

Alma Mater Studiorum - Università di Bologna

DOTTORATO DI RICERCA IN
SCIENZE DELLA TERRA, DELLA VITA E DELL'AMBIENTE

Ciclo 33

Settore Concorsuale: 04/A1 - GEOCHIMICA, MINERALOGIA, PETROLOGIA, VULCANOLOGIA,
GEORISORSE ED APPLICAZIONI

Settore Scientifico Disciplinare: GEO/07 - PETROLOGIA E PETROGRAFIA

CARBONATES AND SULFIDES IN OROGENIC GARNET-BEARING
PERIDOTITES FROM THE ULTEN ZONE AS WITNESSES FOR CARBON AND
SULFUR MOBILITY IN OROGENIC SETTINGS

Presentata da: Giulia Consuma

Coordinatore Dottorato

Giulio Viola

Supervisore

Roberto Braga

Esame finale anno 2021

Table of Contents

Acknowledgements	5
Structure of the Thesis.....	7
Abstract.....	10
The plain language scientific question	12
1 • Introduction	14
1.1 The Carbon Cycle	14
1.1.1 Deep carbon mobility at convergent margins	14
1.2 The Deep Sulfur Cycle.....	16
1.3 Orogenic garnet peridotite: a window to the deep carbon and sulfur mobility in fossil continental collision zone.....	18
Chapter One — References	20
2 • Geological Background.....	27
2.1 The Variscan Orogeny	27
2.2 The Ulten Zone: geological framework	27
2.3 Petrological outline and evolution of the Ulten Zone peridotite	28
2.4 Mineralogical, textural and compositional effects of Alpine overprinting.....	31
2.5 Carbon and sulfur in the Ulten Zone peridotites	32
Chapter Two — References	34
3 • Methods	37
3.1 Scanning Electron Microscopy SEM.....	37
3.2 Electron Microprobe EPMA.....	37
3.3 Optical cathodoluminescence (CL).....	38
3.4 MicroRaman spectroscopy	39
3.5 X-ray fluorescence analyses (XRF)	40
3.6 LA-ICP-MS and LA-MC-ICP-MS	41
3.6.1 Mineral trace element measurements.....	41
3.6.2 In situ Sr isotope: fundamentals of Sr isotope geochemistry.....	42
3.6.2.1 Sr isotope of dolomite and calcite.....	42
3.6.2.2 Sr isotope of clinopyroxene and amphibole.....	43
3.7 Secondary Ion Mass Spectrometry (SIMS)	44
3.7.1 Oxygen isotopes measurements	45
3.7.2 Carbon isotope measurements.....	46

3.7.3 Fundamentals of carbon, oxygen and sulfur isotope geochemistry.....	46
3.7.4 Mounts preparation for SIMS measurements	49
3.7.4.1 Indium mounts preparation for SIMS CAMECA IMS 1280-HR.....	49
3.7.4.2. Epoxy mounts preparation for SIMS CAMECA IMS-1280.....	51
Chapter Three — References.....	52
4 • Carbonate occurrences and constraints on the carbon-bearing fluid sources	55
Article: <i>In situ</i> Sr isotope analysis of mantle carbonate: Constraints on the evolution and sources of metasomatic carbon-bearing fluids in a paleo-collisional setting	55
4.1 Abstract	55
4.2 Introduction.....	56
4.3 Geology and petrology of the Ulten Zone	57
4.4 Analytical methods	61
4.4.1 Scanning electron microscopy (SEM), Electron probe microanalysis (EPMA).....	61
4.4.2 Micro-Raman spectroscopy.....	61
4.4.3 <i>In situ</i> Laser Ablation MC-ICP-MS analyses	62
4.5 Results.....	62
4.5.1 Sample description and petrography.....	62
4.5.2 Major element compositions and micro-Raman spectroscopy.....	68
4.5.3 Sr isotope composition of Ulten Zone carbonates.....	72
4.6 Discussion.....	75
4.6.1 Stage 1: HP carbonation	75
4.6.1.1 <i>Included and interstitial dolomite</i>	75
4.6.1.2 <i>Localized carbonation: carbonates veinlets</i>	77
4.6.2 Stage 2. Carbon re-mobilization via fluid-rock interaction	79
4.7 Conclusion and future directions	79
Chapter Four — References.....	82
5 • Trace elements and C-O isotope signature of texturally-diverse mantle wedge dolomite	86
5.1 Abstract	86
5.2 Introduction.....	88
5.3 Geological background	89
5.3.1 Petrological evolution and metasomatism in the Ulten Zone	89
5.3.2 Sample occurrence and description.....	90
5.4 Methods and analysis strategy.....	93
5.4.1 Cathodoluminescence petrography.....	93

5.4.2 Trace elements compositions	93
5.4.3 SIMS measurements for C and O isotope	94
5.5 Results.....	94
5.5.1 Cathodoluminescence petrography.....	94
5.5.2 Trace elements compositions.....	99
5.5.2.1 Trace elements composition of mantle wedge dolomite	99
5.5.2.2 Trace elements composition of serpentine veins	105
5.5.2.3 Trace elements composition of zircon	106
5.5.3 Stable isotope measurements	107
5.5.3.1 Carbon and oxygen isotope geochemistry of dolomite	107
5.5.3.2 Additional oxygen isotope measurements of zircon and olivine.....	110
5.6 Discussion.....	111
5.6.1 Stable C-O isotope during high pressure metamorphism and the effect of low-T processes	111
5.6.2 Primary mantle carbon mobility under pre-peak conditions.....	113
5.6.3 Carbonic fluid-mediated metasomatism at eclogite-facies conditions.....	114
5.6.4 Crust-mantle mélange exhumation reactivates carbon and elements mobilization.....	116
5.6.5 Preliminary considerations on the combined O isotope of carbonates, zircon, and olivine	119
5.7 Conclusions.....	119
Chapter Five – References	120
6 • The sulfur component of the Ulten Zone peridotite: a piece of the deep Sulfur cycle?	124
Article in review: Multi-stage sulfur and carbon mobility in fossil continental subduction zone: new insights from carbonate-bearing orogenic peridotites.....	124
6.1 Abstract	124
6.2 Introduction.....	125
6.3 Geological setting and metasomatic history	128
6.4 Samples, prior work and sulfide petrography.....	132
6.5 Methods.....	139
6.6 Results.....	140
6.6.1 Whole rock major elements and sulfur concentration	140
6.6.2 Sulfide major element composition and low-pressure re-equilibration.....	142
6.6.3 Sulfide trace element concentrations	146
6.6.4 SIMS Sulfur isotope compositions of pentlandite.....	149
6.6.5 In situ Sr isotope of clinopyroxene and amphibole.....	152

6.7 Discussion.....	153
6.7.1 Fractionation of sulfur isotopes during high-temperature processes and late-stage re-equilibration.....	153
6.7.2 Near-quantitative sulfide extraction during SCLM stabilization and addition during refertilization.....	155
6.7.3 Pre-collision mantle metasomatism (Stage 1).....	156
6.7.4 High-pressure (garnet) metamorphism and recrystallization (Stage 2).....	157
6.7.4.1 <i>Coarse-grained vs Fine-grained peridotite</i>	157
6.7.4.2 <i>Stage 2: The sources of Ulten Zone metasomatic agents</i>	161
6.7.5 Exhumation of crust-mantle mélange and retrogression (Stage 3).....	163
6.7.6 Serpentinization and local effect of fluid-rock interactions on S content and isotope composition (Stage 4).....	164
6.8 Conclusions and implications for sulfur cycling during continent collision.....	166
Chapter Six - References.....	170
7 • Conclusions	178
7.1 Carbon and Sulfur inheritance in the spinel stage.....	178
7.2 High pressure carbonation and sulfidation.....	179
7.3 Channelized carbonation (and sulfidation?).....	180
7.4 Serpentinization as catalyst for decarbonation and desulfidation.....	180
8 • Open questions and future work.....	182
A. Supplementary Material of Chapter 4.....	185
B. Supplementary Material of Chapter 5.....	195
C. Supplementary Material of Chapter 6.....	210

Acknowledgements

How to start! I have so many people to thank. Whatever little or big the support was, many of you contributed to my long and crazy journey of the PhD.

I actually know *where* to start. When I moved to Paris for the internship, I never thought about doing a PhD. I just wanted to have an experience abroad putting my geological degree into practice. Who would have thought that the world of the deep carbon would have intrigued me the most. Thank you, Alberto, for the extraordinary opportunity you gave me. It was during the internship that I realized that maybe there was a little place for me in the crazy scientific world.

But now it's time to go to Bologna!

Roberto, you took a big risk taking me since you did not know me. Thank you for allowing me to travel around the world and for giving me the green light to conduct this PhD. Thank you for your support, and for understanding my humor changes out-of-the-blue. By the way, I will always remember that "*less is more*"!

A special thank goes to Marco L. Fiorentini for the best opportunity I ever dreamed of. I am still surprise about your smiling attitude. Thanks for your prompt availability to host me in Perth and for having introduced me to the ore deposit world.

Thanks to Lukas Baumgartner for assisting me during the late-nigh session at the SwissSIMS laboratory. I was amazed by the University and the high scientific level that circulates in that department.

Many thanks to Sonja Aulbach, I learned a lot working remotely with you this year. You gave me crucial information about the sulfide world, and the manuscript of sulfides wouldn't exist without your scientific support and contribution.

Thanks to Peter Tropper for hosting me several times in Innsbruck and for its tempestive collaboration. Thanks to all the collaborators: Tommaso Giovanardi, Federico Lugli, Maurizio Mazzucchelli, Danilo Bersani, Laure Martin and Anne-Sophie Bouvier.

Martina Tribus (EPMA, University of Innsbruck), Martin Alesh (SIMS, University of Western Australia), Antonio Langone (LA-ICP,MS, University of Pavia) and Claudia Baumgartner (Cathodoluminescence, University of Lausanne) are thanked for assisting me during the analyses.

Thanks to the PLS-UniBO family, we had really nice time working with high-school students!

Francesca, ma chère collègue Parisienne, thank you for the support you have given me through so many skype-calls over the years.

Thank you to all (ex-)PhD students and post-doc, in particular Gabriela, Maria, Valerio, Sara and Simone.

Thanks to ‘the three’ that made me feel at home at the first moment I came here in Bologna: Miriana, Leonardo, Borto. I will always remember the crazy things we have done together, in particular the great all-night-long discussions of life-systems at the Irish Pub drinking an *amaro*. Miriana, thank you so much for being always by my side. Many thanks to all the people I have met during the PhD around the world: thanks to Leonardo, Mattia, Zoneibe, Will, Celso, Marja, Anne. And thank you to the *sante*, Chiara S, Erika, Arianna, Ilaria, Chiara C, Concetta. You are my second family. I miss our time-spent together in Casa del Santo!

Thanks to all my geological friends from Padova.

Mamma, papà. Che posso dire? Il mio passato, presente e futuro è grazie a voi.

Ready for the next step,

Giulia

Structure of the Thesis

This PhD thesis is an original work completed by Giulia Consuma. The first two chapters illustrate the introduction and the state-of-the-art of the research topics. Chapter 3 reports the analytical instrumentations used for this study. Chapter 4 is published in *Lithos*, Chapter 5 will be submitted to a journal for publication and Chapter 6 is an accepted manuscript at *Geochimica et Cosmochimica Acta*. Chapters 7 and 8 are dedicated to the conclusions and open questions for future investigations. Supplementary data of Chapters 4, 5 and 6 is provided in Supplementary Materials at the end of the thesis. Below, I will illustrate a summary for each of the chapters presented in this thesis.

Chapter 1 serves as introduction of the deep Carbon and Sulfur cycle and explains the choice to investigate orogenic garnet peridotites from to track sulfur and carbon mobility in fossil continental collision zones.

Chapter 2 introduces the regional setting, geodynamic framework and the petrological outline of the Ulten Zone peridotites. The background on the carbonate and sulfide occurrences in these peridotites and their interpretations is also reported.

Chapter 3 documents the analytical instrumentations used during the three years of the PhD, implemented with a brief overview of the techniques, relative operating conditions, and sample preparations. Fundamentals to the comprehension of radiogenic and stable isotope geochemistry are also reported.

Chapter 4 is published in *Lithos* (Consuma et al., 2020). This article documents the capability of a mantle wedge to store carbonates at both high-pressure conditions and shallow structural levels. We show that pervasive carbonation occurred at high pressure conditions to form matrix dolomite in textural equilibrium with hornblenditic to pargasitic amphibole and Cl-apatite. Matrix dolomite exhibits relatively unradiogenic Sr isotope values, which indicate the involvement of metasomatizing agents sourced from a depleted mantle wedge and/or from a trondhjemitic igneous activity. During exhumation, carbonic fluid flow is channelized into veins that show heterogeneous Sr isotope values, reflecting both the primary, mantle-like, isotopic composition and

the following interaction with crustal fluids as expected in a crust-mantle mélange. Carbon-remobilization occurred at final stages of exhumation, as late serpeninizing fluids react with dolomite to form calcite/brucite intergrowths and liberate CO₂.

I was responsible for all the analyses presented in this work. Analyses of major elements compositions were performed at the Institute of Mineralogy and Petrography (University of Innsbruck) in collaboration with Peter Tropper and under the guidance of Martina Tribus. In situ Sr isotope measurements of carbonates were carried out at the University of Modena and Reggio Emilia in collaboration with Tommaso Giovanardi, Federico Lugli and Maurizio Mazzucchelli. MicroRaman spectroscopy was conducted at the University of Parma in collaboration with Danilo Bersani.

Chapter 5 will be submitted to a peer-review journal. In this chapter we combined cathodoluminescence observations, trace elements compositions and C-O isotopes of mantle wedge dolomite occurring in different textural positions. This study considers an additional sample consisting of an orthopyroxenite layer within a coarse-grained spinel peridotite. The C-O isotope signature of the dolomite included in this orthopyroxenite layer attests that carbonation may have occurred in an early metasomatic stage, prior to the attainment of high pressure conditions. Moreover, isotopically lighter values of C obtained in a regular-shaped dolomite included in a Cr-rich spinel brought us to re-evaluate the origin of this inclusion, which most likely represents an additional feature that points to carbonate metasomatism prior to spinel and garnet crystallization. Different trace elements compositions of matrix dolomite grains from distinct locations of the Ulten Zone indicate substantial provinciality of the fluids acting at high pressure conditions. The combination of heterogeneous C isotope values together with an intra-vein O isotope homogenization indicates that progressively more diluted fluids may have prompted the full O isotope re-equilibration at low T stages of exhumation in a tectonic mélange.

I conducted the CL petrography, sample preparations and SIMS analyses over the three months period as a visiting researcher at the University of Lausanne, in collaboration with and under the guidance of Lukas Baumgartner, Anne-Sophie Bouvier and Claudia Baumgartner during the cathodoluminescence observations. Trace elements measurements were conducted at the CNR-IGG under the guidance of Antonio Langone.

Chapter 6 is a manuscript accepted at *Geochimica et Cosmochimica Acta* journal.

This work documents an in-depth petrographic study of the sulfur component from the Ulten Zone peridotite. We report a detailed multi-method investigation of the poorly known sulfur speciation and isotopic composition of orogenic mantle as an integral component of the global sulfur cycle, with the aim to delineate a model for sulfide formation and modification in the mantle wedge. We discuss the potential sources and effects of C-O-H-S fluids percolating the mantle wedge during continent collision, with implication for large-scale fluxes. To do this, we combined bulk rock, *in situ* trace elements and sulfur isotope data for sulfides coexisting with multiple generations of carbonate and hydrous minerals. The results allowed us to track the modification of sulfur along the metamorphic stages of peridotite, indicating different episodes, such as inheritance of sulfur from the protolith, sulfidation processes and localized desulfidation during final stages of exhumation. The new dataset is also complemented by *in situ* Sr of amphibole and clinopyroxene.

This work is the result of several international collaborations. I conducted the major elements measurements of sulfides at the University of Innsbruck in collaboration with Peter Tropper and assisted by Martina Tribus; sample preparations and SIMS analyses were conducted during the visiting research period at the University of Western Australia (over two months), in collaboration with Marco L. Fiorentini and Laure Martin. SIMS analyses were also conducted under the guidance of Matvei Aleshin. I prepared the samples/grains for the whole rock analyses, trace elements compositions and Sr isotope measurements that were conducted by Sonja Aulbach and Axel Gerdes from Goethe University Frankfurt.

Chapter 7 summarizes the main conclusions of this PhD thesis.

Chapter 8 reports the future perspective.

Abstract

Convergent plate boundaries are sites of sustained chemical exchanges between the Earth's surface and deep geochemical reservoirs, playing a major role in the global cycle of carbon and sulfur. However, carbon and sulfur recycling processes continue to be hotly debated. A critical gap in the knowledge of the whole *subduction factory*, is given by the limited accessibility to the Earth's interior and to ultramafic lithologies that reside above the subducting plate. In this light, exposed carbonated spinel and garnet peridotite lenses incorporated within migmatites and gneisses in the Ulten Zone of the Central Eastern Italian Alps represent a tangible witness of a long-lasting deep geochemical interplay between continental crust and mantle reservoirs. They record the transition from coarse-grained spinel peridotites to fine-grained garnet-amphibole peridotites, which was prompted by the infiltration of metasomatic liquids as the peridotites were involved in the Variscan subduction architecture and were dragged down to high pressure conditions. Numerous studies have been devoted to foster understanding on the origin and evolution of the peridotite, addressing the question whether the Ulten Zone mantle fragments were affected by 'crustal' or 'mantle' metasomatism. Nevertheless, a limited number of studies were devoted to a detailed investigation of the carbonate metasomatism that affected the Ulten Zone peridotite.

This thesis typically employs a microanalytical approach to provide the first high resolution petrological, geochemical and isotopic study of the carbonates occurring in different peridotite lithotypes and localities of the Ulten Zone. Moreover, the targeted study of carbonates conducted during the work of this PhD revealed an intimate association of these minerals with sulfide phases. This close textural relation brought us to consider the sulfide not as merely subordinate mineral formed upon retrogression, but as a key component to advance our understanding on the deep cycle of carbon and sulfur from the mantle wedge perspective.

I selected peridotites with great care in order to consider (i) peridotites that record different P-T conditions related to different geodynamic setting (i.e. within the lithospheric mantle, within the mantle wedge close to the slab/mantle interface, incorporated within crustal lithologies in a tectonic *mélange*) and (ii) peridotites that contain carbonates and sulfide in different textural sites. This sample suite thus provides the uncommon opportunity to investigate carbon and sulfur metasomatism during the life of a collisional mantle wedge.

Our results indicate that the Variscan lithospheric mantle was initially depleted and sulfide-poor, and that was afterwards percolated by a H₂S-CO₂-bearing melt from the subduction-modified hot

mantle wedge, to form an orthopyroxenite layer containing dolomite with a $\delta^{13}\text{C}$ signature of -12‰ to -8‰ , locally associated with pentlandite of $\delta^{34}\text{S} = +2.77\text{‰}$.

An additional microstructure that can be addressed to early stages of metasomatism is the occurrence of a regular-shaped inclusion of dolomite in a Cr-rich spinel within pyrope-rich porphyroclastic garnet. The timing of the formation of this inclusion is debated throughout this thesis, as it shows microstructural and geochemical signatures that could point to divergent conclusions. However, the regular facets of the crystal inclusion combined with the isotopically light value of $\delta^{13}\text{C} = -8\text{‰}$ are likely related to an early stage of carbon inheritance, prior to spinel and garnet crystallization.

The coarse-grained peridotite samples escaped recrystallization into fine-grained matrix at high pressure conditions. Generally, these peridotites result poor in matrix dolomite. However, when present, little dolomite grains are locally associated with pentlandite grains. It is plausible that, at high pressure conditions, coarse-grained and fine-grained peridotite were affected by different metasomatic agents, as also indicated by the distinct sulfur isotope signature of matrix pentlandite. Within the coarse-grained matrix, pentlandite shows relatively heavy $\delta^{34}\text{S}$ (up to $+3.43\text{‰}$) and elevated Pb abundances. In addition, matrix clinopyroxene grains also carry radiogenic Sr ($^{87}\text{Sr}/^{86}\text{Sr}_{\text{clinopyroxene}} > 0.7053$), indicating an interaction with isotopically heavy melts carrying recycled crustal component, permissive of, but not requiring, involvement of oxidized S species.

Recrystallization of the coarse-grained peridotite to form porphyroclastic to equigranular fine-grained garnet-amphibole peridotite is prompted by infiltration of $\text{H}_2\text{S}-\text{CO}_2$ -bearing crustal fluids variably equilibrated with the depleted mantle before interacting with the peridotites, as indicated by the relatively radiogenic Sr isotope of matrix dolomite and calcite. Pervasive carbonation and sulfidation occurred at high pressure conditions to form matrix dolomite and isotopically lighter matrix pentlandite ($\delta^{34}\text{S} = -1.62$ to $+0.67\text{‰}$) along silicates grain boundaries.

The retrograde path of the Ulten Zone peridotite is characterized by its incorporation in a tectonic mélange mostly formed by previously subducted crustal rocks. Here, channelized carbonic fluid flow through veins of dolomite occurs. These carbonic fluid pathways record heterogeneous Sr and C isotopes, whereas the O isotope is fully equilibrated by late infiltration of progressive diluted low T fluids.

Upon late retrogression, infiltration at low $f\text{S}_2$ of serpentinization fluids of high-crustal affinity played an active role not only in CO_2 release by conversion of dolomite to calcite/brucite intergrowths, but also in local removal of ^{32}S during the final ascent towards shallow structural levels.

The plain language scientific question

The Earth system consists of deeply interconnected natural reservoirs, interacting through biological, chemical and physical processes. This interplay allows the deep Earth to communicate with the Earth's surface through exchange of elements which are essential to life and planet habitability. Among them, carbon (C) and sulfur (S) are not only the backbone of life and ecosystems, but they also affect the Earth's climate, feed the energy of the planet and exert primary control on the genesis of metalliferous deposits. The fundamental role of C and S guide researchers from a broad range of disciplines to investigate their mobility between the Earth's exterior and interior. However, only the surface of the planet is directly accessible to us, whereas the interior is becoming known to us indirectly. To date, a tremendous amount is known about carbon and sulfur mobility through the surficial reservoirs, whereas key questions of the deep processes are still unresolved. The necessity to investigate *deeper*, raises by the fact that the 99% of Earth's Carbon is stored in the core, mantle and crust, with the remaining 1% partitioned between the atmosphere, the biosphere, and the ocean. Likewise, sulfur is mostly stored in the core, but its broad range of valence state (-2 to +6) has crucial implication for the redox conditions of the deep Earth. Constraining the behavior of C and S in the mid- to deep- mantle is therefore important because they have key influence on mantle processes, such as partial melting, element mobility and mantle oxidation state.

Subduction zone, where the denser plate slides underneath the other as tectonic plates collide, is a suitable site for element mobility between mantle and crust. Generally, subduction processes allow carbon and sulfur to reach depths of hundreds of kilometers, and, along this journey towards deeper reservoirs, aqueous fluids may be released and carry carbon and sulfur in the overlying mantle, and ultimately feed arc-volcanism. Investigation of natural samples is critical for a global overview of what really happens in the deep Earth. In this scenario, the fate of carbon and sulfur when the collision involves two continents is much less known and poorly studied with respect to oceanic subduction, but may hide important tiles on the overall cycle of these elements.

The study area of this thesis is the Ulten Zone (central-eastern Italian Alps), a fossil tectono-metamorphic complex that experienced high-pressure conditions and exceptionally preserved the Variscan continental subduction signature in its lithologies, mainly consisting of ultramafic rocks entrapped in high-grade felsic rocks. In the Ulten Zone spinel and garnet peridotite, C and S occur in the form of carbonate and sulfide phases, which are often intimately

associated. They occur in diverse peridotite lithotypes, such as, for example, in coarse-grained spinel peridotite and fine-grained garnet-amphibole peridotite, and in different textural positions (i.e. inclusions, interstitial to matrix silicates, veinlets, in retrograde coronas). Therefore, carbonates and sulfides define characteristic mineral assemblages, which record precise metamorphic stages throughout the involvement of peridotite within the continental subduction architecture.

In this study, we take advantage of the spatial resolution offered by these carbonate and sulfide minerals, which track record of peridotite metamorphic evolution during its involvement within the continental subduction architecture, in order to track the carbon and sulfur transfer from the mantle wedge perspective. In this light, this thesis aims to foster understanding on:

- 1) **The petrographic occurrence of carbonates and sulfides within the Ulten Zone peridotite throughout its metamorphic evolution;**
- 2) **The nature and sources of C-O-H-S metasomatic agents acting in a fossil continental subduction zone, from the orogenic mantle perspective;**
- 3) **The relative timing and geodynamic framework of carbonate and sulfide metasomatism affecting the Ulten Zone peridotite;**
- 4) **The role of the Ulten Zone mantle wedge in the deep carbon and sulfur cycle: is the mantle wedge a carbon locker, a passageway, or *lock-and-release* site for carbon and sulfur?;**
- 5) **The main processes and reactions that drive the carbon and sulfur transfer along the multi-metamorphic history of Ulten Zone peridotites.**

1 • Introduction

1.1 The Carbon Cycle

Among all the known chemical elements, Carbon plays a fundamental role on Earth. With oxidation states spanning from -4 to +4, carbon can both stand alone and form stable bonds with the other elements in a diverse range of forms: solid, fluid, or gas. The combination of carbon with, for example, oxygen to form carbonates, iron to form carbides, or hydrogen to form methane, depends on the surrounding conditions such as pressure, temperature, oxygen fugacity and chemical composition of the system. The recent discoveries of the Deep Carbon Observatory estimate that just 1% of Earth total carbon, corresponding to 43500 Gt (gigatons) is stored above surface in the oceans, on land and in the atmosphere. The remaining amount, 1.85 billion Gt, is included in the crust, mantle and core. The nature and the extent of carbon reservoirs in the deep Earth is therefore fundamental to understanding the global carbon exchanges on the planet. Estimates of carbon from primitive carbonaceous chondritic meteorites show one to two order of magnitude greater than the Earth's abundance of carbon, thus questioning where the missing carbon is stored and how much carbon the deep Earth naturally swallows and exhales.

The main obstacle for an exhaustive understanding of the behavior of carbon at depths is that the deep carbon is mostly inaccessible. However, along the long-lasting geological carbon cycle (> 3Gyrs of uninterrupted exchanges among reservoirs), plate tectonics manage to expose on the surface what was previously locked in the Earth's depths. Exhumed mantle xenolith, high-pressure (HP) and ultra-high-pressure (UHP)/low temperature (LT) metamorphic rocks can in fact be used as a probe to study the deep Earth. In particular, HP-UHP rocks found in subduction settings provide insights into mechanisms that drive the carbonic fluid transfer from the subducting slab to the overlying lithospheric mantle.

1.1.1 Deep carbon mobility at convergent margins

The key questioning in understanding the mobility of C at convergent margins is how much C is stored in the subducting plate and what fraction of it is able to return back to the Earth's surface. In this sense, many studies have been devoted to quantify the fluxes of carbon within a subduction zone, resulting in highly variable global estimates (Fig.1.1; Halama and Bebout, 2021). Following Kelemen and Manning (2015), little carbon is recycled back to the surface, whereas most of it is stored in the lithospheric mantle. In the mantle, carbon is retained in graphite/diamond and in

carbonates, which are refractory and stable at high and very high pressure (Molina and Poli, 2000; Dasgupta & Hirschmann, 2006; Poli et al. 2009). Carbon enters in the mantle through subduction of carbon-bearing lithologies (sediments, altered oceanic crust, hydrate mantle lithosphere) (Staudigel et al., 1989; Alt and Teagle, 1999; Kelemen and Manning 2015), and partly percolate into the overlying mantle ultimately feeding arc volcanism (Dasgupta and Hirschmann, 2010; Burton et al., 2013; Mason et al. 2017).

Active carriers of carbon at high-pressure conditions in subduction settings are low-viscous-mobile aqueous fluids (Scambelluri and Philippot, 2001; Hermann, 2006) with variable amount of carbonic species which, under favorable conditions, facilitate the transfer of carbon at fore- and sub-arc depths during subduction (Piccoli et al., 2016; Vitale Brovarone et al., 2018). COH- fluids, in addition, play a crucial role in melt formation at the slab-wedge interface or on the overlying mantle wedge. The fate of these liquids depends on four variable: pressure/temperature, redox state, activity of silica, activity of water. Carbon transfer in subduction zone is enhanced by different processes, such as metamorphic decarbonation (Molina and Poli, 2000; Kerrick and Connolly, 2001a; Gorman et al., 2006), dissolution via fluid/rock interactions at HP to UHP conditions (Piccoli et al. 2016; Frezzotti et al., 2011; Ague and Nicolescu, 2014; Kelemen and Manning, 2015), carbonate reduction (Malvoisin et al. 2011; Galvez et al., 2013; Vitale et al., 2017; Tao et al., 2018), and partial melting of the carbon-bearing subducting crust (Poli, 2015). Thermodynamic models predict that the greater pulse of carbon release from the slab occurred around 500-800°C at ca. 80-140km depths below the volcanic arc (Connolly, 2005; Gorman and Connolly, 2006; Connolly, 2018). While experimental studies have shown that decarbonation processes result in small fraction of CO₂ in COH-fluids, carbonate dissolution is demonstrated to play a crucial role in mobilizing carbon at high-pressure conditions.

In a summary, many processes may operate during subduction and govern the C exchange through different reservoirs, if favorable conditions are attained. Variability in the global estimates of C is mostly given by the so far attention on individual outcrops rather than regional scales (Halama and Bebout, 2021). Moreover, respect to subduction, the C cycle during collisional orogenesis is less well studied (Halama and Bebout, 2021), despite there is a general consensus that orogenic belts are considered as sources of atmospheric CO₂ (Skelton et al. 2011).

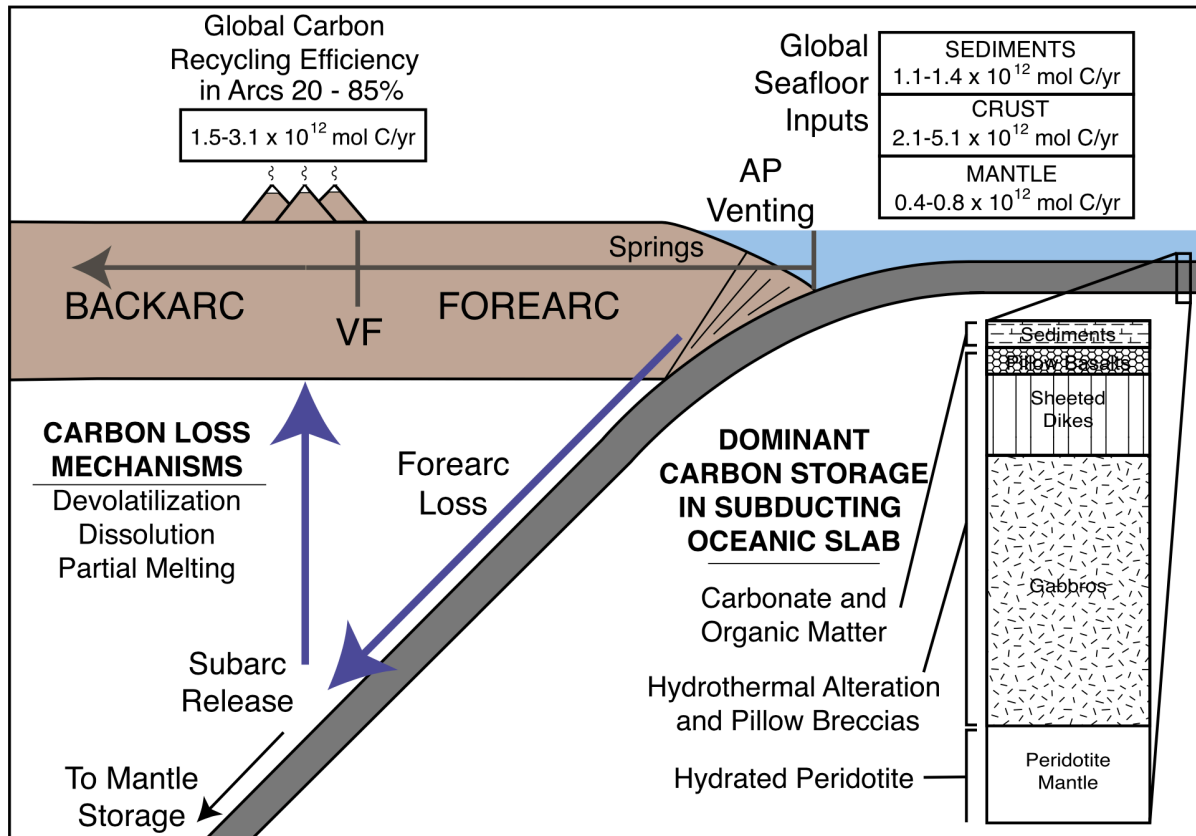


Fig. 1.1 Schematic illustration of an oceanic subduction zone, after Halama and Bebout (2021). The global estimates of C fluxes discussed in Halama and Bebout (2021) (moles of C/year) are shown. They advance a volcanic arc return efficiency (inputs/arc outputs) of ≈ 20 to 85%, highlighting the uncertainties in the various flux estimates after Cook-Kollars et al. (2014), and references therein. This calls for further examinations of the C cycling in margins where the input and output fluxes are better constrained. VF = volcanic front; AP = accretionary prism.

1.2 The Deep Sulfur Cycle

Sulfur (S) is the sixth most abundant element on Earth, with ca. 1.9% by weight, after iron, oxygen, silicon, magnesium, and nickel. In the Earth's mantle, sulfur occurs mostly as accessory sulfide minerals, solid solution or molten sulfides (Harvey et al., 2016; Chowdhury and Dasgupta, 2020), whose distribution and composition are in part controlled by mantle melting, melt mobility, and metasomatism (e.g. Lorand et al. 2004; Lorand et al. 2013; Giuliani et al. 2016). The composition of sulfides from mantle xenoliths and diamond inclusions are shown in Figure 1.2.

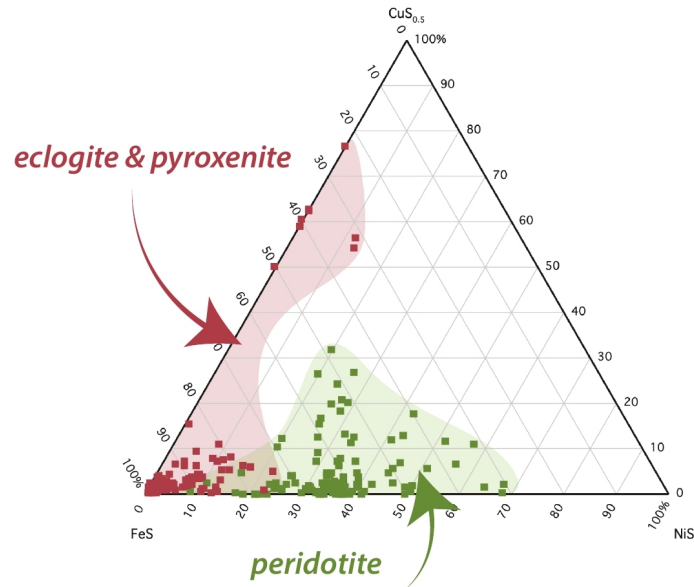


Fig. 1.2 a) Ternary diagram ($\text{CuS}_{0.5}$, FeS and NiS) showing the major element composition of the mantle sulfides (in weight %) modified after Kiseeva et al. (2017).

Like carbon, having different valence states ranging from -2 to +6 and a redox budget of eight electrons, sulfur has the potential to act both as oxidizing agent and transport medium for economically important elements. The sulfur inventory of the deep Earth is modulated by magmatic sulfur degassing at the plate boundaries (e.g. Wallace and Edmonds, 2011, Ding and Dasgupta, 2017), intraplate ocean islands (Ding and Dasgupta, 2018), arcs (e.g., Alt et al., 1993; Chowdhury and Dasgupta, 2019, Kagoshima et al., 2015) and by subduction of sulfides and sulfates back to the deep Earth (Jégo and Dasgupta, 2013, Jégo and Dasgupta, 2014; Tomkins and Evans, 2015, Li et al. 2020). In the last scenario, the relatively high sulfur concentrations and positive isotope values of volcanic rocks and melt inclusions in some arcs, and the presence of sulfate in mantle xenoliths have been attributed to the addition of slab-derived sulfate to arc magmas by fluids. This could also explain the highest oxidation of basaltic melts from subduction setting with respect to the less oxidized fresh MORB formed at divergent plate boundaries (Kelley and Cottrell, 2009; Evans, 2012). Experimental results indicate that slab-derived aqueous fluids are an effective agent for transporting sulfur from the slab to the above mantle wedge (Jégo and Dasgupta, 2013; Tomkins and Evans, 2015). However, a growing numbers of studies have been addressed to better constrain the sulfur mobility and speciation in these settings (i.e. Giacometti et al., 2014; Bénard et al., 2018; Schwarzenbach et al., 2018a; Evans et al., 2014; Tomkins and Evans, 2015; Evans et al., 2017), and they result in contrasting views. On one hand, Pons et al. (2016) and Walters et al. (2019, 2020) provide strong evidences that slab-derived fluids may efficiently transport sulfate, and Evans et al. (2017) and Bénard et al. (2018) invoke the oxidized sulfur species as potential oxidizing agent of the sub-arc mantle. On the other hand, thermodynamic results performed by Piccoli et al.

(2019) stress that aqueous fluids released from a typical oceanic slab are reducing. This is also supported by Li et al. (2020), that, on the base of whole-rock and *in situ* S isotopic compositions, textural constraints and thermodynamic modeling of exhumed high-pressure rocks from a typical oceanic subduction setting, find that slab-derived fluids provide negligible sulfate to oxidize the mantle wedge, and cannot deliver ^{34}S -enriched sulfur to produce the positive signature of arc-settings (Fig. 1.3). It is worth noting that all of these efforts consider the typical oceanic subduction setting from the slab perspective, whereas the sulfur mobility at continental convergent margins from the mantle wedge point of view is much less studied. This thesis will contribute in this sense.

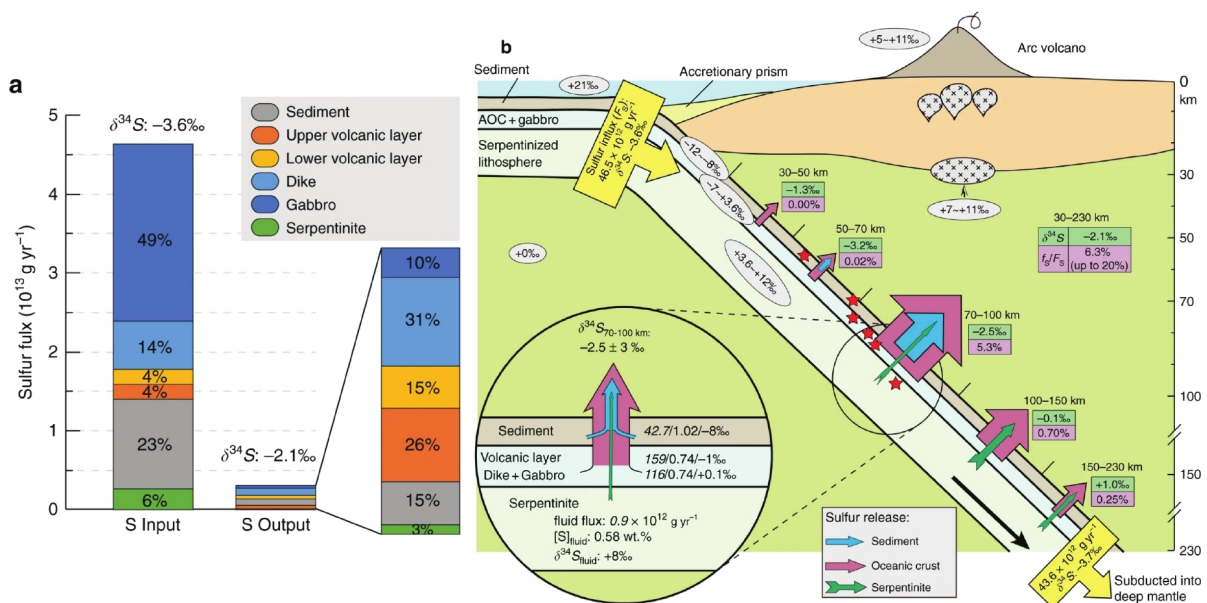


Fig. 1.3 a) Subduction sulfur input and output calculated by Li et al. (2020) at 30-230 km depths; b) Cartoon illustrating the fluid-mediated sulfur liberation in an ocean-continent subduction zone. Estimated S fluxes and S isotopic compositions at various depths and from different lithologies are illustrated. The figure shows how a greater pulse of S release is attained at 70-100km depths. Figure after Li et al. (2020)

1.3 Orogenic garnet peridotite: a window to the deep carbon and sulfur mobility in fossil continental collision zone

Plate subduction and exhumation are major sites for volatile elements exchange between crust and mantle. Numerous studies have been devoted to uncover the fluid regime involved in the so-called ‘Pacific-type’ subduction zones, sites where the collision involves two oceanic plates or one oceanic and one continental, as those in the European Western Alps, North Qilian and Western Tianshan UHP belts in western China (Bebout 1996, 2007; Scambelluri & Philippot 2011; Touret 2001; Ague 2003; Schmidt & Poli 2003; Manning 2004; Gao et al., 2007). Fossil ‘Pacific-type’ subduction zones comprise ophiolite mélangé, island-arc magmatic rocks, and deep-sea sediments, which undergo

metamorphism during subduction at relatively low temperature and (U)HP conditions. On the other hand, some studies have been addressed to unravel the fluid regime during the ‘Alpine-type’ subduction (Philippot & Iii 2000; Jahn et al. 2004; Rumble et al., 2003; Zheng et al., 2003a; Li et al. 2004; Spandler & Hermann 2006), which involves the collision of two continents, and comprises granitic/tonalitic gneiss with minor intercalated metapelite, eclogite and/or peridotite of (U)HP origin (Zhang et al. 2011).

Orogenic garnet-bearing (Alpine-type) peridotite bodies are volumetrically minor but fundamental component within (U)HP metamorphic terranes in many orogenic belts that formed during continental collision and subduction (Brueckner, 1998). Natural occurrences are the Western Gneiss Region in Norway (Hacker et al., 2010), the Alpe Arami (Green et al., 1997) and the Variscan Ulten Zone (Scambelluri et al., 2010) in Italy, the Paleozoic Kokchetav Massif in Kazakhstan (Schertl and Sobolev, 2013), the Triassic Dabie-Sulu (Wu and Zheng, 2013) and the early Paleozoic North Qaidam orogen in China (Chen et al., 2007) (Fig. 1.3). Numerous petrological, geochemical and geochronological studies have recognized crustal signatures in them (Chen et al., 2013; Marocchi et al., 2009; Scambelluri et al., 2006, 2010, 2014; Vrijmoed et al., 2013; Zhang et al., 2011; Yang et al., 2003), which have been ascribed to crustal metasomatism (Zheng et al. 2012). However, the timing and processes that drive crustal metasomatism and the nature and origin of metasomatic agents are still largely unknown (Li et al. 2018).

Once the collision begins, the mantle wedge evolution comprises two main stages: i) a first stage in which orogenic mantle fragments are dragged down close to the slab-wedge interface and interact with slab-derived liquids; ii) a second stage in which the denser ultramafic rocks are incorporated in the subducted continental crust. From that moment, peridotite and the crustal country rocks start to share the metamorphic evolution and exhumation (Brueckner, 1998; Medaris, 1999; Brueckner and Medaris, 2000). Minerals, structures, textures, mineral fabrics and geochemical fingerprints of the mantle wedge subsequently become partly or completely overprinted by features that are typical of the subduction zone type, and this may add complexity in constraining the fluid regime responsible for peridotite metasomatism. Furthermore, the continental collision is often predated by subduction of an oceanic plate (Coleman and Wang, 1995), and the mobility and amounts of aqueous fluids within subduction settings varies whether a continental or oceanic crust is involved. Compared to (U)HP metamorphic gneisses and eclogites, garnet peridotites are anyway more easily able to preserve the petrological records of geochemical processes during subduction and exhumation (Li et al., 2018; Chen et al., 2015; Scambelluri et al., 2010). The presence of metasomatic minerals as a result of modal metasomatism is common, and, in particular, the occurrence of carbonate phases and hydrous minerals (i.e. amphibole and

phlogopite), have been ascribed to metasomatic processes driven by COH-fluids (Zhang et al., 2007; Scambelluri et al., 2008; Malaspina and Tumiati, 2012). On the other hand, the occurrence of sulfides in orogenic garnet peridotites, which can be both related to inheritance of sulfur from mantle precursor or added during metamorphic evolution, is poorly constrained.

For all the reasons above mentioned, orogenic peridotites are an excellent target to foster understanding on the heterogeneous and complex interaction between the mantle and crust, the fluid regime that involve the carbon and sulfur transfer during oceanic and/or continental collision and the composition and the evolution of a mantle wedge above subduction zones.

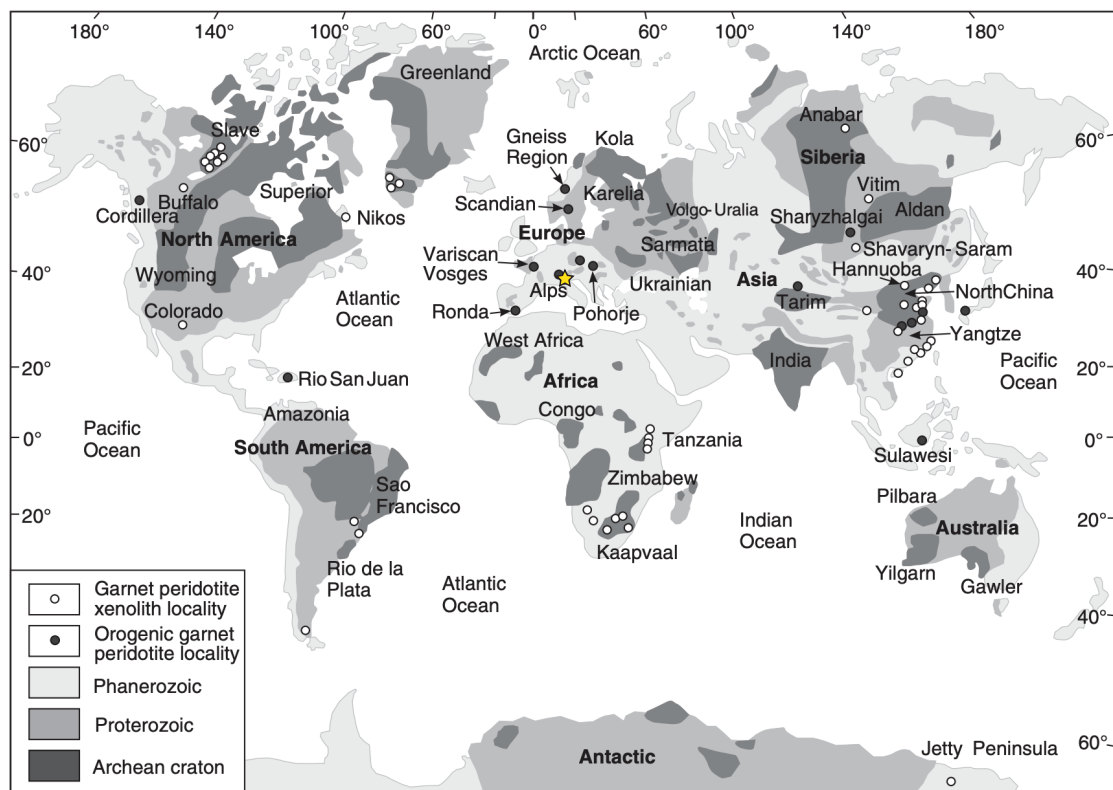


Fig. 1.3: Distribution of global Archean cratons, garnet peridotite xenoliths and orogenic garnet peridotite (the star refers to orogenic garnet peridotite in the study area). Orogenic spinel-facies peridotites are not shown in this map as they occur in abundance worldwide. Figure modified after Tang et al. (2013).

Chapter One — References

- Ague, J.J., 2003. Fluid Infiltration and Transport of Major, Minor, and Trace Elements During Regional Metamorphism of Carbonate Rocks, Wepawaug Schist, Connecticut, USA. *Am. J. Sci.* 303, 753–816. <https://doi.org/10.2475/ajs.303.9.753>
- Ague, J.J., Nicolescu, S., 2014. Carbon dioxide released from subduction zones by fluid-mediated reactions. *Nat. Geosci.* 7, 355–360. <https://doi.org/10.1038/ngeo2143>

- Alt, J.C., Shanks, W.C., Jackson, M.C., 1993. Cycling of sulfur in subduction zones: The geochemistry of sulfur in the Mariana Island Arc and back-arc trough. *Earth Planet. Sci. Lett.* 119, 477–494. [https://doi.org/10.1016/0012-821X\(93\)90057-G](https://doi.org/10.1016/0012-821X(93)90057-G)
- Alt, J.C., Teagle, D.A.H., 1999. The uptake of carbon during alteration of ocean crust. *Geochim. Cosmochim. Acta* 63, 1527–1535. [https://doi.org/10.1016/S0016-7037\(99\)00123-4](https://doi.org/10.1016/S0016-7037(99)00123-4)
- Bebout, G., 1996. Volatile Transfer and Recycling at Convergent Margins: Mass-Balance and Insights from High-P/T Metamorphic Rocks, in: Washington DC American Geophysical Union Geophysical Monograph Series. pp. 179–193. <https://doi.org/10.1029/GM096p0179>
- Bebout, G.E., 2007. Metamorphic chemical geodynamics of subduction zones. *Earth Planet. Sci. Lett.* 260, 373–393. <https://doi.org/10.1016/j.epsl.2007.05.050>
- Bénard, A., Klimm, K., Woodland, A.B., Arculus, R.J., Wilke, M., Botcharnikov, R.E., Shimizu, N., Nebel, O., Rivard, C., Ionov, D.A., 2018. Oxidising agents in sub-arc mantle melts link slab devolatilisation and arc magmas. *Nat. Commun.* 9, 3500. <https://doi.org/10.1038/s41467-018-05804-2>
- Brueckner, H.K., 1998. Sinking intrusion model for the emplacement of garnet-bearing peridotites into continent collision orogens. *Geology* 26, 631–634. [https://doi.org/10.1130/0091-7613\(1998\)026<0631:SIMFTE>2.3.CO;2](https://doi.org/10.1130/0091-7613(1998)026<0631:SIMFTE>2.3.CO;2)
- Brueckner, H.K., Medaris, L.G., 2000. A general model for the intrusion and evolution of “mantle” garnet peridotites in high-pressure and ultra-high-pressure metamorphic terranes. *J. Metamorph. Geol.* 18, 123–133. <https://doi.org/10.1046/j.1525-1314.2000.00250.x>
- Burton, M.R., Sawyer, G.M., Granieri, D., 2013. Deep Carbon Emissions from Volcanoes. *Rev. Mineral. Geochem.* 75, 323–354. <https://doi.org/10.2138/rmg.2013.75.11>
- Chen, R.-X., Zheng, Y.-F., Gong, B., Zhao, Z.-F., Gao, T.-S., Chen, B., Wu, Y.-B., 2007. Oxygen isotope geochemistry of ultrahigh-pressure metamorphic rocks from 200–4000 m core samples of the Chinese Continental Scientific Drilling. *Chem. Geol.* 242, 51–75. <https://doi.org/10.1016/j.chemgeo.2007.03.008>
- Chowdhury, P., Dasgupta, R., 2020. Sulfur extraction via carbonated melts from sulfide-bearing mantle lithologies – Implications for deep sulfur cycle and mantle redox. *Geochim. Cosmochim. Acta* 269, 376–397. <https://doi.org/10.1016/j.gca.2019.11.002>
- Chowdhury, P., Dasgupta, R., 2019. Effect of sulfate on the basaltic liquidus and Sulfur Concentration at Anhydrite Saturation (SCAS) of hydrous basalts – Implications for sulfur cycle in subduction zones. *Chem. Geol.* 522, 162–174. <https://doi.org/10.1016/j.chemgeo.2019.05.020>
- Coleman, R.G., Wang, X., 1995. *Ultrahigh Pressure Metamorphism*. Cambridge University Press.
- Connolly, J.A.D., 2005. Computation of phase equilibria by linear programming: A tool for geodynamic modeling and its application to subduction zone decarbonation. *Earth Planet. Sci. Lett.* 236, 524–541. <https://doi.org/10.1016/j.epsl.2005.04.033>
- Connolly, J.A.D., Galvez, M.E., 2018. Electrolytic fluid speciation by Gibbs energy minimization and implications for subduction zone mass transfer. *Earth Planet. Sci. Lett.* 501, 90–102. <https://doi.org/10.1016/j.epsl.2018.08.024>
- Cook-Kollars, J., Bebout, G.E., Collins, N.C., Angiboust, S., Agards, P., Subduction zone metamorphic pathway for deep carbon cycling: I. Evidence from HP/UHP metasedimentary rocks, Italian Alps. *Chem Geol.* 386, 31-48 (2014).

- Dasgupta, R., Hirschmann, M.M., 2010. The deep carbon cycle and melting in Earth's interior. *Earth Planet. Sci. Lett.* 298, 1–13. <https://doi.org/10.1016/j.epsl.2010.06.039>
- Ding, S., Dasgupta, R., 2018. Sulfur Inventory of Ocean Island Basalt Source Regions Constrained by Modeling the Fate of Sulfide during Decompression Melting of a Heterogeneous Mantle. *J. Petrol.* 59, 1281–1308. <https://doi.org/10.1093/petrology/egy061>
- Ding, S., Dasgupta, R., 2017. The fate of sulfide during decompression melting of peridotite – implications for sulfur inventory of the MORB-source depleted upper mantle. *Earth Planet. Sci. Lett.* 459, 183–195. <https://doi.org/10.1016/j.epsl.2016.11.020>
- Evans, K.A., Elburg, M.A., Kamenetsky, V.S., 2012. Oxidation state of subarc mantle. *Geology* 40, 783–786. <https://doi.org/10.1130/G33037.1>
- Evans, K.A., Reddy, S.M., Tomkins, A.G., Crossley, R.J., Frost, B.R., 2017. Effects of geodynamic setting on the redox state of fluids released by subducted mantle lithosphere. *Lithos* 278–281, 26–42. <https://doi.org/10.1016/j.lithos.2016.12.023>
- Evans, K.A., Tomkins, A.G., Cliff, J., Fiorentini, M.L., 2014. Insights into subduction zone sulfur recycling from isotopic analysis of eclogite-hosted sulfides. *Chem. Geol.* 365, 1–19. <https://doi.org/10.1016/j.chemgeo.2013.11.026>
- Frezzotti, M.L., Selverstone, J., Sharp, Z.D., Compagnoni, R., 2011. Carbonate dissolution during subduction revealed by diamond-bearing rocks from the Alps. *Nat. Geosci.* 4, 703–706. <https://doi.org/10.1038/ngeo1246>
- Galvez, M.E., Beyssac, O., Martinez, I., Benzerara, K., Chaduteau, C., Malvoisin, B., Malavieille, J., 2013. Graphite formation by carbonate reduction during subduction. *Nat. Geosci.* 6, 473–477. <https://doi.org/10.1038/ngeo1827>
- Giacometti, F., Evans, K.A., Rebay, G., Cliff, J., Tomkins, A.G., Rossetti, P., Vaggelli, G., Adams, D.T., 2014. Sulfur isotope evolution in sulfide ores from Western Alps: Assessing the influence of subduction-related metamorphism. *Geochem. Geophys. Geosystems* 15, 3808–3829. <https://doi.org/10.1002/2014GC005459>
- Giuliani, A., Fiorentini, M.L., Martin, L.A.J., Farquhar, J., Phillips, D., Griffin, W.L., LaFlamme, C., 2016. Sulfur isotope composition of metasomatised mantle xenoliths from the Bultfontein kimberlite (Kimberley, South Africa): Contribution from subducted sediments and the effect of sulfide alteration on S isotope systematics. *Earth Planet. Sci. Lett.* 445, 114–124. <https://doi.org/10.1016/j.epsl.2016.04.005>
- Gorman, P.J., Kerrick, D.M., Connolly, J. a. D., 2006. Modeling open system metamorphic decarbonation of subducting slabs. *Geochem. Geophys. Geosystems* 7. <https://doi.org/10.1029/2005GC001125>
- Green, H.W., Dobrzhinetskaya, L., Riggs, E.M., Jin, Z.-M., 1997. Alpe Arami: a peridotite massif from the Mantle Transition Zone? *Tectonophysics, The Adolphe Nicolas Volume* 279, 1–21. [https://doi.org/10.1016/S0040-1951\(97\)00127-3](https://doi.org/10.1016/S0040-1951(97)00127-3)
- Hacker, B.R., Andersen, T.B., Johnston, S., Kylander-Clark, A.R.C., Peterman, E.M., Walsh, E.O., Young, D., 2010. High-temperature deformation during continental-margin subduction & exhumation: The ultrahigh-pressure Western Gneiss Region of Norway. *Tectonophysics* 480, 149–171. <https://doi.org/10.1016/j.tecto.2009.08.012>
- Halama, R. and Bebout G., 2021 Earth's Nitrogen and Carbon Cycles. *Space Science Reviews*, **217**, 45.

- Harvey, J., Warren, J.M., Shirey, S.B., 2016. Mantle Sulfides and their Role in Re–Os and Pb Isotope Geochronology. *Rev. Mineral. Geochem.* 81, 579–649. <https://doi.org/10.2138/rmg.2016.81.10>
- Jégo, S., Dasgupta, R., 2014. The Fate of Sulfur During Fluid-Present Melting of Subducting Basaltic Crust at Variable Oxygen Fugacity. *J. Petrol.* 55, 1019–1050. <https://doi.org/10.1093/petrology/egu016>
- Jégo, S., Dasgupta, R., 2013. Fluid-present melting of sulfide-bearing ocean-crust: Experimental constraints on the transport of sulfur from subducting slab to mantle wedge. *Geochim. Cosmochim. Acta* 110, 106–134. <https://doi.org/10.1016/j.gca.2013.02.011>
- Kagoshima, T., Sano, Y., Takahata, N., Maruoka, T., Fischer, T.P., Hattori, K., 2015. Sulphur geodynamic cycle. *Sci. Rep.* 5, 8330. <https://doi.org/10.1038/srep08330>
- Kelemen, P.B., Manning, C.E., 2015. Reevaluating carbon fluxes in subduction zones, what goes down, mostly comes up. *Proc. Natl. Acad. Sci.* 112, E3997–E4006. <https://doi.org/10.1073/pnas.1507889112>
- Kelley, K.A., Cottrell, E., 2009. Water and the Oxidation State of Subduction Zone Magmas. *Science* 325, 605–607. <https://doi.org/10.1126/science.1174156>
- Kerrick, D.M., Connolly, J. a. D., 2001. Metamorphic devolatilization of subducted marine sediments and the transport of volatiles into the Earth's mantle. *Nature* 411, 293–296. <https://doi.org/10.1038/35077056>
- Li, H.-Y., Chen, R.-X., Zheng, Y.-F., Hu, Z., Xu, L., 2018. Crustal Metasomatism at the Slab-Mantle Interface in a Continental Subduction Channel: Geochemical Evidence From Orogenic Peridotite in the Sulu Orogen. *J. Geophys. Res. Solid Earth* 123, 2174–2198. <https://doi.org/10.1002/2017JB014015>
- Li, J.-L., Schwarzenbach, E.M., John, T., Ague, J.J., Huang, F., Gao, J., Klemd, R., Whitehouse, M.J., Wang, X.-S., 2020. Uncovering and quantifying the subduction zone sulfur cycle from the slab perspective. *Nat. Commun.* 11, 514. <https://doi.org/10.1038/s41467-019-14110-4>
- Lorand, J.-P., Delpech, G., Grégoire, M., Moine, B., O'Reilly, S.Y., Cottin, J.-Y., 2004. Platinum-group elements and the multistage metasomatic history of Kerguelen lithospheric mantle (South Indian Ocean). *Chem. Geol., Highly Siderophile Element Behavior in High Temperature Processes* 208, 195–215. <https://doi.org/10.1016/j.chemgeo.2004.04.012>
- Lorand, J.-P., Luguet, A., Alard, O., 2013. Platinum-group element systematics and petrogenetic processing of the continental upper mantle: A review. *Lithos, Ore deposits and the role of the lithospheric mantle* 164–167, 2–21. <https://doi.org/10.1016/j.lithos.2012.08.017>
- Malvoisin, B., Chopin, C., Brunet, F., Galvez, M.E., 2012. Low-temperature Wollastonite Formed by Carbonate Reduction: a Marker of Serpentinite Redox Conditions. *J. Petrol.* 53, 159–176. <https://doi.org/10.1093/petrology/egr060>
- Mason, E., Edmonds, M., Turchyn, A.V., 2017. Remobilization of crustal carbon may dominate volcanic arc emissions. *Science* 357, 290–294. <https://doi.org/10.1126/science.aan5049>
- Medaris, L.G., 1999. Garnet Peridotites in Eurasian High-Pressure and Ultrahigh-Pressure Terranes: A Diversity of Origins and Thermal Histories. *Int. Geol. Rev.* 41, 799–815. <https://doi.org/10.1080/00206819909465170>
- Molina, J.F., Poli, S., 2000. Carbonate stability and fluid composition in subducted oceanic crust: an experimental study on H₂O–CO₂-bearing basalts. *Earth Planet. Sci. Lett.* 176, 295–310. [https://doi.org/10.1016/S0012-821X\(00\)00021-2](https://doi.org/10.1016/S0012-821X(00)00021-2)

- Philippot, P., Iii, D.R., 2000. Fluid-Rock Interactions during High-Pressure and Ultrahigh-Pressure Metamorphism. *Int. Geol. Rev.* 42, 312–327. <https://doi.org/10.1080/00206810009465085>
- Piccoli, F., Hermann, J., Pettke, T., Connolly, J. a. D., Kempf, E.D., Vieira Duarte, J.F., 2019. Subducting serpentinites release reduced, not oxidized, aqueous fluids. *Sci. Rep.* 9, 19573. <https://doi.org/10.1038/s41598-019-55944-8>
- Piccoli, F., Vitale Brovarone, A., Beyssac, O., Martinez, I., Ague, J.J., Chaduteau, C., 2016. Carbonation by fluid–rock interactions at high-pressure conditions: Implications for carbon cycling in subduction zones. *Earth Planet. Sci. Lett.* 445, 146–159. <https://doi.org/10.1016/j.epsl.2016.03.045>
- Plank, T., Manning, C.E., 2019. Subducting carbon. *Nature* 574, 343–352. <https://doi.org/10.1038/s41586-019-1643-z>
- Poli, S., 2015. Carbon mobilized at shallow depths in subduction zones by carbonatitic liquids. *Nat. Geosci.* 8, 633–636. <https://doi.org/10.1038/ngeo2464>
- Pons, M.-L., Debret, B., Bouilhol, P., Delacour, A., Williams, H., 2016. Zinc isotope evidence for sulfate-rich fluid transfer across subduction zones. *Nat. Commun.* 7, 13794. <https://doi.org/10.1038/ncomms13794>
- Scambelluri, M., Philippot, P., 2001. Deep fluids in subduction zones. *Lithos, Fluid Inclusions: Phase Relationships - Methods - Applications. A Special Issue in honour of Jacques Touret* 55, 213–227. [https://doi.org/10.1016/S0024-4937\(00\)00046-3](https://doi.org/10.1016/S0024-4937(00)00046-3)
- Scambelluri, M., Rampone, E., Braga, R., Malaspina, N., 2010. The Variscan garnet peridotites from the Eastern Alps (Ulten Zone): Records of subduction metasomatism in the mantle wedge. *J. Virtual Explor.* 36, paper 28. <https://doi.org/10.3809/jvirtex.2009.00259>
- Schertl, H.-P., Sobolev, N.V., 2013. The Kokchetav Massif, Kazakhstan: “Type locality” of diamond-bearing UHP metamorphic rocks. *J. Asian Earth Sci., HP-UHP Metamorphic Belts in Asia* 63, 5–38. <https://doi.org/10.1016/j.jseaes.2012.10.032>
- Schmidt, M.W., Poli, S., 2003. Generation of Mobile Components during Subduction of Oceanic Crust. *Treatise Geochem.* 3, 659. <https://doi.org/10.1016/B0-08-043751-6/03034-6>
- Schwarzenbach, E.M., Caddick, M.J., Petroff, M., Gill, B.C., Cooperdock, E.H.G., Barnes, J.D., 2018. Sulphur and carbon cycling in the subduction zone mélange. *Sci. Rep.* 8, 15517. <https://doi.org/10.1038/s41598-018-33610-9>
- Shirey, S., Smit, K., Pearson, D.G., Walter, M., Aulbach, S., Brenker, F., Bureau, H., Burnham, A., Cartigny, P., Chacko, T., Frost, D., Hauri, E., Jacob, D., Jacobsen, S., Kohn, S., Luth, R., Mikhail, S., Navon, O., Nestola, F., Nimis, P., Palot, M., Smith, E., Stachel, T., Stagno, V., Steele, A., Stern, R., Thomassot, E., Thomson, A., Weiss, Y., 2019. *Diamonds and the Mantle Geodynamics of Carbon*. Cambridge University Press.
- Skelton, A. Flux rates for water and carbon during greenschists facies metamorphism. *Geology* **39**, 43-46 (2011).
- Spandler, C., Hermann, J., 2006. High-pressure veins in eclogite from New Caledonia and their significance for fluid migration in subduction zones. *Lithos* 89, 135–153. <https://doi.org/10.1016/j.lithos.2005.12.003>

- Staudigel, H., Hart, S.R., Schmincke, H.-U., Smith, B.M., 1989. Cretaceous ocean crust at DSDP Sites 417 and 418: Carbon uptake from weathering versus loss by magmatic outgassing. *Geochim. Cosmochim. Acta* 53, 3091–3094. [https://doi.org/10.1016/0016-7037\(89\)90189-0](https://doi.org/10.1016/0016-7037(89)90189-0)
- Syracuse, E.M., van Keken, P.E., Abers, G.A., 2010. The global range of subduction zone thermal models. *Phys. Earth Planet. Inter.*, Special Issue on Deep Slab and Mantle Dynamics 183, 73–90. <https://doi.org/10.1016/j.pepi.2010.02.004>
- Tang, Y.-J., Zhang, H.-F., Ying, J.-F., Su, B.-X., 2013. Widespread refertilization of cratonic and circumcratonic lithospheric mantle. *Earth-Sci. Rev.* 118, 45–68. <https://doi.org/10.1016/j.earscirev.2013.01.004>
- Tao, R., Zhang, L., Tian, M., Zhu, J., Liu, X., Liu, J., Höfer, H.E., Stagno, V., Fei, Y., 2018. Formation of abiotic hydrocarbon from reduction of carbonate in subduction zones: Constraints from petrological observation and experimental simulation. *Geochim. Cosmochim. Acta* 239, 390–408. <https://doi.org/10.1016/j.gca.2018.08.008>
- Tomkins, A.G., Evans, K.A., 2015. Separate zones of sulfate and sulfide release from subducted mafic oceanic crust. *Earth Planet. Sci. Lett.* 428, 73–83. <https://doi.org/10.1016/j.epsl.2015.07.028>
- Touret, J.L.R., 2001. Fluids in metamorphic rocks. *Lithos, Fluid Inclusions: Phase Relationships - Methods - Applications*. A Special Issue in honour of Jacques Touret 55, 1–25. [https://doi.org/10.1016/S0024-4937\(00\)00036-0](https://doi.org/10.1016/S0024-4937(00)00036-0)
- Vitale Brovarone, A., Chu, X., Martin, L., Ague, J.J., Monié, P., Groppo, C., Martinez, I., Chaduteau, C., 2018. Intra-slab COH fluid fluxes evidenced by fluid-mediated decarbonation of lawsonite eclogite-facies altered oceanic metabasalts. *Lithos* 304–307, 211–229. <https://doi.org/10.1016/j.lithos.2018.01.028>
- Vitale Brovarone, A., Martinez, I., Elmaleh, A., Compagnoni, R., Chaduteau, C., Ferraris, C., Esteve, I., 2017. Massive production of abiotic methane during subduction evidenced in metamorphosed ophicarbonates from the Italian Alps. *Nat. Commun.* 8, 14134. <https://doi.org/10.1038/ncomms14134>
- Wallace, P.J., Edmonds, M., 2011. The Sulfur Budget in Magmas: Evidence from Melt Inclusions, Submarine Glasses, and Volcanic Gas Emissions. *Rev. Mineral. Geochem.* 73, 215–246. <https://doi.org/10.2138/rmg.2011.73.8>
- Walters, J.B., Cruz-Uribe, A.M., Marschall, H.R., 2020. Sulfur loss from subducted altered oceanic crust and implications for mantle oxidation. *Geochem. Perspect. Lett.* 36–41. <https://doi.org/10.7185/geochemlet.2011>
- Walters, J.B., Cruz-Uribe, A.M., Marschall, H.R., 2019. Isotopic Compositions of Sulfides in Exhumed High-Pressure Terranes: Implications for Sulfur Cycling in Subduction Zones. *Geochem. Geophys. Geosystems* 20, 3347–3374. <https://doi.org/10.1029/2019GC008374>
- Wu, Y.-B., Zheng, Y.-F., 2013. Tectonic evolution of a composite collision orogen: An overview on the Qinling–Tongbai–Hong’an–Dabie–Sulu orogenic belt in central China. *Gondwana Res.* 23, 1402–1428. <https://doi.org/10.1016/j.gr.2012.09.007>
- Zhang, C., van Roermund, H., Zhang, L., 2011. Orogenic Garnet Peridotites, in: *Ultrahigh-Pressure Metamorphism*. Elsevier, pp. 501–540. <https://doi.org/10.1016/B978-0-12-385144-4.00015-1>
- Zhang, H., Yang, T., Hou, Z., Wang, Y., 2020. Magmatic expression of tectonic transition from oceanic subduction to continental collision: Insights from the Middle Triassic rhyolites of the North Qiangtang Block. *Gondwana Res.* 87, 67–82. <https://doi.org/10.1016/j.gr.2020.05.012>

- Zheng, Y.-F., 2009. Fluid regime in continental subduction zones: petrological insights from ultrahigh-pressure metamorphic rocks. *J. Geol. Soc.* 166, 763–782. <https://doi.org/10.1144/0016-76492008-016R>
- Zheng, Y.-F., Fu, B., Gong, B., Li, L., 2003. Stable isotope geochemistry of ultrahigh pressure metamorphic rocks from the Dabie–Sulu orogen in China: implications for geodynamics and fluid regime. *Earth-Sci. Rev.* 62, 105–161. [https://doi.org/10.1016/S0012-8252\(02\)00133-2](https://doi.org/10.1016/S0012-8252(02)00133-2)

2 • Geological Background

2.1 The Variscan Orogeny

The European Variscan belt extends from the Iberian Peninsula to Poland and it formed during a span of time ranging from ca. 380 to 280Ma, comprehending Devonian (419-359Ma), Carboniferous (359 to 299Ma) and early Permian (299 to 252Ma). It is the result of the Pangea accretion following the collision of supercontinents of Laurussia and Gondwana. The Variscan belt was dismembered by rifting and drifting events responsible for the formation of the Adria microplate during the opening of the Mesozoic Tethys, and some portion of the Variscan belt, such as the Austroalpine domain, possibly remained in the northern edge of Adria. Europe and Adria plate margins were re-drown together after the closure of the Tethys by the Alpine collision (Godard et al. 1996). The Alpine Orogeny, occurred between 65 and 2.5 Ma, mostly overprinted the signature of the Variscan belt. Despite this, the pre-Alpine evolution of some exposed metamorphic terranes in the Eastern Alps is still well-preserved by paragenesis and fabrics, as, for example, in the Variscan Ulten Zone.

2.2 The Ulten Zone: geological framework

The Ulten Zone (Andreatta, 1935; Hoinkes & Thöni, 1993), also referred in the literature as *Nonsberg*, *Ultental* or *Ulten unit*, is a Variscan fossilized tectonic mélange attributed to the Upper Austroalpine system of the Central Eastern Italian Alps (Fig. 2.1), a nappe pile of Cretaceous age (Thöni, 1981). The Austroalpine system is separated from the Mesozoic Southern Alps by the North Giudicarie Line, a subset of the main Insubric Lineament, and comprises the Ortler nappe and a southern overlying Tonale nappe, where the Ulten Zone is located. These two nappes are divided by the Pejo Line (Andreatta, 1948), a Cretaceous thrust reactivated during the Tertiary (Martin et al., 1991). The UZ of the Tonale nappe consists of Variscan foliated garnet-kyanite gneisses and migmatites enclosing lenticular ultramafic bodies (Obata and Morten, 1987), generally concordant to the NE-SW trending structure of the nappe and schistosity of the surrounding gneisses. The pre-Alpine signature is weakly overprinted by the Alpine metamorphism, mainly in correspondence of the main tectonic lineaments. Two structural domains of the UZ zone are differentiated by peculiar lithologies and metamorphic grades (Obata and Morten, 1987). The northern domain is bordered by the Pejo Line on the north and Rumo Line on the south, and

contains garnet-kyanite-bearing paragneiss with the assemblage quartz + antiperthitic plagioclase + garnet + kyanite + biotite \pm K-feldspar \pm fibrolitic sillimanite \pm muscovite, grading into migmatites with intercalations of granitic to tonalitic orthogneisses.

The southern domain at the south of the Rumo line shows muscovite schists and paragneiss with quartz + plagioclase + biotite + muscovite garnet \pm staurolite \pm k-feldspar \pm fibrolitic sillimanite \pm epidote.

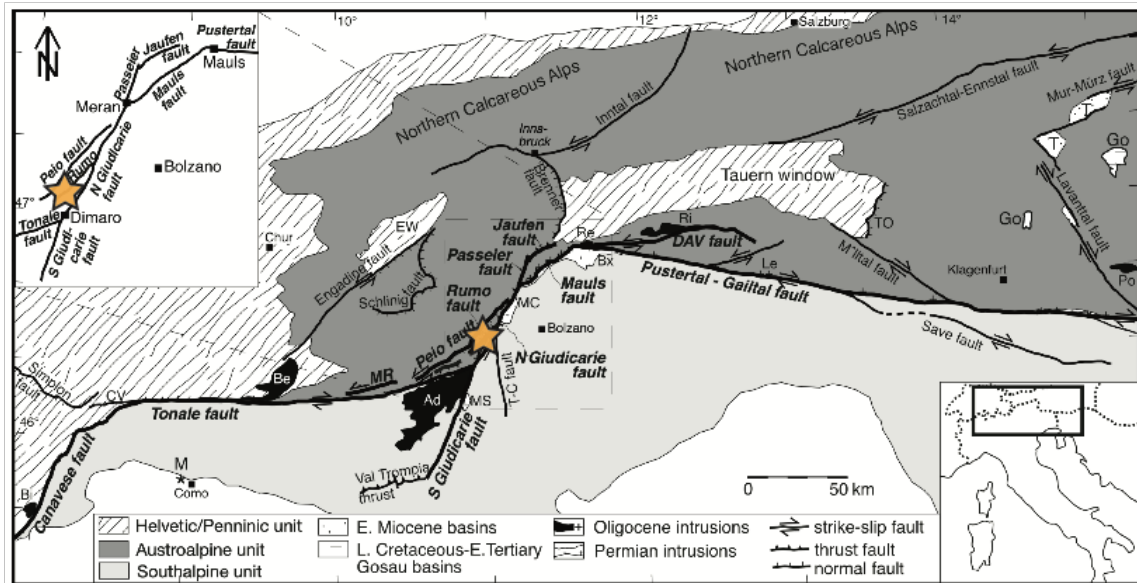


Fig. 2.1 Simplified tectonic sketch map of the Alps showing all major faults related to the Periadriatic fault system (thick black lines) as well as other faults (thin black lines). The stars refer to the study area. Modified after Müller et al. (2001) and reference therein.

2.3 Petrological outline and evolution of the Ulten Zone peridotite

The Ulten Zone ultramafic rocks consist of barrel-shaped peridotites tens to hundreds of meters in size, mostly located along the boundary between the underlying strongly-foliated gneisses and the overlying migmatites and orthogneisses (Morten et al., 2003). Locally, peridotites host layers or bands of pyroxenite, in some cases complexly folded.

Following Obata and Morten (1987), two main textural types of peridotite are recognized: coarse- and fine-grained. The coarse-type has been defined as coarse (Harte, 1977) or protogranular (Mercie and Nicolas, 1975) texture (up to few centimeters in grain size), with predominantly spinel; the fine-type has porphyroclastic to equigranular texture (0.2-1mm in grain size) and is garnet-bearing or garnet-free. Overall, the UZ peridotite shows highly variable petrographic features which track record of the complex tectono-metamorphic evolution during the Variscan Orogeny. The coarse-grained spinel peridotites are usually less deformed and often underwent to extensive fracturing during reactions with fluid. In the field, the fine-type prevails in abundance over the

coarse -type (Obata and Morten, 1987), and the coarse-type sporadically occurs as relics within the fine-grained. Field and petrographic studies have concluded that the less deformed coarse-grained spinel peridotite syn-tectonically recrystallized to foliated fine-grained garnet-amphibole/chlorite-amphibole peridotites. In the following, the specific metamorphic stages, petrographic and tectonic transition with relative mineral assemblages are described. It is worth to note that despite former studies refer to the UZ peridotites as Iherzolite for coarse-type and harzburgite for the fine-type (Rost and Brenneis, 1978), we prefer to simply use the term 'peridotite' as the high modal amounts of amphibole encompasses the IUCS nomenclature.

In the pre-Variscan stage #1 (Fig. 2.2), coarse-grained peridotites made of olivine + enstatite + diopside + Cr-Al spinel with protogranular texture (Obata and Morten, 1987) were intruded by hydrous basic melts ($T > 1400^{\circ}\text{C}$) from deeper lithospheric mantle, leading to LREE and LILE enrichment at spinel facies conditions (1200°C and 1.3-1.6 GPa; Nimis and Morten, 2000).

During stage #2, the continental crust subduction initiated by the Variscan continents collision dragged down the coarse-peridotites as a result of corner flow, and as they approach the slab-wedge interface, the coarse-types have been transitioning to porphyroclastic to fine-grained equigranular peridotites. The porphyroclastic type shows garnet corona around spinel and the occurrence of pale green amphibole in the peridotite matrix (Obata and Morten, 1987). However, well preserved spinel-facies coarse-peridotites are fairly rare in the field and the transitional evolution of the different lithotypes is still somewhat enigmatic.

Fine-grained peridotites show different mineral assemblages, mainly distinguished by the presence/absence of garnet and clinopyroxene, ranging from olivine + orthopyroxene + clinopyroxene + garnet + Ca-amphibole \pm spinel to olivine + orthopyroxene + Ca-amphibole + chlorite (Obata and Morten, 1987). Phlogopite, apatite, dolomite and rare dissakisite-(La) are accessories (Tumiati et al., 2007). Fine-grained peridotites resulted from mylonitization and hydration of the coarse-peridotites that interacted with slab-derived fluids during the Variscan continental collision. The metamorphic peak was estimated around 850°C and 2.7 GPa in eclogite-facies conditions (Nimis and Morten, 2000; Braga and Sapienza, 2007), concomitant to a widespread crystallization of LILE- and LREE-rich amphibole, in textural equilibrium with garnet (Scambelluri et al., 2006). Further studies estimate lower P-T conditions (2.2-2.5 GPa) for the equilibration of hydrous carbonated peridotites (Braga & Sapienza, 2007; Sapienza et al. 2007, 2009; Malaspina & Tumiati, 2012).

Despite it is certain that metamorphism and emplacement of peridotite lenses pre-date the Alpine orogeny, it is not fully understood whether hydration and recrystallization of peridotites occurred. Tumiati et al. (2003) stress that peridotite was already tectonically entrapped into the country rocks

and undergoing simultaneously peak conditions, while Scambelluri et al. (2006) believe that peridotite still resided in the mantle wedge before entrapment in the host gneiss at early stages of exhumation. The first scenario is supported by garnet-whole rock and garnet-clinopyroxene isochrones Sm-Nd ages, which indicate that garnet-facies equilibration and metasomatism in peridotite, and country rocks migmatization occurred at the same time around 340-330 Ma. The second scenario is otherwise supported by the conclusion that the origin of metasomatic fluids is related to the reaction of hydrous anatectic melts with wedge peridotite at the slab-wedge boundary. This reaction produced an orthopyroxene-rich layer and LILE-rich residual fluids forming the garnet + amphibole peridotites. However, despite pyroxenite layers are found in the UZ peridotite (Braga et al., 2007b), the envisaged large-scale production of orthopyroxene at the expense of olivine have not been documented so far (Sapienza et al., 2009). Both the scenarios cannot be fully demonstrated and the question remains open. In addition, hydration of peridotites as a result from country leucosome recrystallization is not supported by the P-T conditions required for the UZ tectono-metamorphic evolution. Marocchi et al. (2007, 2009) and Ionov et al. (2017) suggested that the migmatization of the host gneisses acted only at late stages of metasomatism, while the main metasomatic episodes were governed by slab-derived crustal fluids equilibrating with the lithospheric mantle prior to the Variscan subduction. Stage #3 represents the retrograde evolution of the crust-mantle association, recorded by (i) kelyphitic coronas around garnet in fine-grained garnet-amphibole peridotites (Godard and Martin, 2000) and (ii) the occurrence of fine-grained spinel/chlorite-amphibole peridotite, interpreted as retrograde derivatives from garnet-peridotites (Obata and Morten, 1987; Braga and Sapienza, 2007; Marocchi et al., 2007). Stage #4 indicates further dolomite formation at low pressure and temperature (Sapienza et al., 2009). Ranalli et al. (2005) advanced a two-stage model for the exhumation: (i) a first, fast, driven-buoyancy event followed by (ii) a slow exhumation resulting from slab-breakoff. However, this model has to be taken carefully as it employs at subduction depths of > 100km. All the UZ lithotypes experienced, at different degrees, a post-Variscan exhumation which mostly involved late serpentinization that in some instances erased the previous texture of peridotites.

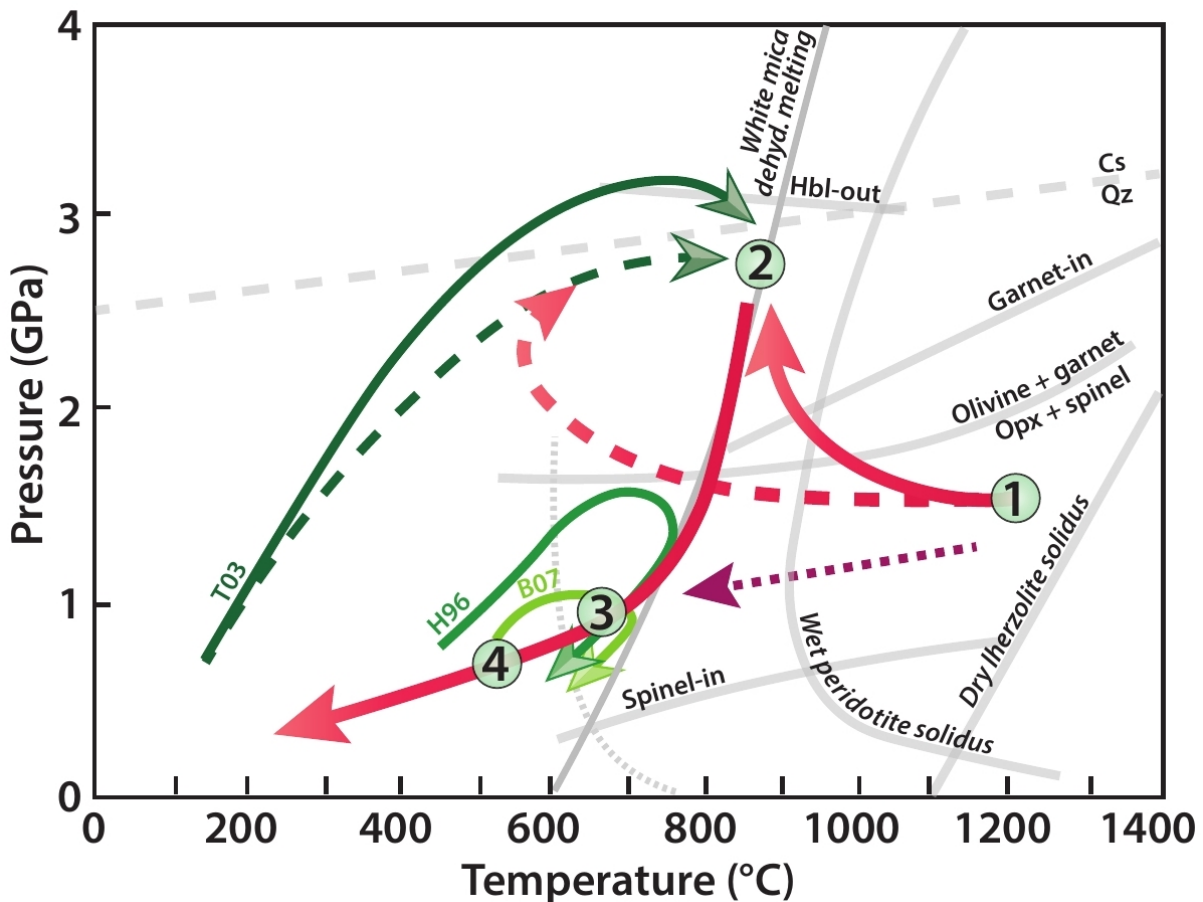


Fig. 2.2: Pressure-Temperature (P-T) evolution of the Ulten Zone crustal rocks and peridotites. The main metasomatic events are taken from Tumiati et al. (2003), Marocchi et al. (2009) and Sapienza et al. (2009). Crustal rock evolutions: T03 from Tumiati et al. (2003); H96 (Hauzenberger et al., 1996) and B07 (Braga et al., 2007a). Peridotite evolution: dashed red line indicates peridotite entrapment during subduction after Nimis and Morten (2000); full red line indicates peridotite entrapment at the beginning of exhumation after Scambelluri et al. (2006). Purple dashed line indicates path of chlorite peridotites which never equilibrated at eclogite-facies conditions, after Marocchi et al. (2007). Gray stippled line indicates the solidus for H₂O-saturated metapelites.

2.4 Mineralogical, textural and compositional effects of Alpine overprinting

Despite the study of the effects of the Alpine overprinting in the peridotite and the country rocks of the Ulten Zone is beyond the scope of this PhD thesis, some first order considerations can be outlined. The Ulten Zone belongs to the Tonale Nappe that largely escaped the Alpine tectono-metamorphic overprint (Godard et al., 1996; Martin et al., 1998). In the Ulten Zone, after the main metamorphic/metasomatic event of Variscan age (330-340 Ma) recorded by gneisses, migmatites, and peridotites, only Ar-Ar and Rb-Sr cooling ages of about 250 Ma were obtained. A weak Alpine overprint led to chlorite, chloritoid and sericite blastesis along localized shear zones within the crustal basement (Martin et al., 1998). In addition, pseudotachylites from retrogressed paragneiss

along the Rumo Line, a minor tectonic line between the Tonale Zone and the Ulten Zone close to our study area, gave Ar-Ar Paleocene ages (Müller et al., 2001). However, there is no field evidence that this Alpine deformation affected the peridotite. Nevertheless, it is plausible that the low-T mineral assemblages we observe in the studied peridotite might be related to the Paleogene collisional phase of the Alpine orogeny. The Ulten peridotite shows variable degree of serpentinization and serpentine veins, whose occurrence, together with calcite/brucite intergrowths, requires aqueous fluid infiltrations at shallow structural levels, with temperature that could be as low as 200-300°C. The lack of time constraints on the development of the low-T assemblages precludes our ability to discuss further the Alpine overprint on the peridotite. This would be an interesting topic for a future scientific endeavor.

2.5 Carbon and sulfur in the Ulten Zone peridotites

The first petrographic evidences of carbonate in the form of dolomite date back to the earlier works of Obata & Morten, (1987) and Godard et al. (1996). Obata & Morten, (1987) find rare large dolomite grains surrounded by apatite within the garnet-bearing fine-type. Godard et al. (1996) also find dolomite only within the recrystallized fine-grained peridotite matrix, and rare dolomite grains included in garnet, attributed to earlier metamorphic stages. Over time, it was clear that the texturally-diverse occurrence of carbonate phases in the UZ peridotite was underestimated and dolomite grains turned out to be more common than previously thought (Rampone and Morten, 2001; Scambelluri et al., 2006; Braga and Sapienza, 2007; Marocchi et al., 2007, 2009; Sapienza et al. 2009; Förster et al. 2017; Gudelius et al. 2019 and Lo Po' et al. 2020). The first detail carbonate petrography is provided by Förster et al. (2017).

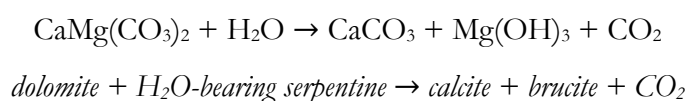
The first attempt in constraining the origin of carbonates is given by Rampone and Morten (2001), that attributed their formation from a residual CO₂-bearing hydrous metasomatic fluid left after the crystallization of leucosomes of the country migmatite during the Variscan subduction. However, high-pressure migmatization of the host rocks is not likely, since the required conditions for partial melting are only reached later in the exhumation stage (Marocchi et al., 2007, 2010; Ionov et al., 2017). Scambelluri et al. (2006) and Sapienza et al. (2009) suggest that C-bearing fluids are extracted by an early hydrous silicate melts derived from the associated crust, testifying C mobilization from the subducting crust to the mantle wedge.

Dolomite grains are reported both in high (eclogite-facies) pressure (about 2.5 GPa, 850-900°C) and low-pressure retrograde peridotites (P 1.5-1.8 GPa, $T < 850^\circ\text{C}$) by Sapienza et al. (2009), who also document the similarity of patterns and element fractionation in the different grains with the

exception of LREE, Ti, Nb, U, Th, Pb abundances, that are of one order greater in the high-pressure type. They interpreted such difference as a reflection of the amphibole occurrence in the high-pressure type, which strongly affects the trace element budget. They therefore envisage the same metasomatic agent for the dolomite in the high-pressure and low-pressure types.

A well-shaped dolomite inclusion in spinel within garnet was interpreted as trapped melt at pre-Variscan times (Förster et al., 2017). The controversy of this inclusion comes out by the occurrence of late calcite+brucite intergrowths and radiating fractures which document with no doubt that at some time during exhumation late metasomatic fluids may have penetrated the fractures formed after garnet crystallization (Consuma et al. 2020). The textural equilibrium of matrix amphibole and minor dolomite indicate that they formed under peak-conditions as carbon bearing hydrous metasomatic agents percolating the peridotite.

Along with dolomite, which is the main C-repository (Sapienza et al., 2009; Förster et al., 2017; Gudelius et al., 2018; Consuma et al., 2020), also magnesite and calcite have been recognized. Minor amounts of magnesite are reported by Malaspina and Tumiati (2012) in a fine-grained porphyroclastic garnet peridotite and by Förster et al. (2017) in a coarse-grained protogranular peridotite. Calcite is reported to occur as polymineralic inclusions in spinel and garnet (Förster et al., 2017; Lo Po' et al. 2020), as few μm -thick veins and as intergrowths with brucite after dolomite (Förster et al., 2017; Gudelius et al. 2019). The latter are only found in highly fine-grained serpentinized peridotite and are always surrounded or somehow connected to serpentine phases. Their shape indicate that they form as pseudomorphs after dolomite and they are interpreted as resulting from dissolution-precipitation processes prompt by infiltration of serpentinizing fluids (Förster et al., 2017), as following:



Serpentinization is therefore not only the most important metamorphic hydration process, but in the UZ peridotite plays a key role in liberating CO_2 during the final exhumation stages. This PhD project will characterize the serpentine phase to the comprehension of the P-T conditions and stability of mineral assemblages throughout the UZ metamorphic evolution.

To date, the S-bearing phases in the Ulten Zone have just been broadly referred as 'sulfides', and to the author's knowledge, there are no petrographic characterization of sulfides occurring in the Ulten Zone peridotites and associated migmatites and gneisses.

This PhD project comes from the evidence of intimate textural associations of carbonate and sulfide. On one hand, carbonate formation in the UZ peridotite is so far best explained by

carbon recycling via subduction fluids at different depths from deep levels to shallow conditions, however, an in situ geochemical approach is needed to constrain their origin; on the other hand, the underestimation of the sulfide occurrence and their possible coupled behavior with carbonates may undervalue the significance of the crust-mantle carbon and sulfur cycling in continental collision settings.

Chapter Two — References

- Andreatta, C., 1935. La formazione gneissico-kinzigitica e le oliviniti di Val d'Ultimo (Alto Adige). *Estr Mem Mus Storia Nat Venezia Trident* 3, 1–160.
- Braga, R., Massonne, H.-J., Morten, L., 2007. An early metamorphic stage for the Variscan Ulten Zone gneiss (NE Italy): evidence from mineral inclusions in kyanite. *Mineral. Mag.* 71, 691–702. <https://doi.org/10.1180/minmag.2007.071.6.691>
- Braga, R., Sapienza, G.T., 2007. The retrograde evolution of a dolomite-bearing hydrous peridotite from the Ulten Zone (Italian Alps). *GeoActa* 6, 37–45.
- Consuma, G., Braga, R., Giovanardi, T., Bersani, D., Konzett, J., Lugli, F., Mazzucchelli, M., Tropper, P., 2020. In situ Sr isotope analysis of mantle carbonates: Constraints on the evolution and sources of metasomatic carbon-bearing fluids in a paleo-collisional setting. *Lithos* 354–355, 105334. <https://doi.org/10.1016/j.lithos.2019.105334>
- Förster, B., Braga, R., Aulbach, S., Lo Pò, D., Bargossi, G.M., Mair, V., 2017. A petrographic study of carbonate phases in the Ulten Zone ultramafic rocks: insights into carbonation in the mantle wedge and exhumation-related decarbonation. *Ofioliti* 42, 105–127.
- Godard, G., Martin, S., 2000. Petrogenesis of kelyphites in garnet peridotites: a case study from the Ulten zone, Italian Alps. *J. Geodyn.* 30, 117–145. [https://doi.org/10.1016/S0264-3707\(99\)00030-7](https://doi.org/10.1016/S0264-3707(99)00030-7)
- Godard, G., Martin, S., Prosser, G., Kienast, J.R., Morten, L., 1996. Variscan migmatites, eclogites and garnet-peridotites of the Ulten zone, Eastern Austroalpine system. *Tectonophysics* 259, 313–341. [https://doi.org/10.1016/0040-1951\(95\)00145-X](https://doi.org/10.1016/0040-1951(95)00145-X)
- Gudelius, D., Aulbach, S., Braga, R., Höfer, H.E., Woodland, A.B., Gerdes, A., 2019. Element Transfer and Redox Conditions in Continental Subduction Zones: New Insights from Peridotites of the Ulten Zone, North Italy. *J. Petrol.* 60, 231–268. <https://doi.org/10.1093/petrology/egy112>
- Harte, B., 2015. Rock Nomenclature with Particular Relation to Deformation and Recrystallisation Textures in Olivine-Bearing Xenoliths. *J. Geol.* <https://doi.org/10.1086/628299>
- Hoinkes, G., Thöni, M., 1993. Evolution of the Ötztal-Stubai, Scarl-Campo and Ulten Basement Units, in: von Raumer, J.F., Neubauer, F. (Eds.), *Pre-Mesozoic Geology in the Alps*. Springer, Berlin, Heidelberg, pp. 485–494. https://doi.org/10.1007/978-3-642-84640-3_29
- Ionov, D.A., Bigot, F., Braga, R., 2017. The Provenance of the Lithospheric Mantle in Continental Collision Zones: Petrology and Geochemistry of Peridotites in the Ulten–Nonsberg Zone (Eastern Alps). *J. Petrol.* 58, 1451–1472. <https://doi.org/10.1093/petrology/egx061>

- Lo Pò, D., Braga, R., Tropper, P., Konzett, J., Mair, V., Bargossi, G.M., 2020. Polymineralic inclusions as tracers of multistage metasomatism in a paleo mantle wedge. *Lithos* 364–365, 105517. <https://doi.org/10.1016/j.lithos.2020.105517>
- Malaspina, N., Tumiati, S., 2012. The role of C-O-H and oxygen fugacity in subduction-zone garnet peridotites. *Eur. J. Mineral.* 24, 607–618. <https://doi.org/10.1127/0935-1221/2012/0024-2213>
- Marocchi, M., Hermann, J., Morten, L., 2007. Evidence for multi-stage metasomatism of chlorite-amphibole peridotites (Ulten Zone, Italy): Constraints from trace element compositions of hydrous phases. *Lithos, Melt-rock reaction processes in the mantle and their bearing on mantle petrology and chemistry* 99, 85–104. <https://doi.org/10.1016/j.lithos.2007.05.010>
- Marocchi, M., Mair, V., Tropper, P., Bargossi, G.M., 2009. Metasomatic reaction bands at the Mt. Hochwart gneiss-peridotite contact (Ulten Zone, Italy): insights into fluid-rock interaction in subduction zones. *Mineral. Petrol.* 95, 251–272. <https://doi.org/10.1007/s00710-009-0043-8>
- Martin, S., Prosser, G., Santini, L., 1991. Alpine deformation along the Periadriatic lineament in the Italian Eastern Alps. *Alp. Deform. Periadriatic Lineament Ital. East. Alps* 5, 118–140.
- Mercier, J.-C.C., Nicolas, A., 1975. Textures and Fabrics of Upper-Mantle Peridotites as Illustrated by Xenoliths from Basalts. *J. Petrol.* 16, 454–487. <https://doi.org/10.1093/petrology/16.1.454>
- Morten, L., Trommsdorff, V., Carswell, D., Compagnoni, R., 2003. Metamorphism and textures of dry and hydrous garnet peridotites, in: *Ultrahigh Pressure Metamorphism. EMU Notes in Mineralogy*, pp. 443–466.
- Müller, W., Prosser, G., Mancktelow, N.S., Villa, I.M., Kelley, S.P., Viola, G., Oberli, F., 2001. Geochronological constraints on the evolution of the Periadriatic Fault System (Alps). *Int. J. Earth Sci.* 90, 623–653. <https://doi.org/10.1007/s005310000187>
- Nimis, P., Morten, L., 2000. P–T evolution of ‘crustal’ garnet peridotites and included pyroxenites from Nonsberg area (upper Austroalpine), NE Italy: from the wedge to the slab. *J. Geodyn.* 30, 93–115. [https://doi.org/10.1016/S0264-3707\(99\)00029-0](https://doi.org/10.1016/S0264-3707(99)00029-0)
- Obata, M., Morten, L., 1987. Transformation of Spinel Lherzolite to Garnet Lherzolite in Ultramafic Lenses of the Austridic Crystalline Complex, Northern Italy. *J. Petrol.* 28, 599–623. <https://doi.org/10.1093/petrology/28.3.599>
- Rampone, E., Morten, L., 2001. Records of Crustal Metasomatism in the Garnet Peridotites of the Ulten Zone (Upper Austroalpine, Eastern Alps). *J. Petrol.* 42, 207–219. <https://doi.org/10.1093/petrology/42.1.207>
- Ranalli, G., Martin, S., Mahatsente, R., 2005. Continental subduction and exhumation: an example from the Ulten Unit, Tonale Nappe, Eastern Austroalpine. *Geol. Soc. Lond. Spec. Publ.* 243, 159–174. <https://doi.org/10.1144/GSL.SP.2005.243.01.12>
- Rost, F., Brenneis, P., n.d. *Die Ultramafite im Bergzug südlich des Ultentales, Provinz Alto Adige (Oberitalien) ~ 30.*
- Sapienza, G.T., Scambelluri, M., Braga, R., 2009. Dolomite-bearing orogenic garnet peridotites witness fluid-mediated carbon recycling in a mantle wedge (Ulten Zone, Eastern Alps, Italy). *Contrib. Mineral. Petrol.* 158, 401–420. <https://doi.org/10.1007/s00410-009-0389-2>

- Scambelluri, M., Hermann, J., Morten, L., Rampone, E., 2006. Melt- versus fluid-induced metasomatism in spinel to garnet wedge peridotites (Ulten Zone, Eastern Italian Alps): clues from trace element and Li abundances. *Contrib. Mineral. Petrol.* 151, 372–394. <https://doi.org/10.1007/s00410-006-0064-2>
- Thöni, M., 1981. Degree and Evolution of the Alpine Metamorphism in the Austroalpine Unit W of the Hohe Tauern in the light of K/Ar and Rb/Sr Age Determinations on Micas. *Jahrb Geol Bundesanst* 124, 111–174.
- Tumiati, S., Godard, G., Martin, S., Klötzli, U., Monticelli, D., 2007. Fluid-controlled crustal metasomatism within a high-pressure subducted mélange (Mt. Hochwart, Eastern Italian Alps). *Lithos* 94, 148–167. <https://doi.org/10.1016/j.lithos.2006.06.009>
- Tumiati, S., Thöni, M., Nimis, P., Martin, S., Mair, V., 2003. Mantle–crust interactions during Variscan subduction in the Eastern Alps (Nonsberg–Ulten zone): geochronology and new petrological constraints. *Earth Planet. Sci. Lett.* 210, 509–526. [https://doi.org/10.1016/S0012-821X\(03\)00161-4](https://doi.org/10.1016/S0012-821X(03)00161-4)

3 • Methods

In the present chapter, all the used analytical instrumentations and relative methods are reported.

3.1 Scanning Electron Microscopy **SEM**

SEM is a powerful tool to study microstructures and to produce images of the surface of investigated sample. In the SEM, a carbon- or gold-coated polished thin section is placed in a chamber under vacuum and investigated by scanning a beam of electrons across the sample. As the electrons interact with the sample, they produce secondary electrons (SE), backscattered electrons (BSE) and characteristic X-rays, which are collected by detectors. BSE signals are related to the atomic number (Z) of minerals and carry information on the composition of the sample and crystal orientation. The resulting BSE show different grey colors. SE signals remain on the surface and are mostly used for color mapping and surface analyses. An energy dispersive X-ray analysis (EDAX), commonly linked to the SEM, measures the energy of X-rays emitted by the irradiated sample and can identify the elements that occur in the samples. EDAX allows analyses of minerals with a grain size bigger than 5 μm .

SEM analyses were carried out at the Dipartimento di Scienze Biologiche Geologiche e Ambientali BiGEGA at University of Bologna in order to identify minerals and to determine semi-quantitatively the mineral compositions. We used a SEM Philips 515B fitted with an EDAX DX4 microanalytical device applying the operating conditions as follows: accelerating voltage of 15 kV, beam current of 2 nA and a spot size $\sim 1\mu\text{m}$. X-ray color mapping was used to detect compositional variations of sulfide grains. All minerals were carefully analyzed, with particular focus on carbonate and sulfide phases. Petrographic thick sections (ca. 100 μm of thickness) and peridotite slices with 5 mm of thickness were gold coated (ca. 10 μm). We choose the use of gold instead of graphite in order to prevent contamination of carbonates.

3.2 Electron Microprobe **EPMA**

EPMA allows qualitative and quantitative analyses using a tungsten filament as an energy source of free electrons. Under fairly optimal conditions, the electrons are focused into a fine beam which penetrate the sample distance up to three times the diameter of the beam. EPMA uses an electron

current up to 1000 times higher as in SEM, in order to allow electrons to displace from the outer shell to inner-shell losing their energy by emission of characteristic X-rays. By comparing the intensity of X-rays from standards with a known composition, we can detect the chemical composition of the investigated material.

Polished thick sections were coated with carbon and major element compositions were determined with the JEOL 8100 SUPERPROBE electron microprobe at the Institute of Mineralogy and Petrography, University of Innsbruck with the analytical conditions: 15 kV accelerating voltage, 10 nA beam current, using wavelength-dispersive spectroscopy (WDS). F-topaz (F), jadeite (Na_2O), orthoclase (K_2O), rutile (TiO_2), rhodonite (MnO), MgO , diopside (CaO), chromite (Cr_2O_3), almandine (FeO), corundum (Al_2O_3), atacamite (Cl), baryte (BaO), Ni-olivine (NiO), and quartz (SiO_2) were used as standards for silicates and oxides analyses, while calcite (CaO), diopside (MgO), strontianite (SrO), rhodonite (MnO) and almandine (FeO) standards were used for carbonates analyses. To avoid carbonate devolatilization during EPMA analyses, the electron beam was defocused to an approximate size of 10×10 microns.

3.3 Optical cathodoluminescence (CL)

Cold optical microscopy cathodoluminescence (OM-CL) is widely used to determine zoning induced by compositional changes in carbonates (Habermann et al. 1996). The CL technique uses light generated by primary, secondary and backscattered electrons that interact with a sample volume, which can be tuned with voltage. Despite CL colors depend on many factors, the trace elements content is the main contributor of luminescence. The main activator elements of carbonate luminescence are Mn^{2+} , Pb^{2+} , Sb^{3+} , Cr^{3+} , $\text{Eu}^{2+}/\text{Eu}^{3+}$, Sm^{3+} , whereas ions Fe^{2+} and Ni^{2+} are the main quencher elements (Götze, 2012). Fe^{2+} and Mn^{2+} are frequently hosted by carbonate minerals and their quantification is pivotal to fully comprehend the resulting effect of luminescence. It is inferred that there is no low Mn^{2+} activation limit for the luminescence in dolomite, and concentrations even up to ~ 15 wt% FeCO_3 shows a weak brownish-red luminescence using an older CL device (Gillhaus et al., 2001).

In order to detect compositional zonation and localize *in-situ* isotope and trace elements analyses, carbonates were investigated using an optical cold-cathodoluminescence (CL) at the University of Lausanne, with a cold cathode ERI-MRTech mounted on a petrological microscope, with a voltage of ca. 8kV and a current of 0.4mA.

3.4 MicroRaman spectroscopy

Raman Spectroscopy is a non-destructive chemical analysis used to provide details about chemical structure, phase and polymorphs, crystallinity and molecular interactions. It is based on the Raman effect, which results in the inelastic scattering of light due to vibration of molecules in an illuminated material. Monochromatic light, normally produced by a laser in the visible range, is focused on the area of interest. When the incident beam interacts with the material under investigation, molecules are excited from a ground state to a virtual energy state. The scattered light can therefore lose or gain energy upon interactions with the investigated material. If a minor increment of the vibrational energy of the molecule occurs, the incident light loses energy and this phenomenon is referred to as Stokes Raman scattering. At the same time, if a small loss of vibrational energy occurs, the scattered light will gain energy and this is called Anti-Stokes Raman scattering. The Stokes and Anti-Stokes vibrational frequencies are respectively shifted to lower and higher energies of the Rayleigh scattering i.e. light that is scattered without a change in energy. The light scattered from the sample is collected by lenses and passed into a spectrometer. The Raman spectrum profile (peak position and relative peak intensity) usually plots intensity versus energy where each peak corresponds to a vibrational frequency in the particular sample. The intensity of a spectrum is directly proportional to concentration and it depends on crystal defects or different orientation of the investigated material.

Micro-Raman analyses were performed in order to distinguish polymorphs of serpentine phases and brucite/periclase minerals at the Department of Mathematical, Physical and Computer Sciences, University of Parma. Polished thick sections and rock chips were investigated with a Horiba Jobin-Yvon LabRam apparatus, equipped with an Olympus microscope with 10x, 100x and ultra long working distance (ULWD) 50x objectives and motorized x-y stage. The 473.1 nm line of a doubled Nd:YAG diode pumped laser was used as excitation source with a spectral resolution of about 2 cm^{-1} . The 473.1 nm source was selected to work in the spectra range with the maximum sensitivity of the detector to enhance the OH stretching signal of the water molecules in the high wavenumber range (3000-4000 cm^{-1}). The spectra were collected using the ULWD 50X objective with repeated acquisition. The background subtraction of each spectrum was performed with the LabSpec software.

3.5 X-ray fluorescence analyses (XRF)

XRF is an acronym for X-ray fluorescence, a non-destructive analytical technique whereby electrons are dislodged from their atomic orbital positions, realizing a burst of energy (fluorescent X-ray) which is characteristic of a specific element. Most atoms have several electron orbitals (K shell, L shell, M shell, for example). When X-ray energy causes electrons to dislocate in and out of these shells, it generates a characteristic spectrum which is the graphical representation of X-ray intensity peaks as a function of energy peaks. The peak energy identifies the element, and the peak height/intensity is generally indicative of its concentration.

XRF was carried out for measuring the whole rock major and minor elements. Following preparation of fused disks from sample powders, concentrations of major, minor and selected trace elements in ten samples were obtained at the Johannes Gutenberg-University Mainz by X-Ray Fluorescence (XRF), using a Phillips Magi XPRO spectrometer and following the procedure outlined in Ionov et al. (2010). Both ultramafic and mafic reference samples are used as external standards, with precisions $\leq 0.6\%$ for elements present at the percent level.

Using the same powders previously prepared for major- and minor-element analysis (Gudelius et al., 2019), sulfur concentrations of nine whole rocks (UN1-UN16) were obtained at Johannes Gutenberg-University Mainz using two methods: (1) via infrared absorption on 1g of powder, using a LECO-Analyzer CS 125, with a detection limit of 30 ppm. The NBS reference material measured as an unknown gave an S concentration of $2,870 \pm 30$ ppm (1σ , $n = 2$), compared to the reference concentration 2,720 ppm; (2) via XRF using the instrument described in section 3.2, where S concentration is calculated from SO_3 . The ultramafic reference material UB-N analyzed as an unknown gave an S concentration of 162 ± 3 ppm ($n = 2$), well within compiled concentration values of 134-206 ppm (GeoReM: <http://georem.mpch-mainz.gwdg.de/>). Average values from the two methods are used for discussion. A further eight samples were analyzed at Karlsruhe Institute of Technology, using a CS 2000 Eltra sulfur analyzer. Steel standard (92400-3050) measured as an unknown gave a S concentration of 360 ppm which agrees well with the accepted value of 370 ± 20 ppm, whereas UB-N gave only 100 pm, lower than the range of compiled values of 134-206 ppm (GeoReM: <http://georem.mpch-mainz.gwdg.de/>).

3.6 LA-ICP-MS and LA-MC-ICP-MS

LA-ICP-MS and LA-MC-ICP-MS are techniques used to achieve accurate and precise element content (down to concentrations of even ppb) and isotopic ratio from ‘thin’ section with a thickness of 80-100 μm . The advantage of these techniques is that they do not require a sample preparation or to make the sample conductive. The laser beam is focused on the samples contained in an air tight chamber and ablates a small amount of material from the target zone, producing ablation pits of 10-200 μm . The ablated material (positively charged ions) is extracted from the argon plasma into the high vacuum of the mass spectrometry via the interface of sampler and skimmer cones. The mass to charge ratio of elements is then measured to evaluate the element content or isotopic ratio of the material under investigation. Internal standard(s) is(are) used to correct for the elemental fractionation caused by sensitivity drift, matrix effect as well as the difference in ablation yield between samples and reference materials (Mukherjee et al., 2014). A detailed overview of LA-ICP-MS and LA-MC-ICP-MS applied to the Earth Sciences can be found in Lin et al. (2016).

3.6.1 Mineral trace element measurements

The trace elements concentration of minerals were analyzed using a triple quadrupole 8900 QQQ (Agilent) coupled to a 193nm excimer laser Geolas 102 (Microlas) housed at the IGG-CNR of Pavia (Italy). Data reduction was carried out using the “Glitter” software package (Van Achterbergh et al., 2001). The spot size was 35 μm , using NIST SRM 610 glass as an external standard and CaO (29wt% for dolomite) as an internal standard. Precision and accuracy estimated on the basaltic glass standard BCR2 and NIST612 were better than 10%.

Trace-element abundances of sulfides were measured following the procedure detailed in Aulbach et al. (2012). Briefly, the Thermo Finnigan Element 2 ICPMS was linked to the above-described laser instrument. Analytical conditions for the LAM include a repetition rate of 7 Hz and laser energy of 90 or 100 mJ, with use of a 25 or 50% attenuator, such that fluences on the sample of <2.5 to 3 J m^{-2} were achieved. Spot sizes for standards and samples were set to 23-50 μm , and multiple spots per grain were analysed, depending on grain size. On the mass spectrometry side, oxide production was minimized to remain below 0.3-0.4% (by monitoring ThO/Th during tuning). External calibration was achieved using two synthetic standards doped with various trace

elements: (1) LaFlamme-Po727 (pyrrhotite containing PGE and Au; Godel et al., 2008) for Au, (2) MASS-1 (pressed Zn sulphide powder; Wilson et al. (2002) for other trace elements. Abundances of Au cannot be quantified in a subset of samples that were Au-coated prior to analysis for multiple S isotopes, as Au may have collected in small pits and cracks in the sulfide grains. Because the standards do not contain a common set of trace elements, accuracy is not independently assessed and results must be considered semi-quantitative. This does not affect conclusions in this study, which rely on relative differences between compositions of sulfides from different peridotite types, textural settings or localities, all obtained with the same method.

Table 3.1. Concentrations in ppm for the two different standards used for calibration and measured as unknowns during two analytical campaigns.

Vs LaFlamme	Mass1 avg	rsde	rsdi	dl	LaFlamme avg	rsde	rsdi	dl	Mass1 avg	rsde	rsdi	dl	LaFlamme avg	rsde	rsdi	dl	
Au197	68	10	11	0,15	46			10	0,11				46			7	0,01
Vs Mass1	Mass1 avg	rsde	rsdi	dl	LaFlamme avg	rsde	rsdi	dl	Mass1 avg	rsde	rsdi	dl	LaFlamme avg	rsde	rsdi	dl	
Co59	60	10	0,14	4,6	9	11	0,13	60	6	0,02	5,6	4	6	0,04			
Ni60	97	10	0,63	1,98	27	17	0,61	97	6	0,17	2,85	11	8	0,27			
Cu63	135849	13	0,57	8,0	16	14	0,51	135218	10	0,24	11,0	8	11	0,39			
Cu65	135456	13	0,70	7,8	15	14	0,63	134222	5	0,36	11,0	9	6	0,59			
Zn66	211051	10	0,86	1,78	25	24	0,80	210434	6	0,40	2,82	34	12	0,64			
As75	65	10	1,52	1,61	36	43	1,44	65	5	0,03	0,25	14	12	0,05			
Se77	51	12	1,28	nd	na	na	1,19	51	7	0,22	na	na	na	0,35			
Se82	51	13	3,44	2,6	16	58	3,22	51	6	0,73	na	na	na	1,21			
Sb121	60	10	0,03	0,181	261	12	0,03	60	5	0,01	0,022	28	24	0,01			
Te125	15,0	12	0,49	0,22	na	93	0,45	15,0	6	0,03	0,03	9	61	0,04			
Pb208	69	14	0,01	0,059	155	21	0,01	68	7	0,00	0,044	21	11	0,00			
Bi209	60	15	0,00	0,0095	43	33	0,00	60	7	0,00	0,0103	16	15	0,00			

Values for 15-24 spot analyses were averaged (avg); rsde average relative standard deviation (%), rsdi average relative within-run uncertainty (%), dl detection limit (ppm); rsde are large for elements not nominally present in the standards (Au in Mass-1; elements except Au in LaFlamme). Certified or working values are reported in Wilson et al. (2002) for Mass-1, Godel et al. (2008) for LaFlamme.

3.6.2 In situ Sr isotope: fundamentals of Sr isotope geochemistry

Strontium widely occurs in nature and its distribution in rocks is mostly controlled by the extent to which Sr^{2+} can substitute for Ca^{2+} in calcium-bearing minerals or K^{+} in potassium feldspar. Strontium has four stable isotopes: ^{88}Sr , ^{87}Sr , ^{86}Sr and ^{84}Sr . The isotopic composition of Sr isotope is variable and depends on the Rb/Sr ratio of the sample from which the strontium is extracted and on the length of time it has been associated with rubidium. The relative abundance of ^{87}Sr among the isotopes of strontium is commonly expressed as the atomic ratio $^{87}\text{Sr}/^{86}\text{Sr}$. Details on strontium isotope geochemistry are reported in Faure and Powell (1972).

3.6.2.1 Sr isotope of dolomite and calcite

In situ Sr isotopes of carbonates occurring in three thick sections and four rock chips of 5 mm thickness, representing both fine- and coarse- grained peridotites, were measured at the Centro

Interdipartimentale Grandi Strumenti (CIGS) of the University of Modena and Reggio Emilia (Italy) using a double focusing MC–ICP–MS with a forward Nier–Johnson geometry (Thermo Fisher Scientific, Neptune™), coupled to a 213 nm Nd:YAG laser ablation system (New Wave Research™). The analytical procedure is the same as of Giovanardi et al. (2018). Laser ablation parameters consisted of a laser spot ranging from 55 μm to 100 μm (see Table 4), a fluence of $\sim 10 \text{ J/cm}^2$, a laser frequency of $\sim 10 \text{ Hz}$ and a He flux of $\sim 0.5 \text{ L/min}$. Signals were acquired in static mode with a block of 250 cycles (including laser warm-up, ~ 50 – 80 cycles of analysis and washout) and an integration time of 0.5 s. Collected m/z were 82Kr, 83Kr, 84Sr, 85Rb, 85.5, 86Sr, 86.5, 87Sr and 88Sr. Masses 85.5 and 86.5 were measured to check doubly charged Yb interferences. Kr was corrected measuring 60 s of gas blank with the laser off. After background subtraction, the remaining signal on mass 82 was used to check the formation of Ca dimers and argides; while mass 83 to check the presence of Er^{2+} . Rb was corrected by calculating the ^{87}Rb contribution to mass 87 by measuring the interference-free ^{85}Rb signal, correcting for instrumental mass fractionation, and using the natural $^{87}\text{Rb}/^{85}\text{Rb}$ ratio. Mass bias normalization was performed through exponential law and a $^{88}\text{Sr}/^{86}\text{Sr}$ ratio of 8.375209. The accuracy of the analyses was checked using an in-house reference material (modern marine shell) (see Table X in Supplementary Material), which yielded a $^{87}\text{Sr}/^{86}\text{Sr}$ ratio of 0.709174 ± 0.000064 (2σ ; $n = 19$), in agreement with modern seawater (0.70917). Three analyses of a second in-house carbonate reference material yielded a $^{87}\text{Sr}/^{86}\text{Sr}$ ratio of 0.707562 ± 0.000018 (2σ), equal to the solution reference value (0.70756 ± 0.00003 ; 2σ) (Weber et al., 2020). Data reduction was performed using a customized excel spreadsheet.

3.6.2.2. Sr isotope of clinopyroxene and amphibole

Rubidium–Sr isotope compositions of clinopyroxene and amphibole were determined *in situ* at Goethe-University Frankfurt using the ThermoFinnigan Neptune MC-ICPMS linked to a Resonetics RESOLUTION M-50-HR laser probe, following details outlined in (Aulbach et al., 2016). The mass spectrometer was operated with Faraday cups in static collection mode, with analyses lasting 45 s with 1 s integration time for gas blank and sample ablation, respectively. The laser probe was run at spot sizes of 90 to 160 μm , a 10 Hz repetition rate and a laser energy of 5–6 J cm^{-1} . Soda-lime glass SRM-NIST 610 was used for empirical determination of the mass bias of $^{87}\text{Rb}/^{85}\text{Rb}$ and of Rb/Sr inter-element fractionation. Analysis of an in-house plagioclase standard (MIR-1) yielded $^{87}\text{Sr}/^{86}\text{Sr}$ (0.703159 ± 0.000017 1 μm , $n = 6$) compared to the TIMS-derived value of 0.703096 ± 0.000050 (Rankenburg et al., 2004). This standard was used for normalization of measured $^{87}\text{Sr}/^{86}\text{Sr}$ in unknowns. Using this procedure USGS glasses BCR-2G and BHVO-2

yielded 0.705016 ± 0.000067 ($n=7$) and 0.703606 ± 0.000045 ($n=7$), respectively, compared to GeoREM preferred values of 0.705003 ± 0.00004 and 0.703469 ± 0.000007 , respectively (<http://georem.mpch-mainz.gwdg.de>). Given that $^{87}\text{Rb}/^{86}\text{Sr}$ in peridotitic clinopyroxene and amphibole is ≤ 0.3 , whereas that in BCR-2 is 0.52, correction for the isobaric interference of ^{87}Rb on ^{87}Sr is considered to be accurate.

3.7 Secondary Ion Mass Spectrometry (SIMS)

SIMS is a destructive, highly-surface-sensitive analytical technique, which provides localized elemental, isotopic and molecular characterization of the sample. An ion source (O^+ or O^{2+} for positive secondary ions, Cs^+ for negative ions) generates the primary ions, which are focused onto the sample to bombard the surface and promote the sputtering effect. During this stage, secondary particles (neutral particles, electrons and positive and negative charged ions) are produced. A mass filtering selects the secondary particles of interest and remove parasitic species from the source. A quadrupole mass spectrometer separates the ejected ions by their mass-to-charge ratio. A range of pumps allow the analyses to run under ultra-high vacuum (UHV) conditions, which are mandatory to prevent sample contaminations and to minimize secondary ion collision with interfering gases. The dependence of the secondary ions to the chemical environment and the sputtering conditions (ion, energy, angle) adds complexity to the measurements. The design of the ion probe allows precise determination of large number of isotopic systems with an excellent precision: mass resolution > 20000 , lateral resolution up to $2\mu\text{m}$ ($10\mu\text{m}$ is usually employed) and depth resolution of hundreds of nm.

Carbon and oxygen isotope measurements were carried out at the SwissSIMS facility (University of Lausanne, Switzerland) using the CAMECA IMS 1280HR large radius multi-collector SIMS. Isotope ratios are reported in δ notation (‰), relative to VDPB – Vienna Standard Mean Ocean Water and VSMOW – Standard Mean Ocean Water, respectively. Carbonate grains representative of the main metasomatic stages from all the peridotite samples were cut from thick sections and pressed into indium mounts with according standard materials placed in the center of the mounts. The same strategy was applied for olivine grains from peridotite MOL1-C and porphyroclastic zircon with dolomite inclusions from peridotite VM2510A.

For the carbonates, we used the following standards: in-house pure dolomite (KPIK; $\delta^{18}\text{O} = 7.6\text{‰} \pm 0.45$ 1.6SD; $\delta^{13}\text{C} = 0.54\text{‰} \pm 0.1$ 1SD), in-house calcite (Ivrea Zone; $\delta^{18}\text{O} = 12.29$; $\delta^{13}\text{C}_{\text{PDB}} = 0.64\text{‰}$) and in-house pure-siderite ($\delta^{18}\text{O} = 9.67$; $\delta^{13}\text{C}_{\text{PDB}} = -7.95$). San Carlos ($\delta^{18}\text{O} = 5.27\text{‰} \pm 0.3$ 0.34SD)

and Plengai ($\delta^{18}\text{O} = 5.29\text{‰} \pm 0.46$ 0.6SD; Li et al. 2010) were used as standards for olivine and zircon respectively. A Bruker Contour GTK white light interferometric microscope was used to check the indium mounts topography and showed accurate conditions for the analyses ($<7\mu\text{m}$ of flatness). As a final step, indium mounts surface was made conductive with a 35-40 nm gold coating.

3.7.1 Oxygen isotopes measurements

Oxygen isotope measurements were carried out on carbonates (dolomite and minor calcite), olivine and zircon. We employed a 10kV, ca. 1.5nA, primary beam of $^{133}\text{Cs}^+$ ions in Gaussian mode focused on the mount surface. The resulting secondary ions were collected by two Faraday cup detectors, with a mass resolving power of 2460 for ^{18}O and ^{16}O , as also reported by (Bégué et al., 2019).

During the session analysis, we conducted regular steps of three measurements of samples and one of standards. Standards were also analyzed at the beginning and ending of the sessions. A pre-sputtering time of 45s was applied to remove the gold coating and the beam was afterwards centered for the SIMS analyses.

Carbonate, zircon, and olivine analyses were corrected for machine drift and IMF – instrumental mass fractionation.

For carbonates along the dolomite-ankerite join, Sliwinski et al. (2015a; 2015b) reported that the $\delta^{18}\text{O}$ bias tends to decrease exponentially by ca. 10‰ with increasing Fe content in dolomite-ankerite. The dolomite from the Ulten Zone peridotite has small but significant amounts of iron, $X_{\text{Fe}} = 0.02$, where $X_{\text{Fe}} = \text{Fe}/(\text{Mg}+\text{Fe})$ (Consuma et al., 2020), that may result in very small IMF ($<1\text{‰}$) in oxygen and even less for carbon during calibration (see also Bégué et al., 2019). The same drift and IMF corrections were applied to olivine, which is forsterite with a major element composition of $\text{Fo}_{88-90}\text{Teph}_{0-2}$.

We here briefly report the standards reproducibility (2SD) for each mount analyzed with SIMS.

- Mount P0345:
 - 1) Carbonates: KPIK standard reproducibility (2SD) at the beginning of the session on 5 points was 0.19‰ and 0.21‰ over the whole session.
 - 2) Zircon: Drift-corrected Plengai 2SD at the beginning of the session on 3 points was 0.18‰ and higher values around 0.62‰ over the whole session.
 - 3) Olivine: Drift-corrected olivine San Carlos 2SD at the beginning of the session on 3 points was 0.21‰ and then 0.34‰ over the whole session.
- Mount P0343 – carbonates:

- 1) Dolomite: KPIK standard reproducibility (2SD) at the beginning of the session on 10 points was 0.37‰ and 0.42‰ over the whole measurement's session.
 - 2) Siderite: in-house siderite standard reproducibility is 0.17‰ over the whole session.
- Mount P0344 – carbonates:
 - 1) Dolomite: KPIK standard reproducibility at the beginning of the session on 6 points was 0.28‰ and 0.35‰ over the whole session.
 - 2) Calcite: in-house standard has 2SD of 0.28‰ over the whole session (just one measurement was taken for calcite).

3.7.2 Carbon isotope measurements

Carbon isotopes of dolomite and one calcite grains were collected using a ca. 1.5nA $^{133}\text{Cs}^+$ primary beam at 10kV in Gaussian mode. ^{12}C and ^{13}C were collected simultaneously on a Faraday Cup and electron multiplier, respectively. As for the oxygen isotope, the same analyses strategy was conducted to measure the carbon isotope in intervals of sample and standards measurements. We here briefly report the standards reproducibility (2SD) for each mount.

- Mount P0345– carbonates:

Dolomite: Drift-corrected KPIK standard reproducibility (2SD) was 0.56‰ at the beginning of the session and 0.95‰ over the whole measurements session.

Siderite: Drift-corrected KPIK standard reproducibility (2SD) was 0.38‰ over the whole measurements session

- Mount P0343 – carbonates:

Dolomite: KPIK standard reproducibility (2SD) was 1.67‰ over the whole measurements session.

Siderite standard reproducibility was 2.03‰

- Mount P0344 – carbonates:

Dolomite: drift-corrected KPIK standard reproducibility (2SD) at the beginning of the session was 1.32‰ and 1.49‰ over the whole session.

Calcite: drift-corrected in-house calcite standard reproducibility was 1.03‰ over the whole session.

3.7.3 Fundamentals of carbon, oxygen and sulfur isotope geochemistry

Isotopes are variants of a given chemical element which differ in the number of neutrons. Therefore, different isotopes for a given element have different atomic mass. As elements are continuously exchanged between Earth's reservoirs, isotopes may be partitioned between phases through chemical and physical processes, called *isotopic fractionation* (Sharp, 2017). Given the

infinitesimal absolute abundances of isotopes, a typical isotope composition is determined by the ratios between one of the less abundant isotope of an element and its main isotope (Kaplan and Hulston, 1966). Because variations in isotopic ratios are also relatively small, stable isotope compositions of low-mass (light) elements such as oxygen, hydrogen, carbon, nitrogen and sulfur are normally reported as delta (δ) values. The delta (δ) notation was introduced by McKinney et al. (1950) to express these relative differences in isotopic ratios between samples and standards, and is reported as parts per thousand (‰) variation relative to a reference material:

$$\delta(\text{‰}) = [(R_{\text{sample}} / R_{\text{standard}} - 1)] * 1000$$

where R denotes the ratio of the heavy to light isotope. As it appears from the δ calculation, the measured isotopic compositions are referred relative to international reference standards (Table 3.1), whose δ values are defined as 0 ‰. $\delta^{18}\text{O}$ values is usually reported relative to SMOW standard (Standard Mean Ocean Water; Craig, 1961) or the equivalent VSMOW (Vienna-SMOW) standard. $\delta^{13}\text{C}$ values are reported relative to either the PDB (Pee Dee Belemnite) or the equivalent VPDB (Vienna-PDB) standard. VSMOW and VPDB are basically identical to the SMOW and PDB standards. The use of the first instead of the second ones is supposed to imply that the measurements were calibrated according to IAEA guidelines for expression of values relative to available reference material on normalized permil scales (Coplen, 1996).

Table 3.1 Internationally accepted standards for isotope measurements (Sharp, 2017)

Ratio	Standard	Value	Reference
$^{13}\text{C}/^{12}\text{C}$	PDB	$11179 \pm 20 \times 10^{-6}$	Zhang et al. (1990)
$^{17}\text{O}/^{16}\text{O}$	SMOW	$379.9 \pm 0.8 \times 10^{-6}$	Li et al. (1988)
$^{18}\text{O}/^{16}\text{O}$	SMOW	$(2005.20 \pm 0.45) \times 10^{-6}$	Baertschi, (1976a)
$^{33}\text{S}/^{32}\text{S}$	VCDT	$78.77 \pm 0.03 \times 10^{-4}$	Ding et al. (2001)
$^{34}\text{S}/^{32}\text{S}$	VCDT	$441.626 \pm 0.039 \times 10^{-4}$	Ding et al. (2001)

Carbon atoms have 6 protons and different isotopes such as ^{12}C , ^{13}C , ^{14}C , having atomic masses of 12, 13, 14, respectively. If ^{12}C is the most abundant in nature (98.93%), ^{13}C accounts only for 1.07%. ^{14}C is the radiogenic isotope, which does not occur in ancient rocks since it decays over geological times ($< 6\text{ky}$). By convention, stable carbon isotope values are reported relative to VPDB (Vienna Pee Dee Belemnite) standard, and, by definition, the $\delta^{13}\text{C}$ of PDB is equal to zero. The resulting isotope values are obtained as following:

$$\delta^{13}\text{C} = [(R_{\text{sample}} / R_{\text{standard}} - 1)] * 1000 \text{ where } R = ^{13}\text{C}/^{12}\text{C}.$$

The measured isotope values result ‘enriched’ if they contain more ^{13}C relative to the standards, whereas they are ‘depleted’ if lesser. Different processes that may affect the Earth’s carbon isotope composition are illustrated in Figure 3.1.

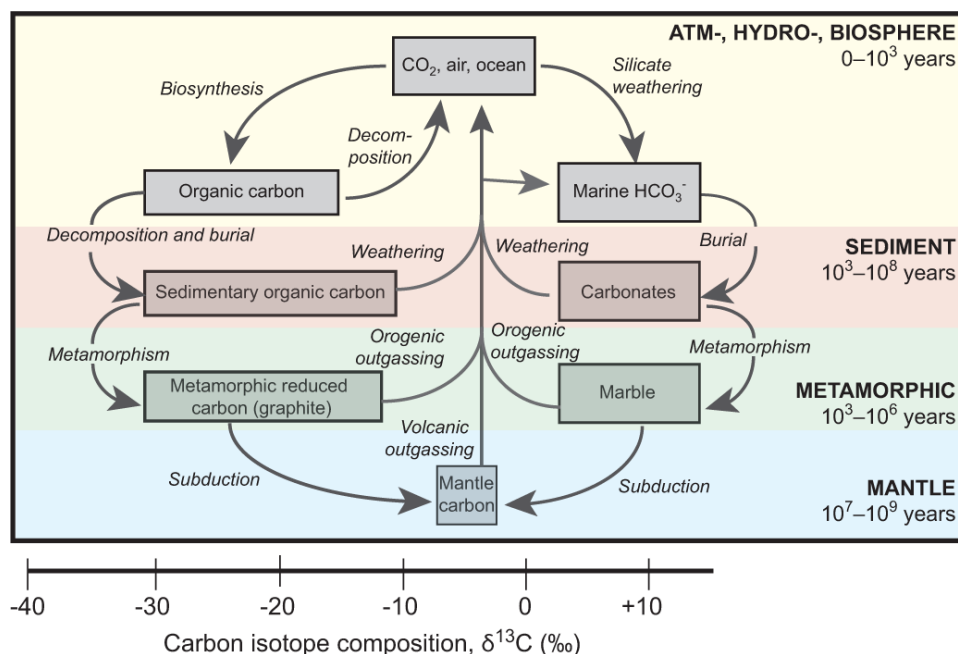


Fig. 3.1 The isotope composition of the Earth’s carbon reservoirs and the processes that modified them. After Suarez et al. (2019).

Oxygen is found in three naturally occurring stable isotopes, ^{18}O , ^{17}O , and ^{16}O , whose nucleus contains eight protons and eight, nine, or ten neutrons respectively. ^{16}O is the most abundant on Earth (99.757%), while ^{17}O (0.038%) and ^{18}O (0.205%) occur in far smaller concentration. Two international reference standards are used to report variations in oxygen isotope ratios, VPDB and VSMOW. Use of the PDB standard for reporting oxygen isotope compositions is restricted to analyses of carbonates of low-temperature origin (oceanic, lacustrine, or pedogenic) in studies of paleoclimate, paleoceanography and carbonate diagenesis. Marine carbonates have $\delta^{18}\text{O}$ values near zero on the VPDB scale, while ocean waters have $\delta^{18}\text{O}$ values near zero on the VSMOW scale. As a result of this relationship, it is not uncommon to see the two scales mixed in published reports, with data for carbonates reported on the VPDB scale and data for waters reported on the VSMOW scale. The oxygen δ notation is reported as following:

$$\delta^{18}\text{O} = \left[\left(\frac{R_{\text{sample}}}{R_{\text{standard}}} - 1 \right) \right] * 1000 \text{ where } R = ^{18}\text{O}/^{16}\text{O}.$$

Sulfur atoms have 16 protons but can have either 16, 17, 18, 19 or 20 neutrons, with different atomic masses (32, 33, 34, 35 and 36 respectively). ^{35}S is radiogenic, whereas the four stable isotopes of sulfur are ^{32}S , ^{33}S , ^{34}S , and ^{36}S , with approximate terrestrial abundances of 95.02%,

0.75‰, 4.21‰, and 0.02‰, respectively (Macnamara and Thode 1950). For sulfide minerals, the main ratio of concern is $^{34}\text{S}/^{32}\text{S}$, despite the ratios $^{33}\text{S}/^{32}\text{S}$ and $^{36}\text{S}/^{32}\text{S}$ have been recently re-evaluated as they show significant variations in Precambrian sulfides and sulfates and Martian sulfides (Farquar and Wing, 2003).

The choice to use the $^{34}\text{S}/^{32}\text{S}$ ratio comes from the fact that 1) it represents the most abundant isotopes of these elements and therefore it facilitates analysis, and 2) isotopic fractionation is governed by mass balance such that different isotopic ratios tend to vary systematically with one another in proportions that can be approximated by the mass differences among the isotopes (Seal, 2006). In other words, it results in linear fractionation trend due to physical and chemical processes known “mass-dependent fractionation” (Urey 1947; Hulston and Thode 1965), which is in distinct contrast to “mass-independent fractionation”. The δ -notation for the $^{34}\text{S}/^{32}\text{S}$ composition of a substance is defined as:

$$\delta^{34}\text{S} = [(R_{\text{sample}} / R_{\text{standard}} - 1)] * 1000 \text{ where } R = ^{34}\text{S}/^{32}\text{S}.$$

The agreed upon reference for sulfur isotopes is Vienna Canyon Diablo Troilite (VCDT) with $\delta^{34}\text{S} = 0.0\text{‰}$ by definition, which is currently defined relative to a silver sulfide reference material IAEA-S-1 with an assigned value of -0.3‰ because the supply of the Canyon Diablo Troilite reference material has been exhausted (Krouse and Coplen 1997). The reference was originally defined by the isotopic composition of troilite (FeS) from the Canyon Diablo iron meteorite. The absolute $^{34}\text{S}/^{32}\text{S}$ ratio for Canyon Diablo Troilite is 4.50045×10^{-3} (Ault and Jensen 1963). The selection of a meteoritic sulfide mineral as the reference for sulfur is useful because meteoritic sulfide is thought to represent the primordial sulfur isotopic composition of Earth (Nielsen et al. 1991). Thus, any variations in the isotopic composition of terrestrial sulfur relative to VCDT reflects differentiation since the formation of Earth (Seal, 2006).

3.7.4 Mounts preparation for SIMS measurements

3.7.4.1 Indium mounts preparation for SIMS CAMECA IMS 1280-HR

Oxygen and carbon isotopes were measured using the CAMECA IMS 1280-HR large radius multi-collector SIMS at the SwissSIMS facility at the University of Lausanne (UNIL, Switzerland). The indium mount preparation required several painstaking steps:

→ Samples topography was checked using a Bruker Contour GTK white light interferometric microscope.

- 20 carbonate grains with a 20x20 μ m clean surface and chemical compositions close to the reference standards were cut from thick sections as much as possible with a diamond wire saw. Since magnesite standards are not available, the UZ magnesite was not considered for the analyses.
- Preparation, polishing and cathodoluminescence of the standards pure dolomite KPIKO, in-house calcite and pure-siderite.
- Preparation of 3 indium mounts: the Al-disk needs to be cleaned and polished to remove any contaminants. Indium tear-drops are inserted into the disk, which is transferred to the hot plate set at the melting temperature of indium, ca. 180°C. After cooling, the indium mount is pressed under 5Ton with a hydraulic press to force the indium into the Al-well and remove air bubbles. If smooth surface is obtained, the grains can be gently pushed into little rooms in indium scavenged previously to make indium not floating out of the well. Return the holder to the hydraulic press. Standard material is placed in the center of the mounts. At each grain pressed, the mount topography was checked using a Bruker Contour GTK white light interferometric microscope, showing accurate conditions for the analyses (< 7 μ m of flatness). Samples are finally coated with 35-40 nm of gold to be ready for the analyses.

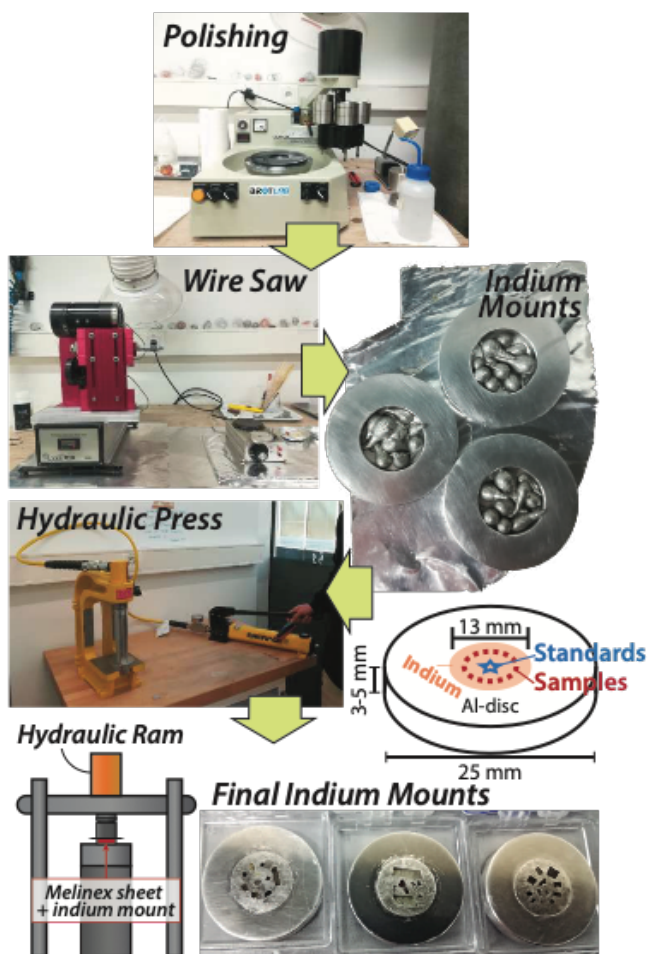


Fig. 3.2: Steps of the preparation of Indium Mounts for CAMECA IMS 1280-HR large radius multi-collector SIMS analyses at the University of Lausanne.

3.7.4.2. Epoxy mounts preparation for SIMS CAMECA IMS-1280

Sulfur isotope compositions were measured *in situ* by secondary-ion mass spectrometry (SIMS) using a Cameca IMS-1280 at the Centre for Microscopy and Microanalysis (CMCA), University of Western Australia. SIMS measurements were undertaken on pentlandite grains from seven peridotites. Grains with a minimum size of 20 μm were previously selected according to the different textural positions and association with carbonates, which track progressive metasomatic episodes during pre-peak, high-pressure-peak and retrograde conditions. All $\delta^{34}\text{S}$ values are reported relative to Vienna Canyon Diablo Troilite – VCDT (Ding et al., 2001). Further details on the procedure are given in LaFlamme et al. (2016).

In situ triple sulfur isotope (^{32}S , ^{33}S , ^{34}S) ratios were measured on a CAMECA IMS1280 ion microprobe at the Centre for Microscopy Characterisation and Analysis, hosted at the University of Western Australia. The cut sections were mounted within 5mm from the centre of 1” diameter epoxy mounts. The mounts were then trimmed to fit the SIMS sample holder together with a resin block containing standards. Care was taken to only mount samples with major element

composition within the 5-10% range of the VMSO standard composition (strictly within Fe: 26-32 wt.%, Ni: 32-39 wt.%; Co < 1-3 wt%) which was used for calibration. After careful cleaning in ethanol and distilled water, the mounts and standard blocs were coated together with ~ 30 nm gold to prevent charging during analysis.

The sample surfaces were sputtered over a 7 x 7 μm area with a 10 kV, Gaussian Cs^+ beam with intensity of ~1.5 nA and total impact energy of 20 keV. Secondary ions were admitted in the double focusing mass spectrometer within a 90 μm entrance slit and focused in the center of a 3000 μm field aperture (x 130 magnification). Energy filtering was applied using a 30 eV band pass with a 5 eV gap toward the high-energy side. All S isotopes were collected simultaneously in Faraday cup detectors fitted with $10^{10} \Omega$ (L2, ^{32}S) and $10^{11} \Omega$ (L1, ^{33}S and H1, ^{34}S) resistors, operating at a mass resolution of ~2400. The ^{33}S and $^{32}\text{S}^1\text{H}$ peaks are not fully resolved under these conditions; thus, the magnetic field was offset slightly to the low-mass side to avoid the interference. The magnetic field was regulated using NMR control. Sample surfaces were bombarded with low energy electrons from a normal incidence electron flood gun for charge compensation. Each analysis includes a pre-sputtering over a 10 x 10 μm area during 30s and the automatic centering of the secondary ions in the field aperture, contrast aperture and entrance slit. Each analysis then consists of a 25 four-second cycles acquisition. The analytical session was monitored in terms of drift using two bracketing standards every 5 sample analyses. Instrumental mass fractionation (IMF) was corrected using the matrix matched reference materials for pentlandite (VMSO) and pyrrhotite (Alexo) (reference values can be found in LaFlamme et al. (2016). IMF correction follows procedure described in LaFlamme et al. (2016).

Chapter Three — References

- Aulbach, S., Gerdes, A., Viljoen, K.S., 2016. Formation of diamondiferous kyanite–eclogite in a subduction mélange. *Geochim. Cosmochim. Acta* 179, 156–176. <https://doi.org/10.1016/j.gca.2016.01.038>
- Aulbach, S., Stachel, T., Seitz, H.-M., Brey, G.P., 2012. Chalcophile and siderophile elements in sulphide inclusions in eclogitic diamonds and metal cycling in a Paleoproterozoic subduction zone. *Geochim. Cosmochim. Acta* 93, 278–299. <https://doi.org/10.1016/j.gca.2012.04.027>
- Ault, W.U., Jensen, M.L., 1963. Summary of sulfur isotope standards, in: *Biogeochemistry of Sulfur Isotopes*. M.L. Jensen (Ed.). Nat. Sci. Found., Symposium Proc., Yale University. pp. 16–29.
- Baertschi, P., 1976a. Absolute 18-O content of standard mean ocean water. *Earth Planet. Sci. Lett.* 31, 341–344.
- Coplen, T.B., 1996. New guidelines for reporting stable hydrogen, carbon, and oxygen isotope-ratio data. *Geochim. Cosmochim. Acta* 60, 3359–3360. [https://doi.org/10.1016/0016-7037\(96\)00263-3](https://doi.org/10.1016/0016-7037(96)00263-3)
- Craig, H., 1961. Isotopic Variations in Meteoric Waters. *Science* 133, 1702–1703. <https://doi.org/10.1126/science.133.3465.1702>

- Ding, T., Valkiers, S., Kipphardt, H., De Bièvre, P., Taylor, P.D.P., Gonfiantini, R., Krouse, R., 2001. Calibrated sulfur isotope abundance ratios of three IAEA sulfur isotope reference materials and V-CDT with a reassessment of the atomic weight of sulfur. *Geochim. Cosmochim. Acta* 65, 2433–2437. [https://doi.org/10.1016/S0016-7037\(01\)00611-1](https://doi.org/10.1016/S0016-7037(01)00611-1)
- Faure, G., Powell, J.L., 2012. *Strontium Isotope Geology*. Springer Science & Business Media.
- Faure, G., Powell, J.L., 1972. *Strontium Isotope Geology*. Springer-Verl. Berl. Heidelb. N. Y. <https://doi.org/10.1017/S0016756800047518>
- Gillhaus, A., Richter, D.K., Meijer, J., Neuser, R.D., Stephan, A., 2001. Quantitative high resolution cathodoluminescence spectroscopy of diagenetic and hydrothermal dolomites. *Sediment. Geol.* 140, 191–199. [https://doi.org/10.1016/S0037-0738\(01\)00062-8](https://doi.org/10.1016/S0037-0738(01)00062-8)
- Götze, J., 2012. Application of Cathodoluminescence Microscopy and Spectroscopy in Geosciences. *Microsc. Microanal.* 18, 1270–1284. <https://doi.org/10.1017/S1431927612001122>
- Gudelius, D., Aulbach, S., Braga, R., Höfer, H.E., Woodland, A.B., Gerdes, A., 2019. Element Transfer and Redox Conditions in Continental Subduction Zones: New Insights from Peridotites of the Ulten Zone, North Italy. *J. Petrol.* 60, 231–268. <https://doi.org/10.1093/petrology/egy112>
- Habermann, D., Neuser, R.D., Richter, D.K., 1996. REE-activated cathodoluminescence of calcite and dolomite: high-resolution spectrometric analysis of CL emission (HRS-CL). *Sediment. Geol.* 101, 1–7. [https://doi.org/10.1016/0037-0738\(95\)00086-0](https://doi.org/10.1016/0037-0738(95)00086-0)
- Hulston, J.R., Thode, H.G., 1965. Variations in the S33, S34, and S36 contents of meteorites and their relation to chemical and nuclear effects. *J. Geophys. Res.* 70, 3475–3484. <https://doi.org/10.1029/JZ070i014p03475>
- Ionov, D.A., Doucet, L.S., Ashchepkov, I.V., 2010. Composition of the Lithospheric Mantle in the Siberian Craton: New Constraints from Fresh Peridotites in the Udachnaya-East Kimberlite. *J. Petrol.* 51, 2177–2210. <https://doi.org/10.1093/petrology/egq053>
- Kaplan, I.R., Hulston, J.R., 1966. The isotopic abundance and content of sulfur in meteorites. *Geochim. Cosmochim. Acta* 30, 479–496. [https://doi.org/10.1016/0016-7037\(66\)90059-7](https://doi.org/10.1016/0016-7037(66)90059-7)
- Krouse, H.R., Coplen, T.B., 1997. *Pure Appl. Chem.*
- LaFlamme, C., Martin, L., Jeon, H., Reddy, S.M., Selvaraja, V., Caruso, S., Bui, T.H., Roberts, M.P., Voute, F., Hagemann, S., Wacey, D., Littman, S., Wing, B., Fiorentini, M., Kilburn, M.R., 2016. In situ multiple sulfur isotope analysis by SIMS of pyrite, chalcopyrite, pyrrhotite, and pentlandite to refine magmatic ore genetic models. *Chem. Geol.* 444, 1–15. <https://doi.org/10.1016/j.chemgeo.2016.09.032>
- Li, W.J., Ni, B.L., Jin, D.Q., Zhang, Q.G., 1988. Measurement of the absolute abundance of O-17 in V-SMOW. *Kexue Tongbao* 33, 1610–1613.
- Lin, J., Liu, Y., Yang, Y., Hu, Z., 2016. Calibration and correction of LA-ICP-MS and LA-MC-ICP-MS analyses for element contents and isotopic ratios. *Solid Earth Sci.* 1, 5–27. <https://doi.org/10.1016/j.sesci.2016.04.002>
- Macnamara, J., Thode, H.G., 1950. Comparison of the Isotopic Constitution of Terrestrial and Meteoritic Sulfur. *Phys. Rev.* 78, 307–308. <https://doi.org/10.1103/PhysRev.78.307>

- McKinney, C.R., McCrea, J.M., Epstein, S., Allen, H.A., Urey, H.C., 1950. Improvements in Mass Spectrometers for the Measurement of Small Differences in Isotope Abundance Ratios. *Rev. Sci. Instrum.* 21, 724–730. <https://doi.org/10.1063/1.1745698>
- Mukherjee, P.K., Khanna, P.P., Saini, N.K., 2014. Rapid Determination of Trace and Ultra Trace Level Elements in Diverse Silicate Rocks in Pressed Powder Pellet Targets by LA-ICP-MS using a Matrix-Independent Protocol. *Geostand. Geoanalytical Res.* 38, 363–379. <https://doi.org/10.1111/j.1751-908X.2013.00260.x>
- Nielsen, H., Pilot, J., 1991. Lithospheric sources of sulphur. *Stable Isotopes: Natural and Anthropogenic Sulphur in the Environment-SCOPE 43* (Krouse, HR and Grinenko, VA, eds.) 43, 65–132.
- Rankenburg, K., Lassiter, J.C., Brey, G., 2004. Origin of megacrysts in volcanic rocks of the Cameroon volcanic chain – constraints on magma genesis and crustal contamination. *Contrib. Mineral. Petrol.* 147, 129–144. <https://doi.org/10.1007/s00410-003-0534-2>
- Sharp, Z., 2017. *Principles of Stable Isotope Geochemistry*, 2nd Edition. <https://doi.org/10.25844/H9Q1-0P82>
- Suarez, C.A., Edmonds, M., Jones, A.P., 2019. Earth Catastrophes and their Impact on the Carbon Cycle. *Elements* 15, 301–306. <https://doi.org/10.2138/gselements.15.5.301>
- Urey, H.C., 1947. The thermodynamic properties of isotopic substances. *J. Chem. Soc. Resumed* 562–581. <https://doi.org/10.1039/JR9470000562>
- Van Achterbergh, E., Ryan, C., Jackson, S., Griffin, W., 2001. Appendix 3, Data reduction software for LA-ICP-MS., in: *Laser-Ablation-ICPMS in the Earth Sciences* (P. Sylvester, Ed.). Mineral. Assoc. Can. Short Course Series. pp. 239–243.
- Weber, M., Lugli, F., Hattendorf, B., Scholz, D., Mertz-Kraus, R., Guinoiseau, D., Jochum, K.P., 2020. NanoSr – A New Carbonate Microanalytical Reference Material for In Situ Strontium Isotope Analysis. *Geostand. Geoanalytical Res.* 44, 69–83. <https://doi.org/10.1111/ggr.12296>
- Wilson, S.A., Ridley, W.I., Koenig, A.E., 2002. Development of sulfide calibration standards for the laser ablation inductively-coupled plasma mass spectrometry technique. *J Anal Spectrom* 17, 406–409. <https://doi.org/10.1039/B108787H>
- Zhang, Q.L., Chang, T.L., Li, W.J., 1990. A calibrated measurement of the atomic- weight of carbon. *Chinese Science Bulletin* 35, 290–296.

4 • Carbonate occurrences and constraints on the carbon-bearing fluid sources

Article: *In situ* Sr isotope analysis of mantle carbonate: Constraints on the evolution and sources of metasomatic carbon-bearing fluids in a paleo-collisional setting

Giulia Consuma, Roberto Braga, Tommaso Giovanardi, Danilo Bersani, Jürgen Konzett, Federico Lugli, Maurizio Mazzucchelli, Peter Tropper

Publication status: published in *Lithos* (2020)

Keywords: Carbon Cycle; peridotite; mantle-wedge; In situ Sr isotope; metasomatism; Ulten Zone

Note: Some additional figures previously reported as Supplementary Material are now reported in the main text.

4.1 Abstract

Carbonate-bearing wedge peridotites attest the mobilization of carbon (C) by slab fluids/melts circulating in a subduction setting. In general, COH fluids are thought to derive from the dehydration/partial melting of the crustal portions of slabs, especially during the exhumation of crust-mantle mélanges along continental subduction channels. In this study we combined textural observations with *in-situ* Sr isotope analyses of mantle carbonates occurring in different microstructural sites to test whether the fluids responsible for the carbonation of a mantle wedge derived from the subducted continental crust or not. We focus on the Ulten Zone peridotites (Eastern Italian Alps) associated with high-grade felsic rocks, where carbonates occur mainly as dolomite and minor magnesite and calcite. Analyses by a laser ablation system coupled to a Neptune MC-ICP-MS on peridotites representing different episodes of a complex metasomatic history, indicate that Sr isotopic variations can be linked to the different microstructural positions of carbonates. The C-metasomatism of UZ peridotites can be outlined in two stages. The first stage is the *HP*-carbonation at peak (eclogite-facies) conditions, with formation of interstitial matrix dolomite in textural equilibrium with hornblende to pargasite amphibole and Cl-apatite. This dolomite exhibits relatively unradiogenic $^{87}\text{Sr}/^{86}\text{Sr}$ present day values of 0.70487 ± 0.00010 ,

requiring different sources with respect to the associated migmatites and the overhanging mantle wedge. Carbonation continued during exhumation, with local injection of C-rich fluids forming dolomite veins in association with tremolite and chlorite. The dolomite vein shows a wide range of $^{87}\text{Sr}/^{86}\text{Sr}$ (0.7036-0.7083), reflecting both the primary composition of carbonates and the consequent interaction with crustal fluids as expected in a crust-mantle mélange. The second stage is C-remobilization during the final exhumation by dolomite dissolution and precipitation of brucite intergrowths with calcite, that exhibits a quite similar Sr composition of the precursor dolomite.

The mantle wedge is therefore capable to store carbonates representing a complex metasomatic evolution from eclogite-facies conditions to very shallow structural levels. Fluids released from subducting slabs of continental lithosphere might be responsible for the crystallization, in the overlying ultramafic rocks, of metasomatic minerals such as amphibole, phlogopite and zircon, but their role on the carbonation of mantle wedge is most likely overestimated. The combination of geochemical, isotopic and textural evidence suggests the contribution of a distinct source of C-bearing fluids for included and interstitial dolomite, which could be likely related to trondhjemitic intrusions or depleted deeper wedge sources. Differently, residual COH-fluids released by the associated stromatic gneisses and orthogneisses acted during the end of exhumation, providing the highest Sr isotope values for the dolomite veins.

4.2 Introduction

At convergent plate boundaries, the interface between subducting slab and overhanging mantle wedge represents a complex region, where a mix of slab- and wedge-derived lithologies plays a key role in the surface-to-mantle volatiles budget on Earth (Bebout and Penniston-Dorland, 2016). In this tectonic setting, the subduction of carbon (C) stored in organic matter and carbonate minerals is partly returned to the surface by slab fluids (Manning, 2014). The occurrence of hydrous and carbonated phases, and the enrichment in incompatible elements of the lithospheric mantle wedge above a subducting slab, testify the fluid-mediated large-scale cycling of elements. The C transfer among different reservoirs is usually related to fluids or melts expelled from the crustal portion of the subducted oceanic lithosphere (carbonated serpentinite, altered crust and sediments). However, many of the studied mantle wedge peridotites are now exposed within variable migmatized felsic gneisses, as a result of continental collision (Brueckner and Medaris, 2000; Zheng, 2012 and references therein). Accordingly, several studies highlight the importance of subducted continental crust as source of metasomatic C-bearing fluids/hydrous melts reacting and enriching the

overhanging mantle wedge (Zanetti et al., 1999; Zheng, 2009; Hermann et al., 2013). An appropriate identification of the C sources during interactions between mantle wedge and subducted continental lithosphere is therefore essential in order to develop a quantitative understanding of the global C flux.

In this study we take advantage of the wealth of data already available on the multiple metasomatic history of the Ulten Zone (UZ) peridotite (northern Italy) to illustrate the formation and the dissolution-precipitation of carbonates at relatively shallow ($P < 3$ GPa) and cold ($T < 850^\circ\text{C}$) conditions. The UZ peridotites record the transition from mantle wedge, coarse-grained, spinel-peridotite to high-pressure, fine-grained, garnet-bearing amphibole-peridotite and, finally to low- P , low- T serpentinized peridotites (Förster et al., 2017; Ionov et al., 2017; Gudelius et al., 2018). Therefore, these rocks offer the opportunity to investigate fluid-driven carbonation at different P - T conditions, along the complex metasomatic evolution of a paleo-mantle wedge involved in continental collision. We combined microstructural observations, major elements compositions, micro-Raman analyses of carbonates and associated minerals, with in situ $^{87}\text{Sr}/^{86}\text{Sr}$ isotopic composition of carbonates as a tracer for investigating the potential sources of C-bearing fluids. The choice of using elemental Sr and $^{87}\text{Sr}/^{86}\text{Sr}$ ratio to shed more light on C-metasomatism is based on the fact that: (i) it is relatively abundant in the carbonates structure due to its easy substitution with Ca^{2+} ; (ii) the partition of Rb into the carbonate crystal structure is hampered because of its large ionic size, and we therefore assume that carbonates may inherit the Sr isotopic composition of C-bearing fluids at the time of their formation and their release from the sources (Dickin, 2018 and references therein); (iii) its concentration and isotopic composition may provide information about fluid sources, elements partitioning, isotopic mixing behavior and extent of fluid-rock interaction (Banner, 1995). *In situ* approaches applied to carbonates can therefore provide the spatial resolution to better constrain the carbon-volatile-element mobilization in a crust-mantle interface and the element exchange at grain-scale.

4.3 Geology and petrology of the Ulten Zone

In the Ulten Valley and Non Valley (Trentino-Alto Adige, Italy), the Ulten Zone is a tectono-metamorphic complex belonging to the Tonale Nappe, Upper Austroalpine domain of the Eastern Alps (Fig. 4.1). The Tonale Nappe forms a SW-NE oriented narrow belt of Variscan metamorphic rocks, bounded by Alpine faults such as the Tonale and Giudicarie lines to the South and the Peio Line to the North (Müller et al., 2001). The UZ consists of strongly foliated garnet-kyanite gneisses and migmatites enclosing lenses of peridotites and pyroxenites (Obata and Morten, 1987). The

main metamorphic overprint is Variscan in age whereas evidences of a weak Eo-Alpine overprint mostly occur along the main tectonic lines (Godard et al., 1996).

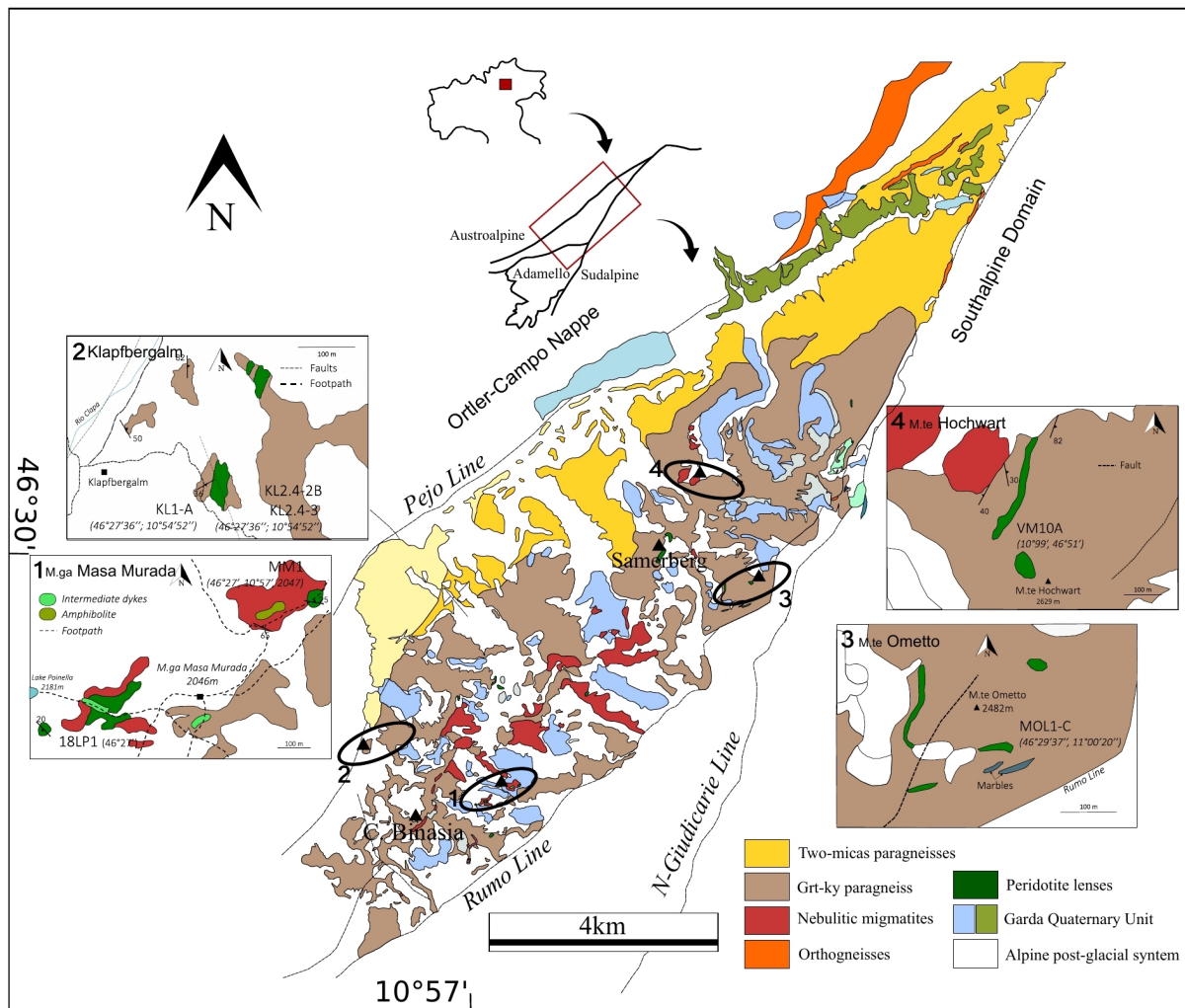


Fig. 4.1: Geological sketch map of the study area showing the localization of the Ulten Zone in the Northeastern Alps and a simplified geological map of the Ulten Zone based on the 1:10.000 sheets Appiano and Rabbi of the Italian Geological Map with samples localization.

Considering the different grain size and metamorphic assemblage, Obata and Morten (1987) classified the UZ peridotites as ranging from less deformed coarse-grained spinel peridotites to foliated fine-grained garnet-amphibole/chlorite-amphibole peridotites: the latter are interpreted as deformed and recrystallized derivatives of the former.

The UZ petrology and metasomatic evolution is the subject of several studies well summarized in Scambelluri et al. (2010) and the sketch of Figure 4.2 contains the main features of an otherwise complex sequence of events.

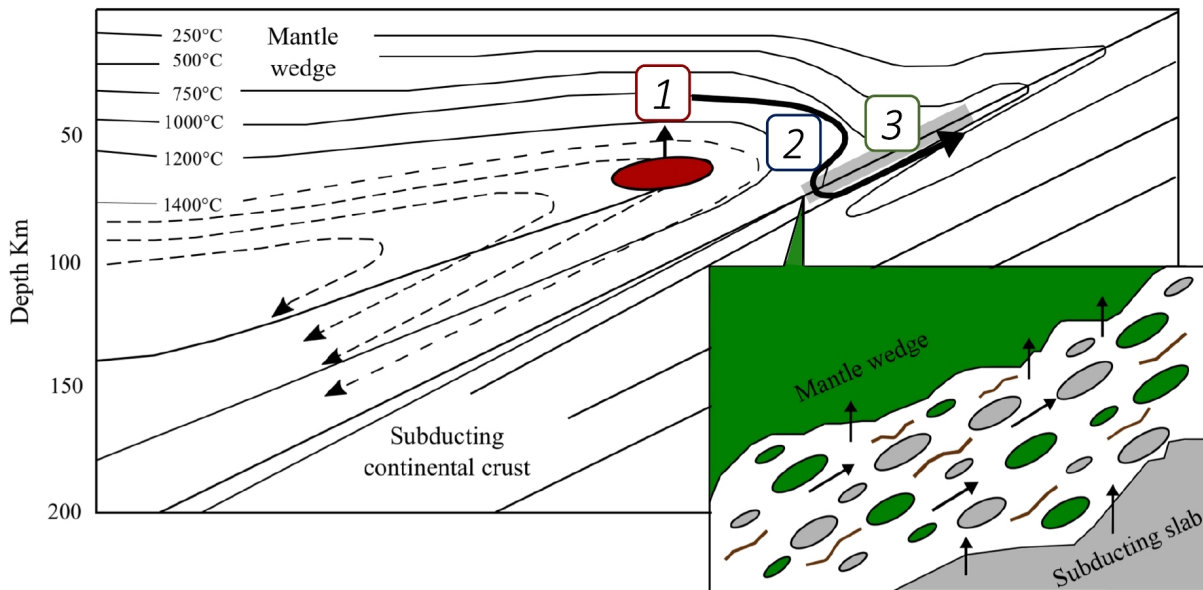


Fig. 4.2: P-T trajectory of the Ulten Zone peridotites showing the different stages as indicated in the text. Infiltration of hot deep melt (red oval) into wedge peridotites in the spinel stage (Stage1); downward flow of mantle wedge peridotites close to the slab-wedge interface due to corner flow (Stage2); exhumation after incorporation of peridotites in a crust-mantle mélange (Stage 3). Redrawn after Nimis and Morten (2000) and Scambelluri et al. (2006).

In stage 1 (Fig. 4.2), coarse-grained peridotites made of olivine + enstatite + diopside + Cr-Al spinel with protogranular texture (Obata and Morten, 1987) were percolated by hydrous basic melts from deeper lithospheric mantle before the Variscan orogeny, leading to LREE and LILE enrichment at spinel facies conditions (1200°C and 1.3-1.6 GPa; Nimis and Morten, 2000).

During stage 2, related to the Variscan subduction, the corner flow dragged the coarse-peridotites close to the slab-wedge interface and caused the transition to porphyroclastic to fine-grained equigranular peridotites. The porphyroclastic type shows garnet corona around spinel and the occurrence of pale green amphibole in the peridotite matrix (Obata and Morten, 1987). However, well preserved spinel-facies coarse-peridotites are fairly rare in the field and the transitional evolution of the different lithotypes is still somewhat enigmatic.

Fine-grained peridotites show different mineral assemblages, mainly distinguished by the presence/absence of garnet and clinopyroxene, ranging from olivine + orthopyroxene + clinopyroxene + garnet + Ca-amphibole \pm spinel to olivine + orthopyroxene + Ca-amphibole + chlorite (Obata and Morten, 1987). Phlogopite, apatite, dolomite and rare dissakisite-(La) are accessories (Tumiati et al., 2007). Fine-grained peridotites resulted from mylonitization and hydration of the coarse-peridotites that interacted with slab-derived fluids during the Variscan continental collision. The metamorphic peak was estimated around 850°C and 2.0-2.5 GPa in eclogite-facies conditions (Nimis and Morten, 2000; Braga and Sapienza, 2007), concomitant to a

widespread crystallization of LILE- and LREE-rich amphibole, in textural equilibrium with garnet (Scambelluri et al., 2006). The timing of the tectonic emplacement into the crust is still uncertain: garnet-whole rock and garnet-clinopyroxene isochrones Sm-Nd ages of Tumiati et al. (2003) suggest that garnet-facies equilibration and metasomatism in peridotite, and country rocks migmatization occurred at the same time, about 340-330 Ma. This argument supported the notion that the tectonic insertion of peridotite into the subducted continental crust occurred at peak conditions (Tumiati et al., 2003). Conversely, Scambelluri et al. (2006) stressed that the incorporation of mantle wedge peridotites into the crustal slab to form a crust-mantle mélange likely occurred shortly after the metamorphic peak.

Stage 3 (Fig. 4.2) represents the retrograde evolution of the crust-mantle association, recorded by (i) kelyphitic coronas around garnet in fine-grained garnet-amphibole peridotites (Godard and Martin, 2000) and (ii) the occurrence of fine-grained spinel/chlorite-amphibole peridotite, interpreted as retrograde derivatives from garnet-peridotites (Obata and Morten, 1987; Braga and Sapienza 2007; Marocchi et al., 2007). All the UZ lithotypes experienced a post-Variscan exhumation and were subjected to variable degrees of serpentinization that in some instances erased the previous texture of peridotites.

The petrographic evidence of amphibole and minor dolomite requires carbon bearing hydrous metasomatic agents. The origin of the hydrous metasomatic fluids with a CO₂ component were at first interpreted by Rampone and Morten (2001) as residual fluids left after the crystallization of leucosomes of the host migmatite during the Variscan subduction. On the other hand, Scambelluri et al. (2006) emphasized that the fluids interacted with the peridotites while the latter still resided in the mantle wedge (i.e. not within a crust-mantle mélange); moreover, the origin of metasomatic fluids were related to the reaction of hydrous anatectic melts with wedge peridotite at the slab-wedge boundary. This reaction produced an orthopyroxene-rich layer and LILE-rich residual fluids forming the garnet + amphibole peridotites. Later studies (Marocchi et al., 2007; Ionov et al., 2017) suggested that the migmatization of the host gneisses plausibly acted only at late stages of metasomatism, while the main metasomatic episodes were governed by slab-derived crustal fluids equilibrating with the lithospheric mantle prior to the Variscan subduction.

Dolomite, previously found in all the UZ textural types, is the main C-repository (Sapienza et al., 2009; Förster et al., 2017; Gudelius et al., 2018). Trace elements analyses of dolomite from stage 2 and stage 3 peridotites indicate that dolomite represents the major repository also for Sr, Ba, Pb and subordinately LREE (Sapienza et al., 2009). Less amounts of magnesite are reported by Malaspina and Tumiati (2012) in a fine-grained porphyroclastic garnet peridotite and by Förster et

al. (2017) in a coarse-grained protogranular peridotite. Only recently, evidences for carbonate dissolution-precipitation processes in these peridotites have been reported (Förster et al., 2017).

4.4 Analytical methods

4.4.1 Scanning electron microscopy (SEM), Electron probe microanalysis (EPMA)

Silicates, carbonates, oxides and sulfides were investigated with SEM and EPMA. Petrographic thick sections (ca. 100 μm of thickness) and peridotite chips with 5 mm of thickness were gold coated for SEM analyses. BSE images were acquired at the Dipartimento di Scienze Biologiche Geologiche e Ambientali, Università di Bologna, using a Scanning Electron Microscope (SEM) Philips 515B fitted with an EDAX DX4 microanalytical device. The operating conditions were: accelerating voltage of 15kV, beam current of 2nA and a spot size $\sim 1\mu\text{m}$. Major element compositions were determined with the JEOL 8100 SUPERPROBE electron microprobe at the Institute of Mineralogy and Petrography, University of Innsbruck, with the analytical conditions: 15 kV accelerating voltage, 10 nA beam current, using wavelength-dispersive spectroscopy (WDS). F-topaz (F), jadeite (Na_2O), orthoclase (K_2O), rutile (TiO_2), rhodonite (MnO), MgO, diopside (CaO), chromite (Cr_2O_3), almandine (FeO), corundum (Al_2O_3), atacamite (Cl), baryte (BaO), Ni-olivine (NiO), and quartz (SiO_2) were used as standards for silicates and oxides analyses, while calcite (CaO), diopside (MgO), strontianite (SrO), rhodonite (MnO) and almandine (FeO) standards were used for carbonates analyses. To avoid carbonate devolatilization during EPM analyses, the electron beam was defocused to an approximate size of 10x10 microns.

4.4.2 Micro-Raman spectroscopy

Micro-Raman spectroscopy was performed for the identification of the serpentine phases and calcite + brucite intergrowths at the Department of Mathematical, Physical and Computer Sciences, University of Parma. Polished thick sections and rock chips were investigated with a Horiba Jobin-Yvon LabRam apparatus, equipped with an Olympus microscope with 10x, 100x and ultra long working distance (ULWD) 50x objectives and motorized x-y stage. The 473.1 nm line of a doubled Nd:YAG diode pumped laser was used as excitation source with a spectral resolution of about 2 cm^{-1} . The 473.1 nm source was selected to work in the spectra range with the maximum sensitivity of the detector to enhance the OH stretching signal of the water molecules in the high wavenumber range ($3000\text{-}4000\text{ cm}^{-1}$). The spectra were collected using the ULWD 50X objective with repeated acquisition. The background subtraction of each spectrum was performed with the LabSpec[®] software.

4.4.3 *In situ* Laser Ablation MC-ICP-MS analyses

In situ Sr isotopes of carbonates occurring in three thick sections and four rock chips of 5 mm thickness, representing both fine- and coarse- grained peridotites, were measured at the Centro Interdipartimentale Grandi Strumenti (CIGS) of the University of Modena and Reggio Emilia (Italy) using a double focusing MC–ICP–MS with a forward Nier–Johnson geometry (Thermo Fisher Scientific, Neptune™), coupled to a 213 nm Nd:YAG laser ablation system (New Wave Research™). The analytical procedure is the same as of Giovanardi et al. (2018).

Laser ablation parameters consisted of a laser spot ranging from 55 μm to 100 μm (see Table 4), a fluence of $\sim 10 \text{ J/cm}^2$, a laser frequency of $\sim 10 \text{ Hz}$ and a He flux of $\sim 0.5 \text{ L/min}$. Signals were acquired in static mode with a block of 250 cycles (including laser warm-up, $\sim 50\text{--}80$ cycles of analysis and washout) and an integration time of 0.5 s. Collected m/z were 82Kr, 83Kr, 84Sr, 85Rb, 85.5, 86Sr, 86.5, 87Sr and 88Sr. Masses 85.5 and 86.5 were measured to check doubly charged Yb interferences. Kr was corrected measuring 60 s of gas blank with the laser off. After background subtraction, the remaining signal on mass 82 was used to check the formation of Ca dimers and argides; while mass 83 to check the presence of Er^{2+} . Rb was corrected by calculating the ^{87}Rb contribution to mass 87 by measuring the interference-free ^{85}Rb signal, correcting for instrumental mass fractionation, and using the natural $^{87}\text{Rb}/^{85}\text{Rb}$ ratio. Mass bias normalization was performed through exponential law and a $^{88}\text{Sr}/^{86}\text{Sr}$ ratio of 8.375209. The accuracy of the analyses was checked using an in-house reference material (modern marine shell) (see Supplementary Table A9), which yielded a $^{87}\text{Sr}/^{86}\text{Sr}$ ratio of 0.709174 ± 0.000064 (2σ ; $n = 19$), in agreement with modern seawater (0.70917). Three analyses of a second in-house carbonate reference material yielded a $^{87}\text{Sr}/^{86}\text{Sr}$ ratio of 0.707562 ± 0.000018 (2σ), equal to the solution reference value (0.70756 ± 0.00003 ; 2σ) (Weber et al., 2019). Data reduction was performed using a customized excel spreadsheet.

4.5 Results

4.5.1 Sample description and petrography

Peridotite samples were collected from the Northeastern part of the UZ (Figs. 4.1 and 4.3), from outcrops or boulders very close to the outcrops (Table 4.1 for sample description, location) (Fig. 4.3).

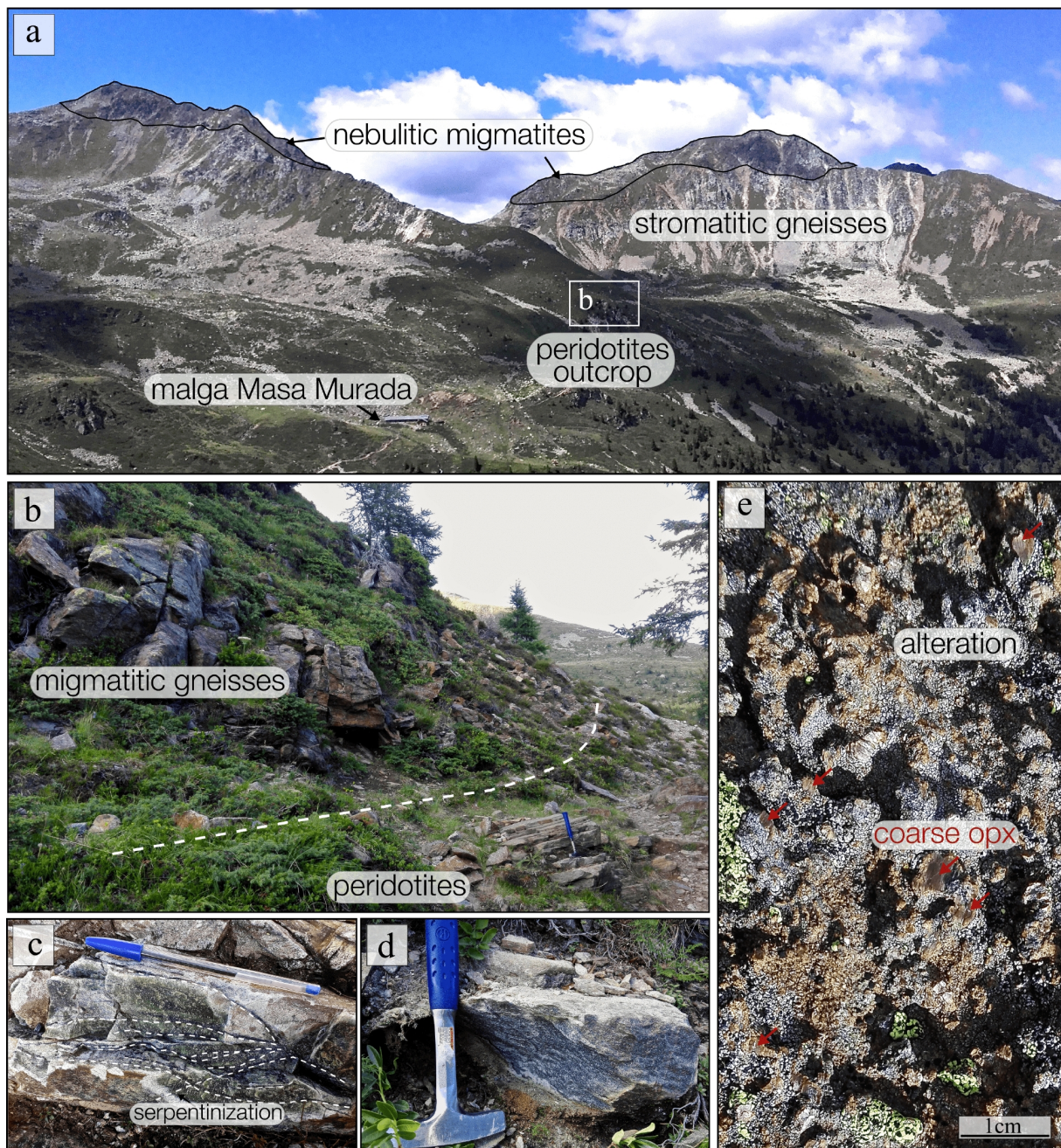


Fig. 4.3: The Ulten Zone peridotites in the field. (a) Overview of the geological setting close to Malga Masa Murada with indication of the peridotite outcrop shown in detail in (b); (c)- (d) Serpentinized fine-grained peridotites; (e) Highly altered coarse-grained peridotite with coarse orthopyroxenes.

Each sample underwent weak up to very strong serpentinization that in some instances overprinted the previous texture. All the samples investigated contain carbonates such as dolomite and, locally, magnesite and calcite (see Table 4.1). From now on, the numbers 1 and 2 refer to first and second generation respectively of olivine, orthopyroxene, clinopyroxene and spinel.

Samples 18LP1 and MOL1-C are coarse-type spinel peridotites consisting mainly of large (1-4 mm) olivine₁, orthopyroxene₁ and spinel₁. Sample 18LP1 shows orthopyroxene₁ with undulose

extinction and kink bands and they are usually rimmed by chlorite of about 150 μm in size. Clinopyroxene₁, exhibiting amphibole and spinel exsolutions, is associated with nearly-dark vermicular spinels₁. The studied chip rock contains a 300 μm wide veinlet crosscutting the matrix and filled with dolomite associated with colorless amphibole and chlorite; here, dolomite occurs as lobate-shaped grains (Fig. 4.5a). This veinlet is perpendicularly crosscut in several places by thin (ca. 50 μm wide) serpentine veins that locally contain dolomite streaks (ca. 25 μm wide) (Fig. 4.5b). Sample MOL1-C does not contain clinopyroxene₁ and mainly consists of strongly fractured olivines₁ and orthopyroxenes₁ showing kink bands. Vermicular dark spinel is often included in coarse green amphiboles. The sample shows a ca. 300 μm wide veinlet consisting of magnesite, serpentine, colorless amphibole and opaque minerals (Fig. 4.5c) cuts by a dolomite vein (ca. 200 μm long) (Fig. 4.5d). When the magnesite + serpentine + colorless amphibole vein encounters coarse crystals of orthopyroxene₁, serpentine minerals grow along orthopyroxene₁ cleavages promoting a black-colored needle-like serpentine microstructure (Figs. 4.4a and 4.5c). Both coarse peridotites probably escaped full mineralogical equilibration under eclogite-facies conditions, as indicated by the absence of garnet.

Table 4.1 Studied peridotite samples from the Ulten Zone.

Sample	Locality	Facies	Texture	Main Assemblage	Carbonates	Serp. Grade	In situ Sr
18LP1	Cima Binasia Nearby Lavazze river (as sample LP6; Ionov et al., 2017)	Spl	C	Ol ₁ + Opx ₁ + Amph + Spl ₁ + Cpx ₁ + Dol + Chl + Phl + Op	Dolomite veinlet (ca. 300 μm wide) cut by thin serpentine veins with dolomite vein included (ca. 25 μm wide). Abundance: < 1%	M	X
MOL1-C	M.te Ometto	Spl	C	Ol ₁ + Opx ₁ + Amph + Spl ₁ + Mgs + Srp + Chl + Phl + Op	Magnesite vein (ca. 300 μm wide) cut by late dolomite vein (ca. 200 μm long).	M	X
MM1	Malga Masa Murada (as sample 300B; Morten and Obata, 1990)	Spl	F	Ol ₂ + Opx ₂ + Amph + Spl ₂ + Srp + Chl + Dol + Op	Matrix dolomite (50-100 μm ; 2% of abundance); dolomite and calcite inclusions (10-50 μm) in magnetite occurring in median line of serpentine vein.	H	X
KL1-A	Klapfbergalm	Grt	F	Ol ₂ + Opx ₂ + Spl ₂ + Grt ₂ + Srp + Op	Calcite plus brucite aggregates; matrix dolomite (ca. 50 μm). Abundance : < 1 %.	H	X
KL2.4-2b KL2.4-3	Klapfbergalm	Grt	P	Ol ₂ + Opx ₂ + Spl ₂ + Grt ₂ + Amph + Srp + Dol + Cal + Op	Dolomite inclusion (ca. 70 μm) in a primary spinel.; calcite plus brucite intergrowths (< 1 %).	H	
VM10A	Mt.e Hochwart	Grt	F	Ol ₂ + Opx ₂ + Spl ₂ + Grt ₂	Matrix dolomite (< 1 % of abundance and ca. 60 μm of size) and a mm-sized dolomite inclusion in porphyroblastic zircon.	No	X

Fine-grained peridotites are the most common textural rock type in the UZ. They have grain size smaller than 0.7 mm and exhibit porphyroblastic to equigranular textures. Sample VM10A is a fine-

grained mylonitic garnet-amphibole-peridotite with a main foliation defined by the preferred orientation of matrix minerals. The main mineralogical association consists of fine-grained olivine₂, orthopyroxene₂, green amphibole, spinel₂ with accessory matrix dolomite (ca. 60 μm) (Fig. 5e) associated with apatite and green amphibole. Allanite locally occurs in the matrix. A porphyroclast (ca. 1 cm) of highly fractured reddish zircon occurs in this rock; it contains a mm-sized dolomite inclusion associated with apatite. Rare small-sized pinkish-garnets occur.

Samples KL2.4-2b and KL2.4-3 are fine-grained garnet-amphibole peridotites and contain porphyroblasts of coarse pink garnet (ca. 1 cm of size) surrounded by a kelyphitic corona made of orthopyroxene + amphibole + clinopyroxene ± spinel (Fig. 4.4b). These garnets are highly fractured and contain mm-sized spinel₁ inclusions. This spinel₁ locally hosts polycrystalline aggregates made of (i) apatite, ilmenite, pentlandite, calcite-brucite intergrowths and phlogopite; (ii) ilmenite, chlorite, apatite, pentlandite. The KL2.4-2b sample description is reported in detail by Förster et al. (2017), who also documented the occurrence of a dolomite inclusion (ca. 70 μm) in a primary spinel included in coarse-grained garnet. Matrix dolomite (ca. 40 μm) occurs commonly in association with green amphibole and apatite. In both samples, calcite occurs as thin veins in the matrix (Fig. 4.5g), included in chlorite and, in some instances, forming intergrowths with brucite. Two generations of serpentine minerals occur, with the first one represented by mesh structure in olivine₂ and bastite in orthopyroxene₂ and the second one forming thin veins crosscutting the matrix with the porphyroblastic garnet and kelyphitic corona.

Sample KL1-A is a fine-grained garnet-amphibole peridotite with the same mineralogy of the previous samples but equigranular texture (ca. 300 μm) (Fig. 4.4c). Here, intergrowths of calcite + brucite associated with relict dolomite occur in the matrix (Fig. 4.5f). Widespread small-sized pinkish-garnets (200-300 μm) occur interstitially in the matrix, always exhibiting a kelyphitic corona of orthopyroxene + amphibole + clinopyroxene ± spinel. This peridotite sample shows mesh and bastite replacement textures of olivine and pyroxene respectively. This sample is also pervaded by thin veins of serpentine and chlorite crosscutting the matrix (Fig. 4.4c).

Sample MM1 is a fine-grained amphibole-chlorite peridotite. This sample comes from a well-studied outcrop which provided sample 300B studied by Morten and Obata (1990), Scambelluri et al. (2006) and Braga and Sapienza (2007). Particularity of the sample is the presence of a ca. 1 cm wide serpentine vein showing concentric zonation with a core filled by magnetite and pentlandite and minor dolomite and calcite, and a border zone including matrix minerals consisting of olivine₂, orthopyroxene₂, green amphibole and spinel₂ (see Figs. 4.5a-b-c-d and Fig. 4.7). Matrix dolomite is

estimated to occur with an abundance of 2%, with a grain-size range of about 50-100 μm and commonly associated with apatite (Figs. 4.5h and 4.7).

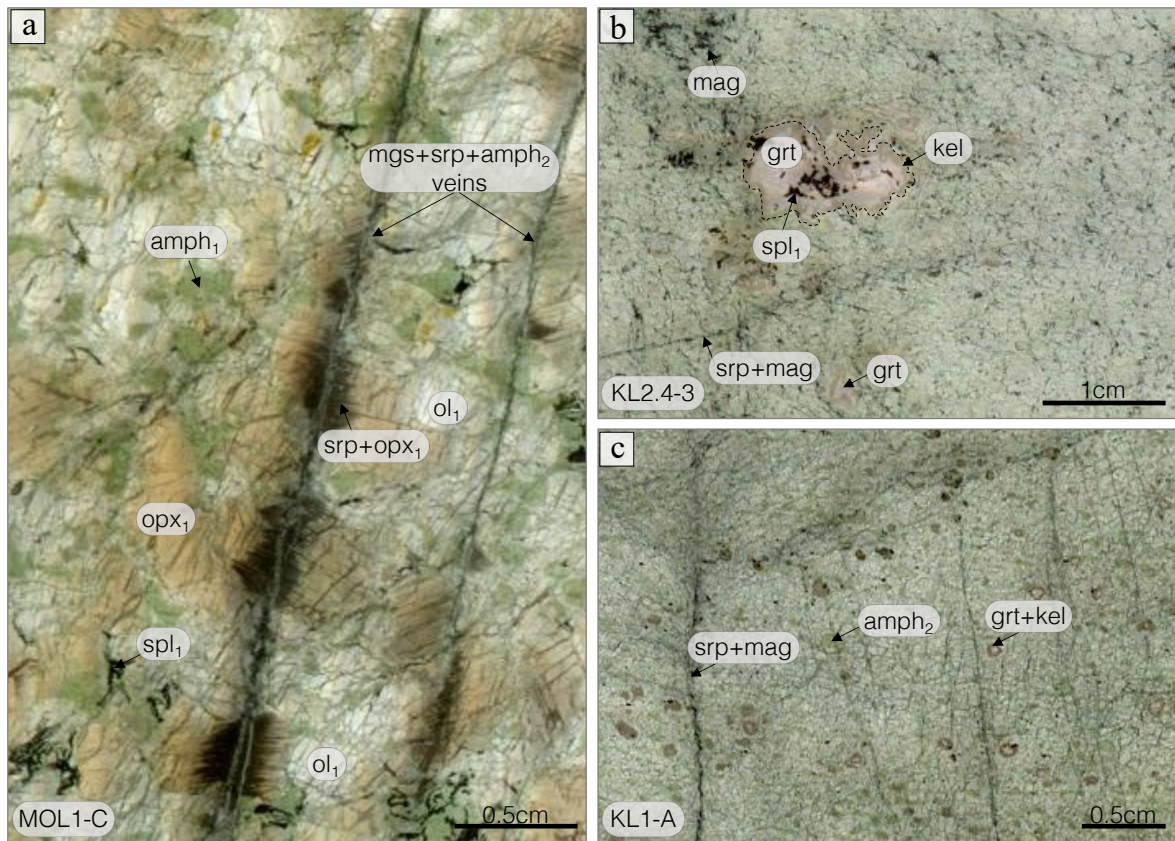


Fig. 4.4: Overview of (a) coarse-grained spinel peridotite MOL1-C with its characteristic serpentine + magnesite + tremolite vein. See text for detailed description. (b) Fine-grained porphyroblastic-garnet-bearing peridotite KL2.4–3. Pinkish-garnet is surrounded by a keliphitic corona containing large spinel inclusions with polycrystalline aggregates. In this peridotite, serpentine occurs in association with magnetite. (c) Fine-grained garnet-bearing peridotite KL1-A. Mineral abbreviations after Whitney and Evans (2010).

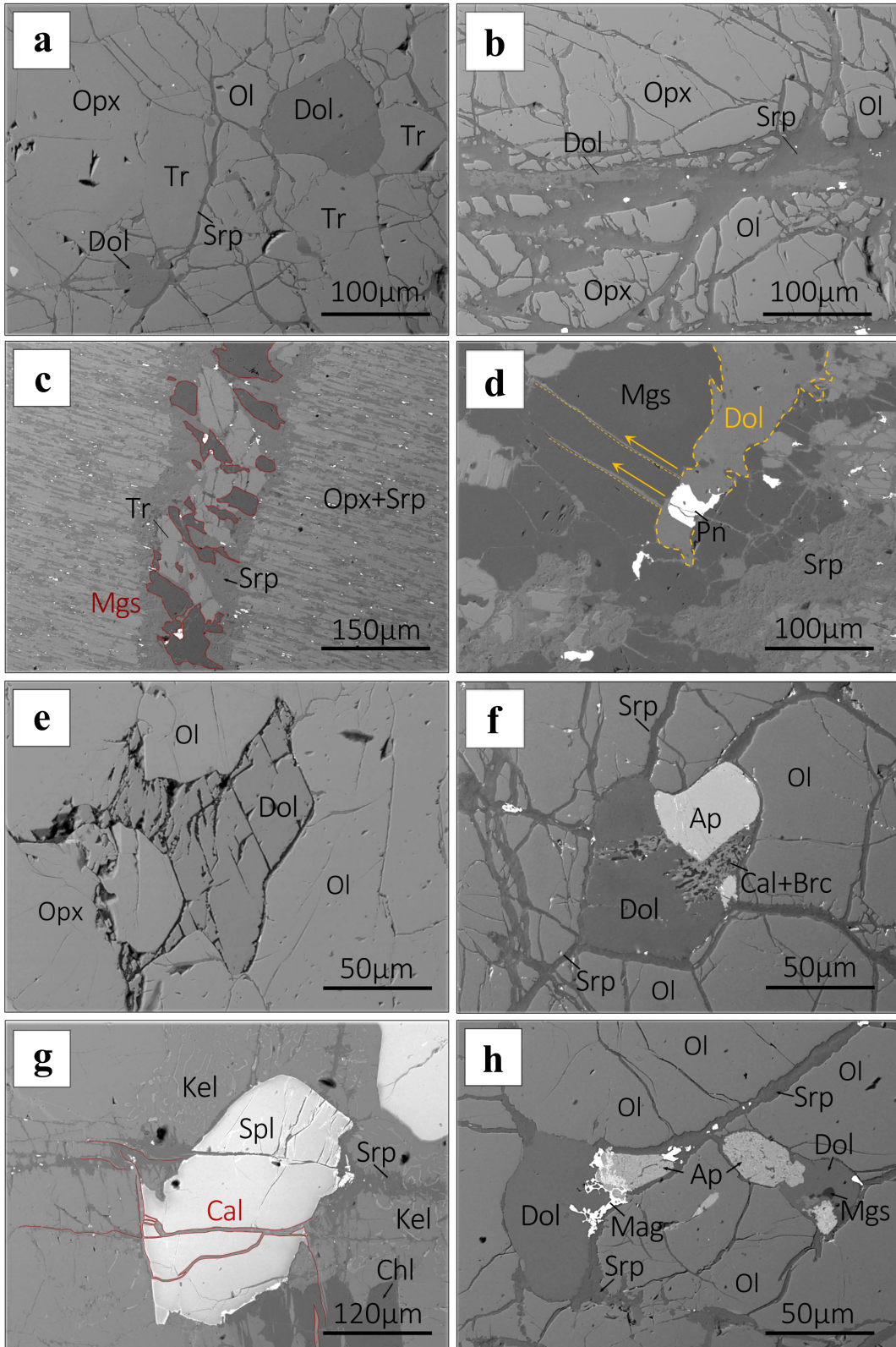


Fig. 4.5: BSE images of carbonates from the Ulten Zone peridotite. (a) 18LP1. Lobate-shaped dolomite grains constituting a veinlet with tremolite and chlorite; (b) 18LP1. Dolomite streaks into a

serpentine vein; (c) MOL1-C. Serpentine vein with magnesite and tremolitic amphibole. Infiltration of the vein into orthopyroxene formed a spectacular needle-shaped microstructure with opaque minerals; (d) MOL1-C. Dolomite vein cutting the magnesite veinlet; (e) VM10A. Interstitial dolomite with perfect cleavage; (f) KL1-A. Matrix dolomite associated with apatite. Note the incipient formation of calcite-brucite intergrowths into dolomite; (g) KL2.4–3. Large spinel cut by a thin calcite vein; (h) MM1. Matrix dolomite (with small magnesite inclusions) associated with apatite and serpentine. Mineral abbreviations after Whitney and Evans (2010).

4.5.2 Major element compositions and micro-Raman spectroscopy

Representative major element compositions of silicate minerals and apatite are listed in Table 4.2 (for all the EPMA analyses see Supplementary Tables A1 to A8) while all the carbonates major element compositions are listed in Table 4.3. The major element compositions commonly do not exhibit variations between coarse-grained and fine-grained rocks and minerals of different generations. *Olivine* is unzoned with $\text{Fo}_{88-90}\text{Teph}_{0-2}$. *Orthopyroxene* is commonly $\text{En}_{90-92}\text{Fs}_{8-10}\text{Wo}_{0-1}$ with Al_2O_3 reaching values up to 2.80 wt.%. Two textural-types of *spinel* are recognized: a first generation of coarse spinel₁ included in porphyroblastic garnets exhibits $\text{Cr}\# \sim 0.43$, where $\text{Cr}\#$ is $\text{Cr}/(\text{Cr}+\text{Al})$, while the second generation of matrix smaller spinel₂ has $\text{Cr}\#$ of about 0.35. *Clinopyroxene* is always diopside ($\text{En}_{46-49}\text{Fs}_{2-3}\text{Wo}_{47-50}$). Green *amphibole* in the matrix is commonly Mg-hornblende and minor pargasite (in samples KL2.4-2b and KL2.4-3). Pargasite is often rimmed by colorless *tremolitic amphibole* ($\text{Al}_2\text{O}_3 \sim 0.25$ wt.%). Considering the three amphibole-types, Na_2O and Al_2O_3 range from 0.1 to 1.6 wt.% and from 0.25 to 16.6 wt.%, respectively. When amphibole occurs in veinlets, its composition is always tremolitic (i.e. magnesite vein with tremolite and serpentine). Unzoned *garnet* is pyrope-rich ($\text{Py}_{51-70}\text{Alm}_{17-30}\text{Sps}_{1-4}\text{Grs}_{11-15}$), with little to no compositional variations between porphyroclasts and small-sized garnets. *Apatite*, always in association with dolomite, exhibits a high Cl content of about 5 wt.%. Serpentine (*lizardite*) replacing olivine and pyroxenes exhibits a Fe content ranging from 1.53 to 9.02 wt.% FeO. In the fine-grained amphibole-chlorite peridotite sample MM1, a composite serpentine vein was characterized by micro-Raman spectroscopy showing lizardite and mixed lizardite/chrysotile compositions (Fig. 4.7). Sheet silicates, represented by chlorite and phlogopite, show Fe contents of 2.22-2.55 and 3.45-5.03 wt.% FeO respectively. The Na_2O content of phlogopite reaches values of 0.13 wt.%.

Carbonate compositions are given in the MgCO_3 - CaCO_3 - FeCO_3 ternary diagram (Fig. 4.6). Unzoned *dolomite* does not exhibit any compositional variations between the different peridotites and microstructural domains. It can be classified as ferroan-dolomite, with X_{FeCO_3} of about 0.02 in all the samples. Similarly, magnesite veinlet shows high Fe content, with X_{FeCO_3} of about 0.05. *Calcite* (together with brucite) was identified using micro-Raman spectroscopy (Fig. 4.7), and it also occurs

as thin veins cutting the matrix or as intergrowths with brucite in association with dolomite (Fig. 4.8). Calcite composition is close to the Ca-carbonate endmember (Fig. 4.6).

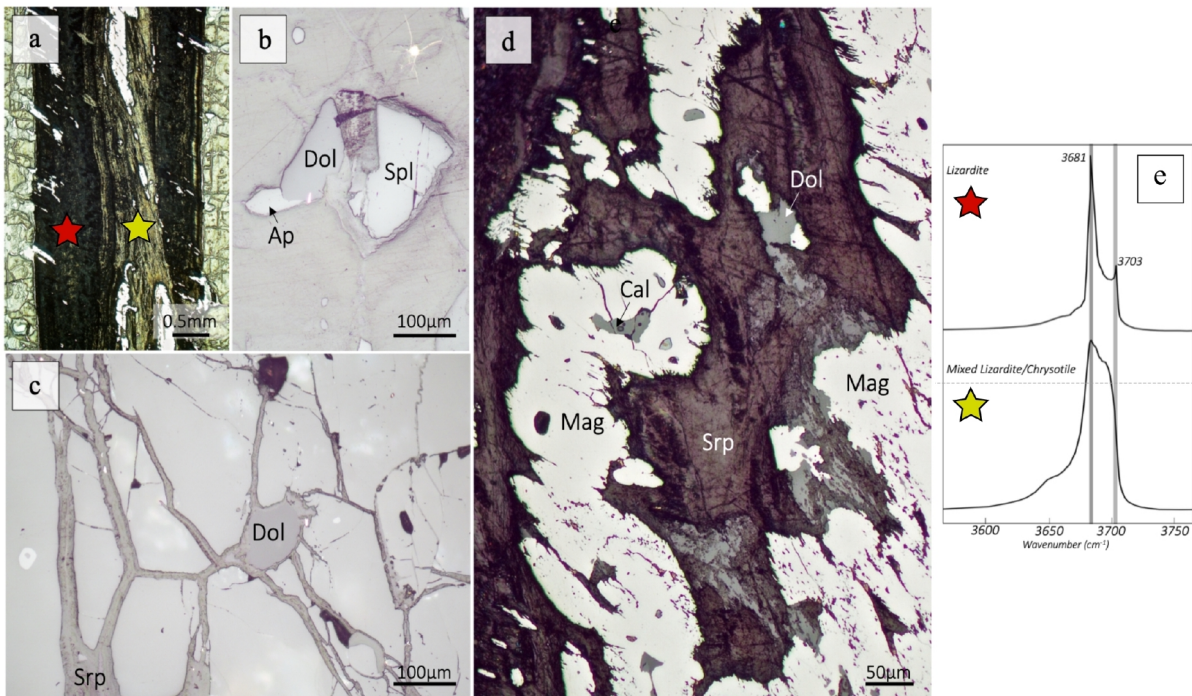
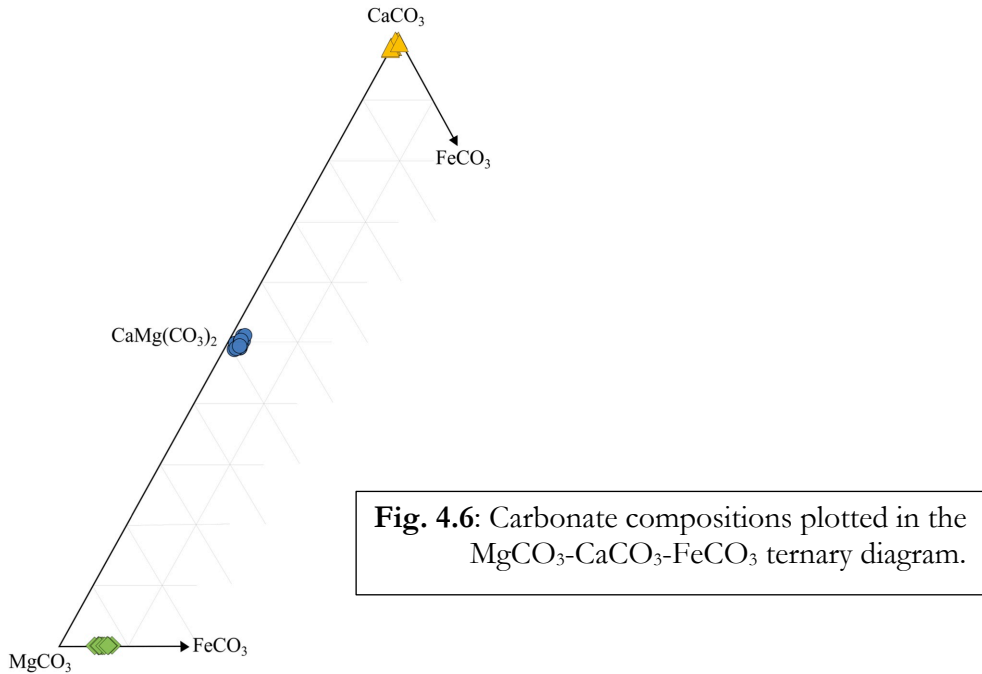


Fig. 4.7: (a) Zoned serpentine-rich vein cutting the MM1 fine-grained amphibole-chlorite peridotite with its constituting minerals under optical reflected light (b)-(c)-(d). (b) Matrix dolomite associated with Cl-apatite and spinel. (c) Matrix dolomite surrounded by serpentine. (d) Vein core consisting of serpentine + magnetite with calcite and dolomite included; (e) Micro-Raman spectra acquired in

4 • Carbonate occurrences and constraints on the carbon-bearing fluid sources

the OH region for a composite serpentine vein. Stars represent the analyzed spots. Mineral abbreviations after Whitney and Evans (2010).

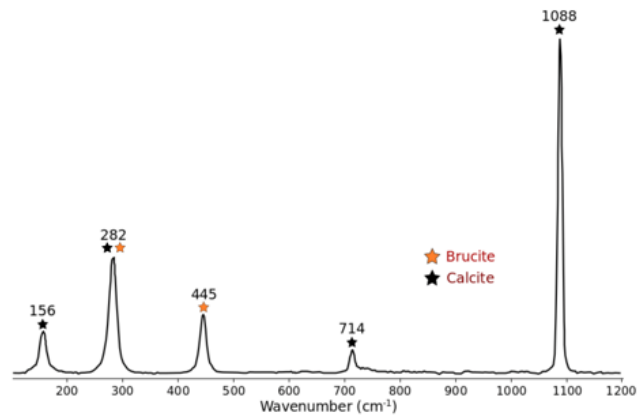
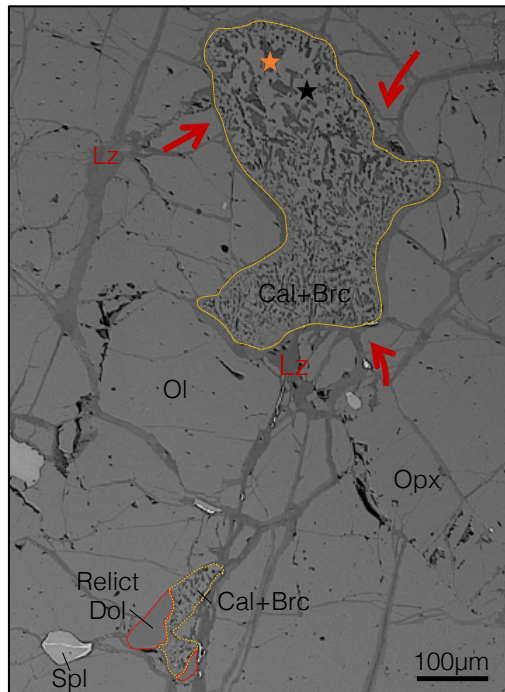


Fig. 4.8: a): BSE image of calcite-brucite intergrowths occurring in the fine-grained garnet- amphibole peridotite KL1-A. The stars indicate the spots of micro-Raman analyses whose spectra are reported in figure. The red arrows indicate serpentine surrounding calcite-brucite intergrowths. Mineral abbreviations after Whitney and Evans (2010).

Table 4.2: Main representative major elements compositions of minerals measured by EPMA.

Mineral M-type sample	Olivine			Enstatite			Diopside			Amphibole			
	C	F		C	F		C	F		C	F	C	
Generation	I	II	I	I	II	II	I	II	Relic in amph				
Comment	m	m	m	m	m	m	m	m		m	m	In mgs vein	In dol+chl+tr vein
SiO ₂	40.89	40.92	40.80	55.96	56.30	56.94	53.84	54.33	54.00	46.76	45.51	57.26	57.43
Al ₂ O ₃	bdl	bdl	bdl	2.80	2.51	1.40	1.41	1.27	1.01	10.88	12.01	1.32	0.91
MgO	49.72	49.04	49.23	33.80	33.84	34.61	17.01	17.22	17.47	19.20	18.33	23.20	23.40
CaO	bdl	bdl	bdl	0.27	0.32	0.18	24.78	24.83	24.23	12.06	12.37	12.86	12.92
K ₂ O	bdl	bdl	bdl	bdl	bdl	0.01	bdl	bdl	bdl	0.15	0.55	bdl	bdl
TiO ₂	bdl	bdl	bdl	bdl	bdl	bdl	0.05	bdl	0.12	0.21	0.48	bdl	bdl
FeO	9.57	9.51	9.37	6.33	6.40	6.29	1.56	1.81	1.70	3.07	2.81	2.09	1.70
MnO	0.14	0.15	0.12	0.19	0.11	0.15	0.07	0.06	bdl	bdl	bdl	0.10	bdl
Cr ₂ O ₃	bdl	bdl	bdl	0.26	0.17	0.18	0.38	0.25	0.29	0.85	1.67	0.16	0.26
Na ₂ O	bdl	bdl	bdl	bdl	bdl	bdl	0.22	0.22	0.23	2.39	1.95	0.37	0.19
NiO	0.41	0.37	0.40	bdl	0.11	0.02	bdl	bdl	bdl	bdl	bdl	0.06	0.07
Sum	100.72	100.06	99.95	99.70	99.81	99.76	99.58	100.18	99.05	95.57	95.68	97.36	96.95
Si	1.00	1.00	1.00	1.94	1.95	1.95	1.97	1.97	1.98	6.64	6.51	7.82	7.88
Ti	-	-	-				0.00	0.00	0.00		0.05		
Al	-	-	-	0.11				0.05	0.04	1.36	2.03	1.82	0.15
Cr	-	-	-	0.01	0.01	0.01	0.01	0.01	0.01	0.10	0.19	0.02	0.03
Fe ³⁺	0.00	0.00	0.00	0.00		0.00	0.00	0.00	0.00	0.34	0.28	0.22	0.11
Fe ²⁺	0.20	0.20	1.90	0.18	0.19	0.18	0.05	0.06	0.05	0.02	0.06	0.07	0.09
Mn	0.00	0.00	0.00	0.01	0.00	0.00	0.00	0.00				0.01	
Mg	1.80	1.79	1.81	1.74	1.74	1.78	0.93	0.93	0.95	4.07	3.91	4.07	4.79
Ca	-	-	-	0.01	0.01	0.01	0.97	0.97	0.95	1.84	1.90	1.84	1.90
Sum	3.01	3.00	3.00	4.01	4.01	4.00	4.01	4.01	4.00	10.55	10.56	10.01	10.00
Mg#	0.90	0.90	0.90	0.91	0.90	0.91	0.95	0.95	0.95	1.00	0.98	1.00	0.96

Mineral M-type sample	Pyrope		Cr-Spinel		Lizardite		Chlorite		Phlogopite		Apatite	
	F		C	F	C	F	C	F	C	F	C	F
Generation	I	II	I	II	I	II						

4 • Carbonate occurrences and constraints on the carbon-bearing fluid sources

Comment	P	m	m	m	In P-grt	m	vein	mesh	vein	In dol+chl+tr vein	m	m	m	m
SiO ₂	41.98	41.82	bdl	0.08	bdl	0.052	41.25	40.02	42.05	30.38	29.85	40.19	37.04	bdl
Al ₂ O ₃	22.6	22.12	45.43	26.47	30.67	37.73	0.34	0.49	0.13	19.08	20.04	14.63	15.07	-
MgO	19.03	18.63	16.13	8.95	9.46	13.93	40.41	39.89	39.53	31.65	32.16	25.53	28.32	bdl
CaO	5.38	5.63	-	-	-	-	bdl	bdl	bdl	0.04	bdl	bdl	bdl	53.45
K ₂ O	-	-	-	-	-	-	bdl	bdl	bdl	-	Bdl	8.35	5.22	-
TiO ₂	bdl	bdl	-	-	0.17	bdl	bdl	bdl	bdl	0.06	0.03	0.21	0.13	-
FeO	9.25	9.70	14.80	24.76	21.24	16.33	2.90	3.72	2.02	2.55	2.22	3.45	5.03	0.41
MnO	0.47	0.63	0.21	0.48	0.49	0.29	bdl	0.12	bdl	bdl	bdl	bdl	0.05	bdl
Cr ₂ O ₃	1.44	1.45	23.09	37.02	35.76	31.01	bdl	bdl	bdl	1.39	1.06	0.76	1.14	-
Na ₂ O	-	-	-	-	-	-	bdl	bdl	bdl	bdl	bdl	0.13	0.04	bdl
NiO	-	-	0.10	-	bdl	bdl	bdl	-	bdl	0.15	0.17	0.17	0.53	-
Cl	-	-	-	-	-	-	-	0.06	0.06	-	-	-	-	5.57
P ₂ O ₅	-	-	-	-	-	-	-	-	-	-	-	-	-	39.57
Sum	100.27	99.73	99.80	97.85	97.86	99.35	84.94	84.43	83.83	85.42	85.60	93.45	92.57	99.21
Si	2.99	3.01	0.00	0.00	0.00	0.00	6.23	6.13	6.38	2.92	2.85	2.87	2.67	-
Ti	-	-	-	0.00	0.00	0.00	-	-	-	0.00	0.00	0.01	0.01	-
Al(IV)	0.01	0.00	-	-	-	-	1.77	1.87	1.62	2.08	2.15	2.13	2.33	-
Al(VI)	1.90	1.87	1.48	0.99	1.12	1.29	-	-	-	0.08	0.11	0.21	-	-
Cr	0.08	0.08	0.51	0.93	0.87	0.71	-	-	-	0.11	0.08	0.03	0.106	-
Fe ³⁺	0.02	0.05	0.00	0.00	0.00	0.00	-	-	-	-	-	-	-	-
Fe ²⁺	0.53	0.54	0.34	0.66	0.55	0.40	0.04	0.05	0.03	0.20	0.18	0.21	0.30	0.06
Mn	0.03	0.04	0.00	0.01	0.01	0.01	-	0.02	-	-	-	-	-	-
Mg	2.02	1.99	0.67	0.43	0.44	0.60	9.09	9.10	8.94	4.53	4.58	2.72	3.04	-
Ca	0.41	0.44	-	-	-	-	-	-	-	0.00	0.00	-	-	10.18
Cl	-	-	-	-	-	-	-	0.016	0.01	-	-	-	-	1.68
P	-	-	-	-	-	-	-	-	-	-	-	-	-	5.97
Sum	8.00	8.00	3.00	3.00	3.00	3.00	15.76	15.86	15.63	9.95	10.00	7.90	7.93	17.90
Mg#	0.79	0.78	0.66	0.43	0.44	0.60	0.96	0.95	0.97	0.96	0.96	0.96	0.90	-

Olivine, enstatite and diopside generations are labeled I and II based on their composition and texture (see text for details); *C* coarse grained; *F* fine grained; *m* mineral in the matrix; *P* porphyroclast; *In P-grt* included in a porphyroblastic garnet; *mesh* mesh structure; *Bdl* below detection limit.

Table 4.3 Representative EPMA analyses of carbonate minerals. Values reported in wt.%. CO₂ reported to 100 for elements recalculations.

Sample	18LP1				MOL1-C				MM1				VM10A				
Type	Coarse				Coarse				Fine				Fine				
Mineral	Dol		Dol		Dol		Mgs		Dol		Dol		Dol		Dol		
Comment	Vein		In opx		Vein w/mgs		Vein		In liz vein		Matrix		In spl		In mag		
n	16	2σ	2	2σ	7	2σ	23	2σ	11	2σ	24	2σ	8	2σ	1	42	2σ
MgO	20.65	0.26	20.79	0.09	20.48	0.16	42.45	1.61	20.36	0.45	20.30	0.27	20.06	0.35	20.58	20.29	0.15
CaO	29.58	0.27	29.61	0.12	29.18	0.48	0.18	0.04	29.47	0.10	29.26	0.32	29.19	0.29	29.87	29.42	0.33
MnO	0.06	0.12	0.08	0.11	0.43	0.38	0.23	0.06	0.03	0.06	0.03	0.07	0.02	0.05	0.27	0.04	0.00
FeO	1.26	0.15	1.21	0.10	1.31	0.39	5.68	2.10	1.24	0.07	1.34	0.09	1.44	0.06	1.96	1.47	0.01
SrO	0.01	0.04	bdl	-	0.09	0.12	bdl	-	0.13	0.11	0.14	0.12	0.20	0.09	bdl	0.05	0.02
CO ₂	48.44	0.27	48.33	0.22	48.51	0.39	51.46	0.71	48.76	0.34	48.92	0.35	49.11	0.41	47.32	48.73	0.12
Sum	100.00	-	100.00	-	100.00	-	100.00	-	100.00	-	100.00	-	100.00	-	100.00	100.00	-
CaCO ₃	49.84	0.46	49.73	0.01	49.38	0.86	0.28	0.06	50.07	0.54	49.89	0.51	50.03	0.58	49.58	49.99	0.53
MgCO ₃	48.41	0.47	48.58	0.01	48.23	0.48	92.47	2.73	48.12	0.64	48.16	0.54	47.83	0.54	47.53	47.97	0.57
MnCO ₃	0.08	0.15	0.10	0.14	0.58	0.50	0.28	0.08	0.04	0.08	0.05	0.09	0.03	0.07	0.35	0.05	0.00
FeCO ₃	1.66	0.20	1.58	0.14	1.73	0.51	6.96	2.66	1.64	0.10	1.78	0.11	1.92	0.08	2.54	1.95	0.02
SrCO ₃	0.01	0.04	0.00	0.00	0.08	0.11	0.00	0.00	0.12	0.10	0.12	0.11	0.18	0.08	0.00	0.05	0.03
Mg/(Mg+Ca)	0.49	0.00	0.49	0.00	0.49	0.01	1.00	0.00	0.49	0.01	0.49	0.01	0.49	0.01	0.49	0.49	0.01

Sample	KL1-A				KL2.4-2b				KL2.4-3				KL1.6			
Type	Fine				Porph-fine				Porph-fine				fine			
Mineral	Dol		Dol		Cal		Dol		Dol		Cal		Cal		Dol	
Comment	Matrix		w/cal+brc		cal+brc		In spl		In spl, w/cal+brc		cal+brc pol.ag.		In spl (in grt)		vein	
n	22	2σ	6	2σ	4	2σ	4	2σ	9	2σ	2	2σ	2	2σ	30	2σ
MgO	20.51	0.23	20.05	0.08	0.33	0.30	20.01	0.30	20.13	1.20	0.38	0.11	0.00	0.00	19.58	0.44

4 • Carbonate occurrences and constraints on the carbon-bearing fluid sources

CaO	29.30	0.20	28.97	0.22	54.33	0.37	29.17	0.16	29.82	1.40	49.48	0.43	57.19	0.08	29.74	0.32
MnO	0.11	0.27	0.02	0.06	bdl		0.05	0.07	0.02	0.04	0.03	0.04	bdl		0.04	0.09
FeO	1.52	0.12	1.63	0.06	bdl		1.60	0.08	1.75	0.46	1.41	0.33	0.41	0.15	1.43	0.18
SrO	0.03	0.07	bdl		0.22	0.05	0.09	0.10	0.05	0.09	0.16	0.22	bdl		0.02	0.05
CO ₂	48.53	0.26	49.33	0.22	45.12	0.09	49.08	0.27	48.24	2.22	48.53	0.15	42.40	0.23	49.20	0.50
Sum	100.00-		100.00 -		100.00 -		100.00-		100.00	-	100.00 -		100.00-		100.00-	
CaCO ₃	49.55	0.22	49.82	0.25	98.93	0.77	49.99	0.45	50.36	1.77	96.59	0.66	99.44	0.20	51.15	0.61
MgCO ₃	48.27	0.39	47.96	0.27	0.85	0.76	47.72	0.46	47.27	1.50	1.04	0.31	000	0.00	46.86	0.68
MnCO ₃	0.15	0.37	0.03	0.08	0.00	0.00	0.07	0.10	0.02	0.05	0.04	0.06	000	0.00	0.05	0.12
FeCO ₃	2.00	0.15	2.18	0.08	0.00	0.00	2.14	0.10	2.29	0.54	2.15	0.51	0.56	0.20	1.92	0.25
SrCO ₃	0.02	0.06	0.00	0.00	0.22	0.05	0.08	0.10	0.05	0.08	0.16	0.23	0.00	0.00	0.02	0.05
Mg/(Mg+Ca)	0.49	0.00	0.49	0.00	0.01	0.01	0.49	0.00	0.48	0.02	0.01	0.00	0.00	0.00	0.48	0.01

bdl—Below detection limit, *w/cal+brc*—associated with cal+brc intergrowths

4.5.3 Sr isotope composition of Ulten Zone carbonates

In situ ⁸⁷Sr/⁸⁶Sr isotope ratio analyses are listed in Table 4.4. Carbonates were previously chosen and detected considering the grain size, the Sr concentration and the microstructural domain. Dolomite is the main C-repository, showing a grain size of mostly 30-70 μm . Calcite veins are too narrow (ca. 20-30 μm wide) to be measured by LA-MC-ICP-MS, while magnesite does not contain Sr. For this study we performed thirty-nine *in situ* analyses. Spot size analyses ranges between 55 and 100 μm , in relation to the carbonate size (see Table 4.4). The ⁸⁷Sr/⁸⁶Sr isotope ratios obtained for all the dolomites are reported in Figure 8 and range between 0.70360 ± 0.00007 and 0.71184 ± 0.00026 (n=36). The distribution of Sr isotopic compositions of all carbonates analyzed is shown in Figure 4.9.

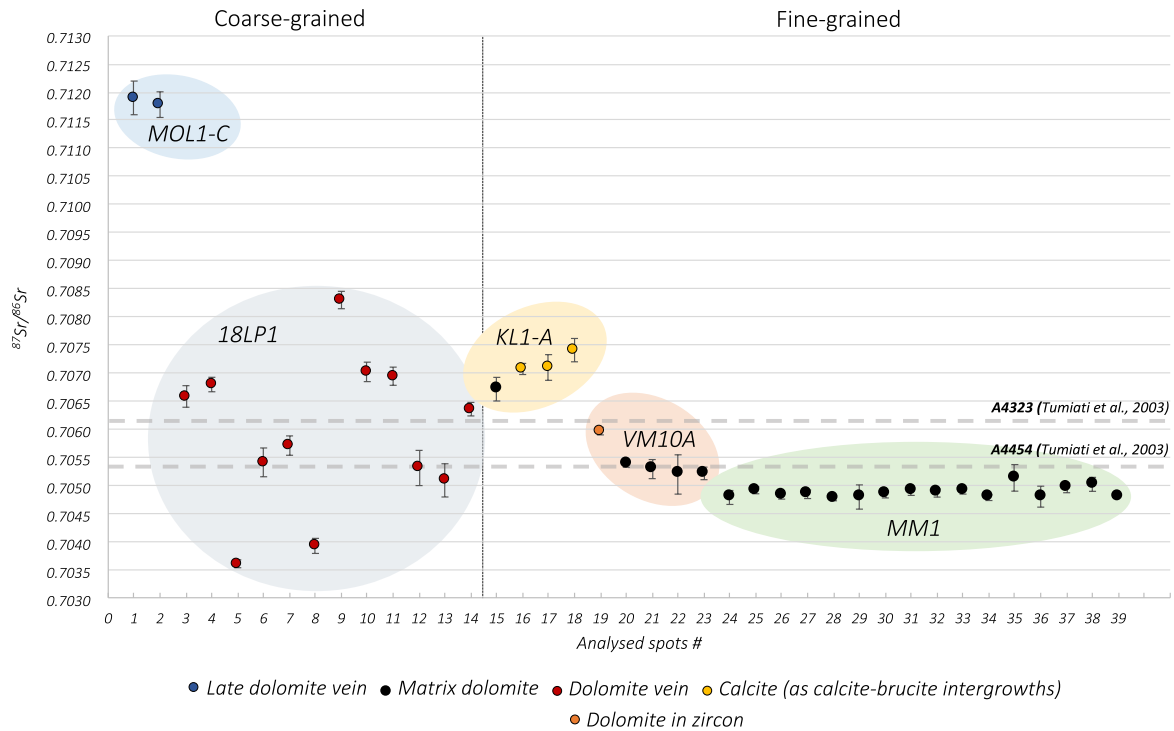


Fig. 4.9: Sr isotope ratios of dolomite and calcite occurring in different microstructural positions measured by LA-MC-ICP-MS. The error bars represent ± 2 standard errors. Whole rock $^{87}\text{Sr}/^{86}\text{Sr}$ ratios of fine-grained garnet-amphibole peridotite A4323 and coarse-grained spinel-garnet peridotite A4454 are from the investigation of Tumiati et al. (2003) and are given here for comparison.

In the coarse-type spinel peridotite *18LP1*, the dolomite vein associated with tremolite and chlorite exhibits highly variable Sr isotopic values ranging from 0.70360 ± 0.00007 to 0.70830 ± 0.00015 ($n=12$) (Figs. 4.8 and 4.10). Two lobate-shaped dolomite grains (spots 5, 8) shown in Figure 4.10 exhibit the lowest values of all UZ carbonates analyzed. In *MOL1-C* late vein dolomite cutting a magnesite vein (Fig. 4.5d) gives an average value of 0.71184 ± 0.00026 ($n=2$), representing the highest radiogenic ratio obtained by the *in-situ* Sr measurements of all Ulten carbonates-bearing peridotites of this study.

In three fine-grained peridotites, both dolomite and (when possible) calcite were analyzed. In Figure 4.9 it can be observed that the Sr isotopic ratio of matrix dolomite is nearly-homogeneous within the same sample and, conversely, different values were obtained from the different fine-type peridotites. In the mylonitic garnet-amphibole peridotite *VM10A*, the $^{87}\text{Sr}/^{86}\text{Sr}$ ratio of matrix dolomite is 0.70529 ± 0.00011 ($n=4$). In the same sample, a large dolomite inclusion (ca. 7 mm long) occurring in a zircon porphyroclast exhibits a $^{87}\text{Sr}/^{86}\text{Sr}$ ratio of 0.70597 ± 0.00007 , obtained by analyzing a line scan along the carbonate grain. In the fine-grained garnet-amphibole peridotite *KL1-A*, the dolomite $^{87}\text{Sr}/^{86}\text{Sr}$ ratio is 0.70671 ± 0.00021 whereas calcite (associated to brucite) gives slightly higher radiogenic values of about 0.70719 ± 0.00018 ($n=3$). It is worth noting that,

given the small size of calcite and brucite and their textural interconnection, both of them were included in the spots analyses. However, brucite is not supposed to incorporate Sr^{2+} and we therefore consider our data as exclusive for calcite. Average value of matrix dolomite in fine-grained amphibole-chlorite peridotite *MM1* is 0.70487 ± 0.00010 (n=16).

Table 4.4. $^{87}\text{Sr}/^{86}\text{Sr}$ and $^{87}\text{Rb}/^{86}\text{Sr}$ isotope ratio measured by LA-MC-ICP-MS for selected carbonates in Ulten Zone peridotites.

Sample and mineral	#	Microstructure	^{88}Sr (V)	$^{87}\text{Rb}/^{86}\text{Sr}$	$^{87}\text{Sr}/^{86}\text{Sr}$	2se	Spot Size (μm)
MOL1-C							
Dolomite	1	Vein	0.8	<0.0001	0.71189	0.00030	65
Dolomite	2	Vein	1.3	0.0002	0.71178	0.00023	65
18LP1							
Dolomite	9	Vein	1.4	<0.0001	0.70830	0.00015	100
Dolomite	10	Vein	1.6	<0.0001	0.70702	0.00017	100
Dolomite	11	Vein	1.3	<0.0001	0.70694	0.00016	100
Dolomite	8	Vein	2.4	<0.0001	0.70392	0.00013	90
Dolomite	7	Vein	1.2	<0.0001	0.70571	0.00017	90
Dolomite	6	Vein	0.8	0.0001	0.70541	0.00026	65
Dolomite	5	Vein	3.0	<0.0001	0.70360	0.00007	65
Dolomite	4	Vein	1.2	0.0003	0.70680	0.00013	65
Dolomite	3	Vein	1.5	0.0001	0.70658	0.00019	100
Dolomite	12	Vein	0.5	<0.0001	0.70531	0.00031	100
Dolomite	13	Vein	0.7	0.0001	0.70509	0.00030	100
Dolomite	14+	Vein	1.6	<0.0001	0.70636	0.00012	100
VM10A							
Dolomite	23	Matrix	3.4	<0.0001	0.70521	0.00011	65
Dolomite	22	Matrix	1.2	<0.0001	0.70519	0.00035	65
Dolomite	20	Matrix	3.4	<0.0001	0.70539	0.00006	65
Dolomite	21	Matrix	1.6	<0.0001	0.70529	0.00017	55
Dolomite	19+	In zircon	1.3	0.0011	0.70597	0.00007	55
KL1-A							
Dolomite	15	Matrix	1.2	0.0004	0.70671	0.00021	65
Calcite	16	In cal+brc	2.4	<0.0001	0.70707	0.00021	65
Calcite	17	In cal+brc	08	<0.0001	0.70709	0.00023	65
Calcite	18	In cal+brc	1.1	<0.0001	0.70741	0.00009	65
MM1							
Dolomite	24	Matrix	4.7	<0.0001	0.70486	0.00007	65
Dolomite	25	Matrix	4.4	<0.0001	0.70489	0.00005	65
Dolomite	26	Matrix	4.6	<0.0001	0.70478	0.00005	65
Dolomite	27	Matrix	4.5	<0.0001	0.70490	0.00008	65
Dolomite	28	Matrix	2.4	<0.0001	0.70502	0.00012	65
Dolomite	29	Matrix	3.3	<0.0001	0.70495	0.00008	65
Dolomite	30	Matrix	3.8	0.0002	0.70491	0.00006	65
Dolomite	31	Matrix	2.0	0.0005	0.70478	0.00012	65
Dolomite	32	Matrix	2.7	0.0004	0.70484	0.00008	65
Dolomite	33	Matrix	4.8	<0.0001	0.70481	0.00005	65
Dolomite	34	Matrix	1.3	<0.0001	0.70479	0.00022	65
Dolomite	35	Matrix	4.2	<0.0001	0.70477	0.00005	65
Dolomite	36	Matrix	2.9	0.0005	0.70484	0.00007	65
Dolomite	37	Matrix	1.7	0.0007	0.70513	0.00024	65
Dolomite	38	Matrix	1.5	0.0004	0.70480	0.00019	65

Dolomite	39	Matrix	3.6	<0.0001	0.70479	0.00006	65
----------	----	--------	-----	---------	---------	---------	----

(+) Analyses were collected along lines using the same spot size for spot analyses (i.e. 55 μm). *cal+brc* – calcite + brucite intergrowths.

4.6 Discussion

Petrographic data indicate that the UZ peridotites, during their complex metasomatic history, underwent carbonation and, locally, dolomite dissolution and calcite reprecipitation. To date, the crustal portion of the subducted continental slab has been considered as the source of the several metasomatic fluids that interacted with the UZ peridotites (Rampone and Morten, 2001; Scambelluri et al., 2006; Sapienza et al., 2009). The presence of hydrous phases (dissakisite-Ce, amphibole and minor phlogopite) enriched in LILE, Th, U, and LREE compared to other incompatible trace elements, as well as the occurrence of large zircon grains (Förster et al., 2017; this study), strongly support this interpretation. On the basis of textures, bulk rock and mineral major and trace element compositions, Ionov et al. (2017) suggested that most of the “crustal” overprint of the UZ occurred into the mantle wedge well below the crust (ca. 850°C at 60-90 km depths), in a supra-subduction setting similar to the mantle wedge sampled by harzburgite xenoliths from the western Pacific. Given the uncertainty of ‘crustal’ vs ‘mantle’ origin of metasomatizing fluids, the Sr concentration and isotopic signature of carbonates of the UZ peridotites may help to shed light on these contrasting views.

We will focus on C-related processes by simply dividing the metasomatic evolution into two main stages: (1) the *HP* carbonation of mantle wedge peridotites at peak (eclogite-facies) conditions and during their early exhumation up to mid-crust depth and (2) the carbon remobilization via fluid-rock interaction during the final exhumation of the crust-mantle mélange, which formed after the incorporation of mantle slivers into the subducted continental crust. The tectonic insertion of the peridotites into the host gneiss is believed to have occurred after peak pressure conditions (Scambelluri et al. 2006). We discuss these two processes separately, referring to them as Stage1 and Stage 2.

4.6.1 Stage 1: HP carbonation

4.6.1.1 Included and interstitial dolomite

The onset of the metasomatic history of the UZ peridotites started with percolation of melts into the spinel-facies mantle wedge, causing the formation of pyroxenite layers (Nimis and Morten, 2000). At this stage there is no petrographic evidence of carbonation. Conversely, the occurrence of lobate-shaped dolomite inclusion in a porphyroclastic zircon and matrix dolomites

in the fine-grained, garnet-bearing peridotites suggests that carbonation occurred when the Ulten peridotites reached peak eclogite-facies conditions (Fig. 4.11). If the zircon and dolomite formation are coeval as the petrographic observation suggests, a time constraint for this early episode of carbonation can be provided by the 333 Ma U-Pb age of zircon from metasomatic reaction bands at the Mt. Hochwart gneiss-peridotite contact (Tumiati et al., 2007), the same locality of sample VM10A of this study. Furthermore, in another fine-grained garnet-bearing peridotite we have a unique microstructural evidence of a dolomite inclusion in Cr-spinel, which is included in a porphyroclastic garnet. Major elements composition obtained with EPMA shows that this inclusion has the same composition as the matrix dolomite and dolomite veins. The origin of this inclusion is yet unknown (i.e. mantle provenance or subducted continental crustal derivation), but the occurrence of fractures in the host garnet may suggest that dolomite precipitation could have been induced during C-rich fluids percolation after spinel and garnet crystallization (in contrast to the interpretation of an early melt-related process in the high- T spinel stage given by Förster et al., 2017). At peak conditions, fluids prompted the precipitation of interstitial dolomite.

During continental collision, the crustal portion of the descending slab consists of the sedimentary cover and its underlying crystalline basement. The subducted lithologies may release fluids into the overhanging mantle wedge and their source can be investigated, at least in part, by considering fluid mobile elements (FME) such as Sr and the $^{87}\text{Sr}/^{86}\text{Sr}$ isotopic ratio. Different sources of the metasomatic liquids were considered for the *HP*-dolomite (both included and interstitial), as reported in Figure 4.12: (i) associated stromatic gneisses and orthogneisses; (ii) Devonian sedimentary cover; (iii) lithospheric mantle; (iv) trondhjemitic dykes and pockets.

- (i) Based on literature, we expected similar Sr isotopic ratio for the carbonates and the associated crustal rocks. However, the high $^{87}\text{Sr}/^{86}\text{Sr}$ ratio of stromatic gneisses (i.e. migmatitic paragneisses that suffered 20-30% degree of partial melting according to Braga and Massonne, 2012) and orthogneisses from the subducted crust and now part of the *mélange*, argues against their role as the sources for C-bearing fluids.
- (ii) It is difficult to assess the role of a sedimentary cover overlying the crystalline basement because of the lack of field evidence of Paleozoic sedimentary successions associated with the UZ crust-peridotite association. Subducted marine carbonates along the oceanic crust subduction prior to the subduction of the continental crust may also play a role in the formation of carbonates in the mantle wedge. However, the Sr isotope values reported by van Geldern et al. (2006) for well-preserved Devonian brachiopod shells ($\text{Mn} < 100$ ppm;

Fe < 400 ppm and Sr > 500 ppm) range from 0.70782 to 0.70804 (during the Emsian-Eifelian boundary and early Famennian respectively), unlikely representing the required sources for the interstitial dolomite in the matrix.

- (iii) The relatively unradiogenic values of matrix carbonates have Sr isotopic values close to those of the coarse-grained spinel-garnet peridotites of Tumiati et al. (2003), as shown in Fig. 4.12. Several studies (i.e. Tumiati et al. 2003 and Scambelluri et al. 2006) highlighted that the UZ peridotites were enriched in incompatible elements by reacting with fluids released from a subducting continental lithosphere undergoing partial melting. In particular, the enrichment of the UZ peridotite took place in the mantle wedge above the subduction zone (Scambelluri et al. 2006) by fluids variably equilibrated with mantle rocks (Ionov et al. 2017). In this scenario, the fluids responsible for the formation of matrix dolomite might have variably reacted with the lithospheric mantle previous depleted in incompatible elements and evolved towards slightly lower Sr isotopic compositions before crystallizing matrix dolomite.
- (iv) The radiogenic Sr signature of few trondhjemitic dykes and pockets described by Del Moro et al. (1999) are close to those reported for the matrix dolomite of the fine-grained mylonitic garnet-amphibole peridotite VM10A from Mt. Hochwart. Based on petrology and whole-rock Sr-Nd isotope geochemistry, Del Moro et al. (1999) interpreted the UZ trondhjemite as melts produced by fluid-assisted anatexis of a metasedimentary lower crust characterized by low Rb/Sr and Sr isotope ratios. Once formed, the trondhjemite melts intruded the UZ migmatitic crust.

4.6.1.2 Localized carbonation: carbonates veinlets

The tectonic insertion of mantle material into the crustal portion of the continental slab occurred after the attainment of maximum pressure conditions, i.e. at the beginning of the exhumation (Scambelluri et al., 2006). During this early phase of upwelling of the crust-mantle mélange, dolomite veins associated with tremolite and chlorite and magnesite + lizardite-crysothile + tremolite vein within the two coarse-type spinel peridotites suggest that carbonation occurs as local injection of C-rich fluids (Fig. 4.11) under different retrograde P - T conditions. The mineral assemblage of the dolomite + tremolite + chlorite vein supports the evidence of a retrograde process prior to serpentinization ($650^{\circ} \leq T \leq 700^{\circ} \text{C}$ at P of ca. 1 GPa) and, in addition, provides a minimum P - T estimate for the formation of the crust-mantle mélange.

The Sr isotopic heterogeneity (0.7035-0.7085; Figs. 4.9 and 4.10) measured in different dolomite grains from the dolomite + tremolite + chlorite vein encompasses the $^{87}\text{Sr}/^{86}\text{Sr}$ values measured from matrix and included dolomite. Most of the inter-grain variability can be explained by the interaction of the matrix and the included dolomite, which show low-Sr isotopic values, with progressively more radiogenic fluid, as it would be expected in mantle rocks closely associated with crustal lithologies. Similarly, late-stage carbonate veins in kimberlites from Beinfontein show a large variability of the Sr-isotope composition, reaching values of 0.70957 ± 116 (2σ). These results were interpreted as a consequence of primary carbonates interaction with crustal fluids (Castillo-Oliver et al., 2018), as we speculate for the UZ dolomite veins. It is not easy to explain the occurrence of low $^{87}\text{Sr}/^{86}\text{Sr}$ ratios (0.7036-0.7039; Figs. 4.9 and 4.10) of two dolomite grains in this vein. As shown in Figure 4.12, these values approach the MORB signature, thus requiring a distinct metasomatic agent with a Sr signature typical of a mantle reservoir depleted in radiogenic Sr, that precipitated primary carbonates without interacting with late-stage metasomatic crustal fluids.

The occurrence of a magnesite vein associated with lizardite-chrysotile and tremolite suggests influx of a local carbonaceous fluid at $T < 600^\circ\text{C}$ during the retrograde path. This vein is cut by a dolomite vein with the highest $^{87}\text{Sr}/^{86}\text{Sr}$ ratio (0.7118-0.7119; Figs. 4.5d and 4.9), which formed after the previously discussed vein dolomite. The highly radiogenic values of this vein suggest that this episode of injection of C-rich fluids occurred when the orogenic mélange, characterized by mingled crustal and mantle components, was already well developed and that infiltrating C-rich crustal fluids introduced significant amounts of radiogenic Sr (Fig. 4.12).

According to the geodynamic scenario of Ranalli et al. (2005), this mélange was brought to mid-crustal depths between 330 and 300 Ma reaching 0.7 GPa at 500°C .

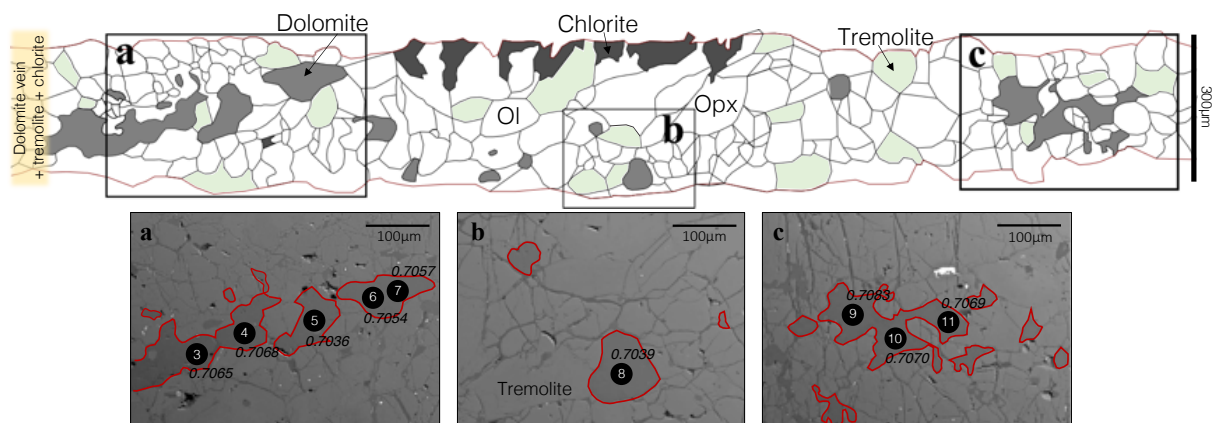


Fig. 4.10: Sketch of a dolomite vein in association with tremolite and chlorite occurring in peridotite 18LP1. BSE images with localization of spots for in situ Sr isotope analyses are also reported.

4.6.2 Stage 2. Carbon re-mobilization via fluid-rock interaction

Following the geodynamic model proposed by Ranalli et al. (2005), after the late Carboniferous fast exhumation, the crust-mantle mélange underwent slow exhumation and cooling during Permian-Triassic times (300-205 Ma). During this slow exhumation, Stage2 carbonation is related to the action of serpentinizing fluids, which in some instances erased the previous mantle texture. Here, C re-mobilization via fluid-rock interaction prevails (blue arrow, Fig. 4.11) as evidenced by the occurrence of (i) calcite + brucite intergrowths surrounded by serpentine (Figs. 4.5f and 4.7) and (ii) thin calcite veins.

The calcite + brucite intergrowths are the result of dolomite breakdown during interaction with aqueous fluids (Figs. 4.5f and 7) (Förster et al., 2017) and were found only in highly serpentinized fine grained garnet-bearing peridotites. Moreover, micro-Raman investigations allowed the identification of lizardite as the serpentine phase surrounding these intergrowths. If serpentinizing fluids were the cause of dolomite dissolution, we therefore argue that the precipitation of calcite + brucite probably occurred at P of about 0.5 GPa and $T < 300^\circ\text{C}$. At this stage the Ulten basement was likely subjected to isostatic adjustment after the conclusion of the Variscan collision (Ranalli et al., 2005).

The formation of thin calcite veins occurring in the matrix and in some instances crosscutting spinel, chlorite and phlogopite, was interpreted by Förster et al. (2017) as a consequence of the influx of serpentinizing fluids that triggered dissolution of the former dolomite and crystallization of calcite + brucite intergrowths with concomitant liberation of CO_2 , following the reaction $\text{CaMg}(\text{CO}_3)_2 + \text{H}_2\text{O} \rightarrow \text{CaCO}_3 + \text{Mg}(\text{OH})_2 + \text{CO}_2$. The release of CO_2 may prompt *in-situ* formation of carbonates (i.e. thin calcite veins) after C saturation was achieved.

During fluid-rock interaction, Sr preferentially partitions into the fluid phase (Banner et al., 1995) and the aqueous serpentinizing fluids, characterized by $^{87}\text{Sr}/^{86}\text{Sr} \approx 0.7070\text{-}0.7075$, dissolved dolomite that provided the local source of Sr. Eventually, the fluid enriched in C and Sr (from dolomite) precipitated relatively Sr-rich calcite. The higher elemental Sr abundance with respect to dolomite is due to the less incompatible behavior of Sr in calcite (Banner et al., 1995).

4.7 Conclusion and future directions

The combination of textural observation of carbonates with *in situ* Sr isotope analyses reveals a more complex metasomatic evolution for the UZ peridotite than previously thought. In

particular, two main conclusions can be drawn: (1) at peak (eclogite facies) conditions, there is not a simple carbon transfer between the crustal portion of a subducted continental and the overhanging wedge, but additional C sources are to be considered and (2) at low-pressure conditions, during the final exhumation stages of an already well developed crust-mantle mélange, the main carbonation process implies dolomite breakdown and calcite reprecipitation by H₂O-rich fluids.

The relatively unradiogenic Sr isotope ratio recorded by included and matrix dolomite, with some grains of a dolomite vein, does not support a simple derivation from fluids emanated from the migmatite host gneisses (Fig. 4.12). The first stage of carbonation thus requires *HP* metasomatic fluids (i.e. at ~ 2.5 GPa and 850°C) likely unrelated to the associated crust (stromatic gneisses and orthogneisses), as already recognized by Marocchi et al. (2009; 2007). We suggest that these *HP* fluids may have variably equilibrated with the depleted lithospheric mantle before the crystallization of matrix dolomite. Residual COH fluids originated from the crystallization of trondhjemite liquids intrusion derived from deeper portions of the Ulten crust or fluids released from Paleozoic carbonate succession and involved into the Variscan orogenesis can be considered as alternative sources for the metasomatic agents infiltrating at peak conditions and before the onset of serpentinization.

During the first stages of exhumation, C-bearing fluids were channeled into veins, giving rise to the veinlet filled with dolomite associated with tremolite and chlorite, followed at lower *P-T* conditions by the formation of the magnesite + lizardite-crysothile + tremolite veins. The fluids released by the crystallization of leucosomes of the host migmatites, showing variable CO₂/H₂O ratios as inferred by Rampone and Morten (2001), seem to be important metasomatic agents only at the end of the exhumation of the crust-mantle mélange, at temperatures consistent with lizardite stability, providing the highest Sr isotope values for the dolomite veins. The infiltration of serpentinizing fluids represents the last metasomatic episode of peridotites, leading to C-remobilization by dolomite dissolution and calcite precipitation with concomitant liberation of CO₂.

Evidence of both *HP* carbonation and carbonates dissolution-reprecipitation make these rocks an effective carbon locker and a “pit-stop” for C-remobilization through a mantle wedge. Consequently, the results of this study have implications for the global comprehension of the so called “Deep Carbon Cycle”. While in situ Sr isotope data have demonstrated useful to give us additional constrains on an overall complex multiphase metasomatic evolution, their main limitation is the restriction to relatively large grains ($\geq 50 \mu\text{m}$) and the less precision compared to dilution techniques. However, our approach ensures the textural control that is mandatory when

multiple generations of metasomatic minerals occur in the same sample and the errors obtained for the Ulten carbonates are far lower than the variability observed, allowing to clearly distinguish the different isotope patterns. Future higher resolution in-situ C and O isotope analyses of carbonates will allow to better constrain the sources of these C-bearing metasomatizing fluids.

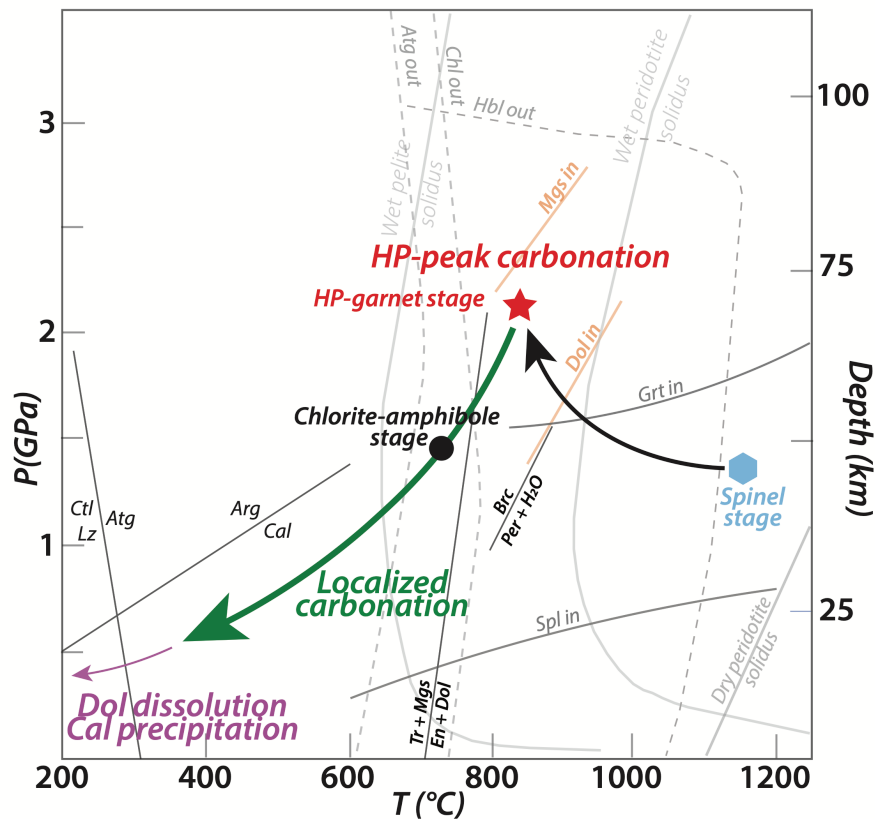


Fig. 4.11: P-T diagram showing the stages of carbonate formation during the metasomatic evolution of the Ulten peridotites modified after Consuma et al. 2020. See text for discussion. Reference curves: Dolomite-in, magnesite-in, dolomite-out, garnet-in curve from Tumiati et al. (2013); tremolite (Tr) + magnesite (Mgs) = enstatite (En) + dolomite (Dol) from Malaspina and Tumiati (2012) for $X_{CO_2} = 0.5$; brucite (Brc) = periclase (Per) + water (H_2O) from Schramke et al. (1982). Antigorite-out curve and chlorite-out curve from Fumagalli and Poli (2005). Antigorite = chrysotile (Ctl) / Lizardite (Liz) from Evans et al. (1976); aragonite = calcite from Johannes and Puhani (1971). The HP-garnet stage and chlorite- amphibole stage correspond to the geothermobarometric data obtained by Nimis and Morten (2000) and Sapienza et al. (2009).

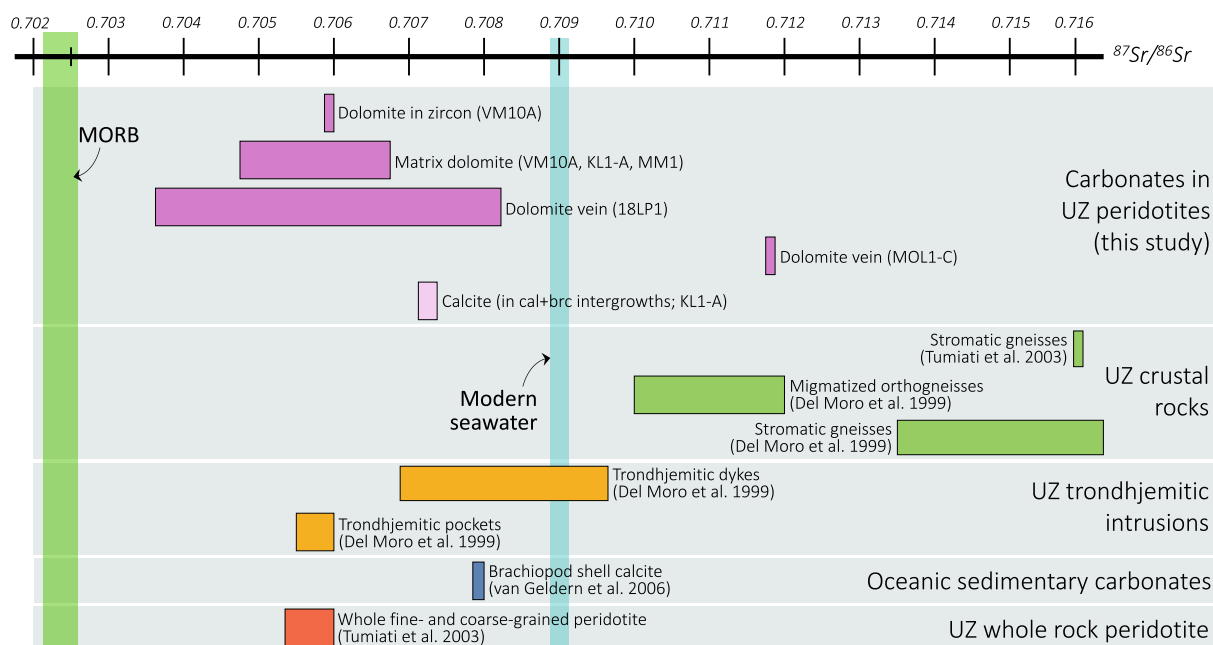


Fig. 4.12: Sr isotopic compositions of carbonates from the Ulten Zone peridotites in comparison with the potential sources of C-bearing fluids. MORB values were taken from Salters and Stracke (2004); the Sr-isotope values of stromatic gneisses and peridotites from Tumiati et al. (2003) and the values of stromatic gneisses, orthogneisses and trondhjemitic intrusions from Del Moro et al. (1999) were recalculated for $t = 330$ Ma, corresponding to the inferred age of the last isotopic homogenization event. The Sr-isotope values for the brachiopod shell calcites from van Geldern et al. (2006) correspond to an Early to Late Devonian (Emsian-Eifelian boundary and early Famennian) age.

Chapter Four — References

- Banner, J.L., 1995. Application of the trace element and isotope geochemistry of strontium to studies of carbonate diagenesis. *Sedimentology* 42, 805-824.
- Bebout, G.E., Penniston-Dorland, S.C., 2016. Fluid and mass transfer at subduction interfaces. The field metamorphic record. *Lithos* 240, 228–258.
- Braga, R., Sapienza, G.T., 2007. The retrograde evolution of a dolomite-bearing hydrous peridotite from the Ulten Zone (Italian Alps). *GeoActa* 6, 37–45.
- Braga, R., Massonne, H.-J., 2012. H₂O content of deep-seated orogenic continental crust: the Ulten Zone, Italian Alps, *International Geology Review* 54, 633-641.
- Brueckner, H.K., Medaris, L.G., 2000. A general model for the intrusion and evolution of ‘mantle’ garnet peridotites in high-pressure and ultra-high-pressure metamorphic terranes. *Journal of Metamorphic Geology* 18, 123–133.
- Castillo-Oliver, M., Giuliani, A., Griffin, W., L., O’Reilly, S., Y., 2018. Characterisation of primary and secondary carbonates in hypabyssal kimberlites: an integrated compositional and Sr-isotopic approach. *Mineralogy and Petrology*, 112, S555-S567.

- Del Moro, A., Martin, S., Prosser, G., 1999. Migmatites of the Ulten Zone (NE Italy), a record of melt transfer in deep crust. *Journal of Petrology* 40, 1803–1826.
- Dickin, A.P., 2018. Radiogenic isotope geology. 3rd edition, Cambridge University Press, 482.
- Evans, B.W., Johannes, W., Oterdoom, H., Trommsdorff, V. 1976. Stability of chrysotile and antigorite in the serpentinite multisystem. *Schweizerische Mineralogische und Petrographische Mitteilungen*, 56, 79-93.
- Förster, B., Braga, R., Aulbach, S., Pò, D.L., Bargossi, G.M.G.M., Mair, V., 2017. A petrographic study of carbonate phases in the Ulten Zone ultramafic rocks: insights into carbonation in the mantle wedge and exhumation-related decarbonation. *Ofioliti* 42, 105–127.
- Fumagalli, P., Poli, S., 2005. Experimentally determined phase relations in hydrous peridotites to 6.5 GPa and their consequences on the dynamics of subduction zones. *Journal of Petrology*, 46, 555-578.
- Gasparri, M., Bechstädt, T., Boni, M., 2006. Massive hydrothermal dolomites in the southwestern Cantabrian Zone (Spain) and their relation to the Late Variscan evolution. *Marine and Petroleum Geology* 23, 543-568.
- Giovanardi, T., Mazzucchelli, M., Lugli, F., Girardi, V.A., Correia, C.T., Tassinari, C.C., Cipriani, A., 2018. Isotopic constraints on contamination processes in the Tonian Goiás Stratiform Complex. *Lithos* 310, 136–152.
- Godard, G., Martin, S., Prosser, G., Kienast, J.R., Morten, L., 1996. Variscan migmatites, eclogites and garnet-peridotites of the Ulten zone, Eastern Austroalpine system. *Tectonophysics* 259, 313–341.
- Gudelius, D., Aulbach S., Braga, R., Höfer, H., Woodland, A.B., Gerdes A., 2018. Element transfer and redox conditions in continental subduction zones: new insights from peridotites of the Ulten Zone, North Italy. *Journal of Petrology* 60, 231-268.
- Hermann, J., Zheng, Y.-F., Rubatto, D., 2013. Deep fluids in subducted continental crust. *Elements* 9, 281–287.
- Ionov, D.A., Bigot, F., Braga, R., 2017. The Provenance of the Lithospheric Mantle in Continental Collision Zones: Petrology and Geochemistry of Peridotites in the Ulten–Nonsberg Zone (Eastern Alps). *Journal of Petrology* 58, 1451–1472.
- Johannes, W., Puhan, D., 1971. The calcite-aragonite transition, reinvestigated. *Contributions to Mineralogy and Petrology* 31, 28-38.
- Malaspina, N., Tumiati, S., 2012. The role of COH and oxygen fugacity in subduction-zone garnet peridotites. *European Journal of Mineralogy* 24, 607–618.
- Manning, C.E., 2014. A piece of the deep carbon puzzle. *Nature Geoscience* 7, 333.

- Marocchi, M., Hermann, J., Morten, L., 2007. Evidence for multi-stage metasomatism of chlorite-amphibole peridotites (Ulten Zone, Italy): constraints from trace element compositions of hydrous phases. *Lithos* 99, 85–104.
- Marocchi, M., Mair, V., Tropper, P., Bargossi, G.M., 2009. Metasomatic reaction bands at the Mt. Hochwart gneiss-peridotite contact (Ulten Zone, Italy): insights into fluid-rock interaction in subduction zones. *Mineralogy and Petrology* 95, 251.
- Martin, S., Godard, G., Prosser, G., Schiavo, A., Bernoulli, D., Ranalli, G., 1998. Evolution of the deep crust at the junction Austroalpine/Southalpine: the Tonale Nappe. *Memorie di Scienze Geologiche* 50, 3–50.
- Morten, L., Obata, M., 1990. Rare earth abundances in the eastern Alpine peridotites, Nonsberg area, Northern Italy. *European Journal of Mineralogy* 643–654.
- Müller, W., Prosser, G., Mancktelow, N.S., Villa, I.M., Kelley, S.P., Viola, G., Oberli, F., 2001. Geochronological constraints on the evolution of the Periadriatic Fault System (Alps). *International Journal of Earth Sciences* 90, 623–653.
- Nimis, P., Morten, L., 2000. P–T evolution of ‘crustal’ garnet peridotites and included pyroxenites from Nonsberg area (upper Austroalpine), NE Italy: from the wedge to the slab. *Journal of Geodynamics* 30, 93–115.
- Obata, M., Morten, L., 1987. Transformation of spinel lherzolite to garnet lherzolite in ultramafic lenses of the Austridic crystalline complex, northern Italy. *Journal of Petrology* 28, 599–623.
- Petrini, R., and Morten, L., 1993. Nd-isotopic evidence of enriched lithospheric domains: an example from the Nonsberg area, Eastern Alps. *Terra Nova* 5, 19–20.
- Rampone, E., Morten, L., 2001. Records of crustal metasomatism in the garnet peridotites of the Ulten Zone (Upper Austroalpine, Eastern Alps). *Journal of Petrology* 42, 207–219.
- Ranalli, G., Martin, S., Mahatsente, R., 2005. Continental subduction and exhumation: an example from the Ulten Unit, Tonale Nappe, Eastern Austroalpine. Geological Society, London, Special Publications 243, 159–174.
- Salters, V.J.M. and Stracke, A., 2004. Composition on the depleted mantle. *Geochemistry Geophysics Geosystems* 5, 1–27.
- Sapienza, G.T., Scambelluri, M., Braga, R., 2009. Dolomite-bearing orogenic garnet peridotites witness fluid-mediated carbon recycling in a mantle wedge (Ulten Zone, Eastern Alps, Italy). *Contributions to Mineralogy and Petrology* 158, 401–420.
- Scambelluri, M., Hermann, J., Morten, L., Rampone, E., 2006. Melt-versus fluid-induced metasomatism in spinel to garnet wedge peridotites (Ulten Zone, Eastern Italian Alps): clues from trace element and Li abundances. *Contributions to Mineralogy and Petrology* 151, 372.

- Schramke, J.A., Kerrick D.M., Blencoe J.G., 1982. Experimental determination of the brucite = periclase + water equilibrium with a new volumetric technique. *American Mineralogist* 67, 269-276.
- Tumiati, S., Thöni, M., Nimis, P., Martin, S., Mair, V., 2003. Mantle–crust interactions during Variscan subduction in the Eastern Alps (Nonsberg–Ulten zone): geochronology and new petrological constraints. *Earth and Planetary Science Letters* 210, 509–526.
- Tumiati, S., Godard, G., Martin, S., Klötzli, U., Monticelli, D., 2007. Fluid-controlled crustal metasomatism within a high-pressure subducted mélange (Mt. Hochwart, Eastern Italian Alps). *Lithos* 94, 148-167.
- Tumiati, S., Fumagalli, P., Tiraboschi, C., Poli, S., 2013. An experimental study on COH-bearing peridotite up to 3.2 GPA and implications for crust-mantle recycling. *Journal of Petrology* 54, 453-479.
- Van Achtebergh, E., Ryan, C.G., Jackson, S.E., Griffin, W.L., Sylvester, P., 2001. Laser-Ablation-ICPMS in the Earth Sciences- Principles and Applications. Mineralogical Association of Canada. 239-243.
- van Geldern, R., Joachimski M.M., Day, J., Jansen, U., Alvarez, F., Yolkin E.A., Ma, X.-P., 2006. Carbon, oxygen and strontium isotope records of Devonian brachiopod shell calcite. *Paleogeography, Palaeoclimatology, Palaeoecology* 240, 47-67.
- Weber, M., Lugli, F., Hattendorf, B., Scholz, D., Mertz-Kraus, R., Guinoiseau, D., Jochum, K.P. (2019) NanoSr-A – new carbonate microanalytical reference material for *In situ* Strontium isotope analysis. *Geostandards and Geoanalytical Research*.
- Whitney, D.L., Evans, B.W., 2010. Abbreviations for names of rock-forming minerals. *American Mineralogist* 95, 185–187.
- Zanetti, A., Mazzucchelli, M., Rivalenti, G., Vannucci, R., 1999. The Finero Phlogopite-Peridotite Massif: An example of subduction-related metasomatism. *Contributions to Mineralogy and Petrology* 134, 107-122.
- Zheng, Y.-F., 2012. Metamorphic chemical geodynamics in continental subduction zones. *Chemical Geology* 328, 5–48.
- Zheng, Y.-F., 2009. Fluid regime in continental subduction zones: petrological insights from ultrahigh-pressure metamorphic rocks. *Journal of the Geological Society* 166, 763–782.

5 • Trace elements and C-O isotope signature of texturally-diverse mantle wedge dolomite

Publication status: to be submitted.

Keywords: Carbonates, dolomite, trace elements, carbon isotope, oxygen isotope, mantle wedge

5.1 Abstract

Garnet bearing peridotite lenses are minor constituents in (ultra-)high-pressure metamorphic terranes, despite they are widely considered as key lithologies to further understanding the crust-mantle interactions in continental collision settings. These rocks occasionally contain carbonate phases, whose investigation may give crucial hints on the carbon mobility throughout collision zone orogens in the Earth's geological past. In the Ulten Zone, migmatites and garnet-kyanite gneisses embedding lenses of carbonated spinel and garnet peridotite witness the entrapment of ancient lithospheric mantle fragments into the continental subduction during the Variscan orogeny, and their exhumation as a crust-mantle *mélange* during a retrograde path. The integration of cathodoluminescence observations, trace elements composition and $\delta^{13}\text{C}$ - $\delta^{18}\text{O}$ of dolomite occurring in different textural positions within the Ulten Zone peridotite allowed us to shed light on the mechanisms, timing and geochemical signature of carbonate metasomatism. Dolomite grains across the peridotite suite show $\delta^{13}\text{C}$ of -16‰ to -8 ‰, $\delta^{18}\text{O}_{\text{VSMOW}}$ of +11‰ to +15‰, and various trace elements compositions. The isotopically lightest values of C, approaching those of mantle carbonates, were measured in a few grains of dolomite found in an orthopyroxenite layer within the coarse-grained spinel peridotite, and in dolomite inclusions within Cr-rich spinel included in garnet, attesting to a pre-peak carbonation metasomatism driven by percolating crust derived mafic melts in the spinel stage. The combination of the C-O isotopic signature ($\delta^{13}\text{C} \sim -10.9\text{‰}$ and $\delta^{18}\text{O}_{\text{VSMOW}} \sim +12.7\text{‰}$), trace elements compositions and previous Sr isotopic data (see Chapter 4) of matrix dolomite occurring along silicates grain boundaries indicate that geochemically different metasomatic agents prompted pervasive carbonation during high pressure conditions. In particular, a pronounced crustal affinity is revealed by the high concentration of B and LILE elements in matrix dolomite occurring in the peridotite from the hybrid contact zone

exposed in the M.te Hochwart. Instead, channelized carbonation initiated shortly after peak conditions is evidenced by veins of dolomite crosscutting both the fine-grained and coarse-grained peridotites, which were part of the exhuming mélange. The C isotope signature of these veins is fairly heterogeneous, encompassing the relatively wide range of $\delta^{13}\text{C}$ of dolomite measured in the study, whereas little variations in the $\delta^{18}\text{O}$ is observed. Oxygen isotope re-equilibration likely occurred within the exhuming crust-mantle mélange, where low T diluted fluids are expected to be liberated from the country gneisses and interact with the entrapped peridotite bodies. The involvement of progressive more diluted fluid is also consistent with the absence or little C isotope homogenization. Final dolomite dissolution is prompted by serpentinizing fluids of crustal affinity, which liberate CO_2 at shallow crustal levels and promote the formation of calcite/brucite intergrowths.

5.2 Introduction

The interface between the subducting slab and the supra-subduction mantle is a structural and lithological complex site that favor melt- and fluid-mediated volatile and elements transfer (Bebout and Penniston-Dorland, 2016; Debret and Sverjensky, 2017; Tumiati and Malaspina, 2019). When pressure reaches 3 GPa, this interface region is usually interested by a mixing of crustal slab and fragments of hanging-wall mantle to form tectonic *mélange* (Bebout and Barton, 2002; Bebout and Penniston-Dorland, 2016; Breeding et al., 2004; Cannaò et al., 2015).

In this regard, exhumed orogenic garnet peridotites found in a few mountain belts worldwide are known to provide natural records from the Earth's otherwise inaccessible interior. Their mineralogy and geochemistry may thus give access to the deep processes that occurred into the mantle fragments that at a certain point were entrapped into the continental subducting slab. This may have occurred under high pressure to ultra-high-pressure (HP-UHP) or late exhumation conditions. Despite this, orogenic mantle wedge involved in fossil continental subduction zones suffers scarce availability of exposed natural samples for direct investigations, thus remaining the least known domain within the *subduction factory* (Scambelluri et al. 2006).

The carbon budget of mantle fragments involved in subduction zones, is dictated by numerous and complex processes occurring at the slab-wedge interface: carbonation and veining favor respectively pervasive and localized carbon storage by carbonate precipitation, whereas carbon release and re-mobilization is triggered by dissolution, decarbonation, melting and formation of carbonic liquids (Frezzotti et al., 2011; Halama and Bebout, 2021; Kelemen and Manning, 2015; Piccoli et al., 2016; Stewart and Ague, 2020; Stewart et al. 2019; Vitale Brovarone et al., 2018). The understanding of these processes requires a targeted approach through detailed petrography, that is mandatory to reveal the mechanisms of carbonic fluid-flow (e.g. pervasive *vs.* channelized) and to understand the structural/mineralogical control of metasomatic agents that percolate the mantle wedge during continental collision.

Mg-rich carbonates are demonstrated to behave conservatively in subduction fluids so that they can be transferred to the deep mantle by subduction (Shen et al., 2018; Tao et al., 2018). Their capacity to store trace elements is also poorly studied, albeit it could be critical to address mantle enrichment processes and recycling of elements through metasomatism of carbonic fluids in response to dehydration of the subducted crust at high pressure conditions.

In this regard, the orogenic spinel and garnet peridotite of the Variscan Ulten Zone offer an ideal target to investigate the mantle wedge dolomite to further understand the carbonate metasomatism acting during and after the Variscan orogeny. As such, Ulten Zone peridotites record (i) pre-peak conditions, where the peridotites are still residing within the mantle wedge (or

lithospheric mantle?) far for the slab; (ii) high-pressure peak conditions, where peridotites are approaching the downgoing crustal slab as a consequence of corner flow, but are still within the mantle wedge; (iii) post-peak, retrograde, conditions where peridotites are incorporated into the upgoing country gneisses to form a tectonic *mélange*. Evidence of carbonate metasomatism in these rocks has been identified via the combination of detailed petrographic study and in situ Sr isotope measurements (Forster et al. 2017; Consuma et al. 2020). However, a deep investigation on stable isotope and trace elements budget of these carbontess is still needed.

We present cathodoluminescence petrography with trace element compositions and integrated C-O stable isotope signature of a texturally diverse dolomite from a mantle wedge involved in continental collision, with the aim to discriminate the processes that governed the poorly studied carbonate metasomatism at high P and T in the mantle wedge, and to provide additional constraints on the geochemical nature of the carbonic metasomatic agents that percolate the mantle wedge during continental collision. We discuss the processes that might have affected the isotope signature upon retrogression and introduce the $\delta^{18}\text{O}$ isotope composition of other crucial mineral phases, zircon and olivine.

5.3 Geological background

5.3.1 Petrological evolution and metasomatism in the Ulten Zone

The Ulten Zone is a fragment of the Variscan lower crust belonging to the Tonale Nappe of the Central Eastern Italian Alps. It forms a narrow belt NW-SE oriented, bounded by the Insubric and Giudicarie line to the south and by the Pejo Line to the north. Leucocratic migmatites, garnet-kyanite gneisses and orthogneisses are representative of the Ulten crust and outcrop as a ‘subduction *mélange*’ (Ranalli et al. 2003) by enclosing barrel-shaped lenses of eclogites and spinel- and garnet-bearing peridotite partially altered to serpentinite \pm chlorite. Peridotites generally form a discontinuous horizon between the garnet-kyanite gneisses and the overlying migmatite and orthogneiss (Martin et al. 1998), but they also occur as boulders detached from outcrops as a consequence of glacial events, thus erasing any form of structural and field characteristic. When found in situ, such as in M.te Hochwart, both crustal rocks and enclosing peridotite bodies are occasionally cut by pegmatitic and trondhjemitic dikes, whereas in some cases these dikes stop at the edge of the peridotite and do not affect the neighboring migmatite (Marocchi et al. 2009).

The Ulten Zone peridotite record the transition from protogranular spinel peridotite to fine-grained garnet-amphibole peridotite and chlorite-amphibole peridotite as a result of the

incorporation of mantle fragments into the downgoing (Godard et al. 1999; Nimis and Morten 2000) or upgoing (Tumiati et al. 2003; Scambelluri et al. 2006) continental slab during the Variscan orogeny. Peak conditions based on pyroxenes-garnet thermobarometry are 2.7 GPa and 850°C (Nimis and Morten, 2000).

The Ulten Zone peridotite underwent a complex multi-stage metasomatism during the prograde to peak and peak to retrograde path. M1 is the early, poorly studied, metamorphic event where percolating melts (possibly slab-derived) led to LREE and LILE enrichment in the overlying spinel peridotite and in the porphyroblastic orthopyroxene of the chlorite peridotite (Scambelluri et al. 2006; Marocchi et al, 2007). This interaction likely occurred at 1200°C and P of 1.5 GPa (Scambelluri et al. 2006). Peak metamorphism occurred at much lower temperature (850°C) but high pressure (< 2.7GPa). Here, the peridotite is affected by aqueous fluid carrying a CO₂ component released by the subducted continental crust, crystallizing pargasite-to-hornblende amphibole, accessory dolomite and favoring the consumption of clinopyroxene to form garnet. Amphibole plays a major role in storing trace elements (Scambelluri 2006; Sapienza 2009), whereas high-pressure dolomite is the major repository for Sr, Ba, Pb and subordinately LREE (Gudelius et al. 2019; Sapienza et al. 2009). Besides trace elements compositions of matrix high-pressure dolomite, the only more detailed investigation on carbonates is presented by the ⁸⁷Sr/⁸⁶Sr signature of dolomite and calcite reported in Consuma et al. (2020). This study reveals that carbonate metasomatism is related to different sources and processes, which requires further investigation. It is unquestionable that the Ulten Zone peridotites were affected by extensive crustal metasomatism, as also indicated by the strong Light Rare Earths (LREE) and Large Ion Lithophile Elements (LILE) enrichment (Rampone and Morten, 2001). However, the origin of the carbonate metasomatism is still largely unknown and recent studies reveal a more complex origin than the simple slab-to-wedge element transfer. This calls for further investigations.

5.3.2 Sample occurrence and description

The herein investigated spinel and garnet peridotite lenses outcrop within migmatites and gneisses in different locations of the Ulten Zone, thus representing different domains of an ancient mantle wedge involved into the Variscan continental subduction and exhumed as a crust-mantle mélange. Carbonated spinel and garnet peridotite are the focus of this study and the sample suite was chosen on the basis of carbonate textural occurrences, major element composition and *in situ* Sr isotope (Consuma et al., 2020). The main phases of carbonate metasomatism are summarized as follows: M1) Pre-peak stage; M2) Peak metamorphism; M3) Retrograde veining; M4) late

serpentinization. Metasomatic phases, petrographic and petrologic characteristics are summarized hereafter and in Table 5.1.

Table 5.1: Selected carbonated spinel and garnet peridotite from the Ulten Zone. For detailed petrography the reader is referred to Chapter 4.

Size	Sample	Lithotype	Facies	Carbonate stage	Serp. Grade	Dolomite	Magnesite	Calcite/brucite intergrowths
C	MOL1-C	peridotite	Spl	#4	M	Late vein	Vein w/srp/tr	No
C	MOL1-C	pyroxenite	Spl	#1	No	Matrix	No	No
C	18LP1	peridotite	Grt	#3	M	Vein	In dol vein	No
F	KL1-A	peridotite	Grt	#2 #4	H	matrix	x	matrix
P	KL2.4-2b	peridotite	Grt	#1 #2 #4	H	In spl/matrix	No	In spl/matrix
F	VM10A	peridotite	Grt	#2	No	matrix	No	No
P	VM25P10A	peridotite	Grt	#1? #2	No	In zircon	No	No
F	MM1	peridotite	Spl	#2	H	matrix	No	No
F	MM1B	Vein in MM1	-	#4	H	In mag	No	No

Size: C—coarse-grained; F—fine-grained; P—porphyroclastic; **Facies:** Spl—spinel; Grt—garnet; **Serpentinization grade:** M—medium; H—high; **Mineral abbreviations:** mag—magnetite; srp—serpentine; tr—tremolite.

Coarse grained spinel peridotite and pyroxenite MOL1-C

The protogranular (coarse-grained; Obata and Morten 1987) lithotype escaping garnet crystallization is rarely preserved in the field, thus explaining the poor literature addressed to the early stages of the Ulten Zone peridotite. The MOL1-C peridotite matrix is coarse-grained equigranular Ol + Opx + Amph + Spl ± Srp, characterized by the absence of relics of clinopyroxene and garnet, which likely indicate an incomplete equilibration under eclogite-facies conditions (Consuma et al., 2020). A magnesite + serpentine + tremolite vein cut the peridotite matrix and is later perpendicularly cut by a thin dolomite vein. As a whole, this peridotite was affected by carbonate metasomatism during M4.

Peridotite MOL1-C also hosts an orthopyroxenite layer characterized by the presence of dolomite locally associated with matrix pentlandite. The latter is interpreted as the result of melt percolation carrying a CO₂ and S component (Chapter 6) in the spinel facies conditions (M#1), in accordance with Scambelluri et al. (2006).

Coarse-grained spinel (± garnet) peridotite 18LP1

A coarse-grained matrix of Ol + Opx + Spl ± Cpx ± Chl ± Grt is crosscut by a vein of dolomite + tremolite + chlorite. Mineralogical assemblages and the superposition of the serpentine veins over the dolomite vein suggest that dolomite formation precedes these serpentinization processes and

it is therefore related to Stage M3 (Consuma et al., 2020). Rare magnesite also occurs within the dolomite vein.

Porphyroblastic garnet-amphibole peridotite KL24.2b and VM25P10A

KL24-2b contains porphyroclastic pyrope-rich garnet that includes mm-sized Cr-rich spinel ($\text{Cr}/(\text{Cr}+\text{Al}) = 0.43$; Consuma et al., 2020) in a matrix of equigranular Ol + Opx + Amph + Spl \pm Cpx. Garnet is surrounded by a kelyphitic corona of Opx + Amph + Cpx + Spl \pm pentlandite. The included spinel grains host very rare regular-shaped inclusions of dolomite associated with calcite/brucite intergrowths, interpreted as a result of dolomite dissolution (Förster et al., 2017). Dolomite inclusion is possibly related to Stage M1, whereas calcite/brucite intergrowths are related to Stage M4. Several spinels also contain different polycrystalline aggregates of carbonates + apatite + sulfides + other metasomatic minerals.

VM25P10A contains a large pink cm-sized zircon in an equigranular olivine + enstatite + hornblende + garnet \pm spinel \pm diopside \pm allanite matrix. Zircon porphyroclast is euhedral and highly fractured, and contains three lobate-shaped dolomite grains which include Cl-apatite and chlorite grains (Figs. 5.1/c and 5.3). This peridotite is not serpentized.

Fine-grained equigranular garnet-amphibole peridotite VM10A, KL1-A and KL1.6

VM10A, KL1-A and KL1.6 are equigranular fine-grained garnet-amphibole peridotites. They are characterized by same mineralogical assemblages with the exception of serpentine, which pervades only peridotite KL1-A and KL1.6 throughout fractures that cut the fine-grained matrix. Dolomite occurs interstitial in peridotite VM10A and KL1-A, whereas it occurs as vein in KL1.6. Calcite/brucite intergrowths are found only in the serpentized peridotites KL1-A and KL1.6, occurring interstitial in the matrix associated with relic dolomite (Fig. 5.2/b1-b2), and within the dolomite veinlet (Fig. 5.2/d), respectively in peridotite KL1-A and KL1.6. VM10A locally contains allanite grains. Calcite+brucite intergrowths related to Stage M4 are found in the matrix of peridotite KL1-A associated with relics of dolomite and surrounded by lizardite. Both samples contain matrix dolomite grains related to Stage M2.

Fine-grained chlorite-amphibole peridotite MM1 and serpentine vein MM1B

MM1 is an equigranular peridotite with a fine-grained matrix of Ol + Opx + Cpx + Spl \pm Chl \pm Dol that is cut by a composite (lizardite/chrysotile) serpentine vein (labelled MM1) carrying a large amount of magnetite \pm dolomite \pm calcite. Matrix dolomite in peridotite MM1 is related to Stage

M2 whereas dolomite and calcite inclusions in magnetite within lizardite/chrysotile vein MM1B to Stage M4 (see Fig. 4.7 in Chapter 4). Calcite/brucite intergrowths were not observed in fine-grained chlorite-amphibole peridotites. None of these samples were investigated by SIMS.

Overall, the investigated peridotites' suite experienced carbonate metasomatism. The coarse-grained peridotite, which represents the precursor of the fine-grained garnet-amphibole lithotypes (Obata and Morten 1987), was mostly affected by channelized carbonation, whereas the recrystallized fine-grained peridotite experienced pervasive carbonation as shown by matrix dolomite.

5.4 Methods and analysis strategy

5.4.1 Cathodoluminescence petrography

Polished thick sections representative of the main metamorphic stages of Ulten Zone peridotites and hosting textural diverse carbonates were prepared for cathodoluminescence (CL) petrography, with the aim to target *in-situ* isotope and trace elements analyses of carbonates. CL observations were conducted at the University of Lausanne using an optical cold cathodoluminescence system ERI-MRTech mounted on a petrological microscope with a voltage of ca. 8kV and a current of 0.4mA. Spots analyses performed with SIMS are reported in overlay with CL images after using QGIS, following the georeferencing method of Linzmeier et al. (2018).

5.4.2 Trace elements compositions

Trace element concentrations were measured in olivine, orthopyroxene, clinopyroxene, spinel, garnet, as well as metasomatic phases such as amphibole, apatite, chlorite, phlogopite, serpentine, zircon and carbonate phases (dolomite and magnesite) on ca. 70 μm polished thick sections at the IGG-CNR, Pavia using a triple quadrupole 8900 QQQ (Agilent) coupled to a 193nm excimer laser Geolas 102 (Microlas) housed at the IGG-CNR of Pavia (Italy). Data reduction was carried out using the “Glitter” software package (Van Achterbergh et al., 2001). LA-ICP-MS measurements were conducted taking care of the mineral grain size, presence of cracks and inclusions and different colors observed under CL investigation. NIST612 standard was used for external sensitivity calibration and the concentrations of SiO₂ and CaO (for dolomite) determined by EPMA were used as internal standards.

5.4.3 SIMS measurements for C and O isotope

Carbon and oxygen isotope measurements were carried out at the SwissSIMS facility (University of Lausanne, Switzerland) using the CAMECA IMS 1280HR large radius multi-collector SIMS. Isotope ratios are reported in δ notation (‰), relative to VDPB – Vienna Standard Mean Ocean Water and VSMOW – Standard Mean Ocean Water, respectively. Carbonate grains representative of the main metasomatic stages from all the peridotite samples were cut from thick sections and pressed into indium mounts with according standard materials placed in the center of the mounts. The same strategy was applied for olivine grains from peridotite MOL1-C, and the highly-fractured porphyroclastic zircon that hosts lobate-shaped dolomite grains from the peridotite VM25P10A. A Bruker Contour GTK white light interferometric microscope was used to check the indium mounts topography and showed accurate conditions for the analyses ($<7\mu\text{m}$ of flatness). As a final step, the surface of indium mounts was made conductive with a 35-40 nm gold coating.

5.5 Results

5.5.1 Cathodoluminescence petrography

With the aim to target *in situ* analyses of carbonates, CL petrography was performed in order to reveal some petrographic features otherwise hidden under optic polarized microscopy and BSE imaging. Contents of Fe, Mn and trace elements are critical in enhancing and quenching luminescence of the investigated material. The Ulten Zone dolomite contains significant Fe content ($X_{\text{FeCO}_3} = 0.02$; Consuma et al. 2020), which may quench the luminescence (Habermann et al. 2000). On the other hand, CL imaging is highly sensitive to trace element variations and to concentrations of Mn^{2+} , which is an efficient activator of the luminescence even at ppm-levels (Habermann et al., 2000). The measured concentrations of $\text{Mn}^{2+} > 500$ ppm (Table 5.3) in the investigated dolomite grains allowed the use of CL colors and superposition criteria to recognize different stages of carbonate metasomatism. CL colors of dolomite, calcite, and porphyroclastic zircon are summarized in Table 5.2 and illustrated in Figures 5.1, 5.2 and 5.3. As a whole, the relative chronology of dolomite formation based on CL colors is: dark green, dull green, dark red, light green, orange, bright yellow.

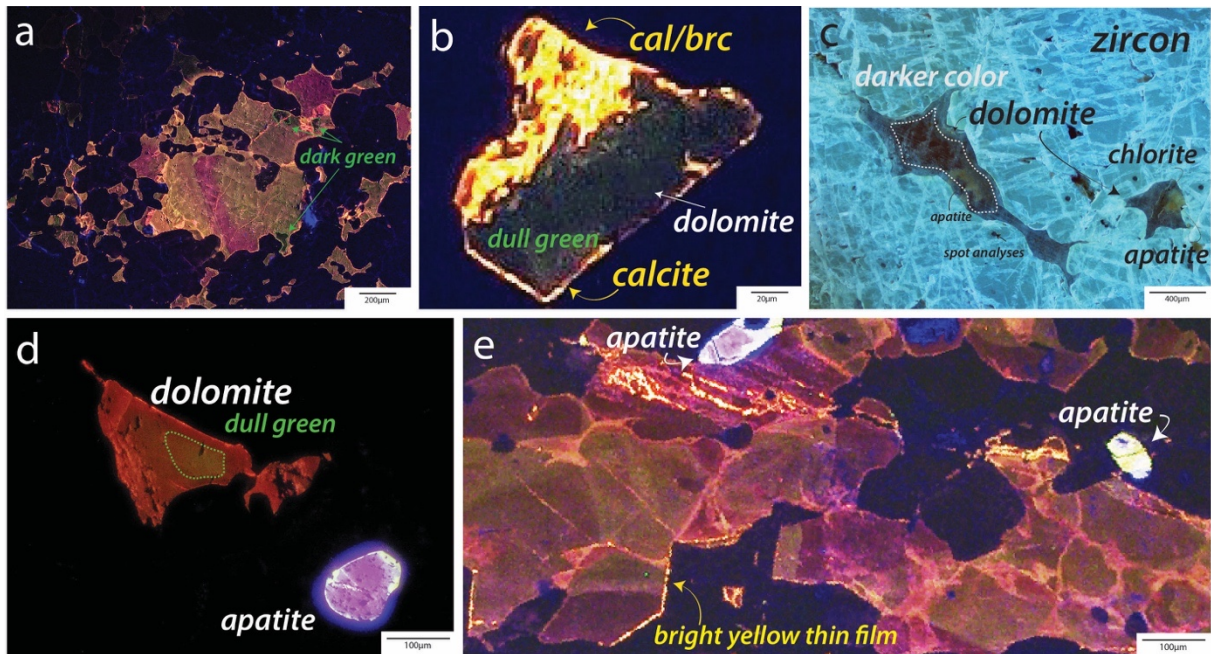


Fig. 5.1: CL images of carbonates representative of the main textural occurrences. **a)** interstitial dolomite in the orthopyroxenite layer within the coarse-grained spinel peridotite MOL1-C. Here, all the CL colors observed in the Ulten Zone dolomite are visible.; **b)** The regular-shaped dolomite is included in a Cr-rich primary spinel within pyrope-rich garnet (peridotite KL24-2b). We distinguish a dull green color of the dolomite which is rimmed by a bright yellow thin film of calcite. The bright yellow color is given by the calcite that is finely intergrown with brucite.; **c)** Two grains of dolomite, one including apatite and one including chlorite + apatite, are characterized by lobate-shaped boundaries with the host zircon. The CL colors of dolomite is depressed by the high luminescence of the host zircon, however, a dull green color is observed. **d)** A dolomite grain interstitial to matrix silicates in the fine-grained garnet-amphibole peridotite VM10A. The dull green core is surrounded by a red rim that in turn is surrounded by a thin bright orange film. Note that apatite is also luminescent and zoned; **e)** heterogeneous CL colors of dolomite in the vein from peridotite 18LP1. The dull green color suggests growth zoning. Please note that the brightness of the CL colors is emphasized with the use of Photoshop program.

Dolomite interstitial to orthopyroxene (Fig. 5.1a) in the orthopyroxenite layer from the coarse-grained spinel peridotite MOL1-C shows various CL colors, which are also observed in dolomite vein from the coarse-grained spinel (\pm garnet) peridotite 18LP1 (Fig. 5.1e). In some cases, the discrimination of the observed CL colors is made enigmatic by their ambiguous superposition, which is possibly related to the contemporaneity of liquids infiltration defined by a different geochemical signature.

The regular-shaped dolomite inclusions associated with calcite/brucite intergrowths within large spinel in garnet shows a dull-green color, which corresponds to the oldest generation, surrounded by the orange color towards the rim and finally rimmed by bright yellow calcite thin films (Figs. 5.1 and 5.2). Of interest are the radial fracture infillings of bright yellow calcite, which emerges along fractures in the coarse spinel. These fracture infillings originate from the kelyphitic

corona to cut apatite which is part of a polycrystalline inclusion (Fig. 5.2/a). The same color sequence is found in the dolomite interstitial to matrix silicates.

Highly fractured zircon shows weak zoning under optical CL (Fig. 5.3), but a more intense blue color is observed towards the rim. The light-blue core of the zircon hosts three lobate-shaped dolomite grains (Fig. 5.1/c), whose CL colors are quenched by the high CL response of the host mineral. It is anyway visible the dull green color that characterizes the core of dolomite grains, whereas the rim recalls the CL color of the host.

The dolomite vein from the coarse-grained spinel (\pm garnet) peridotite 18LP1, previously analyzed by *in situ* Sr isotope (Consuma et al., 2020), shows a wide range of colors. Differently from the interstitial matrix dolomite within the orthopyroxenite layer, the dark red colors are likely related to Stage 1, followed by dark green (Stage 2), dull green (Stage 3), light green (Stage 4), orange (Stage 5), bright yellow (Stage 6) (Fig. 5.1). Of interest is the dull green color dolomite domain, which shows growth zoning.

Magnesite, which does not show luminescence under CL, was not considered because magnesite standards are not available for SIMS measurements.

Table 5.2: Summary of observed CL colors of Ulten Zone carbonates and zircon.

Mineral	Texture	CL color
Dolomite	Inclusion	Dull green surrounded by thin film of bright yellow calcite
Dolomite	Interstitial to matrix silicates	Dark orange and dull green usually rimmed by bright orange thin films.
Dolomite	Interstitial to matrix silicates in pyroxenite layer	Dark red (Stage #1), dark green (Stage #2), dull green (Stage #3), light green (Stage #4), orange (Stage #5), bright yellow (Stage #6)
Dolomite	Vein	Dark red (Stage #1), dark green (Stage #2), dull green (Stage #3), light green (Stage #4), orange (Stage #5), bright yellow (Stage #6)
Calcite	Intergrowths with brucite, thin films filling fractures, dolomite rims, mineral cleavage	Bright yellow (to note, luminescence can result in different brightness as a result of different operating conditions used to emphasize the luminescence of the grain under investigation).
Zircon	Porphyroclast	Light blue. Intra-grain slight zonation with more intense blue, also shown at the rim.

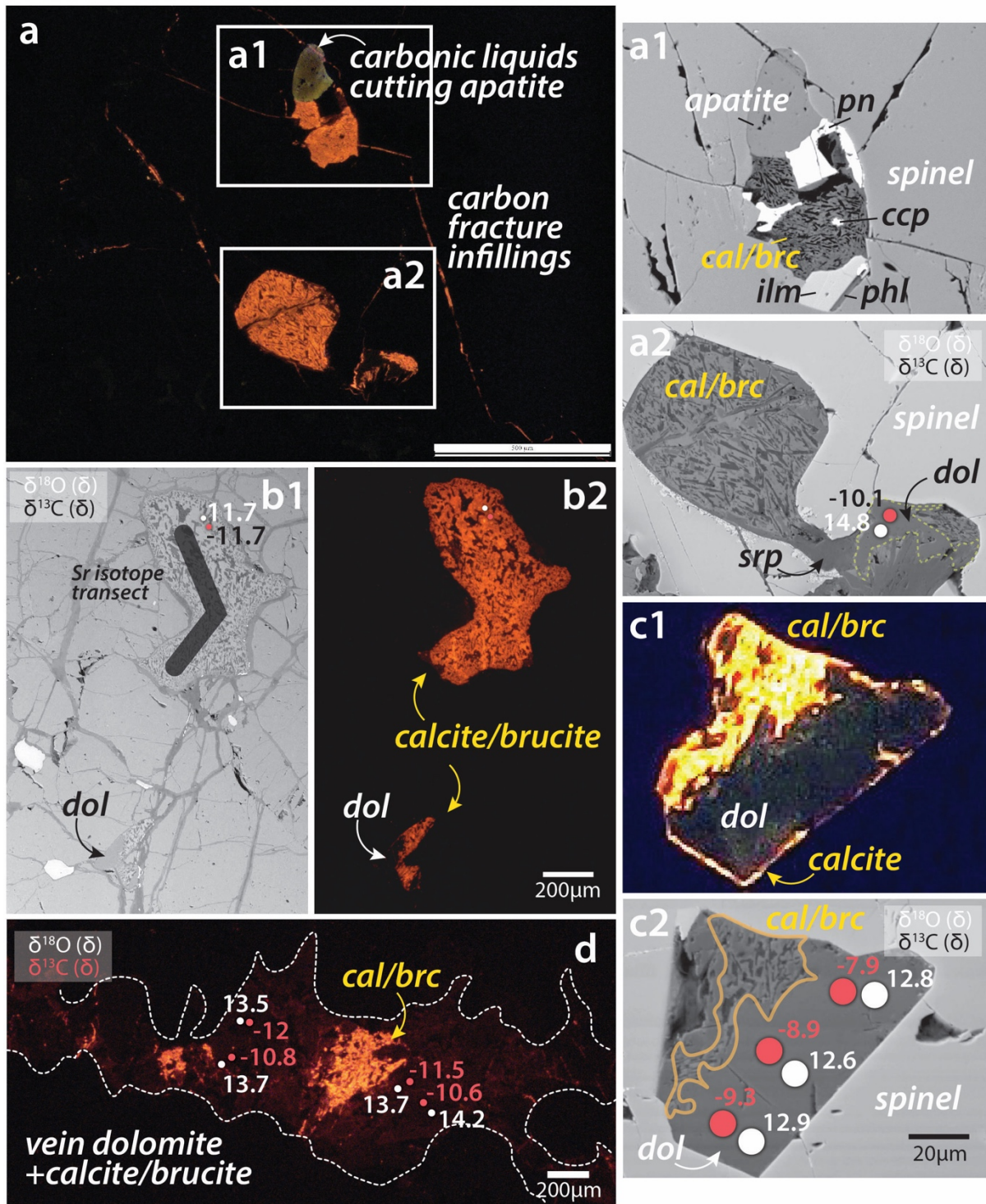


Fig. 5.2: Microstructural occurrence of calcite/brucite intergrowths in the Ulten Zone peridotite. *a*) CL imaging of polycrystalline inclusion in spinel within garnet, showing carbonates as fracture infillings in the spinel; *a1-a2*) Zoomed in BSE images of calcite/brucite intergrowths with relics of dolomite inclusion within coarse spinel included in coarse garnet; *b1*) BSE and *b2*) CL imaging of matrix calcite/brucite intergrowths with relic of precursor dolomite. The surrounding serpentine is lizardite (Consuma et al. 2020) and the transect used to measure the Sr isotope is also shown; *c1*) CL and *c2*) BSE imaging of a dolomite inclusion in a coarse spinel included in garnet surrounded by a bright yellow thin film of calcite and intimately associated with calcite/brucite intergrowths; *d*) dolomite vein from peridotite KL1.6 with calcite/brucite intergrowths formed along the vein as

5 • Trace elements and C-O stable isotope signature of texturally diverse mantle wedge dolomite

evidenced by the CL imaging. SIMS spots analyses with relative measured C and O isotopes are reported.

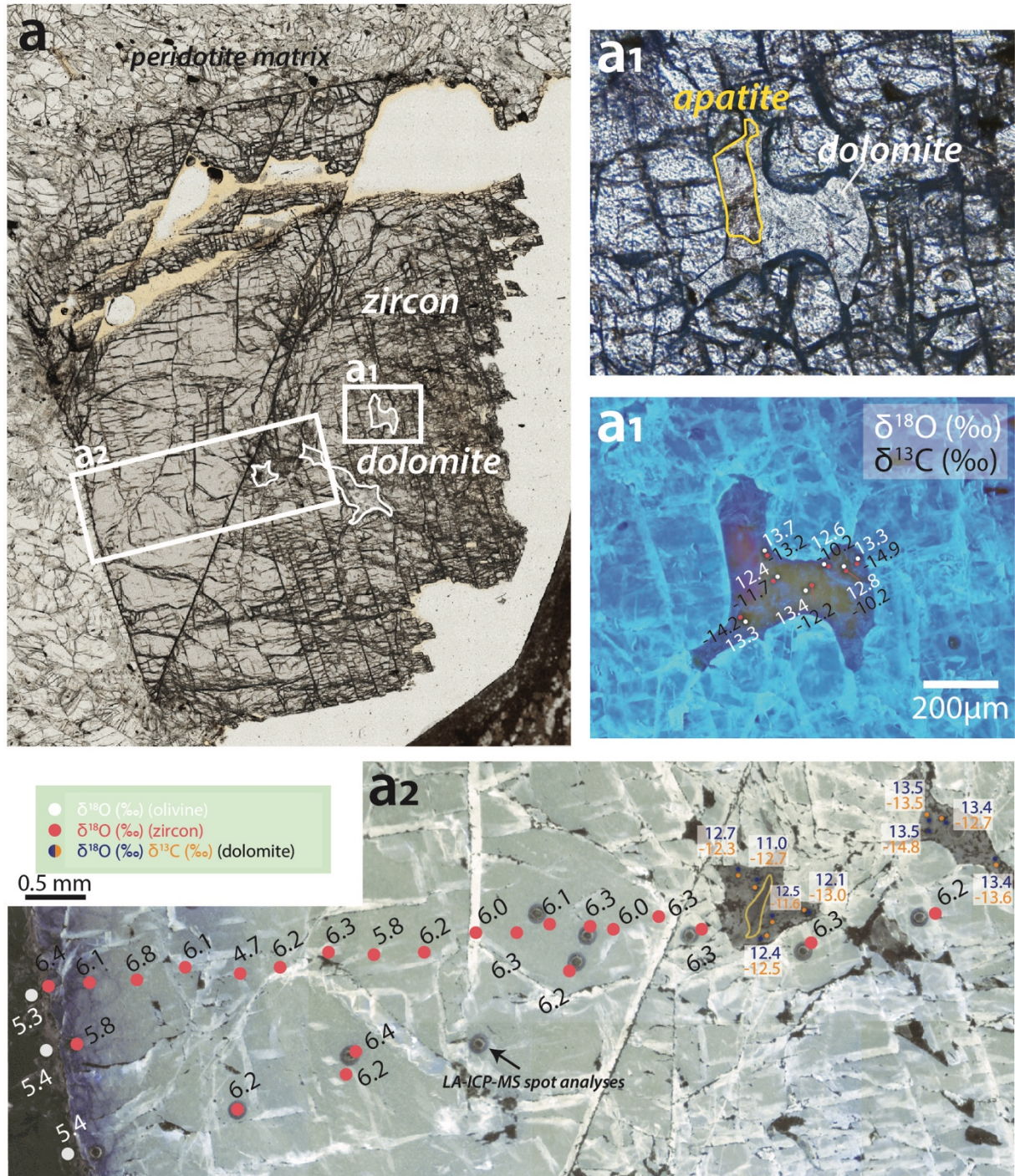


Fig. 5.3: a) scan image under plane polarized light of highly fractured zircon with inclusions of dolomite (+ apatite + chlorite) within fine-grained matrix from the coarse-grained spinel (\pm garnet) peridotite VM25P10A; a1) zoom in of a dolomite inclusion with apatite; a2) CL image of a1. The dull green dolomite core is visible whereas the rim is light blue/darker blue; a3) CL image of zircon and locations of the spot analyses.

5.5.2 Trace elements compositions

Trace element compositions were measured in carbonates as they occur within an orthopyroxenite layer (within coarse-grained spinel peridotite), included in spinel and zircon, interstitial to silicates in the peridotite matrix, as veinlets crosscutting the peridotite matrix. Additional crucial metasomatic phases, such as serpentine and zircon, were analysed. The description of trace element measurements of the main peridotite-forming minerals, largely documented in literature (e.g. Gudelius et al., 2019; Marocchi et al., 2007; Sapienza et al., 2009; Scambelluri et al., 2010, 2006), is reported in a Supplementary Paragraph B1, whereas the full dataset in Supplementary Tables B1 to B10.

5.5.2.1 Trace elements composition of mantle wedge dolomite

The average trace elements composition of dolomite from different textural positions and peridotite lithotypes is reported in Table 5.3, whereas the full dataset is reported in Supplementary Table B11 and illustrated in Figures from 5.4 to 5.8. For comparison, we report the values of matrix dolomite investigated by Sapienza et al. (2009) from both eclogite-facies and retrograde peridotite. Trace element concentrations of the associated crustal rocks and of trondhjemites dikes after Tumiati et al. (2007) are also reported.

In the interstitial dolomite found in the orthopyroxenite layer from the coarse-spinel peridotite MOL1-C, no significant compositional differences in terms of trace elements are found among the CL colors (Fig. 5.4). The enrichment of LREE over HREE is here less marked with L_{AN}/Yb_N that reaches a maximum value of 55. Among LILE, of note, the Na reaches values up to 40ppm.

5 • Trace elements and C-O stable isotope signature of texturally diverse mantle wedge dolomite

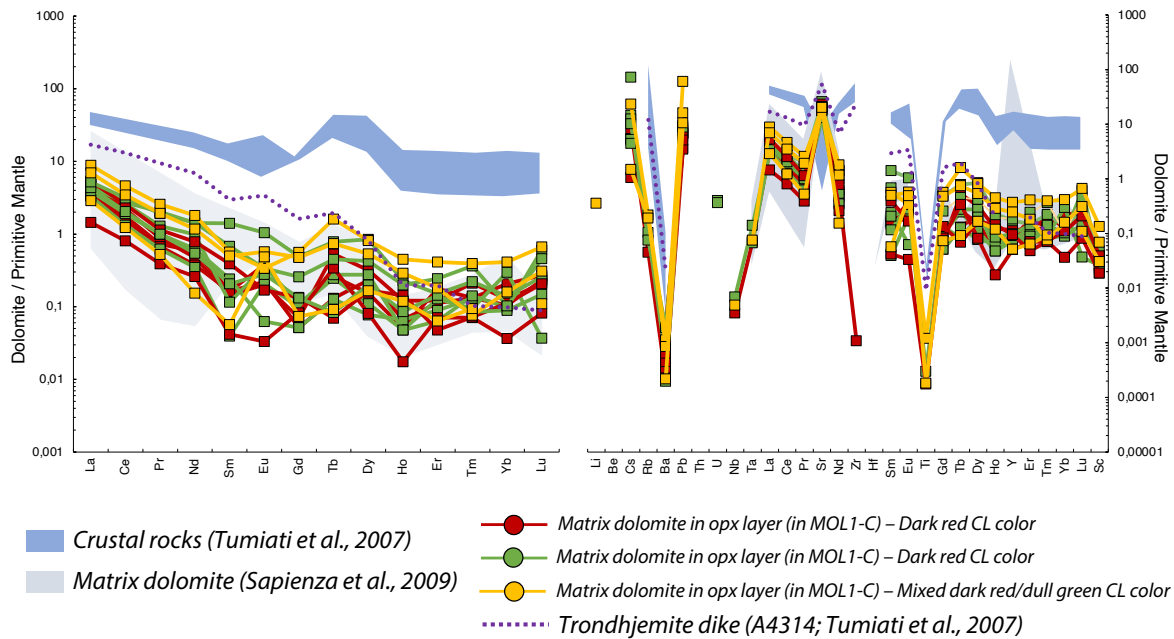


Fig. 5.4: Trace elements composition of matrix dolomite within an orthopyroxenite layer intruding the coarse-grained spinel peridotite MOL1-C. Normalization values after McDonough and Sun (1995).

Figure 5.5. shows the trace elements composition of dolomite grains included in a coarse spinel within garnet (Figs. 5.2/c1 and c2) and in a porphyroclastic zircon (Fig. 5.3).

Dolomite included in Cr-rich spinel within garnet is depleted in HREE, which are usually below detection limit. It is variably enriched in Ti (av. 7ppm; n=2), Cr (av. 395ppm; n=2), Co (av. 13.7ppm; n=2), Ni (av. 84.4ppm; n=2), Zn (av. 12.7ppm; n=2), and Pb (av. 5.41ppm; n=2). Notably, this inclusion is markedly enriched in Sr (>1000ppm) and Ba (76.9ppm) relative to all the other textural positions). Detectable abundances of W = 0.12ppm are also observed. Of note, this inclusion has been investigated with two spot analyses, which exhibit respectively absent and negative Eu anomaly ($Eu/Eu^* = 0.57$).

Dolomite grains included in zircon exhibit the highest concentrations of LREE, which result markedly enriched over HREE (La_N/Yb_N up to 1818). This enrichment is particularly evident in the dolomite grain with included apatite, which shows La abundances that reach up to 165ppm (the highest value for the Ulten Zone carbonates). A second dolomite grain with included apatite and chlorite shows minor La concentrations (up to 71ppm) and a less pronounced LREE enrichment over HREE (La_N/Yb_N up to 86).

5 • Trace elements and C-O stable isotope signature of texturally diverse mantle wedge dolomite

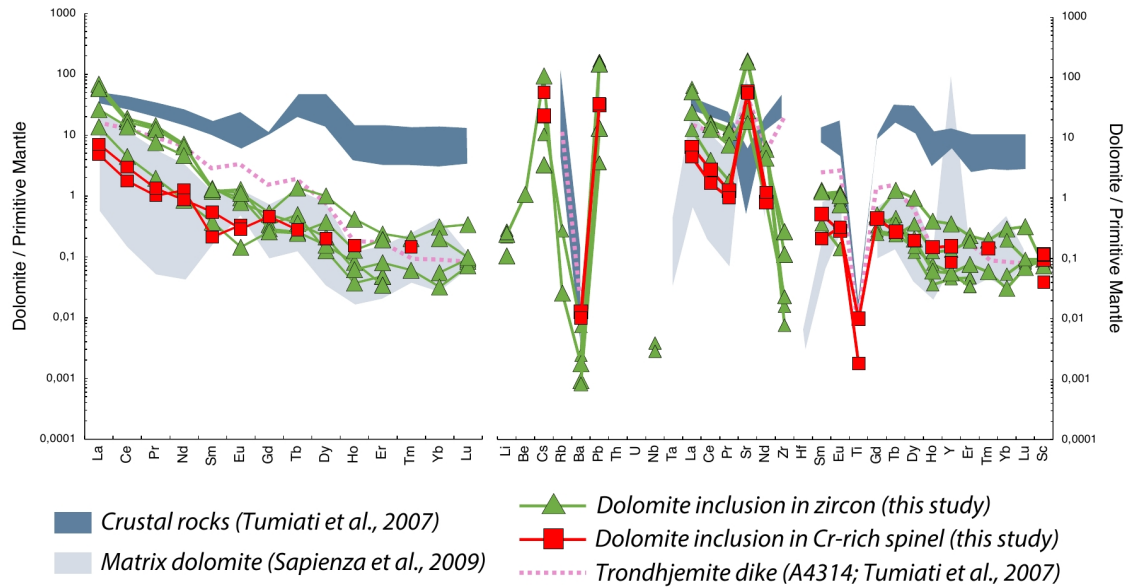


Fig. 5.5: Trace elements composition of dolomite inclusions in spinel and in zircon from fine-grained garnet-amphibole peridotite KL2.4-2b and porphyroclastic fine-grained garnet-amphibole peridotite VM25P10A.

Dolomite grains interstitial to matrix silicates of peridotite VM10A shows a more pronounced enrichment of LREE over HREE ($186 < La_N/Yb_N < 501$) with respect to those from peridotite KL1-A ($12 < La_N/Yb_N < 38$) (Fig. 5.6). Given the small size of 30-50 μ m of the interstitial dolomite, the spot analyses ablated together the CL colors of the core (dull green) and those of the rim (red-orange). The matrix dolomite from Klapfbergalm (KL1-A) is more depleted in La than the dolomite from Mt. Hochwart (VM10A) and it shows always detectable amounts of HREE. The Eu anomaly is always positive, and more marked in dolomite from KL1-A.

5 • Trace elements and C-O stable isotope signature of texturally diverse mantle wedge dolomite

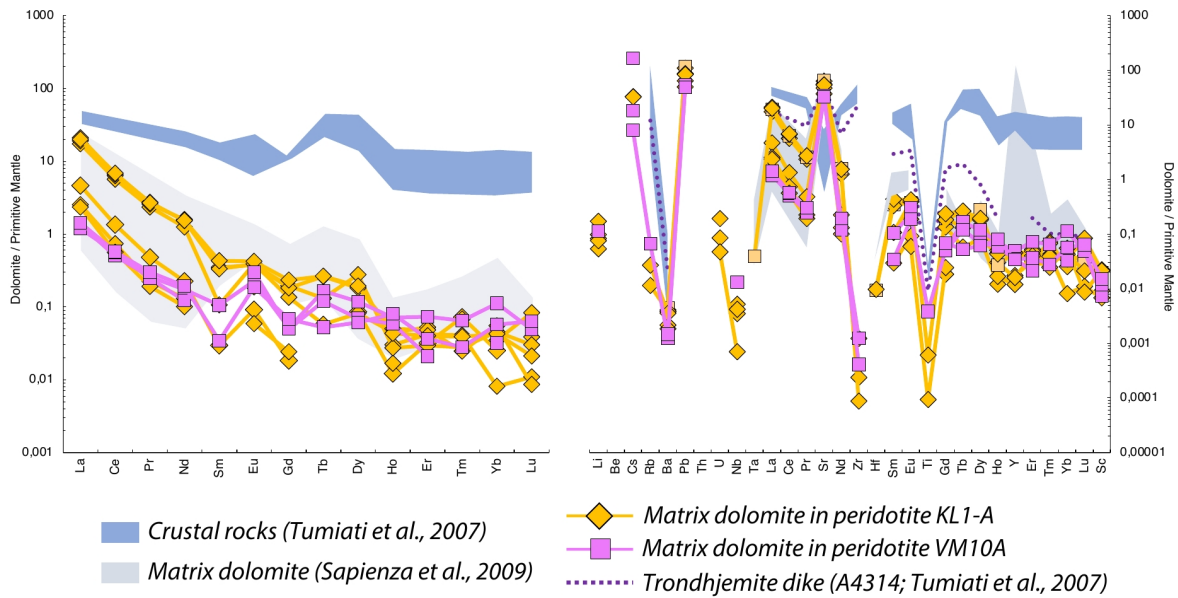


Fig. 5.6: Trace elements composition of matrix dolomite from peridotite samples KL1-A and VM10A.

The REE features of interstitial dolomite from the retrograde spinel peridotite MM1B+MM1 (Fig. 5.7) agree with those of peridotite VM10A, with $104 < L_{a_N}/Y_{b_N} < 1787$ and a marked positive Eu anomaly ($Eu/Eu^* = 3.5$ to 5.9).

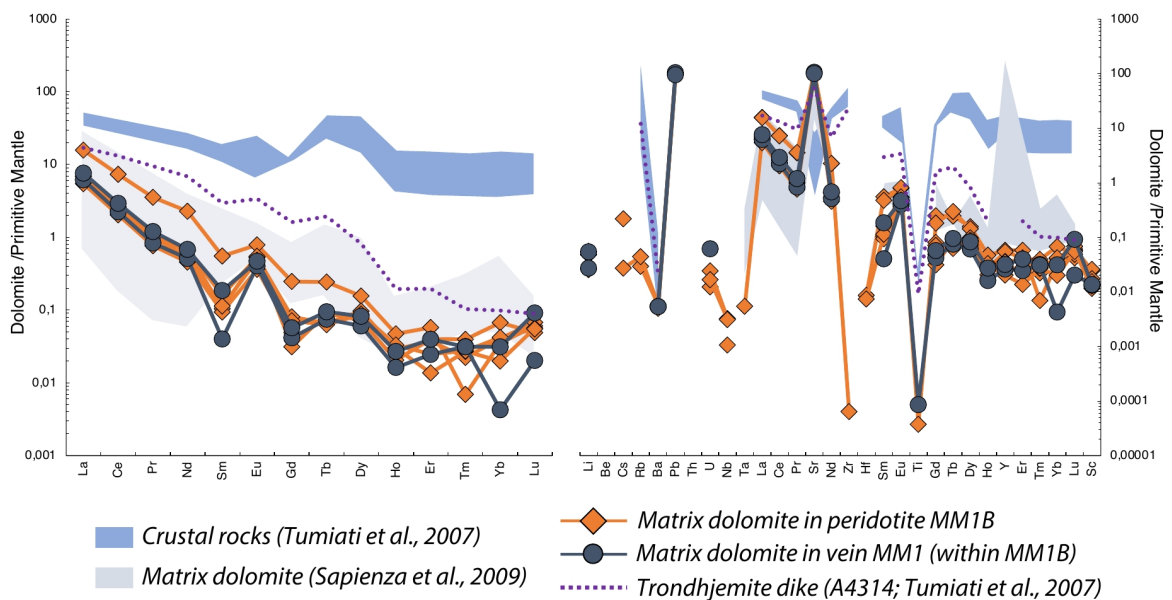


Fig. 5.7: Trace elements composition of matrix dolomite from fine-grained chlorite-amphibole peridotite MM1B and of the serpentine vein MM1.

Regarding the trace elements composition of the dolomite vein crosscutting the coarse-grained the 18LP1 peridotite matrix (Fig. 5.8), the REE slope varies relative to the different CL colors and shows a decreasing trend from the dark red dolomite (La_N/Lu_N up to 319 to the mixed red-green dolomite ($La_N/Lu_N = 66$). The dull green and green-yellow dolomite show REE patterns less steep than the dark-red and mixed red-green dolomite, with an average La_N/Lu_N of 33 (n=4) and 32-37 respectively.

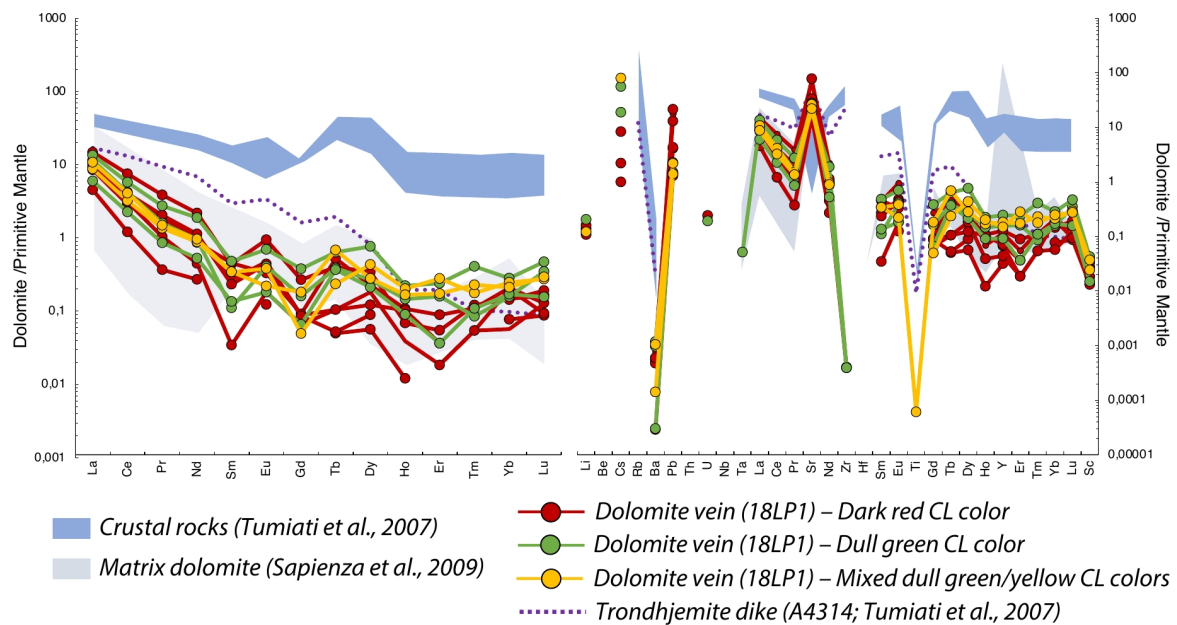


Fig. 5.8: Trace elements composition of dolomite vein from coarse-grained peridotite 18LP1, with correspondent CL colors.

Overall, **dolomite** shows enrichment of LREE over HREE. Interestingly, it shows compositional variations among the textural positions and, as expected, among the observed CL colors. In accordance with Sapienza et al. (2009) and Gudelius et al (2019), the Eu anomaly (Eu/Eu^*) is systematically positive in almost all the textural positions and peridotite lithotypes. However, we observe errant slightly negative anomalies for dolomite included in spinel ($Eu/Eu^* = 0.57$) and interstitial dolomite showing red CL color found in the pyroxenite layer ($Eu/Eu^* = 0.5-0.7$). Among high field strength elements (HFSE; namely Nb, Ta, Zr, Th, U), Hf and Nb are always below detection limit, whereas the other HFSE, when detectable, reflect the textural position and relative paragenesis. For example, Ti is up to 12ppm in the dolomite inclusion associated with tiny rutile grain (2 μm in grain-size) in the coarse spinel (included in garnet) and in very low concentrations in matrix dolomite in pyroxenite layer from the coarse-spinel peridotite MOL1-C

5 • Trace elements and C-O stable isotope signature of texturally diverse mantle wedge dolomite

(bdl to 1.4ppm). Zr concentrations are detectable only when dolomite is included in zircon, reaching contents of 3ppm Zr.

Magnesite has REE often below the detection limit or in very low concentrations (full measurements are detailed in Supplementary Table B12; **Calcite** grains are too small to allow LA-ICP-MS analyses and trace element concentrations are not available.

Table 5.3 Average trace elements composition of dolomite (ppm).

type	Peridotite								Pyroxenite layer in CS					
	P-FGA		FGA		FSA		CG		CS					
sample	KL24-2b	VM25P10A	VM10A	VM10A	KL1-A	MM1	MM1-B	18LP1	18LP1	18LP1	18LP1	MOL1-C	MOL1-C	MOL1-C
texture	In spl	In zrn	m-core	m-rim	matrix	matrix	matrix	vein	vein	vein	vein	matrix	matrix	matrix
n	2	5	6	1	3	2	6	8	2	4	1	5	6	3
CL color	dull green	dull green	dull green	red	dull green	dull green	dull green	red	green-yellow	green	green-red	red	dull green	red-green
Li	bdl	0,37	0,13	0,27	0,18	0,07	0,07	0,18	0,19	0,24	0,03	bdl	bdl	0,57
Be	bdl	0,08	bdl	<0,00	bdl	bdl	bdl	bdl	bdl	bdl	<0,00	bdl	bdl	bdl
B	bdl	18,19	5,72	18,8	11,6	12,41	8,03	9,65	9,22	8,04	4,42	16,7	16,8	16,1
Na	11,8	110,7	5,29	4,24	12,1	bdl	bdl	6,50	3,98	7,21	0,35	29,7	27,9	39,1
Sc	1,28	1,40	0,29	0,15	0,18	0,22	0,29	0,40	0,50	0,44	0,58	0,48	0,53	1,26
Ti	7,07	bdl	0,30	<0,24	4,57	0,10	0,04	0,15	0,07	0,19	0,19	0,21	0,36	0,83
V	4,36	0,17	0,29	0,15	0,43	0,18	0,20	1,26	0,14	1,11	5,94	0,19	0,27	0,61
Cr	395	2,23	4,77	4,06	10,09	4,87	4,18	189	bdl	230	609	5,38	6,81	6,54
Mn	686	998	560	600	582	575	654	3005	734	2633	8775	705	681	793
Co	13,74	8,16	9,92	9,56	10,48	9,20	9,69	8,65	4,62	5,89	7,06	8,55	10,10	10,00
Ni	84,4	31,6	77,5	59,5	56,4	67,6	67,6	65,9	34,3	40,9	53,3	68,7	82,5	73,6
Cu	1,07	2,23	7,42	<0,06	bdl	0,01	0,04	0,07	0,07	0,01	0,06	bdl	0,18	bdl
Zn	12,72	9,51	6,44	8,09	8,72	7,17	6,34	7,29	5,99	5,99	5,25	8,26	9,40	9,23
Rb	bdl	0,09	0,01	<0,02	0,04	bdl	0,02	0,01	bdl	0,01	0,01	0,03	0,05	0,12
Sr	1124	2410	1121	734	673	2032	2029	802	479	496	260	389	381	391
Y	0,53	0,58	0,15	0,05	0,17	0,12	0,17	0,29	0,71	0,72	0,20	0,37	0,50	0,96
Zr	bdl	0,93	0,00	0,01	0,01	bdl	0,00	0,00	bdl	0,00	0,01	0,01	bdl	bdl
Nb	bdl	0,00	0,00	0,00	0,01	bdl	0,00	bdl	bdl	0,00	0,00	0,00	0,00	0,00
Mo	bdl	0,07	0,06	0,04	0,08	0,07	0,07	0,06	0,04	0,11	0,07	0,03	0,07	0,02
Cs	0,84	0,70	0,69	0,69	1,34	bdl	0,00	0,32	1,67	0,52	bdl	0,10	0,42	0,26
Ba	76,9	17,8	23,6	14,1	8,71	35,4	35,9	3,60	3,94	4,00	1,68	5,04	5,37	4,84
La	3,85	29,4	9,15	1,64	0,85	4,45	6,14	5,63	6,32	7,18	4,13	2,40	2,86	4,04
Ce	3,97	24,16	7,67	1,24	0,92	4,32	6,74	5,81	6,13	7,28	3,04	2,97	3,85	5,18
Pr	0,30	2,51	0,47	0,06	0,07	0,26	0,46	0,41	0,36	0,48	0,18	0,19	0,33	0,42
Nd	1,32	6,47	1,30	0,16	0,20	0,75	1,42	1,14	1,16	1,58	0,45	0,62	1,11	1,30
Sm	0,15	0,44	0,10	bdl	0,03	0,05	0,10	0,11	0,14	0,13	0,06	0,07	0,18	0,15
Eu	0,05	0,13	0,04	0,03	0,04	0,07	0,09	0,06	0,05	0,06	0,02	0,03	0,06	0,07
Gd	0,25	0,21	0,07	bdl	0,03	0,03	0,06	0,07	0,06	0,12	0,04	0,05	0,10	0,20
Tb	0,01	0,02	0,01	0,00	0,00	0,00	0,01	0,01	0,02	0,02	0,00	0,01	0,01	0,03
Dy	0,05	0,09	0,04	bdl	0,02	0,02	0,03	0,04	0,09	0,11	0,04	0,05	0,08	0,12
Ho	0,02	0,02	0,01	0,00	0,01	0,00	0,00	0,01	0,03	0,03	0,01	0,01	0,02	0,04
Er	bdl	0,05	0,02	bdl	0,02	0,01	0,02	0,02	0,10	0,07	0,02	0,05	0,06	0,10
Tm	0,01	0,01	0,00	0,00	0,00	0,00	0,00	0,00	0,01	0,02	0,00	0,01	0,01	0,01
Yb	bdl	0,07	0,02	bdl	0,03	0,01	0,02	0,05	0,10	0,10	0,02	0,05	0,06	0,13
Lu	bdl	0,01	0,00	0,00	0,00	0,00	0,00	0,01	0,02	0,02	0,01	0,01	0,02	0,02
Hf	bdl	bdl	0,00	bdl	bdl	bdl	0,00	bdl	bdl	bdl	bdl	bdl	bdl	bdl
Ta	bdl	bdl	0,00	bdl	bdl	bdl	0,00	0,00	bdl	0,00	bdl	0,00	0,00	0,00
W	0,12	0,18	bdl	0,01	bdl	bdl	bdl	bdl	0,01	0,01		0,03	bdl	bdl
Pb	5,41	16,9	13,7	7,42	7,49	14,9	14,6	1,67	0,27	0,22	0,28	0,75	1,15	4,37

5 • Trace elements and C-O stable isotope signature of texturally diverse mantle wedge dolomite

Th	bdl	bdl	0,001	bdl	bdl	0,00	0,00	0,00	bdl	0,00	0,00	bdl	bdl	bdl
U	bdl	bdl	0,002	bdl	bdl	0,00	0,00	0,00	bdl	0,00	bdl	bdl	bdl	bdl
La _N /Lu _N	-	330	456	65,5	23,4	123	171	77,1	34,2	32,6	65,8	18,8	28,7	20,65
Ce/Ce*	0,90	0,68	0,90	0,98	0,92	0,98	0,97	0,93	0,98	0,94	0,84	1,06	0,96	0,97
Eu/Eu*	0,74	1,31	1,59	-	3,78	5,85	3,52	2,27	1,51	1,49	1,15	-	1,80	3,10
La _N /Sm _N	15,6	41,3	56,2	-	18,7	60,7	37,8	31,9	28,3	34,9	45,5	24,7	29,5	26,8
La _N /Yb _N	-	305	402	-	19,79	391	240	75,6	42,69	50,5	122	35,2	-	-
Sm _N /Yb _N		-7,41	7,16	-	1,06	6,43	6,34	2,37	1,51	1,44	2,68	1,64	-	-

5.5.2.2 Trace elements composition of serpentine veins

We analyzed the trace elements composition of serpentine veins that cut at high angle the main dolomite + tremolite + chlorite vein in the coarse-grained peridotite 18LP1, of the lizardite/chrysotile vein MM1B containing magnetite and of the thinner veins that originates from it and cut the fine-grained matrix of chlorite-amphibole peridotite MM1 (Fig. 5.9).

Overall, serpentine veins show an enrichment of LREE over MREE ($2.88 < \text{La}_N/\text{Nd}_N < 4.20$ in peridotites MM1B and MM1 and $2.20 < \text{La}_N/\text{Nd}_N < 6.94$ in 18LP1) and variable enrichment of MREE relative to HREE (Sm_N/Lu_N up to 2.33 in MM1 and up to 1.41 in 18LP1). Serpentine veins are generally low (up to 1.35 ppm) in Sr, which preferentially partitions into the associated dolomite. B content is relatively high, ranging between 8 and 19 ppm in the serpentine veins of peridotite 18LP1, and reaching higher concentrations in the serpentine veins of chlorite-amphibole peridotite MM1 and MM1B, varying between 33 and 78 ppm. For comparison, seawater contains 4.6 ppm B whereas depleted and/or primitive mantle contains 0.06 and 0.3 ppm B, respectively (Deschamps et al., 2013).

On the contrary, Li content is higher in peridotite 18LP1 relative to MM1B, with concentrations up to 15 ppm in the former and up to 5 ppm in the latter. Pb content ranges between 0.05 (in MM1) and 0.52 ppm (in 18LP1). Ba is up to 11ppm in veins from 18LP1a, whereas is up to 0.5 ppm when from MM1 and MM1B. Some HFSE, such as Th, U and Zr, are also markedly more enriched in the serpentine veins from peridotite 18LP1 relative to peridotite MM1B.

Eu anomalies (Eu_N/Eu^* up to 3) are generally positive, with the exception of one slightly negative anomaly for the serpentine vein crosscutting the dolomite vein in peridotite 18LP1. This vein also shows a marked enrichment of REE compared to the other veins from the same sample.

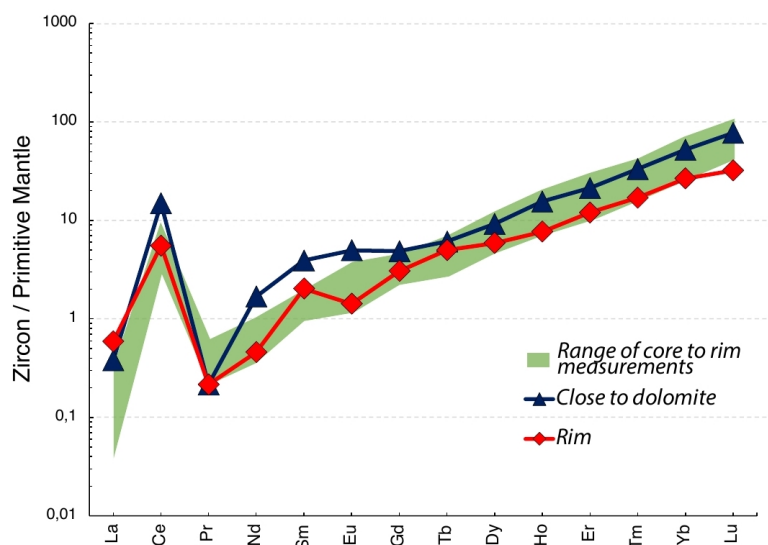


Fig. 5.10: REE trace elements pattern of zircon. The green shade covers all the measurements taken along a profile core-to-rim ($n=6$), with the exception of the measurements taken in correspondence to the rim and in proximity of the included dolomite. Normalized to primitive mantle (values after McDonough and Sun, 1995).

5.5.3 Stable isotope measurements

5.5.3.1 Carbon and oxygen isotope geochemistry of dolomite

The $\delta^{13}\text{C}$ signature versus $\delta^{18}\text{O}$ of the investigated carbonates is illustrated in Figure 5.11, whereas the frequency of $\delta^{13}\text{C}$ for each carbonate textural occurrence with the correspondent CL color is reported in Figure 5.11. Supplementary Table B12 reports the full data-set.

Overall, carbonates show a range of $\delta^{13}\text{C}$ values between -16‰ and -8‰ and $\delta^{18}\text{O}$ values between $+11\text{‰}$ and $+15\text{‰}$.

In the coarse-grained peridotite, petrographic evidence of interstitial dolomite is rare. However, the coarse-grained spinel MOL1-C contains an orthopyroxenite layer which hosts pervasive matrix dolomite (Fig. 5.1a). This dolomite has an average of $\delta^{13}\text{C}$ of -10.43‰ , $1\sigma = 1.0\text{‰}$, and $\delta^{18}\text{O}$ of 12.45 , $1\sigma = 0.39\text{‰}$. Two spot analyses, corresponding to dark red and dull green CL colors, show the isotopically heaviest value of the investigated dolomite (average $\delta^{13}\text{C} = -8.2\text{‰}$; $1\sigma = 0.02\text{‰}$), approaching the C signature of mantle carbonates (-2 to -8‰ ; Giuliani et al., 2014) (Fig. 5.11). On the other hand, the measured $\delta^{18}\text{O}$ plots outside the $\delta^{18}\text{O}$ mantle range (~ 6 - 8‰ ; Giuliani et al., 2014). No statistically significant correlations between the stable isotope signature and the CL colors was observed.

Euhedral dolomite (\pm calcite/brucite intergrowths) included in the Cr-rich spinel within porphyroclastic garnet (Fig. 5.2/a-b) has a relatively heavy $\delta^{13}\text{C}$ averaging -8.7‰ , $1\sigma=0.8\text{‰}$ and a $\delta^{18}\text{O}$ of 12.8‰ , $1\sigma = 0.1\text{‰}$.

A spot analysis taken from a dolomite relic inclusion in another Cr-rich spinel, associated with calcite/brucite intergrowths and serpentine (Fig. 5.2/a2) exhibits a $\delta^{13}\text{C}$ of $-10.1\text{‰} \pm 0.5$ (2se) and a $\delta^{18}\text{O}$ of $14.8\text{‰} \pm 0.5$ (2se).

Three lobate-shaped dolomite inclusions occur in the core of a highly fractured slightly zoned zircon (Fig. 5.3). One dolomite grain previously analysed by in situ Sr isotope (see Consuma et al., 2020; Chapter 4) (Fig. 5.3) shows an average of $\delta^{13}\text{C}$ of -12.4 , $1\sigma=1.8\text{‰}$ and $\delta^{18}\text{O} = 13.1\text{‰}$, $1\sigma=0.5$. The lightest C isotope signature of around -14.9‰ is measured in the dolomite rim, close to the boundary with the host zircon. Another dolomite inclusion (\pm apatite) has an average of $\delta^{13}\text{C}$ of -13.8‰ , $1\sigma=0.8$ and $\delta^{18}\text{O} = +13.5$, $1\sigma=0.1$ (Figs. 5.3/a1), whereas the grain including apatite and chlorite (Figs. 5.1/c and Fig. 5.3) has an average of $\delta^{13}\text{C}$ of -12.29‰ , $1\sigma=0.5$ and $\delta^{18}\text{O} = +12.3$, $1\sigma=0.7$.

The unique matrix dolomite (associated with pentlandite and chlorite (see Fig. 6.3/c in see Chapter 6) from the coarse-grained peridotite MOL1-C analysed by SIMS shows an average of $\delta^{13}\text{C}$ of -12.7‰ , $1\sigma = 0.2\text{‰}$ and $\delta^{18}\text{O}$ of $+12.4\text{‰}$, $1\sigma = 0.7\text{‰}$.

Overall, matrix dolomite from the fine-grained garnet-amphibole peridotite VM10A and KL1-A shows an average of -10.9 , $1\sigma=1.0\text{‰}$ and $\delta^{18}\text{O} = 12.7\text{‰}$, $1\sigma=0.3$.

Specifically, the matrix dolomite grains from peridotite VM10A (Fig. 5.1/d) show $\delta^{13}\text{C}$ values averaging -11‰ , $1\sigma = 1.2\text{‰}$ with the $\delta^{13}\text{C}$ value of -8.8‰ measured in correspondence of the rim (red CL color). Intra-grain $\delta^{18}\text{O}$ is fairly homogeneous with an average value of $12.6 \pm 0.4\text{‰}$ ($n=4$; 2se). The $\delta^{13}\text{C}$ and $\delta^{18}\text{O}$ of dolomite grains from peridotite KL-1A average -10.8‰ , $1\sigma = 0.8\text{‰}$ and $+12.7\text{‰}$, $1\sigma = 0.3\text{‰}$.

Four SIMS measurements were carried out in the dolomite vein from peridotite KL1-6, which locally contains calcite/brucite intergrowths (Fig. 5.2/d). Spots analysis were taken in the proximity of the intergrowths, showing an average of $\delta^{13}\text{C} = -11.1\text{‰}$, $1\sigma = 0.7\text{‰}$ and $\delta^{18}\text{O} = 13.6\text{‰}$, $1\sigma = 0.5\text{‰}$.

The vein of dolomite + chlorite + tremolite crosscutting the coarse-grained spinel \pm garnet peridotite 18LP1 has an average of $\delta^{13}\text{C}$ of -11.9‰ , $1\sigma = 1.7\text{‰}$ ($n=29$) and a fairly homogeneous $\delta^{18}\text{O}$ of $+12.5\text{‰}$, $1\sigma = 0.4$. The lighter C isotope values, such as the measured $\delta^{13}\text{C}$ of -8.8‰ in correspondence of the CL dull green color, approach the mantle-like signature.

5 • Trace elements and C-O stable isotope signature of texturally diverse mantle wedge dolomite

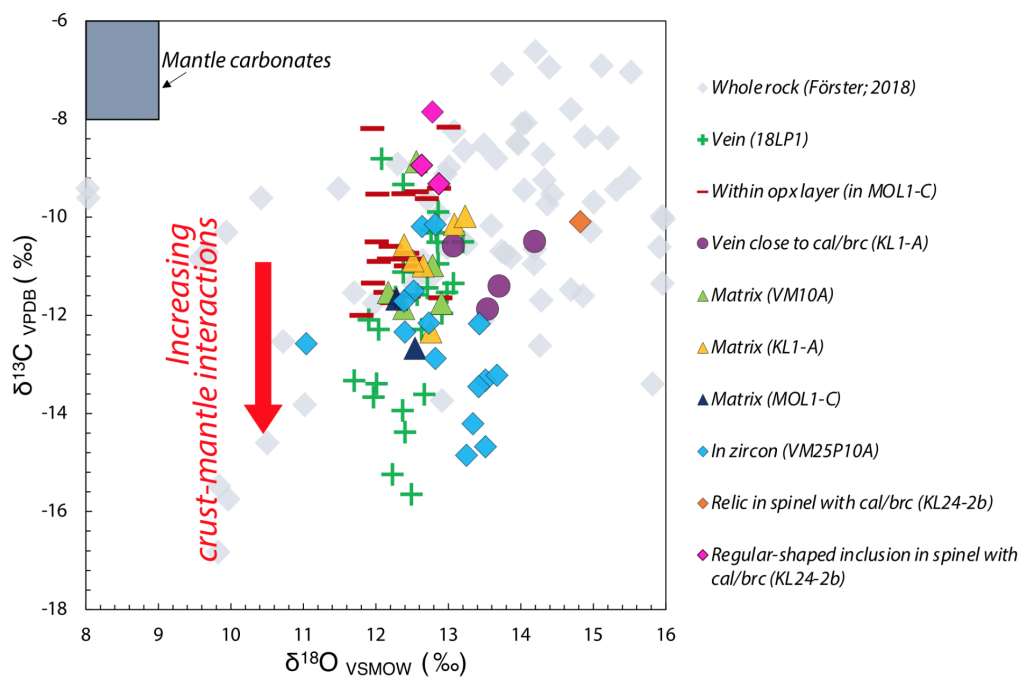


Fig. 5.11: $\delta^{13}\text{C}$ versus $\delta^{18}\text{O}$ of dolomite occurring in different textural positions across the peridotite suite, measured by SIMS. For comparison, whole rock C-O isotope measurements of the carbonated Ulten Zone peridotites after Förster (2018) are reported. The dark field represents the stable isotope signature of mantle carbonates; taken from Giuliani et al. (2014).

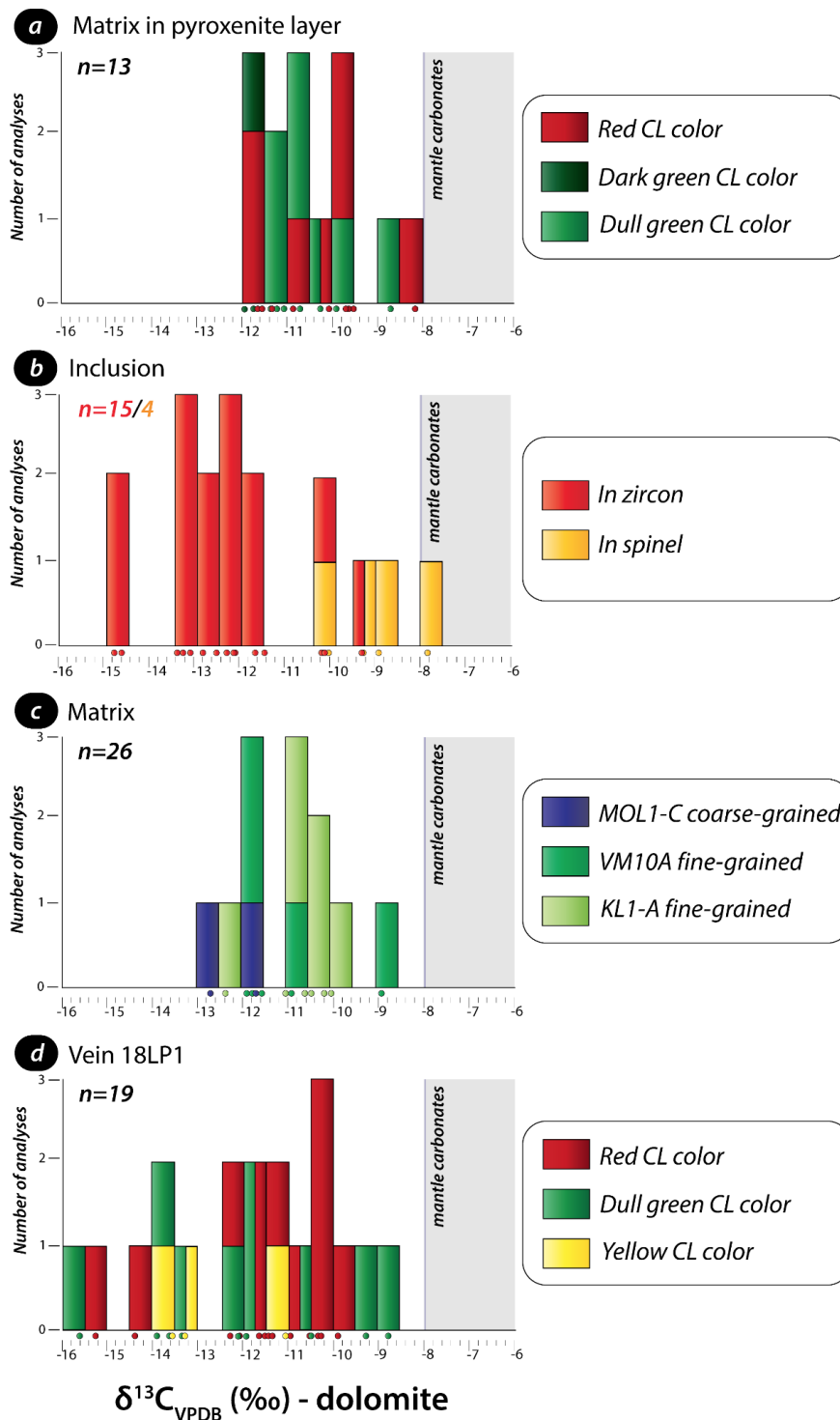


Fig. 5.12: $\delta^{13}\text{C}$ distribution of dolomite from the main textural occurrences. $\delta^{13}\text{C}$ range of mantle carbonates is also reported for comparison.

5.5.3.2 Additional oxygen isotope measurements of zircon and olivine

Further $\delta^{18}\text{O}$ isotope compositions were taken for a mm-sized porphyroclastic zircon in the fine-grained garnet-amphibole peridotite V25P10A (Fig. 5.3) and associated fine-grained olivine (Fig.

5.13). Care was taken to analyse both the olivine grains at the contact with the zircon rim and olivine grains in the matrix. Additional coarse- and fine-grained olivine grains from the coarse-grained spinel peridotite MOL1-C were analysed. All the olivine grains (both fine and coarse) were analysed along rim to core profiles (see Supplementary Table B13 for the full dataset).

Porphyroclastic zircon shows positive $\delta^{18}\text{O}$ values ranging from + 5.8 to + 6.8 ‰ (Fig. 5.3/c), with an intra-grain variability of about 1‰. The outlier value of +4.7‰ corresponds to the dark blue CL zoning of zircon. These values fall outside the typical mantle range ($5.3\text{‰} \pm 0.3\text{‰}$; Valley, 2003).

Olivine is $\text{Fo}_{88-90}\text{Teph}_{0-2}$, with no compositional variations between the fine-grained and coarse-grained matrix (Consuma et al., 2020). The rims of the fine-grained olivines at the zircon boundary typically show higher $\delta^{18}\text{O}$ values of about +5.3‰, and the average O isotope values of fine-grained matrix olivine grains is +5.3‰ (n=14), spanning from +4.8‰ to +5.5‰.

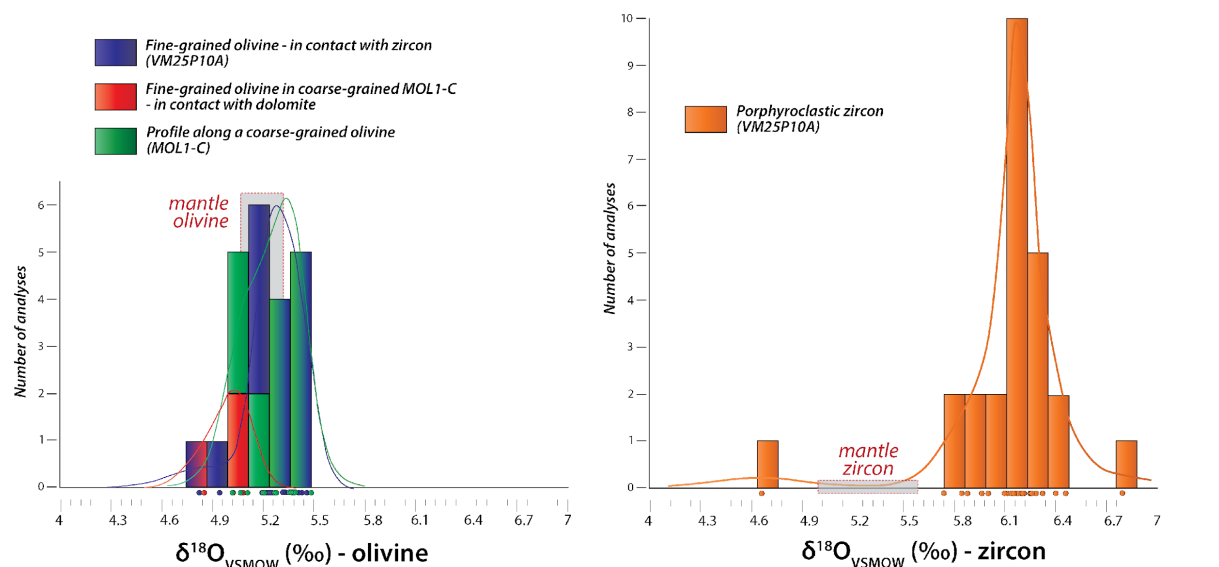


Fig. 5.13: On the left: $\delta^{18}\text{O}$ signature of olivine occurring as (i) fine-grained grains in contact with zircon boundaries; (ii) fine-grained grains in recrystallized domain of the coarse-grained peridotite MOL1-C. Here, olivines are in contact with matrix dolomite and magnesite; (iii) coarse-grained grain (6 mm in size) within coarse peridotite MOL1-C measured along a profile. On the right, $\delta^{18}\text{O}$ of slightly CL zoned porphyroclastic zircon. Of note, the outlier is measured in correspondence of the dark blue CL domain of the zircon rim. Kernel Density Estimate (KDE) curves are also reported.

5.6 Discussion

5.6.1 Stable C-O isotope during high pressure metamorphism and the effect of low-T processes

The Ulten Zone peridotite is known to have experienced a strong metasomatic overprint. Hornblenditic amphibole, dolomite, chlorite and tremolite are among the mineralogical evidence

of this metasomatism, that was characterized by multiple aqueous and carbonic melt and fluid infiltrations throughout the Variscan orogeny. In Chapter 4 (Consuma et al., 2020) we have advanced three main mechanisms for carbon mobilization acting in the Ulten Zone peridotite:

- (1) at high pressure conditions, pervasive carbonic fluid flow permeated the peridotites (mostly the fine-grained ones) still residing within the mantle wedge, forming matrix dolomite along the silicates grain boundaries;
- (2) channelized carbonic fluid flow occurred shortly after peak conditions (i.e. starting from 330Ma; Scambelluri et al., 2006) when the peridotite was incorporated in the country rocks;
- (3) serpentinization at crustal levels (up to 25 km depths; Consuma et al. 2020) provokes dolomite dissolution to form calcite/brucite intergrowths and liberate CO₂.

As such, the Ulten Zone peridotite has been unquestionably affected by progressive more diluted fluids, possibly originated from the country gneisses, within the flowing upwards mélange at low T conditions. These low temperature processes may have severe geochemical effects by modifying the stable isotope composition of the investigated material, shifting the values away from the starting isotope signature. The range of $\delta^{13}\text{C}$ (-16‰ and -8 ‰) and $\delta^{18}\text{O}$ (+11‰ and +15‰) of the investigated Ulten Zone dolomite has to be considered in the light of these aspects, and a careful knowledge of the surrounding conditions (i.e. geodynamic context, petrography, T and subordinately P and $f(\text{O}_2)$) is mandatory. Given the high extent of fluid/rock interactions recorded by the Ulten Zone peridotite and the trend, considering the textural positions, towards isotopically lighter values, the changing in $\delta^{13}\text{C}$ and $\delta^{18}\text{O}$ isotopic composition of the metamorphic carbonates, is most plausibly attributed to interactions with external C-O-H fluids during high pressure and retrograde conditions (Ague and Nicolescu, 2014; Galvez et al., 2013a, 2013b).

Considering the greater extent of fluid/rock interaction within the mélange, the little variation of the $\delta^{18}\text{O}$ of about 1‰ at the thin section scale (10cm³) in the vein crosscutting the coarse-grained peridotite 18LP1, which has been shown in Chapter 4 to have highly heterogeneous ⁸⁷Sr/⁸⁶Sr, could be explained by potential full isotopic re-equilibration prompted by low-T fluids generated by the neighbouring gneisses. This would be also consistent with the work of Bebout et al. (2013), who attest the full re-equilibration of calcite with dehydration fluids originated from the neighbouring metapelite at the low T of about 450°C and 650°C. Besides, according with Cook-Kollars et al. (2014), the absence of homogenization of the $\delta^{13}\text{C}$ of carbonates in the same vein, and the trend toward isotopically lighter values are consistent with a very low C content in the infiltrating fluids derived from the neighbouring gneisses. A few crustal rocks (stromatic migmatites and garnet-staurolite gneisses from Valle Lavazzé close to Malaga Murada) were measured by

Förster B. (PhD Thesis, 2017) in their bulk carbon content, ranging between 0.050 and 0.220 wt.%, and $\delta^{13}\text{C}$ signature, spanning from -33‰ in the migmatites to -25‰ in the gneisses. Low C concentrations could be addressed to the presence of accessory crystalline graphite, as reported by Langone et al. (2011) in a garnet-kyanite gneiss. Nevertheless, another C-bearing phase that could occur in the crust is carbonaceous material, which has been recently demonstrated to be more efficiently mobilized respect to the crystalline graphite during subduction at depths < 110km (Tumiati et al., 2020; Vitale Brovarone et al., 2020).

The following paragraphs are devoted to evaluate the several stages of carbonate metasomatism that affected the Ulten Zone peridotite via fluid and melt-mediated processes as it was located in different wedge's position relative to the Variscan continental subduction architecture (i.e. within the mantle wedge domain, proximal to the slab, mantle/crust interface, tectonic mélange).

5.6.2 Primary mantle carbon mobility under pre-peak conditions

Earlier studies stress that the Ulten Zone peridotite protolith resided in a lithospheric mantle and was afterwards metasomatized by percolating hot mafic melt, possibly crust-derived, to form pyroxenite layers in the spinel stage (1200°C at ca. 1.5GPa, Nimis and Morten (2000); Scambelluri et al. 2006). The melt-mediated episode caused a LREE- and Li-enrichment to the starting spinel lherzolites. Differently from the previous chapter, we have available for the study the orthopyroxenite layer intruding the coarse-grained spinel peridotite MOL1-C, which most plausibly corresponds to this Stage 1. Carbonation likely affected the peridotite, by forming dolomite within the orthopyroxenite layer through multiple episodes of liquid infiltration, as indicated by the growth zoning of dolomite under CL. The observed variability of CL colors of this dolomite combined with the large range of $\delta^{13}\text{C}$ (-8‰ to -12‰) does not show any significant correlation. The $\delta^{13}\text{C}$ value of -8‰ is close to the mantle isotopic range and may represent preserved mantle values of the carbonate-bearing silicate melt, in accordance with Nimis and Morten (2000). Negative values relative to the mantle box range usually require an involvement of a metasomatic agent with lighter C isotope composition or the shift towards lighter values ($\delta^{13}\text{C} = -12‰$) may be explained by later episodically fluid-mediated metasomatism.

The lowest $\delta^{13}\text{C}$ range of -9‰ to -8‰ approaching the mantle signature obtained in the regular-shaped dolomite inclusion within a Cr-rich spinel brought us to re-evaluate the origin of this inclusion (see Chapter 4). Microstructurally, this inclusion reveals different aspects that may point

to opposite timing of formation: (1) regular shape defined by straight facets of the dolomite indicates carbonate inheritance prior to spinel and garnet crystallization; (2) the presence of radial fractures in the garnet may facilitate infiltration of low T fluids to react with the pre-existing minerals; (3) the intimate association of dolomite with calcite/brucite intergrowths is a compelling evidence of dolomite dissolution due to serpentinizing fluids migrating through spinel and garnet fractures under low-T conditions. Low T fluid infiltration is also evidenced by the CL bright yellow thin film rimming the inclusion (Fig. 5.1b). Geochemically, this inclusion contains high amounts of Sr (>1000ppm) and Ba (>70ppm), which may point to melt-mediated recycling of crustal components. Enrichment in Co, Ni, Cr, Ti, V, Zn in this dolomite can be addressed to elements diffusion from the Cr-rich spinel host and the associated tiny grain of rutile. The recognition of textural features and mineral assemblages indicating the dissolution of dolomite as it interacts with serpentinizing fluids to form calcite/brucite intergrowths may also be supported by the trend of $\delta^{13}\text{C}$ towards slightly lighter $\delta^{13}\text{C}$ within a few tens of microns across, that may indicate local devolatilization of carbon.

5.6.3 Carbonic fluid-mediated metasomatism at eclogite-facies conditions

Peak-pressure conditions were attained at ca. 850°C and 2.7GPa (Nimis and Morten, 2000). The geotectonic scenario of the Ulten Zone at this stage is controversial. Most plausibly, peridotites were still residing in the mantle wedge above the crustal slab at high pressure conditions, whereas their incorporation into the country gneisses occurred shortly after, during early stages of exhumation (Scambelluri et al. 2006). Nevertheless, crust-mantle interactions unquestionably initiated at this point time (HP), as it is evidenced by preserved inclusions of dissakisite-(La) in garnet (Marocchi et al., 2009; Tumati et al., 2005) and by the radiogenic in situ Sr isotope signature of matrix hornblende (see Chapter 6).

There is a general consensus that interstitial dolomite precipitated from a mixture of aqueous and carbonic fluids within the garnet stability field: the coexistence of high pressure matrix dolomite with the garnet is confirmed by the HREE depleted composition of dolomite (about 0.1 x CI) (Sapienza et al., 2009; this study). Consuma et al. (2020) found relatively radiogenic Sr isotope values for high pressure matrix dolomite, thus indicating that crust-derived liquids variably equilibrated with a depleted mantle source during percolation of the overlying mantle wedge. Pervasive carbonation of the peridotite through porous flow is envisaged at high pressure conditions, where the fluid/rock ratio is low and the O isotope of dolomite may equilibrate with the O isotope composition of the surrounding silicate matrix.

Overall, matrix dolomite shows a wide range of $\delta^{13}\text{C}$ from -13‰ to -9‰ where the lowest values are obtained for the dolomite grains in the coarse-spinel peridotite MOL1-C matrix, whereas those from fine-grained garnet-amphibole peridotites VM10A and KL1-A display higher values.

Of note, dolomite from peridotite VM10A, sampled from the hybrid contact zone exposed in Mt. Hochwart, shows significant positive correlation trends by the pairs Sr-Pb and Sr-Ba (Fig. 5.9). The exposed crust-mantle tectonic contact is well known to host a few peculiar metasomatic phases such as zircon (Marocchi et al., 2009, 2010; this study), tourmaline, and dissakisite (Tumiati et al., 2005). It is thus not surprising that the matrix dolomite from this locality stores the highest abundances of a typical crustal element like B (up to 19ppm towards the rim), the highest enrichment of LREE over HREE (large $\text{La}_\text{N}/\text{Lu}_\text{N}$), significant abundances of LILE elements such as Sr, Cs, Ba and detectable amounts of HFSE Zr, Nb, Hf, Ta, Th and U.

In the matrix dolomite from this sample, the variability of $\delta^{13}\text{C}$, combined with dull green contoured by dark orange CL colors, and trace element compositional variations among core and rim, together with $^{87}\text{Sr}/^{86}\text{Sr}$ isotope values of 0.705 (Consuma et al. 2020) points to the infiltration of carbonic-fluids from different sources (i.e. subduction-related and depleted mantle) carrying incompatible elements.

A slightly different geochemical signature is observed for matrix dolomite from peridotite KL1-A from Klappbergalm. Here the Sr-Pb and Sr-Ba correlation is less pronounced of those found in Mt. Hochwart, and compared to the Mt. Hochwart sample it exhibits a more flat trace element pattern, with a weak enrichment of LREE and a pronounced positive Eu anomaly (up to 4). The higher $^{87}\text{Sr}/^{86}\text{Sr}$ of 0.707 signature of these dolomite grains combined with lower $\delta^{13}\text{C}$ indicate that the metasomatic agents are geochemically different from those that percolate Mt. Hochwart, with a more pronounced subduction-related crustal imprint.

The matrix dolomite preserved in retrograde chlorite-amphibole peridotite is characterized by high contents of Sr (> 2000ppm), Ba (>36ppm) and Pb (>14ppm). The slight but significant positive Sr-Pb correlation (Fig. 5.9) and the marked positive Eu anomaly (up to 6; Fig. 5.4) points to subduction-related crustal fluids. Unfortunately, given the pervasive serpentinization of these samples and the impossibility to reach the required flatness of the thin section surface, these samples were not considered for SIMS analyses.

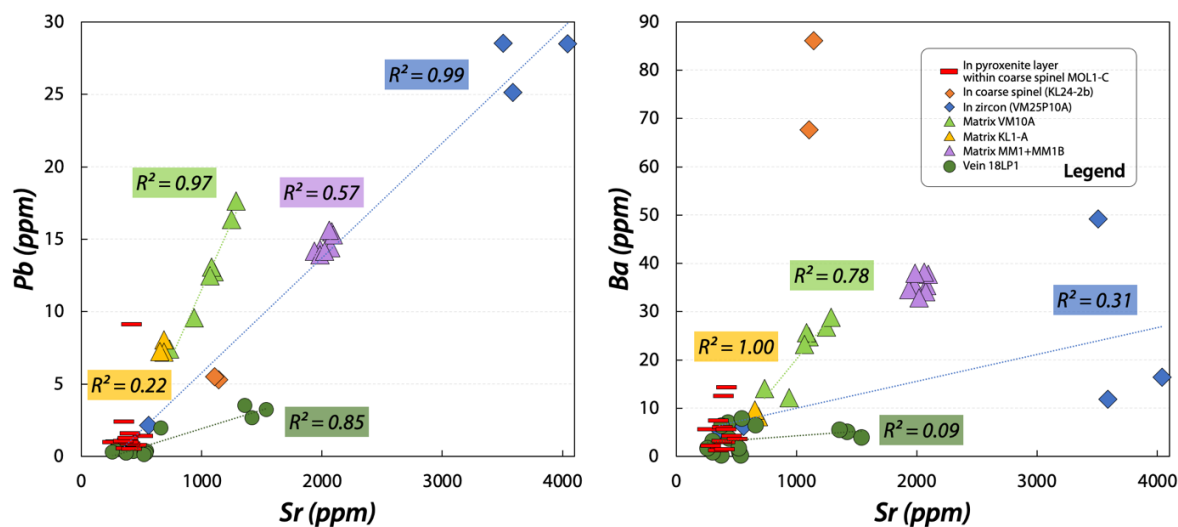


Fig. 5.14: Abundances of Sr versus Pb (ppm) for dolomite grains occurring in different textural positions. R-squared values are reported. Of note, matrix dolomite within the pyroxenite layer does not show any Sr-Pb statically significant correlation.

5.6.4 Crust-mantle *mélange* exhumation reactivates carbon and elements mobilization

The retrograde evolution of the Ulten Zone starts when mantle wedge fragments of the Ulten Zone are incorporated into exhuming country rock gneisses to form a tectonic *mélange* (Scambelluri et al., 2006). At this stage, hydration of peridotite from crustal fluids is largely documented in the literature (i.e. Marocchi et al. 2007; Sapienza et al. 2009; Marocchi et al. 2009; Tumiati et al. 2005). Zircon grains found in fine-grained peridotite strongly testifies to the introduction of exotic crustal hydrous fluids carrying HFSE (Tumiati et al. 2003; Forster, 2018; Gudelius et al., 2019). Here, carbonic aqueous fluids are channelized into veins to form dolomite + tremolite + chlorite, which crosscut the coarse-grained peridotite matrix 18LP1 at around 1GPa and 650-700°C (Consuma et al., 2020). The marked heterogeneity of in situ Sr isotope values measured by Consuma et al. (2020) in this vein, ranging from 0.7035 to 0.7085, encompasses both the $^{87}\text{Sr}/^{86}\text{Sr}$ signature of a depleted mantle ($^{87}\text{Sr}/^{86}\text{Sr}=0.7026$; Workman and Hart, 2005) and the country crustal gneisses ($^{87}\text{Sr}/^{86}\text{Sr}=0.716189$; Tumiati et al., 2003). This variability is also recognized in the $\delta^{13}\text{C}$ signature, which ranges between -16‰, corresponding to the lowest value for Ulten Zone carbonates and -9‰. If the Sr isotope signature correlates with the CL colors (Fig. 5.15 and Table 5.4), no significant correlations between $\delta^{13}\text{C}$ and CL colors were observed.

We interpret the dark red CL color with $^{87}\text{Sr}/^{86}\text{Sr}=0.7035$ and $\delta^{13}\text{C} = -8‰$ to represent primary mantle carbonates which have been metasomatized by later, crust-derived, incoming aqueous fluids that originate the dull green color. These exotic fluids must have episodically infiltrated the peridotite, as evidenced by the growth zoning of the dull green color in the vein (Fig.

5.1/e). The primary mantle composition later affected by crustal contamination can be also explained by the lack of significant Eu anomalies together with marked positive Eu anomalies in different spots analyses from the same vein and dark red CL color. Exhumation-related serpentinization plays a critical role in mobilizing volatiles and fluid-mobile elements during peridotite hydration. Serpentine plays a significant role as a sink and source of fluid mobile elements (FME) during metamorphism and subduction (Deschamps et al., 2013). In particular, serpentine can contain large amounts of B and Li, or being enriched in semi volatile and chalcophile elements like As, Sb, Pb, and large ion lithophile elements LILE like Sr Rb Cs Ba, Th and U. As such, in situ analyses can be used to evaluate the distribution and mobilization of FME at different P-T conditions. Petrographic observations indicate that serpentine veins cut both the peridotite matrix and the former dolomite vein, and they therefore compete with carbonates for the FME storage. Serpentinization of the coarse-grained peridotite 18LP1 possibly occurred in the early stages of exhumation, carrying B, Ba and Li. On the other hand, serpentinization of the chlorite-amphibole peridotite MM1+MM1B occurred later in the geotectonic scenario, as indicated by the lizardite-chrysotile composition and crustal components (i.e. marked positive Eu anomaly and higher concentrations of B). Carbon mobilization is finally reactivated by the dissolution of dolomite to form calcite/brucite intergrowths and liberate CO₂ in the system at shallow structural levels (Förster et al., 2017; Consuma et al. 2020). Liberation of CO₂ at shallow levels could contribute to late formation of calcite veins randomly found in some fine-grained peridotite or being recycled through the surficial C cycle.

5 • Trace elements and C-O stable isotope signature of texturally diverse mantle wedge dolomite

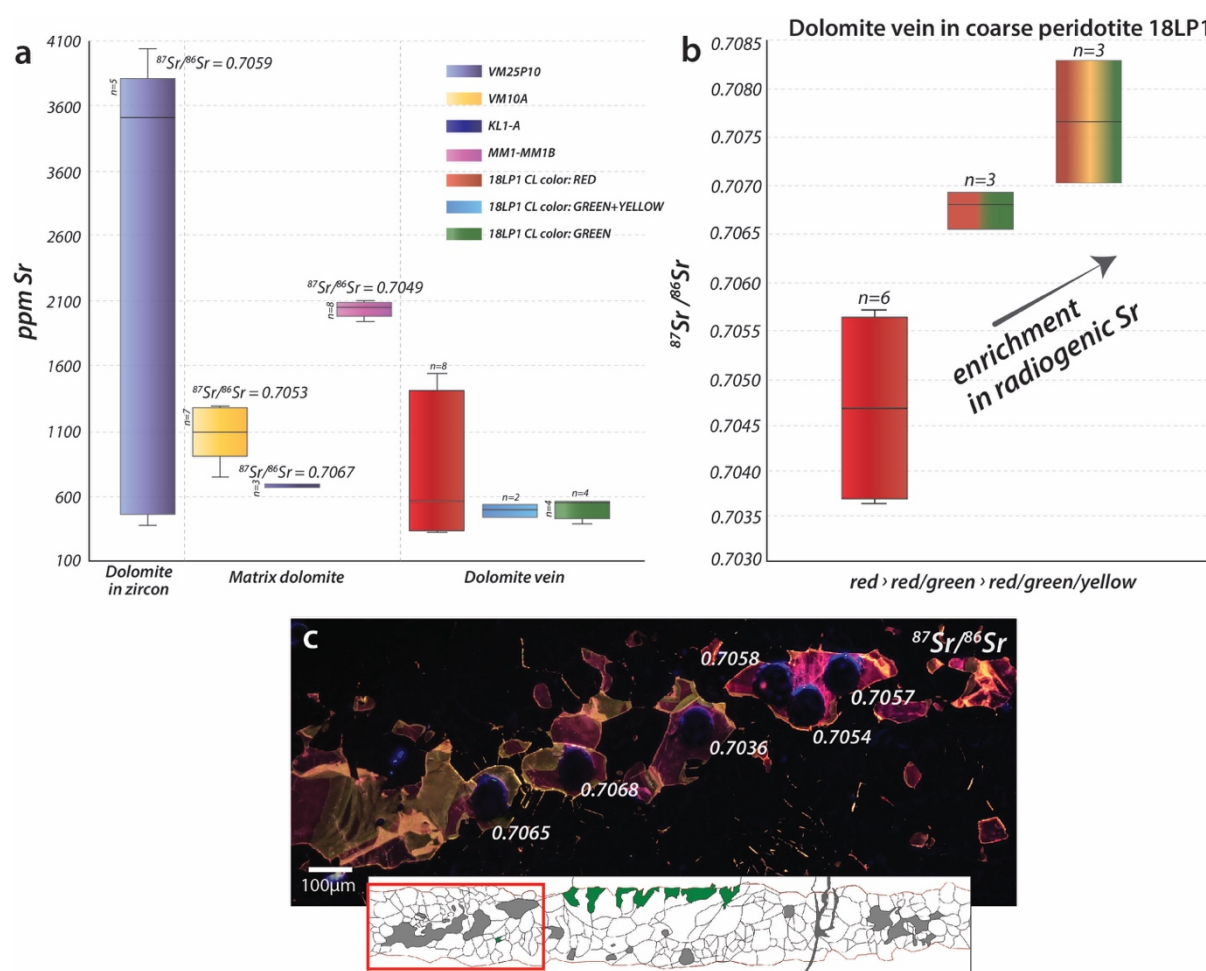


Fig. 5.15: *a*) Sr abundances in dolomite from the different textural positions analyzed by *in situ* Sr isotope (Consuma et al. 2020); *b*) in situ Sr isotope relative to the CL colors observed in the vein from peridotite 18LP1; *c*) portion of the vein shown in its CL colors and relative $^{87}\text{Sr}/^{86}\text{Sr}$ signature. Note that, for the vein from 18LP1, some mixtures of CL colors have not been analyzed for both the measurements reported in *a* and *b* due to lack of analytical requirements (i.e. size of the grain too small to be analyzed by LA-ICP-MC-MS). Of note, the dull green CL colors show growth zoning.

Table 5.4: Reported values of in situ Sr isotope measured by Consuma et al. (2020) with the relative CL color.

Peridotite 18LP1	#	CL color	^{88}Sr (V)	$^{87}\text{Rb}/^{86}\text{Sr}$	$^{87}\text{Sr}/^{86}\text{Sr}$	2se	Spot Size (µm)
Dolomite	9	Red/green/yellow	1.4	<0.0001	0.70830	0.00015	100
Dolomite	10	Red/yellow	1.6	<0.0001	0.70702	0.00017	100
Dolomite	11	Red/green	1.3	<0.0001	0.70694	0.00016	100
Dolomite	8	Red	2.4	<0.0001	0.70392	0.00013	90
Dolomite	7	Red	1.2	<0.0001	0.70571	0.00017	90
Dolomite	6	Red	0.8	0.0001	0.70541	0.00026	65
Dolomite	5	Red	3.0	<0.0001	0.70360	0.00007	65
Dolomite	4	Red/green	1.2	0.0003	0.70680	0.00013	65
Dolomite	3	Red/green	1.5	0.0001	0.70658	0.00019	100
Dolomite	12	Red	0.5	<0.0001	0.70531	0.00031	100
Dolomite	13	Red	0.7	0.0001	0.70509	0.00030	100
Dolomite	14+	Mixed	1.6	<0.0001	0.70636	0.00012	100

5.6.5 Preliminary considerations on the combined O isotope of carbonates, zircon, and olivine

We have seen that the low T fluids/peridotite interaction within the exhuming tectonic mélange could have led to a high degree of $\delta^{18}\text{O}$ homogenization in the dolomite. The obtained $\delta^{18}\text{O}$ values of the zircon in this study fall outside the typical mantle range ($5.3\text{‰} \pm 0.3\text{‰}$; Valley, 2003) and are more consistent with a crustal source. For comparison, negative to low $\delta^{18}\text{O}$ of -11.3 to +0.9 were measured by Li et al. (2016) in zircon from orogenic peridotite in the Sulu orogen. These values were interpreted to reflect the zircon growth from metasomatic fluids originated from a deeply subducted continental crust during an early exhumation. $\delta^{18}\text{O}$ values of zircon and olivine in contact with dolomite were used to perform preliminary oxygen isotope thermometry. Calculations were performed using the ThermoOx 1.0.1 software and the database DBOXYGEN 2.0.3 (Vho et al., 2019). We obtained temperature of ca. 300°C for included dolomite within the host zircon and 400°C for matrix dolomite (with magnesite) with fine-grained olivine. This may suggest that externally-derived fluids may have reset the $\delta^{18}\text{O}$ compositions at low temperature. Future detailed studies are needed to fully comprehend the effect of low T on the O isotope composition of zircon at appropriate P-T conditions.

5.7 Conclusions

The mantle wedge is probably the least known domain within the subduction factory (Kelemen and Manning, 2015). It is therefore fortunate that the Ulten Zone peridotites can give us the opportunity to study C-related reactions throughout a complex metamorphic evolution. Integrated CL petrography, trace elements and C-O isotopic study were used on mantle wedge diverse dolomite that evidences various carbonic fluid flow upon high-pressure and retrograde conditions.

The main results we found are:

1. The first melt-mediated metasomatic episode is recorded by the percolation of a hot (1400°C; Nimis and Morten, 2000) $\text{H}_2\text{S-CO}_2$ -bearing mafic melt intruded into a coarse-grained peridotite, which promoted pervasive carbonation (in the form of matrix dolomite) into a newly formed pyroxenite layer. Further interaction of a matrix dolomite with primary mantle signature ($\delta^{13}\text{C} = -8\text{‰}$) with later infiltration of isotopically lighter fluids/melts is recorded by the wide range of measured $\delta^{13}\text{C}$ values that reaches -12‰. This pre-peak stage is also recorded by the $\delta^{13}\text{C}$ values of -8‰ recorded by the unique preserved dolomite

inclusion with a regular shape within the coarse spinel also indicates this first pre-peak metasomatic episode.

2. At high pressure conditions (ca. 850°C, < 2.7 GPa; Nimis and Morten, 2000). Pervasive flow along grain boundaries, mediated by carbonic fluids carrying incompatible trace elements, form eclogite-facies dolomite, whose various trace elements compositions reflect the involvement of geochemically different metasomatic agents and the provinciality of the fluid sources. Dolomite from the hybrid contact zone of Mt. Hocwhart is critical for the LILE and HFSE mobility, whereas carbonic fluids from Klppferbgalm shows minor enrichment in LREE but a higher crustal affinity. Peridotite VM10A is not serpentinized and the variation in the $\delta^{13}\text{C}$ is better explained through late addition of external isotopically lighter $\delta^{13}\text{C}$ fluid (possibly neighbouring migmatites and gneisses), and/or leaching of $\delta^{13}\text{C}$ by external metasomatic agents. This is also supported by the observed different CL colors (dull green surrounded by dark orange), which suggest infiltrations of different fluids.
3. The isotopically heterogeneous dolomite vein also reflects several fluid infiltrations from a mixing of depleted mantle and crustal sources, which may have variably affected the $\delta^{13}\text{C}$ signature. Of note, further growth zoning revealed by the dull green CL color in the vein also points to episodically fluid infiltrations. Low T dilute fluids carrying minor to low concentration of C within the mélange have prompted the re-equilibration $\delta^{18}\text{O}$ values of dolomite, whereas the $\delta^{13}\text{C}$ signature is weakly affected.
4. Upon late retrogression, serpentinizing fluids of high crustal affinity are channelized into veins crosscutting previous veins of carbonates and enhancing dolomite dissolution to form calcite/brucite intergrowths and liberate CO_2 .

Acknowledgements

This project is funded by Marco Polo Scholarship given to GC. The University of Lausanne is thanked for hosting GC as a PhD visiting student. Antonio Langone and Claudia Baumgartner are thanked for assisting G.C. during the trace elements analyses and cathodoluminescence petrography.

Chapter Five – References

Baumgartner, L.P., Valley, J.W., 2001. Stable Isotope Transport and Contact Metamorphic Fluid Flow. *Rev. Mineral. Geochem.* 43, 415–467. <https://doi.org/10.2138/gsrmg.43.1.415>

- Bebout, G.E., Barton, M.D., 2002. Tectonic and metasomatic mixing in a high-T, subduction-zone mélange—insights into the geochemical evolution of the slab–mantle interface. *Chem. Geol.* 187, 79–106. [https://doi.org/10.1016/S0009-2541\(02\)00019-0](https://doi.org/10.1016/S0009-2541(02)00019-0)
- Bebout, G.E., Penniston-Dorland, S.C., 2016. Fluid and mass transfer at subduction interfaces—The field metamorphic record. *Lithos* 240–243, 228–258. <https://doi.org/10.1016/j.lithos.2015.10.007>
- Breeding, C.M., Ague, J.J., Bröcker, M., 2004. Fluid–metasedimentary rock interactions in subduction-zone mélange: Implications for the chemical composition of arc magmas. *Geology* 32, 1041–1044. <https://doi.org/10.1130/G20877.1>
- Cannaò, E., Agostini, S., Scambelluri, M., Tonarini, S., Godard, M., 2015. B, Sr and Pb isotope geochemistry of high-pressure Alpine metaperidotites monitors fluid-mediated element recycling during serpentinite dehydration in subduction mélange (Cima di Gagnone, Swiss Central Alps). *Geochim. Cosmochim. Acta* 163, 80–100. <https://doi.org/10.1016/j.gca.2015.04.024>
- Consuma, G., Braga, R., Giovanardi, T., Bersani, D., Konzett, J., Lugli, F., Mazzucchelli, M., Tropper, P., 2020. In situ Sr isotope analysis of mantle carbonates: Constraints on the evolution and sources of metasomatic carbon-bearing fluids in a paleo-collisional setting. *Lithos* 354–355, 105334. <https://doi.org/10.1016/j.lithos.2019.105334>
- Debret, B., Sverjensky, D.A., 2017. Highly oxidising fluids generated during serpentinite breakdown in subduction zones. *Sci. Rep.* 7, 10351. <https://doi.org/10.1038/s41598-017-09626-y>
- Förster, B., 2018. MULTI-STAGE METASOMATISM IN A MANTLE-WEDGE AND EXHUMATION MÉLANGE: NEW INSIGHTS FROM THE PERIDOTITES OF THE ULTEN ZONE (EASTERN ALPS, ITALY). *Plinius* 41–48. <https://doi.org/10.19276/plinius.2018.01006>
- Förster, B., Braga, R., Aulbach, S., Lo Pò, D., Bargossi, G.M., Mair, V., 2017. A petrographic study of carbonate phases in the Ulten Zone ultramafic rocks: insights into carbonation in the mantle wedge and exhumation-related decarbonation. *Ofioliti* 42, 105–127.
- Frezzotti, M.L., Selverstone, J., Sharp, Z.D., Compagnoni, R., 2011. Carbonate dissolution during subduction revealed by diamond-bearing rocks from the Alps. *Nat. Geosci.* 4, 703–706. <https://doi.org/10.1038/ngeo1246>
- Gudelius, D., Aulbach, S., Braga, R., Höfer, H.E., Woodland, A.B., Gerdes, A., 2019. Element Transfer and Redox Conditions in Continental Subduction Zones: New Insights from Peridotites of the Ulten Zone, North Italy. *J. Petrol.* 60, 231–268. <https://doi.org/10.1093/petrology/egy112>
- Habermann, D., Neuser, R.D., Richter, D.K., 2000. Quantitative High Resolution Spectral Analysis of Mn²⁺ in Sedimentary Calcite, in: Pagel, M., Barbin, V., Blanc, P., Ohnenstetter, D. (Eds.), *Cathodoluminescence in Geosciences*. Springer, Berlin, Heidelberg, pp. 331–358. https://doi.org/10.1007/978-3-662-04086-7_13
- Ionov, D., Harmer, R.E., 2002. Trace element distribution in calcite[^]dolomite carbonatites from Spitskop: inferences for differentiation of carbonatite magmas and the origin of carbonates in mantle xenoliths. *Earth Planet. Sci. Lett.* 16.
- Kelemen, P.B., Manning, C.E., 2015. Reevaluating carbon fluxes in subduction zones, what goes down, mostly comes up. *Proc. Natl. Acad. Sci.* 112, E3997–E4006. <https://doi.org/10.1073/pnas.1507889112>

- Linzmeier, B.J., K. Kitajima, A.C. Denny, and J.N. Cammack (2018). Making maps on a micro meter scale, *Eos*, 99.
- Marocchi, M., Hermann, J., Morten, L., 2007. Evidence for multi-stage metasomatism of chlorite-amphibole peridotites (Ulten Zone, Italy): Constraints from trace element compositions of hydrous phases. *Lithos, Melt-rock reaction processes in the mantle and their bearing on mantle petrology and chemistry* 99, 85–104. <https://doi.org/10.1016/j.lithos.2007.05.010>
- Marocchi, M., Mair, V., Tropper, P., Bargossi, G.M., 2009. Metasomatic reaction bands at the Mt. Hochwart gneiss-peridotite contact (Ulten Zone, Italy): insights into fluid-rock interaction in subduction zones. *Mineral. Petrol.* 95, 251–272. <https://doi.org/10.1007/s00710-009-0043-8>
- Marocchi, M., Marschall, H.R., Konzett, J., Tropper, P., Ludwig, T., Mair, V., Bargossi, G.M., 2011. Metasomatic tourmaline in hybrid contact-bands between gneiss and peridotite in the Ulten zone of the Eastern Italian Alps: chemistry and boron isotopic composition. *Can. Mineral.* 49, 245–261. <https://doi.org/10.3749/canmin.49.1.245>
- McDonough, W.F. and Sun, S., 1995. The composition of the Earth. *Chem. Geol.* **120**, 223–253.
- Piccoli, F., Vitale Brovarone, A., Beyssac, O., Martinez, I., Ague, J.J., Chaduteau, C., 2016. Carbonation by fluid–rock interactions at high-pressure conditions: Implications for carbon cycling in subduction zones. *Earth Planet. Sci. Lett.* 445, 146–159. <https://doi.org/10.1016/j.epsl.2016.03.045>
- Rampone, E., Morten, L., 2001. Records of Crustal Metasomatism in the Garnet Peridotites of the Ulten Zone (Upper Austroalpine, Eastern Alps). *J. Petrol.* 42, 207–219. <https://doi.org/10.1093/petrology/42.1.207>
- Sapienza, G.T., Scambelluri, M., Braga, R., 2009. Dolomite-bearing orogenic garnet peridotites witness fluid-mediated carbon recycling in a mantle wedge (Ulten Zone, Eastern Alps, Italy). *Contrib. Mineral. Petrol.* 158, 401–420. <https://doi.org/10.1007/s00410-009-0389-2>
- Scambelluri, M., Hermann, J., Morten, L., Rampone, E., 2006. Melt- versus fluid-induced metasomatism in spinel to garnet wedge peridotites (Ulten Zone, Eastern Italian Alps): clues from trace element and Li abundances. *Contrib. Mineral. Petrol.* 151, 372–394. <https://doi.org/10.1007/s00410-006-0064-9>
- Scambelluri, M., Rampone, E., Braga, R., Malaspina, N., 2010. The Variscan garnet peridotites from the Eastern Alps (Ulten Zone): Records of subduction metasomatism in the mantle wedge. *J. Virtual Explor.* 36, paper 28. <https://doi.org/10.3809/jvirtex.2009.00259>
- Shen, J., Li, S.-G., Wang, S.-J., Teng, F.-Z., Li, Q.-L., Liu, Y.-S., 2018. Subducted Mg-rich carbonates into the deep mantle wedge. *Earth Planet. Sci. Lett.* 503, 118–130. <https://doi.org/10.1016/j.epsl.2018.09.011>
- Stewart, E.M., Ague, J.J., Ferry, J.M., Schiffries, C.M., Tao, R.-B., Isson, T.T., Planavsky, N.J., 2019. Carbonation and decarbonation reactions: Implications for planetary habitability. *Am. Mineral.* 104, 1369–1380. <https://doi.org/10.2138/am-2019-6884>
- Stewart, E.M., Ague, J.J., 2020. Pervasive subduction zone devolatilization recycles CO₂ into the forearc. *Nat. Commun.* 11, 6220. <https://doi.org/10.1038/s41467-020-19993-2>
- Tao, R., Zhang, L., Tian, M., Zhu, J., Liu, X., Liu, J., Höfer, H.E., Stagno, V., Fei, Y., 2018. Formation of abiogenic hydrocarbon from reduction of carbonate in subduction zones: Constraints from

5 • Trace elements and C-O stable isotope signature of texturally diverse mantle wedge dolomite

- petrological observation and experimental simulation. *Geochim. Cosmochim. Acta* 239, 390–408. <https://doi.org/10.1016/j.gca.2018.08.008>
- Tumiati, S., Godard, G., Martin, S., Klötzli, U., Monticelli, D., 2007. Fluid-controlled crustal metasomatism within a high-pressure subducted mélange (Mt. Hochwart, Eastern Italian Alps). *Lithos, Melting, Metasomatism and Metamorphic Evolution in the Lithospheric Mantle* 94, 148–167. <https://doi.org/10.1016/j.lithos.2006.06.009>
- Tumiati, S., Godard, G., Martin, S., Nimis, P., Mair, V., Boyer, B., 2005. Dissakisite-(La) from the Ulten zone peridotite (Italian Eastern Alps): A new end-member of the epidote group. *Am. Mineral.* 90, 1177–1185. <https://doi.org/10.2138/am.2005.1710>
- Tumiati, S., Malaspina, N., 2019. Redox processes and the role of carbon-bearing volatiles from the slab–mantle interface to the mantle wedge. *J. Geol. Soc.* 176, 388–397. <https://doi.org/10.1144/jgs2018-046>
- Tumiati, S., Thöni, M., Nimis, P., Martin, S., Mair, V., 2003. Mantle–crust interactions during Variscan subduction in the Eastern Alps (Nonsberg–Ulten zone): geochronology and new petrological constraints. *Earth Planet. Sci. Lett.* 210, 509–526. [https://doi.org/10.1016/S0012-821X\(03\)00161-4](https://doi.org/10.1016/S0012-821X(03)00161-4)
- Valley, J.W., 1986. Chapter 13. STABLE ISOTOPE GEOCHEMISTRY of METAMORPHIC ROCKS, in: Valley, J.W., Taylor, H.P., O'Neil, J.R. (Eds.), *Stable Isotopes in High Temperature Geological Processes*. De Gruyter, Berlin, Boston, pp. 445–490. <https://doi.org/10.1515/9781501508936-018>
- Vho A., Lanari P., Rubatto. D (2019). Internally-consistent database for oxygen isotope fractionation between minerals. *Journal of Petrology*, **60**, 2101–2130
- Vitale Brovarone, A., Chu, X., Martin, L., Ague, J.J., Monié, P., Groppo, C., Martinez, I., Chaduteau, C., 2018. Intra-slab COH fluid fluxes evidenced by fluid-mediated decarbonation of lawsonite eclogite-facies altered oceanic metabasalts. *Lithos* 304–307, 211–229. <https://doi.org/10.1016/j.lithos.2018.01.028>

6 • The sulfur component of the Ulten Zone peridotite: a piece of the deep Sulfur cycle?

Article accepted: Multi-stage sulfur and carbon mobility in fossil continental subduction zone: new insights from carbonate-bearing orogenic peridotites

Giulia Consuma, Sonja Aulbach, Roberto Braga, Laure A.J. Martin, Peter Tropper, Axel Gerdes and Marco L. Fiorentini

Publication status: accepted at *Geochimica et Cosmochimica Acta* (14/04/2021)

Keywords: sulfur isotopes; sulfide; mantle wedge; orogenic garnet peridotite

Note: Some additional figures previously reported as Supplementary Material are now reported in the main text.

6.1 Abstract

The volatile transfer in subduction zones and the role of sulfate as a vector for the mobilization of oxidized components from down-going slabs remain hotly debated issues. Orogenic spinel and garnet peridotite lenses from the Ulten Zone (Eastern Alps, Italy), exhumed as part of felsic metamorphic terranes in continental collision zones, bear witness to mass transfer processes in these pivotal environments.

In this study, we report a multi-method investigation of mantle sulfides coexisting with four generations of carbonates, indicating coupled sulfur and carbon mobility throughout the peridotites' metamorphic evolution as part of the Variscan subduction architecture. Detailed petrography, bulk rock measurements, *in situ* chemical and geochemical analyses of sulfides as well as Sr isotope analyses of associated clinopyroxene and amphibole are combined with the aim to constrain the origin, nature and effect of multiple C-O-H-S-bearing fluids and melts the peridotite interacted with. The first, pre-peak, metasomatic pulse (Stage 1) is represented by an H₂S-CO₂-bearing melt from the subduction-modified hot mantle wedge, which formed a pyroxenite layer hosting matrix pentlandite with $\delta^{34}\text{S}$ of +2.77‰. Heavier $\delta^{34}\text{S}$ (up to +3.43‰), radiogenic Sr

($^{87}\text{Sr}/^{86}\text{Sr}_{\text{clinopyroxene}} > 0.7052$) and elevated Pb abundances recorded in coarse-grained garnet peridotite under eclogite-facies peak-conditions (Stage 2) are ascribed to interaction with isotopically heavy melts carrying recycled crustal component, permissive of, but not requiring, involvement of oxidized S species. Matrix carbonates occasionally occur in the coarse-grained peridotite. Conversely, isotopically lighter matrix pentlandite ($\delta^{34}\text{S} = -1.62$ to $+0.67\text{‰}$), and radiogenic Sr in amphibole ($^{87}\text{Sr}/^{86}\text{Sr} = 0.7056$) and associated dolomite (published data), from fine-grained garnet-amphibole peridotite may point to involvement of H_2S - CO_2 -bearing crustal fluids, which variably equilibrated with the mantle before interacting with the peridotites. Sulfide and amphibole in retrogressed spinel peridotite reveal the highest contents of fluid-mobile elements (As, Sb) and $^{87}\text{Sr}/^{86}\text{Sr}_{\text{amphibole}}$ up to 0.7074, suggesting late interaction with isotopically heavy crustal fluids at high fluid-rock ratios. The post-peak Stage 3 marks the entrapment of peridotites into a tectonic *mélange*. Here, kelyphitization of garnet is catalyzed by further ingress of a S-bearing fluid ($\delta^{34}\text{S} = -0.38\text{‰}$), while carbonate veining with occasional sulfides bear witness to channelized fluid flow. Textural observations indicate that, during Stage 4, serpentinization of peridotites at low f_{S_2} played an active role not only in CO_2 release by conversion of dolomite to calcite + brucite intergrowths, but also in local removal of ^{32}S during the final exhumation stage. Late channelized sulfur remobilization is evidenced by the serpentine + magnetite (\pm millerite \pm calcite) vein carrying > 300 ppm S.

Overall, the relatively narrow range of sulfur isotope composition ($\delta^{34}\text{S} = -1.62$ to $+3.76\text{‰}$) is indicative for a limited interaction with isotopically heavy crustal liquids, and points to a subordinate role of subduction-derived sulfate throughout the extended fluid(melt)/rock evolution of the Ulten Zone peridotites, first in the mantle wedge and then as part of a tectonic *mélange*.

6.2 Introduction

Sulfur (S) is a minor component in the mantle, yet it is thought to exert a key control on mantle redox conditions as well as ore-forming processes (e.g., Tomkins and Evans, 2015; Evans et al., 2017; Holwell et al., 2019). In xenoliths and orogenic peridotites, S is mostly stored in sulfides, such as pentlandite, pyrrhotite, chalcopyrite, monosulfide-solid-solution (mss) and intermediate-solid-solution (iss) (e.g., Lorand et al., 2013; Kiseeva et al., 2017; Vaughan and Corkhill, 2017). The speciation and mobility of S in subduction zones is of particular interest because magmas in convergent-margin settings have been shown to be more oxidized than those from spreading ridges (e.g., Kelley and Cottrell, 2009; Evans, 2012), and with a redox budget of eight electrons, S has been invoked as a potential oxidizing agent (Evans et al., 2017; Bénard et al., 2018).

Development of cutting-edge analytical techniques and improvement of thermodynamic modeling tools have recently led to major advances in constraining the speciation, sources and mobility of sulfur in oceanic subduction settings and associated ore deposit formation (e.g., Evans et al. 2014; Schwarzenbach et al., 2018a, Li et al., 2020; Walters et al., 2020). However, major uncertainties persist for several reasons, such as (i) the lack of defined sulfide solid solution models for thermodynamic modelling; (ii) the limited control on physicochemical conditions (e.g. oxygen fugacity) determining S speciation and behavior, (iii) the lack of data from the mantle wedge, prevented by the small size of mantle sulfides, which remains a less-well known domain within the subduction factory.

In addition, the recent resultant research efforts produced conflicting lines of evidence for the behavior of S in subduction zones and for its contribution to the oxidation state of the sub-arc mantle region. Thus, exhumed mafic and ultramafic rocks from the island of Syros (Greece), interpreted as blocks detached from the lithospheric slab to form a subduction channel mélange under blueschist-facies conditions, were shown to have bulk-rock S isotopic signatures inherited from seawater alteration and overprinted by sediment-derived fluids mobilizing S along the plate interface (Schwarzenbach et al., 2018a). Evans et al. (2014) find complex S isotopic zoning of pyrite grains in eclogites originating as subducted oceanic crust from the Zermatt-Saas zone (Western Alps) and the Pouébo terrane (New Caledonia), which they ascribe to S loss during prograde metamorphism and sulfide growth at the earliest stage of exhumation. Similarly, Walters et al. (2019) describe sulfides of metasomatic origin from a global suite of exhumed high-pressure rocks, that yield a wide range of S isotopic compositions interpreted as having precipitated from sulfate-bearing fluids. Bénard et al. (2018) also maintain that oxidized slab components have the potential to oxidate the sub-arc mantle, by documenting dissolved S^{6+} in spinel-hosted glass inclusions in sub-arc mantle xenoliths brought to the surface by a recent volcanic activity in the Kamchatka (Russia) and West Bismarck arcs (Papua New Guinea). On the other hand, Li et al. (2020) show most S to be present as reduced species, and argue for limited S release in slab fluids. These constraints are based on a combination of petrographic observations, whole-rock and *in situ* S isotope measurements and thermodynamic modelling of sulfide-bearing high-pressure rocks and veins from the southwestern Tianshan (ultra-)high-pressure (U-HP) metamorphic belt (China). Thermodynamic modelling results of Piccoli et al. (2019) also support the reducing nature of dehydrated slab fluids at sub-arc depth. Giacometti et al. (2014) report little evidence for S mobilization during metamorphism from microtextural and *in situ* S isotopic analysis of exhumed meta-ophiolites from the Western Alps. Two-stage release of S during subduction is predicted by the thermodynamic modelling results of Walters et al. (2020), with a small flux of reduced S at

shallow depths and elevated S fluxes from deep, cold oxidized slabs via the release of sulfate and sulfide species. Although Tomkins and Evans (2015) also predict a two-stage release process, they model anhydrite dissolution into fluids at low temperatures and the release of H₂S when pyrite converts to pyrrhotite at higher temperatures.

Despite the importance of orogenic mantle peridotites as proxies for deep and retrograde-fluid-mediated volatile exchange between crust and mantle (Scambelluri et al., 2010), few studies have investigated the S speciation and isotopic composition of orogenic mantle rocks as an integral component of the global S cycle. Orogenic spinel lherzolites in the North-Eastern Pyrénées yielded negative values of $\delta^{34}\text{S} = -3.2\text{‰}$ to represent an ancient S depletion event in the upper mantle, whereas positive values up to +3.3‰ of pyroxenite intrusions were interpreted to reflect various enriched mantle sources (Chaussidon and Lorand, 1990). The positive shift in the $\delta^{34}\text{S}$ of sulfides up to +5.4‰ from the garnet-bearing pyroxenites in the Western Gneiss Region of Norway (Rielli et al., 2018) are ascribed to contamination from oceanic slab-derived oxidized fluids, whereas negative values down to -10.0‰ are attributed to fluids, which originated from the enclosing gneisses or subducted oceanic sediments.

We focus on this little-explored facet of the S cycle, by investigating well-characterized orogenic spinel and garnet peridotites from the Ulten Zone (UZ) in the Eastern Alps that originated as continental mantle that became involved in continent-continent collision during the Variscan Orogeny. Displaying a diversity of compositional and mineralogical features, including several generations of hydrous and carbonate minerals, the UZ peridotites have been the subject of multiple investigations, with a focus on unravelling the element cycles in convergent margin settings (Rampone and Morten, 2001; Scambelluri et al., 2006; Hermann et al., 2006; Marocchi et al., 2009; Sapienza et al., 2009; Marocchi et al., 2010; Scambelluri et al., 2010; Marocchi et al., 2011; Braga and Massonne, 2012; Förster et al., 2017; Ionov et al., 2017; Gudelius et al., 2019; Consuma et al., 2020; Lo Pò et al., 2020). The occurrence of sulfides in the UZ peridotites and their petrological implications have so far been overlooked as an important source of information on the behavior of S in fossil continental subduction zones. In this regard, taking advantage of the spatial resolution and textural control afforded by *in situ* analyses of single sulfide grains, we use S isotopes as a sensitive tracer of the speciation and source of S in high pressure orogenic settings. Additional constraints on the nature of metasomatic agents can be inferred from the variation in the trace element composition of texturally diverse pentlandite, which is known to reflect changes in the physicochemical fluid parameters (e.g., pressure, temperature, oxygen fugacity). Dehydration and partial melting lead to a depletion of the upper mantle in fluid-mobile and magmaphile

elements, respectively, including the chalcophile elements As, Sb, Se, Te and Pb (Hattori et al., 2002; Hattori and Guillot, 2003). As a consequence, their enrichment in the mantle wedge is usually explained by the supply of these elements from slab-derived fluids and melts that percolate and metasomatize the supra-subduction mantle. These variable chalcophile elements (e.g., Barnes, 2016) would be expected to follow sulfide complexes (e.g., as HS⁻) mobilized in fluids and melts. *In-situ* determination of S isotopic and trace element compositions of pentlandite, combined with whole-rock analyses, *in situ* Sr isotope compositions of amphibole and clinopyroxene, and published *in situ* Sr isotope of the associated carbonates, allow to delineate a model for the formation and modification of sulfide and associated carbonates, and to discuss the potential sources and effects of C-O-H-S liquids percolating the mantle wedge during continental collision.

6.3 Geological setting and metasomatic history

The Ulten Zone (UZ) is a Variscan tectonic unit located in the Tonale Nappe (Eastern Alps) (Fig. 6.1). It is part of the metamorphic basement of the Austroalpine domain, interpreted as a constituent of Gondwana before its involvement in the Variscan collision with Laurussia (Regorda et al., 2020). In this unit, relicts of high pressure (HP) metamorphism are preserved as lenses of ultramafic rocks (mostly garnet-bearing peridotites and eclogites) within host rocks such as migmatites and garnet-kyanite gneisses.

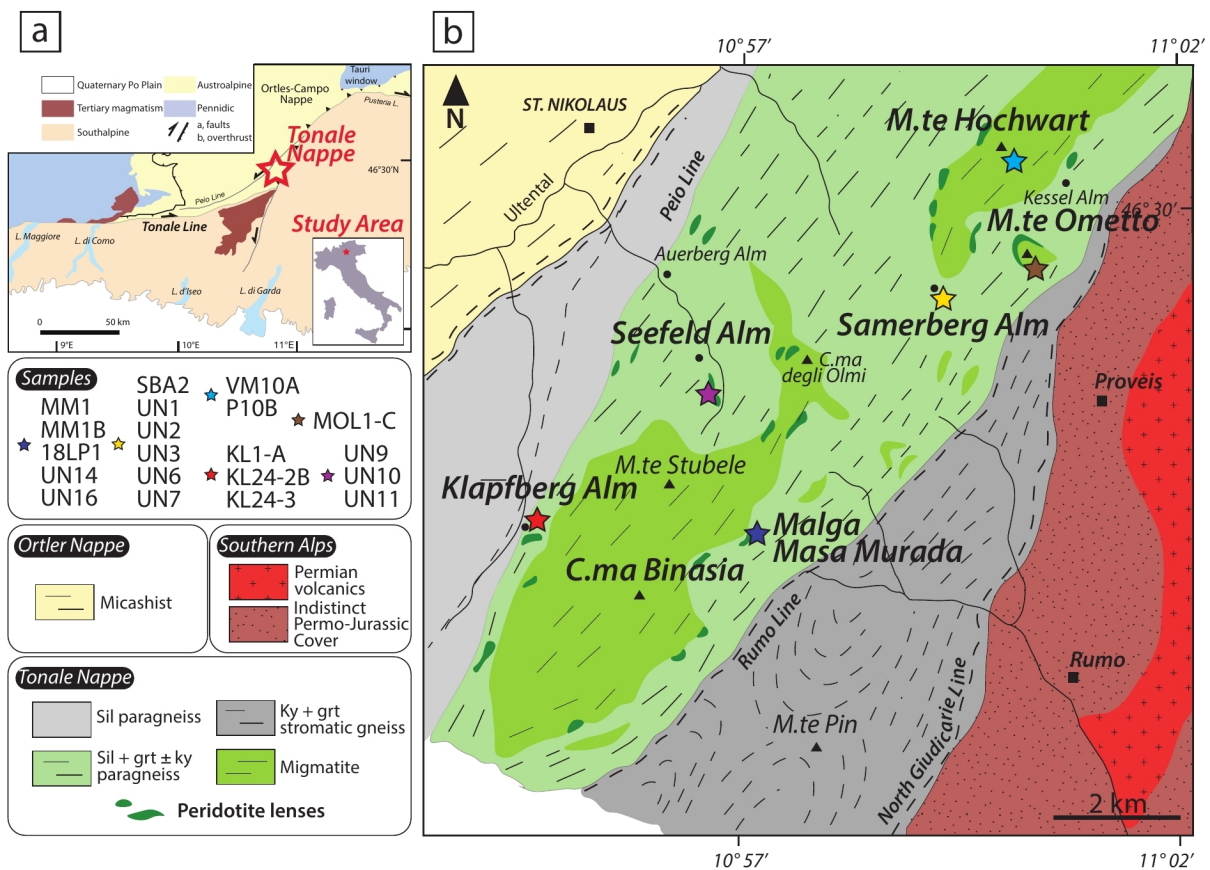


Fig. 6.1: Geological sketch map of the central and Eastern Alps modified after Langone et al. (2011). (b) Geological-structural map of the Ulten Zone modified after Tumati et al. (2003) and Consuma et al. (2020). The reader is referred to Consuma et al. (2020) and (Gudelius et al., 2019) for the exact location of the samples.

The peridotites first resided in a supra-subduction zone mantle wedge at relatively high temperature (about 1200°C), followed by re-equilibration under eclogite-facies HP conditions of ~850°C and pressure of 2.2-2.7 GPa (Nimis and Morten, 2000; Braga and Sapienza, 2007), as a result of their movement toward deeper portions of the upper mantle during continental crust subduction along a relatively cold path (Figs. 6.2a-b). Prior to or contemporaneously with the attainment of eclogite-facies conditions, the former coarse-protogranular peridotites experienced deformation and recrystallization into fine-grained peridotites, with formation of garnet and amphibole at the expense of spinel and clinopyroxene. The post-collisional stage comprises the development of a crust-peridotite tectonic mélange, and the onset of its exhumation is estimated to begin at around 330 Ma (Tumati et al., 2003). The three different lithologies described by Obata and Morten (1987) synthesize the different stages of peridotite evolution: (1) (pre-peak) coarse-grained protogranular spinel peridotite (CS) that transforms into a variety with coronitic garnet (CG), consisting of olivine + enstatite + diopside + Cr-Al spinel (\pm garnet); (2) (peak)

porphyroclastic (P-FGA) to equigranular fine-grained garnet-amphibole peridotite (FGA) consisting of olivine + orthopyroxene + clinopyroxene + garnet + Ca-amphibole + spinel; and (3) (post-peak/exhumation) fine-grained spinel (chlorite-amphibole) peridotite (FSA) with olivine + orthopyroxene + Ca-amphibole + chlorite ± spinel. All the UZ peridotites were variably serpentinized as they were involved in a crust-mantle mélange along the exhumation path. The exceptional complexity of the study area results from polyphase C-O-H-metasomatism along the Variscan continent collision (i.e. peak pressure conditions and retrogression afterwards), during which inputs of metasomatic liquids percolated the overlying orogenic mantle wedge inducing the formation of hydrous and carbonate phases.

On the basis of the high modal amphibole contents with a strong LILE/HSFE fractionation, Rampone and Morten (2001) suggested that the metasomatic agents of the high-pressure hydrous metasomatism are fluids with a low CO₂/H₂O ratio sourced from the neighboring crustal rocks. Nevertheless, carbonate phases related to the progressive metasomatic stages occur ubiquitous in the Ulten Zone peridotites, the petrography of which is described in detail in Förster et al. (2017). Inclusion of dolomite in coarse spinel, itself enclosed in garnet, was ascribed as a trapped melt during the high-temperature metasomatic stage in the mantle wedge (Stage 1 in Fig. 2a-b), despite the radiating fracturing which may point to a late metasomatic process (Consuma et al. 2020). Formation of interstitial dolomite with minor magnesite has been ascribed as a peak-pressure feature, while late exhumation-related serpentinization caused dolomite dissolution and formation of calcite+brucite intergrowths via the reaction $\text{CaMg}(\text{CO}_3)_2 + \text{H}_2\text{O} \rightarrow \text{CaCO}_3 + \text{Mg}(\text{OH})_3 + \text{CO}_2$. This reaction implies CO₂ liberation from peridotites now entrapped in a crust-mantle mélange (Förster et al., 2017). Subsequent *in situ* Sr isotope measurements of the UZ carbonates have shown multiple signatures related to their textural positions (Consuma et al., 2020): relatively unradiogenic ⁸⁷Sr/⁸⁶Sr of ~ 0.705 in matrix dolomite in equilibrium with garnet was taken as evidence that fluid sources variably equilibrated with a depleted mantle reservoir percolated the peridotite at high-pressure peak conditions. In contrast, variably radiogenic ⁸⁷Sr/⁸⁶Sr (0.7036 to 0.7083) was ascribed to hybridized sources (i.e. mixing of depleted mantle and crustal liquids) generated after the entrapment of peridotites into crustal rocks during the exhumation stage (Consuma et al., 2020). The occurrence of these carbonates commonly in intimate association with sulfides in different textural positions proves that metasomatic fluids and melts played a continuous role in the mobility not only of carbon but also of sulfur in the mantle wedge and tectonic mélange, and thus opens new questions regarding their role in the global S cycle.

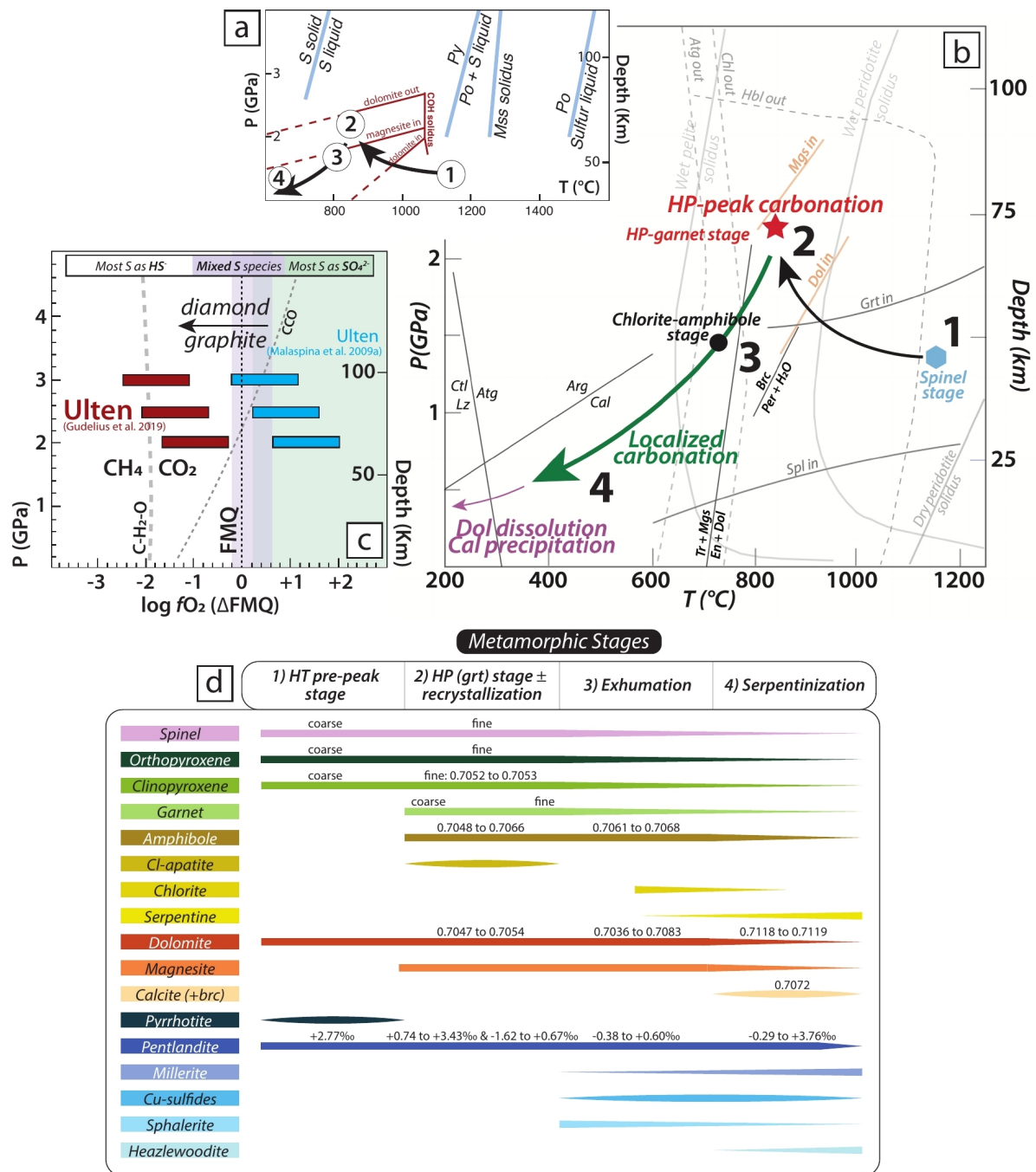


Figure 6.2: (a-b) Pressure (P)-Temperature (T) diagram modified after Consuma et al. (2020) showing the pressure-temperature evolution of the Ulten Zone peridotites, with respect to various metasomatic stages and phase relations for COH-bearing species. The experimentally determined melting curves of sulfur, pyrrhotite, Mss and decomposition of pyrite are taken from Brazhkin et al. (1999), Zhang et al. (2015) and Bataleva et al. (2018). Dolomite-in, magnesite-in, dolomite-out, garnet-in curves from Tumiati et al. (2013); tremolite (Tr) + magnesite (Mgs) = enstatite (En) + dolomite (Dol) are from Malaspina and Tumiati (2012) for $X_{CO_2}=0.5$; brucite (Brc) = periclase (Per) + water (H_2O) from Schramke et al. (1982). Antigorite-out curve and chlorite-out curve from (Fumagalli and Poli, 2005). Antigorite (Atg) = chrysotile (Ctl) / lizardite (Liz) are from Evans et al. (1976); aragonite (Arg) = calcite (Cal) from Johannes and Puhan (1971). P-T conditions of Stage 2 are taken from Nimis and Morten (2000) and Sapienza et al. (2009). **Sulf**—sulfide, **Po**—pyrrhotite, **Py**—pyrite, **Mss**—monosulfide solid solution.

- (c) Ranges and average values of oxygen fugacity relative to the fayalite–magnetite–quartz buffer (FMQ) for the Ulten Zone peridotites for various pressures (GPa), as well as CHO speciation, modified from Cannaò and Malaspina (2018) and Gudelius et al. (2019). Note the offset to higher fO_2 obtained by Malaspina et al. (2009), who, using the same method, obtained higher $Fe^{3+}/\sum Fe$ in garnet from their samples. Fields denote fO_2 where most S in basalt glass (Jugo et al., 2010) and in sediment glass (Canil and Fellows, 2017) is present as HS^- ($\sim FMQ$ and maximum $FMQ \leq 0.2$, respectively) and as $H_2SO_4^{2-}$ ($\sim FMQ+2$ and minimum $FMQ \geq 0.2$, respectively), with mixed species at intermediate fO_2 in the basalt.
- (d) Table showing the presence of rock-forming minerals, hydrous minerals, carbonates and sulfides as linked to distinct metamorphic stages (1-4) of the Ulten Zone peridotites. Grain size is qualitatively indicated for spinel, orthopyroxene, clinopyroxene and garnet. *In situ* Sr isotope compositions are reported for clinopyroxene, amphibole (this study) and for dolomite, calcite (Consuma et al., 2020). S isotope compositions of pentlandite measured by SIMS (this study) are also shown. **HT**—high temperature, **HP**—high pressure, **grt**—garnet.

6.4 Samples, prior work and sulfide petrography

We investigated twenty orogenic peridotite samples from different localities of the Ulten Zone (Fig. 6.1), as being representative of different domains of the Variscan Ulten Zone mantle wedge. The selection was guided by the motivation to include specimens that are representative of the metamorphic and metasomatic stages, mineral assemblages, and presence of carbonates and sulfides.

Ten samples encompassing coarse spinel peridotites (UN1, UN2), fine-grained garnet-amphibole peridotites (UN3, UN6, UN7, UN9, UN10, UN14) and fine-grained spinel-amphibole peridotites (UN8, UN16) were previously studied in detail for their petrography, bulk-rock and mineral major-, minor- and trace-elements composition, as well as for garnet Fe speciation (Gudelius et al., 2019). Their study shows that LILE, LREE and some HFSE are co-enriched and reveal significant compositional differences between sampling localities (Samerberg vs. Seefeld/Malga Masa Murada; Fig. 6.1), which are ascribed to different positions of the peridotite bodies relative to the slab during subduction and exhumation. Despite evidence for a strong metasomatic overprint, Fe^{3+}/Fe^{2+} in garnet remains low (< 0.046), and oxygen fugacities relative to the fayalite-magnetite-quartz buffer FMQ ($\Delta \log fO_2$) of -2.4 to -0.32 are calculated for $P=2$ GPa, suggesting reducing conditions in the mantle wedge beneath the Ulten Zone (Gudelius et al., 2019). Conversely, Malaspina et al. (2009) find more oxidizing conditions (FMQ to FMQ+2 calculated at $P = 3$ GPa) in FGA peridotites from the Malga Masa Murada and Samerberg areas. Thus, the UZ records heterogeneous redox conditions of various mantle wedge and tectonic *mélange* domains (Fig. 6.2c).

An additional seven samples were previously investigated by Consuma et al. (2020) (18LP1, MOL1-C, KL2.4-2b, KL2.4-3, VM10A, KL1-A, MM1), integrating petrography, *in situ* major elements,

Raman analyses and *in situ* Sr isotopes of dolomite and calcite. Their results show that HP carbonation of the UZ peridotite led to matrix dolomite formation from fluids variably equilibrated with a depleted mantle reservoir, indicating the efficiency of the mantle wedge, as represented by UZ peridotites, in storing carbonates. During exhumation, further percolation of hybridized fluids (sourced both from mantle and associated migmatites) may have metasomatized the peridotites as part of a crust-mantle mélange, as suggested by the large range of $^{87}\text{Sr}/^{86}\text{Sr}$ obtained for carbonate veins crosscutting the peridotite matrix. Dissolution of carbonates prevail during late exhumation-related serpentinization, as testified by pseudomorphs of calcite+brucite intergrowths after dolomite first described by Förster et al. (2017).

The porphyroclastic fine-grained garnet-amphibole peridotite P10B was first investigated by Lo Pò et al. (2020). Based on mineral chemistry and thermodynamic modelling, they interrogate the formation of polymineralic inclusions (PI) in highly fractured cm-sized garnet. PI are proposed to crystallize as incoming saline brines flow throughout fractures in garnet and locally interact with it along the post-Variscan, retrograde path.

For the purpose of the present study, two additional peridotite samples were investigated: (i) MM1B, which represents the composite serpentine vein crosscutting the matrix of FSA peridotite MM1; and (ii) coarse-grained peridotite SBA2, the only carbonate-free sample (CGn). Classification of the samples with sulfide assemblages, salient published data and analyses performed in this study are synthesized in Table 6.1.

Table 6.1. Ulten Zone peridotites analyzed in this study, carbonate and sulfide assemblages, and some salient characteristics.

Sample	logfO ₂ (ΔFMQ) @2 GPa	Carbonates	<i>in situ</i> ⁸⁷ Sr/ ⁸⁶ Sr carbonates (av.)	Geodynamic stage at carbonate addition	<i>in situ</i> ⁸⁷ Sr/ ⁸⁶ Sr cpx (av.)	<i>in situ</i> ⁸⁷ Sr/ ⁸⁶ Sr amph (av.)	Sulfide assemblage	Sulfide mode (wt%)	Bulk S (ppm)
CS Coarse-grained spinel peridotite									
MOL1-C	-	Mgs ± Do	0.71183	Mélange - ex	-	-	Pn ± Hz	-	212
CGn Carbonate-free coarse-grained garnet peridotite									
SBA2	-	No	-	no C addition	-	-	Pn	-	166
CG Coarse-grained garnet/spinel with coronitic garnet peridotite									
18LP1	-	Do ± Mgs	0.70360 to 0.70830 (vein)	Mélange - ex	-	-	Pn ± Hz	-	170
UN1	-0.96	Do	-	MW-HP peak	0.70543	-	Po ± Pn ± Ccp	0.06	187
UN2	-1.46	Do	-	MW-HP peak	0.70548	-	Pn	0.05	168
P-FGA Porphyroclastic fine-grained garnet amphibole peridotite									
KL24-2b	-	Do ± Cal+Brc	-	MW-HP peak	0.70534	-	Pn ± Sp ± Hz	-	-
KL24-3	-	Do ± Cal+Brc	-	MW-HP peak	-	-	Pn ± Sp ± Ccp ± Cc	-	128
P10B	-	Do	-	MW-HP peak	0.70531	-	Po ± Pn ± Ccp	-	240
UN3	-1.29	Do	-	MW-HP peak	0.70569	-	Pn ± Po ± Hz	0.02	58
UN6	-1.72	Do	-	MW-HP peak	0.70532	-	Pn ± Mil ± Hz	0.03	107
UN7	-1.09	Do	-	MW-HP peak	0.70543	-	Pn ± Hz	0.02	65
FGA Fine-grained garnet amphibole peridotite									
KL1-A	-	Do ± Cal+Brc	0.70671 (m)	MW-HP peak	-	-	Pn ± Hz ± Ccp	-	280
VM10A	-	Do	0.70597 (in zrn)	MW-HP peak	0.70539	-	Pn ± Ccp	-	202
UN9	-1.38	Do	0.70527 (m)	MW-HP peak	-	-	Pn	0.02	68
UN14	-1.30	Cal+Brc	-	Mélange - ex	0.70737	-	Pn	0.09	288
FSA Fine-grained spinel (chlorite-amphibole) peridotite									
MM1/MM1B	-	Do	0.70486 (m)	MW-HP peak	-	-	Mil ± Pn ± Hz	-	228/329
UN8	-	Do ± Cal+Brc	-	Mélange - ex	0.70678 (n=5)	-	Pn ± Hz	0.01	40
UN16	-	Do ± Cal+Brc	-	Mélange - ex	0.70778 (n=6)	-	Pn	0.04	135

Carbonate assemblages and Sr isotope compositions in carbonate from Consuma et al. (2020), logfO₂ values from Gudeřius et al. (2019), sulfide modes and bulk S contents reported in Table S2 (Electronic Annex C), initial Sr isotope compositions in clinopyroxene and amphibole reported in Table S6 (Electronic Annex C). P10B and KL2.4-2b/3 sulfide assemblages from polycrystalline inclusions in garnet and spinel respectively. Minerals: **Mgs**—magnesite; **Do**—dolomite; **Cal+Brc**—calcite + brucite intergrowths; **Pn**—pentlandite; **Po**—pyrrhotite; **Mil**—millerite; **Hlz**—heazlewoodite; **Sp**—sphalerite; **Ccp**—chalcopyrite; **Cc**—chalcocite. Textural positions: **m**—matrix; **in zrc**—included in zircon. Geodynamic setting: **MW**—mantle wedge; **ex**—exhumation.

Sulfides occur as discrete monophase and subordinately as polyphase grains with different shapes (rounded grains, elongated, blocky, skeletal or irregular) and grain size (up to 150 μm). They show various stages of alteration, ranging from none, to partial or strong alteration and fracturing, as illustrated in Figure 6.3.

Six texturally distinct sulfide types are recognized linked to the different metamorphic stages of the UZ peridotites (Fig. 6.2d):

1. *Polycrystalline Inclusions (PI) (Stage 1-4)*: Sulfide inclusions in a cm-sized garnet and in spinel included in mm-sized garnet occur as part of PI with grain size varying from 5 to 30 μm (Fig. 6.3a-b).
 - *Included in cm-sized garnet* (peridotite P10B): Pyrrhotite (\pm pentlandite) is solely included in garnet from this sample, whereas monophase pentlandite dominates in the matrix (Fig. 6.3a). PI fill a fracture crosscutting the host garnet from the rim through the core. Here, PI show a complex association of unusual minerals (amphibole + dolomite + chlorite + pentlandite + pyrrhotite + apatite + kinoshitalite + sapphirine + garnet included in amphibole; Lo Pò et al., 2020).
 - *Included in spinel (enclosed in garnet)* (peridotites KL2.4-2b and KL2.4-3): They occur as assemblages of apatite + ilmenite + dolomite + pentlandite; calcite-brucite intergrowths + Cl-apatite + pentlandite + ilmenite + phlogopite + chalcopyrite (Fig. 6.3b); calcite + ilmenite + Cl-apatite + pentlandite. The PI containing the assemblage of native Cu + ilmenite + Cl-apatite + amphibole occur within radiating fractures, linking the PI to the host spinel rim. Occasionally, PI (e.g. amphibole + ilmenite + sphalerite + calcite + pentlandite) occur within, but at the edge of, coarse-grained spinel connected with the surrounding kelyphitic corona.
2. *Discrete sulfide inclusions (Stage 1-2)*: Orthopyroxene grains, Cr-rich spinel in garnet, Cr-poor spinel in the matrix and kelyphitic corona host different types of sulfides, whereas no sulfides are found in olivine. Notably, kelyphite around spinel and garnet commonly hosts sulfides (mostly pentlandite) of exceptionally large dimensions (30-150 μm ; Fig. 6.3d). They commonly occur at the edge of coarse spinel following the directions of the kelyphite growths or at the edge of the corona in contact with the peridotite matrix (e.g. pentlandite with magnetite exsolutions and cut by late chlorite flakes; pentlandite + sphalerite + native-Cu blebs associated with Cl-apatite and cut by chlorite flakes; 30 μm zoned chalcopyrite grain).
3. *Interstitial sulfides (Stage 2)*: They occur at silicate grain boundaries and commonly in close spatial relationship with matrix dolomite (Fig. 6.3c). In the coarse-grained peridotite (CS + CG +

CGn), they are usually anhedral or subhedral with rounded or elongated shapes and sizes from 10 to 50 μm . The carbonate-free peridotite SBA2 contains only five fractured blocky monophase pentlandite grains with no alteration features. In CS and CG peridotites MOL1-C and 18LP1, interstitial sulfides occur mainly as pentlandite + millerite assemblages partially replaced by magnetite. In MOL1-C, pentlandite (partly replaced and rimmed by thin magnetite) + heazlewoodite + dolomite + serpentine assemblage is cut by chlorite flakes (Fig. 6.3c). In the FGA peridotites KL1-A and VM10A, pentlandite grows interstitially to olivine, orthopyroxene and pargasitic to hornblenditic amphibole. It is locally associated with disseminated dolomite. Nickeline blebs (Ni, As) are found within disseminated rounded pentlandite in association with Cl-apatite in FGA peridotite VM10A. It is worth noting that this peridotite is very weakly serpentinized.

4. *In carbonate veins (Stage 3)*: Pentlandite + millerite cut by late chlorite flakes (with magnetite filling the cleavage) are hosted in a vein predominantly formed by dolomite (and minor magnesite) + tremolite + serpentine that cuts the peridotite matrix 18LP1 (Fig. 6.3e). Monophase pentlandite also occurs not directly within the vein but in spatial proximity with it (i.e. few μm away from the vein). A nickeline bleb enclosed into pentlandite partially replaced by magnetite is also documented.
5. *In matrix serpentine or serpentine vein (Stage 4)*: P-FGA peridotites KL2.4-2b and KL2.4-3 show pentlandite + magnetite exsolutions contoured by chalcopyrite blebs. Exceptionally in these two samples, sphalerite can also be found included in matrix serpentine, as single phase or polyphase-assemblages (pentlandite + sphalerite + chalcocite). Matrix serpentine in FSA peridotite MM1 is dominated by pentlandite rarely replaced by millerite or heazlewoodite. Conversely, the composite serpentine + magnetite (\pm calcite \pm dolomite) vein MM1B, crosscutting the matrix of peridotite MM1, hosts fractured elongated-to-rounded millerite in intimate association with Ni-oxide grains with sizes of ~ 30 and $20 \mu\text{m}$ respectively. Nickeline blebs (NiAs; 3-5 μm on average) occasionally occur within pentlandite (\pm magnetite) grains associated with serpentine (e.g. in peridotites MOL1-C, 18LP1 and VM10A). Pentlandite enclosed in the serpentine + magnesite + tremolite vein (peridotite MOL1-C) is replaced by pseudomorphs of magnetite (Fig. 6.3e). Perpendicularly to this vein, serpentine + pentlandite + magnetite fills the cleavage of the host mm-sized enstatite, rarely containing small nickeline blebs.
6. *In halos, apophyses and sulfide-filled fractures (Stage 2-3-4)*: Diffuse sulfide material is commonly observed in i) halos around discrete sulfide grains, ii) apophyses leading into sulfide-filled

fractures and iii) sulfide in fractures apparently unconnected to discrete sulfide grains (Fig. 6.3f). In megacrysts, similar observations are ascribed to decrepitation of the sulfide during heating in contact with host basalt (Andersen et al., 1987), a mechanism that does not apply here. It is noteworthy that such features are observed both in fine-grained garnet amphibole peridotite and in spinel peridotite and therefore not (exclusively) related to late-stage retrogression.

To sum up, in order of decreasing abundance, sulfides occur mostly interstitial to silicates and are associated with matrix dolomite, enclosed in veins of serpentine and carbonates (dolomite, magnesite) and finally as inclusions (in coarse spinel and few grains in silicates), coexisting with dolomite and calcite. Interstitial pentlandite is by far the most dominant sulfide phase occurring in all the UZ peridotite samples, with an average grain size of 5-150 μm , followed by heazlewoodite and millerite mostly found in association with pentlandite in serpentine and carbonate veins. Pentlandite inclusions are common in spinel as a discrete phase or PI, while pyrrhotite (\pm pentlandite) occurs as PI in cm-sized garnet in peridotite P10B, except for few matrix pyrrhotite grains in the “UN” sample suite. Finally, few sphalerite, chalcopyrite and chalcocite grains occur only in P-FGA peridotites, mostly within coarse-grained spinel and kelyphite (KL24-2b, KL24-3, VM10A, P10B).

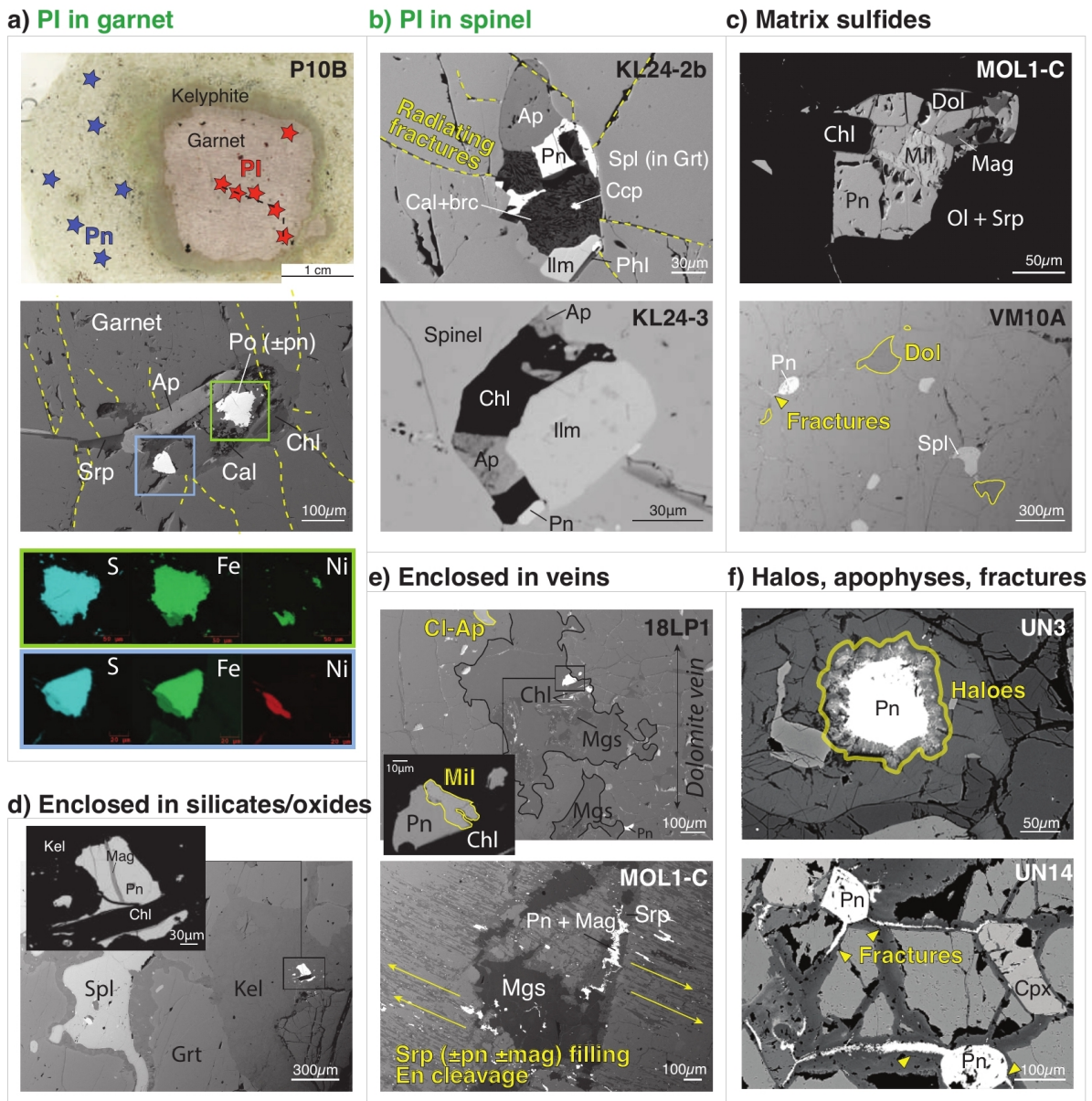


Figure 6.3. Photomicrographs, back-scattered electron images, and color maps illustrating the textural settings of sulfides in Ulten Zone peridotites. (a) Scan image of thin section P10B with stars indicating locations of polyphase inclusions (PI) in garnet and matrix pentlandite (modified after Lo Pò et al. 2020) along with a BSE image of a PI and relative color mapping showing major element compositions of Po + Pn. (b) Coarse spinel enclosing PI. Note calcite + brucite intergrowths associated with pentlandite (KL24-2b). PI in spinel with ilmenite + chlorite + apatite + pentlandite (KL24-3); (c) matrix pentlandite in intimate association with dolomite (MOL1-C) and in close relationship with dolomite (VM10A). (d) kelyphite corona enclosing pentlandite cut by a chlorite flake and magnetite string; (e) dolomite vein (+ magnesite) enclosing pentlandite + millerite cut by chlorite flake (18LP1); magnesite + serpentine + tremolite vein enclosing pentlandite partially replaced by magnetite pseudomorphs (MOL1-C); (f) halos and apophyses around pentlandite (UN3) and pentlandite-fracture fillings (UN14).

6.5 Methods

Each analytical method and the specifics on quality control measures are detailed in Chapter Three – Methods. Samples were examined in polished thin section and slices of peridotite of 3 mm thickness by optical transmitted and reflected light using a polarized optical microscope, and by Scanning Electron Microscopy (SEM) for X-ray maps at the Department of Biological, Geological and Environmental Sciences, University of Bologna, Italy.

Bulk rock major- and minor-element compositions along with selected trace elements were acquired by X-Ray-Fluorescence, using a Phillips Magi XPRO spectrometer at Johannes Gutenberg-University Mainz. Results are shown in the Supplementary Table C1. The same instrument, and a LECO-Analyzer CS 125, were used to obtain bulk-rock S concentrations for a subset of samples (UN1-UN16) for which major- and minor-element compositions had been previously determined (Gudelius et al., 2019). Remaining S concentration measurements were carried out at Karlsruhe Institute of Technology, also using a LECO instrument. Individual results are provided in Supplementary Table C2. Sulfide major- and minor-element concentrations were obtained *in situ* by EPMA, using a JEOL JXA-8100 Superprobe electron probe microanalyser at the Institute of Mineralogy and Petrography, University of Innsbruck and a JEOL JXA-8900 at Goethe-University Frankfurt. Results and summary are shown in Supplementary Table C3.

Trace-element abundances were determined *in situ* in sulfides following the procedure detailed in Aulbach et al. (2012). Measurement statistics for two separate analytical campaigns are reported in detail in Table 3.1 of Chapter 3, whereas the full dataset is given in Supplementary Table C4. Abundances of Au cannot be quantified in a subset of samples that were Au-coated prior to analysis for multiple S isotopes, as Au may have collected in small pits and cracks in the sulfides.

The Rb-Sr isotopic composition of clinopyroxene and amphibole (Table C5 in Supplementary Material) was obtained *in situ* by laser ablation microprobe (LAM) multi-collector inductively-coupled plasma mass spectrometry (MC-ICPMS), using a Resonetics RESolution M-50-HR laser probe linked to a ThermoFinnigan Neptune mass spectrometer at the Goethe-University Frankfurt, as reported previously in Aulbach et al. (2016) and described in Chapter Three.

Sulfur isotope compositions were measured *in situ* by secondary-ion mass spectrometry (SIMS) using a Cameca IMS-1280 at the Centre for Microscopy and Microanalysis (CMCA), University of Western Australia. SIMS measurements were undertaken on 30 pentlandite grains from seven peridotite samples and results are reported in Table 6.4. Grains with a minimum size of 20 μm were previously selected according to the different textural positions and association with carbonates, which track progressive metasomatic episodes during pre-peak, high-pressure-peak and retrograde conditions. All $\delta^{34}\text{S}$ values are reported relative to Vienna Canyon Diablo Troilite – VCDT (Ding et al., 2001). Further details on the procedure are given in LaFlamme et al. (2016).

6.6 Results

6.6.1 Whole rock major elements and sulfur concentration

New whole rock compositions are reported in Supplementary Table C1 and illustrated together with published data (UN series) in Figure 6.4. Loss On Ignition (LOI) ranges between 0.37 and 13.10 wt.%, in line with the degree of serpentinization. The highest value of 13.10 wt.% is from the serpentine vein MM1B previously hand-picked from FSA peridotite MM1. Contents of Al_2O_3 in the UZ peridotites range between 1.40 and 3.12 wt.%, while CaO ranges from 0.44 to 2.84 wt.%, TiO_2 from 0.02 to 0.11 wt.% and MgO from 37.87 to 42.79 wt.%. For comparison, primitive and depleted mantle have estimated Al_2O_3 concentrations of 4.45 and 4.28 wt.%, respectively, CaO of 3.55 and 3.50 wt.%, TiO_2 contents of 0.201 and 0.19 wt.% and MgO contents of 37.8 and 38.22 wt.%, respectively (McDonough and Sun, 1995; Salters and Stracke, 2004).

Sulfur concentrations for eighteen peridotite samples are reported in Figures 6.4, 6.5, and in Supplementary Figure C2. The full dataset is reported in Supplementary Table C2. Overall, the S content of the orogenic peridotites ranges from as low as a few tens to hundreds ppm, averaging 171 (± 45 ; $n=18$) ppm with a median value of 169 ppm.

Coarse-grained garnet peridotite (CG) shows an average value of 180 ± 28 ppm ($n=5$), fine-grained garnet amphibole peridotite (FGA) an average value of 160 ± 34 ppm ($n=9$) and three fine-grained spinel peridotites (FSA) have wide sulfur concentration ranging from 40 to 228 ppm. The serpentine + magnetite \pm sulfide (mostly millerite) \pm calcite \pm dolomite vein MM1B reaches the highest value of 329 ppm S. Again for comparison, primitive and depleted mantle have S concentrations of 250 and 60-119 ppm, respectively (Alt et al., 2007; McDonough and Sun, 1995; Salters and Stracke, 2004).

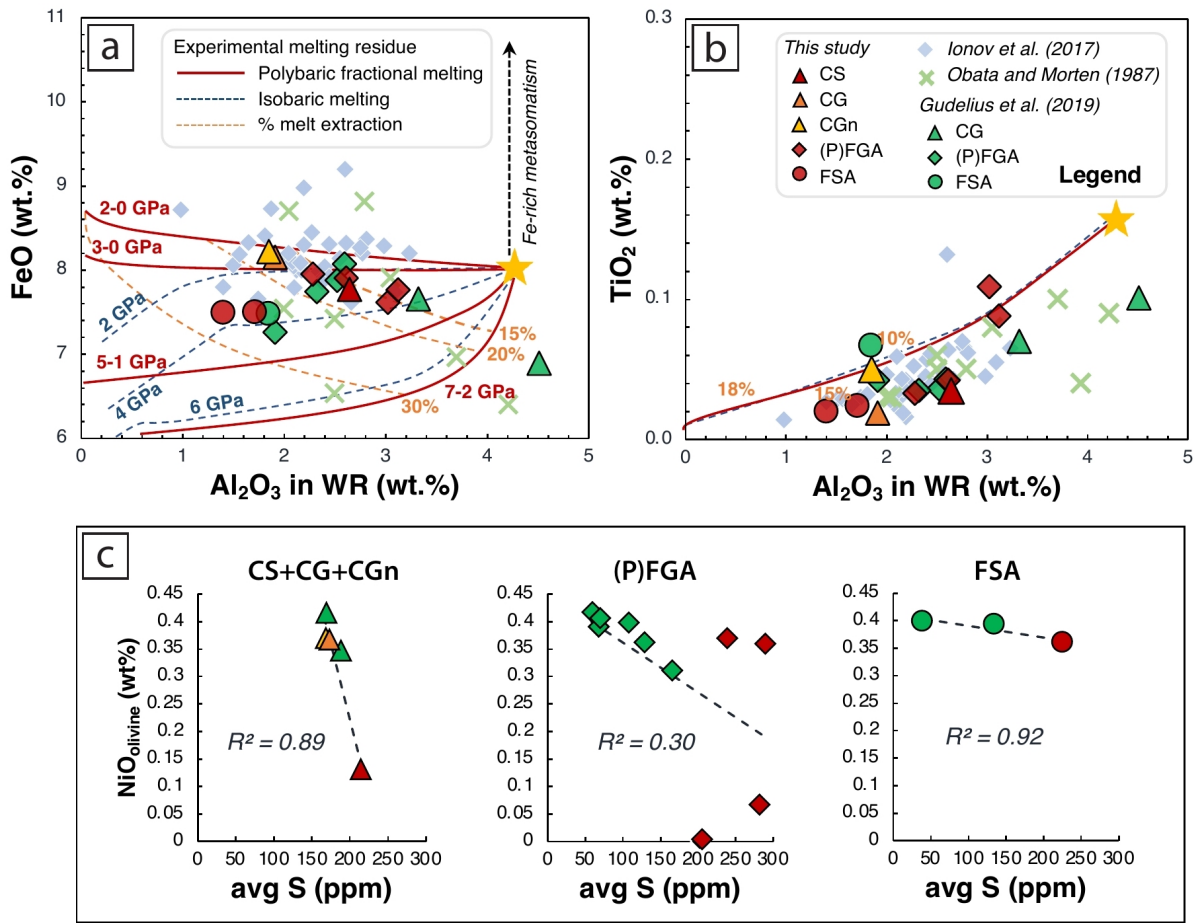


Figure 6.4: (a) FeO and (b) TiO₂ (wt%) as a function of Al₂O₃ of whole-rock peridotite analyses from the Ulten Zone investigated in this study (data in Table S3, Obata and Morten, 1987, Ionov et al. 2017 and Gudelius et al., 2019). Shown for comparison in (a) are residues from batch melting at 2, 4 and 6 GPa (stippled blue lines) and from polybaric fractional melting of primitive mantle (PM—yellow star) at 2-0, 3-0, 5-1 and 7-2 GPa (thick red lines), as well as contours of % melt extracted (orange lines) (from Herzberg, 2004). Shown for comparison in (b) are paths for polybaric fractional melting of PM at 1.5-0.5 and 2.5-0.5 GPa. Low TiO₂ contents at a given Al₂O₃ in the UZ peridotites compared to the model suggest formation from a more depleted source. (c) NiO (wt.%) of olivine grains vs bulk S concentration (ppm). Values of NiO taken from Gudelius et al. (2019) and Consuma et al. (2020).

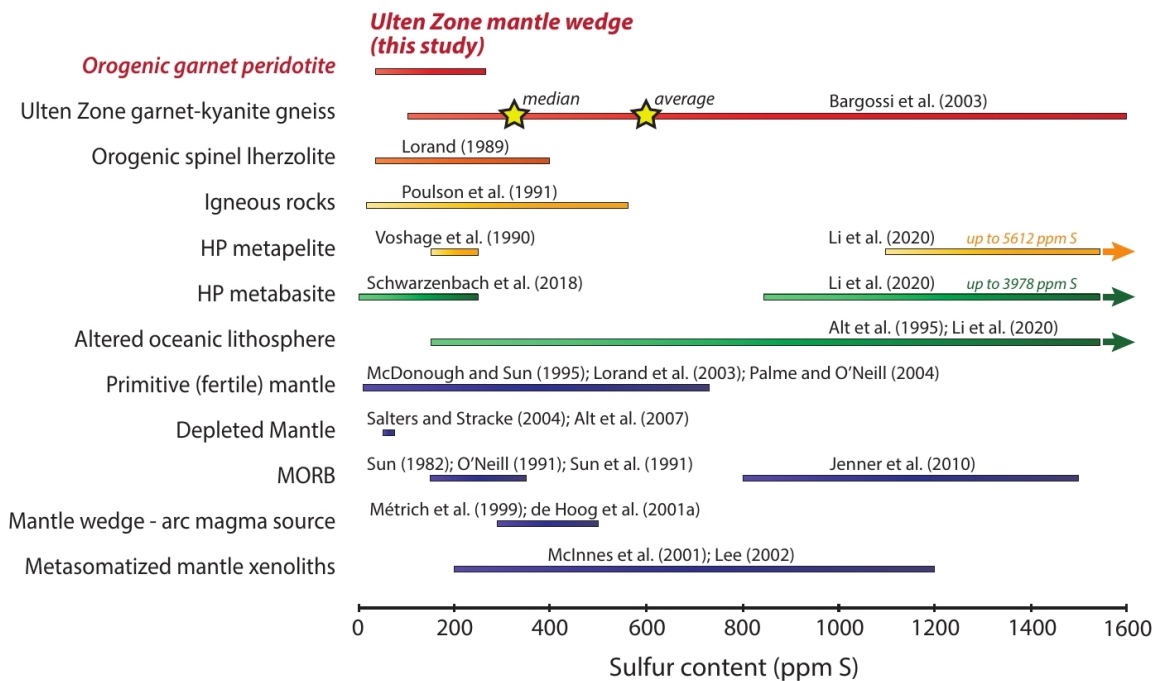


Figure 6.5: Sulfur contents (in ppm S) in the Ulten Zone peridotites (this study) compared to those in different mantle and crustal reservoirs (references in panel).

6.6.2 Sulfide major element composition and low-pressure re-equilibration

The dataset comprises 295 sulfide grains analyzed for their major element compositions (Fig. 6.6 and Supplementary Table C3); Table 6.2 reports the average major element concentrations of pentlandite grains according to their different textural positions while Appendix shows Backscatter-Electron (BSE) images of all analyzed sulfides in UN series samples.

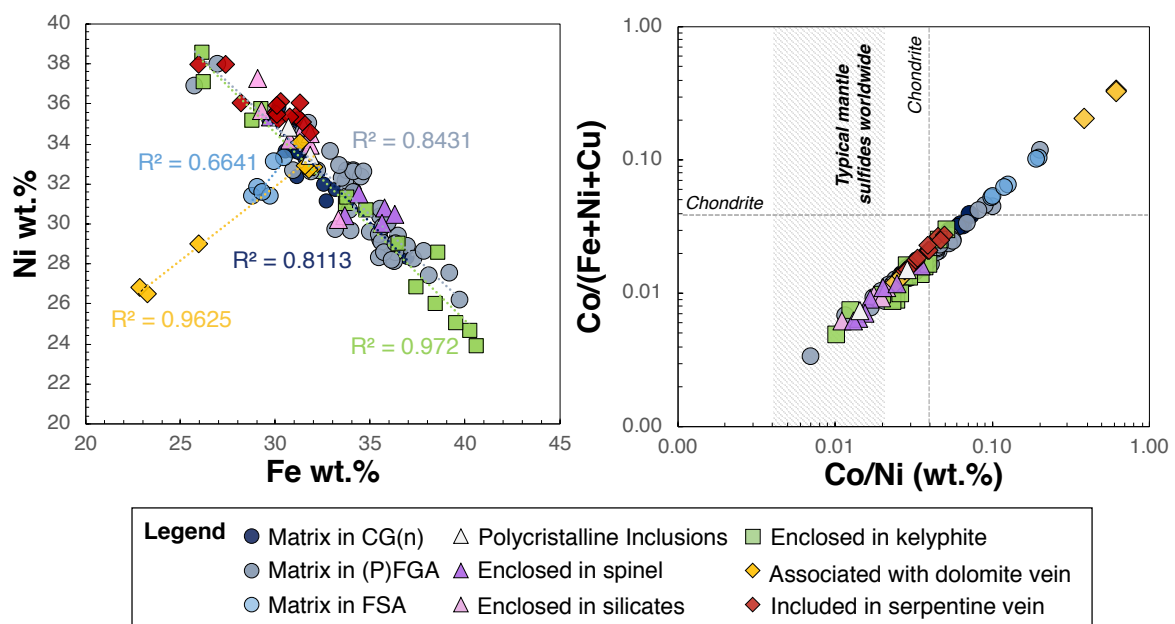


Figure 6.6: Pentlandite compositions (EPMA) colour-coded according to different textural positions; (a) Ni *vs.* Fe; (b) Co/(Fe+Ni+Cu) ratio *vs.* Co/Ni ratio. Chondritic ratios from McDonough and Sun, (1995); worldwide sulfide Co/metal ratios (according to Wang et al. 2010) shown for comparison.

Pentlandite is compositionally heterogeneous with 22.8-39.5 wt.% Fe, 28.8-37.8 wt.% Ni and below detection limit (bdl)-16.6 wt.% Co. Here, pentlandite with Ni > 36wt.% is classified as Ni-pentlandite (mostly found in serpentine vein), and that with Co > 6wt.% as Co-pentlandite (mostly found associated with carbonate veins and in FSA peridotites). Data show that pentlandite enclosed in coarse spinel included in garnet (occurring both as discrete grain and PI) and in silicates, as well as most of the matrix pentlandite grains in P-FGA and FGA peridotites and some pentlandite enclosed in kelyphitic coronas around garnet fall in the “typical” mantle sulfide range according to Wang et al. 2010 (Fig. 6.6). Conversely, the other sulfides, such as those found in the matrix of CGn peridotite SBA2 and those included in a serpentine vein show higher Co/(Fe+Ni+Cu) and Co/Ni ratio with respect to the mantle sulfides.

The Ni/(Ni+Fe) ratio of pentlandite averages 0.46 (± 0.05), ranging from 0.34 to 0.59, except for three Ni-pentlandite grains with ratios >0.60. In CGn peridotite SBA2, pentlandite shows a relatively high Co-content, with an average of 1.89 wt.% (n=10). The Co-content increases in FSA peridotites MM1 and vein MM1B with an average of 5.6 wt.% (n=7), while the highest value (Co = 16.6 wt.%) is reached in few pentlandite grains enclosed in the dolomite vein of peridotite 18LP1. Millerite and heazlewoodite (\pm pentlandite) with Ni > 63.6 wt.% are the dominant phases in peridotite MM1 and vein MM1B. Cu-enriched pentlandite is found in grains enclosed in kelyphitic coronas around garnet, with Cu concentration from bdl-2.6 wt.%. Nickel and Fe in pentlandite occurring in peridotites 18LP1, MM1 and MM1B are positively correlated; conversely, a negative correlation is shown for pentlandite in fine, prophyroclastic, garnet-amphibole peridotites (Fig. 6.6). The overall occurrence of pentlandite in the studied peridotites is consistent with the typical sulfide component of orogenic mantle (Alard et al., 2000), and the measured Ni/(Ni+Fe) ratio of about 0.46 (± 0.05) is also similar to those found in mantle xenoliths (e.g., Szabó and Bodnar, 1995; Guo et al., 1999; Aulbach et al., 2004; Aulbach et al., 2019).

Pyrrhotite shows homogeneous chemical compositions, with a sulfur content of about 50.40 at.% (± 0.19). The Ni content is always below detection limit. Minor Cu-sulfides are represented by few tiny blebs (max. 5 μm) of chalcopyrite and chalcocite, except for one chalcopyrite grain of 30 μm size found enclosed in kelyphite. The metal/S ratio of chalcopyrite averages 0.97 (± 0.01). Only two chalcocite grains were found in sample KL2.4-2b.

Table 6.2. Average major element compositions of pentlandite in different microstructural positions.

Pentlandite	n	S wt.%	Fe wt.%	Ni wt.%	Co wt.%	Cu wt.%	Total
PI	2	34.07(0.25)	31.28(0.83)	34.15(0.98)	0.74(0.37)	bdl	100.38(0.89)
In spinel (no PI)	7	34.14(0.16)	33.64(2.71)	32.03(2.40)	0.64(0.23)	bdl	100.62(0.94)
Matrix in CS/CG(n)	16	34.02(0.33)	31.89(1.78)	33.06(1.90)	1.47(0.62)	bdl	100.71(1.01)
Matrix in FGA	47	33.92(0.89)	34.44(2.70)	30.93(2.60)	1.29(1.11)	bdl	100.76(1.09)
Matrix in FSA	6	33.87(0.23)	29.56(0.61)	32.09(0.87)	4.48(1.36)	bdl	100.11(1.11)
In kelyphite	14	33.94(0.46)	34.58(5.10)	30.25(4.85)	0.90(0.43)	1.72(0.54)	100.42(1.00)
In silicates	7	33.84(0.19)	31.07(1.53)	34.38(2.14)	0.69(0.15)	bdl	100.11(1.07)
W/ dolomite vein	7	33.64(0.56)	28.39(4.20)	30.69(3.18)	6.82(7.57)	bdl	99.84(0.58)
In serpentine vein	13	34.34(0.12)	29.87(1.72)	35.92(1.02)	1.31(0.28)	bdl	101.59(0.80)

PI—polycrystalline inclusions; **W/dolomite vein**—associated with dolomite vein; **bdl**—below detection limit. **CS**—Coarse-grained spinel peridotite, **CGn**—Carbonate-free coarse-grained garnet peridotite, **CG**—Coarse-grained garnet/spinel with coronitic garnet peridotite, **(P)FGA**—Porphyroclastic and non-porphyroclastic fine-grained garnet amphibole peridotite, **FSA**—Fine-grained spinel (chlorite-amphibole) peridotite. Standard deviations reported in parentheses.

The high-temperature precursors of the UZ sulfides can be revealed by comparing their major chemical compositions to experimentally determined phase relations at various temperatures in the ternary diagram S-Fe-(Ni+Co) in at.% (Fig. 6.7). This indicates that minor pyrrhotite and dominant pentlandite could be derived from re-equilibration of mss to low temperature (T). In addition, in the ternary system Fe_9S_8 – Ni_9S_8 – Co_9S_8 , experimental studies have shown that the pentlandite composition is temperature-dependent (Kaneda et al., 1986) and can reflect the condition under which it forms (e.g., Lorand and Grégoire, 2006; LaFlamme et al., 2016). Most of the investigated pentlandite grains plot within the entire field of stability for T of 200°C and 300°C (Fig. 6.7b), which is consistent with low-T assemblages ($\leq 300^\circ\text{C}$) re-equilibrated from high-T-(mono)sulfides, whereby a higher Co content shifts the stability field of pentlandite formation to higher T (c. 300°C). Pentlandite can also originate by crystallization from metasomatic Ni-Cu-rich sulfide melts with high metal/S ratios (Lorand et al., 2013).

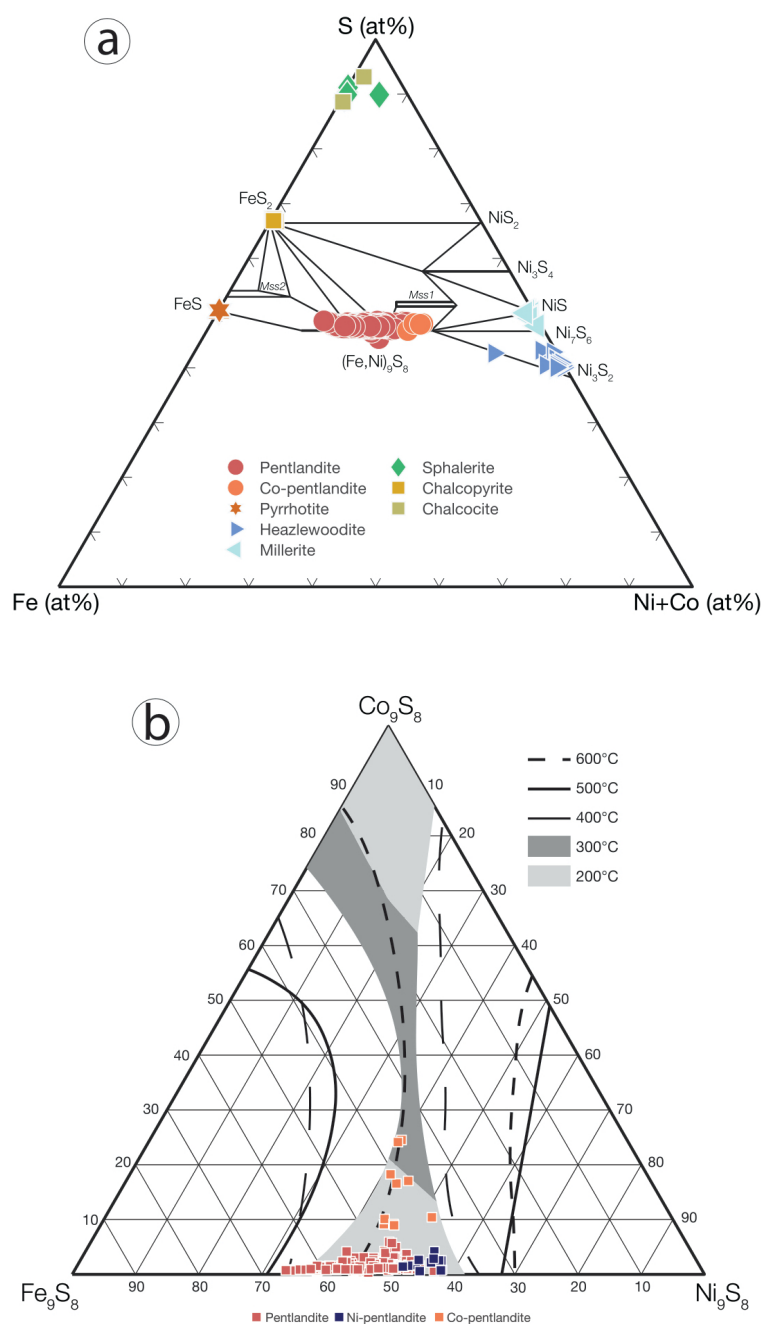


Figure 6.7: (a) Ternary diagram of the system S-Fe-(Ni+Co) at 250°C and atmospheric pressure showing the composition of the studied sulfides in the Ulten Zone peridotites (in atomic units). Phase relations and Mss1 and Mss2 compositional fields after Craig (1973) and Lorand and Grégoire, (2006). (b) Stability of pentlandite in the ternary system Fe₉S₈-Co₉S₈-Ni₉S₈ (expressed in mol%) (Kaneda et al., 1986). Most of the studied pentlandite grains plot within the stability field for T of 200°C to 600°C.

6.6.3 Sulfide trace element concentrations

Trace elements were measured in pentlandite and pyrrhotite from the UN suite samples, peridotite P10B, and from pentlandite previously measured by SIMS. A few millerite grains were also analyzed.

Pyrrhotite from PI in garnet shows Ni concentrations ranging from 119 to 8332 ppm, Cu from 22 to 569 ppm, Zn from 0.96 to 7.41 ppm, As from 0 to 30 ppm, Se from 2 to 24 ppm, Ag from 0.08 to 0.70 ppm, Sb from 0.07 to 0.82 ppm, Te from bdl to 1.3 ppm, Pb from 1.7 to 22.6 ppm and Bi from 0.2 to 1.1 ppm. Median values are reported in Table 6.3 and illustrated in Figure 6.8, while for the full trace-element dataset the reader is referred to Supplementary C4.

Siderophile and chalcophile element concentrations in pentlandite span a large range of values. Arsenic is the most abundant trace element, ranging from 1 to 1213 ppm (median 514 ppm; n=86). Abundances of Zn range from bdl to 535 ppm, maintaining low concentrations in matrix pentlandite from peridotite P10B (bdl-1.73 ppm). Selenium and Te are always present in detectable abundances, ranging from 12 to 211 ppm (median=81 ppm; n= 86) and from 1 to 89 ppm (median=14 ppm; n=80) respectively, while Ag ranges from bdl to 51.67 ppm (median = 1 ppm; n=86). Concentrations of Sb are usually low (from bdl to 40 ppm; median 1 ppm; n=80), except for few matrix pentlandite grains in FSA peridotites UN8 and UN16, and when in association with a dolomite vein or enclosed in a serpentine vein of peridotite MOL1-C (here Sb values are always > 13 ppm). By contrast, matrix pentlandite from P-FGA peridotite P10B varies from 0.07 to 0.28 ppm and the pentlandite in PI in spinel shows Sb concentration of 7.1 ppm. Pb is from 0.9 to 1730 ppm (median=9 ppm; n=80) and Bi from 0.1 to 15.6 ppm (median=1 ppm; n=80).

Table 6.3. Median values of trace element contents (ppm) in sulfides from Ulten Zone peridotites.

Type	CG	FGA	FSA	P10B	P10B	P-FGA	CS	CG (P)FGA	CS	CGn	P-FGA	CG	
Sulfide	Pn	Pn	Pn	Pn	Po	Pn	Pn	Pn	Pn	Pn	Pn	Pn	
Textural setting	-	-	-	PI in grt	PI in grt	PI in spl	matrix	matrix	matrix	In srp vein	matrix	In kel	w/do vein
Co	3669	4270	4060	5236	33	7276	8136	5478	4745	6370	12636	5927	6010
Ni	290	308	391	339	1,234	376	401	333	334	363	369	250	368
Cu	2146	811	10	25	217	64	bdl	229	121	210	60	2550	3261
Zn	5	3	1.71	1.55	2	18.7	4	7	7	26	31	1.34	4
As	401	450	860	462	1	842	798	784	645	606	461	156	865
Se	108	83	64	80	11.8	20	50	106	90	46	60	92	96
Ag	8	1.36	0.29	0.08	0.17	0.12	0.03	0.16	0.15	0.07	0.25	0.58	5
Sb	0.21	0.77	1.94	0.18	0.12	7	10.5	7	3	15.06	0.85	1.54	9
Te	24	13.6	12.1	15.1	0.48	7	12.4	22.61	15.4	8	12.2	16.5	18.9

6 • The sulfur component of the Ulten Zone peridotite: a piece of the deep Sulfur cycle?

Pb	30	14.7	4	5	5	3.17	2	1.54	4	13.1	34	9	9
Bi	0.39	0.71	2.23	0.32	0.49	0.90	1.70	0.76	0.69	3	1.13	0.26	1.18

Au contents not available for samples previously gold-coated for SIMS analyses. **Pn**—pentlandite; **Po**—pyrrhotite; **PI**—polycrystalline aggregates. **CS**—Coarse-grained spinel peridotite, **CGn**—Carbonate-free coarse-grained garnet peridotite, **CG**—Coarse-grained garnet/spinel with coronitic garnet peridotite, **(P)FGA**—(Porphyroclastic) fine-grained garnet amphibole peridotite, **FSA**—Fine-grained spinel (chlorite-amphibole) peridotite.

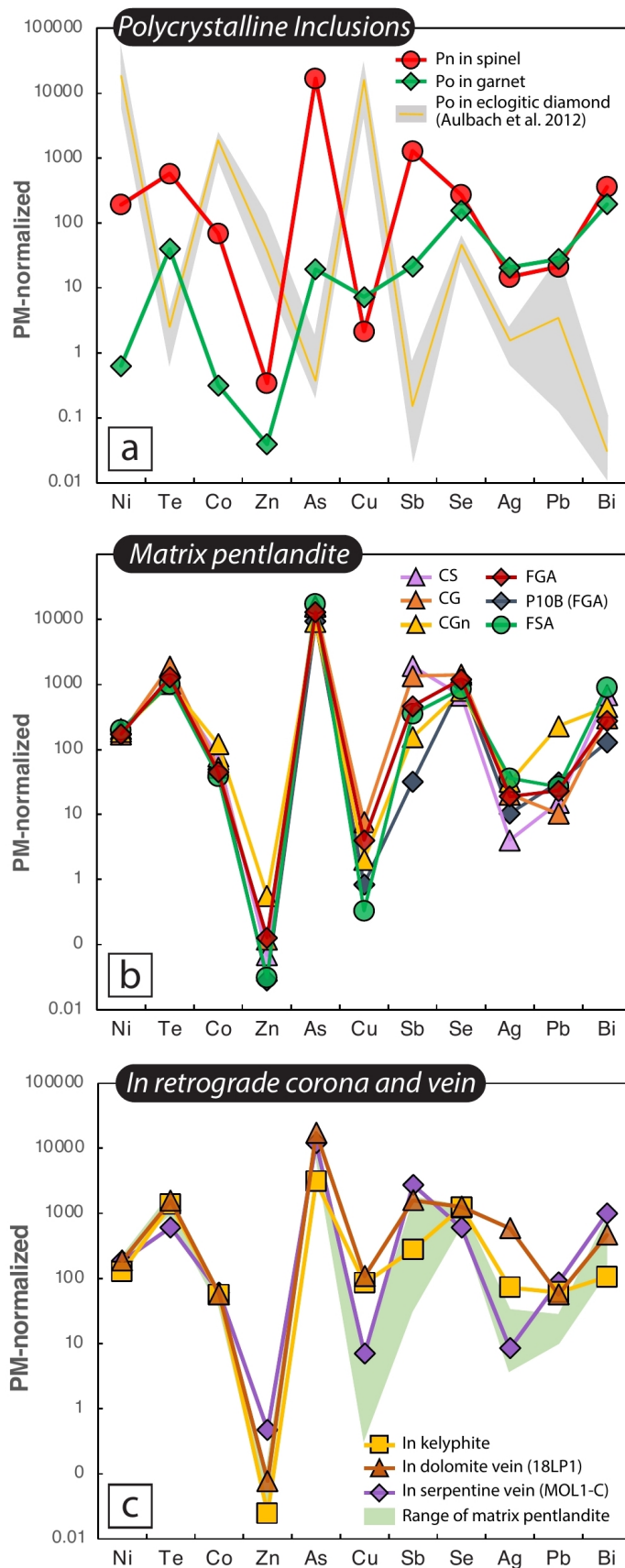


Figure 6.8: Primitive-mantle normalized trace element compositions of pentlandite and pyrrhotite (primitive mantle of McDonough and Sun, 1995). For simplicity, only medians for coarse and fine peridotites, and for different textural positions are reported. Element order corresponds to decreasing compatibility during partial melting of primitive mantle (from Aulbach et al., 2012). Shown for comparison in (a) is range of abundances in pyrrhotite included in eclogitic diamond and obtained using the same method employed in this study (Aulbach et al., 2012). Shown for comparison in (c) is the range of matrix pentlandite compositions shown in (b). **CS**—Coarse-grained spinel peridotite, **CGn**—Carbonate-free coarse-grained garnet peridotite, **CG**—Coarse-grained garnet/spinel with coronitic garnet peridotite, **(P)FGA**—Porphyroclastic and non-porphyroclastic fine-grained garnet amphibole peridotite, **FSA**—Fine-grained spinel (chlorite-amphibole) peridotite. **Po**—pyrrhotite, **Pn**—pentlandite.

6.6.4 SIMS Sulfur isotope compositions of pentlandite

Since the textural context of the sulfides provides crucial information on the stage during which S was potentially added or removed (Fig. 6.2d), *in situ* acquisition of S isotopic composition of sulfides is indispensable. Only a few grains showed a suitable size and composition (close to matrix-matched standards) for SIMS analysis. Results are listed in Table 6.4 and shown in Figure 6.9.

In the coarse-grained spinel peridotite MOL1-C, a pyroxenite layer hosts a pentlandite grain with values of $+2.77 \pm 0.37\text{‰}$ (1σ , $n=2$), whereas the matrix pentlandite associated with dolomite (Fig. 6.3c) in the peridotite matrix averages $+3.11 \pm 0.38\text{‰}$ ($n = 6$). Pentlandite grains exhibit a wide isotopic range when occurring in serpentine + magnesite + tremolite vein crosscutting the peridotite MOL1-C, with $\delta^{34}\text{S}$ values ranging from $-0.29 \pm 0.34\text{‰}$ to $+3.76 \pm 0.36\text{‰}$. These two extreme values were measured in the same serpentine-enclosed pentlandite grain.

Matrix pentlandite in the only carbonate-free sample (SBA2), a coarse-grained garnet peridotite, consistently shows relatively heavy $\delta^{34}\text{S}$, with an average of $+2.71 \pm 0.43\text{‰}$ ($n=14$). Except for one grain showing $+0.74 \pm 0.41\text{‰}$, the other grains are $\geq 1.52 \pm 0.45\text{‰}$, reaching a maximum value of $+3.54 \pm 0.35\text{‰}$. There is no significant intra-grain isotopic variability.

The CG peridotite 18LP1 contains a dolomite vein with pentlandite showing the highest Co values. Given the restricted range of Co imposed by the sulfide standard to be measured by SIMS, only few grains could be analyzed, yielding an average value of $+0.80 \pm 0.40\text{‰}$ ($n=4$) for pentlandite enclosed or locally associated with the dolomite vein, while pentlandite included in coarse spinel gives $\delta^{34}\text{S} = -0.18 \pm 0.45\text{‰}$.

The Mann-Whitney U Test (Supplementary Annotation C1) reveals a significant difference between the $\delta^{34}\text{S}$ values of pentlandite within the fine-grained and the coarse-grained peridotite lithotypes, at a level of significance of 1% ($p < 0.00001$). The isotopic values of pentlandite in the fine-grained peridotite are significantly lighter than those in the coarse-grained peridotite.

The single pentlandite in PI in coarse spinel (in turn included in garnet) exhibits $\delta^{34}\text{S} = +0.46 \pm 0.34\text{‰}$. Two matrix pentlandite grains in the fine-grained peridotite KL1-A, which are intimately associated with matrix dolomite, show values of $-1.62 \pm 0.42\text{‰}$ and $-1.14 \pm 0.39\text{‰}$ respectively. Matrix pentlandite in sample KL2.4-3 averages $+0.31 \pm 0.34\text{‰}$ ($n=3$) with little intra-grain isotope variability. Within the same peridotite, a pentlandite grain found in kelyphite around spinel and cut by a chlorite flake averages $-0.38 \pm 0.31\text{‰}$ ($n=3$). In peridotite VM10A, matrix pentlandite $\delta^{34}\text{S}$ ranges from $-1.32 \pm 0.40\text{‰}$ to $+0.67 \pm 0.40\text{‰}$ with an average of $-0.21 \pm 0.41\text{‰}$ ($n=12$).

Overall, the S isotope compositions obtained for the UZ pentlandite grains range between $-1.62 \pm 0.42\text{‰}$ and $+3.76 \pm 0.36\text{‰}$. Matrix pentlandite from fine-grained peridotites is isotopically light, with an average of $\delta^{34}\text{S} = -0.11 \pm 0.39\text{‰}$ ($n=15$), ranging from $-1.62 \pm 0.42\text{‰}$ to $+0.67 \pm 0.40\text{‰}$. Conversely, matrix pentlandite from coarse-grained peridotites is isotopically heavy, with an average $\delta^{34}\text{S} = +2.48\text{‰} \pm 0.41\text{‰}$ (1σ , $n=25$) and ranging between $+0.41 \pm 0.42\text{‰}$ to $+3.76\text{‰} \pm 0.36\text{‰}$. For comparison, $\delta^{34}\text{S}$ of the depleted mantle is estimated at $-1.28 \pm 0.33\text{‰}$ (Labidi et al., 2013).

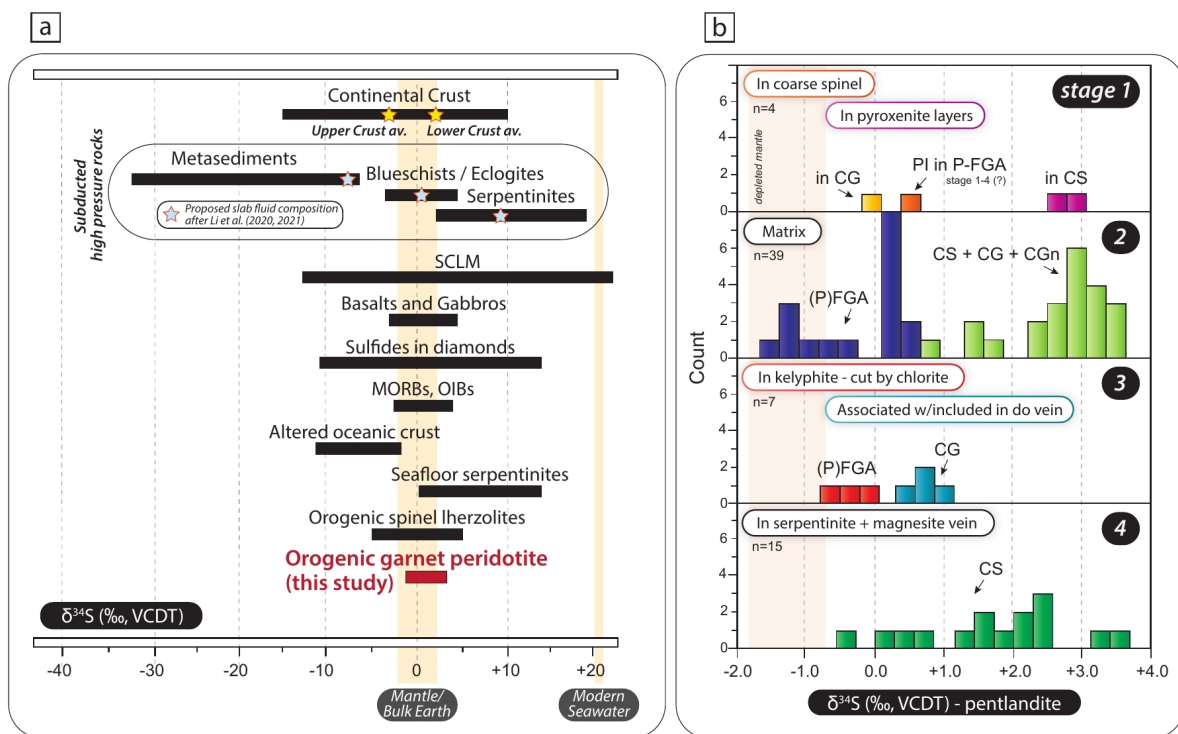


Figure 6.9: (a) Sulfur isotope variations of this study compared to those in different reservoirs (Giuliani et al., 2016, and references therein), in high-pressure rocks reported in Li et al. (2020) and references therein, in slab fluids estimated by Walters et al. (2019) and Li et al. (2020), pelagic sediments from Schwarzenbach et al. (2018) and Li et al. 2020, and in sulfides (green line) and sulfates (orange line) from altered oceanic lithosphere and serpentinite (Schwarzenbach et al., 2018a,b; Li et al., 2020); (b) Histograms showing the sulfur isotope compositions in pentlandite in various textural settings measured by SIMS (this study). The yellow box corresponds to the depleted mantle value range, following Labidi et al. (2013) ($\delta^{34}\text{S} = -1.28 \pm 0.25\text{‰}$) and Labidi et al. (2014) ($\delta^{34}\text{S} = -1.40 \pm 0.50\text{‰}$). **CS**—Coarse-grained spinel peridotite, **CGn**—Carbonate-free coarse-grained garnet peridotite, **CG**—Coarse-grained garnet/spinel with coronitic garnet peridotite, **(P)FGA**—Porphyroclastic plus non-porphyroclastic fine-grained garnet amphibole peridotite, **FSA**—Fine-grained spinel (chlorite-amphibole) peridotite. **PI**—polycrystalline inclusions. **VCDT**—Vienna Canyon Diablo Troilite standard.

Table 6.4. $\delta^{34}\text{S}$ ‰ (VCDT) measurements by SIMS of individual pentlandite (Pn) grains.

Grain/spot	Textural setting of pentlandite	$\delta^{34}\text{S}$ (‰)	2σ (‰)	Stage
KL24-2b (P-FGA)				
3S-GC-Mount5-b_pn1	Pl in spinel (in garnet)	0.46	0.34	1-4
KL2.4-3 (P-FGA)				
3S-GC-Mount2-pn1@1	Matrix	0.33	0.34	2
3S-GC-Mount2-pn1@2	Matrix	0.37	0.33	2
3S-GC-Mount2-pn1@3	Matrix	0.24	0.34	2
3S-GC-Mount2-pn2@1	In kelyphite	-0.13	0.32	3
3S-GC-Mount2-pn2@2	In kelyphite	-0.44	0.32	3
3S-GC-Mount2-pn2@3	In kelyphite	-0.57	0.31	3
KL1-A (FGA)				
3S-GC-Mount5-c-pn1@1	Matrix	-1.62	0.42	2
3S-GC-Mount5-c-pn2@1	Matrix	-1.14	0.39	2
VM10A (FGA)				
3S-GC-Mount7-d-pn1@1	Matrix	-0.37	0.38	2
3S-GC-Mount7-d-pn1@2	Matrix	0.19	0.37	2
3S-GC-Mount8-pn1@1	Matrix	0.17	0.31	2
3S-GC-Mount8-pn2@1	Matrix	0.67	0.40	2
3S-GC-Mount8-pn2@2	Matrix	0.15	0.41	2
3S-GC-Mount8-pn2@3	Matrix	0.22	0.41	2
3S-GC-Mount4-c-pn1@1r	Matrix	0.12	0.48	2
3S-GC-Mount4-c-pn1@2r	Matrix	0.56	0.50	2
3S-GC-Mount6-pn1@1	Matrix	-1.07	0.39	2
3S-GC-Mount6-pn1@2	Matrix	-1.32	0.40	2
3S-GC-Mount6-pn1@3	Matrix	-1.25	0.41	2
3S-GC-Mount6-pn2@1	Matrix	-0.64	0.44	2
18LP1 (CG)				
3S-GC-Mount5-d_pn1@1	In coarse spinel	-0.18	0.45	1-2
3S-GC-Mount7-a-pn1@1	In dolomite vein	1.13	0.37	3
3S-GC-Mount7-b-pn1@1	Matrix w/dolomite vein	0.75	0.41	2
3S-GC-Mount7-b-pn1@2	Matrix w/dolomite vein	0.89	0.41	2
3S-GC-Mount7-b-pn1@3	Matrix w/dolomite vein	0.41	0.42	2
MOL1-C (CS)				
3S-GC-Mount5-a-pn1@1	Matrix	1.59	0.38	2
3S-GC-Mount5-a-pn1@2	Matrix	1.70	0.40	2
3S-GC-Mount3-rerun-a-pn1@1	In serpentine vein	3.58	0.39	4
3S-GC-Mount3-rerun-a-pn1@2	In serpentine vein	2.80	0.26	4
3S-GC-Mount3-rerun-a-pn2@1	In serpentine vein	-0.29	0.34	4
3S-GC-Mount3-rerun-a-pn2@2	In serpentine vein	0.56	0.37	4
3S-GC-Mount3-rerun-a-pn2@3	In serpentine vein	3.76	0.36	4
3S-GC-Mount4-a-pn1@1	In serpentine vein	2.58	0.24	4
3S-GC-Mount1-a-pn1@1r	In serpentine vein	2.20	0.45	4
3S-GC-Mount4-a-pn1@3r	In serpentine vein	2.24	0.47	4
3S-GC-Mount4-a-pn1@4r	In serpentine vein	0.20	0.41	4
3S-GC-Mount4-a-pn1@5r	In serpentine vein	1.71	0.48	4
3S-GC-Mount4-a-pn1@6r	In serpentine vein	1.52	0.47	4
3S-GC-Mount4-a-pn2@1r	In serpentine vein	1.69	0.49	4
3S-GC-Mount4-a-pn3@1r	In serpentine vein	1.97	0.47	4
3S-GC-Mount4-d-pn1@1r	In serpentine vein	2.50	0.50	4
3S-GC-Mount4-d_pn1@2r	In serpentine vein	0.71	0.50	4
3S-GC-Mount3-rerun-b-pn1@1	Matrix in pyx layer	2.83	0.35	1
3S-GC-Mount3-rerun-b-pn1@2	Matrix in pyx layer	2.70	0.38	1
3S-GC-Mount3-rerun-c-pn1@1	Matrix w/mil/dol	2.40	0.36	2
3S-GC-Mount3-rerun-c-pn1@2	Matrix w/mil/dol	2.98	0.41	2
3S-GC-Mount3-c-pn1@02	Matrix w/mil/dol	3.30	0.38	2
3S-GC-Mount3-c-pn1@03	Matrix w/mil/dol	3.34	0.39	2
3S-GC-Mount3-c-pn1@04	Matrix w/mil/dol	3.22	0.37	2
3S-GC-Mount3-c-pn1@05	Matrix w/mil/dol	3.43	0.38	2
SBA2 (CGn)				
3S-GC-Mount1-a-rerun2-pn1@1	Matrix	2.50	0.45	2
3S-GC-Mount1-a-rerun2-pn1@2	Matrix	2.54	0.37	2
3S-GC-Mount1-a-rerun2-pn2@1	Matrix	3.60	0.44	2
3S-GC-Mount1-a-rerun2-pn2@2	Matrix	2.98	0.43	2
3S-GC-Mount1-a-rerun2-pn2@3	Matrix	3.07	0.43	2
3S-GC-Mount1-b-rerun2-pn1@2	Matrix	2.94	0.41	2
3S-GC-Mount1-b-rerun2-pn1@3	Matrix	3.38	0.43	2
3S-GC-Mount1-b-rerun2-pn1@4	Matrix	3.54	0.35	2
3S-GC-Mount1-b-rerun2-pn1@1	Matrix	2.61	0.39	2
3S-GC-Mount1-c-rerun2-pn1@1	Matrix	2.85	0.49	2
3S-GC-Mount1-c-rerun2-pn1@2	Matrix	3.02	0.48	2
3S-GC-Mount1-c-rerun2-pn1@3	Matrix	2.68	0.49	2
3S-GC-Mount1-c-rerun2-pn1@4	Matrix	1.52	0.45	2
3S-GC-Mount1-c-rerun2-pn3@1	Matrix	0.74	0.41	2

'Stage' corresponds to the metamorphic stage of pentlandite growths; **Stage 1**—Pre-peak, **Stage 2**—High-pressure peak conditions, **Stage 3**—Exhumation, **Stage 4**—Serpentinization – see Fig. 6.9 for a summary.

Matrix w/mil/dol—Interstitial pentlandite intimately associated with millerite and dolomite. **In pyx layer**—included in pyroxenite layer in peridotite MOL1-C. **CS**—Coarse-grained spinel peridotite, **CGn**—Carbonate-free coarse-grained garnet peridotite, **CG**—Coarse-grained garnet/spinel with coronitic garnet peridotite, **P-FGA**—Porphyroclastic fine-grained garnet amphibole peridotite, **FGA**—fine-grained garnet-amphibole peridotite.

6.6.5 In situ Sr isotope of clinopyroxene and amphibole

Laser ablation MC-ICP-MS analyses were performed on 15 clinopyroxene grains from 5 UZ peridotite samples (total of 25 analyses; Fig. 6.10 and Supplementary Table C5). Clinopyroxene in the two fine-grained garnet-amphibole peridotites P10B and VM10A sampled from Mt. Hochwart (Fig. 6.1) shows an average measured $^{87}\text{Sr}/^{86}\text{Sr}$ value of 0.70538 ± 0.000076 (1σ , $n = 11$). The porphyroclastic garnet-amphibole peridotite sample KL2.4-2b from Klappfbergalm (Fig. 6.1) shows similar $^{87}\text{Sr}/^{86}\text{Sr}$ with 0.70535 ± 0.00012 (1σ , $n = 4$). Clinopyroxene grains from the two coarse-grained peridotite samples UN1 and UN2 from Samerberg area (Fig. 6.1) show similarly radiogenic values of 0.70544 ± 0.00015 and 0.7055 ± 0.0020 . The lower standard deviation obtained for clinopyroxene in fine-grained amphibole peridotite compared to coarse-grained protogranular peridotites (using the same method in the same laboratory) suggests a greater degree of isotopic homogenization of the former, which was subjected to recrystallization and retrogression.

Furthermore, 23 amphibole grains from 8 samples were analyzed for their *in situ* Sr isotope compositions ($n=41$ analyses; Table S6.5). Measured $^{87}\text{Sr}/^{86}\text{Sr}$ of amphibole in the P-FGA peridotites UN3, UN6 (from Samerberg) and UN7 (from Seefeld) averages 0.70548 ± 0.00006 (1σ , $n = 15$), while peridotite UN10 from Seefeld shows more radiogenic values of 0.70597 ± 0.00009 ($n = 4$), and the most radiogenic value is found in peridotite UN14 from Malga Masa Murada with 0.70705 ± 0.00006 ($n = 6$). The FSA peridotites UN8 from Seefeld and UN16 from near Malga Masa Murada exhibit $^{87}\text{Sr}/^{86}\text{Sr}$ of 0.70679 ± 0.00008 ($n = 5$) and 0.70779 ± 0.00011 ($n = 6$), respectively. For comparison, the primitive and depleted mantle have estimated $^{87}\text{Sr}/^{86}\text{Sr}$ of 0.7045 and 0.7026, respectively (Workman and Hart, 2005). Whereas the low $^{87}\text{Rb}/^{86}\text{Sr}$ ratio of the clinopyroxenes (average 0.02) imply that initial $^{87}\text{Sr}/^{86}\text{Sr}$ ratios (at 330 Ma; Tumati et al., 2003) are not much different from the measured ones, this is not the case for amphiboles with an average $^{87}\text{Rb}/^{86}\text{Sr}$ ratio of 0.14 (Supplementary Table C5). For the purpose of the following discussion, the initial values will be used for both clinopyroxene and amphibole.

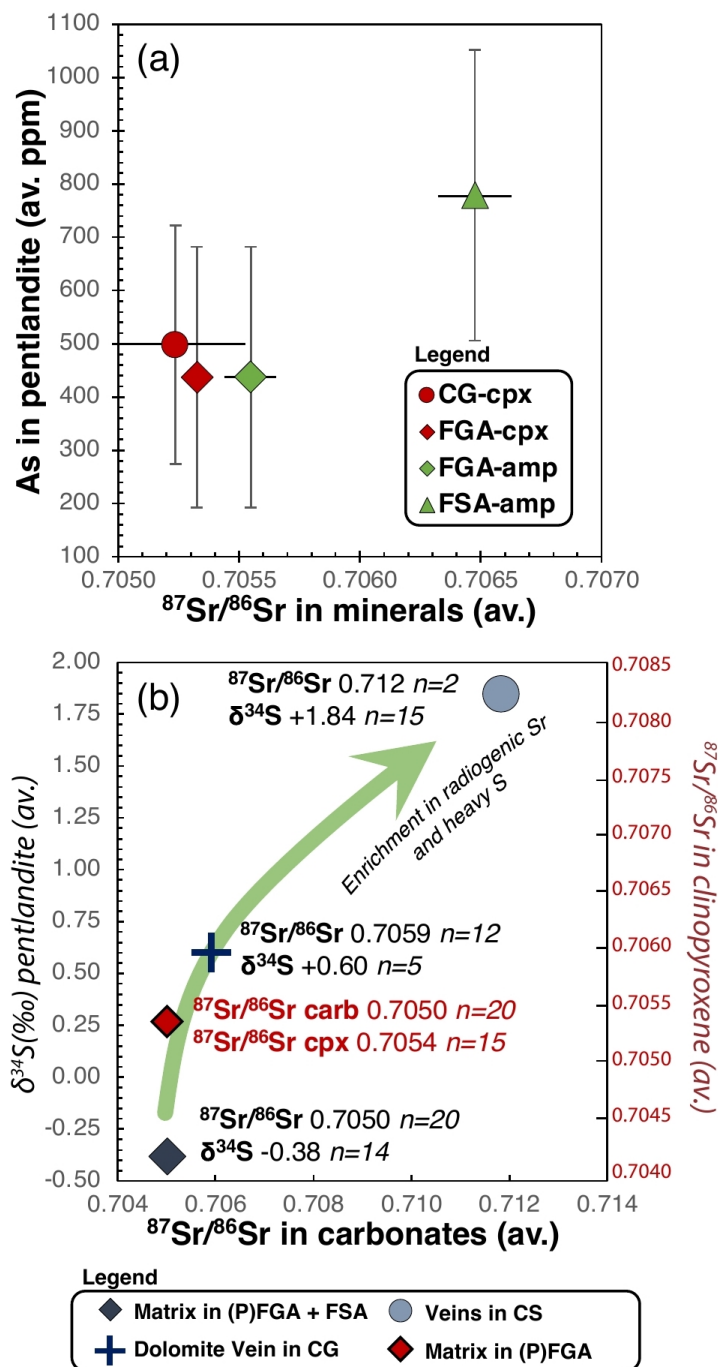


Figure 6.10. *In situ* Sr isotope ratios of (a) amphibole and clinopyroxene compared to As concentrations in the associated pentlandite. Values are reported as total averages for the different lithotypes. **CS**—Coarse-grained spinel peridotite, **CG**—Coarse-grained garnet/spinel with coronitic garnet peridotite, **(P)FGA**—Porphyroclastic and non-porphyroclastic fine-grained garnet amphibole peridotite, **FSA**—Fine-grained spinel (chlorite-amphibole) peridotite. (b) *In situ* Sr isotope compositions of clinopyroxene vs S isotope of pentlandite (this study) and vs *in situ* Sr isotope compositions of carbonates (Consuma et al. 2020). The small number of data points is due to the rare occurrence of clinopyroxene combined with the typically small grain size of clinopyroxene and carbonates, which precludes laser ablation sampling of large enough volumes for statistically meaningful Sr isotope analysis. Further limitations are imposed by the requirement of using matrix-matched sulfide grains for SIMS analyses.

6.7 Discussion

6.7.1 Fractionation of sulfur isotopes during high-temperature processes and late-stage re-equilibration

Few studies have systematically examined the combined geochemical and isotopic signature of sulfides from orogenic mantle domains as a probe to investigate the nature of high-pressure and exhumation processes in collisional settings. The full set of metasomatic and re-equilibration

processes affecting the UZ peridotites throughout their evolution dictates their sulfide mineralogy as well as their chemical and sulfur isotope composition. As these processes may produce sulfur isotopic fractionations, the effects of high-temperature processes and low-temperature re-equilibration of the sulfide assemblage on $\delta^{34}\text{S}$ have to be considered before attempting any interpretation on the relationships between sulfur isotope signatures and source/s.

Pentlandite is not stable at upper mantle conditions experienced by UZ peridotites during their multi-stage evolution (Fig. 6.2a-b). It either formed together with minor amounts of pyrrhotite, now in part replaced by magnetite, from a high-temperature monosulfide precursor (Fig. 6.7a), or precipitated directly from a metasomatic metal-rich fluid (Lorand and Grégoire, 2006; Lorand et al., 2013; Giuliani et al., 2016). Prior modelling has demonstrated that the S isotopic fractionation between pentlandite and a precursor monosulfide solid solution (mss) is limited to 0.7 ‰ for equal proportions of pentlandite and mss, and low temperature of pentlandite formation (300°C; Giuliani et al., 2016). Given the dominance of pentlandite in the low-temperature assemblages in the UZ peridotites, it is argued that the $\delta^{34}\text{S}$ signature of pentlandite largely reflects that of its high-temperature precursor. Furthermore, since the pH of fluids does not induce significant isotope fractionation at the metamorphic conditions of subduction zones (Giacometti et al., 2014), the measured $\delta^{34}\text{S}$ of pentlandite is considered to be broadly representative of the bulk rock that interacted with various S-bearing metasomatic fluids or melts. The sulfur isotope composition is also not modified by high-pressure prograde metamorphism of subducted rocks (Evans et al., 2014; Li et al., 2021), and the S isotopic fractionation between solid sulfide and sulfide melt or H_2S in reduced fluids is negligible (Ohmoto and Rye, 1979; Li and Liu, 2006; Marini et al., 2011). Instead, significant fractionation occurs between oxidized and reduced S species (up to 4-5‰) even at mantle temperatures (i.e. $T > 900^\circ\text{C}$; Ohmoto and Rye, 1979). During the Variscan subduction and subsequent exhumation, the precursor sulfide to pentlandite may have interacted with, or precipitated from, fluids or melts containing oxidized or reduced S species.

Sulfate is recycled with sediments and altered oceanic crust (Alt and Shanks, 2006; Schwarzenbach et al., 2018b), and it usually preserves a positive S isotope signature close to the seawater composition (Alt, 1995; Alt and Shanks, 2011; Li et al., 2021). The timing and mechanisms of sulfate-to-sulfide reduction remain poorly constrained, since so far no sulfate grains have been found in equilibrium with mineral assemblages of HP-UHP subducted metamorphic rocks (Li et al., 2021 and references therein). Of note, Li et al. (2021) measured isotopically heavy $\delta^{34}\text{S}$ signature (+25‰) for pyrite in veins from subducted HP metamorphic rocks from the Southwestern Tianshan HP-UHP metamorphic belt (northwestern China), which exceptionally documents that

the seawater sulfate-derived $\delta^{34}\text{S}$ signature may be retained even at great depths (i.e. 70 km depth). The authors suggest that reduction of sulfate to sulfide may have occurred during pre-subduction hydrothermal alteration or contemporaneous with subduction at fore-arc depths, implying that no isotope fractionation occurred (Li et al., 2021). On the other hand, a fractionation value of $\sim 20\text{‰}$ between dissolved sulfate and pyrite precipitation was modeled for fluid migration throughout the slab-mantle interface at 300°C , reaching up to 120‰ depending on distance from the source, pathway and amount of pyrite precipitation (Walters et al., 2019).

In the UZ peridotites, the high oxygen fugacity of FMQ to FMQ+2 estimated by Malaspina et al. (2009) at 3GPa approaches conditions where significant proportions of oxidized S should be present (Jugo et al., 2010). However, the oxygen fugacity conditions recorded by the UZ peridotites investigated in this study ($<\text{FMQ}$ at 2 GPa; Gudelius et al., 2019) are far too reducing to allow the presence of significant amounts of sulfate. Moreover, despite the restricted range of S isotope values in the UZ peridotite, we observe a clear distinction among the lithotypes and textural occurrences. We therefore propose that multiple melt-and-fluid/rock interactions occurred during and after the Variscan Orogeny, and we discuss the nature of the fluid sources in Section 6.4.2. Although a larger range of $\delta^{34}\text{S}$ values (-10.0 to $+5.4\text{‰}$) is documented in mantle wedge sulfides from the Western Gneiss Region (Norway) by Rielli et al. (2018), the reported S signature is referred to sulfides from lenses of pyroxenite and websterite enclosed within peridotite bodies. Peridotite and pyroxenite may record different geochemical processes and, consequently, there are no sulfur isotope compositions from garnet peridotites available in the literature to allow comparison with the data presented in our study.

6.7.2 Near-quantitative sulfide extraction during SCLM stabilization and addition during refertilization

The sulfur isotope composition of sub-continental lithospheric mantle (SCLM), which stabilizes by extraction of variable degrees of partial melt (e.g., Griffin et al., 2004), remains poorly constrained and has been mostly addressed in studies of sulfide inclusions in diamonds from mantle xenoliths, showing a $\delta^{34}\text{S}$ range between -4‰ and $+6\text{‰}$ (Chaussidon et al., 1987; Farquhar, 2002; Thomassot et al., 2009). In the Ulten Zone, during high-temperature pre-peak conditions (Stage 1), the coarse-grained protogranular peridotites containing the assemblage olivine + enstatite + diopside + Cr-Al spinel reside in the continental lithospheric mantle and equilibrate at 1200°C and 1.3-1.6 GPa (Nimis and Morten, 2000). Their study may therefore provide insights into mantle wedge evolution before its entrainment into the Variscan subduction architecture. Samples in this

study appear to fall along a curved array with respect to bulk-rock TiO_2 and Al_2O_3 , both of which are moderately incompatible (Fig. 6.4). Such arrays result from partial melt extraction.

In accord with Ionov et al. (2017) and Gudelius et al. (2019), major element compositions indicate mostly ~15-25% of melt extraction (Fig. 6.4a), although this is a minimum estimate if refertilization occurred (Gudelius et al., 2019). At such melt fractions, the sulfide component would have been exhausted, depending on oxygen fugacity and S concentration (Keays, 1995; Mungall et al., 2006). For example, for Al_2O_3 contents of 2-2.3 wt.% recorded in some UZ peridotites (Fig. 6.4a), less than 100 ppm S would be expected to remain in the mantle for fractional melt extraction at 3 GPa and an oxygen fugacity of FMQ-2 (Aulbach et al., 2016). If melt extraction occurred at a lower pressure, then S concentrations in the residue would be even lower, given increasing S solubility in silicate melt at sulfide saturation with decreasing pressure (Mavrogenes and O'Neill, 1999). In this light, the UZ peridotites containing >100 ppm S (Supplementary Table C2 and Figure C2) almost certainly experienced S addition. Furthermore, sulfidation of peridotite has been shown to cause Fe-Ni zoning in olivine (Papike et al., 1995; Bataleva et al., 2016). Although such zoning is not observed in the UZ olivine (Gudelius et al., 2019; Consuma et al., 2020), higher NiO contents in olivine are observed in S-poor peridotites relative to olivine from S-rich peridotites, consistent with Ni extraction from olivine during metasomatic sulfide addition (Fig. 6.4c).

Hereafter, for each metamorphic stage, we discuss (i) the textural relationship of sulfides with the coexisting carbonates and hydrous minerals; (ii) the process and related metasomatic agents that may have modified the sulfide component throughout the evolution of peridotites; (iii) the relevant conditions (P-T- $f\text{O}_2$ - $f\text{S}_2$) that may have exerted a major control on the nature of sulfides and their mobility with respect to the melt/fluid phase. We conclude with the potential implications that our findings may have for the understanding of the coupled sulfur-carbon cycling during continental collision.

6.7.3 Pre-collision mantle metasomatism (Stage 1)

Stage 1 is represented by rare coarse-grained spinel peridotites containing pyroxenite layers (Nimis and Morten, 2000), with only one sample available for this study (MOL1-C). During this stage, percolation of a hydrous basic melt induces an enrichment in the lithospheric mantle of LREE, LILE and Li at spinel-facies conditions (Nimis and Morten, 2000; Scambelluri et al., 2006). Precipitation of this melt prompts the formation of sulfide-bearing pyroxenite layers within the peridotite. The $\delta^{34}\text{S}$ signature ($+2.77 \pm 0.37\text{‰}$; $n=2$) of matrix pentlandite in pyroxenites is heavier than that estimated for continental lithospheric mantle ($+1.35 \pm 0.25 \text{‰}$; Fiorentini et al., 2018),

and similar to the $\delta^{34}\text{S}$ signature (up to +5.4‰) of sulfides contained in pyroxenite lenses within peridotite bodies from the Western Gneiss Region (Rielli et al., 2018). Similarly, pentlandite associated with dolomite in the surrounding peridotite matrix is also isotopically heavy ($+3.11 \pm 0.38\text{‰}$; $n = 6$).

Euhedral inclusions of dolomite in primary spinel within porphyroclastic garnet from fine-grained UZ peridotite, may represent relics that testify to the percolation of carbon-bearing liquids prior to Stage 2 garnet growth (Förster et al., 2017). The aforementioned petrographic and isotopic evidence indicate the presence of (possibly subduction-related) isotopically heavy S in the source of the melts involved in Stage 1 metasomatism. Temperature and oxygen fugacity are the main factors that dictate the solubility and speciation of sulfur in silicate melts (Clemente et al. 2004; Jugo et al. 2010; Jégo and Dasgupta, 2014; Canil and Fellows, 2017). Experimental data on the sulfide vs. sulfate stability in basaltic and sediment glasses (Jugo et al., 2010; Canil and Fellows, 2017) suggest that the melt is saturated in sulfide (S^{2-}) rather than in sulfate (S^{6+}) at oxygen fugacity lower than around the FMQ buffer. In this light, the relatively reducing nature ($<\text{FMQ}$; Gudelius et al., 2019) of the investigated samples is suggested to also indicate a system dominated by reduced S species. Additionally, the overall lack of identifiable reduced carbon species (i.e. graphite or disordered carbonaceous material; e.g., Vitale Brovarone et al., 2020) in the UZ peridotites requires carbon to be present mostly as carbonate (CO_2). We speculate that any S added from melt leaving a lithospheric mantle source would have involved an H_2S - CO_2 -bearing agent, consistent with suggestions that mantle fluids are H_2S -dominated (Eggler and Lorand, 1993).

6.7.4 High-pressure (garnet) metamorphism and recrystallization (Stage 2)

6.7.4.1 Coarse-grained vs Fine-grained peridotite

With the onset of the Variscan Orogeny, the corner flow initiated by continental subduction dragged the UZ peridotites deeper into the lithospheric mantle towards the slab-wedge interface, causing their textural transition from coarse protogranular to porphyroclastic and finally fine-grained equigranular. The peak conditions were attained at $\sim 850^\circ\text{C}$ and 2.2-2.7 GPa (Nimis and Morten, 2000; Braga and Sapienza, 2007). At this stage, the UZ peridotites still resided in the mantle wedge (Scambelluri et al., 2006), where matrix pentlandite coexisted along with high-pressure matrix phases, such as recrystallized olivine and pyroxenes, pargasitic to hornblenditic amphibole, garnet, and dolomite. Thus, the S isotopic composition of pentlandite may reflect peak-garnet conditions with superposed local interaction with retrograde fluids. The Mann-Whitney U Test allows to distinguish two populations of matrix sulfides with respect to $\delta^{34}\text{S}$: one from fine-grained

peridotite ($\delta^{34}\text{S} = -0.11\text{‰} \pm 0.39$; 1σ , $n=15$) and one from the coarse-grained counterpart ($\delta^{34}\text{S} = +2.35\text{‰} \pm 0.43\text{‰}$; 1σ , $n=18$). Thus, despite the limited range of measured sulfur isotope signature for the entire data set (-1.62 to $+3.76$ ‰), differences in the source of sulfur for texturally diverse sulfides are detected. Moreover, some coupling between the $\delta^{34}\text{S}$ signature of pentlandite and trace elements becomes evident when not only the textural positions (Fig. 6.11), but also the different sampling localities are considered. This suggests some provinciality with respect to the nature of metasomatism (see Supplementary Figure C1), as previously recognized based on lithophile element contents (Gudelius et al., 2019).

Coarse-grained garnet peridotite. The positive $\delta^{34}\text{S}$ values obtained from a population of matrix pentlandite in the coarse-grained garnet peridotites are distinct from the proposed depleted mantle range of $\delta^{34}\text{S}$ of $-1.28 \pm 0.33\text{‰}$ (Labidi et al., 2013), from the suggested mantle wedge composition of 0‰ (Li et al., 2020), and from the proposed composition of continental lithospheric mantle ($+1.35 \pm 0.25\text{‰}$; Fiorentini et al., 2018). Combined with elevated S abundances (≥ 166 ppm; Table 1), the measured isotope values require addition of isotopically heavy S, either from an enriched mantle source as recognized by Ionov et al. (1992) or involving processes inducing heavy S isotope enrichment, such as fractionation of isotopically light sulfide (Walters et al., 2019). The initial Sr isotopic composition of clinopyroxene in two coarse-grained peridotites ($^{87}\text{Sr}/^{86}\text{Sr}=0.70509$ - 0.70538 ; Table 1) is more radiogenic than that of the primitive or depleted mantle (0.7045 and 0.7026 , respectively; Workman and Hart, 2005), and also indicates that the enrichment in radiogenic Sr pre-dates the entrapment of peridotites into the tectonic mélange. Indeed, coarse-grained UZ peridotites show evidence for interaction with crust-derived silicic melts (Gudelius et al., 2019). Figure 6.11 shows that the isotopically heavy $\delta^{34}\text{S}$ signature of pentlandite in coarse-grained peridotites is coupled with elevated Pb concentrations, but not with elevated abundances of other fluid-mobile elements, such as As and Sb, which may again point to a continental crustal contaminant carried by a melt rather than a fluid. Indeed, for sulfide- rather than sulfate-saturated sediment-derived melts, Sb will be depleted in the melt relative to As and Pb (Canil and Fellows, 2017), which corresponds to the systematics observed for sulfide in the coarse-grained peridotite (Fig. 6.11).

Fine-grained garnet-amphibole peridotite. Following the interpretation of Obata and Morten (1987), the fine-grained lithotypes record re-crystallization of the coarse-grained peridotites during downward movement into the deeper portion of the supra-subduction mantle. Compared to coarse-grained

peridotites, the average sulfur isotope composition of matrix pentlandite from fine-grained peridotites is distinctly lower ($\delta^{34}\text{S} = -0.11\text{‰} \pm 0.39$; 1σ , $n=15$), with a few grains within the DM value of $\delta^{34}\text{S} = -1.28 \pm 0.33\text{‰}$ (Labidi et al., 2013), as shown in Figure 6.9. Although the relationship between the coarse- and the fine-grained peridotite remains unclear, the latter clearly documents interaction with crust-derived hydrous fluids based on elevated contents of fluid-mobile lithophile elements (Gudelius et al., 2019). This may be corroborated by sulfide compositions, where the contents of the fluid-mobile elements As and Sb, which are highly soluble in aqueous fluids (Jochum and Verma, 1996), are slightly more elevated in fine-grained than in coarse-grained peridotites (Fig. 6.11). In addition, Se and Te abundances are markedly higher in fine-grained peridotites, and, as strongly chalcophile elements (e.g., Barnes, 2016), might be expected to follow the sulfide anion. Thus, formation from reduced and slightly isotopically heavy (with respect to DM) reduced S species is inferred during this stage. At $> 30\text{km}$ depth, reduced S species carrying As(-1), Sb and Te may be sourced from the subducted slab and dissolved in hot aqueous fluids (Hattori and Guillot, 2007), where they dominate over oxidized species and are efficiently mobilized (Li et al., 2020).

Initial $^{87}\text{Sr}/^{86}\text{Sr}$ of matrix amphibole from high-pressure fine-grained peridotites is elevated, ranging from 0.705334 ± 0.00006 to 0.70691 ± 0.00006 , again pointing to the addition of an isotopically evolved crustal component, either from the surrounding gneisses or from seawater-altered slab components (considering that the $^{87}\text{Sr}/^{86}\text{Sr}$ of seawater at 330Ma was equal to 0.7078; Peterman et al., 1970). Variable equilibration of the resultant fluids with unradiogenic mantle material prior to metasomatizing the UZ peridotites can explain the variable $^{87}\text{Sr}/^{86}\text{Sr}$ signature. This was previously invoked to explain relatively unradiogenic *in situ* $^{87}\text{Sr}/^{86}\text{Sr}$ values of ~ 0.705 of matrix dolomite formed under eclogite-facies conditions (Consuma et al., 2020). The heterogeneous nature of Stage 2 metasomatism is also reflected in the S concentration of fine-grained peridotites, which encompasses the entire range of 40 to 288 ppm in this study. This suggests local variations in terms of S concentration and/or degrees of S saturation levels due to multiple fluid infiltration, causing only minor sulfide addition in some (e.g., peridotite UN-3 with a sulfide mode of 0.02 wt%) and abundant sulfide addition in other samples (e.g., peridotite UN-14 with sulfide mode of 0.09 wt%). Interestingly, the aforementioned peridotites were sampled from Samerberg and Malga Masa Murada, which also respectively show evidence for lower and higher levels of lithophile fluid-mobile element enrichment, suggestive of more and less distal positions relative to the source of the metasomatic fluids (Gudelius et al., 2019).

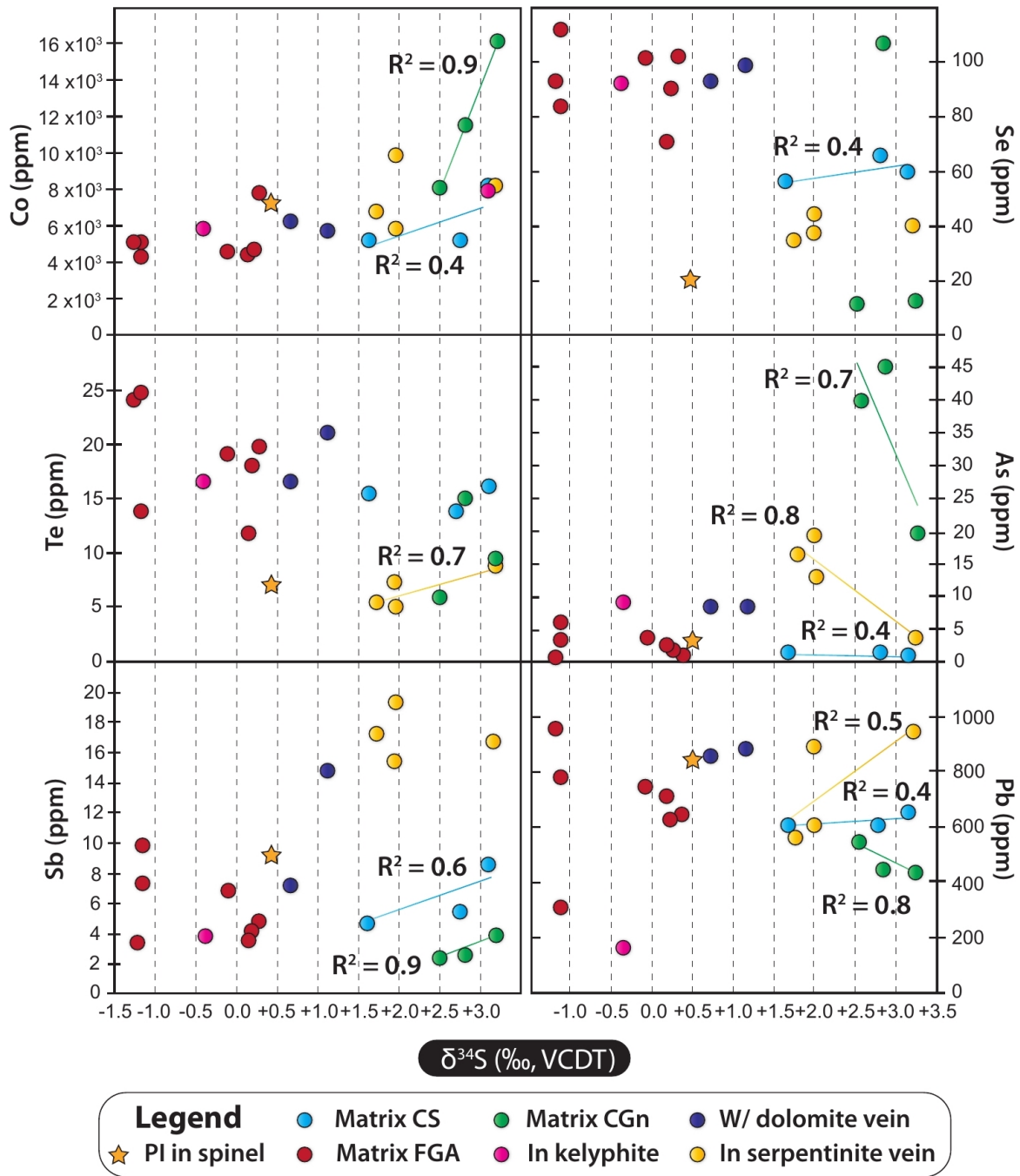


Figure 6.11: Trace element concentrations (Co, Se, Te, Pb, Sb, As) versus $\delta^{34}\text{S}$ measured in pentlandite in the Ulten Zone peridotites distinguished by textural positions. When significant, correlation fitting lines and respective R^2 are reported. **CS**—Coarse-grained spinel peridotite, **CGn**—Carbonate-free coarse-grained garnet peridotite, **CG**—Coarse-grained garnet/spinel with coronitic garnet peridotite, **(P)FGA**—Porphyroclastic and non-porphyroclastic fine-grained garnet amphibole peridotite, **FSA**—Fine-grained spinel (chlorite-amphibole) peridotite. **Po**—pyrrhotite, **Pn**—pentlandite.

6.7.4.2. *Stage 2: The sources of Ulten Zone metasomatic agents*

The early stages of the Ulten Zone continental subduction were characterized by a continental crust possibly still attached to a mature oceanic slab (Ranalli et al., 2005). In this light, possible sources capable of furnishing sulfur to the mantle wedge are subducted altered oceanic crust, overlying metasediments, metaserpentinites and enclosing gneisses. The low fO_2 recorded in the investigated UZ peridotites (Fig. 6.2c) does not preclude that isotopically heavy sulfide with $\delta^{34}S$ up to +3.76 ‰ formed by reduction of oxidized S species under appropriate conditions. Oxidized S could derive from seawater-altered oceanic lithosphere, which records a large range of $\delta^{34}S$ values (-50 to +20 ‰) in seafloor hydrothermal sedimentary pyrite, but with a predominantly negative isotopic signature (Canfield & Farquhar, 2009). In contrast, sulfates in serpentinite and metabasic rocks from Syros, as analogs of subducted lithosphere, record dominantly heavier $\delta^{34}S$ of +15.7 to +20.8‰ and +3.5 to +20.1‰, respectively (Schwarzenbach et al., 2018a). In exhumed high-pressure rocks, metasomatic sulfides with a much larger range of $\delta^{34}S$ (-21.7 to +13.9‰) than in the UZ peridotites are ascribed to the combined effects of isotope fractionations due to sulfate reduction and fluid evolution as a result of precipitation of isotopically light sulfide (Walters et al., 2019). Li et al. (2021) collate a comprehensive dataset of sulfides from worldwide HP-UHP metamorphic terranes. Combined with new data, they find a $\delta^{34}S$ signature of -33 to -6‰ in metasediments, $\delta^{34}S$ of -4 to +4‰ in metabasite/metagabbros, and $\delta^{34}S$ of +2 to +18‰ in HP serpentinites.

Given the *mélange* setting of Ulten Zone peridotites, the continental crust may also be a source of isotopically heavy S, either by direct formation from H_2S if the lighter value applies, or by sulfate reduction if the heavier value applies.

The availability of both S and Sr isotopic data from this study and from the literature allows some constraints to be placed on the sources and amount of contaminant involved in the formation of sulfides and associated clinopyroxene or amphibole (Fig. 6.12). The garnet-kyanite gneisses of continental crust enclosing the UZ peridotites contain a large range of S concentrations (100 to 1600ppm S; Bargossi et al., 2003) with an average of ~ 600 ppm S ($n=12$), and a Sr content of ~ 130 ppm (Tumiati et al., 2003). Their S isotopic composition is unknown, but metapelites metamorphosed under amphibolite-facies conditions from the Kinzigite Formation of the Ivrea Zone ($\delta^{34}S$ values of +3.6‰ to +10.1‰; Fiorentini et al., 2018) may represent reasonable analogues that can be used to model mixing with the depleted mantle. This is because of the contemporaneity of the Variscan metamorphic event and because of the similar chemical composition with the UZ garnet-kyanite gneisses.

6 • The sulfur component of the Ulten Zone peridotite: a piece of the deep Sulfur cycle?

Figure 6.12 shows the binary mixing between a depleted mantle (DM) reservoir with plausible slab-derived sources in a closed system (full dataset in Supplementary Table C6). The sample scatter reflects the variability of the S and Sr concentrations and isotopic composition of melts/fluids and their evolution between leaving the source and their interaction with the Ulten Zone peridotites. Results show that $\ll 10\%$ of a continental crust component with $\delta^{34}\text{S}$ values $+10.1\text{‰}$ and 600ppm of S are required to explain the S-Sr isotopic composition of UZ fine-grained peridotite during Stage 2. Concentrations of several 100 ppm S may be expected for a crustal melt, and of several 1000 ppm S for a fluid equilibrated with crustal rock (Supplementary Table C6). Conversely, in accordance with trace element composition and with the lack of carbonates, the outlier CGn peridotite SBA2 points to a liquid carrying isotopically heavy S, which percolated the mantle wedge in the Samerberg Area, and which can be explained by invoking a third S source derived from isotopically heavy, but less radiogenic serpentinite (Fig. 6.12). In this scenario, formation of isotopically heavy sulfide by reduction of sulfate, accompanied by isotopic fractionation of several ‰ at the estimated conditions of 850°C (cf., Ohmoto and Rye, 1979) is not required, nor is it precluded by the data.

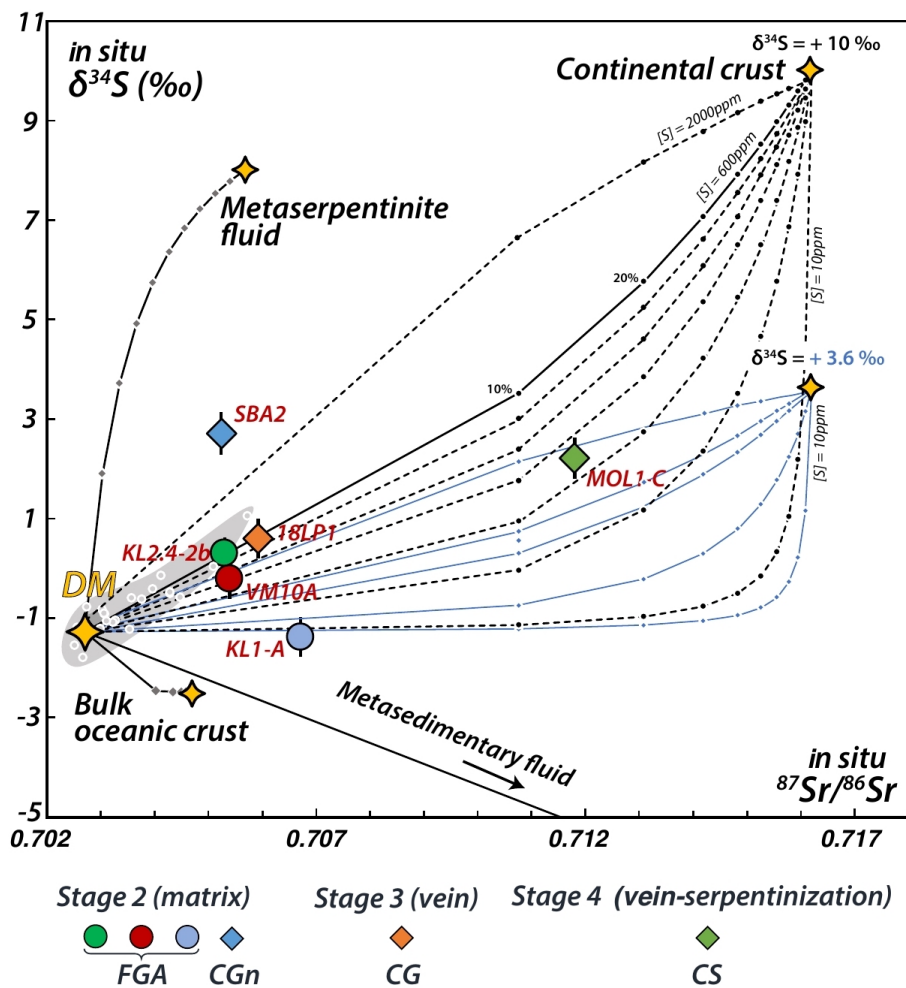


Figure 6.12: $\delta^{34}\text{S}$ in pentlandite (this study) vs. $^{87}\text{Sr}/^{86}\text{Sr}$ in coexisting carbonate, clinopyroxene and amphibole (this study and Consuma et al., 2020). Note that MOL1-C refers to the carbonates(+serpentine)-bearing vein crosscutting the coarse spinel peridotite of Figure 6. 3e. Mixing trends between depleted mantle (DM) source and possible slab-derived melt and fluid sources. The continental crustal (CC) component may be a melt or a fluid with variable S concentrations as shown. A single Sr concentration (~ 130 ppm) is assumed for the purpose of modeling, since in our study the Sr concentration in fluid and melt is estimated to vary less than two-fold. Light grey area and individual data for glasses dredged on the South Atlantic ridge from Labidi et al. (2013). Input data with references, as well as the effect of varying Sr concentration on the curvature of the mixing lines, is reported in Supplementary Table C6.

6.7.5 Exhumation of crust-mantle mélange and retrogression (Stage 3)

Shortly after the attainment of peak-P conditions, UZ peridotites became part of a crust-mantle mélange (Scambelluri et al., 2006), where they were exposed to infiltration of channelized C-O-H fluids and late serpentinization along a fast exhumation path in the late Carboniferous (Ranalli et al. 2005; Consuma et al. 2020), with conditions of 650-700 °C and P ranging between 2.2 and 1 GPa (Figs. 6.2a-b). Two types of sulfides represent this stage and are interpreted as retrograde: (1) sulfide grains in retrograde kelyphitic coronas around garnet, and (2) those included and associated

with a dolomite + tremolite + chlorite vein. Late pyrite in retrograde coronas reported in few studies has been interpreted as a result of late influx of S-rich fluids which were produced deeper in the slab (c.f., Evans et al., 2014; Giacometti et al., 2014), possibly involving redox reactions (Walters et al., 2019). Similarly, the presence of pentlandite in garnet coronas of UZ peridotites suggests that partial kelyphitization was catalyzed by ingress of a S-bearing fluid. Corona-associated pentlandite averages $\delta^{34}\text{S}$ of -0.38‰ (1σ ; $n=3$), with negligible intra-grain variability. This grain is also cut by a late chlorite flake, whose cleavage is filled with magnetite, suggesting its formation above the chlorite-out reaction (i.e. at $\sim 750\text{--}800^\circ\text{C}$ and P of 1.7 GPa), that is, somewhat warmer than the conditions inferred earlier ($650\text{--}700^\circ\text{C}$; Consuma et al. 2020). No carbonates occur in these retrograde coronas. Low Pb, As and Sb contents (Fig. 6.11) suggest kelyphitization at low fluid-rock ratios, consistent with incomplete garnet breakdown.

On the basis of mineral assemblages and textural relationships, it is suggested that the pentlandite-hosting dolomite vein formed prior to serpentinization at $T = 650^\circ\text{C}\text{--}700^\circ\text{C}$ and $P = 1\text{GPa}$ (Consuma et al. 2020). Along this vein, enclosed pentlandite associated with millerite exhibits $\delta^{34}\text{S} = +1.13 \pm 0.38\text{‰}$, which is somewhat higher than the values of pentlandite in kelyphite and interstitial to silicates. Furthermore, a distinct fluid source is otherwise required to explain the lower $\delta^{34}\text{S}$ of $0.68 \pm 0.40\text{‰}$ ($n=3$) for matrix pentlandite spatially close to the dolomite vein, found in peridotite sample 18LP1. The heterogeneity of the measured *in situ* Sr isotopes of this dolomite vein ($^{87}\text{Sr}/^{86}\text{Sr}=0.7035\text{--}0.7085$) was interpreted to reflect retrograde hybridized C-fluids channelized into the peridotites during exhumation, when the crust-peridotite *mélange* was already formed (Consuma et al. 2020). Coupled S and Sr isotopic ratios related to dolomite veining during early exhumation (in coarse peridotite 18LP1) and even more so in serpentinite + magnesite vein MOL1 -C suggest higher degrees of contamination from a continental crustal source (Fig. 6.12). High Se and Te contents, together with intermediate to high Sb and As concentrations, suggest that this was a hydrous fluid carrying HS^- as the dominant S species.

6.7.6 Serpentinization and local effect of fluid-rock interactions on S content and isotope composition (Stage 4)

The latest stage recording metasomatic modification of UZ peridotites is the serpentinization that occurred over a span of temperatures ($<600^\circ\text{C}$ to 300°C) along a slow and cooling exhumation path during the Permian-Triassic (300-205Ma; Ranalli et al. 2005; Consuma et al. 2020).

The high-T phase of Stage 4 is characterized by veining of serpentine + magnesite + tremolite crosscutting the coarse spinel peridotite MOL1-C, an assemblage which indicates a temperature of

formation of $< 600^{\circ}\text{C}$ on the retrograde path (Consuma et al. 2020). Pentlandite grains enclosed in this vein locally show textural alteration features, including (i) magnetite pseudomorphs after pentlandite and (ii) association with heazlewoodite grains. The pentlandite \pm heazlewoodite \pm magnetite assemblages documented here and previously studied in kimberlite-borne mantle xenoliths from the Kaapvaal craton (Giuliani et al. 2016; Lorand and Grégoire, 2006), could originate from partial desulfidation of the low-T sulfide assemblage during serpentinization, which is a common feature of mantle peridotites (e.g. Lorand, 1989).

Desulfurization of pentlandite to awaruite (not observed in the UZ peridotite) and/or heazlewoodite represents the lowest S fugacity for a sulfide assemblage (see Fig. 8 in Lorand and Grégoire, 2006). Furthermore, the relatively wide S isotopic range of these pentlandite grains ($\delta^{34}\text{S} = -0.29$ to $+3.76\text{‰}$) attests to the strongly heterogeneous effect of serpentinization on the S isotope signature, and it reflects minimal isotopic homogenization at the vein scale. Importantly, this vein is texturally cut by late dolomite vein with highly radiogenic Sr ($^{87}\text{Sr}/^{86}\text{Sr} > 0.7118$; Table 6.1).

The low-T phase of Stage 4 is characterized by dolomite dissolution via serpentinization and formation of pseudomorphs of calcite + brucite intergrowths, found in several fine-grained garnet-amphibole peridotite (Förster et al., 2017; Consuma et al. 2020; Gudelius et al., 2019; this study), and by the composite serpentine vein MM1B hosting magnetite + millerite with minor calcite and dolomite.

Several PI included in coarse spinel are intimately associated with calcite + brucite intergrowths and decrepitation features (i.e. radiating fractures; Fig. 6.3), and therefore represent Stage 4 processes. Nevertheless, the $\delta^{34}\text{S}$ ($+0.46 \pm 0.34\text{‰}$) of pentlandite in PI is only moderately heavier than the suggested depleted mantle with $\delta^{34}\text{S}$ of $-1.28 \pm 0.33\text{‰}$ (Labidi et al., 2013). The PI assemblages (Fig. 6.3b) may point to the involvement late, C-S-bearing saline, possibly seawater-derived agents, as previously suggested (Lo Pò et al., 2020). Indeed, saline, oxidizing, sulphate-bearing brines have been implicated in sulfide dissolution in subduction mélanges (Schwarzenbach et al., 2018a), corresponding to the tectonic setting where UZ peridotites were serpentinized. Experimental studies performed by Bataleva et al. (2018) reveal that interaction of olivine with sulfate and C-bearing brines may induce mantle sulfide and carbonate formation via the reaction $\text{olivine} + \text{anhydrite} + \text{C} \rightarrow \text{diopside} + \text{S}_0 + \text{CO}_2$, followed by olivine sulfidation. If so, the relatively low $\delta^{34}\text{S}$ of PI sulfide requires a low-T origin when the isotopic fractionation would be largest. For examples, Walters et al. (2019) model fractionations of some 20‰ for pyrite precipitation from sulfate at 300°C . Pentlandite in the PI has also moderate to high contents of the fluid-mobile elements Sb and As, but low Se and Te compared to other samples (Fig. 6.8). This may indicate

limited addition of Se and Te by saline media where concentrations may be low due to limited availability of the HS⁻ ligand, with which chalcophile elements could complex.

Last, in contrast to textural evidences for desulfurization and dedolomitization, high bulk S contents (> 300 ppm) and high As and Sb concentrations in sulfides from the serpentine vein (Fig. 6.8) indicates channelized S-enriched fluid infiltration during Stage 4 (in the form of millerite grains) near the area of Malga Masa Murada.

To conclude, together with the possible involvement of oxidizing H₂S-poor saline fluids in the formation of PI, serpentinization appears to be associated with highly localized processes. These may involve sulfide dissolution in S-undersaturated oxidizing saline fluids, perhaps sourced from metasediments (Schwarzenbach et al., 2018a), sulfide precipitation when such fluids reach S saturation, and removal of isotopically light S in reducing hydrous fluids, such as those associated with dehydration of oceanic mantle (Piccoli et al., 2019).

6.8 Conclusions and implications for sulfur cycling during continent collision

We provide a new perspective of sulfur and carbon mobility in continental subduction zones from the viewpoint of the previously poorly studied mantle wedge. A first-order observation is the intimate association between carbonates and sulfides, which occur in different textural positions related to the multi-metamorphic evolution of the Ulten Zone orogenic peridotite, as summarized in the conceptual sketch of Figure 6.13. Using detailed petrography with bulk-rock data as well as high-resolution chemical and isotopic analyses of sulfides and associated metasomatic minerals (amphibole, clinopyroxene, carbonates), we demonstrate that the high-pressure orogenic mantle domain from the Variscan Ulten Zone repeatedly interacted with multiple metasomatic agents variably enriched in sulfur and carbon.

(1) The Variscan lithospheric mantle was initially depleted and sulfide-poor, and subsequently inherited a sulfur component during an early stage, when hot, H₂S-CO₂-bearing melts leaving a subduction-modified source invaded the overlying spinel-facies peridotite in the mantle wedge, leading to precipitation of sulfide-bearing pyroxenite with $\delta^{34}\text{S}_{\text{pentlandite}}$ of +2.77 ‰. A reported dolomite inclusion in coarse spinel indicates carbonate mobility at this early stage.

(2) Under peak eclogite-facies P-T conditions, heterogeneous melt and fluid sources variably enriched in carbon, isotopically heavy sulfur and radiogenic Sr were involved: (i) the positive shifts of $\delta^{34}\text{S}$ (up to +3.43‰) from typical mantle values, and radiogenic $^{87}\text{Sr}/^{86}\text{Sr}_{\text{clinopyroxene}} > 0.7053$ suggest that, at high-pressure conditions, coarse-grained garnet peridotites interacted with

³⁴S- and Pb-enriched crustal melts prior to their becoming part of a crust-mantle mélange. Matrix carbonate is usually rare in the coarse peridotite. (ii) The hydrous fluids interacting with mantle rocks during recrystallization and deformation from coarse- to fine-grained peridotites added radiogenic Sr ($^{87}\text{Sr}/^{86}\text{Sr}_{\text{amphibole}} \sim 0.7061$, this study) and had a heterogeneous effect on the bulk S content (58 to 288 ppm S), as S was variably added or removed. The presence of dolomite with $^{87}\text{Sr}/^{86}\text{Sr} \sim 0.705$ (Consuma et al., 2020) suggests that carbon was also mobilized at this stage. Given Sr isotopic evidence for a crustal fluid source, the low $\delta^{34}\text{S} = -1.62$ to $+0.67\text{‰}$ compared to the coarse-grained peridotites is suggestive to reflect involvement of a sulfide- rather than sulfate-bearing fluid. The observed S-Sr isotopic relationship in the fine-grained peridotite can be satisfied if a depleted mantle source is contaminated by $\ll 10\%$ of radiogenic and isotopically heavy fluids sourced from the neighboring garnet-kyanite paragneisses, with minor contribution of less radiogenic metaserpentine-derived fluid.

(3) Shortly after peak P-T conditions the crust-mantle mélange interacted with hybridized fluids, leading to formation of a dolomite veinlet with heterogeneous Sr isotope values ($^{87}\text{Sr}/^{86}\text{Sr} = 0.7036$ to 0.7083 ; Consuma et al., 2020), which is intimately associated with (mostly) Copentlandite and pentlandite with $\delta^{34}\text{S}$ close to 0‰ .

(4) Exhumation-related serpentinization in the crust-mantle mélange had a markedly heterogeneous effect on sulfur isotopes. Pentlandite grains enclosed in a serpentine + magnesite vein crosscutting the coarse-grained peridotite matrix, and texturally cut by a late dolomite vein with $^{87}\text{Sr}/^{86}\text{Sr} = 0.711$ (Consuma et al. 2020), show a broad range of $\delta^{34}\text{S}$ between -0.29 and $+3.76\text{‰}$. Furthermore, the presence of magnetite as pseudomorphs after pentlandite indicates local desulfurization with inferred preferential loss of ^{32}S , whereas the S concentration of 300 ppm in a cm-sized vein of serpentine + magnetite \pm millerite \pm calcite crosscutting the fine spinel peridotite indicates sulfur pathways during late exhumation stages. The presence of pentlandite as part of polycrystalline inclusions in spinel associated with calcite + brucite intergrowths indicates that local desulfurization may have been coupled with dissolution of the associated dolomite and subsequent release of CO_2 .

The recorded oxidation state of the studied peridotites likely precludes stabilization of sulfate, but is permissive of carbonate as opposed to graphite stability, as confirmed by petrographic observations. The close association of sulfides and carbonates at all stages of mantle wedge evolution indicates that peak metamorphic pervasive fluids and melts, and channelized fluids generated during late exhumation, may serve as pathways for coupled S and C transport under the investigated conditions. Similar petrographic features have been advocated by Blanks et al. (2020)

to document the critical role of carbon in facilitating the sulfide mobility across the mantle-crust transition, thus being critical for the metallogenic processes. Further studies of the physical and chemical mechanism behind the S-C intimate association might help to shed light in this regard. As a whole, S and C should therefore be considered together in the discussion of the mantle wedge redox evolution. Despite evidence for long-lasting and polyphase metasomatic processes involving slab-derived C-O-H-S fluids and melts (Fig. 6.12), the measured S isotope values of the UZ pentlandite display a narrow range ($\delta^{34}\text{S} = -1.62 \pm 0.42\text{‰}$ to $+3.76 \pm 0.36\text{‰}$), which suggests that reduction of sulfate (S^{6+}) to sulfide species (S^{2-}) had a limited role throughout the Ulten Zone peridotite metamorphic evolution. Importantly, this study provides petrographic and geochemical evidence in support of a dominantly reduced nature of slab-derived sulfur-bearing subduction liquids in the orogenic mantle wedge under high-pressure conditions and during subsequent exhumation within the tectonic *mélange*, suggesting that S is not the dominant agent causing oxidation of the mantle wedge in this setting.

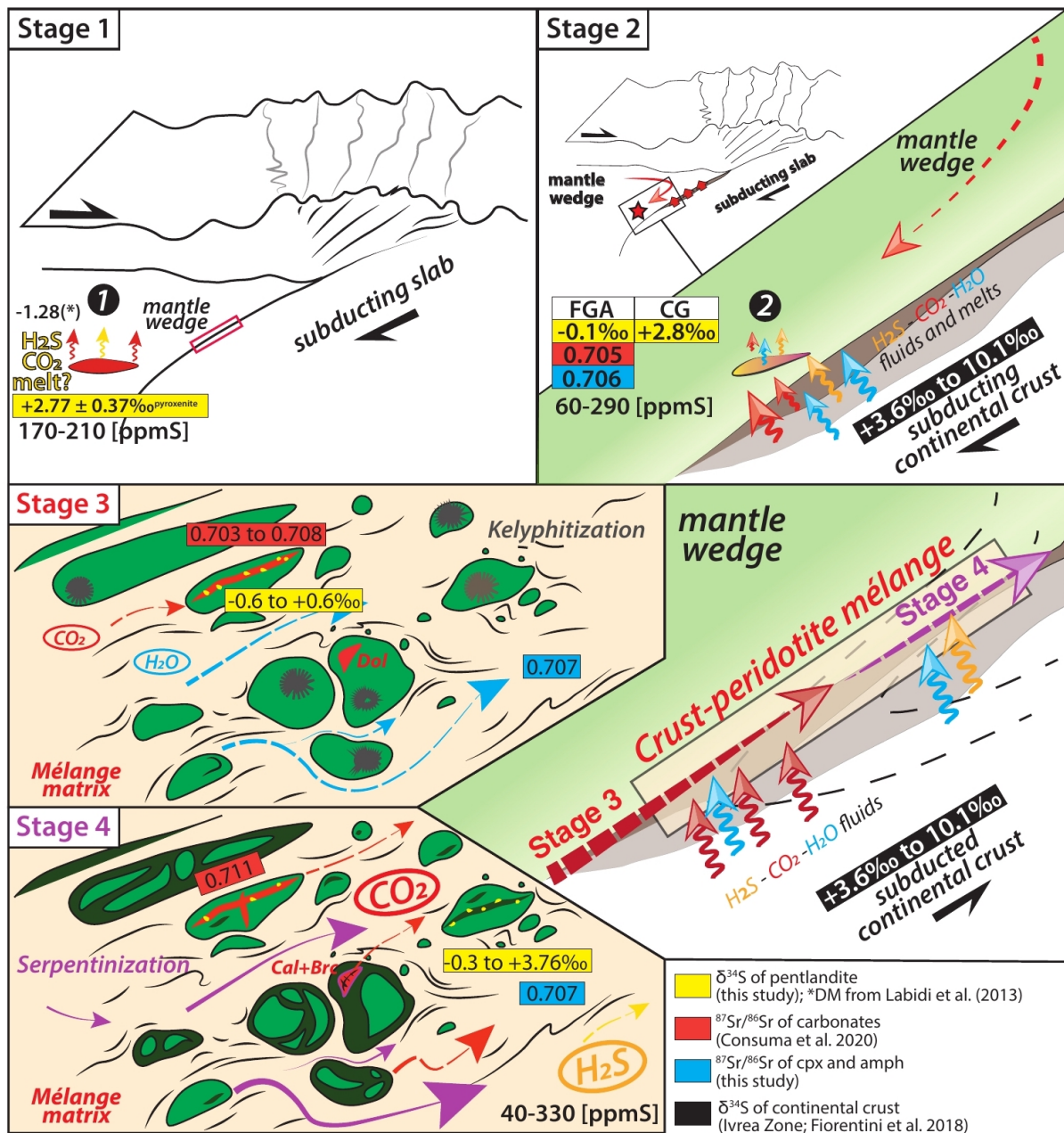


Figure 6.13: Conceptual model of the metamorphic stages of the Ulten Zone peridotites, see discussion for details. **Stage 1**— Only a small residual sulfur component would have remained after ca. 15-25% of melt extraction. Concentrations of 170-210 ppm S with a heavy $\delta^{34}\text{S}$ signature may reflect percolation by reduced, H₂S-CO₂-bearing hydrous basic melts from the subduction-modified deeper lithospheric mantle. **Stage 2**—At peak (garnet) conditions, when UZ peridotites still reside in the mantle wedge, sulfur is introduced into peridotites from heterogeneous melt and fluid sources, which variably equilibrated with the depleted mantle and possibly mixed with de-serpentinization fluids. **Stage 3**— The supra-depleted mantle S isotope signature again require addition of heavy sulfur. **Stage 4**—Sulfur and CO₂ are variously released from the mantle-crust mélange during late-stage serpentinization, while high S concentrations (>300 ppm) in a serpentine vein suggest efficient mobilization throughout channelized fluid flow.

Acknowledgements

This manuscript is part of the Ph.D. project of G.C. and has been financially supported by Almaidea-UniBO and FFARB to R.B. FIERCE is financially supported by the Wilhelm and Else Heraeus Foundation and by the Deutsche Forschungsgemeinschaft (DFG, INST 161/921-1 FUGG and INST 161/923-1 FUGG), which is gratefully acknowledged. Financial support was also provided by the Australian Research Council through the Centre of Excellence for Core to Crust Fluid Systems (CE1100001017), as well as the Minerals Research Institute of Western Australia. M. Tribus (University of Innsbruck) is thanked for assisting G.C. during EPMA analyses at University of Innsbruck. At University of Mainz, Nora Groschopf is thanked for providing top-quality XRF data, and for guidance during acquisition of S concentrations, and Dejan Prelevic for facilitating the work. At Goethe-University Frankfurt, the expert assistance of Alexander Schmidt in the mass spectrometry laboratory is gratefully acknowledged. The authors acknowledge the technical, and the scientific assistance from the Australian Microscopy & Microanalysis Research Facility at the Centre for Microscopy, Characterisation & Analysis of The University of Western Australia (UWA). The School of Earth Sciences at UWA is particularly thanked for hosting G.C. during her visiting research activity.

Chapter Six - References

- Alard O., Griffin W. L., Lorand J. P., Jackson S. E. and O'Reilly S. Y. (2000) Non-chondritic distribution of the highly siderophile elements in mantle sulphides. *Nature* **407**, 891–894.
- Alt J. C. (1995) Sulfur isotopic profile through the oceanic crust: Sulfur mobility and seawater-crustal sulfur exchange during hydrothermal alteration. *Geology* **23**, 585.
- Alt J. C., Shanks W. C., Bach W., Paulick H., Garrido C. J. and Beaudoin G. (2007) Hydrothermal alteration and microbial sulfate reduction in peridotite and gabbro exposed by detachment faulting at the Mid-Atlantic Ridge, 15°20'N (ODP Leg 209): A sulfur and oxygen isotope study: hydrothermal alteration processes. *Geochem. Geophys. Geosyst.* **8**.
- Andersen T., Griffin W. L. and O'Reilly S. Y. (1987) Primary sulphide melt inclusions in mantle-derived megacrysts and pyroxenites. *Lithos* **20**, 279–294.
- Aulbach S., Griffin W. L., Pearson N. J., O'Reilly S. Y., Kivi K. and Doyle B. J. (2004) Mantle formation and evolution, Slave Craton: constraints from HSE abundances and Re–Os isotope systematics of sulfide inclusions in mantle xenocrysts. *Chem. Geol.* **208**, 61–88.
- Aulbach S., Stachel T., Seitz H.-M. and Brey G. P. (2012) Chalcophile and siderophile elements in sulphide inclusions in eclogitic diamonds and metal cycling in a Paleoproterozoic subduction zone. *Geochim. Cosmochim. Acta* **93**, 278–299.
- Aulbach S., Gerdes A. and Viljoen K. S. (2016) Formation of diamondiferous kyanite–eclogite in a subduction mélange. *Geochim. Cosmochim. Acta* **179**, 156–176.
- Aulbach S., Mungall J. E. and Pearson D. G. (2016) Distribution and Processing of Highly Siderophile Elements in Cratonic Mantle Lithosphere. *Rev. Mineral. Geochem.* **81**, 239–304.

6 • The sulfur component of the Ulten Zone peridotite: a piece of the deep Sulfur cycle?

- Aulbach S., Heaman L. M., Jacob D. E. and Viljoen K. S. (2019) Ages and sources of mantle eclogites: ID-TIMS and in situ MC-ICPMS Pb-Sr isotope systematics of clinopyroxene. *Chem. Geol.* **503**, 15–28.
- Bataleva Y. V., Palyanov Y. N., Borzdov Y. M. and Sobolev N. V. (2016) Sulfidation of silicate mantle by reduced S-bearing metasomatic fluids and melts. *Geology* **44**, 271–274.
- Bataleva Y. V., Palyanov Y. and Borzdov Y. (2018) Sulfide Formation as a Result of Sulfate Subduction into Silicate Mantle (Experimental Modeling under High P,T-Parameters). *Minerals* **8**, 373.
- Bénard A., Klimm K., Woodland A. B., Arculus R. J., Wilke M., Botcharnikov R. E., Shimizu N., Nebel O., Rivard C. and Ionov D. A. (2018) Oxidising agents in sub-arc mantle melts link slab devolatilisation and arc magmas. *Nat. Commun.* **9**.
- Blanks D.E., Holwell D.A., Fiorentini M.L., Moroni M., Giuliani A., Tassara S., Gonzalez-Jiménes J.M., Boyce A.J., and Ferrari E. (2020) Fluxing of mantle carbon as a physical agent for metallogenic fertilization of the crust. *Nat Commun.* **11**, 4342
- Braga R. and Massonne H.-J. (2012) H₂O content of deep-seated orogenic continental crust: the Ulten Zone, Italian Alps. *Int. Geol. Rev.* **54**, 633–641.
- Braga R. and Sapienza G. T. (2007) The retrograde evolution of a dolomite-bearing hydrous peridotite from the Ulten Zone (Italian Alps). *GeoActa* **6**, 37–45.
- Brazhkin V. V., Popova S. V. and Voloshin R. N. (1999) Pressure–temperature phase diagram of molten elements: selenium, sulfur and iodine. *Physica B: Condens. Matter* **265**, 64–71.
- Chaussidon M. and Lorand J.-P. (1990) Sulphur isotope composition of orogenic spinel lherzolite massifs from Ariege (North-Eastern Pyrenees, France): An ion microprobe study. *Geochim. Cosmochim. Acta* **54**, 2835–2846.
- Chaussidon M., Albarède F. and Sheppard S. M. F. (1987) Sulphur isotope heterogeneity in the mantle from ion microprobe measurements of sulphide inclusions in diamonds. *Nature* **330**, 242–244.
- Consuma G., Braga R., Giovanardi T., Bersani D., Konzett J., Lugli F., Mazzucchelli M. and Tropper P. (2020) In situ Sr isotope analysis of mantle carbonates: Constraints on the evolution and sources of metasomatic carbon-bearing fluids in a paleo-collisional setting. *Lithos* **354–355**, 105334.
- Creighton S., Stachel T., Matveev S., Höfer H., McCammon C. and Luth R. W. (2009) Oxidation of the Kaapvaal lithospheric mantle driven by metasomatism. *Contrib. Mineral. Petrol.* **157**, 491–504.
- Ding T., Valkiers S., Kipphardt H., De Bièvre P., Taylor P. D. P., Gonfiantini R. and Krouse R. (2001) Calibrated sulfur isotope abundance ratios of three IAEA sulfur isotope reference materials and V-CDT with a reassessment of the atomic weight of sulfur. *Geochim. Cosmochim. Acta* **65**, 2433–2437.
- Eggler D. H. and Lorand J. P. (1993) Mantle sulfide geobarometry. *Geochim. Cosmochim. Acta* **57**, 2213–2222.
- Evans B.W., Johannes, W., Oterdoom, H., Trommsdorff, V. (1976). Stability of chrysotile and antigorite in the serpentinite multisystem. *Schweiz. Mineral. Petrogr. Mitt.* **56**, 79–93.
- Evans K. A. (2012) The redox budget of subduction zones. *Earth-Sci. Rev.* **113**, 11–32.
- Evans K. A., Reddy S. M., Tomkins A. G., Crossley R. J. and Frost B. R. (2017) Effects of geodynamic setting on the redox state of fluids released by subducted mantle lithosphere. *Lithos* **278–281**, 26–42.

6 • The sulfur component of the Ulten Zone peridotite: a piece of the deep Sulfur cycle?

- Evans K. A., Tomkins A. G., Cliff J. and Fiorentini M. L. (2014) Insights into subduction zone sulfur recycling from isotopic analysis of eclogite-hosted sulfides. *Chem. Geol.* **365**, 1–19.
- Farquhar J. (2002) Mass-Independent Sulfur of Inclusions in Diamond and Sulfur Recycling on Early Earth. *Science* **298**, 2369–2372.
- Fiorentini M. L., LaFlamme C., Denyszyn S., Mole D., Maas R., Locmelis M., Caruso S. and Bui T.-H. (2018) Post-collisional alkaline magmatism as gateway for metal and sulfur enrichment of the continental lower crust. *Geochim. Cosmochim. Acta* **223**, 175–197.
- Förster B., Braga R., Aulbach S., Pò D. L., Bargossi G. M. G. M. and Mair V. (2017) A petrographic study of carbonate phases in the Ulten Zone ultramafic rocks: insights into carbonation in the mantle wedge and exhumation-related decarbonation. *Ophioliti* **42**, 105–127.
- Fumagalli P. and Poli S. (2005) Experimentally Determined Phase Relations in Hydrous Peridotites to 6.5 GPa and their Consequences on the Dynamics of Subduction Zones. *J. Petrol.* **46**, 555–578.
- Giacometti F., Evans K. A., Rebay G., Cliff J., Tomkins A. G., Rossetti P., Vaggelli G. and Adams D. T. (2014) Sulfur isotope evolution in sulfide ores from Western Alps: Assessing the influence of subduction-related metamorphism. *Geochem., Geophys., Geosyst.* **15**, 3808–3829.
- Giuliani A., Fiorentini M. L., Martin L. A. J., Farquhar J., Phillips D., Griffin W. L. and LaFlamme C. (2016) Sulfur isotope composition of metasomatised mantle xenoliths from the Bultfontein kimberlite (Kimberley, South Africa): Contribution from subducted sediments and the effect of sulfide alteration on S isotope systematics. *Earth Planet. Sci. Lett.* **445**, 114–124.
- Griffin W. L., Belousova E. A., Shee S. R., Pearson N. J. and O'Reilly S. Y. (2004) Archean crustal evolution in the northern Yilgarn Craton: U–Pb and Hf-isotope evidence from detrital zircons. *Precambrian Res.* **131**, 231–282.
- Gudelius D., Aulbach S., Braga R., Höfer H. E., Woodland A. B. and Gerdes A. (2019) Element Transfer and Redox Conditions in Continental Subduction Zones: New Insights from Peridotites of the Ulten Zone, North Italy. *J. Petrol.* **60**, 231–268.
- Guo J., Griffin W. L. and O'Reilly S. Y. (1999) Geochemistry and Origin of Sulphide Minerals in Mantle Xenoliths: Qilin, Southeastern China. *J. Petrol.* **40**, 1125–1149.
- Hermann J., Spandler C., Hack A. and Korsakov A. V. (2006) Aqueous fluids and hydrous melts in high-pressure and ultra-high pressure rocks: Implications for element transfer in subduction zones. *Lithos* **92**, 399–417.
- Herzberg C. (2004) Geodynamic Information in Peridotite Petrology. *J. Petrol.* **45**, 2507–2530.
- Holwell D. A., Fiorentini M., McDonald I., Lu Y., Giuliani A., Smith D. J., Keith M. and Locmelis M. (2019) A metasomatized lithospheric mantle control on the metallogenic signature of post-subduction magmatism. *Nat. Commun.* **10**.
- de Hoog J. C. M., Mason P. R. D. and van Bergen M. J. (2001) Sulfur and chalcophile elements in subduction zones: constraints from a laser ablation ICP-MS study of melt inclusions from Galunggung Volcano, Indonesia. *Geochim. Cosmochim. Acta* **65**, 3147–3164.
- Ionov D. A., Hoefs J., Wedepohl K. H. and Wiechert U. (1992) Content and isotopic composition of sulphur in ultramafic xenoliths from central Asia. *Earth and Planetary Science Letters* **111**, 269–286.

6 • The sulfur component of the Ulten Zone peridotite: a piece of the deep Sulfur cycle?

- Ionov D. A., Bigot F. and Braga R. (2017) The Provenance of the Lithospheric Mantle in Continental Collision Zones: Petrology and Geochemistry of Peridotites in the Ulten–Nonsberg Zone (Eastern Alps). *J. Petrol.* **58**, 1451–1472.
- Jenner F. E., O'Neill H. ST. C., Arculus R. J. and Mavrogenes J. A. (2010) The Magnetite Crisis in the Evolution of Arc-related Magmas and the Initial Concentration of Au, Ag and Cu. *J. Petrol.* **51**, 2445–2464.
- Jochum K. P. and Verma S. P. (1996) Extreme enrichment of Sb, Tl and other trace elements in altered MORB. *Chemical Geology* **130**, 289–299.
- Jugo P. J. (2009) Sulfur content at sulfide saturation in oxidized magmas. *Geology* **37**, 415–418.
- Jugo P. J., Luth R. W. and Richards J. P. (2005) Experimental data on the speciation of sulfur as a function of oxygen fugacity in basaltic melts. *Geochim. Cosmochim. Acta* **69**, 497–503.
- Johannes, W. and Puhan, D. (1971). The calcite-aragonite transition, reinvestigated. *Contrib. Mineral. Petrol.* **31**, 28–38.
- Kaneda H., Takenouchi S. and Shoji T. (1986) Stability of pentlandite in the Fe-Ni-Co-S system. *Miner. Deposita* **21**, 169–180.
- Keays R. R. (1995) The role of komatiitic and picritic magmatism and S-saturation in the formation of ore deposits. *Lithos* **34**, 1–18.
- Kelley K. A. and Cottrell E. (2009) Water and the Oxidation State of Subduction Zone Magmas. *Science* **325**, 605–607.
- Kiseeva E. S., Fonseca R. O. C. and Smythe D. J. (2017) Chalcophile Elements and Sulfides in the Upper Mantle. *Elements* **13**, 111–116.
- Labidi J., Cartigny P. and Moreira M. (2013) Non-chondritic sulphur isotope composition of the terrestrial mantle. *Nature* **501**, 208–211.
- Labidi J., Cartigny P., Hamelin C., Moreira M. and Dosso L. (2014) Sulfur isotope budget (^{32}S , ^{33}S , ^{34}S and ^{36}S) in Pacific–Antarctic ridge basalts: A record of mantle source heterogeneity and hydrothermal sulfide assimilation. *Geochim. Cosmochim. Acta* **133**, 47–67.
- LaFlamme C., Martin L., Jeon H., Reddy S. M., Selvaraja V., Caruso S., Bui T. H., Roberts M. P., Voute F., Hagemann S., Wacey D., Littman S., Wing B., Fiorentini M. and Kilburn M. R. (2016) In situ multiple sulfur isotope analysis by SIMS of pyrite, chalcopyrite, pyrrhotite, and pentlandite to refine magmatic ore genetic models. *Chem. Geol.* **444**, 1–15.
- Langone, A., Braga, R., Massonne, H.-J., Tiepolo, M., 2011. Preservation of old (prograde metamorphic) U–Th–Pb ages in unshielded monazite from the high-pressure paragneisses of the Variscan Ulten Zone (Italy). *Lithos* **127**, 68–85.
- Lee C.-T. y A. (2002) Platinum-group element geochemistry of peridotite xenoliths from the Sierra Nevada and the Basin and Range, California. *Geochim. Cosmochim. Acta* **66**, 3987–4005.
- Li Y. and Liu J. (2006) Calculation of sulfur isotope fractionation in sulfides. *Geochimica et Cosmochimica Acta* **70**, 1789–1795.

- Li J.-L., Schwarzenbach E. M., John T., Ague J. J., Huang F., Gao J., Klemd R., Whitehouse M. J. and Wang X.-S. (2020) Uncovering and quantifying the subduction zone sulfur cycle from the slab perspective. *Nat. Commun.* **11**, 514.
- Lo Pò D., Braga R., Tropper P., Konzett J., Mair V. and Bargossi G. M. (2020) Polymineralic inclusions as tracers of multistage metasomatism in a paleo mantle wedge. *Lithos*, **364-365**, 105517.
- Lorand J. P. (1989) Abundance and distribution of Cu-Fe-Ni sulfides, sulfur, copper and platinum-group elements in orogenic-type spinel lherzolite massifs of Arirge (northeastern Pyrenees, France). *Earth Planet. Sci. Lett.* **93**, 50–64.
- Lorand J.-P. and Grégoire M. (2006) Petrogenesis of base metal sulphide assemblages of some peridotites from the Kaapvaal craton (South Africa). *Contrib. Miner. Petrol.* **151**, 521–538.
- Lorand J.-P., Alard O., Luguët A. and Keays R. R. (2003) Sulfur and selenium systematics of the subcontinental lithospheric mantle: Inferences from the Massif Central xenolith suite (France). *Geochim. Cosmochim. Acta* **67**, 4137–4151.
- Lorand J.-P., Luguët A. and Alard O. (2013) Platinum-group element systematics and petrogenetic processing of the continental upper mantle: A review. *Lithos* **164-167**, 2–21.
- Malaspina N. and Tumiatì S. (2012) The role of COH and oxygen fugacity in subduction-zone garnet peridotites. *Eur. J. Mineral.* **24**, 607–618.
- Malaspina N., Poli S. and Fumagalli P. (2009) The oxidation state of metasomatized mantle wedge: insights from C–O–H-bearing garnet peridotite. *J. Petrol.* **50**, 1533–1552.
- Marini L., Moretti R. and Accornero M. (2011) Sulfur Isotopes in Magmatic-Hydrothermal Systems, Melts, and Magmas. *Reviews in Mineralogy and Geochemistry* **73**, 423–492.
- Marocchi M., Mair V., Tropper P. and Bargossi G. M. (2009) Metasomatic reaction bands at the Mt. Hochwart gneiss-peridotite contact (Ulten Zone, Italy): insights into fluid-rock interaction in subduction zones. *Mineral. Petrol.* **95**, 251.
- Marocchi M., Hermann J., Tropper P., Bargossi G. M. and Mair V. (2010) Amphibole and phlogopite in “hybrid” metasomatic bands monitor trace element transfer at the interface between felsic and ultramafic rocks (Eastern Alps, Italy). *Lithos* **117**, 135–148.
- Marocchi M., Marschall H. R., Konzett J., Tropper P., Ludwig T., Mair V. and Bargossi G. M. (2011) Metasomatic tourmaline in hybrid contact-bands between gneiss and peridotite in the Ulten zone of the Eastern Italian Alps: chemistry and boron isotopic composition. *Can. Mineral.* **49**, 245–261.
- Mavrogenes J. A. and O'Neill H. St. C. (1999) The relative effects of pressure, temperature and oxygen fugacity on the solubility of sulfide in mafic magmas. *Geochim. Cosmochim. Acta* **63**, 1173–1180.
- McDonough W. F. and Sun S. (1995) The composition of the Earth. *Chem. Geol.* **120**, 223–253.
- McInnes B. I. A., Gregoire M., Binns R. A., Herzig P. M. and Hannington M. D. (2001) Hydrous metasomatism of oceanic sub-arc mantle, Lihir, Papua New Guinea: petrology and geochemistry of fluid-metasomatised mantle wedge xenoliths. *Earth Planet. Sci. Lett.* **188**, 169–183.
- Métrich N., Schiano P., Clocchiatti R. and Maury R. C. (1999) Transfer of sulfur in subduction settings: an example from Batan Island (Luzon volcanic arc, Philippines). *Earth Planet. Sci. Lett.* **167**, 1–14.

6 • The sulfur component of the Ulten Zone peridotite: a piece of the deep Sulfur cycle?

- Mungall J. E., Hanley J. J., Arndt N. T. and Debecdelievre A. (2006) Evidence from meimechites and other low-degree mantle melts for redox controls on mantle-crust fractionation of platinum-group elements. *Proc. Natl. Acad. Sci.* **103**, 12695–12700.
- Nimis P. and Morten L. (2000) P–T evolution of ‘crustal’ garnet peridotites and included pyroxenites from Nonsberg area (upper Austroalpine), NE Italy: from the wedge to the slab. *J. Geodyn.* **30**, 93–115.
- O’Neill H. St. C. (1991) The origin of the moon and the early history of the earth—A chemical model. Part 2: The earth. *Geochim. Cosmochim. Acta* **55**, 1159–1172.
- Obata M. and Morten L. (1987) Transformation of spinel lherzolite to garnet lherzolite in ultramafic lenses of the Austridic crystalline complex, northern Italy. *J. Petrol.* **28**, 599–623.
- Ohmoto, H., & Rye, R. O. (1979). Isotopes of sulfur and carbon. In H. L. Barnes (Ed.), *Geochemistry of Hydrothermal Ore Deposits*, (pp. 517–611). New York: Wiley.
- Ono S., Keller N. S., Rouxel O. and Alt J. C. (2012) Sulfur-33 constraints on the origin of secondary pyrite in altered oceanic basement. *Geochim. Cosmochim. Acta* **87**, 323–340.
- Palme H. and O’Neill H. St. C. (2007) Cosmochemical Estimates of Mantle Composition. In *Treatise on Geochemistry* Elsevier. 1–38.
- Papike J. J., Spilde M. N., Fowler G. W., Layne G. D. and Shearer C. K. (1995) The Lodran primitive achondrite: petrogenetic insights from electron and ion microprobe analysis of olivine and orthopyroxene. *Geochim. Cosmochim. Acta* **59**, 3061–3070.
- Peterman Z. E., Hedge C. E. and Tourtelot H. A. (1970) Isotopic composition of strontium in sea water throughout Phanerozoic time. *Geochim. Cosmochim. Acta* **34**, 105–120.
- Piccoli F., Hermann J., Pettke T., Connolly J. A. D., Kempf E. D. and Vieira Duarte J. F. (2019) Subducting serpentinites release reduced, not oxidized, aqueous fluids. *Sci. Rep.* **9**, 1–7.
- Poulson S. R., Kubišius W. P. and Ohmoto H. (1991) Geochemical behavior of sulfur in granitoids during intrusion of the South Mountain batholith, Nova Scotia, Canada. *Geochim. Cosmochim. Acta* **55**, 3809–3830.
- Rampone E. and Morten L. (2001) Records of crustal metasomatism in the garnet peridotites of the Ulten Zone (Upper Austroalpine, Eastern Alps). *J. Petrol.* **42**, 207–219.
- Regorda A., Lardeaux J.-M., Roda M., Marotta A. M. and Spalla M. I. (2020) How many subductions in the Variscan orogeny? Insights from numerical models. *Geosci. Front.* **11**, 1025–1052.
- Rielli A., Tomkins A. G., Nebel O., Raveggi M., Jeon H., Martin L. and Ávila J. N. (2018) Sulfur isotope and PGE systematics of metasomatised mantle wedge. *Earth Planet. Sci. Lett.* **497**, 181–192.
- Salters V. J. and Stracke A. (2004) Composition of the depleted mantle. *Geochem. Geophys. Geosyst.* **5**, Q05B07.
- Sapienza G. T., Scambelluri M. and Braga R. (2009) Dolomite-bearing orogenic garnet peridotites witness fluid-mediated carbon recycling in a mantle wedge (Ulten Zone, Eastern Alps, Italy). *Contrib. Mineral. Petrol.* **158**, 401–420.
- Scambelluri M., Hermann J., Morten L. and Rampone E. (2006) Melt-versus fluid-induced metasomatism in spinel to garnet wedge peridotites (Ulten Zone, Eastern Italian Alps): clues from trace element and Li abundances. *Contrib. Mineral. Petrol.* **151**, 372.

- Scambelluri M., Rampone E., Braga R. and Malaspina N. (2010) The Variscan garnet peridotites from the Eastern Alps (Ulten Zone): records of subduction metasomatism in the mantle wedge. In: (Eds.) Marco Beltrando, Angelo Peccerillo, Massimo Mattei, Sandro Conticelli, and Carlo Doglioni, *J. Virtual Explor.* **36**. doi: 10.3809/jvirtex.2009.00259
- Schramke J.A., Kerrick D.M. and Blencoe J.G. (1982) Experimental determination of the brucite = periclase + water equilibrium with a new volumetric technique. *Am. Min.* **67**, 269–276.
- Schwarzenbach E. M., Caddick M. J., Petroff M., Gill B. C., Cooperdock E. H. G. and Barnes J. D. (2018a) Sulphur and carbon cycling in the subduction zone mélange. *Sci. Rep.* **8**, 15517.
- Schwarzenbach E. M., Gill B. C. and Johnston D. T. (2018b) Unraveling multiple phases of sulfur cycling during the alteration of ancient ultramafic oceanic lithosphere. *Geochim. Cosmochim. Acta* **223**, 279–299.
- Sun S.-S. (1982) Chemical composition and origin of the earth's primitive mantle. *Geochim. Cosmochim. Acta* **46**, 179–192.
- Sun S.-S., Wallace D. A., Hoatson D. M., Glikson A. Y. and Keays R. R. (1991) Use of geochemistry as a guide to platinum group element potential of mafic-ultramafic rocks: examples from the west Pilbara Block and Halls Creek Mobile Zone, Western Australia. *Precambrian Res.* **50**, 1–35.
- Szabó Cs. and Bodnar R. J. (1995) Chemistry and origin of mantle sulfides in spinel peridotite xenoliths from alkaline basaltic lavas, Nógrád-Go˝mo˝r Volcanic Field, northern Hungary and southern Slovakia. *Geochim. Cosmochim. Acta* **59**, 3917–3927.
- Thomassot E., Cartigny P., Harris J. W., Lorand J. P., Rollion-Bard C. and Chaussidon M. (2009) Metasomatic diamond growth: A multi-isotope study (¹³C, ¹⁵N, ³³S, ³⁴S) of sulphide inclusions and their host diamonds from Jwaneng (Botswana). *Earth Planet. Sci. Lett.* **282**, 79–90.
- Tomkins A. G. and Evans K. A. (2015) Separate zones of sulfate and sulfide release from subducted mafic oceanic crust. *Earth Planet. Sci. Lett.* **428**, 73–83.
- Tumiati S., Thöni M., Nimis P., Martin S. and Mair V. (2003) Mantle–crust interactions during Variscan subduction in the Eastern Alps (Nonsberg–Ulten zone): geochronology and new petrological constraints. *Earth Planet. Sci. Lett.* **210**, 509–526.
- Tumiati S., Fumagalli P., Tiraboschi C. and Poli S. (2013) An Experimental Study on COH-bearing Peridotite up to 3.2 GPa and Implications for Crust–Mantle Recycling. *J. Petrol.* **54**, 453–479.
- Vaughan D. J. and Corkhill C. L. (2017) Mineralogy of Sulfides. *Elements* **13**, 81–87.
- Voshage H., Hofmann A. W., Mazzucchelli M., Rivalenti G., Sinigoi S., Raczek I. and Demarchi G. (1990) Isotopic evidence from the Ivrea Zone for a hybrid lower crust formed by magmatic underplating. *Nature* **347**, 731–736.
- Walters J. B., Cruz-Uribe A. M. and Marschall H. R. (2019) Isotopic Compositions of Sulfides in Exhumed High-Pressure Terranes: Implications for Sulfur Cycling in Subduction Zones. *Geochem. Geophys. Geosyst.* **20**, 3347–3374.
- Walters J. B., Cruz-Uribe A. M. and Marschall H. R. (2020) Sulfur loss from subducted altered oceanic crust and implications for mantle oxidation. *Geochem. Perspect. Lett.* **13**, 36–41.
- Wang, K.-L., O'Reilly, S.Y., Honda, M., Matsumoto, T., Griffin, W.L., Pearson, N.J., Zhang, M., 2010. Co-rich sulfides in mantle peridotites from Penghu Islands, Taiwan: Footprints of Proterozoic mantle

6 • The sulfur component of the Ulten Zone peridotite: a piece of the deep Sulfur cycle?

plumes under the Cathaysia Block. *J. Asian Earth Sci.* **37**, 229–245.
<https://doi.org/10.1016/j.jseaes.2009.08.008>

Workman R. K. and Hart S. R. (2005) Major and trace element composition of the depleted MORB mantle (DMM). *Earth Planet. Sci. Lett.* **231**, 53–72.

Zhang Z., Lentsch N. and Hirschmann M. M. (2015) Carbon-saturated monosulfide melting in the shallow mantle: solubility and effect on solidus. *Contrib. Miner. Petrol.* **170**, 47.

7 • Conclusions

The last decade has seen remarkable advancements in understanding the forms, processes and fate of the deep C during subduction. Compared to C, the deep cycling of S dictated by subduction processes has been a niche topic since the very few years, albeit, they both represent critical elements for maintaining the chemical heterogeneity of the deep Earth.

C and S are unquestionably mobilized at high-pressure conditions, whose mobility is favored by fluids and melts released by the subducting crust via dehydration and melting processes. At favorable conditions, these fluids and melts may enhance C and S transfer throughout the supra-subduction mantle, prompting carbonates and sulfides formation. In this geodynamic scenario, this thesis contributes to advance our understanding in the deep C and S mobility in fossil continental subduction zone, by investigating them from the orogenic mantle perspective, which represents the least domain of the whole *subduction factory*.

This knowledge gap is because of different reasons, such as: (1) the limited accessibility to rocks that record crust-mantle interactions at (U)HP conditions; (2) the absence of post-magmatism and arc volcanics to directly quantify the volatiles discharge from the mantle; (3) the tiny grain-size of C- and S-bearing minerals formed in the orogenic mantle, which make them difficult to investigate without the use of cutting-edge analytical techniques and detailed petrography.

This thesis is among the first reports of a multi-microanalytical investigation of carbonates and sulfides stored into orogenic garnet peridotites exhumed as part of felsic metamorphic terranes. I combined a short field-survey with detailed petrography and petrological, geochemical, and isotopic analyses to shed light on the hitherto unconstrained carbonate and sulfide metasomatism that affected the mantle wedge fragments of the Eastern Italian Alps, which were involved in a paleo-subduction channel during the Variscan Orogeny.

Forms, processes, mechanisms of carbon- and sulfur-bearing fluid/melt flow and types of metasomatic agents are elucidated. All these findings are hereafter summarized across the whole metamorphic sequence recorded by the peridotite.

7.1 Carbon and Sulfur inheritance in the spinel stage

The Ulten Zone lithospheric mantle was initially depleted and sulfide-poor. Bulk rock major elements compositions, in accord with the literature, show that the Ulten Zone peridotite

experienced ca. 15-25% of melt extraction. As such melt fractions, we expect a complete exhaustion of the sulfide component in the peridotite. Measured S concentrations of > 100ppm thus certainly indicate that the Ulten Zone peridotite experienced S addition. An early event of S and C addition occurred when a hot, H₂S-CO₂-bearing melt leaving a subduction-modified source invaded the overlying spinel-facies peridotite in the mantle wedge, leading to precipitation of dolomite- and sulfide-bearing orthopyroxenite. The reducing nature of the investigated peridotite (<FMQ) is consistent with the occurrence of pentlandite grains within the orthopyroxenite layer, which show a $\delta^{34}\text{S}$ signature of +2.77 ‰. However, the relatively reducing nature does not preclude the formation of carbonate phases in the peridotite. It is worth noting that no identifiable reduced carbon species were found. The dolomite in local association with pentlandite shows variable $\delta^{13}\text{C}$ values of -12‰ to -8‰. This range of isotopic values is interpreted to represent mantle carbon later affected by multiple episodes of isotopically lighter liquid infiltrations, as additionally indicated by the growth zoning of dolomite observed under cathodoluminescence. These late liquids are possibly crustal fluids released by the neighboring gneisses.

A light $\delta^{13}\text{C}$ signature of -8‰ is also obtained in the regular-shaped dolomite included in a Cr-rich spinel within porphyroclastic garnet. The origin of this inclusion is questionable as it shows microstructural features that clearly involved late metasomatic processes (i.e. association with calcite/brucite intergrowths; highly fractured garnet). However, the inclusion shows high concentrations of Sr (>1000ppm) and Ba (>70ppm), which may point to melt-mediated recycling of crustal components and its light C isotope signature may be addressed to C inheritance prior to spinel and garnet crystallization.

7.2 High pressure carbonation and sulfidation

Within the garnet stability field, at ca. 850°C and < 2.7GPa, geochemically heterogeneous fluid sources are involved:

(i) the positive shifts of $\delta^{34}\text{S}$ (up to +3.43‰) from typical mantle values measured in matrix pentlandite grains, and the radiogenic signature of clinopyroxene ($^{87}\text{Sr}/^{86}\text{Sr}_{\text{clinopyroxene}} > 0.7053$) suggest that, at high-pressure conditions, coarse-grained garnet peridotites were enriched in radiogenic crustal components carrying ^{34}S prior to their involvement in a crust-mantle mélange. Matrix carbonate is usually rare in the coarse-grained peridotite. However, the occurrence of matrix magnesite + dolomite grains in a coarse-grained peridotite offers a few grains available for *in situ* analyses, showing a $\delta^{13}\text{C}$ signature of about -13‰.

(ii) Fluids interacting with mantle rocks during recrystallization and deformation from coarse- to fine-grained peridotites added radiogenic Sr ($^{87}\text{Sr}/^{86}\text{Sr}_{\text{amphibole}} \sim 0.7061$) and had an heterogeneous effect on the bulk S content (58 to 288 ppm S), as S was variably added or removed. Given evidence for a crustal fluid source (i.e. high fluid-mobile-elements concentrations in pentlandite, such as As, Sb, Te), the low $\delta^{34}\text{S}$ (-1.62 to +0.67‰) in the matrix pentlandite from the fine-grained peridotite compared to the isotopic values measured in the coarse-grained peridotites indicate an involvement of a slightly isotopically heavy (with respect to the depleted mantle) H_2S -bearing fluid. Given the intimate association of matrix dolomite with matrix pentlandite, these fluids were also able to carry C and form matrix dolomite along silicates grain boundaries, showing an average value of $\delta^{13}\text{C}$ of -11‰ and a relatively un-radiogenic $^{87}\text{Sr}/^{86}\text{Sr}$ ratio of ~ 0.705 . We propose that, at this evolutionary stage, a depleted mantle source is expected to have been contaminated by $\ll 10\%$ of strongly radiogenic isotopically heavy continental crust \pm serpentinite-derived fluids with heavy S and less radiogenic Sr.

7.3 Channelized carbonation (and sulfidation?)

Shortly after the attainment of peak-P conditions the Ulten Zone peridotite is entrapped in a tectonic *mélange* together with the neighboring gneisses. Here, peridotite bodies were exposed to channelized infiltration of hybridized C-O-H fluids that form veinlets of dolomite crosscutting the peridotite matrix. The heterogeneous range of the $^{87}\text{Sr}/^{86}\text{Sr}$ ratio (0.7036 to 0.7083), and of $\delta^{13}\text{C}$ (-16 to -8‰) measured in these veins, is consistent with an extensive crust/mantle interaction in the *mélange*. Moreover, little variation of the $\delta^{18}\text{O}$ (+12 to +13‰) was observed, indicating that diluted fluids possibly originated from the gneisses within the *mélange* and interacted with the peridotite at very low T, allowing a full re-equilibration of the O isotope signature. Multiple fluids infiltration at this stage is also evidenced by the growth zoning of dolomite visible under cathodoluminescence. A few pentlandite grains hosted by this vein has a $\delta^{34}\text{S}$ signature close to 0‰.

7.4 Serpentinization as catalyst for decarbonation and desulfidation

Upon late retrogression, serpentinizing aqueous fluids had marked heterogeneous effects carbon and sulfur. During the peridotite ascent towards shallow structural levels (up to 25 km depths), incoming serpentinizing fluids reacted with precedently formed dolomite (included, matrix, and vein). This scenario enhances isotope fractionation through release of isotopically heavy ^{13}C , which would generate isotopically lighter residue as shown by dolomite relics included

in spinel associated with calcite/brucite intergrowths. Therefore, dolomite hydration testifies decarbonation and liberation of CO₂.

Likewise, the relatively wide range of $\delta^{34}\text{S}$ (-0.29 and +3.76‰) recorded by pentlandite grains enclosed in a serpentine + magnesite vein, combined with the presence of magnetite pseudomorphs after pentlandite indicates local desulfurization with inferred preferential loss of ³²S.

The texturally-late vein of dolomite with ⁸⁷Sr/⁸⁶Sr of 0.711 that cut the previous magnesite vein, and a very late vein of serpentine + magnetite ± millerite ± calcite crosscutting a fine-grained chlorite-amphibole peridotite with measured sulfur concentrations of 300 ppm, indicates that radiogenic crustal carbonation and sulfur addition may have occurred as channelized fluid-flow at the very latest metamorphic stage.

To conclude, this thesis demonstrates that the Ulten Zone peridotite contains petrological and geochemical features of both retention and release of C and S throughout its involvement in the Variscan continental subduction architecture and subsequent exhumation as a tectonic mélange. In this sense, the orogenic mantle domains of the Ulten Zone in the Variscan Eastern Italian Alps most likely acted as a pit-stop (lock and release) of C and S.

8 • Open questions and future work

– **Nature of metasomatic agents.**

Now that we have a detailed dataset on carbonates and sulfides occurring into the Ulten Zone peridotite, a comparable investigation of carbon and sulfur within the neighboring rocks is needed. In fact, albeit the overall geochemical record reported in this thesis gives first crucial hints of a plausible nature for the carbonic and sulfur-bearing metasomatic agents of the peridotite, these data need to be compared with the country rocks.

Open questions are: In which form carbon and sulfur occur in migmatites and gneisses? Which is their geochemical signature? Is their crustal imprint already affecting the carbonates and sulfide inventory of peridotites at high pressure conditions, where peridotites are still residing within the mantle wedge, close to the slab - mantle wedge interface? In addition, in order to further detect any structural and field relation of the pervasive fluid flow and fluid pathways between the two lithologies, a focus on the localities of the Ulten Zone that preserved the field relations (when peridotite are found *in situ* within crustal rocks) is the first approach that needs to be taken.

– **Extending the database of dolomite inclusions within primary coarse spinels. Are these dolomite grains the marker of the pre-peak carbonation and sulfidation?**

Preserved regular shape of carbonate inclusions are exceptionally rare. One exceptional inclusion of dolomite with a regular shape has been detected so far and is reported in this thesis. Pentlandite also variably occurs along with dolomite and calcite/brucite intergrowths forming polycrystalline inclusions in Cr-rich spinel and garnet porphyroclasts. These polycrystalline inclusions record textural and petrological evidence of late processes, and further detailed investigation in this regard is needed to constrain their origin and enlarge the dataset of melt-mediated processes in the spinel stage.

– **Thermodynamic modelling and experiments:**

In general, there is limited work on the solubility behavior of carbonate minerals under high-pressure conditions, in particular for dolomite and magnesite, and experimental constraints designed with the data reported in this thesis would be useful to recreate the studied carbonated peridotite via interaction with melts at fluids at P and T compatible with those reported in this study. Thermodynamic modelling is crucial to investigate carbonate behavior when

experiments and empirical data are lacking, and a new generation of solution models for sulfides (and carbonates) might help to enhance our capacity to perform forward modelling on orogenic peridotites in both closed and open systems.

– **Mass balances calculations and quantification of fluxes.**

Once the carbon and sulfur inventory of the neighboring crustal rocks is investigated, the implementation of our data to the global fluxes of carbon and sulfur into subduction zones will be mandatory for quantifying the contribution of an orogenic mantle wedge to the deep carbon and sulfur cycling.

A. Supplementary Material of Chapter 4

Table A1: Major elements compositions (wt%) of olivine. Formula based on 4 oxygens.

rock type	F	F	F	F	F	F	F	P	P	P	F	F	F	F	F	F	C	C	C	C	C	C
sample	MM1	KL24-2B	KL24-2B	KL24-2B	VM10A	KL1-A	KL1-A	KL1-A	KL1-A	KL1-A	MOL1-C	MOL1-C	MOL1-C	MOL1-C	18LP1	18LP1						
texture	m	m	m	m	m	m	m	m	m	m	m	m	m	m	m	m	m	m	m-coarse	m-coarse	m-coarse	m-coarse
name	ol1	ol2	ol3	ol5	ol6	ol7	ol9	ol2	ol7	ol8	ol1	ol1	ol1	ol2	ol4	ol5	ol2	ol3	ol7	ol8	ol1	ol2
MgO	50.1	49.24	49.54	49.89	49.92	50.22	49.18	47.30	49.31	49.40	48.10	49.35	49.19	49.21	49.23	49.07	49.40	49.04	49.68	49.72	49.58	49.35
Al ₂ O ₃	bdl	bdl	bdl	bdl	bdl	bdl	bdl	bdl	bdl	bdl	bdl	bdl	bdl	bdl	bdl							
SiO ₂	40.85	40.53	40.66	40.56	40.53	40.59	40.96	40.62	40.69	40.27	40.66	40.79	40.52	40.73	40.80	40.30	50.50	40.92	40.99	40.89	41.06	40.79
Cr ₂ O ₃	bdl	bdl	bdl	bdl	bdl	bdl	0.36	0.03	bdl	bdl	0.05	bdl	bdl	bdl	bdl	bdl	bdl	bdl	bdl	bdl	bdl	0.01
MnO	0.16	0.12	0.12	0.12	0.18	0.14	0.14	0.31	0.19	0.12	0.18	0.16	0.13	0.18	0.12	0.10	0.11	0.16	bdl	0.14	0.15	0.16
FeO	9.54	9.65	9.52	9.42	9.30	9.49	9.32	10.83	9.93	9.08	9.04	10.73	9.22	9.20	9.37	9.44	9.56	9.51	9.47	9.57	9.40	9.64
NiO	0.36	0.42	0.34	0.35	0.34	0.34	0.38	0.37	0.37	0.35	bdl	0.37	bdl	bdl	bdl	bdl	0.39	bdl	bdl	bdl	0.37	0.37
Sum	101.01	100.02	100.18	100.34	100.26	100.77	100.36	99.46	100.50	99.27	0.05	0.37	bdl	99.32	99.52	98.91	99.96	89.96	90.67	90.61	91.01	90.51
Si	0.99	0.99	0.99	0.99	0.99	0.99	1.00	1.01	0.99	0.99	1.01	0.99	1.00	1.00	1.00	1.00	1.00	1.00	1.00	1.00	1.00	1.00
Al	-	-	-	-	-	-	-	-	-	-	-	-	-	-	-	-	-	-	-	-	-	-
Cr	-	-	-	-	-	-	0.01	0.00	-	-	0.00	-	-	-	-	-	-	-	-	-	0.00	-
Fe ²⁺	0.19	0.20	0.19	0.19	0.19	0.19	0.19	0.22	0.20	0.19	0.19	0.22	0.19	0.19	0.19	0.20	0.20	0.20	0.19	0.20	0.19	0.20
Ni	0.01	0.01	0.01	0.01	0.01	0.01	0.01	0.01	0.01	0.01	-	0.01	-	-	-	-	0.00	-	-	-	0.01	0.01
Mn	0.00	0.00	0.00	0.00	0.00	0.00	0.00	0.01	0.00	0.00	0.00	0.00	0.00	0.00	0.00	0.00	0.00	0.00	0.00	0.00	0.00	0.00
Mg	1.81	1.80	1.81	1.82	1.82	1.82	1.79	1.75	1.80	1.82	1.78	1.79	1.81	1.80	1.80	1.81	1.81	1.79	1.81	1.81	1.80	1.80
Sum	3.01	3.01	3.01	3.01	3.01	3.01	3.00	2.99	3.01	3.01	2.99	3.01	3.00	3.00	3.00	3.00	3.00	3.00	3.00	3.00	3.00	3.00
Fo	90.20	89.98	90.16	90.31	90.38	90.29	90.26	88.33	89.67	90.54	90.29	88.98	90.36	90.34	90.24	90.17	90.10	90.04	90.34	90.13	90.25	89.97
Fa	9.64	9.90	9.72	9.57	9.44	9.57	9.60	11.35	10.13	9.34	9.52	10.86	9.50	9.47	9.63	9.73	9.78	9.80	9.66	9.73	9.60	9.86
Teph	0.16	0.12	0.12	0.12	0.18	0.14	0.14	0.33	0.20	0.13	0.19	0.17	0.14	0.18	0.13	0.10	0.11	0.16	0.00	0.14	0.15	0.17
#Mg	90.35	90.09	90.16	90.42	90.54	90.42	90.39	88.62	89.85	90.65	90.46	89.13	90.49	90.51	90.35	90.26	90.21	90.19	90.34	90.25	90.39	90.12

F–fine-grained; C–coarse-grained; P–porphyroclastic texture; m–matrix. #Mg=Mg/(Mg+Fe²⁺)

Table A2: Major elements compositions (wt%) of orthopyroxene and clinopyroxene. Formula based on 6 oxygens.

rock type	C	C	C	C	C	C	C	C	C	C	F	P	P	P	P	P	P	F
sample	MOL1-C	KL1-A	KL2.4-2b	KL2.4-2b	KL2.4-2b	KL2.4-2b	KL2.4-2b	KL2.4-2b	VM10A									
mineral	opx	opx	opx	opx	opx	opx	opx	opx	opx									
texture	C-m	m	m	C-m	C-m	C-m	C-m	C-m	C-m	m	m	m	m	m	m	m	m	m
name	opx1	opx3	opx2	opx4	opx6	opx6/2	opx7	opx7/2	opx8	opx8	opx8	opx1	opx3	opx3/2	opx4	opx5	opx8	opx1
Na ₂ O	bdl	bdl	bdl	bdl	bdl	bdl	0.04	bdl	0.04	bdl	bdl	bdl	0.35	0.30	0.28	0.30	0.24	0.14
MgO	34.11	33.84	34.36	33.79	33.79	33.74	33.80	33.65	34.23	34.61	34.61	16.00	16.55	16.77	17.04	16.85	32.83	
Al ₂ O ₃	1.65	2.51	2.43	3.00	2.63	3.18	2.80	4.64	1.71	1.52	1.54	1.47	1.35	1.16	1.28	1.01	1.63	
SiO ₂	56.84	56.30	56.69	55.43	56.66	55.78	55.96	54.41	57.13	57.08	56.21	52.21	53.36	54.10	54.40	53.32	55.67	
K ₂ O	bdl	bdl	bdl	bdl	bdl	bdl	bdl	bdl										
CaO	0.11	0.32	0.12	0.34	0.25	0.30	0.27	0.11	0.22	0.24	0.24	24.39	24.58	24.63	24.40	24.73	0.36	
TiO ₂	bdl	bdl	0.12	0.10	0.10	0.11	0.09	bdl										
Cr ₂ O ₃	0.17	0.17	0.20	0.32	0.31	0.35	0.26	0.70	0.10	0.20	0.15	0.78	0.65	0.96	0.31	0.24	0.21	
MnO	0.17	0.11	0.20	0.18	0.14	0.22	0.19	0.17	0.12	0.20	0.19	bdl	bdl	0.08	0.09	bdl	0.17	
FeO	6.61	6.39	6.55	6.21	6.27	6.13	6.33	6.47	6.48	6.22	6.07	1.69	1.59	2.01	1.82	1.71	5.76	
Sum	99.66	99.81	100.59	99.41	100.16	99.80	99.70	100.24	100.01	99.88	99.08	96.99	98.52	100.14	99.78	98.22	96.90	
Si	1.97	1.95	1.94	1.93	1.95	1.93	1.94	1.88	1.97	1.97	1.96	1.96	1.97	1.97	1.98	1.97	1.98	
Ti	-	-	-	-	-	-	-	-	-	-	-	0.00	0.00	0.00	0.00	0.00	0.00	
Al	0.07	0.10	0.10	0.12	0.11	0.13	0.11	0.19	0.07	0.06	0.06	0.06	0.06	0.05	0.05	0.04	0.07	
Cr	0.00	0.00	0.01	0.01	0.01	0.01	0.01	0.02	0.00	0.01	0.00	0.02	0.02	0.03	0.01	0.01	0.01	
Fe ²⁺	0.19	0.18	0.19	0.18	0.18	0.18	0.18	0.19	0.19	0.18	0.18	0.05	0.05	0.06	0.06	0.05	0.17	
Mn	0.00	0.00	0.01	0.01	0.00	0.01	0.01	0.00	0.00	0.01	0.01	-	-	0.00	0.00	-	0.00	
Mg	1.76	1.74	1.76	1.75	1.73	1.74	1.74	1.73	1.76	1.76	1.80	0.90	0.91	0.91	0.92	0.93	1.74	
Ca	0.00	0.01	0.00	0.01	0.01	0.01	0.01	0.00	0.01	0.01	0.01	0.98	0.97	0.96	0.95	0.98	0.01	
Na	-	-	-	-	-	-	-	0.00	-	-	-	0.03	0.02	0.02	0.02	0.02	0.01	
Sum	4.00	4.01	4.01	4.01	3.99	4.00	4.01	4.02	4.00	4.00	4.02	4.01	4.00	4.01	4.00	4.01	4.00	
Wo	0.20	0.60	0.22	0.65	0.48	0.58	0.52	0.21	0.41	0.45	0.45	50.19	49.76	49.22	48.72	49.51	0.72	
En	90.01	89.88	90.14	90.06	90.14	90.22	89.89	90.07	89.93	90.35	90.64	45.81	46.62	46.63	47.34	46.94	89.95	
Fs	9.79	9.52	9.64	9.29	9.38	9.20	9.44	9.72	9.52	9.20	8.92	2.71	2.51	3.14	2.84	2.67	8.85	
N° Mg	90.19	90.42	90.34	90.65	90.57	90.75	90.49	90.26	90.43	90.76	91.04	94.41	94.89	93.70	94.35	95.61	91.04	

Table A2: Continued

Rock type	F	F	F	F	F	F	P	F	F	F	F	F	C	C	C	C	C	C	C	C
sample	VM10A	VM10A	VM10A	VM10A	VM10A	VM10A	KL2.4-2b	KL1-A	KL1-A	KL1-A	KL1-A	KL1-A	18LP1							
Mineral	opx	cpx	cpx	cpx	cpx	cpx	cpx	cpx	cpx	cpx	cpx	cpx	cpx	cpx	cpx	cpx	cpx	opx	opx	opx
texture	in C-splamph-core	m	m	m	m	C-m	m	m	m	m	m	m	C-cpx	C-cpx	C-cpx	C-cpx	m	m	m	m
name	opx3	cpx1	cpx2	cpx3	cpx4	cpx5	cpx5	cpx6	cpx7	opx1	opx2	opx3	cpx1	cpx2	cpx3	cpx5	opx3	opx4	opx1	opx2
Na ₂ O	0.00	0.20	0.24	0.22	0.16	0.31	0.25	0.20	0.28	0.02	0.01	0.01	0.23	0.28	0.23	0.22	bdl	0.01	0.20	0.01
MgO	32.81	17.02	16.71	17.22	17.46	16.43	17.72	17.16	17.18	34.59	34.98	35.10	17.10	17.16	16.96	17.01	33.27	34.20	33.26	34.15
Al ₂ O ₃	1.53	1.11	1.31	1.27	1.06	1.60	1.08	1.02	1.09	1.62	1.67	1.57	2.32	2.56	2.28	1.41	2.78	2.30	2.45	2.93
SiO ₂	55.08	54.13	54.04	54.33	54.64	52.60	53.39	54.33	53.98	57.05	56.74	56.56	53.07	52.61	52.18	53.84	55.74	56.37	56.31	56.46
K ₂ O	bdl	bdl	bdl	bdl	bdl	bdl	bdl	bdl	bdl	bdl	bdl	bdl	bdl	0.02	0.01	bdl	bdl	bdl	0.05	0.01
CaO	0.20	24.88	24.79	24.83	24.77	24.08	24.27	24.49	23.81	0.22	0.21	0.20	23.85	23.81	24.13	24.78	0.17	0.14	1.00	0.23
TiO ₂	bdl	bdl	0.12	0.08	0.08	bdl	0.12	0.14	bdl	0.05	0.02	0.04	0.10	0.09	0.08	0.05	bdl	0.02	0.01	0.01
Cr ₂ O ₃	0.21	0.25	0.27	0.25	0.18	0.45	0.28	0.23	0.27	0.15	0.17	0.14	0.61	0.64	0.48	0.38	0.26	0.26	0.32	0.33
MnO	0.14	0.11	bdl	bdl	bdl	0.10	0.12	0.09	0.12	0.15	0.14	0.16	0.07	0.08	0.03	0.07	0.14	0.14	0.20	0.15
FeO	5.86	1.77	1.67	1.81	1.74	1.81	1.86	1.75	1.77	5.76	5.75	5.42	1.41	1.29	1.37	1.56	6.02	6.16	6.06	5.99
Sum	95.88	99.46	99.18	100.00	100.16	97.41	99.18	99.40	98.49	99.67	99.76	99.31	98.93	98.64	97.86	99.58	98.45	99.74	99.86	100.27
Si	1.98	1.98	1.98	1.97	1.98	1.96	1.96	1.98	1.98	1.97	1.96	1.96	1.95	1.94	1.94	1.97	1.95	1.95	1.95	1.94
Ti	0.00	0.00	0.00	0.00	0.00		0.00	0.00		0.00	0.00	0.00	0.00	0.00	0.00	0.00		0.00	0.00	0.00
Al	0.06	0.05	0.06	0.05	0.05	0.07	0.05	0.04	0.05	0.07	0.07	0.06	0.10	0.11	0.10	0.06	0.11	0.09	0.10	0.12
Cr	0.01	0.01	0.01	0.01	0.01	0.01	0.01	0.01	0.01	0.00	0.00	0.00	0.02	0.02	0.01	0.01	0.01	0.01	0.01	0.01
Fe ₂₊	0.18	0.05	0.05	0.05	0.05	0.06	0.06	0.05	0.05	0.17	0.17	0.16	0.04	0.04	0.04	0.05	0.18	0.18	0.18	0.17
Mn	0.00	0.00				0.00	0.00	0.00	0.00	0.00	0.00	0.00	0.00	0.00	0.00	0.00	0.00	0.00	0.01	0.00
Mg	1.75	0.93	0.91	0.93	0.94	0.91	0.97	0.93	0.94	1.78	1.80	1.81	0.93	0.94	0.94	0.93	1.73	1.76	1.72	1.75
Ca	0.01	0.97	0.97	0.97	0.96	0.96	0.96	0.96	0.94	0.01	0.01	0.01	0.94	0.94	0.96	0.97	0.01	0.01	0.04	0.01
Na	0.00	0.01	0.02	0.02	0.01	0.02	0.02	0.01	0.02	0.00	0.00	0.00	0.02	0.02	0.02	0.02	-	0.00	0.01	0.00
K	-	-	-	-	-	-	-	-	-	-	-	-	-	0.00	0.00	-	-	-	0.00	0.00
Sum	4.00	4.00	4.00	4.00	4.01	4.01	4.02	4.00	4.00	4.00	4.01	4.01	4.01	4.01	4.02	4.01	3.99	4.00	4.01	4.00
Wo	0.39	49.46	29.79	49.08	48.79	49.22	47.86	48.90	48.01	0.42	0.39	0.38	48.51	48.80	49.03	49.49	0.34	0.27	1.91	0.43
En	90.54	47.08	46.70	47.36	47.85	46.73	48.42	47.67	48.20	91.02	91.16	91.64	48.40	48.54	47.95	47.27	90.48	90.54	88.37	90.62
Fs	9.07	2.75	2.62	2.79	2.87	2.89	2.85	2.73	2.79	8.50	8.41	7.93	2.24	2.05	2.17	2.43	9.18	9.15	9.03	8.92
N° Mg	90.89	94.49	94.69	94.43	94.71	94.18	94.44	94.59	97.54	91.46	91.56	92.03	95.58	95.95	95.66	95.11	90.78	90.82	90.73	91.04

Table A3: Major elements compositions (wt%) of garnet. Formula based on 12 oxygens.

Rock Type	P	P	P	P	P	P	F	F	F	F	F	F	F	F	F	F	F	F	F	F
Sample	KL24-2B	KL24-2B	KL24-2B	KL24-2B	KL24-2B	KL24-2B	KL1-A	KL1-A	KL1-A	KL1-A	KL1-A	KL1-A	KL1-A	KL1-A	KL1-A	KL1-A	KL1-A	KL1-A	VM10A	VM10A
texture	m w/k	P	P	m w/k	m w/k	P	m	m	m	m	m	m	m	m	m	m	m	m	m w/k	m w/k
name	grt1	grt2	grt3	grt4	grt4	grt5	grt1	grt1-rim	grt3	grt3-rim	grt4	grt6	grt5	grt7	grt7	grt1	grt2-core			
Spot	85	88	89	92	315	332	462	463	472	473	478	484	486	491	146					
SiO ₂	40,88	42,05	41,78	40,65	41,98	42,42	42,13	42,21	41,74	41,23	41,82	42,04	41,85	41,02	41,55	41,55	42,11			
TiO ₂	0,06	0,04	0,04	bdl	bdl	0,05	0,11	0,06	0,03	0,05	bdl	0,08	0,07	0,06	0,04	0,04	0,09			
Al ₂ O ₃	21,52	22,37	21,93	21,34	22,66	21,91	22,32	22,20	22,09	21,77	22,12	21,95	22,35	21,92	22,58	21,90				
Cr ₂ O ₃	1,86	1,39	1,41	1,40	1,44	1,65	1,39	1,51	1,45	1,52	1,45	1,42	1,48	1,41	0,83	1,88				
FeO	14,91	9,47	9,08	12,04	9,25	8,60	9,39	9,49	9,91	11,36	9,70	10,13	9,88	9,89	9,38	9,73				
MnO	1,82	0,60	0,61	0,70	0,47	0,46	0,58	0,56	0,66	0,85	0,63	0,61	0,60	0,66	0,65	0,56				
MgO	14,07	19,05	18,44	16,36	19,03	19,25	18,97	18,90	18,06	16,74	18,63	17,82	18,38	18,52	18,51	18,80				
CaO	5,64	5,71	5,91	5,95	5,38	5,39	5,34	5,32	5,84	5,77	5,63	5,70	5,43	5,35	5,81	5,53				
Sum	100,76	100,68	99,20	98,44	100,27	99,72	100,23	100,25	99,78	99,29	99,99	99,75	100,03	98,83	99,34	100,60				
Si	3,01	2,99	3,02	3,00	2,99	3,04	3,01	3,02	3,01	3,01	3,00	3,04	3,01	2,98	2,99	3,01				
Ti	0,00	0,00	0,00	0,00	0,00	0,00	0,01	0,00	0,00	0,00	0,00	0,00	0,00	0,00	0,00	0,00				
Al	1,87	1,87	1,87	1,86	1,91	1,85	1,88	1,87	1,88	1,87	1,87	1,87	1,89	1,88	1,92	1,84				
Cr	0,11	0,08	0,08	0,08	0,08	0,09	0,08	0,09	0,08	0,09	0,08	0,08	0,08	0,08	0,05	0,11				
Fe ₃₊	0,01	0,06	0,01	0,06	0,02	0,00	0,01	0,00	0,02	0,01	0,05	0,00	0,01	0,08	0,05	0,03				
Fe ₂₊	0,91	0,50	0,54	0,69	0,53	0,52	0,55	0,57	0,58	0,69	0,54	0,61	0,59	0,52	0,52	0,55				
Mn ₂₊	0,11	0,04	0,04	0,04	0,03	0,03	0,04	0,03	0,04	0,05	0,04	0,04	0,04	0,04	0,04	0,03				
Mg	1,54	2,02	1,99	1,80	2,02	2,06	2,02	2,01	1,94	1,82	1,99	1,92	1,97	2,00	1,99	2,00				
Ca	0,44	0,44	0,46	0,47	0,41	0,41	0,41	0,41	0,45	0,45	0,43	0,44	0,42	0,42	0,45	0,42				
Sum	8,00	8,00	8,00	8,00	8,00	8,00	8,00	8,00	8,00	8,00	8,00	8,00	8,00	8,00	8,00	8,00				
Al IV	0,00	0,01	0,00	0,00	0,01	0,00	0,00	0,00	0,00	0,00	0,00	0,00	0,00	0,02	0,01	0,00				
Al VI	1,87	1,87	1,87	1,86	1,90	1,85	1,88	1,87	1,88	1,87	1,87	1,87	1,89	1,85	1,91	1,84				
Fe ₂₊ oct	0,02	0,00	0,04	0,00	0,00	0,05	0,03	0,04	0,02	0,03	0,00	0,05	0,01	0,00	0,00	0,02				
Mg oct	0,00	0,00	0,00	0,00	0,00	0,00	0,00	0,00	0,00	0,00	0,00	0,00	0,00	0,00	0,00	0,00				
Tetr.	3,01	3,00	3,02	3,00	3,00	3,04	3,01	3,02	3,01	3,01	3,00	3,04	3,01	3,00	3,00	3,01				
Y site	2,00	2,01	2,00	2,00	2,00	2,00	2,00	2,00	2,00	2,00	2,00	2,00	2,00	2,00	2,01	2,00				
X site	2,99	2,99	2,98	3,00	3,00	2,96	2,99	2,98	2,99	2,99	3,00	2,96	2,99	2,98	2,99	2,99				
Prp	0,51	0,67	0,66	0,60	0,68	0,68	0,67	0,67	0,64	0,60	0,66	0,64	0,65	0,67	0,66	0,66				
Alm	0,30	0,17	0,18	0,23	0,18	0,17	0,18	0,19	0,19	0,23	0,18	0,20	0,20	0,17	0,17	0,18				

Supplementary Material • CHAPTER 4

Grs	0,15	0,15	0,15	0,16	0,14	0,14	0,14	0,13	0,15	0,15	0,14	0,15	0,14	0,14	0,15	0,14
Sps	0,04	0,01	0,01	0,01	0,01	0,01	0,01	0,01	0,01	0,02	0,01	0,01	0,01	0,01	0,01	0,01

Table A4. Major elements compositions (wt%) of amphibole recalculated using the spreadsheet from Ridolfi et al. (2018).

Spot	4	5	15	16	23	34	35	39	40	41	66	68	135	136	137	138	139	140	143	144	145	
Rock Type	F	F	F	F	F	F	F	F	F	F	F	F	C	C	C	C	C	C	C	C	C	
sample name	MM1	MM1	MM1	MM1	18LP1	18LP1	18LP1	18LP1	18LP1	18LP1	18LP1	18LP1	18LP1									
texture	am-1	am-2	am3	am4	am5	am6	am7	am8	am9	am10	am11	am11	am1	am2	am3	am4	am5	am6	am7	am8	am9	
	m	m	m-core	m-rim	m	m	min	srp	veinin	srp	veinin	srp	vein	in spl	m	in vein						
SiO ₂	46.32	46.91	46.55	52.83	56.29	45.73	56.45	46.33	45.93	46.14	47.83	46.51	55.14	57.01	57.43	57.21	57.62	53.18	44.18	45.05	54.16	
TiO ₂	0.13	0.19	0.15	bdl	bdl	0.26	0.00	0.30	0.28	0.26	0.11	0.21	0.06	0.064	0.04	0.086	0.045	0.044	0.236	0.224	0.048	
Al ₂ O ₃	13.07	12.07	12.93	6.03	2.07	12.84	1.67	12.05	12.56	12.80	10.56	11.95	3.2	0.915	0.91	1079.00	0.9	5.59	14.27	13.58	4.39	
Cr ₂ O ₃	0.776	0.879	0.588	0.467	0.227	1.25	0.14	1.15	1095.00	1.03	1377.00	1.19	0.529	0.239	0.26	0.276	0.14	0.72	1.19	1.28	0.52	
FeOtot	2.45	2.5	2.54	1.81	1.49	2.57	1.48	2.48	2.39	2.55	2.5	2.6	1.86	1.84	1.70	1.86	1.73	2.02	2.98	2.88	2.01	
MnO	0.083	0.072	bdl	bdl	bdl	0.07	bdl	bdl	bdl	bdl	bdl	bdl	0.074	0.072	bdl	0.062	0.058	0.026	0.093	0.026	0.107	
NiO+ZnO	0.15	0.111	0.086	0.094	0.122	0.124	0.084	0.111	0.105	0.099	0.053	0.098	0.117	0.064	0.08	0.09	0.138	0.13	0.112	0.09	0.104	
MgO	18.56	19.05	18.88	21.25	22.86	18.58	23.17	18.99	18.67	18.82	19.07	18.61	22.43	23.29	23.40	23.83	23.83	21.37	18.28	18.21	21.93	
CaO	12.56	12.6	12.61	12.87	13.06	12.41	13.05	12.6	12.35	12.44	12.63	12.34	13.19	12.76	12.92	12.67	12.9	12.81	12.36	12.62	12.84	
Na ₂ O	1.86	1.84	1.76	0.8	0.329	1.73	0.235	1.58	1.7	1.63	1.54	1.72	0.552	0.2	0.19	0.191	0.203	1.00	1.9	1.98	0.84	
K ₂ O	0.717	0.243	0.545	0.221	0.044	0.786	0.03	0.787	0.651	0.742	0.601	0.696	0.061	0.041	bdl	bdl	0.025	0.138	1.31	1154.00	0.087	
F	bdl	0.041	0.027	0.055	bdl	bdl	0.021	0.049	bdl	0.061	bdl	0.011	bdl	bdl	0.01	bdl	bdl	bdl	0.033	0.037	0.013	
Cl	0.156	0.081	0.16	0.091	0.046	0.019	0.041	0.083	0.058	0.052	0.192	0.21	0.049	0.006	0.00	0.016	0.018	0.097	0.036	0.085	0.086	
Si	6.52	6.61	6.54	7.34	7.76	6.50	7.78	6.56	6.54	6.53	6.76	6.60	7.58	7.86	7.88	7.82	7.85	7.35	6.29	6.38	7.47	
Al	1.48	1.39	1.46	0.66	0.24	1.50	0.22	1.44	1.46	1.47	1.24	1.40	0.42	0.14	0.12	0.17	0.14	0.65	1.71	1.62	0.53	
Ti	0.00	0.00	0.00	0.00	0.00	0.00	0.00	0.00	0.00	0.00	0.00	0.00	0.00	0.00	0.00	0.01	0.00	0.00	0.00	0.00	0.00	
Sum T	8.00	8.00	8.00	8.00	8.00	8.00	8.00	8.00	8.00	8.00	8.00	8.00	8.00	8.00	8.00	8.00	8.00	8.00	8.00	8.00	8.00	
Al	0.69	0.61	0.68	0.33	0.09	0.64	0.05	0.58	0.64	0.66	0.52	0.60	0.10	0.01	0.03	0.00	0.00	0.26	0.69	0.65	0.18	
Ti	0.01	0.02	0.02	0.00	0.00	0.03	0.00	0.03	0.03	0.03	0.01	0.02	0.01	0.01	0.00	0.00	0.00	0.00	0.03	0.02	0.00	
Cr	0.09	0.10	0.07	0.05	0.02	0.14	0.02	0.13	0.12	0.12	0.15	0.13	0.06	0.03	0.03	0.03	0.02	0.08	0.13	0.14	0.06	
Ni+Zn	0.02	0.01	0.01	0.01	0.01	0.01	0.01	0.01	0.01	0.01	0.01	0.01	0.01	0.01	0.01	0.01	0.01	0.02	0.01	0.01	0.01	
Fe ³⁺	0.24	0.21	0.27	0.20	0.17	0.20	0.17	0.24	0.26	0.23	0.19	0.30	0.20	0.15	0.11	0.16	0.16	0.21	0.25	0.24	0.23	
Mg	3.90	4.00	3.96	4.40	4.70	3.93	4.76	4.01	3.96	3.97	4.02	3.94	4.60	4.79	4.79	4.85	4.84	4.40	3.88	3.85	4.51	
Fe ²⁺	0.05	0.09	0.03	0.01	0.00	0.11	0.00	0.05	0.03	0.07	0.10	0.01	0.01	0.06	0.09	0.06	0.04	0.02	0.11	0.10	0.00	
Mn	0.01	0.01	0.00	0.00	0.00	0.01	0.00	0.00	0.00	0.00	0.00	0.00	0.01	0.01	0.00	0.01	0.01	0.00	0.01	0.00	0.01	
ΔC	0.00	0.04	0.03	0.00	0.00	0.08	0.01	0.05	0.05	0.08	0.00	0.01	0.00	0.05	0.05	0.11	0.07	0.00	0.10	0.02	0.01	
Ca	1.90	1.90	1.90	1.92	1.93	1.89	1.93	1.91	1.88	1.88	1.91	1.88	1.94	1.88	1.90	1.85	1.88	1.90	1.89	1.92	1.90	
Na	0.10	0.05	0.07	0.08	0.07	0.04	0.06	0.03	0.07	0.03	0.09	0.12	0.06	0.05	0.05	0.03	0.04	0.10	0.01	0.06	0.09	
Ca	0.00	0.00	0.00	0.00	0.00	0.00	0.00	0.00	0.00	0.00	0.00	0.00	0.00	0.00	0.00	0.00	0.00	0.00	0.00	0.00	0.00	
Na	0.41	0.45	0.41	0.13	0.02	0.44	0.00	0.40	0.40	0.41	0.33	0.36	0.09	0.00	0.00	0.02	0.01	0.17	0.51	0.48	0.13	
K	0.13	0.04	0.10	0.04	0.01	0.14	0.00	0.14	0.12	0.13	0.11	0.13	0.01	0.01	0.00	0.00	0.00	0.02	0.24	0.21	0.02	
(Na+K) _A	0.54	0.49	0.50	0.17	0.02	0.58	0.00	0.54	0.52	0.55	0.44	0.48	0.10	0.01	0.00	0.02	0.02	0.19	0.75	0.69	0.15	
Sum A	0.54	0.49	0.50	0.17	0.02	0.58	0.00	0.54	0.52	0.55	0.44	0.48	0.10	0.01	0.00	0.02	0.02	0.19	0.75	0.69	0.15	
OH	1.96	1.96	1.93	1.95	1.99	1.91	1.98	1.87	1.91	1.86	1.95	1.91	1.98	2.00	2.00	2.00	2.00	1.98	1.83	1.86	1.97	
F	0.00	0.02	0.01	0.02	0.00	0.00	0.01	0.02	0.00	0.03	0.00	0.00	0.00	0.00	0.00	0.00	0.00	0.00	0.01	0.02	0.01	
Cl	0.04	0.02	0.04	0.02	0.01	0.00	0.01	0.02	0.01	0.01	0.05	0.05	0.01	0.00	0.00	0.00	0.00	0.02	0.01	0.02	0.02	
O	0.00	0.00	0.02	0.00	0.00	0.08	0.00	0.09	0.08	0.10	0.00	0.04	0.00	0.00	0.00	0.00	0.00	0.00	0.15	0.10	0.00	
sum W	2.00	2.00	2.00	2.00	2.00	2.00	2.00	2.00	2.00	2.00	2.00	2.00	2.00	2.00	2.00	2.00	2.00	2.00	2.00	2.00	2.00	
M _r	838.59	836.38	836.67	824.47	818.55	841.23	817.40	840.05	838.11	839.29	837.67	838.64	823.13	818.53	817.99	818.61	818.27	826.00	847.94	846.23	824.27	
2CTi-WO	0.02	0.04	0.01	0.00	0.00	-0.03	0.00	-0.02	-0.02	-0.04	0.02	0.01	0.01	0.01	0.01	0.00	0.00	0.01	-0.10	-0.05	0.01	
Mg#	0.93	0.93	0.93	0.95	0.96	0.93	0.97	0.93	0.93	0.93	0.93	0.93	0.96	0.96	0.96	0.96	0.96	0.95	0.92	0.92	0.95	
Mg/(Mg+Fe ²⁺)	0.99	0.98	0.99	1.00	1.00	0.97	1.00	0.99	0.99	0.98	0.98	1.00	1.00	0.99	0.98	0.99	0.99	1.00	0.97	0.97	1.00	

Table A4 continued

Spot	71	105	106	118	120	309	310	318	321	322	323	326	327	345	131	145	147	402	403	406	415	420	422	423	424
Rock Type	P	P	P	P	P	P	P	P	P	P	P	P	P	P	F	F	F	C	C	C	C	C	C	C	C
Sample name	KL24-2B am1	KL24-2B am3	KL24-2B am_r2	KL24-2B am_r4	KL24-2B am_r6	KL24-2B am4	KL24-2B am_r7	KL24-2B am5	KL24-2B am_r7	KL24-2B am6	KL24-2B am_r8	KL24-2B am_r9	KL24-2B am7	KL24-2B am8	VM10 A am6	VM10 A am6	VM10 A am6	MOL1 -C am2	MOL1 -C am2/2	MOL1 -C am1	MOL1 -C am_r1	MOL1 -C am_r2	MOL1 -C m_r3	MOL1 -C am3	MOL1 -C am4
Texture	m w/opx incl	m	m	m	zoned amph with incl	in ol	m	in in am_r7	m	m	m	in amph 7	m	m	m w/spl ex	in c-cpx	in grt	in tr	m	m	in mgs vein	in mgs around mgs vein	in mgs vein	in mgs vein	in mgs vein
SiO ₂	45,71	47,30	56,87	45,66	55,48	45,02	45,54	44,75	56,42	44,55	57,16	56,72	44,88	45,47	49,91	45,91	49,47	47,40	55,29	47,18	57,31	57,48	57,56	57,04	57,26
TiO ₂	0.491	0.387	0.133	0.544	0.215	0.472	0.46	0.563	bdl	0.556	0.087	0.113	0.532	0.532	0.117	0.324	0.146	0.131	0.107	0.147	0.033	bdl	bdl	bdl	bdl
Al ₂ O ₃	12.07	11.52	2.09	12.52	2.22	12.36	12.49	12.88	1.25	12.99	1.20	1.66	12.75	12.16	9.34	11.04	10.17	10.02	2.61	10.62	1.34	0.81	1.24	1.14	1.32
Cr ₂ O ₃	1.46	0.71	0.35	1.32	0.74	1.30	1.30	1.33	0.20	1.33	0.29	0.20	1.40	1.41	0.29	1.46	0.79	1.14	0.50	0.91	0.17	bdl	0.25	0.18	0.16
FeO _{tot}	2.68	2.72	1.82	2.70	2.25	3.36	2.86	2.79	1.62	3.18	1.88	1.64	3.07	2.60	2.62	3.56	2.47	3.14	2.16	3.10	2.23	2.02	2.02	2.26	2.09
MnO	bdl	bdl	bdl	bdl	0.078	bdl	bdl	bdl	bdl	bdl	bdl	bdl	0.078	0.074	bdl	bdl	bdl	0.111	0.06	0.09	0.084	bdl	0.082	bdl	0.097
NiO+ZnO	0.134	0.123	0.058	0.115	0.024	bdl	bdl	0.14	0.00	0.141	bdl	0.118	0.034	0.094	bdl	bdl	bdl	0.11	0.00	0.116	0.118	0.104	0.105	0.067	0.056
MgO	18.41	17.97	21.94	18.15	21.43	18.39	18.29	18.65	23.36	18.30	22.92	23.28	18.52	18.31	19.33	18.22	18.86	19.41	22.74	19.58	23.62	23.57	23.40	23.85	23.20
CaO	12.96	13.24	13.38	12.89	13.31	12.12	12.28	12.59	13.16	12.66	13.34	13.05	12.22	12.66	12.92	12.65	12.96	12.34	12.47	12.52	12.21	12.78	12.78	12.08	12.86
Na ₂ O	2.08	1.82	0.26	1.86	0.32	2.22	1.92	1.97	0.20	2.04	0.19	0.32	2.08	1.87	1.18	2.62	1.17	2.05	0.65	2.08	0.28	0.19	0.25	0.25	0.37
K ₂ O	0.66	0.293	bdl	0.827	0.072	0.639	0.633	0.666	bdl	0.693	0.024	bdl	0.658	0.627	0.198	0.073	0.117	0.574	0.073	0.561	0.014	bdl	bdl	bdl	bdl
F	0.054	0.056	0.046	0.057	0.039	0.055	0.108	bdl	0.08	0.087	bdl	bdl	0.097	0.00	bdl	0.057	bdl	bdl	bdl	0.065	0.028	bdl	0.082	0.014	0.046
Cl	0.062	0.143	0.045	0.048	0.038	0.00	0.033	0.035	0.00	0.028	0.00	0.019	0.02	0.036	0.111	0.111	0.1	0.099	0.03	0.088	0.034	bdl	0.032	0.03	0.021
Si	6.51	6.77	7.87	6.50	7.78	6.45	6.51	6.39	7.80	6.37	7.86	7.76	6.41	6.50	7.03	6.60	6.96	6.72	7.63	6.65	7.82	7.88	7.84	7.82	7.82
Al	1.49	1.23	0.13	1.50	0.22	1.55	1.49	1.61	0.20	1.63	0.14	0.24	1.59	1.50	0.97	1.40	1.04	1.28	0.37	1.35	0.18	0.12	0.16	0.18	0.18
Ti	0.00	0.00	0.00	0.00	0.00	0.00	0.00	0.00	0.00	0.00	0.00	0.00	0.00	0.00	0.00	0.00	0.00	0.00	0.00	0.00	0.00	0.00	0.00	0.00	0.00
Sum T	8.00	8.00	8.00	8.00	8.00	8.00	8.00	8.00	8.00	8.00	8.00	8.00	8.00	8.00	8.00	8.00	8.00	8.00	8.00	8.00	8.00	8.00	8.00	8.00	8.00
Al	0.54	0.71	0.21	0.60	0.14	0.54	0.61	0.56	0.00	0.56	0.05	0.03	0.56	0.55	0.59	0.47	0.65	0.39	0.06	0.42	0.04	0.01	0.04	0.00	0.03
Ti	0.05	0.04	0.01	0.06	0.02	0.05	0.05	0.06	0.00	0.06	0.01	0.01	0.06	0.06	0.01	0.04	0.02	0.01	0.01	0.02	0.00	0.00	0.00	0.00	0.00
Cr	0.16	0.08	0.04	0.15	0.08	0.15	0.15	0.15	0.02	0.15	0.03	0.02	0.16	0.16	0.03	0.17	0.09	0.13	0.05	0.10	0.02	0.00	0.03	0.02	0.02
Ni+Zn	0.02	0.01	0.01	0.01	0.00	0.00	0.00	0.02	0.00	0.02	0.00	0.01	0.00	0.01	0.00	0.00	0.00	0.01	0.00	0.01	0.01	0.01	0.01	0.01	0.01
Fe ³⁺	0.10	0.00	0.00	0.13	0.00	0.27	0.26	0.25	0.19	0.26	0.07	0.19	0.24	0.22	0.06	0.06	0.02	0.27	0.23	0.25	0.19	0.16	0.16	0.23	0.22
Mg	3.91	3.83	4.52	3.85	4.48	3.93	3.89	3.97	4.81	3.90	4.70	4.75	3.95	3.90	4.06	3.90	3.96	4.10	4.68	4.12	4.80	4.82	4.75	4.87	4.72
Fe ²⁺	0.22	0.33	0.21	0.19	0.26	0.13	0.08	0.08	0.00	0.12	0.15	0.00	0.13	0.09	0.25	0.37	0.27	0.10	0.02	0.11	0.06	0.07	0.07	0.03	0.02
Mn	0.00	0.00	0.00	0.00	0.01	0.00	0.00	0.00	0.00	0.00	0.00	0.00	0.01	0.01	0.00	0.00	0.00	0.01	0.01	0.01	0.01	0.00	0.01	0.00	0.01
ΔC	0.00	0.00	0.00	0.00	0.00	0.07	0.04	0.08	0.02	0.07	0.00	0.02	0.10	0.01	0.00	0.00	0.00	0.03	0.06	0.04	0.14	0.07	0.07	0.16	0.03
Ca	1.98	2.00	1.98	1.97	2.00	1.86	1.88	1.92	1.95	1.93	1.96	1.91	1.87	1.94	1.95	1.95	1.95	1.87	1.84	1.89	1.79	1.88	1.87	1.77	1.88
Na	0.02	0.00	0.02	0.03	0.00	0.07	0.08	0.00	0.03	0.00	0.04	0.07	0.03	0.05	0.05	0.05	0.05	0.10	0.09	0.06	0.07	0.05	0.07	0.07	0.09
Ca	0.00	0.03	0.00	0.00	0.00	0.00	0.00	0.01	0.00	0.00	0.00	0.00	0.00	0.00	0.00	0.00	0.00	0.00	0.00	0.00	0.00	0.00	0.00	0.00	0.00
Na	0.55	0.50	0.05	0.48	0.09	0.55	0.45	0.55	0.02	0.57	0.01	0.02	0.55	0.46	0.27	0.68	0.27	0.47	0.08	0.50	0.00	0.00	0.00	0.00	0.01
K	0.12	0.05	0.00	0.15	0.01	0.12	0.12	0.12	0.00	0.13	0.00	0.00	0.12	0.11	0.04	0.01	0.02	0.10	0.01	0.10	0.00	0.00	0.00	0.00	0.00
(Na+K) _A	0.67	0.56	0.05	0.63	0.10	0.66	0.57	0.67	0.02	0.69	0.02	0.02	0.67	0.58	0.31	0.69	0.29	0.57	0.09	0.61	0.00	0.00	0.00	0.00	0.01
Sum A	0.67	0.59	0.05	0.63	0.10	0.66	0.57	0.68	0.02	0.70	0.02	0.02	0.67	0.58	0.31	0.69	0.29	0.57	0.09	0.61	0.00	0.00	0.00	0.00	0.01
OH	1.89	1.69	1.80	1.86	1.83	1.87	1.84	1.84	1.97	1.80	2.00	2.00	1.82	1.91	1.97	1.95	1.98	1.98	1.99	1.95	1.98	2.00	1.96	1.99	1.98
F	0.02	0.03	0.02	0.03	0.02	0.02	0.05	0.00	0.03	0.04	0.00	0.00	0.04	0.00	0.00	0.03	0.00	0.00	0.00	0.03	0.01	0.00	0.04	0.01	0.02
Cl	0.01	0.03	0.01	0.01	0.01	0.00	0.01	0.01	0.00	0.01	0.00	0.00	0.00	0.01	0.03	0.03	0.02	0.02	0.01	0.02	0.01	0.00	0.01	0.01	0.00
O	0.07	0.25	0.17	0.11	0.14	0.10	0.11	0.15	0.00	0.16	0.00	0.00	0.13	0.08	0.00	0.00	0.00	0.00	0.00	0.00	0.00	0.00	0.00	0.00	0.00
sum W	2.00	2.00	2.00	2.00	2.00	2.00	2.00	2.00	2.00	2.00	2.00	2.00	2.00	2.00	2.00	2.00	2.00	2.00	2.00	2.00	2.00	2.00	2.00	2.00	2.00
M ^r	845,8	840,9	821,9	844,9	826,5	844,8	841,3	844,6	818,3	847,1	820,0	818,4	845,1	842,6	831,1	846,7	831,7	841,4	821,8	841,6	818,3	817,9	818,9	817,6	819,0
2CTi-	1	5	5	2	0	4	4	5	4	3	7	6	7	0	0	3	0	9	9	7	3	5	6	1	6
WO	0.03	-0.17	-0.15	0.01	-0.10	0.00	-0.01	-0.03	0.00	-0.04	0.02	0.02	-0.02	0.03	0.02	0.07	0.03	0.03	0.02	0.03	0.01	0.00	0.00	0.00	0.00
Mg#	0.92	0.92	0.96	0.92	0.94	0.91	0.92	0.92	0.96	0.91	0.96	0.96	0.91	0.93	0.93	0.90	0.93	0.92	0.95	0.92	0.95	0.95	0.95	0.95	0.95
Mg/(Mg+Fe ₂)	0.95	0.92	0.96																						

Table A4 continued

Spot Rock Type Sample name Text. Pos.	425 C MOL1-C am5 m	426 C MOL1-C am5/2 m	429 C MOL1-C am5/3 min	430 C MOL1-C am6 mgs vein	440 C MOL1-C am7 m	443 F KL1-A am1 m	451 F KL1-A am2 m	490 F KL1-A am7 m	495 F KL1-A am9 m	497 F KL1-A am10 m	35 P KL24-3 am1 m	42 P KL24-3 am2 in C-grt	43 P KL24-3 am3 in C-grt	45 P KL24-3 am4 in C-grt	51 P KL24-3 kel-am kel	61 P KL24-3 am6 in C-spl	90 P KL24-3 am12/2 m	209 P KL24-3 am5r2 m	211 P KL24-3 am9r m	220 P KL24-3 am10r m	
SiO ₂	46,76	46,67	46,98	57,46	49,17	46,01	45,51	45,61	45,58	45,86	44,19	44,42	50,78	42,88	45,06	57,16	56,17	44,74	57,61	57,31	
TiO ₂	0,209	0,257	0,213	0,00	0,155	0,517	0,475	0,508	0,404	0,43	0,625	0,565	0,238	0,594	0,576	0,088	0,087	0,504	bdl	bdl	
Al ₂ O ₃	10,88	11,83	11,13	1,51	8,48	11,99	12,01	12,33	12,41	12,33	13,31	14,3	9,13	16,58	13,07	1,03	1,71	12,99	0,71	0,944	
Cr ₂ O ₃	0,85	0,99	0,92	0,25	1,06	1,27	1,67	1,51	1,34	1,09	1,29	1,64	0,20	1,57	1,40	0,63	0,22	1,21	0,16	0,15	
FeOtot	3,07	2,88	3,16	2,17	2,85	2,75	2,81	3,13	3,20	2,85	3,12	2,45	1,95	2,35	3,15	1,77	1,74	3,15	1,49	1,55	
MnO	bdl	0,097	0,106	bdl	bdl	bdl	bdl	0,08	bdl	bdl	0,119	0,08	bdl	bdl	bdl	bdl	0,007	0,07	0,00	0,041	
NiO+ZnO	0,127	0,115	0,112	0,135	0,107	0,128	bdl	0,133	bdl	bdl	bdl	0,103	bdl	bdl	0,148	bdl	0,082	0,107	0,04	0,108	
MgO	19,20	19,24	19,55	23,37	20,39	18,45	18,33	17,98	18,12	18,15	18,12	18,43	20,64	17,17	17,99	23,03	22,77	17,88	23,11	22,80	
CaO	12,06	12,34	12,42	12,54	12,3	12,62	12,37	12,45	12,58	12,77	12,62	12,02	12,61	12,17	12,61	13,29	13,17	12,65	13,31	13,29	
Na ₂ O	2,39	2,38	2,26	0,36	1,97	2,05	1,95	2,02	2,02	2,10	1,83	2,36	1,13	2,37	1,88	0,09	0,31	2,07	0,11	0,07	
K ₂ O	0,149	0,197	0,177	bdl	0,245	0,581	0,548	0,702	0,65	0,5	0,687	0,221	0,023	0,212	0,754	0,007	0,046	0,449	bdl	bdl	
F	0,069	0,059	0,11	0,013	0,121	0,07	0,107	bdl	bdl	bdl	0,069	0,049	bdl	bdl	0,065	0,08	0,035	bdl	bdl	bdl	
Cl	0,148	0,125	0,152	0,022	0,11	0,076	0,086	0,068	0,116	0,153	0,037	0,00	0,073	0,131	0,071	0,00	0,011	0,15	0,027	0,03	
Si	6,64	6,56	6,61	7,81	6,90	6,54	6,51	6,50	6,49	6,55	6,34	6,31	7,03	6,12	6,42	7,85	7,78	6,40	7,94	7,94	
Al	1,36	1,44	1,39	0,19	1,10	1,46	1,49	1,50	1,51	1,45	1,66	1,69	0,97	1,88	1,58	0,15	0,22	1,60	0,06	0,06	
Ti	0,00	0,00	0,00	0,00	0,00	0,00	0,00	0,00	0,00	0,00	0,00	0,00	0,00	0,00	0,00	0,00	0,00	0,00	0,00	0,00	
Sum T	8,00	8,00	8,00	8,00	8,00	8,00	8,00	8,00	8,00	8,00	8,00	8,00	8,00	8,00	8,00	8,00	8,00	8,00	8,00	8,00	
Al	0,46	0,52	0,45	0,05	0,30	0,55	0,54	0,57	0,58	0,63	0,60	0,70	0,52	0,91	0,62	0,02	0,06	0,60	0,06	0,09	
Ti	0,02	0,03	0,02	0,00	0,02	0,06	0,05	0,05	0,04	0,05	0,07	0,06	0,02	0,06	0,06	0,01	0,01	0,05	0,00	0,00	
Cr	0,10	0,11	0,10	0,03	0,12	0,14	0,19	0,17	0,15	0,12	0,15	0,18	0,02	0,18	0,16	0,07	0,02	0,14	0,02	0,02	
Ni+Zn	0,01	0,01	0,01	0,01	0,01	0,01	0,00	0,02	0,00	0,00	0,00	0,01	0,00	0,00	0,02	0,00	0,01	0,01	0,00	0,01	
Fe ³⁺	0,34	0,23	0,26	0,20	0,26	0,21	0,28	0,20	0,24	0,05	0,27	0,17	0,20	0,28	0,24	0,07	0,13	0,30	0,01	0,00	
Mg	4,07	4,03	4,10	4,74	4,27	3,91	3,91	3,82	3,85	3,86	3,88	3,90	4,26	3,65	3,82	4,72	4,70	3,82	4,75	4,71	
Fe ²⁺	0,02	0,11	0,11	0,05	0,07	0,11	0,06	0,17	0,14	0,29	0,11	0,12	0,03	0,00	0,14	0,14	0,07	0,08	0,16	0,18	
Mn	0,00	0,01	0,01	0,00	0,00	0,00	0,00	0,01	0,00	0,00	0,01	0,01	0,00	0,00	0,00	0,00	0,00	0,01	0,00	0,00	
ΔC	0,03	0,06	0,07	0,08	0,05	0,00	0,03	0,02	0,00	0,00	0,08	0,16	0,06	0,09	0,05	0,02	0,00	0,00	0,00	0,01	
Ca	1,84	1,86	1,87	1,83	1,85	1,92	1,90	1,90	1,92	1,95	1,92	1,83	1,87	1,86	1,93	1,96	1,95	1,94	1,97	1,97	
Na	0,14	0,08	0,06	0,09	0,10	0,08	0,08	0,08	0,08	0,05	0,00	0,01	0,07	0,05	0,03	0,02	0,05	0,06	0,03	0,02	
Ca	0,00	0,00	0,00	0,00	0,00	0,00	0,00	0,00	0,00	0,00	0,02	0,00	0,00	0,00	0,00	0,00	0,00	0,00	0,00	0,00	
Na	0,52	0,57	0,56	0,00	0,44	0,49	0,46	0,48	0,48	0,54	0,51	0,64	0,23	0,60	0,49	0,00	0,04	0,51	0,00	0,00	
K	0,03	0,04	0,03	0,00	0,04	0,11	0,10	0,13	0,12	0,09	0,13	0,04	0,00	0,04	0,14	0,00	0,01	0,08	0,00	0,00	
(Na+K) _s	0,55	0,60	0,59	0,00	0,48	0,59	0,56	0,61	0,60	0,63	0,64	0,68	0,24	0,64	0,63	0,00	0,04	0,60	0,00	0,00	
Sum A	0,55	0,60	0,59	0,00	0,48	0,59	0,56	0,61	0,60	0,63	0,65	0,68	0,24	0,64	0,63	0,00	0,04	0,60	0,00	0,00	
OH	1,93	1,94	1,91	1,99	1,92	1,88	1,82	1,90	1,90	1,94	1,80	1,82	1,98	1,75	1,79	1,97	1,98	1,88	1,99	1,97	
F	0,03	0,03	0,05	0,01	0,05	0,03	0,05	0,00	0,00	0,03	0,02	0,00	0,00	0,03	0,03	0,02	0,00	0,00	0,00	0,00	
Cl	0,04	0,03	0,04	0,01	0,03	0,02	0,02	0,02	0,03	0,04	0,01	0,00	0,02	0,03	0,02	0,00	0,00	0,04	0,01	0,01	
O	0,00	0,00	0,00	0,00	0,00	0,07	0,11	0,08	0,07	0,02	0,16	0,16	0,00	0,22	0,16	0,00	0,00	0,08	0,00	0,02	
sum W	2,00	2,00	2,00	2,00	2,00	2,00	2,00	2,00	2,00	2,00	2,00	2,00	2,00	2,00	2,00	2,00	2,00	2,00	2,00	2,00	
M _r	838,23840,05840,69	818,66836,42842,62842,43845,36844,14843,42845,53842,31824,76841,50846,19820,14820,26844,44818,04818,83																			
2CTI-WO	0,04	0,05	0,05	0,00	0,03	0,04	0,00	0,03	0,02	0,07	-0,02	-0,04	0,05	-0,09	-0,04	0,02	0,02	0,03	0,00	-0,02	
Mg#	0,92	0,92	0,92	0,95	0,93	0,92	0,92	0,91	0,91	0,92	0,91	0,93	0,95	0,93	0,91	0,96	0,96	0,91	0,97	0,96	
Mg/(Mg+Fe ²⁺)	1,00	0,97	0,97	0,99	0,98	0,97	0,98	0,96	0,97	0,93	0,97	0,97	0,99	1,00	0,97	0,97	0,98	0,98	0,97	0,96	

Table A5: Continued

Rock type	F	F	F	F	F	F	F	F	F	F	F	F	F	F	F	F
Sample	KL1-A	KL1-A	KL1-A	KL1-A	KL1-A	KL1-A	MM1	MM1	MM1	MM1	MM1	MM1	MM1	MM1	MM1	MM1
Comment	spl12	spl13	spl14	spl15	cp1	spl6	spl-1	spl-2	spl3	spl6	spl7	spl9	spl8	spl10	spl12	spl11
Text	in amph	m	m	m	in am	in ol	min	srp	vein	m	m	m	m	m	m	m
MgO	11,56	10,70	11,83	10,66	12,82	11,93	13,93	17,07	14,25	14,47	19,59	18,99	14,99	15,20	15,76	14,94
Al ₂ O ₃	32,97	29,58	33,84	30,79	32,52	30,87	37,73	47,54	38,35	38,88	56,72	55,12	41,26	42,36	42,47	41,66
SiO ₂	0,07	0,01	0,05	0,05	4,63	0,06	0,05	0,05	0,04	0,07	0,05	0,08	0,03	0,04	0,05	0,03
TiO ₂	bdl	bdl	bdl	0,17	0,06	0,43	bdl	bdl	0,05	bdl	bdl	0,05	bdl	0,01	0,01	bdl
Cr ₂ O ₃	34,30	35,78	34,14	35,54	27,64	35,04	31,01	20,87	31,17	30,04	12,08	12,70	27,19	25,89	25,26	26,63
MnO	0,36	0,46	0,34	0,41	0,33	0,34	0,29	0,24	0,32	0,35	0,18	0,13	0,31	0,25	0,23	0,20
FeO	18,94	19,63	18,43	19,95	16,57	20,53	16,33	13,14	16,19	15,84	10,40	10,97	15,43	15,13	14,43	15,16
CoO	bdl	bdl	bdl	bdl	bdl	0,00	bdl	bdl	bdl	bdl	bdl	bdl	bdl	bdl	bdl	bdl
NiO	bdl	bdl	bdl	0,05	0,09	0,18	bdl	0,11	0,06	0,01	0,26	0,19	0,12	0,13	0,03	0,07
ZnO	bdl	bdl	bdl	bdl	bdl	bdl	bdl	bdl	bdl	bdl	bdl	bdl	bdl	bdl	bdl	bdl
Fe ₂ O ₃	bdl	bdl	bdl	bdl	bdl	bdl	bdl	bdl	bdl	bdl	bdl	bdl	bdl	bdl	bdl	bdl
Sum	98,19	96,16	98,63	97,62	94,67	99,38	99,35	99,02	100,43	99,67	99,28	98,23	99,34	99,00	98,24	98,69
Si				0,00	0,14	0,00			0,00			0,00		0,00	0,00	
Ti				0,00	0,00	0,01			0,00			0,00		0,00	0,00	
Al	1,17	1,09	1,19	1,12	1,15	1,10	1,29	1,54	1,29	1,31	1,75	1,73	1,38	1,41	1,42	1,40
V	0,00	0,00	0,00	0,00	0,00	0,00	0,00	0,00	0,00	0,00	0,00	0,00	0,00	0,00	0,00	0,00
Cr	0,82	0,89	0,81	0,87	0,66	0,84	0,71	0,45	0,70	0,68	0,25	0,27	0,61	0,58	0,57	0,60
Fe ₂ ⁺	0,48	0,52	0,46	0,51	0,42	0,52	0,40	0,30	0,39	0,38	0,23	0,24	0,37	0,36	0,34	0,36
Fe ₃ ⁺	0,00	0,00	0,00	0,00	0,00	0,00	0,00	0,00	0,00	0,00	0,00	0,00	0,00	0,00	0,00	0,00
Mn	0,01	0,01	0,01	0,01	0,01	0,01	0,01	0,01	0,01	0,01	0,00	0,00	0,01	0,01	0,01	0,00
Mg	0,52	0,50	0,53	0,49	0,57	0,54	0,60	0,70	0,61	0,62	0,76	0,75	0,63	0,64	0,67	0,63
Co																
Ni				0,00	0,00	0,00			0,00	0,00	0,01	0,00	0,00	0,00	0,00	0,00
Zn																
Sum	3,00	3,01	3,00	3,00	2,95	3,02	3,00	3,00	3,00	3,00	3,00	3,00	3,00	3,00	3,00	3,00
Cr/(Cr+Al)	0,41	0,45	0,40	0,44	0,36	0,43	0,36	0,23	0,35	0,34	0,13	0,13	0,31	0,29	0,29	0,30
Mg/(Mg+Fe ²⁺)	0,52	0,49	0,53	0,49	0,58	0,51	0,60	0,70	0,61	0,62	0,77	0,76	0,63	0,64	0,66	0,64

Table A5: Continued

Rock type	F	F	F	F	F	F	F	F	F	C	C	C	C	C	C	C
Sample	MM1	18LP1	18LP1	18LP1	18LP1	18LP1	18LP1	18LP1								
Comment	spl12	spl14	spl15	spl16	spl17	spl18	spl19	spl20	spl21	spl1	spl2	spl3	spl4	spl5	spl6	spl7
Text	m	m	m	m	m	min	srp	vein	srp	vein	m	in amph	m	m-core	m-rim	C-m
MgO	14,55	12,32	9,21	17,41	17,19	12,89	16,16	16,03	17,14	14,34	15,78	16,13	14,18	16,56	18,24	18,71
Al ₂ O ₃	39,81	29,40	21,43	49,46	48,91	34,92	45,04	45,17	48,02	41,40	44,63	45,43	39,56	48,29	51,59	52,00
SiO ₂	0,06	0,64	1,48	0,04	0,06	0,04	0,05	0,03	0,01	0,08	0,34	0,04	0,04	0,01	0,04	0,48
TiO ₂	0,06	0,01	0,02	0,04	bdl	bdl	0,01	0,02	bdl	0,03	0,05	bdl	0,04	0,05	bdl	0,04
Cr ₂ O ₃	28,64	37,59	37,51	19,03	19,39	33,15	23,03	23,40	20,67	26,09	22,91	23,09	29,00	20,06	16,37	16,02
MnO	0,29	0,38	0,44	0,17	0,20	0,36	0,28	0,28	0,23	0,23	0,23	0,21	0,23	0,19	0,15	0,17
FeO	15,82	19,13	23,40	12,95	13,14	17,03	14,14	14,15	13,10	16,31	15,05	14,80	16,81	13,68	11,92	11,60
CoO	bdl	bdl	bdl	bdl	bdl											
NiO	0,06	0,06	3,66	0,18	0,15	0,17	0,09	0,13	0,18	0,10	0,07	0,10	0,11	0,17	0,32	0,30
ZnO	bdl	bdl	bdl	bdl	bdl											
Fe ₂ O ₃	bdl	bdl	bdl	bdl	bdl											
Sum	99,28	99,53	97,15	99,28	99,04	98,56	98,80	99,20	99,36	98,57	99,06	99,80	99,97	99,01	98,63	99,32
Si	0,00	0,02	0,05	0,00			0,00	0,00		0,00	0,01	0,00	0,00	0,00	0,00	0,01
Ti	0,00	0,00	0,00	0,00			0,00	0,00		0,00	0,00		0,00	0,00		0,00
Al	1,34	1,05	0,83	1,58	1,57	1,22	1,48	1,48	1,55	1,40	1,47	1,48	1,33	1,56	1,64	1,64
V	0,00	0,00	0,00	0,00	0,00	0,00	0,00	0,00	0,00	0,00	0,00	0,00	0,00	0,00	0,00	0,00
Cr	0,65	0,90	0,97	0,41	0,42	0,78	0,51	0,51	0,45	0,59	0,51	0,51	0,66	0,44	0,35	0,34
Fe ₂ ⁺	0,38	0,48	0,64	0,29	0,30	0,42	0,33	0,33	0,30	0,39	0,35	0,34	0,40	0,31	0,27	0,26
Fe ₃ ⁺	0,00	0,00	0,00	0,00	0,00	0,00	0,00	0,00	0,00	0,00	0,00	0,00	0,00	0,00	0,00	0,00
Mn	0,01	0,01	0,01	0,00	0,00	0,01	0,01	0,01	0,01	0,01	0,01	0,01	0,00	0,01	0,00	0,00
Mg	0,62	0,55	0,45	0,71	0,70	0,57	0,67	0,66	0,70	0,61	0,66	0,67	0,60	0,68	0,73	0,74
Co																
Ni	0,00	0,00	0,10	0,00	0,00	0,00	0,00	0,00	0,00	0,00	0,00	0,00	0,00	0,00	0,01	0,01
Zn																
Sum	3,00	3,01	3,05	3,00	3,00	3,00	3,00	3,00	3,00	3,00	3,00	3,00	3,00	3,00	3,00	3,00
Cr/(Cr+Al)	0,33	0,46	0,54	0,21	0,21	0,39	0,26	0,26	0,22	0,30	0,26	0,25	0,33	0,22	0,18	0,17
Mg/(Mg+Fe ²⁺)	0,62	0,53	0,41	0,71	0,70	0,57	0,67	0,67	0,70	0,61	0,65	0,66	0,60	0,68	0,73	0,74

Table A6: Major elements compositions (wt%) of apatite. Formula based on 26 O, OH, F, Cl.

Rock Type	P	F	F
-----------	---	---	---

Sample	KL24-2B	VM10A	VM10A
Mineral	ap	ap	ap
Text. Pos.	in spl (PA)	in ol	in ol
Spot	170	174	175
Sample	KL2.4-2b_ap1	VM10A_ap1	VM10A_ap2
P ₂ O ₅	39.99	39.57	40.68
CaO	52.43	53.45	54.72
SrO	0.35	0.21	0.00
FeO	0.48	0.41	0.20
MgO	0.18	bdl	bdl
Cl	4.92	5.57	5.31
Tot	98.35	99.21	100.91
O=F	0	0	0
O=Cl	1.11	1.26	1.20
Tot*	97.24	97.95	99.71
P	6.04	5.96	5.99
Ca	10.01	10.18	10.20
Sr	0.04	0.02	0.00
Fe	0.07	0.06	0.03
Mg	0.05		
Cl	0.14	1.68	1.57
Sum	16.34	17.90	17.79

Table A7: Major elements compositions (wt%) of serpentine.

Sample name	KL2.4-2B srp1	KL2.4-2B _srp2	KL2.4-2B srp3	KL2.4-2B srp4	KL2.4-2B _srp1	KL2.4-2B srp2	KL1-A srp1	KL2.4-3 srp1	KL2.4-3 srp2	KL2.4-3 srp3	MM1 srp2	MM1 srp3	MM1 srp4	MM1 srp5
Text. Pos.	mesh	mesh	mesh	mesh	mesh	mesh	vein	mesh	mesh	mesh	vein	vein	vein	vein
No.	107	108	109	116	307	325	449	33	41	52	20	24	28	42
F	0,02	0,04	0,04	0,04	0,03	0,03	0,06	0,01	0,03	0,05	0	0,001	0	0
Na ₂ O	0,00	0,02	0,02	0,03	0,00	0,03	0,03	0,00	0,10	0,01	0,018	0	0,008	0,009
Cl	0,05	0,27	0,20	0,05	0,06	0,07	0,15	0,07	0,03	0,09	0,12	0,198	0,115	0,064
TiO ₂	0,01	0,09	0,09	0,06	bdl	0,04	0,82	0,03	0,00	0,00	0,007	0,036	0	0
MnO	0,06	0,39	0,32	0,11	0,12	0,18	0,11	0,12	0,00	0,30	0	0,052	0,029	0,056
MgO	36,36	31,96	31,01	38,85	39,89	39,05	38,91	38,73	31,68	38,39	41,03	38,59	39,14	39,53
CaO	0,01	0,00	0,00	0,01	bdl	bdl	0,02	0,03	0,05	0,07	0,014	0,083	0	0,021
Cr ₂ O ₃	0,00	0,08	0,03	0,01	bdl	bdl	0,00	0,03	0,05	0,01	0	0,234	0	0,036
FeO	3,33	9,02	8,60	4,87	3,72	4,98	4,84	3,73	1,53	3,36	1,87	2,27	2,74	2,02
Al ₂ O ₃	0,08	1,27	1,41	0,04	0,49	bdl	0,03	0,22	2,15	1,48	0	1,125	0,427	0,129
K ₂ O	0,02	0,16	0,13	0,01	0,01	bdl	0,04	bdl	0,10	0,00	0	0	0	0,006
BaO	0,01	bdl	0,07	bdl	0,03	bdl	0,09	bdl	bdl	bdl	0,024	0,006	0,015	0,04
NiO	0,27	0,07	0,21	0,26	bdl	0,33	0,33	0,33	0,10	0,20	0,077	0,025	0,054	0,207
SiO ₂	40,27	34,72	33,30	39,01	40,02	35,96	38,38	40,97	55,77	40,47	42,07	41,11	44,03	42,05
Sum	80,48	78,09	75,41	83,35	84,37	80,67	83,80	84,27	91,59	84,44	85,231	83,731	86,558	84,169

Sample name	MM1 srp6	MM1 srp7	MM1 srp8	MM1 srp9	MM1 srp10	MM1 srp11	MM1 srp12	MM1 srp13	MM1 srp14	18LP1 srp1	18LP1 srp2	18LP1 srp3	18LP1 srp4	18LP1 srp5
Text. Pos.	vein	vein	vein	vein	vein	vein	vein	vein	vein	vein	vein	vein	vein	vein
No.	43	44	45	46	49	58	62	63	64	150	154	155	157	158
F	0	0	0	0	0	0	0	0	0	0	0	0	0	0,01
Na ₂ O	0,033	0,016	0,012	0,007	0	0	0	0,013	0	0,006	0	0	0,009	0
Cl	0,086	0,054	0,066	0,154	0,047	0,102	0,111	0,104	0,143	0,035	0,021	0,068	0,037	0,036
TiO ₂	0	0,011	0,018	0	0,017	0,05	0,029	0	0,023	0,032	0	0	0,018	0,011
MnO	0,069	0,041	0,055	0	0,024	0,128	0,069	0,047	0,058	0,247	0,14	0,067	0,021	0
MgO	39,46	39,87	39,68	39,06	38,51	38,01	39,51	39,29	38,9	32,53	35,27	40,41	40,7	41,48
CaO	0,017	0,02	0,027	0,019	0,003	0,036	0,049	0,084	0,022	0,229	0,014	0,031	0,035	0,011
Cr ₂ O ₃	0,024	0,043	0	0	0	0	0,152	0,089	0,313	0,005	0,007	0,033	0,027	0
FeO	2,1	1,87	1,96	2,48	2,23	2,34	2,02	1,98	2,25	10,45	7,42	2,9	1,91	1,34
Al ₂ O ₃	0,194	0,347	0,264	0,214	0,175	0,148	0,509	0,572	1,366	1,013	0,303	0,336	0,068	0,079
K ₂ O	0	0	0,011	0	0	0	0	0	0	0,012	0	0	0,004	0,006
BaO	0,015	0	0	0	0,022	0,025	0,038	0	0	0	0	0	0	0,069
NiO	0,19	0,198	0,184	0,191	0,118	0,176	0,188	0,241	0,172	0,056	0,025	0,122	0	0,029
SiO ₂	42,15	41,81	41,17	41,39	41,25	41,01	41,76	41,71	42,05	41,32	42,42	41,25	42,22	42,99
Sum	84,339	84,281	83,448	83,514	82,396	82,026	84,435	84,131	85,298	85,936	85,62	85,216	85,049	86,061

Table A8: Major elements compositions (wt%) of chlorite and phlogopite.

<i>Rock type</i>	<i>F</i>	<i>F</i>	<i>F</i>	<i>F</i>	<i>C</i>	<i>F</i>	<i>F</i>	<i>F</i>	<i>F</i>	<i>F</i>	<i>F</i>	<i>F</i>	<i>F</i>
<i>Sample</i>	<i>MM1</i>	<i>MM1</i>	<i>MM1</i>	<i>MM1</i>	<i>18LP1</i>	<i>18LP1</i>	<i>18LP1</i>	<i>18LP1</i>	<i>18LP1</i>	<i>18LP1</i>	<i>18LP1</i>	<i>18LP1</i>	<i>KL1-A</i>
<i>Mineral</i>	<i>phl</i>	<i>phl</i>	<i>chl</i>	<i>chl</i>	<i>chl</i>	<i>chl</i>	<i>chl</i>	<i>chl</i>	<i>chl</i>	<i>chl</i>	<i>phl</i>	<i>phl</i>	<i>chl</i>
<i>Comment</i>	<i>phl2</i>	<i>phl2 new</i>	<i>chl1</i>	<i>chl2</i>	<i>chl1</i>	<i>chl4</i>	<i>chl4/2</i>	<i>chl5</i>	<i>chl6</i>	<i>chl7</i>	<i>phl1</i>	<i>phl2</i>	<i>chl1</i>
	<i>m</i>	<i>m</i>	<i>m</i>	<i>m</i>	<i>opx rim - vein</i>	<i>in vein</i>	<i>in vein</i>	<i>in vein</i>	<i>m</i>				
Na ₂ O	0,05	0,04	0,02	bdl	bdl	bdl	0,03	bdl	0,01	bdl	0,11	0,13	0,03
MgO	28,33	28,32	32,16	32,27	31,65	31,56	31,47	32,24	31,61	32,69	25,88	25,53	32,50
Al ₂ O ₃	14,49	15,07	20,04	19,06	19,08	19,38	19,40	19,91	19,41	16,52	14,90	14,63	18,62
SiO ₂	35,22	37,04	29,85	30,71	30,38	29,75	29,55	29,96	30,11	31,13	39,25	40,19	30,96
K ₂ O	4,96	5,22	bdl	bdl	0,01	0,04	0,04	0,01	0,04	0,01	8,03	8,35	bdl
CaO	bdl	bdl	bdl	0,01	0,04	0,01	bdl	0,01	bdl	0,04	bdl	bdl	0,10
TiO ₂	0,15	0,13	0,03	0,06	0,06	0,01	bdl	0,01	0,02	0,05	0,15	0,21	0,03
Cr ₂ O ₃	1,10	1,14	1,06	0,69	1,39	1,24	1,08	1,26	1,28	1,92	0,78	0,57	0,67
MnO	0,02	0,05	0,00	0,02	0,03	0,03	0,03	0,02	0,02	0,01	0,02	0,01	0,04
FeO	4,72	5,03	2,22	2,26	2,55	2,46	2,65	2,53	2,50	2,37	2,84	3,45	2,91
NiO	1,16	0,53	0,17	0,15	0,15	0,17	0,17	0,18	0,17	0,23	0,21	0,17	0,20
BaO	0,19	0,13	bdl	bdl	0,04	bdl	0,01	bdl	0,01	0,03	0,21	0,21	bdl
F	0,04	0,04	0,05	0,05	bdl	0,01	0,03	0,06	0,01	bdl	bdl	0,00	bdl
Cl	0,19	0,20	0,04	0,02	0,04	0,02	0,03	0,03	0,05	0,05	0,15	0,20	0,02
O ≡ F,Cl	-0,06	-0,06	-0,03	-0,03	-0,01	-0,01	-0,02	-0,03	-0,02	-0,01	-0,03	-0,04	0,00
Sum	90,57	92,86	85,62	85,28	85,41	84,66	84,46	86,20	85,21	85,02	92,48	93,61	86,08
Si	2,62	2,67	2,85	2,94	2,92	2,88	2,87	2,85	2,90	3,01	2,83	2,87	2,95
Ti	0,01	0,01	0,00	0,00	0,00	0,00	0,00	0,00	0,00	0,00	0,01	0,01	0,00
Al	1,27	1,28	2,26	2,15	2,16	2,21	2,22	2,23	2,20	1,88	1,27	1,23	2,09
Cr	0,06	0,06	0,08	0,05	0,11	0,10	0,08	0,09	0,10	0,15	0,04	0,03	0,05
Fe ²⁺	0,29	0,30	0,18	0,18	0,20	0,20	0,22	0,20	0,20	0,19	0,17	0,21	0,23
Mn	0,00	0,00	0,00	0,00	0,00	0,00	0,00	0,00	0,00	0,00	0,00	0,00	0,00
Mg	3,14	3,04	4,58	4,61	4,53	4,56	4,56	4,58	4,53	4,71	2,78	2,72	4,62
Ca	0,00	0,00	0,00	0,00	0,00	0,00	0,00	0,00	0,00	0,00	0,00	0,00	0,01
Na	0,01	0,01	0,00	0,00	0,00	0,00	0,01	0,00	0,00	0,00	0,02	0,02	0,01
K	0,47	0,48	0,00	0,00	0,00	0,00	0,00	0,00	0,00	0,00	0,74	0,76	0,00
Ni	0,07	0,03	0,01	0,01	0,01	0,01	0,01	0,01	0,01	0,02	0,01	0,01	0,02
Zn	0,00	0,00	0,00	0,00	0,00	0,00	0,00	0,00	0,00	0,00	0,00	0,00	0,00
Ba	0,01	0,00	0,00	0,00	0,00	0,00	0,00	0,00	0,00	0,00	0,01	0,01	0,00
F	0,01	0,01	0,01	0,02	0,00	0,00	0,01	0,02	0,00	0,00	0,00	0,00	0,00
Cl	0,02	0,02	0,01	0,00	0,01	0,00	0,00	0,01	0,01	0,01	0,02	0,02	0,00
Sum	7,98	7,93	10,00	9,97	9,95	9,97	9,99	10,00	9,97	9,98	7,90	7,90	9,98
Al IV	2,38	2,33	2,15	2,06	2,08	2,12	2,13	2,15	2,10	1,99	2,17	2,13	2,05
Al VI	-	-	0,11	0,09	0,08	0,09	0,09	0,09	0,10	-	0,20	0,21	0,04
A site	0,48	0,49	0,01	0,00	0,00	0,01	0,01	0,00	0,01	0,00	0,75	0,78	0,03

Table A9. ⁸⁷Sr/⁸⁶Sr values and 2se of reference material analyzed during carbonate isotopic analyses (Weber et al., 2019)

<i>Analysis</i>	<i>Sample</i>	<i>⁸⁷Sr/⁸⁶Sr</i>	<i>2se</i>
Line1	nanopellet	0.70755	0.00003
Spot8	nanopellet	0.70756	0.00013
Spot33	nanopellet	0.70757	0.00014
Spot9	seashell	0.70917	0.00005
Spot10	seashell	0.70915	0.00004
Spot18	seashell	0.70916	0.00005
Spot19	seashell	0.70914	0.00005
Spot31	seashell	0.70918	0.00006
Spot32	seashell	0.70914	0.00005
Spot34	seashell	0.70917	0.00008

Spot35	seashell	0.70924	0.00007
Spot40	seashell	0.70910	0.00005
Spot48	seashell	0.70920	0.00005
Spot49	seashell	0.70917	0.00009
Spot54	seashell	0.70916	0.00006
Spot55	seashell	0.70917	0.00006
Spot56	seashell	0.70919	0.00007
Spot62	seashell	0.70920	0.00006
Spot65	seashell	0.70920	0.00005
Spot66	seashell	0.70922	0.00006
Spot68	seashell	0.70919	0.00007
Spot69	seashell	0.70915	0.00006

B. Supplementary Material of Chapter 5

Supplementary annotation B1: Trace elements composition of the main peridotite-forming minerals

Olivine shows a REE sub-chondritic pattern, excepting for one matrix olivine enriched in La. This olivine exhibits also an enrichment in Li, Be, Ba, Pb, Th, U and Ce. A positive Pb and weak positive Li anomalies characterize all the olivine crystals analyzed. The coarse olivine in coarse-grained peridotite MOL1-C is more depleted in LILE and HFSE (excepting in some instances for elements such as Pb, La and Ce) with respect to the matrix olivine in fine-grained samples. The systematic change of Li according to the different metamorphic stages of the peridotites agrees with the work of Scambelluri et al. (2006).

The coarse **orthopyroxenes** in samples MOL1-C and 18LP1 show a spoon-shaped REE pattern. The REE, LILE and HFSE contents are higher for coarse orthopyroxene respect to the matrix orthopyroxenes occurring in fine-grained samples, occasionally excepting for Hf and Sm. LILE and HFSE in matrix dolomite are always below the Primitive Mantle values with occasionally exception of Ba, Pb and weak positive anomalies for U and Sc.

The REE content of **spinel** is commonly below the detection limit. Matrix coarse spinel in MOL1-C sample shows strong positive anomaly for Ba and Pb.

Amphibole in all microstructural textures shows typical spoon-shaped REE patterns with more flattened pattern for matrix coarse amphibole in MOL1-C and tremolitic amphibole in vein in 18LP1. It exhibits a LREE enriched pattern with variable degree of enrichment in LREE compared to MREE ($La_N/Gd_N=1.61-8.99$). Hornblenditic amphibole from fine-grained peridotites MM1 and MM1B shows an enrichment in LREE and large LREE/HREE fractionation with respect to the coarse hornblenditic amphibole from MOL1-C sample and tremolitic amphibole in vein from 18LP1 sample. Amphibole is always characterized by flat HREE pattern. As suggested by Scambelluri et al. (2006), the high HREE suggest that amphibole is not in equilibrium with garnet. This can be explained by the amphibole formation during a retrogression stage or by the lack of achievement of garnet stability field during the evolution of peridotites (i.e. for coarse grained spinel peridotite MOL1-C). All amphiboles display a high LILE content with $Ba_N > Rb_N$ and $U_N > Th_N$, with distinct positive anomaly for Ba and Pb.

Matrix **garnet** surrounded by a kelyphitic corona in the sample VM10A shows typical LREE depletion ($La_N/Yb_N \ll 1$). All the analyses exhibit positive Ba, Pb and U anomalies and negative Sr and Ti anomalies (consistent with matrix garnet reported by Sapienza et al., 2009).

Apatite shows an enrichment of LREE over REE ($La_N/Yb_N = 218-5239$). It is strongly enriched in Ba, Pb Th and U. Cl-apatite included in coarse spinel as polycrystalline aggregates with calcite/brucite

intergrowths + pentlandite + relic dolomite shows higher HREE than the other textural position, with the exception of the negative anomaly of Yb. The lowest HREE in apatite occurs when it is included in zircon together with dolomite. Overall, Th content ranges from 0.6 to 20.5 ppm and U from 0.1 up to 13.9ppm when it is included in coarse spinel.

Respect to the apatite reported by [Sapienza et al. \(2009\)](#), it exhibits also positive anomalies for HREE and HFSE.

The **chlorite** REE pattern show very low concentration of REE and HFSE. Positive anomalies for Ba and Pb.

Phlogopite was analyzed only in the sample MOL1-C. The HREE contents are low and commonly below detection limit. However, it shows a positive spike for Li, Rb, Ba, Nb, Ta, Sr and Ti.

Table B1: Trace element concentrations of olivine

type Mount Sample Mineral Texture Name #	FGA			CS							CG					
	VM25P10A ol m-w/zr 1ol1 4	VM25P10A ol m-w/zr 1ol2 5	VM25P10A ol m-w/zr 1ol3 6	MOL1-C ol 2ol1 17	MOL1-C ol 2ol2 18	MOL1-C ol 2ol3 19	MOL1-C ol 2ol4 20	MOL1-C ol 2ol5 21	MOL1-C ol large ol1a 22	RUN3 ol large ol1b 23	RUN3 ol ol2a 26	RUN3 ol ol2b 27	18LP1 ol w/do vein 3ol1 15	18LP1 ol w/dovein 7ol1 26		
SIMS spot	Ol1#2	Ol1#5	Ol1#													
Li7	4,13	3,48	3,81	2,20	2,75	4,79	5,60	2,45	1,76	1,83	1,92	1,86	5,06	6,80		
Be9	<0.00	<0.00	<0.00	<0.00	<0.00	<0.00	<0.00	<0.00	<0.00	<0.00	<0.00	<0.00	<0.00	<0.00		
B11	14,10	12,92	14,71	11,59	14,5	14,8	13,2	14,7	7,12	6,69	7,99	7,78	23,2	15,5		
Na23	1,32	<0.88	<0.72	<0.61	<0.81	308	<0.72	0,75	na	na	na	na	4,28	<0.82		
Al27	2,97	0,52	1,79	0,62	2,62	0,65	1,16	1,64	6,00	0,31	0,24	0,44	155	1,71		
K39	<2.01	<2.22	<1.79	<1.62	<2.10	4,76	<1.86	<1.71	na	na	na	na	5,95	<1.96		
Ca43	<36.6	<37.7	<33.3	32,9	<38.6	<26.6	<29.1	35,16	16,08	7,05	<5.78	<6.78	85,6	<32.6		
Ca44	102	94,8	86,2	59,4	71,7	78,5	59,3	59,9	81,85	74,7	85,48	80,7	135	29,58		
Sc45	1,21	1,16	1,09	1,39	1,36	1,15	1,06	1,23	1,15	1,17	1,13	1,10	1,78	1,37		
Ti47	25,5	9,78	11,74	7,68	8,03	3,93	6,89	4,75	11,51	8,95	3,40	3,38	7,08	6,59		
V51	0,45	0,17	0,20	0,33	0,28	0,11	0,20	0,27	0,28	0,25	0,23	0,20	1,73	0,37		
Cr53	3,46	<2.32	3,31	5,74	13,6	2,26	4,89	7,23	2,19	4,97	4,48	4,34	49,58	3,16		
Mn55	1017	1033	1037	935	946	992	935	954	1012	1008	1062	1050	981,6	999		
Co59	151	151	148	161	167	160	166	170	154	156,76	164	165	142	151		
Ni60	3101	3080	3026	3472	3528	3190	3458	3563	4255	4291	3781	3785	2746	2852		
Cu63	<0.05	<0.05	<0.03	<0.03	<0.06	0,11	0,05	0,04	0,01	0,02	<0.003	<0.004	10,78	<0.05		
Zn66	29,1	26,8	27,3	75,2	74,4	55,1	59,47	70,03	19,20	21,5	61,2	59,8	35,2	33,2		
Rb85	<0.02	<0.01	0,01	<0.01	0,01	<0.01	<0.01	<0.012	0,00	<0.002	0,00	0,01	<0.02	<0.02		
Sr88	<0.00	0,00	<0.00	0,00	0,00	1,25	0,00	0,03	0,00	<0.00	0,01	0,00	0,26	<0.00		
Y89	<0.00	0,00	<0.00	<0.00	<0.00	0,00	<0.00	0,00	0,00	0,00	0,00	0,00	0,00	<0.01		
Zr90	<0.00	<0.00	0,02	0,03	0,01	<0.00	<0.00	0,02	0,00	0,00	0,00	0,00	0,03	0,00		
Nb93	0,05	0,01	0,02	<0.00	0,00	<0.01	<0.00	0,00	<0.00	0,00	0,00	0,00	0,01	0,00		
Mo95	0,08	0,16	0,16	0,09	<0.05	0,12	0,15	0,11	0,11	0,12	0,11	0,14	0,06	0,06		
Cs133	<0.01	<0.01	<0.01	<0.01	<0.01	<0.01	<0.01	<0.01	na	na	na	na	<0.01	<0.01		
In	na	na	na	na	na	na	na	na	0,00	0,00	0,00	0,00	na	na		
Ba138	0,00	0,01	0,01	<0.00	<0.00	0,90	0,01	0,02	<0.00	0,00	0,00	0,00	0,25	<0.00		
La139	<0.00	<0.00	0,01	0,00	0,00	0,00	<0.00	0,01	0,00	0,00	0,00	0,00	0,05	<0.00		
Ce140	<0.00	<0.00	0,00	0,00	0,00	0,02	0,00	0,02	<0.00	<0.00	0,00	0,00	0,08	<0.00		
Pr141	<0.00	<0.00	<0.00	<0.00	<0.00	<0.00	<0.00	<0.00	<0.00	<0.00	0,00	<0.00	0,00	0,00		
Nd146	<0.00	0,01	<0.00	<0.00	<0.00	<0.00	<0.03	<0.00	<0.00	<0.00	0,00	0,00	<0.00	<0.00		
Sm149	0,01	<0.00	<0.00	<0.00	<0.00	<0.00	<0.00	<0.00	<0.00	<0.00	<0.00	<0.00	<0.00	<0.00		
Eu151	<0.02	<0.00	<0.00	<0.00	<0.00	<0.00	<0.00	<0.00	<0.00	<0.00	<0.00	<0.00	<0.00	0,00		
Gd157	<0.04	<0.00	<0.00	<0.00	<0.00	<0.00	<0.00	<0.00	<0.00	<0.00	<0.00	<0.00	<0.00	<0.00		
Tb159	<0.00	<0.00	<0.00	<0.00	<0.00	<0.00	<0.00	<0.00	<0.00	<0.00	0,00	<0.00	<0.00	<0.00		
Dy163	<0.00	<0.00	<0.00	<0.00	<0.00	<0.00	<0.00	<0.00	<0.00	0,00	<0.00	<0.00	<0.00	0,01		
Ho165	<0.00	<0.00	<0.00	<0.00	<0.00	<0.00	<0.00	<0.00	<0.00	<0.00	<0.00	<0.00	<0.00	0,00		
Er167	<0.00	<0.00	<0.00	<0.00	<0.00	<0.00	<0.00	<0.00	0,00	<0.00	<0.00	<0.00	<0.00	<0.00		
Tm169	0,00	<0.00	<0.00	<0.00	<0.00	<0.00	<0.00	<0.00	0,00	<0.00	<0.00	<0.00	<0.00	<0.00		
Yb173	<0.00	<0.00	<0.00	<0.00	<0.00	<0.00	<0.00	<0.00	0,00	0,00	0,00	0,00	<0.00	<0.00		
Lu175	<0.00	<0.00	0,00	<0.00	<0.00	<0.00	0,00	<0.00	0,00	0,00	0,00	0,00	0,00	<0.00		
Hf177	<0.00	<0.00	<0.00	<0.00	<0.00	<0.00	<0.00	<0.03	<0.00	<0.00	<0.00	<0.00	<0.00	<0.00		
Ta181	<0.00	<0.00	<0.00	0,00	<0.00	<0.00	0,00	<0.00	<0.00	<0.00	0,00	<0.00	<0.00	<0.01		
W182	<0.00	0,01	0,01	<0.00	<0.00	0,12	<0.00	0,05	na	na	na	na	0,02	<0.00		
Pb208	0,04	<0.03	0,05	<0.023	<0.03	1,49	<0.04	<0.02	0,01	0,00	0,01	0,01	0,40	0,01		
Th232	<0.00	<0.00	0,00	0,00	<0.00	0,00	<0.00	0,03	<0.00	0,00	0,00	0,00	0,09	<0.00		
U238	<0.00	0,00	0,00	0,00	0,00	<0.00	<0.00	0,05	<0.00	0,00	0,01	0,00	0,02	<0.00		

Table B1. Continued.

Type	FGA					FSA								
Mount	KL1-A	KL1-A	KL1-A	KL1-A	KL1-A	RUN1	RUN1	RUN1	RUN2	RUN2	RUN2	RUN2	RUN5	
Sample	KL1-A	KL1-A	KL1-A	KL1-A	KL1-A	MM1	MM1	MM1	MM1B	MM1B	MM1B	MM1B	VM10A	
Mineral	ol	ol	ol	ol	ol	ol	ol	ol	ol	ol	ol	ol	ol	
Texture	m	m	matrix-fine	matrix-fine	matrix-fine	matrix	matrix	matrix	matrix	matrix	matrix	matrix	matrix	
Name	2ol1	2ol2	1ol1	1ol1	1ol2	ol1a	ol1b	ol1c	ol1a	ol1b	ol2a	ol2b	ol1	
#	19	20	25	5	7	8	9	10	14	15	27	28	19	
Li7	7,03	5,38	4,92	3,87	4,56	5,02	5,57	2,99		5,34	4,50	5,15	6,73	
Be9	<0.00	<0.00	<0.00	<0.00	<0.00	0,03	<0.00	0,05	<0.00	<0.00	<0.00	<0.00	<0.00	
B11	13,98	17,63	13,29	40,74	39,1	18,0	18,63	23,9	9,37	9,78	9,29	9,34	7,87	
Na23	<0.73	41,82	<0.90	<0.60	10,8	na	na	na	na	na	na	na	na	
Al27	1,68	2,41	2,47	1,54	3,70	47,18	56,71	4036,52	1,11	1,90	2,16	2,95	5,98	
K39	<1.80	<2.12	<2.25	<1.64	<1.78	na	na	na	na	na	na	na	na	
Ca43	37,87	<32.8	<42.5	38,4	52,5	81,5	61,9	658	41,1	55,2	59,3	35,1	48,7	
Ca44	47,51	56,23	62,33	50,8	41,6	75,8	68,2	648	86,5	105	92,7	96,6	150	
Sc45	1,27	1,41	1,13	1,55	1,53	1,31	1,19	4,52	1,44	1,48	1,09	1,21	2,66	
Ti47	29,8	30,2	24,20	14,1	30,7	11,0	5,60	74,3	11,7	15,8	13,60	16,51	28,6	
V51	0,44	0,48	0,51	0,40	0,47	0,39	0,36	26,1	0,24	0,27	0,30	0,38	0,39	
Cr53	6,42	5,87	4,87	2,83	3,20	10,6	11,1	686	4,67	6,45	4,63	5,17	3,61	
Mn	1146	1172	931	977	1023	1128	1120	985	1080	1082	1069	1085	1604	
Co	163	164	160	156	163	137	135	66,8	147	1467	139	144	173	
Ni	3151	2981	3280	3147	3333	3397	3322	1454	3518	3526	3161	3223	4086	
Cu	<0.05	<0.06	<0.05	<0.05	<0.05	0,06	0,11	0,47	<0.003	0,01	0,02	<0.003	<0.004	
Zn	79,7	81,1	47,5	53,1	54,7	30,0	29,3	26,8	24,8	25,6	23,1	23,5	22,1	
Rb	<0.02	<0.01	<0.02	<0.01	<0.01	0,01	0,00	0,64	0,00	<0.002	<0.002	<0.002	0,00	
Sr	<0.01	0,01	<0.01	0,00	0,01	0,11	0,04	0,47	<0.001	0,00	0,02	0,00	<0.00	
Y	0,00	0,00	0,00	0,00	0,00	0,00	0,00	0,04	0,00	0,00	0,00	0,00	<0.00	
Zr	<0.02	0,02	0,01	<0.00	0,01	0,01	0,01	0,18	0,01	0,01	0,01	0,00	0,00	
Nb	0,01	0,04	0,02	0,01	0,03	0,04	0,02	0,06	0,02	0,04	0,05	0,06	0,07	
Mo	0,06	0,12	0,05	0,05	0,05	0,13	0,08	0,10	0,12	0,10	0,11	0,12	0,16	
Cs	<0.01	0,04	<0.01	<0.01	<0.01	na	na	na	na	na	na	na	na	
In	na	na	na	na	na	0,00	0,00	0,00	0,00	0,00	0,00	<0.0004	<0.0003	
Ba	0,01	0,03	<0.00	<0.00	0,02	0,01	0,01	0,35	0,00	0,00	0,06	0,00	<0.00	
La	0,00	0,00	<0.00	<0.00	<0.00	0,05	0,02	0,56	0,00	<0.00	0,00	0,00	<0.00	
Ce	<0.01	0,00	<0.00	<0.00	<0.00	0,06	0,01	0,64	<0.001	<0.0001	0,00	0,00	<0.00	
Pr	0,00	<0.00	<0.00	<0.00	<0.00	0,00	<0.00	0,04	<0.0002	<0.00	0,00	<0.00	<0.00	
Nd	<0.00	<0.00	<0.00	<0.00	<0.00	0,01	0,00	0,13	<0.001	<0.00	0,00	<0.00	<0.00	
Sm	0,01	<0.00	<0.00	<0.00	<0.00	<0.001	<0.00	0,01	<0.001	<0.00	<0.001	<0.00	0,00	
Eu	<0.00	<0.00	<0.00	<0.00	<0.00	<0.00	<0.00	0,00	<0.0004	<0.00	0,00	0,00	<0.00	
Gd	<0.00	<0.00	<0.00	<0.00	<0.00	<0.00	<0.00	0,00	<0.001	0,00	<0.00	<0.00	<0.00	
Tb	<0.00	<0.00	<0.00	<0.00	<0.00	<0.00	<0.00	0,00	<0.00	<0.00	<0.00	<0.00	<0.00	
Dy	<0.00	<0.00	<0.00	<0.00	<0.00	<0.00	<0.00	0,00	<0.00	0,00	<0.00	<0.00	<0.00	
Ho	<0.00	<0.00	<0.00	<0.00	<0.00	0,00	<0.00	0,00	<0.00	<0.00	<0.00	0,00	0,00	
Er	<0.00	0,01	<0.00	<0.00	<0.00	<0.00	<0.00	0,01	<0.00	0,00	<0.00	<0.00	<0.00	
Tm	<0.01	<0.00	<0.01	<0.00	<0.00	<0.00	<0.00	<0.0001	0,00	0,00	0,00	<0.0002	<0.00	
Yb	0,01	<0.043	<0.00	<0.00	<0.00	<0.00	<0.0004	0,02	0,00	0,00	0,00	0,01	0,01	
Lu	<0.01	<0.00	<0.00	0,00	<0.00	0,00	0,00	0,00	<0.00	0,00	0,00	0,00	0,00	
Hf	<0.00	<0.00	<0.00	<0.00	<0.00	<0.00	<0.00	0,01	0,00	0,00	<0.00	<0.00	<0.00	
Ta	<0.00	0,00	<0.00	<0.00	0,00	<0.00	0,00	0,00	0,00	0,00	0,00	0,00	0,00	
W	<0.00	<0.00	0,03	<0.00	0,01	na	na	na	na	na	na	na	na	
Pb	0,05	0,12	<0.03	0,02	0,09	0,01	0,02	0,65	0,01	<0.002	0,00	<0.002	0,00	
Th	<0.00	<0.00	<0.00	<0.00	<0.00	0,00	0,00	0,69	0,00	0,00	0,00	<0.00	0,00	
U	<0.00	<0.00	0,01	<0.00	<0.00	<0.0002	0,00	0,06	<0.0002	<0.0003	0,00	0,00	<0.0002	

Table B2. Trace element concentrations of orthopyroxene

type	CS		FGA						FSA						
	RUN3	RUN3	RUN3	RUN3	RUN4	RUN4	RUN5	RUN5	KL1A	KL1A	KL1A	RUN2	RUN2	RUN2	RUN2
Sample	MOL1-C	MOL1-C	MOL1-C	MOL1-C	18LP1	18LP1	VM10A	VM10A	KL1A	KL1A	KL1A	MM1B	MM1B	MM1B	MM1B
Mineral	large	large	large	large	large	large	matrix								
Name	opx1a	opx1b	opx2a	opx2b	opx1a	opx1b	opx1a	opx1b	2opx1	1opx1	1opx2	opx1a	opx1b	opx2a	opx2b
#	5	6	24	25	18	19	15	16	22	4	6	17	18	19	20
Li	1,45	1,60	2,34	2,54	3,40	3,84	6,02	5,43	2,46	1,17	1,83	1,20	1,53	7,04	7,61
Be	0,07	0,09	0,14	0,20	0,10	0,05	<0.00	<0.00	<0.00	0,06	<0.00	0,15	0,05	<0.00	<0.00
B	8,63	7,69	6,91	7,48	3,91	3,70	9,76	7,51	10,6	25,1	26,6	7,83	7,49	12,4	11,4
Na	na	na	na	na	na	na	na	na	10,0	20,5	36,8	na	na	na	na
K	na	na	na	na	na	na	na	na	<2.48	<2.03	12,9	na	na	na	na
Sc	10,3	13,2	20,5	21,3	12,6	14,4	1,60	1,54	5,11	6,78	6,47	8,11	7,80	1,84	1,81
Ti	120	152	248	246	104	111	7,78	8,84	262	315	355	131	128	18,1	22,0
V	81,6	99,3	116	116	104	107	0,27	0,40	48,5	53,5	62,5	58,6	59,6	0,65	0,62
Cr	3123	3180	4398	3766	2805	2587	2,18	3,97	1223	932	1217	1280	1243	9,63	12,9
Mn	1281	1253	1171	1191	1175	1205	1535	1539	1007	936	1114	1087	1073	1571	1557
Co	53,1	59,3	61,8	58,7	53,90	52,4	198	197	53,2	48,8	53,4	47,9	47,7	206	203
Ni	498	619	767	742	654	637	4214	4100	574	501	584	542	549	4720	4673

Supplementary Material • CHAPTER 5

Cu	0,31	0,05	0,58	0,22	0,21	0,12	<0.01	<0.01	<0.07	<0.05	0,06	0,02	0,05	<0.01	0,01
Zn	145	242	58,4	58,3	52,2	38,9	27,8	29,02	54,2	47,1	61,3	26,6	28,2	33,4	33,2
Rb	0,39	0,42	0,34	0,52	0,03	0,04	<0.01	0,02	<0.02	<0.01	0,14	<0.002	0,14	0,00	0,02
Sr	2,45	1,39	4,47	4,19	2,24	1,97	0,75	0,55	0,03	0,04	0,12	0,06	0,17	<0.00	0,00
Y	0,37	0,27	0,63	0,56	0,18	0,27	<0.00	<0.01	0,04	0,06	0,06	0,04	0,04	0,00	0,00
Zr	0,23	0,22	0,06	0,06	0,34	0,29	0,00	0,00	0,24	0,38	0,33	0,25	0,24	0,01	0,01
Nb	0,12	0,12	0,04	0,03	0,15	0,10	0,02	0,01	0,01	0,00	0,01	0,01	0,02	0,10	0,10
Mo	0,14	0,14	0,18	0,12	0,16	0,22	0,19	0,17	0,05	<0.06	0,07	0,10	0,11	0,21	0,16
Cs	na	na	na	na	na	na	na	na	<0.01	0,00	0,07	na	na	na	na
In	0,01	0,01	0,01	0,01	0,01	0,01	0,00	<0.001	na	na	na	0,01	0,01	0,00	0,00
Ba	3,55	2,88	3,88	5,20	2,29	1,70	0,61	0,15	0,08	0,01	0,51	0,02	0,19	<0.00	0,00
La	0,14	0,15	0,13	0,14	0,18	0,13	0,04	0,00	0,00	0,00	0,01	0,00	0,02	<0.00	<0.00
Ce	0,40	0,33	0,16	0,20	0,32	0,33	0,04	0,01	0,02	0,00	0,00	0,01	0,03	<0.00	<0.00
Pr	0,05	0,04	0,01	0,02	0,04	0,04	0,00	<0.00	<0.00	0,00	0,00	0,00	0,00	0,00	<0.00
Nd	0,22	0,15	0,03	0,04	0,14	0,16	<0.004	0,00	<0.00	<0.00	0,01	0,01	0,01	0,00	<0.00
Sm	0,06	0,04	0,00	0,01	0,03	0,03	0,01	<0.00	<0.00	<0.00	0,02	0,01	0,01	<0.002	<0.00
Eu	0,02	0,01	0,01	0,00	0,01	0,01	<0.00	<0.00	<0.00	<0.00	<0.01	0,00	0,00	<0.00	<0.00
Gd	0,03	0,02	0,02	0,02	0,02	0,04	<0.00	0,00	<0.00	<0.00	<0.00	<0.00	0,01	<0.00	<0.00
Tb	0,01	0,00	0,01	0,00	0,00	0,01	<0.00	<0.00	0,00	0,00	0,00	<0.001	0,00	<0.00	<0.00
Dy	0,06	0,04	0,08	0,06	0,02	0,03	<0.004	<0.00	0,01	0,01	<0.00	0,01	0,00	<0.001	<0.00
Ho	0,01	0,01	0,02	0,02	0,01	0,01	<0.00	<0.00	0,00	<0.00	0,01	0,00	0,00	<0.00	<0.00
Er	0,05	0,04	0,10	0,09	0,03	0,03	<0.00	<0.00	<0.00	0,01	0,01	0,01	0,01	<0.00	<0.00
Tm	0,01	0,01	0,02	0,01	0,01	0,00	<0.00	0,00	0,00	0,00	<0.003	0,00	0,00	<0.0003	<0.00
Yb	0,07	0,08	0,21	0,19	0,06	0,09	0,00	0,00	<0.00	0,02	0,03	0,03	0,03	<0.00	<0.00
Lu	0,01	0,01	0,03	0,03	0,01	0,02	<0.00	0,00	<0.00	0,00	0,01	0,00	0,00	0,00	0,00
Hf	0,00	0,00	0,02	0,01	0,01	0,01	<0.00	<0.00	0,01	0,01	<0.00	0,01	0,01	<0.00	<0.00
Ta	0,01	0,00	<0.00	<0.00	0,02	0,01	<0.00	<0.00	0,00	0,00	0,00	0,00	0,00	0,00	0,00
W	na	na	na	na	na	na	na	na	<0.00	0,00	0,01	na	na	na	na
Pb	1,06	0,34	1,31	1,90	na	0,07	0,08	<0.003	<0.05	0,23	0,19	0,03	0,05	<0.002	0,01
Th	0,13	0,13	0,13	0,10	0,20	0,09	0,00	0,00	0,00	0,00	0,00	0,00	0,00	<0.00	0,00
U	0,05	0,07	0,07	0,05	0,06	0,03	0,01	0,00	<0.00	0,00	<0.00	0,01	0,01	<0.00	0,00

Table B3: Trace element concentrations of clinopyroxene

Sample	RUN4	RUN4
	18LP1	18LP1
	clinopyroxene	clinopyroxene
Texture Name	porph cpx1a	porph cpx1b
#	005	006
L17	12,8	12,3
Be9	<0.00	0,47
B11	7,74	<1.18
Al27	15606	16777
Sc45	71,6	70,2
Ti47	514	555
V51	228	235
Cr53	4195	5361
Mn55	547	498
Fe57	13162	12309
Co59	13,7	15,3
Ni60	376	368
Cu63	0,43	0,44
Zn66	21,9	33,4
Rb85	0,41	0,10
Sr88	42,1	41,2
Y89	6,07	6,07
Zr90	0,46	0,31
Nb93	0,07	0,08
Mo95	<0.02	<0.00
In115	0,01	0,03
Ba138	3,73	1,68
La139	3,99	4,13
Ce140	8,42	9,11
Pr141	0,91	0,98
Nd146	3,45	3,95
Sm147	0,36	0,63
Eu153	0,09	0,06
Gd157	0,39	0,65
Tb159	0,07	0,12
Dy163	0,91	0,72
Ho165	0,27	0,18
Er166	0,44	0,80
Tm169	0,14	0,11
Yb172	0,87	0,66
Lu175	0,13	0,15
Hf178	0,05	<0.00
Ta181	<0.002	0,01
Pb208	1,15	0,53
Th232	0,36	0,15

Table B4: Trace element concentrations of spinel

Run Sample Mineral Texture Name #	P-FGA			FSA			CS			CG			FGA		
	KL24-2B spinel in grt 2sp1 8,00	KL24-2B spinel in grt 2sp2 9,00	KL24-2B spinel in grt 3sp1 13,00	RUN1 MM1 spinel matrix spl1 17	RUN1 MM1 spinel matrix spl2a 18	RUN1 MM1 spinel matrix spl2b 19	RUN2 MM1B spinel matrix spl1a 16	RUN3 MOL1-C spinel matrix spl1 20	RUN3 MOL1-C spinel matrix spl2 21	RUN4 18LP1 spinel porph spl1a 7	RUN4 18LP1 spinel porph spl1b 8	RUN4 18LP1 spinel porph spl2 27	RUN5 VM10A spinel matrix spl1 8	RUN5 VM10A spinel matrix spl2 9	RUN5 VM10A spinel matrix spl3 22
Li7	1,30	0,82	0,74	1,12	1,47	2,00	2,58	<46.44	<7.33	4,91	4,66	5,64	0,47	0,87	0,78
Be9	<0.00	<0.69	<0.00	<0.00	0,14	0,07	<0.00	<0.00	<0.00	0,09	<0.00	<0.09	0,10	0,17	<0.00
B11	20,4	29,3	30,5	12,4	18,1	11,5	11,36	1208	473	5,54	7,18	6,65	5,11	4,70	4,89
Na23	<3.15	<3.00	<1.52	na	na	na	na	na	na	na	na	na	na	na	na
Si29	1254	1606	1711	836	1394	1843	1419	163605	163604	1580	1200	306	268	848	1456
Ca43	<170	<160	119	151	35,8	113,2	<31.3	21370	<3114	242	241	185	58,2	131	148
Ca44	64,8	<60.5	<30.6	<3.48	<4.38	<4.92	<5.02	<3065	<462	7,33	<4.46	<5.20	<4.14	<4.62	73,3
Sc45	2,56	1,52	0,75	0,06	0,12	0,22	0,13	21,1	16,2	0,09	0,14	0,10	0,22	0,15	0,82
Ti47	2323	1120	1906	88,5	78,4	72,14	275	20834	6667	209	156	87,84	443	338	241
V51	1359	1331	1304	565	904	984	908	59441	15691	601	609	653	1263	1008	1261
Mn55	2025	1881	1990	1034	1040	1059	1131	101075	26584	918	902	962	1490	1511	1729
Co59	254	285	241	593	583	628	720	57823	14298	531	516	641	606	676	379
Ni60	939	757	404	557	847	964	1396	50391	12726	2624	2616	2498	616	695	266
Cu63	0,14	0,20	<0.09	0,09	<0.02	0,05	0,09	<13.7	16,04	0,09	0,08	<0.02	0,03	0,16	0,36
Zn66	2056	2178	1817	4096	3783	4091	4484	829682	204524	2468	2467	3246	2742	2941	1188
Rb85	0,10	0,06	0,08	0,03	<0.01	<0.01	<0.01	<6.54	9,41	<0.01	0,02	0,07	<0.01	0,02	0,03
Sr88	0,02	0,02	0,03	0,04	0,08	0,05	0,03	51,24	10,33	0,02	0,04	0,02	<0.01	0,05	0,03
Y89	<0.00	<0.00	<0.00	<0.00	0,00	0,00	<0.00	1,17	0,72	<0.001	0,01	<0.00	0,01	0,00	0,01
Zr90	0,50	0,38	1,12	0,43	0,39	0,36	0,59	53,50	15,65	0,57	0,56	0,60	0,84	0,72	0,83
Nb93	0,36	0,47	0,41	0,49	0,52	0,51	0,65	75,02	18,32	0,61	0,65	0,64	0,89	0,97	1,02
Mo95	0,23	0,09	0,17	0,15	0,12	0,17	0,18	7,98	1,72	0,16	0,14	0,12	0,16	0,24	0,23
Cs133	<0.04	<0.04	<0.02	na	na	na	na	na	na	na	na	na	na	na	na
ln115	na	na	na	<0.001	0,01	0,00	0,00	1,37	<0.15	0,01	0,00	0,00	0,00	<0.002	<0.001
Ba138	0,02	0,01	0,04	0,01	0,19	0,11	0,01	76,14	36,48	0,38	0,01	0,00	0,02	<0.00	0,02
La139	<0.00	<0.00	<0.00	<0.00	0,08	0,03	<0.002	<0.00	<0.00	0,01	<0.002	<0.00	0,03	<0.00	<0.00
Ce140	<0.00	<0.00	<0.00	<0.001	0,12	0,04	0,01	0,99	0,41	0,01	<0.002	<0.001	0,01	0,00	0,01
Pr141	<0.00	<0.00	<0.00	<0.001	0,02	0,01	<0.00	<0.00	<0.12	0,00	<0.002	<0.00	<0.00	<0.00	<0.00
Nd146	<0.00	<0.00	<0.00	<0.003	0,05	0,02	<0.00	<0.00	<0.00	<0.00	0,01	<0.00	<0.01	<0.00	<0.00
Sm149	<0.00	<0.00	<0.00	0,01	0,03	<0.00	<0.01	6,25	<0.00	0,01	<0.00	<0.00	0,02	0,02	<0.01
Eu151	<0.00	<0.00	0,01	<0.00	<0.00	<0.001	<0.00	<0.00	<0.00	<0.002	<0.00	<0.00	<0.00	<0.00	<0.00
Gd157	<0.00	<0.00	<0.00	<0.00	<0.00	<0.00	<0.00	<0.00	<0.00	<0.00	<0.00	<0.00	<0.00	<0.00	<0.00
Tb159	<0.00	<0.00	<0.00	0,00	<0.00	<0.00	<0.00	<0.00	<0.00	<0.003	<0.001	<0.00	<0.001	<0.00	<0.00
Dy163	<0.00	<0.00	<0.00	<0.00	<0.00	<0.003	<0.00	<0.00	<0.00	<0.00	<0.00	<0.00	<0.004	<0.00	0,01
Ho165	<0.00	<0.00	<0.00	<0.00	<0.00	<0.001	<0.00	<0.00	<0.00	<0.001	<0.00	<0.00	<0.00	<0.00	0,00
Er167	<0.00	<0.07	<0.00	<0.00	0,00	<0.00	0,00	<0.00	<0.00	<0.00	<0.00	<0.00	<0.00	<0.00	<0.00
Tm169	0,01	<0.00	<0.00	<0.001	<0.001	<0.00	<0.00	<0.00	0,18	<0.002	<0.001	<0.00	<0.00	<0.001	<0.00
Yb173	<0.00	<0.00	<0.00	<0.00	0,00	<0.00	0,01	<0.00	<0.00	<0.006	<0.005	<0.00	<0.00	<0.00	<0.00
Lu175	0,01	<0.00	<0.00	<0.00	<0.00	<0.00	<0.00	0,92	<0.00	<0.00	<0.00	<0.00	0,00	<0.00	<0.00
Hf177	<0.00	<0.00	<0.00	<0.00	<0.00	<0.00	<0.00	<0.00	<0.00	<0.00	<0.00	<0.00	<0.00	<0.00	<0.00
Ta181	<0.00	<0.00	<0.00	<0.00	0,00	<0.00	<0.00	<0.00	<0.00	0,00	0,00	<0.00	<0.00	0,00	<0.00
W182	<0.00	<0.00	0,24	na	na	na	na	na	na	na	na	na	na	na	na
Pb208	<0.11	<0.09	<0.05	<0.01	0,09	<0.01	<0.01	115	15,9	0,01	0,01	0,02	0,03	0,03	0,01
Th232	0,01	<0.00	<0.00	0,00	0,01	0,01	0,04	<0.86	1,00	0,01	0,01	0,01	0,14	0,01	0,01
U238	<0.00	<0.00	<0.00	<0.00	0,00	0,00	0,00	1,06	1,32	0,00	0,01	<0.001	0,08	0,00	0,01

Table B5: Trace element concentrations of garnet.

Type Sample Mineral Texture Name #	FGA			P-FGA			
	VM10A garnet m grt1a 017	VM10A garnet m grt1b 01	VM10A garnet m grt2a 020	VM10A garnet m grt2b 021	KL24-2b garnet coarse 2gr1 011	KL24-2b garnet coarse 2gr2 012	KL24-2b garnet coarse 3gr1 014
Li	0,51	0,39	0,75	0,76	1,01	0,85	17,4
Be	<0.00	<0.00	<0.00	<0.00	<0.00	<0.00	<0.00
B	3,56	4,00	4,66	5,43	18,3	15,2	236
Sc	117	126	108	110	89,3	86,9	831
Ti	114	174	99,1	116	172	173	2912
V	91,0	127	95,2	94,9	97,6	99,6	1280
Cr	8107	11058	7469	8001	9028	9165	113700
Mn	4561	4697	4583	4519	4271	4232	51860
Fe	81836	82538	82720	81063	74360	74810	970274
Co	33,5	34,5	34,1	35,06	37,3	38,6	544
Ni	2,88	3,85	3,60	4,03	6,58	8,15	154
Cu	0,01	0,20	0,61	0,13	<0.06	<0.06	1,41
Zn	3,72	4,52	3,92	4,06	9,23	11,9	184

Supplementary Material • CHAPTER 5

Rb	0,01	0,01	0,08	0,07	<0.03	<0.01	<0.32
Sr	0,05	0,11	0,08	0,07	0,03	0,06	1,64
Y	13,9	22,9	14,7	14,7	18,3	17,1	142
Zr	6,75	11,6	6,70	6,69	12,3	12,6	131,4
Nb	0,04	0,07	0,04	0,06	0,05	0,03	0,21
Mo	0,46	0,48	0,53	0,50	0,27	0,29	3,31
Cs	na	na	na	na	<0.01	<0.01	<0.17
In	0,04	0,03	0,02	0,02	na	na	na
Ba	0,00	0,03	0,16	0,08	0,01	0,00	2,19
La	0,01	0,01	0,02	0,02	<0.00	0,00	0,06
Ce	0,07	0,12	0,05	0,07	0,01	0,01	0,74
Pr	0,03	0,05	0,03	0,03	0,00	0,01	0,27
Nd	0,35	0,57	0,25	0,39	0,13	0,13	3,23
Sm	0,28	0,48	0,23	0,26	0,22	0,27	4,08
Eu	0,15	0,27	0,14	0,17	0,17	0,16	3,07
Gd	0,68	1,29	0,66	0,75	0,75	0,80	15,9
Tb	0,21	0,35	0,20	0,23	0,30	0,31	3,84
Dy	2,10	3,36	2,09	2,17	2,44	2,33	25,0
Ho	0,51	0,92	0,56	0,54	0,64	0,58	4,58
Er	1,81	3,11	1,79	1,93	1,87	1,56	9,06
Tm	0,29	0,49	0,28	0,29	0,26	0,23	1,08
Yb	2,45	4,37	2,27	2,09	1,78	1,48	7,30
Lu	0,36	0,65	0,32	0,29	0,24	0,22	0,47
Hf	0,07	0,14	0,09	0,07	0,15	0,15	0,77
Ta	0,00	0,00	<0.00	<0.00	<0.00	<0.00	<0.00
W	na	na	na	na	<0.00	<0.00	<0.00
Pb	0,00	0,08	0,04	0,03	0,02	<0.04	3,14
Th	0,01	0,02	0,01	0,00	0,01	0,00	<0.00
U	0,07	0,14	0,05	0,06	0,04	0,02	0,79

Table B6. Trace element concentrations of amphibole

Type	CS		CG				FGA			FSA					
Run	run3	run3	run4	run4	run4	run4	run4	run4	run5	run1	run2	run2	run2	run2	
Sample	MOL1-C	MOL1-C	18LP1	18LP1	18LP1	18LP1	18LP1	KL1A	VM10A	MM1	MM1	MM1B	MM1B	MM1B	
Mineral	amph	amph	tremolite	tremolite	amph corona	amph corona	tremolite	amph	amph	amph	amph	amph	amph	amph	
Texture			vein	vein	opx	opx	w/do vein	m w/do		matrix	matrix	matrix	matrix	matrix	
Name	amph1a	amph1b	amph1a	amph1b	amph2a	amph2b	3amph1	2amph1	amph1	amph1a	amph1b	amph1a	amph1b	amph2a	amph2b
#	13	14	14	15	16	17	14	21	12	13	14	33	34	35	36
Li	4,43	4,19	0,36	0,37	6,50	8,33	5,25	14,14	6,15	3,66	3,02	5,91	7,67	5,86	12,51
Be	0,16	0,33	<0.00	0,06	0,20	0,21	0,06	0,87	0,22	0,92	0,81	2,02	2,53	2,86	2,65
B	10,69	12,25	15,44	16,16	7,93	10,59	7,02	21,85	7,81	16,44	16,90	35,98	37,2	36,17	38,63
Ca	85764	85764	81573	81130	82135	87606	13,00	13,0	81600	13,00	13,00	33,00	33,0	33,00	33,00
Sc	57,5	58,6	23,2	20,1	66,57	77,21	54,8	50,5	51,4	69,6	68,3	224	219	201	215
Ti	827	800	222	210,2	980	1297	602	2545	1463	1427	1431	4231	4377	4571	4567
V	252	258	77,9	69,2	358	422	253	435	380	496	497	1021	1045	1074	1108
Cr	6894	7259	1453	2862	7198	7992	6031	10093	8943	8294	10219	23161	22956	23180	23925
Mn	438	436	548	497	328	435	464	698	362	419	391	869	965	892	1105
Fe	24863	25258	15486	15039	21240	24163	21740	33539	21715	26350	25146	56721	66878	56809	76648
Co	31,1	32,8	24,4	26,1	30,0	32,7	32,6	36,9	29,3	35,1	34,0	84,4	87,3	85,2	95,0
Ni	822	836	651	647	757	786	862	900	761	938	914	2219	2295	2268	2385
Cu	1,56	1,54	5,17	0,22	1,96	1,85	2,01	1,78	1,49	1,30	1,32	3,60	3,53	3,58	3,18
Zn	20,8	25,5	10,6	23,1	9,89	12,0	12,6	37,2	7,93	14,7	13,30	24,3	28,0	24,4	31,1
Rb	2,92	2,96	0,06	0,07	3,66	5,94	2,15	20,1	10,4	20,1	20,48	47,8	43,8	45,0	52,4
Sr	39,7	39,8	20,6	21,9	247	40,3	63,8	185	224	670	569	1018	1207	1322	1136
Y	5,40	5,64	2,94	1,96	11,0	12,8	6,19	7,73	7,03	5,91	5,18	22,7	22,9	17,0	19,03
Zr	3,17	3,07	2,54	1,47	9,71	10,4	3,92	26,3	17,64	18,1	18,4	55,5	57,5	55,6	54,71
Nb	0,65	0,65	0,19	0,14	4,45	7,68	0,54	4,43	5,02	14,6	13,6	29,7	33,3	35,7	32,7
Mo	0,07	0,07	0,07	0,08	0,07	0,05	0,06	0,07	0,08	0,07	0,07	0,10	0,15	0,12	0,14
Cs	na	na	na	na	na	na	na	1,46	na	na	na	na	na	na	na
In	0,07	0,07	0,01	0,01	0,06	0,08	na	na	0,05	0,07	0,07	0,15	0,15	0,18	0,16
Ba	16,9	17,4	2,89	1,14	177	257	38,8	232	920	1869	1385	3729	4102	4627	3699
La	2,46	2,47	1,02	0,76	16,0	18,3	7,68	5,27	13,9	23,2	23,79	55,6	58,0	59,9	59,2
Ce	6,37	6,19	2,96	2,13	47,4	54,4	11,5	13,67	26,9	64,7	61,9	126	137	148	139
Pr	0,68	0,69	0,47	0,32	6,59	7,89	1,18	1,97	2,90	8,20	7,69	15,1	16,8	181	16,8
Nd	2,87	2,90	2,59	1,63	30,5	38,0	4,42	9,30	12,0	35,2	33,2	68,3	75,6	80,0	72,4
Sm	0,62	0,62	0,62	0,49	4,94	6,07	0,89	2,11	1,88	5,26	4,86	10,2	12,0	12,0	11,4
Eu	0,24	0,26	0,17	0,11	1,08	1,38	0,16	0,63	0,47	1,19	1,11	2,25	2,55	2,74	2,49
Gd	0,61	0,57	0,53	0,26	3,02	3,84	0,65	1,99	1,42	2,65	2,51	6,20	6,53	6,43	5,89
Tb	0,11	0,11	0,08	0,04	0,36	0,44	0,14	0,26	0,19	0,30	0,26	0,71	0,82	0,71	0,69
Dy	0,86	0,88	0,54	0,32	2,08	2,46	0,96	1,53	1,45	1,49	1,28	4,41	4,55	3,72	3,98
Ho	0,20	0,21	0,11	0,07	0,42	0,49	0,23	0,31	0,26	0,22	0,20	0,81	0,86	0,64	0,72
Er	0,66	0,70	0,35	0,28	1,32	1,46	0,68	0,81	0,86	0,52	0,49	2,60	2,50	1,82	2,07
Tm	0,10	0,11	0,05	0,04	0,18	0,19	0,13	0,11	0,12	0,06	0,07	0,40	0,36	0,23	0,31

Supplementary Material • CHAPTER 5

Yb	0,84	0,90	0,46	0,32	1,43	1,77	0,94	0,83	1,18	0,44	0,58	3,42	3,05	2,02	2,62
Lu	0,12	0,12	0,06	0,05	0,20	0,23	0,16	0,12	0,16	0,05	0,08	0,48	0,43	0,28	0,36
Hf	0,06	0,07	0,14	0,07	0,33	0,38	0,12	1,09	0,59	0,58	0,56	1,73	2,04	1,97	1,74
Ta	0,02	0,02	0,01	0,01	0,22	0,34	0,03	0,20	0,18	0,39	0,45	1,15	1,29	1,26	1,16
W	na	na	na	na	na	na	0,03	0,13	na						
Pb	0,37	0,37	0,29	0,25	3,45	7,40	1,81	11,9	14,8	23,9	21,7	39,5	38,3	47,3	38,0
Th	0,19	0,22	0,09	0,09	0,44	0,57	0,47	0,80	1,32	0,56	0,69	3,04	2,87	2,46	2,92
U	0,14	0,14	0,02	0,04	0,36	0,32	0,27	0,60	0,83	1,48	1,59	2,94	3,23	3,87	3,45

Table B7: Trace element concentrations of apatite.

Sample	KL24-2B	VM25P10	VM25P10	VM10A	18LP1	18LP1	18LP1	18LP1	MM1	MM1	MM1B	18LP1
Type	P-FGA	P-FGA	P-FGA	P-FGA	CG	CG	CG	CG	FSA	FSA	FSA	CG
Mineral	ap	ap	ap	ap	ap	ap	ap	ap	ap	ap	ap	ap
Texture	PA	in zr	in zr	matrix	vein	vein	vein	vein	m	m	m	m
Name	2ap1	4ap1	4ap2	5ap1	5ap1	3ap1	3ap2	7ap1	ap1	ap2	ap1	ap1
#	010	020	021	029	008	010	012	027	007	015	013	024
Li	<1.25	0,34	0,16	0,72	0,18	<0.15	<0.18	0,22	0,35	0,35	1,95	0,25
Be	<0.00	<0.00	<0.00	0,06	<0.00	<0.00	<0.00	<0.00	<0.01	<0.00	<0.00	<0.00
B	65,7	11,1	10,15	12,7	4,96	<5.75	8,52	<8.66	9,47	10,7	28,0	1,96
Na	315	413	208	302	204	158	172	88,1				
K	96,8	3,68	<3.09	<2.73	4,33	<2.78	<3.03	<3.86				
Sc	8,07	<0.09	<0.09	0,14	<0.06	<0.09	<0.09	<0.11	0,04	0,04	0,08	0,19
Ti	5896	7,45	8,06	6,16	7,80	6,64	6,02	5,59	5,27	6,40	10,20	44,8
V	5105,76	11,25	13,13	15,54	2,19	0,89	2,76	2,58	1,70	0,94	0,94	1,79
Cr	615494	<1.59	<1.60	<1.48	<1.72	<2.11	<2.16	<3.11	0,19	<0.11	0,70	1,31
Mn	8500	58,0	56,38	54,3	69,22	49,51	96,01	72,8	141	205	1167	118,00
Fe	525995	136	155	152	292	234	673	104	1467	567	65324	988,84
Co	1016	0,44	0,82	0,20	1,05	0,15	0,23	0,02	0,58	0,21	5,79	1,73
Ni	2862	18,5	18,0	8,06	1,36	0,70	1,41	0,22	22,9	13,43	7,01	39,78
Cu	24,8	89,1	133	0,87	0,25	0,40	0,25	<0.09	0,12	0,07	0,22	0,08
Zn	7166	0,33	0,42	0,42	1,24	0,59	0,75	<0.59	1,51	1,63	3,88	1,23
Rb	<0.23	<0.03	<0.02	<0.01	0,01	<0.03	<0.02	<0.02	0,02	0,08	<0.002	0,00
Sr	2537	6524	6554	1898	4520	5285	4914	4448	1853	2226	831	4027
Y	20,0	3,63	3,68	9,67	9,11	6,25	11,73	10,3	12,6	4,16	6,78	7,83
Zr	2,59	0,04	0,16	0,03	<0.00	0,01	0,01	0,00	0,01	0,01	0,01	0,01
Nb	2,83	0,03	0,02	0,17	<0.00	<0.00	0,02	0,03	0,09	0,00	0,00	0,03
Mo	0,54	<0.04	0,02	0,04	0,04	<0.06	0,04	<0.00	0,03	0,04	0,19	0,01
Cs	<0.16	<0.02	0,04	<0.02	<0.01	<0.01	<0.02	<0.03				
Ba	53,0	44,8	42,4	17,5	52,3	24,8	29,4	6,95	13,4	12,0	20,8	11,8
La	119	480	586	475	399	296	478	447	905	492	221	365
Ce	358	557	691	349	319	229	378	347	897	485	323	351
Pr	36,7	58,9	73,1	17,9	17,5	13,1	21,3	18,4	49,4	24,7	21,08	20,2
Nd	123	181	221	37,1	47,9	32,9	57,3	45,1	116	57,1	56,3	53,63
Sm	19,9	12,9	14,7	2,70	4,13	3,33	4,29	3,58	6,95	3,17	4,01	4,75
Eu	3,00	1,02	1,18	0,84	0,91	0,74	1,28	1,18	2,86	1,75	2,00	1,07
Gd	8,26	5,00	6,24	2,42	2,46	1,79	2,91	2,48	4,56	1,87	2,21	2,66
Tb	1,14	0,31	0,39	0,35	0,24	0,25	0,34	0,26	0,39	0,14	0,21	0,28
Dy	4,68	1,15	1,08	1,86	1,85	1,18	1,97	1,64	2,38	0,95	1,16	1,50
Ho	0,74	0,16	0,16	0,42	0,35	0,27	0,41	0,39	0,51	0,15	0,23	0,31
Er	1,64	0,41	0,23	0,95	0,86	0,70	1,25	0,94	1,34	0,46	0,74	0,95
Tm	0,16	0,02	0,04	0,13	0,17	0,08	0,19	0,16	0,16	0,05	0,09	0,13
Yb	0,37	0,25	0,08	0,99	1,02	0,33	1,49	1,07	1,09	0,27	0,68	1,07
Lu	0,13	<0.00	0,02	0,17	0,12	0,09	0,24	0,26	0,17	0,05	0,10	0,15
Hf	<0.00	<0.00	<0.00	<0.00	<0.00	<0.00	<0.00	<0.00	<0.00	<0.00	<0.00	<0.00
Ta	<0.00	<0.00	<0.00	<0.00	<0.00	<0.00	<0.00	<0.00	0,00	<0.00	<0.00	<0.00
W	3,44	0,13	0,18	1,32	0,27	0,06	0,12	0,13	na	na	na	na
Pb	28,0	24,7	25,9	14,90	7,36	7,04	11,5	10,4	5,35	3,10	0,26	11,04
Th	10,7	3,26	3,79	76,1	10,3	0,95	24,6	21,0	33,1	3,59	20,1	19,2
U	13,9	0,36	0,73	13,7	1,66	0,14	3,78	2,78	2,10	0,30	2,26	3,82

Table B8: Trace element concentrations of zircon measured along a profile rim-to-core.

Sample	VM25P10A							
	rim	close to do						
Texture								
Name	1zr1	1zr2	1zr3	1zr4	1zr5	1zr6	1zr7	1zr8
Mineral	zircon	zircon	zircon	zircon	zircon	zircon	zircon	zircon
#	007	008	009	010	011	012	013	014
SIMS spot								
Li	37,9	3,05	4,91	2,58	1,86	10,1	3,51	7,62
Be	<0.00	<0.29	<0.00	<0.00	<0.00	<0.00	<0.00	<0.00
B	6,6	<5.15	<5.38	<5.32	<5.33	<5.23	<5.31	<4.61

Supplementary Material • CHAPTER 5

Na	0,98	<0.87	<0.94	<0.94	1,07	<0.93	<0.89	4,14
Mg25	<1.31	<0.00	0,44	<0.35	<0.00	<0.37	0,96	<0.32
Al27	8,19	17,4	10,8	30,7	38,5	14,8	22,0	16,2
K	2,89	<2.26	<2.36	<2.36	<2.35	<2.33	<2.29	<2.07
Ca43	<33.3	<39.0	32,2	<42.5	<44.6	<38.3	<35.4	<33.0
Ca44	53,8	<15.6	34,7	26,1	37,3	54,9	39,7	<14.6
Sc	274	261	301	274	279	286	269	268
Ti	1222	1184	1190	1168	1199	1205	1176	1189
V	<0.04	<0.06	0,11	0,16	0,1	0,18	0,08	0,16
Cr	1,97	<2.14	<2.33	<2.33	<2.09	<2.20	<2.27	<1.87
Mn	0,84	<0.45	<0.48	<0.46	0,49	<0.46	<0.46	<0.42
Co	<0.02	<0.01	<0.02	<0.01	<0.00	<0.01	<0.00	<0.01
Ni	0,34	<0.06	<0.06	0,06	0,02	<0.00	0,02	0,11
Cu	<0.04	<0.06	0,19	<0.04	<0.05	0,06	1,24	3,16
Zn	0,47	0,36	<0.38	<0.26	0,64	0,54	0,4	0,28
Rb	<0.01	<0.016	<0.02	<0.02	<0.01	0,02	<0.02	<0.02
Sr	0,09	0,105	0,08	0,05	0,15	0,15	0,11	0,08
Y	13,6	11,8	32,8	17,0	16,3	22,7	15,5	17,1
Zr	443473	432350	429643	430794	443172	448642	441608	442926
Nb	0,92	0,81	0,76	0,55	0,66	1,32	0,90	1,15
Mo	0,50	0,43	0,349	0,45	0,57	0,55	0,46	0,57
Cs	<0.01	<0.01	<0.02	<0.01	<0.01	<0.02	<0.01	<0.01
Ba	0,01	0,01	0,02	0,01	0,03	0,04	0,05	0,14
La	0,14	0,01	0,01	0,01	0,06	0,09	0,05	0,1
Ce	3,40	3,33	2,12	1,88	2,09	9,14	5,93	6,68
Pr	0,02	0,03	0,03	0,02	0,04	0,02	0,05	0,06
Nd	0,21	0,219	0,33	0,17	0,30	0,77	0,49	0,49
Sm	0,30	0,294	0,25	0,18	0,15	0,58	0,33	0,31
Eu	0,08	0,15	0,17	0,08	0,07	0,28	0,12	0,22
Gd	0,61	0,48	0,94	0,53	0,49	0,97	0,61	0,87
Tb	0,18	0,11	0,26	0,14	0,104	0,22	0,13	0,20
Dy	1,45	1,27	3,19	1,46	1,46	2,27	1,19	1,77
Ho	0,42	0,41	1,18	0,56	0,607	0,85	0,49	0,53
Er	1,92	1,66	5,14	2,77	2,34	3,41	2,33	2,29
Tm	0,42	0,42	1,08	0,60	0,65	0,82	0,58	0,49
Yb	4,29	4,22	11,9	6,81	6,01	8,41	5,44	5,49
Lu	0,79	1,01	2,67	1,45	1,36	1,90	1,18	1,28
Hf	5887	5775	6044	5936	6245	6456	6315	6419
Ta	0,50	0,3	0,26	0,20	0,17	0,30	0,22	0,29
W	<0.00	<0.00	<0.00	<0.00	<0.00	<0.00	<0.00	0,04
Pb	10,6	0,97	0,78	0,36	0,36	0,86	0,4	1,07
Th	305	29,2	16,9	11,3	8,38	21,9	10,6	25,1
U	439	52,2	59,9	46,8	44,4	61	39,2	48,8

Table B9. Trace element concentrations of serpentine phases.

type	FSA						CG				
	run1	run1	run2	run2	run2	run2	run4	run4	run4	run4	run4
RUN	run1	run1	run2	run2	run2	run2	run4	run4	run4	run4	run4
Sample	MM1	MM1	MM1-B	MM1-B	MM1-B	MM1-B	18LP1	18LP1	18LP1	18LP1	18LP1
Texture			vein	vein	vein	vein	vein	vein	vein	vein	vein
Name	srp1	srp2	srp1a	srp1b	srp2a	srp2b	srp1a	srp1b	srp2a	srp2b	srp3
#	020	021	009	010	025	026	009	010	025	026	028
Li7	2,84	0,64	4,93	5,13	3,16	2,44	13,88	13,3	14,8	14,25	9,08
Be9	0,03	0,05	0,07	0,13	0,14	<0.00	<0.00	0,10	<0.00	<0.00	<0.00
B11	77,8	41,7	52,6	62,4	49,2	33,0	8,11	7,82	17,2	19,03	17,3
Al27	1986	549	4546	1147	1192	619	9885	8896	3939	4531	6673
Si28	41,50	41,5	42,0	42,0	41,5	41,5	42,00	42,0	42,0	42,0	42,1
Ca43	97,08	102	262	131	166	159	225	139	19,2	66,6	184
Ca44	152	128	308	181	195	153	331	296	180	230	289
Sc45	4,11	2,65	5,11	3,91	3,97	2,13	15,68	11,4	4,37	6,06	21,8
Ti47	32,4	28,68	90,8	29,9	41,9	33,1	96,2	80,8	39,7	51,6	144
V51	6,86	3,04	39,2	5,28	5,57	3,06	94,67	65,8	31,3	48,6	78,0
Cr53	644	17,14	1217,00	5,01	8,92	8,59	1481	932	521	844	1419
Mn55	587	408	675	570	370	249	503	432	422	539	465
Fe57	20721	17380	24279	23187	18293	15996	29384	27349	31261	31066	29558
Co59	19,5	13,5	23,1	14,2	15,5	17,5	20,1	22,7	26,9	16,9	29,0
Ni60	1465	1566	776	599	731	716	222	221	488	194	557
Cu63	0,01	0,03	0,02	0,01	0,05	0,97	0,18	0,03	0,04	0,03	0,14
Zn66	67,4	17,9	25,3	19,6	17,3	20,3	25,3	17,7	17,6	19,9	21,7
Rb85	0,10	0,01	0,21	0,38	0,09	0,09	0,40	0,50	0,26	0,26	0,11
Sr88	0,49	0,41	1,35	0,40	0,53	0,37	0,45	0,40	0,22	0,30	0,29
Y89	0,28	0,23	0,27	0,28	0,34	0,23	0,06	0,06	0,07	0,09	0,81
Zr90	0,21	0,16	0,21	0,09	0,36	0,16	0,04	0,05	0,06	0,15	1,49

Supplementary Material • CHAPTER 5

Nb93	0,21	0,10	0,11	0,09	0,12	0,07	0,01	0,01	0,03	0,04	0,14
Mo95	0,15	0,18	0,23	0,36	0,23	0,09	0,07	0,07	0,23	0,18	0,10
In115	0,01	0,00	0,00	0,01	0,00	0,01	0,00	0,01	0,01	0,00	0,01
Ba138	0,41	0,34	0,48	0,31	0,60	0,25	10,94	8,71	3,15	4,19	3,59
La139	1,40	1,07	2,70	1,39	1,57	0,85	0,18	0,13	0,25	0,42	1,31
Ce140	3,03	2,27	5,08	2,70	2,76	1,67	0,24	0,24	0,50	0,93	2,91
Pr141	0,25	0,18	0,39	0,23	0,24	0,12	0,02	0,01	0,04	0,08	0,26
Nd146	0,89	0,58	1,24	0,77	0,78	0,57	0,05	0,06	0,17	0,31	1,15
Sm147	0,09	0,07	0,14	0,10	0,09	0,08	0,01	0,01	0,04	0,06	0,17
Eu153	0,04	0,04	0,09	0,10	0,07	0,04	0,01	0,01	0,01	0,02	0,04
Gd157	0,06	0,05	0,05	0,09	0,04	0,02	<0.00	0,01	0,02	0,02	0,21
Tb159	0,01	0,00	0,01	0,01	0,01	0,00	0,00	<0.00	0,00	0,00	0,03
Dy163	0,05	0,05	0,05	0,06	0,06	0,05	0,00	<0.00	0,01	0,01	0,16
Ho165	0,01	0,01	0,01	0,01	0,01	0,01	0,00	0,00	0,00	0,01	0,03
Er166	0,03	0,02	0,03	0,03	0,05	0,02	0,01	0,00	0,02	0,01	0,12
Tm169	0,01	0,01	0,00	0,01	0,01	0,00	0,00	0,00	0,00	<0.00	0,01
Yb172	0,06	0,03	0,04	0,06	0,06	0,03	0,03	0,02	0,01	0,04	0,20
Lu175	0,02	0,00	0,01	0,01	0,01	0,01	0,01	0,01	0,00	0,01	0,02
Hf178	0,00	0,00	0,01	<0.00	0,01	0,01	<0.00	<0.00	<0.00	0,00	0,09
Ta181	0,00	0,00	0,00	0,00	0,00	0,00	<0.00	0,00	0,00	<0.00	0,00
Pb208	0,05	0,08	0,18	0,09	0,15	0,21	0,18	0,21	0,52	0,36	0,08
Th232	0,05	0,08	0,09	0,09	0,10	0,04	0,04	0,29	0,19	0,68	0,11
U238	0,03	0,03	0,04	0,02	0,04	0,03	0,02	0,04	0,04	0,09	0,03

Table B10. Trace element concentrations of chlorite and phlogopite

Lithotype	FSA			CS					CG			CS		
	run1	run1	run2	run2	run2	run2	run3	run3	run4	run4	run4	run3	run3	
Sample	MM1	MM1	MM1B	MM1B	MM1B	MM1B	MOL1-C	MOL1-C	18LP1	18LP1	18LP1	MOL1-C	MOL1-C	
Mineral	chlorite	phlogopite	phlogopite											
Texture	w/dol	w/dol	matrix	matrix	matrix	matrix	w/phl	w/phl	matrix	matrix	in vein			
Name	chl1a	chl1b	chl1a	chl1b	chl2a	chl2b	chl2a	chl2b	chl1a	chl1b	chl2a	phl1a	phl1b	
#	005	006	029	030	031	032	011	012	011	012	013	009	010	
Li7	0,90	0,86	0,96	0,93	1,07	1,12	0,77	0,89	1,79	1,74	1,79	101,13	88,88	
Be9	<0.00	<0.00	<0.00	<0.00	0,04	<0.02	0,04	<0.00	<0.00	<0.00	<0.00	0,05	0,13	
B11	17,84	14,22	8,24	6,50	9,37	8,13	6,84	6,79	7,33	5,99	5,29	7,36	7,53	
Ca43	92,2	107	241	251	51,3	80,7	128	158	13359	229	400	168,07	175	
Ca44	34,4	37,01	36,9	48,4	31,14	30,1	47,4	58,4	12857	92,6	155	75,19	73,2	
Sc45	3,65	3,80	3,99	3,42	3,31	3,43	3,53	3,53	2,95	3,08	2,44	2,28	2,28	
Ti47	193	251	223	175	165	163	147	141	157	137	119	1260	1214	
V51	140	146	148	121	113	114	120	119	166	148	135	93,9	90,3	
Cr53	5253	4864	6335	7202	6278	6503	10669	10543	7074	7234	8129	4368	4519	
Mn55	90,8	87,8	91,94	101	188	93,9	92,4	88,3	170	84,8	91,8	49,75	47,9	
Fe57	20756	20176	20242	21061	22135	20907	24248	24060	21516	20794	20861	16453	16044	
Co59	46,2	45,4	45,6	48,3	50,3	48,4	57,8	57,3	47,72	46,3	46,6	37,6	37,5	
Ni60	1679	1687	1604	1698	1770	1733	2012	2010	1560	1519	1537	1297	1281	
Cu63	0,22	0,50	<0.01	0,04	0,03	0,04	0,02	0,07	0,45	0,42	0,12	0,71	0,85	
Zn66	18,32	20,2	12,4	13,8	11,8	12,0	28,7	26,8	22,2	16,2	15,9	15,3	15,8	
Rb85	0,03	0,06	0,25	0,66	0,22	0,04	0,09	<0.01	0,51	0,44	0,31	195	180	
Sr88	0,07	0,02	0,02	0,09	0,03	0,14	0,03	0,10	2,42	0,11	0,22	14,3	15,4	
Y89	<0.001	<0.0003	0,00	<0.0003	<0.00	<0.00	0,00	<0.001	0,00	0,00	<0.00	0,04	0,05	
Zr90	0,03	0,02	0,04	0,05	0,04	0,04	0,06	0,08	0,03	0,06	0,06	0,06	0,05	
Nb93	0,15	0,20	0,17	0,14	0,12	0,13	0,08	0,07	0,11	0,08	0,08	0,68	0,60	
Mo95	<0.002	0,01	0,01	0,01	0,03	<0.004	0,00	0,04	<0.01	0,02	0,01	<0.004	0,00	
In115	0,02	0,02	0,02	0,02	0,01	0,02	0,02	0,02	0,02	0,02	0,01	0,01	0,01	
Ba138	0,10	0,19	0,79	2,41	0,68	0,19	0,17	0,15	6,33	1,41	1,82	832	900	
La139	0,00	0,00	0,00	0,01	<0.00	<0.00	0,00	0,00	0,02	0,02	0,01	0,00	0,02	
Ce140	0,01	0,00	0,00	0,01	0,00	<0.00	0,00	<0.001	0,02	0,02	0,02	<0.002	0,02	
Pr141	<0.0001	<0.00	0,00	<0.00	<0.00	0,00	0,00	0,00	<0.00	0,00	0,00	0,00	0,00	
Nd146	0,00	<0.00	<0.00	<0.00	<0.00	<0.00	<0.00	<0.003	<0.00	0,00	0,01	0,00	0,00	
Sm147	<0.001	<0.00	<0.002	<0.00	0,01	<0.00	<0.00	<0.00	<0.00	<0.00	<0.00	0,00	<0.003	
Eu153	<0.001	<0.00	<0.00	<0.00	<0.00	<0.00	<0.00	<0.0007	<0.00	<0.00	<0.00	0,01	0,02	
Gd157	<0.00	<0.00	<0.00	<0.00	<0.00	<0.00	0,00	<0.00	<0.00	<0.00	<0.00	<0.00	<0.00	
Tb159	0,00	<0.00	<0.00	<0.00	<0.00	<0.00	<0.00	<0.00	<0.00	<0.00	<0.00	<0.00	<0.00	
Dy163	<0.00	<0.001	<0.00	<0.00	<0.00	<0.00	<0.00	<0.00	<0.00	<0.00	<0.00	<0.00	<0.00	
Ho165	<0.0004	<0.00	<0.00	<0.00	<0.00	<0.00	<0.00	<0.00	<0.00	0,01	<0.00	<0.00	<0.00	
Er166	<0.001	<0.00	<0.00	<0.00	<0.00	<0.00	<0.00	<0.00	<0.00	<0.00	<0.00	<0.00	<0.00	
Tm169	0,00	<0.0003	0,00	<0.00	<0.0003	<0.00	<0.00	0,00	0,00	<0.00	<0.0004	<0.00	<0.001	
Yb172	<0.00	<0.00	<0.00	<0.00	<0.00	<0.00	<0.00	<0.00	0,01	<0.00	<0.00	<0.00	0,00	
Lu175	0,00	<0.0003	<0.00	<0.00	<0.00	<0.00	<0.00	0,00	<0.00	<0.00	<0.00	<0.001	<0.00	
Hf178	0,00	<0.00	<0.00	<0.00	<0.00	<0.00	<0.00	<0.00	<0.001	<0.00	<0.00	0,01	0,01	
Ta181	0,00	0,01	0,00	0,01	<0.00	0,00	0,00	0,00	0,01	0,00	<0.00	0,02	0,02	
Pb208	0,07	0,03	0,04	0,11	0,01	0,09	0,04	0,14	0,02	0,04	0,07	0,68	0,85	
Th232	0,00	0,01	0,00	0,00	0,00	0,00	<0.00	<0.001	0,00	0,00	<0.001	0,23	0,30	
U238	0,00	0,01	0,00	<0.00	<0.001	0,00	0,00	<0.00	0,01	0,00	0,00	0,01	0,01	

Tab B11. Trace element compositions of carbonates (dolomite and minor magnesite) in ppm.

Supplementary Material • CHAPTER 5

Type	P-FGA															FGA		
	P0344	P0344	P0344	P0344	P0344	P0344	P0345	P0345	P0344	P0344	RUN5	RUN5	RUN5	RUN5	RUN5	P0343	P0343	P0343
Mounts	P0344	P0344	P0344	P0344	P0344	P0344	P0345	P0345	P0344	P0344	RUN5	RUN5	RUN5	RUN5	RUN5	P0343	P0343	P0343
Sample	KL24-2B	KL24-2B	VM25P10	VM25P10	VM25P10	VM25P10	VM25P10	VM25P10	VM10A	VM10A	VM10A	VM10A	VM10A	VM10A	VM10A	KL1A	KL1A	KL1A
Texture	in sp	in sp	in zr	in zr w/chl	m-green-core	m-red-rim	matrix	matrix	matrix	matrix	matrix	m-core	matrix	vein				
Mineral	do	do	do	do	do	do	do	do	do	do	do							
Name	3do1	3do2	4do1	4do2	4do3	1do1	1do2	5do1	5do2	dol1	dol2a	dol2b	dol3	dol3b	2do1	1do1	4do1	
#	015	016	017	018	019	015	016	027	028	005	006	007	013	014	023	024	009	
SIMS			@4	@1				@2										
CL color	dull green	red	dull green															
Li	<0.43	<0.46	0.37	0.47	0.40	0.18	0.42	<0.21	0.27	0.16	0.09	0.16	0.13	0.12	0.18	<0.15	<0.14	
Be	<0.00	<0.00	<0.00	<0.00	0.08	<0.00	<0.00	<0.00	<0.00	<0.00	<0.00	<0.00	<0.00	<0.00	<0.00	<0.00	<0.00	
B	<20.2	<18.8	23.0	19.1	21.9	12.7	14.2	13.7	18.8	5.26	5.36	2.81	3.78	3.38	12.6	8.48	13.8	
Na	8.78	14.8	23.0	20.9	489	12.01	7.06	5.29	4.24						24.1	4.79	7.24	
Sc	1.89	0.66	1.33	1.34	1.57	1.22	1.56	<0.13	0.15	0.11	0.35	0.31	0.36	0.35	0.12	0.19	0.24	
Ti	11.9	2.17	<0.25	<0.16	<0.21	<0.24	<0.20	<0.22	<0.24	0.11	0.05	<0.03	<0.04	0.73	4.57	<0.18	<0.38	
V	7.35	1.36	0.19	0.12	0.23	0.16	0.13	0.24	0.15	0.17	0.30	0.27	0.33	0.45	0.78	0.22	0.30	
Cr	595.3	195	<1.18	<1.40	<1.26	1.95	2.51	4.96	4.06	4.04	3.19	4.90	5.06	6.44	19.3	5.74	5.24	
Mn	724	647	1047	1082	1181	962	718	597	599	522	534	543	593	576	606	558	582	
Co	14.51	12.9	8.23	9.66	8.37	8.19	6.36	10.4	9.56	9.06	9.61	10.1	10.2	10.02	10.49	10.4	10.6	
Ni	90.15	78.6	24.14	25.5	27.2	37.5	43.68	66.2	59.5	63.91	78.5	79.5	90.2	86.6	64.4	48.1	56.7	
Cu	1.07	<0.23	1.36	0.23	0.27	9.20	0.11	<0.11	<0.06	0.33	9.22	11.1	10.5	5.98	<0.06	<0.05	<0.07	
Zn	15.71	9.72	10.23	9.26	13.4	9.07	5.58	<5.46	8.09	6.50	6.10	7.21	6.25	6.12	8.72	8.39	9.04	
Rb	<0.07	<0.09	0.17	<0.02	0.02	<0.02	<0.02	<0.02	<0.02	<0.00	<0.00	<0.00	0.01	0.02	0.04	<0.03	<0.01	
Sr	114	1105	3507	4040	3588	558	359	1102	734	939	1249	1287	1084	1067	684	684	651	
Y	0.68	0.37	0.20	0.25	0.25	1.62	0.59	0.08	0.05	0.07	0.18	0.20	0.19	0.19	0.21	0.15	0.15	
Zr	<0.08	<0.00	0.17	0.08	1.22	2.91	0.24	<0.00	0.01	<0.00	0.00	<0.00	0.00	<0.001	0.01	<0.00	0.00	
Nb	<0.03	<0.00	0.00	0.00	<0.00	<0.00	<0.00	<0.01	0.00	0.00	<0.00	<0.00	0.00	0.00	0.01	<0.00	<0.00	
Mo	<0.15	<0.14	0.06	0.06	0.07	0.12	0.06	<0.07	0.04	0.04	0.06	0.06	0.07	0.08	0.09	0.06	0.10	
Cs	0.49	1.18	0.50	0.24	2.23	0.08	0.48	0.69	0.69						0.17	0.38	3.48	
Ba	86.1	67.7	49.2	16.5	11.8	6.24	5.50	24.9	14.1	12.19	26.8	28.8	25.6	24.0	8.25	8.22	9.67	
La	4.58	3.11	39.1	44.5	37.5	17.1	8.83	3.01	1.64	1.52	11.3	12.4	13.6	13.0	0.87	0.77	0.93	
Ce	4.97	2.96	31.0	31.5	27.8	22.9	7.44	2.25	1.24	0.94	9.46	10.7	11.2	11.5	0.84	0.94	0.96	
Pr	0.34	0.26	3.35	3.63	3.15	1.92	0.50	0.12	0.06	0.05	0.60	0.65	0.69	0.68	0.07	0.06	0.08	
Nd	1.08	1.56	8.60	8.92	8.04	5.74	1.07	0.28	0.16	0.13	1.57	1.98	1.91	1.93	0.22	0.15	0.24	
Sm	0.22	0.09	0.49	0.52	0.55	0.52	0.15	0.01	<0.00	<0.00	0.04	0.14	0.13	0.18	0.04	<0.00	0.01	
Eu	0.04	0.05	0.20	0.14	0.12	0.17	0.02	0.01	0.03	0.01	0.06	0.06	0.06	0.06	0.04	0.05	0.03	
Gd	0.25	<0.00	0.18	0.16	0.27	0.29	0.14	0.01	<0.00	0.01	0.07	0.11	0.10	0.13	0.03	0.03	0.04	
Tb	0.01	<0.02	0.02	0.01	0.01	0.05	0.01	<0.00	0.00	<0.00	0.00	0.00	0.01	0.01	0.01	0.00	0.00	
Dy	<0.00	0.05	0.03	0.04	0.05	0.25	0.09	0.02	<0.00	<0.00	0.02	0.07	0.04	0.05	0.03	0.02	0.02	
Ho	0.02	<0.03	0.01	0.01	0.01	0.06	0.02	0.00	0.00	0.00	0.01	0.00	0.01	0.01	0.01	0.01	0.01	
Er	<0.00	<0.00	0.02	0.02	0.04	0.10	0.08	0.01	<0.00	0.02	0.02	0.01	0.02	0.02	0.03	0.01	0.02	
Tm	0.01	<0.00	<0.05	<0.00	0.00	0.01	<0.01	0.00	0.00	0.00	<0.00	0.00	0.00	0.00	0.00	<0.00	0.00	
Yb	<0.00	<0.00	<0.00	0.02	0.01	0.14	0.09	0.01	<0.00	0.00	0.02	0.02	0.02	0.02	0.05	0.01	0.03	
Lu	<0.00	<0.00	0.01	0.01	0.00	0.02	0.01	<0.00	0.00	0.00	0.01	0.00	0.00	0.00	0.00	<0.00	0.00	
Hf	<0.00	<0.00	<0.00	<0.00	<0.00	<0.14	<0.00	<0.00	<0.00	<0.00	<0.00	<0.00	<0.00	<0.00	<0.00	<0.00	<0.00	
Ta	<0.00	<0.00	<0.00	<0.00	<0.00	<0.00	<0.00	<0.01	<0.00	<0.001	<0.00	0.00	<0.00	<0.00	<0.00	<0.00	<0.00	
W	0.12	<0.00	0.09	<0.00	<0.00	0.28	<0.00	<0.07	0.01						<0.00	<0.00	<0.00	
Pb	5.29	5.52	28.5	28.5	25.1	2.16	0.57	12.8	7.42	9.58	16.4	17.6	13.1	12.5	8.05	7.20	7.23	
Th	<0.00	<0.00	<0.00	<0.00	<0.00	<0.00	<0.00	<0.00	<0.00	0.00	<0.001	<0.00	<0.00	0.00	<0.00	<0.00	<0.00	
U	<0.00	<0.00	<0.00	<0.00	<0.00	<0.00	<0.00	0.00	<0.01	<0.01	0.00	<0.00	0.00	<0.0003	<0.00	<0.00	<0.00	

Tab B11. Continued.

Type	FSA								CS								
	RUN1	RUN1	RUN2	RUN2	RUN2	RUN2	RUN2	RUN2	P0344	P0344	P0344	P0344	P0344	P0344	P0344	P0344	
Mounts	RUN1	RUN1	RUN2	RUN2	RUN2	RUN2	RUN2	RUN2	P0344	P0344	P0344	P0344	P0344	P0344	P0344	P0344	
Sample	MM1	MM1	MM1-B	MM1-B	MM1-B	MM1-B	MM1-B	MM1-B	MOL1C	MOL1C	MOL1C	MOL1C	MOL1C	MOL1C	MOL1C	MOL1C	
Texture																	
Mineral	do	do	do	do	do	do	do	do	do	do	do	do	do	do	do	do	
Name	dol1a	dol2	dol1a	dol1b	dol2a	dol2b	dol3a	dol3b	6do1	6do2	6do3	6do4	6do5	6do6	7do1	7do2	
#	011	016	005	006	007	008	011	012	031	032	033	034	035	036	037	038	
SIMS									@13	@14	@15	@16	@17	@18			
CL color									red	red	red	green	green	green	green	red	
Li	0.04	0.09	0.09	0.08	0.08	<0.03	0.04	0.08	<0.15	<0.14	<0.20	<0.14	<0.14	<0.21	<0.10	<0.15	
Be	<0.00	<0.00	<0.00	<0.00	<0.00	<0.00	<0.00	<0.00	<0.00	<0.00	<0.00	<0.00	<0.00	<0.00	<0.00	<0.00	
B	12.08	12.74	7.56	8.22	8.52	9.74	6.33	7.83	11.1	10.1	17.57	8.17	13.3	18.4	19.4	20.3	
Na									27.9	13.0	5.94	26.6	21.5	22.6	57.9	95.6	
Sc	0.21	0.22	0.40	0.42	0.28	0.25	0.19	0.21	0.31	0.66	0.52	0.42	0.37	0.50	0.62	0.30	
Ti	<0.08	0.10	<0.02	0.04	<0.03	<0.04	<0.02	<0.02	<0.29	<0.34	<0.52	<0.24	<0.26	<0.248	<0.33	0.21	
V	0.20	0.17	0.23	0.24	0.18	0.21	0.18	0.15	0.07	0.22	0.17	0.19	0.22	0.32	0.42	0.22	
Cr	5.91	3.82	5.02	4.53	4.34	3.76	3.69	3.76	<1.77	3.76	5.45	4.27	10.32	8.97	6.83	5.44	
Mn	580	570	657	734	641	609	626	658	619	648	643	631	645	728	738	969	
Co	9.20	9.20	9.48	10.1	9.65	10.1	9.33	9.52	7.81	8.79	9.89	9.64	10.21	10.98	8.57	6.06	
Ni	65.8	69.5	74.6	75.1	67.4	67.1	59.5	61.7	57.8	68.3	85.5	82.9	84.8	88.3	63.4	45.35	
Cu	<0.007	0.01	0.03	0.03	0.02	<0.01	0.05	0.04	<0.06	<0.08	<0.08	<0.08	<0.07	<0.09	<0.07	<0.07	
Zn	7.55	6.79	6.26	6.29	6.87	6.13	6.46	6.00	7.47	7.95	9.20	8.40	7.73	9.31	12.04	7.37	
Rb	<0.004	<0.00	<0.002	0.02	0.03	<0.005	<0.002	<0.002	0.03	<0.02	<0.02	<0.03	0.06	0.05	<0.02	<0.02	
Sr	2083	1982	2073	2096	2062	1935	1985	2020	370	420	287	262	382	393	510	460	
Y	0.11	0.14	0.25	0.23	0.15	0.15											

Supplementary Material • CHAPTER 5

Gd157	0,02	0,03	0,13	0,10	0,04	0,02	0,03	0,04	<0.044	0,04	0,03	0,05	0,03	0,06	0,27	0,05
Tb159	0,00	0,00	0,01	0,01	0,00	0,00	<0.0004	0,00	0,01	0,02	0,00	0,01	0,00	0,01	0,03	0,01
Dy163	0,01	0,02	0,04	0,04	0,02	0,02	0,02	0,02	0,04	0,08	0,06	0,03	0,02	0,07	0,21	0,02
Ho165	0,00	0,00	0,01	0,00	0,00	0,00	0,00	0,00	0,01	0,02	0,01	0,01	0,01	0,01	0,03	0,00
Er167	0,01	0,02	0,03	0,02	0,02	0,02	0,01	0,01	0,08	0,05	0,05	0,06	0,04	0,03	0,07	0,03
Tm	0,00	0,00	0,00	0,00	0,00	0,00	0,00	0,00	0,01	0,01	0,01	0,01	0,01	0,01	0,02	0,00
Yb	0,01	0,00	0,02	0,01	0,02	0,03	0,01	0,02	0,09	0,06	0,05	0,13	<0.048	0,04	0,06	0,02
Lu	0,01	0,00	0,00	0,00	0,00	0,00	0,00	0,00	0,02	0,01	0,02	0,00	0,02	0,04	0,02	0,01
Hf	<0.00	<0.00	0,00	<0.00	<0.00	<0.00	<0.00	0,00	<0.00	<0.00	<0.00	<0.00	<0.00	<0.00	<0.00	<0.00
Ta	<0.00	<0.00	<0.0003	<0.001	0,00	<0.0005	<0.00	<0.0002	<0.008	<0.00	0,00	0,00	0,01	<0.00	<0.00	<0.01
W									<0.00	<0.00	<0.00	<0.00	<0.00	<0.00	<0.00	0,03
Pb	15,5	14,3	14,42	15,3	15,6	14,2	13,9	14,2	0,55	0,53	1,01	1,00	1,15	0,99	1,42	0,77
Th	0,00	<0.0004	<0.0004	<0.00	<0.0003	0,00	0,00	<0.00	<0.00	<0.00	<0.0243	<0.00	<0.00	<0.00	<0.00	<0.00
U	<0.0004	0,00	0,00	<0.001	<0.0004	0,00	0,00	<0.0002	<0.00	<0.00	<0.00	<0.00	<0.00	0,01	<0.00	<0.00

Tab B11. Continued.

Type	CS						CG										
	P0344	P0344	P0344	P0344	P0344	P0344	P0343	P0343	P0343	P0343	P0343	P0343	P0343	P0344	P0344	P0344	P0344
Mounts	MOL1-C	MOL1-C	MOL1-C	MOL1-C	MOL1-C	MOL1-C	18LP1	18LP1	18LP1	18LP1	18LP1	18LP1	18LP1	18LP1	18LP1	18LP1	18LP1
Sample							vein	vein	vein	vein	vein	vein	vein	vein	vein	vein	vein
Texture							do	do	do	do	do	do	do	do	do	do	do
Mineral	do	do	do	do	do	do	do	do	do	do	do	do	do	do	do	do	do
Name	7do3	7do4	7do5	8do1	8do2	8do3	5do1	5do2	5do3	5do4	3do1	3do2	7do1	7do2	7do3	7do4	
#	039	040	041	042	043	044	004	005	006	007	do	do	do	do	do	do	
SIMS				@1	@6	@7											
CL color	red	green	green	red-green	red-green	red-green	dark red	green	Yellow-green	dark red	red	green	green	red	red	green-yellow	
Li	<0.14	<0.14	<0.18	0,57	<0.18	<0.14	0,28	0,33	0,19	<0.15	0,22	<0.15	<0.19	0,17	0,26	<0.18	
Be	<0.00	<0.00	<0.00	<0.00	<0.00	<0.00	<0.00	<0.00	<0.00	<0.00	<0.00	<0.00	<0.00	<0.00	<0.00	<0.00	
B	24,1	17,9	23,5	16,1	16,17	16,19	10,3	10,2	11,6	12,7	11,2	6,81	11,7	10,7	14,0	6,84	
Na	5,87	8,33	30,2	82,8	25,2	9,39	15,5	6,36	4,91	7,87	9,28	20,3	1,74	5,64	9,36	3,05	
Sc	0,63	0,52	0,78	2,16	1,12	0,50	0,62	0,40	0,60	0,55	0,21	0,69	0,24	0,30	0,45	0,39	
Ti	<0.29	0,36	<0.33	<0.35	1,44	0,22	<0.19	<0.15	<0.16	<0.32	<0.49	<0.19	<0.27	<0.217	<0.37	0,07	
V	0,29	0,24	0,24	0,65	0,58	0,59	0,30	0,12	0,17	0,23	0,14	0,17	0,08	0,23	0,17	0,11	
Cr	6,88	5,37	5,11	7,12	4,00	8,49	4,54	2,99	<1.61	5,51	3,27	2,76	<2.45	3,93	4,41	<2.36	
Mn	648	645	702	743	899	736	680	831	819	646	602	698	622	688	645	648	
Co	10,2	10,3	10,9	11,0	8,36	10,64	9,89	5,45	4,25	7,67	7,62	7,03	5,32	10,1	9,54	4,98	
Ni	86,7	89,7	85,8	90,6	66,5	63,6	78,5	34,0	35,6	65,9	62,6	50,3	35,5	65,6	71,4	33,1	
Cu	<0.08	<0.09	0,18	<0.11	<0.09	<0.06	<0.07	<0.07	0,07	<0.07	0,10	<0.08	<0.09	<0.09	<0.08	<0.05	
Zn	9,30	9,38	9,51	9,23	10,8	7,65	8,04	5,64	6,23	6,02	7,07	7,25	6,29	6,38	7,04	5,74	
Rb	<0.02	<0.02	<0.02	0,13	0,11	<0.01	<0.02	<0.01	<0.01	<0.02	<0.02	<0.02	<0.02	<0.02	<0.01	<0.01	
Sr	407	352	386	353	416	403	1423	547	434	440	304	376	540	1543	663	524	
Y	0,41	0,42	0,79	1,59	1,06	0,22	0,49	0,67	0,64	0,55	0,14	1,05	0,39	0,19	0,29	0,78	
Zr	<0.00	<0.00	<0.00	<0.00	<0.00	<0.00	<0.00	<0.00	<0.00	<0.00	<0.00	0,00	0,00	<0.00	0,00	<0.00	
Nb	<0.00	<0.00	<0.01	<0.00	<0.00	0,00	<0.00	<0.01	<0.00	<0.00	<0.00	<0.00	<0.01	<0.00	<0.01	<0.00	
Mo	<0.09	0,07	0,05	0,01	0,03	<0.05	0,06	<0.07	<0.03	0,08	0,07	0,06	<0.06	0,04	0,02	0,04	
Cs	<0.02	0,09	1,51	0,49	0,03	<0.01	1,36	1,17	1,67	0,18	0,05	0,39	<0.03	<0.01	0,02	<0.02	
Ba	2,96	1,30	6,08	7,46	5,61	1,44	5,06	7,79	6,95	3,65	3,14	6,36	0,20	3,94	6,48	0,93	
La	3,46	2,83	3,37	5,73	4,51	1,87	9,61	7,44	5,65	5,52	2,94	8,73	3,88	5,74	6,06	6,98	
Ce	4,26	3,43	5,26	7,69	5,81	2,05	12,5	7,06	5,41	4,82	2,02	9,66	3,78	6,87	6,80	6,85	
Pr	0,29	0,25	0,49	0,65	0,49	0,13	0,98	0,41	0,34	0,38	0,09	0,70	0,22	0,47	0,52	0,38	
Nd	0,98	0,68	1,79	2,26	1,46	0,19	2,73	1,19	1,11	1,08	0,34	2,37	0,66	1,28	1,42	1,20	
Sm	0,16	0,08	0,28	0,23	0,20	0,02	0,18	0,05	0,14	0,18	<0.00	0,20	0,06	0,11	0,10	0,14	
Eu	0,03	0,04	0,05	0,05	0,09	0,08	0,15	0,06	0,06	0,05	0,02	0,11	0,03	0,07	0,07	0,03	
Gd	0,07	0,07	0,14	0,31	0,26	0,04	0,15	0,09	0,03	0,05	<0.00	0,21	0,04	0,05	0,05	0,10	
Tb	0,00	0,00	0,02	0,06	0,03	0,00	0,01	0,01	0,01	0,02	0,00	0,02	0,01	0,00	0,00	0,02	
Dy	0,04	0,05	0,10	0,20	0,13	0,04	0,09	0,07	0,11	0,06	0,01	0,19	0,05	0,05	0,02	0,07	
Ho	0,02	0,01	0,03	0,07	0,04	0,02	0,01	0,02	0,03	0,02	0,00	0,03	0,01	0,01	<0.01	0,03	
Er	0,02	0,06	0,11	0,18	0,08	0,03	0,02	0,07	0,12	0,04	<0.00	0,11	0,02	0,01	0,01	0,08	
Tm	0,00	0,01	0,02	0,03	0,01	0,01	0,01	0,01	0,01	0,01	<0.00	0,03	0,01	0,00	0,00	0,02	
Yb	0,05	0,04	0,05	0,18	0,07	<0.00	0,07	0,07	0,11	0,09	0,03	0,12	0,08	0,03	0,09	0,09	
Lu	0,01	0,01	0,03	0,05	0,02	0,01	0,01	0,02	0,02	0,01	0,01	0,03	0,01	0,01	0,01	0,02	
Hf	<0.00	<0.00	<0.00	<0.00	<0.00	<0.00	<0.00	<0.00	<0.00	<0.00	<0.00	<0.00	<0.00	<0.00	<0.05	<0.00	
Ta	<0.00	<0.00	<0.00	0,00	<0.00	<0.00	<0.00	0,00	<0.00	<0.00	<0.00	<0.00	<0.00	<0.00	<0.00	<0.00	
W	<0.00	<0.00	<0.00	<0.00	<0.00	<0.00	<0.00	0,01	0,01	<0.00	<0.00	<0.00	<0.00	<0.00	<0.00	<0.00	
Pb	0,87	1,05	1,28	2,40	9,12	1,59	2,66	0,34	0,33	0,62	0,64	0,22	0,21	3,20	1,95	0,21	
Th	<0.00	<0.00	<0.03	<0.00	<0.00	<0.00	<0.00	<0.00	<0.00	0,00	<0.00	<0.00	<0.00	<0.00	<0.00	<0.00	
U	<0.00	0,01	<0.00	<0.00	<0.00	<0.00	<0.00	0,00	<0.00	<0.0176	<0.00	<0.00	<0.00	<0.00	<0.00	<0.00	

Table B11. Continued.

Type	CG					CS			
	P0344	14	15	16	17	9,00	11,00	12,00	13,00
Mounts	18LP1	18LP1	18LP1	18LP1	18LP1	MOL1-C	MOL1-C	MOL1-C	MOL1-C
Sample									
Texture	vein	vein	vein	vein	vein	vein	vein	vein	vein
Mineral	032SMPL	do	do	do	do	mgs	mgs	mgs	mgs
Name	7do5	dol1a	dol1b	dol2	dol3	mgs1a	mgs1c	mgs2a	mgs2b
#	32	21	22	23	29	15	17	18	19
SIMS		vicino #36	vicino #36		close srp cut	-	-	-	-
CL color	red	red-green	green	red	red	-	-	-	-
Li7	<0.18	0,03	0,16	0,06	0,10	<0.01	0,02	0,28	0,30
Be9	<0.00	<0.00	<0.00	<0.00	<0.00	<0.00	<0.00	<0.00	<0.00
B11	12,1	4,42	3,48	2,27	4,44	4,06	4,16	3,97	4,53
Na23	3,91	0,35	0,42	0,33	0,16	0,08	0,03	0,95	1,98
Sc45	0,57	0,58	<0.05	0,10	<0.08	0,08	<0.02	<0.03	0,06
Ti47	<0.26	0,19	0,19	0,20	0,09	0,02	0,02	0,11	0,41
V51	0,14	5,94	4,06	5,79	3,05	0,46	1,12	1,53	3,33
Cr53	<3.07	609	685	664	638	1272	1304	1423	1470
Mn55	642	8775	8380	10838	9299	29547	30308	35541	36756
Co59	6,73	7,06	5,75	10,1	7,55	26,22	26,4	32,7	32,5
Ni60	46,3	53,3	44,0	72,4	64,2	253	247	241,04	231

Cu63	<0.08	0,06	0,01	0,04	<0.005	0,02	<0.003	0,03	0,02
Zn66	6,71	5,25	4,78	6,76	10,3	12,04	12,41	12,93	13,30
Rb85	<0.03	0,01	0,01	0,01	0,00	0,00	0,01	0,01	0,00
Sr	377	260	524	1361,23	305	0,10	0,25	0,14	0,07
Y	0,30	0,20	0,75	0,17	0,15	0,00	0,00	0,01	0,00
Zr	0,00	0,01	<0.002	<0.00	<0.00	0,00	<0.00	<0.00	0,00
Nb	<0.00	0,00	0,00	<0.00	<0.00	<0.0003	<0.00	<0.001	<0.00
Mo	<0.08	0,07	0,15	0,10	0,04	0,14	0,19	0,14	0,18
Cs	<0.03	<0.001	0,00	<0.001	0,00	0,00	0,00	0,00	0,00
Ba	0,19	1,68	1,66	5,48	0,82	0,13	0,12	0,12	0,02
La	6,72	4,13	8,66	5,10	3,38	0,002	0,004	0,001	0,003
Ce	5,22	3,04	8,61	6,08	2,16	0,001	0,003	0,002	0,003
Pr	0,26	0,18	0,62	0,44	0,11	<0.00	0,0004	<0.00	<0.00
Nd	0,56	0,45	2,08	1,27	0,44	<0.00	<0.00	0,002	<0.001
Sm	0,01	0,06	0,22	0,11	0,08	<0.00	<0.00	<0.00	<0.00
Eu	0,03	0,02	0,04	0,10	0,02	<0.00	<0.001	<0.00	<0.00
Gd	0,04	0,04	0,14	0,06	<0.00	<0.00	<0.00	<0.00	0,0021
Tb	0,00	0,00	0,01	0,00	0,00	<0.00	<0.00	<0.00	<0.00
Dy	0,03	0,04	0,13	0,03	0,01	<0.00	<0.00	<0.00	0,001
Ho	0,02	0,01	0,04	0,01	0,00	0,0003	<0.00	<0.00	0,0003
Er	0,02	0,02	0,09	0,02	0,02	0,001	<0.001	<0.00	<0.0006
Tm	<0.00	0,00	0,02	0,00	0,00	0,0003	<0.00	<0.00	<0.00
Yb	0,06	0,02	0,12	0,02	0,02	0,002	0,002	0,01	0,01
Lu	0,01	0,01	0,03	0,01	0,00	0,001	0,001	0,002	0,003
Hf	<0.00	<0.00	<0.00	<0.00	<0.00	<0.00	<0.00	<0.00	<0.00
Ta	<0.00	<0.00	<0.00	0,00	<0.00	<0.00	<0.00	<0.00	<0.00
W	<0.00								
Pb	0,19	0,28	0,10	3,51	0,59	0,03	0,01	0,01	0,01
Th	<0.00	0,00	0,00	0,00	<0.00	<0.00	<0.00	<0.00	<0.00
U	0,00	<0.001	0,00	0,00	<0.00	<0.00	<0.00	<0.00	0,00

Table B12: Drift- and matrix effect-corrected $\delta^{13}\text{C}$ and $\delta^{18}\text{O}$ values for dolomite from the Ulten Zone peridotite.

	Texture	Grain	CL color	$\delta^{13}\text{C}_{\text{VPDB}} (\text{‰})$	2se	$\delta^{18}\text{O}_{\text{SMOW}} (\text{‰})$	2se
VM25P10A							
P03345	in zrn w/chl/ap	dol1 #1	dark blue	-12,34	0,84	12,40	0,43
	in zrn very close to ap	dol1 #2	dark blue	-11,51	0,62	12,52	0,40
	in zrn w/chl/ap	dol1 #3	dark blue	-12,88	0,70	12,82	0,40
	in zrn w/chl/ap	dol1 #4	dark blue	-12,16	0,77	12,73	0,40
	in zrn w/chl/ap	dol1 #5	dark blue	-12,58	0,62	11,04	0,26
P03345	in zrn w/ap	dol2 #1	dark blue	-14,68	0,62	13,51	0,40
	in zrn w/ap	dol2 #2	dark blue	-13,32	0,62	13,51	0,30
	in zrn w/ap	dol2 #3	dark blue	-13,45	0,62	13,42	0,40
P03344	In zrn w/ap	dol4 #1	blue - rim	-14,85	0,68	13,25	0,39
	In zrn w/ap	dol4 #2	blue – close to rim	-10,19	0,69	12,64	0,38
	In zrn w/ap	dol4 #3	dull green	-10,15	0,77	12,82	0,35
	In zrn w/ap	dol4 #4	dull green - core	-12,17	0,74	13,43	0,36
	In zrn - close to apatite	dol4 #5	dull green	-11,71	0,78	12,39	0,35
	In zrn w/ap	dol4 #6	dull green - rim	-13,22	0,84	13,67	0,41
	In zrn w/ap	dol4 #7	dull green - rim	-14,21	0,85	13,34	0,42
MOL1-C							
P0345	matrix	dol3 #1	red	-11,67	0,65	12,29	0,39
	matrix	dol4 #1	red	-12,67	0,63	12,54	0,39
KL2.4-2b							
P0344	in spl w/cal+brc	dol3 #1	dull green	-9,32	0,69	12,87	0,31
	in spl w/cal+brc	dol3 #2	dull green - core	-8,94	0,69	12,63	0,38
	in spl w/cal+brc	dol3 #3	dull green	-7,85	0,70	12,78	0,41
	in spl w/cal+brc	dol2 #1	red (?)	-10,09	0,69	14,82	0,48
VM10A							
P0344	matrix	dol5 #1	red - rim	-8,87	0,86	na	na
	matrix	dol5 #2	dull green	-11,75	0,71	12,90	0,40
	matrix	dol5 #3	red - rim	-11,53	0,76	12,17	0,37
	matrix	dol5 #4	red/green	-10,98	0,69	12,78	0,27
	matrix	dol5 #5	red/yellow	-11,86	0,69	12,39	0,49
KL1-A							
P0343	matrix-rim	dol1 #1	red - rim	-10,43	0,76	13,08	0,43
	matrix-core	dol1 #2	red - core	-10,14	0,61	13,23	0,34

Supplementary Material • CHAPTER 5

	matrix	dol2 #1	red	-9,98	0,61	12,65	0,38
	matrix	dol2 #2	red/yellow - rim	-10,99	0,61	12,51	0,37
	matrix	dol2 #3	red	-10,88	0,73	12,39	0,47
	matrix	dol4 #1	red - core	-10,57	0,63	12,76	0,40
	matrix	dol4 #2	red - rim	-12,33	0,63	12,77	0,33
KL1-6							
P0343	vein	dol6 #1	red	-11,40	0,62	13,70	0,42
	vein	dol6 #2	red	-10,49	0,62	14,19	0,49
	vein	dol6 #3	red	-11,87	0,82	13,54	0,29
	vein	dol6 #4	red	-10,58	0,62	13,07	0,39
18LP1							
P0343	vein	dol3 #1	dark red	-15,24	0,71	12,23	0,38
	vein	dol3 #2	dark red	-14,38	0,76	12,40	0,36
	vein	dol3 #3	red	-12,09	0,59	11,90	0,28
	vein	dol3 #4	red	-10,32	0,62	12,83	0,40
	vein	dol3 #5	red	-12,29	0,76	12,04	0,39
	vein	dol3 #6	red	-11,35	0,75	13,07	0,43
	vein	dol3 #7	red	-11,53	0,63	12,98	0,33
	vein	dol3 #8	red	na	na	12,87	0,34
	vein	dol5 #5	red	-11,44	0,92	12,71	0,24
	vein	dol5 #6	red	-10,26	0,62	12,76	0,36
	vein	dol5 #4	red	-10,95	0,63	12,86	0,51
	vein	dol7#6	dark red	-11,63	0,63	12,27	0,35
	vein	dol 7#9	red	na	na	12,30	0,39
	vein	dol7#10	red //(O close y)	-10,50	0,63	13,20	0,37
	vein	dol #12	dark red	-9,89	0,63	12,86	0,39
	vein	dol5 #1	red-dull green	-9,33	na	12,38	0,39
	vein	dol5#2	dull green	-15,65	0,86	12,49	0,33
	vein	dol7#1	dull green	-11,96	0,64	12,91	0,29
	vein	dol7#2	dark green	-13,94	0,86	12,37	0,50
	vein	dol7#3	dark green	-13,39	0,62	12,01	0,35
	vein	dol7#4	dull green	-11,58	0,62	12,57	0,35
	vein	dol7#5	dull green	-13,67	0,65	11,97	0,32
	vein	dol7#8	dull green	-10,51	0,62	12,85	0,30
	vein	dol 7#9	dull green	-12,12	0,63	na	na
	vein	dol7#11	dull green	-8,81	0,63	12,08	0,30
	vein	dol7#13	dull green	-12,29	0,63	12,63	0,47
	vein	dol5 #3	yellow (O g/y)	-13,61	0,59	12,67	0,53
	vein	dol7#7	Yellow/red	-11,12	0,62	12,38	0,43
	vein	dol7#14	yellow (O g/y)	-13,33	0,66	11,70	0,37
Pyroxenite layer in MOL1-C							
	matrix	dol6 #1	dark green	-11,74	0,71	12,22	0,52
		dol6#5	dark green	-10,5	0,7	12,01	0,40
		dol6 #8	dark green (?)	-12	0,69	11,8	0,37
		dol8#1	dull green	na	na	12,85	0,41
		dol7#8	green	-8,16	0,69	13	0,35
		dol6#7	green	-10,59	0,7	12,2	0,38
		dol6#9	green	-10,9	0,69	12,04	0,37
		dol6#10	green	-10,73	0,7	12,43	0,42
		dol6#11	green	-10,23	0,7	na	na
		dol6#3	green	-9,87	0,71	na	na
		dol6#4	green	-11,31	0,71	na	na
		dol6#16	green	-11,34	0,7	11,96	0,43
		dol#5	red-green	na	na	12,78	0,55
		dol8#6	red-green	na	na	12,96	0,37
		dol8#9	red-green	-9,41	0,69	12,87	0,41
		dol7#3	red-green (?)	-10,85	0,72	12,18	0,38
		dol8 #3	red	na	na	12,70	0,36

dol6#6	red	-9,69	0,7	na	na
dol6#12	red	-9,53	0,74	12,02	0,34
dol6#13	red	-8,19	0,71	11,95	0,33
dol6#14	red	-11,53	0,82	12,13	0,41
dol6#15	red	-11,61	0,82	12,45	0,45
dol7#1	red	-10,02	0,71	na	na
dol7#2	red	-10,85	0,68	12,49	0,49
dol8#8	red	-9,62	0,84	12,70	0,39
dol8#2	red	na	na	12,29	0,44
dol8#10	red	na	na	12,97	0,37
dol6#2	yellow	-11,64	0,7	12,89	0,36
dol6#17	Green/yellow	-10,78	0,7	na	na
dol7#3	Red/green	-10,85	0,72	12,18	0,38
dol7#4		-9,52	0,7	12,38	0,45
dol7#5	Red/yellow	-10,05	0,8	na	na
dol #6	Red/green	-10,99	0,71	12,41	0,39
dol7#7		-9,48	0,7	12,56	0,44
dol7#10		na	na	13,23	0,39

Table B13: Drift- and matrix effect-corrected $\delta^{18}\text{O}$ values for zircon and forsterite from the porphyroclastic fine-grained garnet-amphibole peridotite VMP2510A, from M.te Hochwart.

ZIRCON						
Peridotite	Grain	Label	Texture	$\delta^{18}\text{O}$ corr \pm 2sig		X Mg
VM25P10A		unk_d18O_P0345_Zr@1	Rim – blue CL	5,89	0,32	
		unk_d18O_P0345_Zr@02	Rim – blue CL	5,84	0,33	
		unk_d18O_P0345_Zr@03		6,16	0,32	
		unk_d18O_P0345_Zr@04	Light blue-green	6,19	0,35	
		unk_d18O_P0345_Zr@05	Light blue-green	6,43	0,37	
		unk_d18O_P0345_Zr@06		6,19	0,27	
		unk_d18O_P0345_Zr@07		6,30	0,32	
		unk_d18O_P0345_Zr@08		6,15	0,32	
		unk_d18O_P0345_Zr@09		6,34	0,28	
		unk_d18O_P0345_Zr@10		6,17	0,26	
		unk_d18O_P0345_Zr@11		6,20	0,32	
		unk_d18O_P0345_Zr@12		6,47	0,37	
		unk_d18O_P0345_Zr_profile@1	Close to dolomite	6,25	0,35	
		unk_d18O_P0345_Zr_profile@02		5,97	0,37	
		unk_d18O_P0345_Zr_profile@03		6,05	0,32	
		unk_d18O_P0345_Zr_profile@04		6,26	0,34	
		unk_d18O_P0345_Zr_profile@05		6,02	0,29	
		unk_d18O_P0345_Zr_profile@06		6,15	0,27	
		unk_d18O_P0345_Zr_profile@07		5,76	0,26	
		unk_d18O_P0345_Zr_profile@08		6,34	0,37	
		unk_d18O_P0345_Zr_profile@09		6,15	0,34	
		unk_d18O_P0345_Zr_profile@10	Blue CL color	4,66	0,26	
		unk_d18O_P0345_Zr_profile@11		6,13	0,36	
		unk_d18O_P0345_Zr_profile@12		6,77	0,34	
		unk_d18O_P0345_Zr_profile@13	Close to rim – green/blue	6,14	0,34	
		unk_d18O_P0345_Zr_profile@14	Rim – blue CL	6,39	0,27	

OLIVINE						
Peridotite	Grain	Label	Texture	$\delta^{18}\text{O}$ corr \pm 2sig		X Mg (Mg/Mg+Fe)
VM25P10A	O1 – bordering with zircon	unk_d18O_P0345_O1@1	rim w/zircon	5,43	0,23	
		unk_d18O_P0345_O1@02	→ profile rim to core →	5,22	0,25	
		unk_d18O_P0345_O1@03	→ core	5,24	0,36	
	O12 – bordering with zircon	unk_d18O_P0345_O1@04	close to rim w/zircon	5,43	0,31	
		unk_d18O_P0345_O1@05	→ profile rim to core →	4,95	0,23	

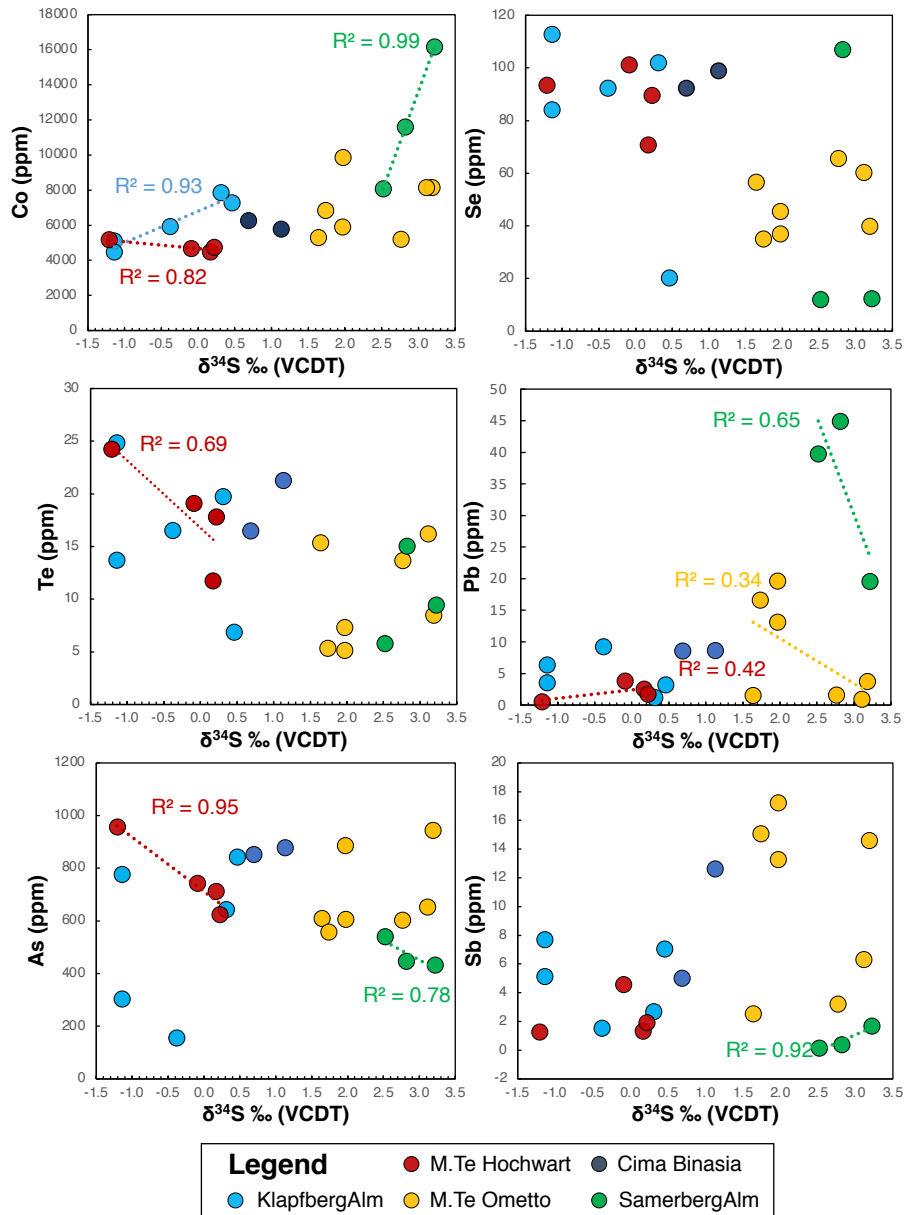
Supplementary Material • CHAPTER 5

		unk_d18O_P0345_OI1@06	→ olivine core	5,25	0,31
OI3 – bordering with zircon		unk_d18O_P0345_OI1@07	close to rim w/zircon	5,38	0,25
		unk_d18O_P0345_OI1@08	→ rim to core	5,33	0,34
OI4 – fine-grained matrix		unk_d18O_P0345_OI1@09	rim	5,24	0,22
		unk_d18O_P0345_OI1@10	→ towards core →	5,23	0,26
		unk_d18O_P0345_OI1@11	→ towards core	5,20	0,30
		unk_d18O_P0345_OI1@12	close to rim (other crystal facet)	5,46	0,27
		unk_d18O_P0345_OI1@13	→ core	5,42	0,23
OI 5 – fine-grained matrix		unk_d18O_P0345_OI1@14	rim with OI4	5,37	0,29
		unk_d18O_P0345_OI1@15	→ profile rim to core →	5,34	0,29
		unk_d18O_P0345_OI1@16	→ core →	5,22	0,34
		unk_d18O_P0345_OI1@17	→ towards opposite rim	4,83	0,27
MOL1-C	OI1 – coarse-grained matrix	unk_d18O_P0345_OI1_profile@1		5,12	0,30
		unk_d18O_P0345_OI1_profile@2		5,20	0,26
		unk_d18O_P0345_OI1_profile@3		5,21	0,20
		unk_d18O_P0345_OI1_profile@4		5,09	0,26
		unk_d18O_P0345_OI1_profile@5		5,36	0,26
		unk_d18O_P0345_OI1_profile@6		5,27	0,31
		unk_d18O_P0345_OI1_profile@7		5,08	0,24
		unk_d18O_P0345_OI1_profile@8		5,36	0,33
		unk_d18O_P0345_OI1_profile@9		5,10	0,28
		unk_d18O_P0345_OI1_profile@10		5,30	0,17
		unk_d18O_P0345_OI1_profile@11		5,40	0,24
		unk_d18O_P0345_OI1_profile@12		5,41	0,31
		unk_d18O_P0345_OI1_profile@13		5,00	0,26
		unk_d18O_P0345_OI1_profile@14		5,49	0,34
		unk_d18O_P0345_OI1_profile@15		5,40	0,26
		unk_d18O_P0345_OI1_profile@16		5,38	0,29
OI2 in fine-grained domain w/magnesite and dolomite		unk_d18O_P0345_OI2@1	Core (olivine with magnesite +dol)	4,87	0,31
		unk_d18O_P0345_OI2@2		5,03	0,26
		unk_d18O_P0345_OI2@3	Bordering with dol3#1	5,09	0,26

C. Supplementary Material of Chapter 6

Figure C1

Trace element concentrations (Co, Se, Te, Pb, As, Bi) versus $\delta^{34}\text{S}$ measured in pentlandite from different sampling locations in the Ulten Zone.



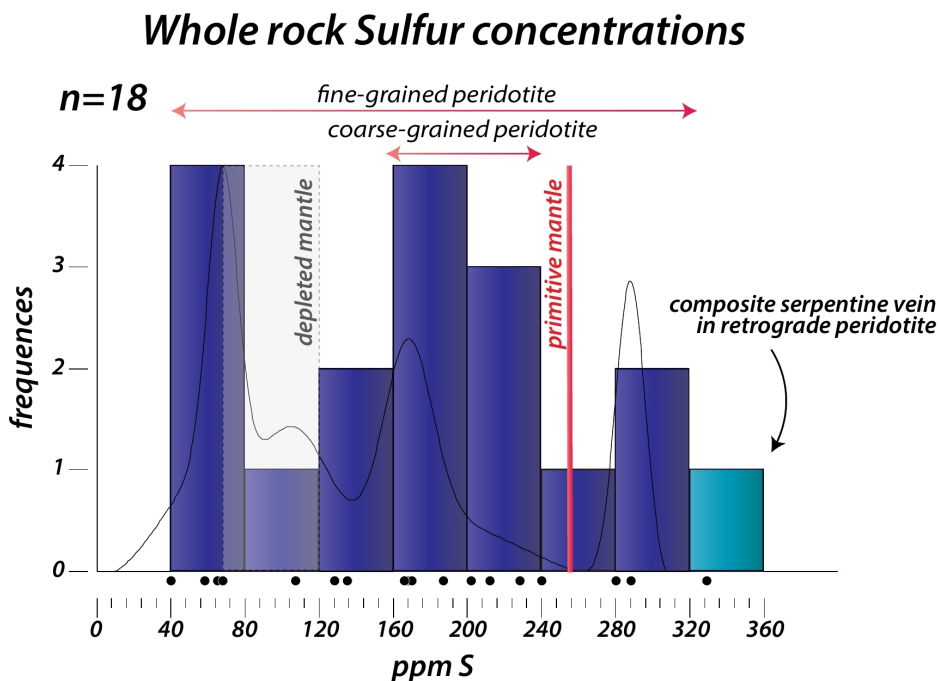


Figure C2: Sulfur concentrations of the Ulten Zone peridotites. The full dataset is reported in Supplementary Table C2.

Table C1: Major- and minor-element concentrations (wt%) of Ulten Zone peridotites

Sample	Rock Type	SiO ₂	TiO ₂	Al ₂ O ₃	Fe ₂ O ₃	FeOcalc	MnO	MgO	CaO	Na ₂ O	K ₂ O	P ₂ O ₅	Cr ₂ O ₃	NiO	LOI	Sum	V	Co	Zn
		(ppm) (ppm) (ppm)																	
MOL1-C	Cs	45.42	0.04	2.64	8.64	7.77	0.13	38.86	1.92	0.20	0.08	0.00	0.46	0.25	1.55	100.21	64	100	80
SBA2	CGn	43.68	0.05	1.85	9.14	8.22	0.13	41.90	2.67	0.13	0.01	0.00	0.22	0.29	0.40	100.49	54	117	59
18LP1	CG	43.10	0.02	1.91	9.06	8.15	0.13	42.71	1.51	0.06	0.02	0.00	0.37	0.30	0.86	100.07	50	113	51
KL24-3	P-FGA	41.97	0.11	3.02	8.47	7.62	0.12	38.11	2.42	0.26	0.12	0.01	0.41	0.26	5.34	100.62	68	102	52
P10B	P-FGA	44.15	0.04	2.61	8.79	7.91	0.13	39.96	2.59	0.15	0.04	0.00	0.40	0.27	0.72	99.88	66	111	39
VM10A	FGA	43.75	0.03	2.28	8.84	7.95	0.13	41.58	2.20	0.11	0.03	0.01	0.41	0.28	0.37	100.05	55	110	43
KL1-A	FGA	44.87	0.09	3.12	8.63	7.77	0.13	38.33	2.84	0.24	0.07	0.00	0.37	0.25	1.15	100.12	67	101	56
MM1B-Srp Vein	FSA	38.96	0.02	1.40	8.33	7.50	0.07	37.87	0.44	0.01	0.02	0.00	0.34	0.27	13.10	100.86	40	33	37
MM1	FSA	43.46	0.02	1.71	8.34	7.50	0.12	42.79	1.43	0.07	0.04	0.01	0.41	0.29	1.83	100.54	48	112	44

LOI—Loss on ignition; **Mg#**: molar Mg/(Mg+Fe^{total}). **Cs**—Coarse-grained spinel peridotite, **CGn**—Carbonate-free coarse-grained garnet peridotite, **CG**—Coarse-grained garnet/spinel with coronitic garnet peridotite, **P-FGA**—Porphyroclastic fine-grained garnet amphibole peridotite, **FGA**—Porphyroclastic fine-grained garnet amphibole peridotite, **FSA**—Fine-grained spinel (chlorite-amphibole) peridotite.

Table C2. Whole rock sulfur concentrations (ppm) of Ulten Zone peridotites

Type	Samples	S XRF	S Leco	avg ppm	rsd
CS	MOL1-C			212,00	
CG	UN1	244,30	129,00	186,65	43,68

PhD Activities

CG	UN2	152,19	184,00	168,09	13,38
CG	18LP1			170,00	
CGn	SBA2			166,00	
FGA	UN3	48,06	67,40	57,73	23,69
FGA	UN6	92,11	121,00	106,56	19,17
FGA	UN7	116,14	14,00	65,07	111,00
FGA	UN9	64,08	72,00	68,04	8,23
FGA	UN14	304,38	272,00	288,19	7,94
FGA	KL24-3			128,00	
FGA	KL1-A			280,00	
FGA	P10B			240,00	
FGA	VM10A			202,00	
FSA	MM1B			228,00	
FSA	UN16	248,31	21,00	134,65	119,37
FSA	UN8	64,08	16,00	40,04	84,91
FSA-vein	MM1			329,00	

XRF: calculated from SO₃ concentrations obtained by X-Ray Fluorescence spectroscopy, LECO: obtained from infrared absorption rsd = relative standard deviation. During XRF analysis, ultramafic reference material UB-N, a serpentinite, gave an S concentration of 162±3 ppm (n = 2), during infrared spectroscopy the NBS reference material gave an S concentration of 2,870±30 ppm (n = 2). Sulfide modes were calculated by assuming all S resides in a pentlandite with ~33 wt% S (i.e. the average of pentlandite from Ulten Zone peridotites). CS—Coarse-grained spinel peridotite, CGn—Carbonate-free coarse-grained garnet peridotite, CG—Coarse-grained garnet/spinel with coronitic garnet peridotite, FGA—Fine-grained garnet amphibole peridotite, FSA—Fine-grained spinel (chlorite-amphibole) peridotite.

Table C3: Major element compositions (wt.%) of sulfides from the Ulten Zone peridotites

Pentlandite				S	Fe	Ni	Co	Cu	Zn	Pb	Total
Comment	Sulfide	No.	Textural Position								
Detection Limit (ppm)				100	400	300	400	500	450		
UN1_2_s2_8	pentlandite	na		33,13	34,96	29,93	0,87	bdl	bdl	0,11	99,03
UN1_2_s3_1	pentlandite	na		33,11	33,97	30,90	0,90	bdl	bdl	0,12	99,14
UN1_2_s4_1	pentlandite	na		33,34	33,21	31,50	1,02	bdl	bdl	0,12	99,24
UN1_2_s5_1	pentlandite	na		33,12	36,35	28,38	0,89	bdl	bdl	0,11	99,04
UN1_2_s6_4	pentlandite	na		33,39	34,65	29,47	0,78	0,22	bdl	0,08	98,70
UN1_2_s7_5	pentlandite	na		32,28	31,46	32,55	1,42	bdl	bdl	0,11	97,94
UN1_2_s10b_2	pentlandite	na		30,97	29,05	34,04	1,05	bdl	bdl	0,08	95,29
UN1_2_s11_5	Ni-pn	na		33,02	28,78	36,09	1,14	bdl	bdl	0,10	99,21
UN1_2_s11b_3	pentlandite	na		32,00	31,03	32,43	1,13	bdl	bdl	0,13	96,79
UN1_2_s12gross_3	pentlandite	na		33,20	34,84	30,11	0,93	bdl	bdl	0,14	99,28
UN2_2_s1_6	pentlandite	na		33,38	37,04	26,68	0,92	bdl	bdl	0,12	98,24
UN2_2_s3_5	pentlandite	na		33,18	36,20	28,29	1,30	bdl	bdl	0,10	99,18
UN2_2_s4a_3	pentlandite	na		33,35	37,86	26,65	1,02	bdl	bdl	0,09	99,08
UN2_2_s4b_3	pentlandite	na		33,44	38,33	25,70	0,98	0,61	bdl	0,12	99,19
UN2_2_s5_4	pentlandite	na		33,13	36,82	27,60	0,65	0,33	bdl	0,11	98,71
UN2_2_s7d_3	pentlandite	na		33,01	30,13	32,37	3,20	bdl	bdl	0,09	98,90
UN2_2_s7h_3	Ni-pn	na		32,47	26,05	37,19	2,84	bdl	bdl	0,10	98,74
UN2_2_s8_5	pentlandite	na		33,22	38,20	26,49	0,93	bdl	bdl	0,10	99,02
UN2_2_s8kl_3	pentlandite	na		33,16	37,42	27,07	0,93	bdl	bdl	0,12	98,83
UN2_2_s9_5	pentlandite	na		33,18	37,26	27,56	0,75	bdl	bdl	0,09	98,93

PhD Activities

UN2_2_s10_4	pn inhomo	na	33,63	40,02	24,60	0,79	bdl	bdl	0,11	99,22
UN2_2_s11_4	pentlandite	na	33,36	37,04	27,11	0,79	0,73	bdl	0,06	99,13
UN3_2_s1_3	pentlandite	na	33,06	30,34	33,82	1,79	bdl	bdl	0,09	99,20
UN3_2_s1b_5	pentlandite	na	33,09	34,60	30,03	1,07	bdl	bdl	0,12	99,02
UN3_2_s2_5	pentlandite	na	33,04	31,08	31,97	2,60	bdl	bdl	0,11	98,88
UN3_2_s3_5	pentlandite	na	33,09	30,39	33,84	1,70	bdl	bdl	0,10	99,21
UN3_2_s4_5	pentlandite	na	33,23	34,91	29,53	1,24	bdl	bdl	0,10	99,09
UN3_2_s5_8	pn inhomo	na	32,14	33,67	26,71	0,91	4,96	bdl	0,09	98,55
UN3_2_s6d_5	pentlandite	na	33,10	35,13	29,56	0,95	bdl	bdl	0,09	98,95
UN3_2_s6h_4	pentlandite	na	32,74	34,40	28,69	0,89	1,92	bdl	0,08	98,77
UN3_2_s7homo_5	pentlandite	na	33,03	31,04	33,81	0,89	bdl	bdl	0,10	98,94
UN3_2_s7heterogross_4	pentlandite	na	32,87	35,62	28,66	0,73	0,69	bdl	0,11	98,76
UN3_2_s8_5	pentlandite	na	32,91	34,23	30,63	0,88	bdl	bdl	0,08	98,82
UN6_2_s2a_5	pentlandite	na	33,27	36,27	28,81	0,84	bdl	bdl	0,11	99,42
UN6_2_s2b_5	pentlandite	na	33,16	34,98	30,34	0,74	bdl	bdl	0,09	99,36
UN6_2_s3_5	pentlandite	na	33,17	35,12	29,89	0,85	bdl	bdl	0,12	99,23
UN6_2_s4_5	pentlandite	na	32,53	36,27	27,25	0,53	bdl	bdl	0,10	96,72
UN6_2_s6_2	pentlandite	na	33,29	36,66	28,52	0,77	0,14	bdl	0,13	99,56
UN6_2_s7_5	pentlandite	na	33,19	35,41	29,32	1,14	bdl	bdl	0,10	99,22
UN6_2_s8_5	pentlandite	na	33,20	31,41	33,60	0,91	bdl	bdl	0,08	99,28
UN6_2_s9d_5	pentlandite	na	33,19	31,34	32,61	1,08	bdl	bdl	0,11	98,38
UN6_2_s9h_2	pentlandite	na	32,72	28,30	36,42	1,09	bdl	bdl	0,10	98,74
UN6_2_s10_5	pentlandite	na	33,14	35,16	29,93	0,89	bdl	bdl	0,11	99,29
UN7_1_s1_5	pentlandite	na	33,19	34,85	29,97	1,06	bdl	bdl	0,11	99,24
UN7_1_s2biga_5	pentlandite	na	33,14	30,76	33,61	1,52	bdl	bdl	0,14	99,29
UN7_1_s2bigb_5	pentlandite	na	32,95	30,58	33,30	1,43	bdl	bdl	0,09	98,44
UN7_1_s3d_5	pentlandite	na	33,16	31,57	32,97	1,58	bdl	bdl	0,09	99,43
UN7_1_s4ko_3	pentlandite	na	33,07	29,82	34,05	1,04	bdl	bdl	0,10	98,13
UN7_1_s4go_5	pentlandite	na	33,10	34,93	30,18	0,75	bdl	bdl	0,10	99,10
UN7_1_s4gu_5	pentlandite	na	33,15	34,23	30,32	0,96	bdl	bdl	0,10	98,85
UN7_1_s5_5	pentlandite	na	32,94	33,99	30,38	0,97	bdl	bdl	0,09	98,48
UN7_1_s6_5	pentlandite	na	33,11	34,54	30,08	1,19	bdl	bdl	0,11	99,13
UN7_1_s7_5	pentlandite	na	33,09	32,98	31,85	1,04	bdl	bdl	0,10	99,12
UN7_1_s8_5	pentlandite	na	33,14	32,63	32,14	1,17	bdl	bdl	0,12	99,33
UN7_1_s9_10	pentlandite	na	33,16	37,69	27,49	0,61	bdl	bdl	0,10	99,13
UN7_1_s10_5	pentlandite	na	33,07	34,48	29,05	2,06	0,18	bdl	0,10	98,97
UN7_1_s11_5	pentlandite	na	33,10	31,65	32,24	1,86	bdl	bdl	0,11	99,03
UN7_1_s13_7	pentlandite	na	33,18	31,35	32,51	1,83	bdl	bdl	0,11	99,02
UN7_1_s9kl_3	pentlandite	na	33,39	38,36	26,33	0,63	bdl	bdl	0,12	98,91
UN7_1_s9h_2	pentlandite	na	33,12	36,58	28,42	0,80	bdl	bdl	0,05	99,03
UN8_1_s1_4	pentlandite	na	32,92	26,07	38,70	0,53	bdl	bdl	0,09	98,39
UN8_1_s2h_5	pentlandite	na	32,88	29,80	30,34	6,23	bdl	bdl	0,10	99,40
UN8_1_s3_4	pentlandite	na	32,93	31,94	31,67	1,90	bdl	bdl	0,05	98,66
UN8_1_s5l_5	pentlandite	na	33,03	32,12	32,37	1,18	bdl	bdl	0,10	98,91
UN8_1_s5r_5	pentlandite	na	33,11	31,60	32,72	1,30	bdl	bdl	0,10	98,94
UN8_1_s6ld_3	pentlandite	na	33,13	31,77	32,32	1,59	bdl	bdl	0,07	99,00
UN8_1_s7_5	pentlandite	na	33,09	30,99	32,34	2,37	bdl	bdl	0,09	98,87
UN8_1_s8m_3	pentlandite	na	33,12	29,38	30,06	6,88	bdl	bdl	0,10	99,67
UN9_s1_5	pentlandite	na	33,57	37,72	27,36	0,70	bdl	bdl	0,09	99,51
UN9_s2_5	pentlandite	na	33,59	39,25	25,75	0,49	0,12	bdl	0,12	99,34
UN9_s3_5	pentlandite	na	33,10	37,51	27,42	0,76	bdl	bdl	0,08	98,98
UN9_s4_5	pentlandite	na	33,42	37,04	28,11	0,72	bdl	bdl	0,09	99,51
UN9_s5_5	pentlandite	na	33,58	34,64	30,58	0,84	bdl	bdl	0,09	99,79
UN9_s6_4	pentlandite	na	33,02	35,30	29,26	0,90	0,14	bdl	0,08	98,75
UN9_s7_5	pentlandite	na	33,51	36,34	28,89	0,74	bdl	bdl	0,08	99,66
UN9_s8_5	pentlandite	na	33,48	33,14	31,71	0,98	bdl	bdl	0,10	99,50

PhD Activities

UN9_s9_5	pentlandite	na		33,49	39,12	25,57	0,70	0,32	bdl	0,09	99,35
UN9_s10a_5	pentlandite	na		33,33	36,89	28,06	0,77	bdl	bdl	0,08	99,25
UN9_s10b_4	pentlandite	na		33,23	36,56	28,49	0,80	bdl	bdl	0,11	99,26
UN10_s1_5	pentlandite	na		33,06	35,05	30,31	0,59	bdl	bdl	0,10	99,17
UN10_s2_5	pentlandite	na		33,02	36,13	28,91	0,61	bdl	bdl	0,13	98,91
UN10_s3_5	pentlandite	na		33,21	34,06	31,04	0,65	bdl	bdl	0,11	99,14
UN10_s4_5	pentlandite	na		33,45	34,99	30,33	0,65	bdl	bdl	0,07	99,52
UN10_s5_5	pentlandite	na		33,61	38,93	26,06	0,69	bdl	bdl	0,10	99,49
UN10_s6a_3	pentlandite	na		33,34	35,85	29,46	0,65	bdl	bdl	0,10	99,50
UN10_s6bdunkel_3	pentlandite	na		33,39	36,30	28,68	0,61	bdl	bdl	0,09	99,18
UN10_s7innen_3	pentlandite	na		33,70	37,07	28,15	0,59	bdl	bdl	0,10	99,74
UN10_s8_5	pn hetero	na		34,32	25,56	36,46	0,51	1,25	bdl	0,11	98,21
UN10_s9a_2	pentlandite	na		33,03	35,20	29,50	0,60	bdl	bdl	0,12	98,47
UN10_s9b_3	pentlandite	na		33,47	35,54	29,98	0,60	bdl	bdl	0,09	99,76
UN10_s9c_3	pentlandite	na		33,52	38,31	26,98	0,53	bdl	bdl	0,10	99,50
UN10_s10_5	pentlandite	na		33,55	39,38	26,08	0,41	bdl	bdl	0,12	99,57
UN14_s1_3	pentlandite	na		33,35	38,00	26,65	0,58	0,27	bdl	0,13	99,00
UN14_s2_3	pentlandite	na		33,47	40,16	24,33	0,53	0,50	bdl	0,10	99,12
UN14_s3_4	pentlandite	na		33,50	40,00	24,71	0,65	0,20	bdl	0,08	99,16
UN14_s4a_4	pentlandite	na		33,70	38,10	26,41	0,70	bdl	bdl	0,09	99,04
UN14_s4b_5	pentlandite	na		32,92	38,70	25,65	0,71	0,13	bdl	0,13	98,28
UN14_s5_4	pentlandite	na		33,67	38,58	25,88	0,71	0,61	bdl	0,11	99,59
UN14_s6_4	pentlandite	na		32,84	35,58	28,26	0,76	1,05	bdl	0,10	98,61
UN14_s7_1	pentlandite	na		33,57	38,75	25,98	0,69	bdl	bdl	0,11	99,23
UN14_s8_2	pentlandite	na		33,49	39,84	24,99	0,63	0,10	bdl	0,11	99,18
UN14_s9_3	pentlandite	na		33,52	38,17	26,29	0,68	0,31	bdl	0,11	99,09
UN14_s10_4	pentlandite	na		33,15	38,31	26,60	0,77	bdl	bdl	0,10	99,07
UN14_s11_4	pentlandite	na		33,51	39,59	25,14	0,68	0,12	bdl	0,11	99,16
UN14_s12g_2	pentlandite	na		33,58	40,27	23,02	0,46	1,58	bdl	0,10	99,01
UN14_s12k_2	pentlandite	na		33,47	36,98	27,77	0,74	bdl	bdl	0,13	99,13
UN14_s13a_3	pentlandite	na		33,62	40,82	21,77	0,49	2,03	bdl	0,14	98,91
UN14_s13b_3	pentlandite	na		33,54	38,10	26,73	0,76	0,07	bdl	0,13	99,34
UN16_s1_5	pentlandite	na		33,17	34,90	29,79	0,84	bdl	bdl	0,13	98,92
UN16_s2_5	pentlandite	na		33,55	37,00	27,39	0,63	bdl	bdl	0,11	98,70
UN16_s3_5	pentlandite	na		33,29	30,67	34,43	0,75	bdl	bdl	0,10	99,27
UN16_s4_4	pentlandite	na		33,31	35,97	28,91	0,81	bdl	bdl	0,09	99,21
UN16_s5_4	pentlandite	na		33,17	35,60	29,00	0,80	bdl	bdl	0,09	98,77
UN16_s6g_4	pentlandite	na		33,46	33,32	31,53	0,69	bdl	bdl	0,08	99,17
UN16_s6k_4	pentlandite	na		33,35	31,92	32,02	0,82	bdl	bdl	0,08	98,28
UN16_s7a_2	pentlandite	na		33,35	34,46	30,44	0,66	bdl	bdl	0,09	99,08
SBA2_pn1	pentlandite	130,00	matrix	34,28	34,21	31,65	1,32	bdl	bdl	na	101,55
SBA2_pn2	pentlandite	131,00	matrix	33,97	29,70	35,22	1,89	bdl	bdl	na	100,85
SBA2_pn3	pentlandite	132,00	matrix	33,99	33,19	31,67	2,09	bdl	bdl	na	101,04
SBA2_pn4	pentlandite	133,00	matrix	34,06	30,55	33,65	2,12	bdl	bdl	na	100,46
SBA2_pn5	pentlandite	134,00	in srp vein	34,22	32,00	33,38	1,79	bdl	bdl	na	101,47
SBA2_pn6	Ni-pn	135,00	in srp vein	33,10	26,27	39,08	1,73	bdl	bdl	na	100,28
SBA2_pn7	pentlandite	136,00	matrix	33,89	30,82	33,83	2,05	bdl	bdl	na	100,77
SBA2_pn8	pentlandite	137,00	matrix	33,95	30,92	33,59	2,46	bdl	bdl	na	100,92
SBA2_pn9	pentlandite	138,00	matrix	34,04	36,97	28,27	0,84	bdl	bdl	na	100,17
SBA2_pn10	pentlandite	139,00	matrix	33,98	30,22	35,79	2,60	bdl	bdl	na	102,63
18LP1_pn1	pentlandite	171,00	matrix	34,11	31,18	32,37	1,11	bdl	bdl	na	99,37
18LP1_pn2	pentlandite	172,00	matrix	33,67	31,58	33,32	1,09	bdl	bdl	na	99,68
18LP1_pn3	pentlandite	173,00	matrix	33,92	32,58	31,94	1,01	bdl	bdl	na	100,12
18LP1_pn4	pentlandite	175,00	matrix	33,88	31,20	33,55	1,13	bdl	bdl	na	99,78
18LP1_pn5	pentlandite	176,00	w/dolomite vein	33,93	32,03	32,87	1,03	bdl	bdl	na	99,89
18LP1_pn6	Co-pn	177,00	w/dolomite vein	34,05	22,85	26,82	16,58	bdl	bdl	na	100,34

PhD Activities

18LP1_pn6-2	Co-pn	178,00	w/dolomite vein	33,81	23,27	26,49	16,28	bdl	bdl	na	99,98
18LP1_pn7	pentlandite	179,00	matrix	33,88	31,93	32,77	0,89	bdl	bdl	na	99,77
18LP1_pn8	pentlandite	180,00	matrix	33,30	32,70	31,15	0,84	1,77	bdl	na	99,76
18LP1_pn9	pentlandite	181,00	in orthopyroxene	33,90	30,72	34,19	0,81	bdl	bdl	na	99,62
18LP1_pn10	pentlandite	182,00	in dol vein (w/millerite)	33,41	31,76	32,70	0,80	1,05	bdl	na	99,82
18LP1_pn11	pentlandite	184,00	in dol vein (w/millerite)	33,95	31,28	34,06	0,95	bdl	bdl	na	100,50
18LP1_pn12	pentlandite	185,00	in dol vein (w/millerite)	33,86	31,59	32,91	0,88	bdl	bdl	na	99,61
18LP1_pn13	Co-pn	187,00	matrix close to dol vein	32,45	25,95	29,00	11,23	bdl	bdl	na	98,72
18LP1_mil4	Co-pn	188,00	matrix close to dol vein	33,80	24,37	29,82	11,44	bdl	bdl	na	99,49
18LP1_pn14	pentlandite	189,00	in orthopyroxene	33,90	29,25	35,68	0,64	bdl	bdl	na	99,47
18LP1_pn15	pentlandite	190,00	in coarse spl (in opx)	34,05	29,73	35,35	0,59	bdl	bdl	na	99,82
18LP1_pn16	pentlandite	191,00	in coarse spl (in opx)	33,91	30,05	35,60	0,72	bdl	bdl	na	100,42
MOL1-C_pn1	pentlandite	41,00	in srp	34,48	30,06	35,82	1,54	bdl	bdl	na	102,01
MOL1-C_pn3	Ni-pn	43,00	in srp vein	34,20	25,92	38,00	1,72	bdl	bdl	na	100,01
MOL1-C_pn4	pentlandite	45,00	in srp vein	34,12	30,01	35,53	1,38	bdl	bdl	na	101,15
MOL1-C_pn4_2	pentlandite	46,00	in srp vein	34,34	30,12	35,25	1,39	bdl	bdl	na	101,19
MOL1-C_pn7	Ni-pn	49,00	in srp	34,24	28,16	36,08	1,78	bdl	bdl	na	100,39
MOL1-C_pn8	pentlandite	50,00	in srp vein	34,39	31,39	35,09	1,14	bdl	bdl	na	102,23
MOL1-C_pn8-2	pentlandite	51,00	in srp vein	34,50	31,07	35,43	1,17	bdl	bdl	na	102,45
MOL1-C_pn10	pentlandite	53,00	in srp (in opx)	34,38	30,90	35,73	1,14	bdl	bdl	na	102,25
MOL1-C_pn11	pentlandite	55,00	in srp vein	34,39	30,76	35,36	1,05	bdl	bdl	na	101,63
MOL1-C_pn12	Ni-pn	56,00	in srp vein	34,33	30,28	36,15	1,10	bdl	bdl	na	101,99
MOL1-C_pn13	Ni-pn	57,00	in srp vein	34,37	31,26	36,07	1,00	bdl	bdl	na	102,90
MOL1-C_pn14	Ni-pn	59,00	in srp vein	34,29	27,39	37,99	1,49	bdl	bdl	na	101,28
MOL1-C_pn15	pentlandite	60,00	in srp vein	34,42	30,06	35,48	1,66	bdl	bdl	na	101,89
MOL1-C_pn16	pentlandite	61,00	in srp vein	34,58	31,85	34,57	1,00	bdl	bdl	na	102,02
MOL1-C_pn17	pentlandite	62,00	in srp (in opx)	34,15	30,55	35,49	0,93	bdl	bdl	na	101,37
MOL1-C_pn18	pentlandite	63,00	in srp vein	34,28	30,04	35,91	1,21	bdl	bdl	na	101,58
MOL1-C_pn19	pentlandite	64,00	matrix w/dolomite	34,55	31,29	35,00	1,06	bdl	bdl	na	102,12
MOL1-C_pn20	pentlandite	66,00	matrix	34,77	31,22	35,20	1,02	bdl	bdl	na	102,31
KL2.4-2b_pn1	pentlandite	5,00	in kelyphite	33,90	29,25	35,75	1,04	bdl	bdl	na	100,01
KL2.4-2b_pn2-dark-zoning	Ni-pn	9,00	in kelyphite	34,13	26,24	37,11	1,91	bdl	bdl	na	100,02
KL2.4-2b_pn5	pentlandite	11,00	in srp	32,91	33,73	32,12	1,77	bdl	bdl	na	100,73
KL2.4-2b_pn6	pentlandite	12,00	in srp	33,95	35,52	29,17	1,64	bdl	bdl	na	100,45
KL2.4-2b_pn7	pentlandite	13,00	in kelyphite	33,93	33,75	30,99	0,86	bdl	bdl	na	99,64
KL2.4-2b_pn8	pentlandite	14,00	PI in spinel	33,89	31,86	33,46	0,48	bdl	bdl	na	99,76
KL2.4-2b_pn9	pentlandite	16,00	in kelyphite	34,44	34,80	30,70	0,32	bdl	bdl	na	100,37
KL2.4-2b_pn10	pentlandite	18,00	in kelyphite	34,18	40,58	23,88	0,59	1,85	0,18	na	101,27
KL2.4-2b_pn10-2	pentlandite	19,00	in kelyphite	33,86	38,42	26,00	0,92	2,55	bdl	na	101,88
KL2.4-2b_pn10-3	pentlandite	24,00	in kelyphite	33,63	40,24	24,65	0,58	1,66	bdl	na	100,79
KL2.4-2b_pn11	pentlandite	26,00	in spinel	34,11	35,72	30,77	0,47	bdl	bdl	na	101,29
KL2.4-2b_pn11-2	pentlandite	27,00	in spinel	34,24	36,31	30,51	0,43	bdl	bdl	na	101,88
KL2.4-2b_pn12	pentlandite	28,00	PI in spinel	34,25	30,69	34,84	1,00	bdl	bdl	na	101,01
KL2.4-2b_pn13	pentlandite	31,00	in kelyphite	32,61	28,82	35,13	1,62	1,13	bdl	na	99,39
KL2.4-2b_pn14	pentlandite	33,00	in spinel	34,40	34,40	31,50	0,41	bdl	bdl	na	100,80
KL2.4-2b_pn15	pentlandite	34,00	in srp	33,91	36,05	28,71	2,91	bdl	bdl	na	101,69
KL2.4-2b_pn16	pentlandite	35,00	in kelyphite	34,56	38,59	28,53	1,07	bdl	bdl	na	102,84
KL2.4-2b_pn17	pentlandite	36,00	in spinel	34,20	35,60	30,04	1,07	bdl	bdl	na	101,03
KL2.4-2b_pn18	pentlandite	37,00	in srp	34,16	35,55	30,38	0,52	bdl	bdl	na	100,67
KL2.4-2b_pn19	pentlandite	38,00	in srp	34,12	34,15	31,59	0,22	0,32	bdl	na	100,58
KL2.4-2b_pn20	pentlandite	39,00	in srp	33,81	35,01	29,61	0,85	bdl	bdl	na	100,30
KL2.4-2b_pn21	pentlandite	40,00	in srp	34,24	36,51	29,40	0,74	bdl	bdl	na	101,02
KL2.4-3_pn1	pentlandite	93,00	in kelyphite	34,23	37,46	26,83	1,06	bdl	bdl	na	99,73
KL2.4-3_pn2	pentlandite	94,00	in Ca-amphibole	33,77	33,31	30,25	0,59	bdl	bdl	na	98,29
KL2.4-3_pn3	pentlandite	96,00	in srp	33,96	38,10	27,43	1,02	bdl	bdl	na	100,95
KL2.4-3_pn3-2	pentlandite	97,00	in srp	34,17	39,72	26,18	1,08	bdl	bdl	na	101,71

PhD Activities

KL2.4-3_pn4	pentlandite	100,00	in srp	34,07	36,28	28,11	1,11	bdl	bdl	na	99,58
KL2.4-3_pn5	pentlandite	102,00	in srp	33,85	26,99	38,00	0,44	bdl	bdl	na	99,38
KL2.4-3_pn6	pentlandite	103,00	in srp	33,86	35,47	29,46	1,35	bdl	bdl	na	100,25
KL2.4-3_pn7	pentlandite	104,00	in srp	34,08	36,96	28,85	0,95	bdl	bdl	na	100,94
KL2.4-3_pn8	pentlandite	105,00	in kelyphite	34,12	36,49	28,98	0,87	bdl	bdl	na	100,66
KL2.4-3_pn9	pentlandite	106,00	in kelyphite	33,79	39,50	25,02	0,66	1,39	bdl	na	100,36
KL2.4-3_pn10	pentlandite	109,00	in coarse spinel	34,05	33,66	30,42	0,76	bdl	bdl	na	99,07
KL2.4-3_pn11	pentlandite	110,00	in kelyphite	33,70	33,80	31,31	0,63	bdl	bdl	na	99,59
KL2.4-3_pn12	Ni-pn	111,00	in kelyphite	34,01	26,18	38,58	0,48	bdl	bdl	na	99,39
KL2.4-3_pn13	pentlandite	112,00	in srp	34,44	35,60	29,07	1,30	bdl	bdl	na	100,44
KL2.4-3_pn14	pentlandite	113,00	in srp	33,95	35,51	28,28	1,53	bdl	bdl	na	99,38
KL2.4-3_pn15	pentlandite	114,00	in srp	33,92	33,90	30,70	1,40	bdl	bdl	na	100,00
KL2.4-3_pn16	pentlandite	115,00	in srp	34,38	35,70	29,82	0,96	bdl	bdl	na	101,02
KL2.4-3_pn17	pentlandite	116,00	in srp	33,62	36,38	28,53	1,11	bdl	bdl	0,00	99,78
KL24-3_thick_pn1	pentlandite	196,00	in srp	33,60	35,75	28,57	1,52	bdl	bdl	0,00	99,76
KL24-3_thick_pn1-2	pentlandite	197,00	in srp	33,78	36,14	28,17	1,59	bdl	bdl	0,00	100,04
KL24-3_thick_pn2	pentlandite	198,00	nd	33,60	33,96	29,66	0,97	bdl	bdl	0,00	98,28
KL24-3_thick_pn3	pentlandite	199,00	nd	33,45	30,95	32,64	1,26	bdl	bdl	0,00	98,35
KL24-3_thick_pn4	pentlandite	200,00	in srp	33,54	33,19	29,70	2,09	bdl	bdl	0,00	98,78
KL24-3_thick_pn5	Co-pn	201,00	in srp (w/dolomite)	28,43	25,76	36,91	7,47	bdl	bdl	0,00	98,68
KL1-A_pn1	pentlandite	67,00	matrix	34,13	32,22	32,69	1,52	bdl	bdl	0,00	100,68
KL1-A_3	pentlandite	71,00	matrix w/dol	34,48	33,76	32,66	1,28	bdl	bdl	0,00	102,21
KL1-A_pn3-2	pentlandite	72,00	matrix w/dol	34,03	34,14	32,69	1,47	bdl	bdl	0,00	102,43
KL1-A_pn4	pentlandite	73,00	matrix	34,14	31,87	32,62	2,94	bdl	bdl	0,00	101,72
KL1-A_pn4-2	pentlandite	74,00	matrix	34,37	31,82	32,80	2,71	bdl	bdl	0,00	101,89
KL1-A_pn8	pentlandite	81,00	matrix	34,14	37,29	28,22	0,73	bdl	bdl	0,00	100,54
KL1-A_pn9	pentlandite	82,00	matrix	34,33	31,57	34,16	0,67	bdl	bdl	0,00	100,90
KL1-A_pn10	pentlandite	83,00	matrix	34,41	33,50	32,27	1,28	bdl	bdl	0,00	101,51
KL1-A_pn11	pentlandite	84,00	matrix	34,34	34,56	32,35	1,53	bdl	bdl	0,00	103,01
KL1-A_pn12	pentlandite	85,00	matrix	34,35	35,88	29,94	0,67	bdl	bdl	0,00	101,30
KL1-A_pn13	pentlandite	86,00	matrix	34,66	37,83	28,62	0,70	bdl	bdl	0,00	101,85
KL1-A_pn14	pentlandite	87,00	w/srp/dolomite	34,58	32,88	33,61	0,84	bdl	bdl	0,00	102,08
KL1-A_pn15	pentlandite	88,00	w/srp/dolomite	34,20	34,12	32,57	1,02	bdl	bdl	0,00	102,16
VM10A_pn1	pentlandite	120,00	matrix	34,31	35,92	30,06	0,64	bdl	bdl	0,00	101,02
VM10A_pn2	pentlandite	121,00	matrix	34,08	34,68	32,61	0,67	bdl	bdl	0,00	102,15
VM10A_pn3	pentlandite	122,00	matrix w/dolomite	34,04	31,49	34,61	0,84	bdl	bdl	0,00	101,01
VM10A_pn4	pentlandite	123,00	matrix	34,14	36,37	29,02	0,62	bdl	bdl	0,00	100,26
VM10A_pn5	Ni-pn	124,00	in orthopyroxene	34,08	29,03	37,27	0,41	bdl	bdl	0,00	100,97
VM10A_pn6	pentlandite	125,00	in spl	34,22	30,45	34,10	0,66	bdl	bdl	0,00	99,59
VM10Athick_pn1	pentlandite	140,00	matrix	34,17	39,19	27,51	0,58	bdl	bdl	0,00	101,58
VM10Athick_pn2	pentlandite	141,00	m w/ap	34,17	31,76	35,01	0,61	bdl	bdl	0,00	101,57
VM10Athick_pn2-2	pentlandite	142,00	m w/ap	33,53	31,61	34,28	0,76	bdl	bdl	0,00	100,26
VM10Athick_pn3	pentlandite	143,00	in orthopyroxene	34,02	31,52	34,84	0,83	bdl	bdl	0,00	101,41
VM10Athick_pn4	pentlandite	144,00	included in garnet 2	33,57	31,82	33,92	0,79	bdl	bdl	0,00	100,26
VM10Athick_pn4-2	pentlandite	145,00	included in garnet 2	33,66	31,85	34,51	0,73	bdl	bdl	0,00	100,77
VM10Athick_pn5	pentlandite	146,00	matrix	34,10	33,38	32,91	0,77	bdl	bdl	0,00	101,17
VM10Athick_pn6	pentlandite	147,00	matrix w/chalcopyrite	33,91	35,54	30,73	0,62	bdl	bdl	0,00	100,99
MM1_pn1	pentlandite	161,00	matrix	33,75	30,46	33,29	3,32	bdl	bdl	0,00	100,82
MM1_pn1-2	pentlandite	162,00	matrix	34,11	29,94	33,08	3,39	bdl	bdl	0,00	100,70
MM1_pn2	Co-pn	164,00	matrix	33,73	28,80	31,38	6,26	bdl	bdl	0,00	100,23
MM1_pn2-2	Co-pn	166,00	matrix	34,22	29,09	31,82	6,16	bdl	bdl	0,00	101,38
MM1B_mil1	Co-pn	192,00	in serpentine	34,09	25,74	27,50	12,23	bdl	bdl	0,00	99,69
MM1B_pn1	pentlandite	194,00	matrix	33,71	29,72	31,40	3,96	bdl	bdl	0,00	98,96
MM1B_pn1-2	pentlandite	195,00	matrix	33,71	29,32	31,56	3,80	bdl	bdl	0,00	98,57
UN8_1_s2hh_5	Ni-pn	na	nd	30,68	16,38	48,95	3,42	bdl	bdl	0,12	99,60
UN7_1_s3h_4	pn hetero	na	nd	31,16	19,96	47,53	0,95	bdl	bdl	0,07	99,76

PhD Activities

UN8_1_s6lh_3	pn hetero	na	nd	32,01	25,69	40,25	1,16	bdl	bdl	0,11	99,33
Comment	Sulfide		Textural Position	S	Fe	Ni	Co	Cu	Zn	Pb	Total
UN1_2_s2_7	pyrrhotite		matrix	36,41	62,14	0,10	0,12	bdl	bdl	0,13	98,92
UN1_2_s12kleinoben_3	pyrrhotite		matrix	36,52	62,08	0,11	0,11	bdl	bdl	0,12	98,97
UN1_2_s13_5	pyrrhotite		matrix	36,48	62,30	bdl	0,11	bdl	bdl	0,12	99,04
UN2_2_s10_5	pyrrhotite		matrix	36,44	62,08	bdl	0,11	bdl	bdl	0,14	98,92
UN7_1_s9d_2	pyrrhotite		matrix	36,01	61,32	bdl	0,10	0,91	bdl	0,11	98,49
UN7_1_s9_4	po hetero		matrix	36,00	62,46	bdl	0,10	bdl	bdl	0,11	98,74
Comment	Mineral	No.	Textural Position	S	Fe	Ni	Co	Cu	Zn	Pb	Total
MOL1-C_mil2	millerite	54	matrix	30,64	2,33	68,52	bdl	0,23	bdl	na	101,72
MOL1-C_mil4	heazlewoodite	65	matrix	27,96	1,24	72,60	0,02	0,13	bdl	na	101,99
18LP1_mil1	heazlewoodite	174	in serpentine	29,57	2,72	68,11	0,17	0,07	bdl	na	100,64
18LP1_mil2	heazlewoodite	183	in dol vein (w/pn)	27,45	1,43	71,77	bdl	1,13	bdl	na	101,80
18LP1_mil3	heazlewoodite	186	in dol vein (w/pn)	28,75	2,14	69,77	0,03	bdl	bdl	na	100,69
KL2.4-2b_aw1	heazlewoodite	25	in kelyphite	27,96	1,73	71,05	bdl	bdl	bdl	na	100,99
KL1-A_pn2	heazlewoodite	69	matrix with dolomite	27,69	0,79	70,17	0,09	0,07	bdl	na	98,92
KL1-A_pn2-2	heazlewoodite	70	matrix with dolomite	28,65	0,75	68,92	0,08	bdl	0,06	na	98,62
KL1-A_pn7	heazlewoodite	79	in serpentine	28,35	1,02	71,28	0,29	bdl	0,02	na	101,05
MM1_mil1	millerite	149	in srp + mag vein	36,47	0,86	65,04	0,06	bdl	bdl	na	102,45
MM1_mil1-2	millerite	150	in srp + mag vein	36,14	1,81	64,86	0,02	bdl	0,10	na	103,01
MM1_mil3	millerite	151	in srp + mag vein	35,21	0,48	63,96	0,08	0,11	0,03	na	99,93
MM1_mil4	millerite	152	in srp + mag vein	36,43	1,06	64,36	0,12	0,02	0,02	na	102,03
MM1_mil5	millerite	153	in srp + mag vein	34,53	1,09	63,56	0,29	0,07	bdl	na	99,60
MM1_mil6	millerite	154	in srp + mag vein	35,20	1,31	65,33	0,08	0,04	bdl	na	101,99
MM1_mil6-2	millerite	155	in srp + mag vein	33,86	0,83	67,11	0,02	0,01	bdl	na	101,84
MM1_mil7	millerite	156	in srp + mag vein	36,45	1,71	64,41	0,39	0,24	bdl	na	103,23
MM1_mil8	heazlewoodite	157	in serpentine	27,35	0,58	73,34	0,13	0,05	bdl	na	101,66
MM1_mil9	heazlewoodite	158	in srp + mag vein	27,28	0,40	74,11	0,16	0,09	0,04	na	102,17
MM1_mil11	heazlewoodite	163	in srp	27,51	0,44	73,77	0,02	0,06	0,06	na	101,87
MM1B_mil1-2	heazlewoodite	193	in srp	27,20	1,64	71,61	0,09	0,09	bdl	na	100,69
MM1B_mil2	heazlewoodite	202	in srp/dol	27,24	0,36	71,52	0,10	bdl	bdl	na	99,34
UN7_1_s12_2	heazlewoodite	na		26,92	0,95	70,91	0,24	bdl	bdl	0,11	99,17
UN7_1_s3h_3	heazlewoodite	na		27,34	3,50	69,79	0,11	bdl	bdl	bdl	100,86
UN8_1_s7_3	heazlewoodite	na		27,08	1,49	71,29	0,01	bdl	bdl	bdl	99,93
UN8_1_s8h_3	heazlewoodite	na		26,94	1,74	71,82	0,15	bdl	bdl	bdl	100,82
UN2_2_s7_1	heazlewoodite	na		29,15	11,87	58,02	1,17	bdl	bdl	0,13	100,46
UN3_2_s2h_5	heazlewoodite	na		26,76	1,95	71,69	0,06	bdl	bdl	bdl	100,57
KL2.4-3_cpy1	chalcocite	99	in srp w/pn/sphalerite	21,33	4,56	0,17	0,08	73,62	0,26	na	100,01
VM10Athick_cpy1	chalcocite	148	w/pentlandite	22,15	2,18	0,68	0,01	76,69	0,16	na	101,87
KL2.4-3_cpy2	chalcopyrite	107	in kelyphite	35,36	29,92	0,15	bdl	33,17	bdl	na	98,68
KL2.4-3_cpy2-2	chalcopyrite	108	in kelyphite	35,58	30,04	0,85	0,03	32,76	bdl	na	99,33
UN1_2_s2_6	chalcopyrite	na		35,04	30,56	0,08	0,05	33,32	bdl	0,10	99,16
UN1_2_s13klein_3	chalcopyrite	na		34,82	29,78	0,03	0,06	33,39	bdl	0,12	98,24
KL24-3_cpy2	chalcopyrite	127		34,97	29,41	0,36	0,06	33,45	0,18	na	98,43
KL2.4-2b_sf1	sphalerite	17	in pn10 (in kel)	33,89	6,76	0,24	bdl	0,96	58,25	na	100,14
KL2.4-2b_pn2-repeat	sphalerite	7	sphalerite	34,08	2,95	3,70	0,22	1,11	58,78	na	100,84
KL2.4-3_sf1-2	sphalerite	98	in srp w/pn/ccp	34,46	6,15	0,25	0,02	0,24	59,24	na	100,36
KL2.4-3_sf2	sphalerite	101	in srp	34,48	5,75	0,02	0,02	0,07	59,07	na	99,41
KL24-3 sf1	sphalerite	95	in kelyphite	34,56	6,38	0,41	bdl	0,85	59,70	na	101,90
UN1_2_s5sym_4	alt pn			17,41	33,13	11,23	0,11	15,38	bdl	0,10	77,37
UN8_1_s6rh_2	hz hetero			27,73	2,35	69,62	0,08	bdl	bdl	0,06	99,95
UN14_s2_2	FeCuNi sf			26,42	32,62	17,07	0,34	18,52	bdl	0,11	95,10
UN14_s5_1	FeCuNi sf			26,83	23,78	15,51	0,39	30,76	bdl	0,11	97,39

Ni-pn–Ni-rich pentlandite; **Co-pn**–Co-rich pentlandite; **PI**–polycrystalline inclusions; **hz**–heazlewoodite; **na**–not analyzed; **bdl**–below detection limit

Table C4: Trace element compositions (in ppm) of sulfides from the Ulten Zone peridotites

Comment	Sulfide	Texture	Type	Au	Co	Cu	Zn	As	Se	Ag	Sb	Te	Pb	Bi
Median CGA				1,11	3669,83	2146,35	5,07	401,30	107,83	8,02	0,21	24,04	30,14	0,39
1s				1,15	5966,22	3059,66	4,44	259,24	41,51	3,38	0,38	25,18	124,55	0,56
UN3.2 S	pn	n.a.	FGA	0,26	3166,38	3570,56	0,61	445,43	64,01	5,80	0,48	14,31	2,01	0,31
UN3.2 S1	pn	n.a.	FGA	0,15	6077,24	12200,01	2,41	514,17	74,63	42,61	0,46	12,03	102,25	0,33
UN6.2 S7	pn	n.a.	FGA	bdl	6345,08	32,85	0,88	495,13	117,66	2,62	1,85	33,68	2,56	0,25
UN7 S1	pn	n.a.	FGA	0,06	5040,26	764,29	28,12	385,50	84,55	1,46	1,09	12,95	46,00	0,36
UN7 S10	pn	n.a.	FGA	bdl	10584,53	1655,93	185,44	370,38	99,58	2,71	0,74	27,30	62,84	0,22
UN7 S11	pn	n.a.	FGA	bdl	9471,06	14,28	1,90	342,77	72,62	0,18	1,61	4,16	4,33	0,56
UN7 S3	pn	n.a.	FGA	0,45	6507,86	31,04	1,08	604,48	63,02	1,26	1,96	11,89	21,78	1,89
UN7 S4	pn	n.a.	FGA	bdl	3480,73	581,76	535,73	182,55	58,48	2,12	0,18	9,98	13,90	0,99
UN7 S7	pn	n.a.	FGA	1,59	4958,43	254,52	112,20	422,91	80,29	6,98	1,03	12,13	31,58	0,41
UN7 S8	pn	n.a.	FGA	bdl	6297,09	598,75	2,50	417,30	89,79	1,20	1,22	12,37	586,12	0,65
UN9 S1	pn	n.a.	FGA	1,37	3290,38	530,29	50,39	195,09	91,48	0,32	0,28	13,27	3,38	5,93
UN9 S10a	pn	n.a.	FGA	0,18	3551,63	111,30	1,54	810,71	114,41	0,11	0,16	31,75	1,02	0,29
UN9 S10b	pn	n.a.	FGA	0,81	4323,54	1935,81	7,26	432,81	118,57	1,91	0,51	20,78	73,80	13,60
UN9 S2	pn	n.a.	FGA	bdl	2245,59	1590,95	10,16	29,20	86,75	0,57	0,38	1,01	12,43	6,34
UN9 S4	pn	n.a.	FGA	bdl	3746,49	993,07	47,02	883,43	145,27	0,70	0,13	42,84	23,69	1,78
UN9 S5	pn	n.a.	FGA	bdl	3285,02	1741,43	34,78	421,11	103,68	10,16	0,55	17,75	69,23	8,77
UN9 S6	pn	n.a.	FGA	na	4451,31	389,62	2,61	580,79	116,67	0,09	1,43	13,54	2,70	1,43
UN9 S7	pn	n.a.	FGA	18,38	3749,89	159,26	0,92	781,65	150,46	0,49	0,17	38,79	4,99	0,46
UN9 S8	pn	n.a.	FGA	bdl	5591,07	42,71	1,76	921,28	147,35	0,25	0,81	57,60	8,78	0,75
UN14 S3	pn	n.a.	FGA	0,12	3170,29	4726,10	1,52	4,85	58,25	0,60	bdl	0,96	25,99	0,39
UN14 S4	pn	n.a.	FGA	0,57	3145,23	1096,04	1,45	1,45	57,23	0,40	0,03	0,32	39,81	5,01
UN14 S5	pn	n.a.	FGA	0,16	3596,41	9657,10	280,85	74,48	78,08	2,37	0,05	10,31	24,95	4,83
UN14 S7	pn	n.a.	FGA	bdl	3603,12	4386,47	49,03	145,41	107,09	1,01	bdl	30,48	15,44	4,39
1s				4,04	2068,45	6527,88	119,49	231,42	25,11	11,17	1,40	12,13	304,08	3,79
UN8 S1	pn	n.a.	FSA	bdl	3906,17	19532,67	20,12	268,52	81,97	0,76	0,39	28,57	11,07	14,48
UN8 S3	pn	n.a.	FSA	bdl	8799,74	2,09	1,37	910,95	61,78	0,08	20,40	12,61	4,46	3,96
UN8 S5	pn	n.a.	FSA	bdl	6234,53	6,40	0,96	1074,72	58,78	bdl	7,45	8,76	0,60	1,13
UN8 S6	pn	n.a.	FSA	0,06	6840,12	2,40	1,43	935,58	57,52	0,12	9,25	11,78	2,31	2,15
UN8 S7	pn	n.a.	FSA	0,24	9323,00	9,94	4,89	279,97	77,85	0,21	40,10	22,67	20,22	6,53
UN16 S1	pn	n.a.	FSA	<0.109	3835,06	3,49	<0.76	741,87	65,91	<0.031	2,14	10,77	1,97	0,16
UN16 S10	pn	n.a.	FSA	<0.17	4192,53	9,97	1,71	745,89	60,12	0,06	0,81	9,13	1,07	0,85
UN16 S11	pn	n.a.	FSA	0,14	3680,55	9,18	1,88	875,69	72,69	bdl	0,60	14,03	3,08	0,63
UN16 S3	pn	n.a.	FSA	bdl	3489,13	174,45	1,79	582,04	61,36	0,68	1,00	8,51	4,79	3,63
UN16 S4	mil	n.a.	FSA	bdl	5126,36	1967,16	1,90	1213,33	84,84	0,79	14,75	10,59	39,52	2,31
UN16 S6	pn	n.a.	FSA	0,17	3751,74	12,13	1,38	846,17	61,96	0,32	1,73	13,43	3,59	2,63
UN16-S9	pn	n.a.	FSA	bdl	3928,93	39,23	1,38	872,92	68,13	0,29	1,19	12,32	4,45	1,74
Min				0,06	3489,13	2,09	0,96	268,52	57,52	0,06	0,39	8,51	0,60	0,16
Max				0,24	9323,00	19532,67	20,12	1213,33	84,84	0,79	40,10	28,57	39,52	14,48
Median FSA				0,15	4060,73	9,96	1,71	859,55	63,94	0,29	1,94	12,05	4,02	2,23
1s				0,07	2071,06	5607,92	5,60	284,70	9,43	0,30	11,92	6,02	11,29	3,92
ULT3bpn1	pn	in px layer	CS	na	5205,76	<DL	2,26	603,09	65,53	0,05	3,20	13,68	1,54	0,55
ULT3cpn	pn	matrix	CS	na	8143,04	<DL	2,48	651,93	60,24	0,03	6,32	16,23	0,86	1,25
ULT3cmi	mil	matrix	CS	na	3488,09	5,82	bdl	584,37	66,50	1,11	5,84	11,73	18,15	1,24
ULT4bpn1	pn	matrix	CG	na	5478,77	228,88	6,58	783,74	105,74	0,16	7,35	22,61	1,54	0,76
ULT5apn1	pn	matrix	CS	na	5282,70	2,94	3,33	609,28	56,54	bdl	2,54	15,38	1,47	0,41
ULT5cpn2	pn	matrix	FGA	na	5099,17	6,69	10,72	303,84	84,19	0,27	5,13	13,70	3,48	1,04
ULT6pn1	pn	matrix	FGA	na	5158,69	5,59	bdl	957,29	93,38	<DL	1,26	24,27	0,47	0,73
ULT7dpn1	pn	matrix	FGA	na	4655,07	492,16	1,67	743,46	101,09	0,14	4,56	19,08	3,77	0,69
ULT8pn1	pn	matrix	FGA	na	4480,49	8,03	2,70	711,76	70,81	bdl	1,33	11,76	2,48	0,36
ULT8pn3	pn	matrix	FGA	na	4745,99	52,67	1,34	623,38	89,66	0,15	1,91	17,80	1,68	0,28
ULT2pn1	pn	matrix	FGA	na	7837,58	120,88	32,65	643,12	101,91	0,12	2,68	19,76	1,15	0,19
ULT5cpn2	pn	matrix	CGn	na	4472,05	1680,18	12,06	775,95	112,77	0,30	7,70	24,87	6,33	6,30
ULT1apn1	pn	matrix	CGn	na	8057,55	1664,22	71,62	539,93	12,00	4,18	0,15	5,77	39,74	1,16
ULT1apn2	pn	matrix	CGn	na	16160,45	9,18	21,44	432,90	12,31	0,23	1,69	9,47	19,52	1,30

PhD Activities

ULT1bpn1	pn	matrix	CGn	na	11599,77	79,40	21,64	446,66	106,94	0,28	0,40	15,03	44,85	0,63	
Min - CGn					4472,05	9,18	12,06	432,90	12,00	0,23	0,15	5,77	6,33	0,63	
Max - CGn					16160,45	1680,18	71,62	775,95	112,77	4,18	7,70	24,87	44,85	6,30	
Median - CGn					9828,66	871,81	21,54	493,30	59,63	0,29	1,04	12,25	29,63	1,23	
ULT2pn2	pn	in kel	FGA	na	5927,25	2549,60	1,34	155,86	92,32	0,58	1,54	16,51	9,22	0,26	
ULT7apn1	pn	w/do vein	CG	na	5773,44	2269,82	<3.96	877,81	98,84	0,37	12,62	21,27	8,63	1,37	
ULT7bpn1	pn	w/do vein	CG	na	6246,63	4253,15	4,26	852,82	92,30	9,08	5,02	16,48	8,51	0,98	
ULT3aPn1	pn	in srp	CS	na	8130,66	<DL	5,05	943,59	39,86	<DL	14,59	8,50	3,72	2,16	
ULT4apn1	pn	in srp	CS	na	6841,68	77,96	bdl	558,46	35,11	0,04	15,06	5,33	16,55	2,58	
ULT4apn3	pn	in srp	CS	na	5883,26	342,54	25,86	886,14	45,51	<0.083	13,26	7,31	19,59	2,62	
ULT4apn4	pn	in srp	CS	na	9863,12	476,41	bdl	605,59	37,03	0,09	17,22	5,13	13,10	1,62	
Min - srp					5883,26	77,96	5,05	558,46	35,11	0,04	13,26	5,13	3,72	1,62	
Max - srp					9863,12	476,41	25,86	943,59	45,51	0,09	17,22	8,50	19,59	2,62	
ULT4apn2	pn / Si	in srp	CS	na	6370,97	32,88	53,14	1248,39	49,21	0,11	22,65	9,59	5,10	2,51	
ULT4cpn1	pn / Si	matrix	FGA	na	4701,11	198,73	7,36	645,13	92,95	0,13	1,54	12,07	29,44	0,60	
ULT5cpn1	pn / Si	matrix	FGA	na	7338,60	530,23	33,04	865,50	81,12	0,25	4,10	15,31	7,92	1,25	
ULT8pn2	pn / Si	matrix	FGA	na	4329,46	151,81	6,66	568,22	78,58	<DL	1,20	13,85	4,37	0,71	
ULT1cpn1	pn / Si	matrix	CGn	na	13672,57	41,28	39,97	475,28	119,23	0,19	1,30	17,65	28,58	1,09	
ULT5bpn	pn	Pl in spl	FGA	na	7276,15	63,91	18,77	842,21	20,28	0,12	7,06	6,88	3,17	0,90	
P10B2pn1	pn	matrix	FGA(P10B)	bdl	5196,84	25,35	<DL	482,01	86,85	0,08	0,21	15,12	1,30	0,17	
P10B2pn2	pn	matrix	FGA(P10B)	bdl	5236,91	233,40	1,43	449,84	83,79	1,13	0,28	17,35	4,68	0,52	
P10Bpn3	pn	matrix	FGA(P10B)	0,08	5272,14	14,43	1,73	242,00	79,28	0,07	0,18	15,30	1,58	0,04	
P10Bpn4	pn	matrix	FGA(P10B)	0,03	4474,32	5,89	1,66	529,93	78,51	0,06	0,07	14,31	5,21	0,32	
P10Bpn5	pn	matrix	FGA(P10B)	0,03	5542,07	36,24	0,87	462,23	79,51	0,21	0,15	11,42	6,50	0,74	
Min					0,03	4474,32	5,89	0,87	242,00	78,51	0,06	0,07	11,42	1,30	0,04
Max					0,08	5542,07	233,40	1,73	529,93	86,85	1,13	0,28	17,35	6,50	0,74
Median pn					0,03	5236,91	25,35	1,55	462,23	79,51	0,08	0,18	15,12	4,68	0,32
1s					0,03	398,36	95,90	0,39	111,15	3,59	0,46	0,08	2,15	2,30	0,28
P10Bpo1	po	Pl in grt	FGA	0,01	48,87	116,61	2,29	30,48	2,19	0,21	0,82	1,27	2,71	0,23	
P10Bpo3	po	Pl in grt	FGA	bdl	13,10	569,10	0,96	0,62	12,88	0,12	0,06	0,27	5,67	0,74	
P10B4po1	po	Pl in grt	FGA	<0.039	138,44	22,11	7,41	0,44	23,75	0,70	0,17	<DL	22,57	1,15	
P10B4po2	po	Pl in grt	FGA	bdl	17,89	317,58	2,02	1,33	10,66	0,08	0,07	0,48	1,71	0,15	
Min					0,01	13,10	22,11	0,96	0,44	2,19	0,08	0,06	0,27	1,71	0,15
Max					0,01	138,44	569,10	7,41	30,48	23,75	0,70	0,82	1,27	22,57	1,15
Median po					0,01	33,38	217,09	2,15	0,97	11,77	0,17	0,12	0,48	4,19	0,49
1s					58,11	242,18	2,88	14,85	8,88	0,29	0,37	0,53	9,75	0,47	
UN14 S3	pn	n.a.	FGA	0,12	3170,29	4726,10	1,52	4,85	58,25	0,60	<DL	0,96	25,99	0,39	
UN14 S4	pn	n.a.	FGA	0,57	3145,23	1096,04	1,45	1,45	57,23	0,40	0,03	0,32	39,81	5,01	
UN14 S5	pn	n.a.	FGA	0,16	3596,41	9657,10	280,85	74,48	78,08	2,37	0,05	10,31	24,95	4,83	
UN14 S7	pn	n.a.	FGA	bdl	3603,12	4386,47	49,03	145,41	107,09	1,01	<DL	30,48	15,44	4,39	
Median pristine					0,16	3383,35	4556,29	25,28	39,67	68,17	0,81	0,04	5,63	25,47	4,61
1s					0,25	255,41	3529,70	133,65	68,13	23,35	0,89	0,01	14,07	10,04	2,19
UN14 S13alt	pn alt	n.a.	FGA	bdl	4100,81	19949,90	745,10	0,98	61,29	2,86	0,04	0,37	37,10	3,04	
UN14 S6alt	pn alt	n.a.	FGA	bdl	4100,52	3994,06	26,51	8,26	71,44	1,81	0,06	1,17	3,69	3,47	
UN14 S9alt	pn alt	n.a.	FGA	bdl	3297,20	2512,44	241,08	27,34	63,85	0,55	<DL	5,72	19,67	0,41	
Median alt					4100,52	3994,06	241,08	8,26	63,85	1,81	0,05	1,17	19,67	3,04	
1s					463,88	9668,24	368,88	13,61	5,28	1,16	0,02	2,89	16,71	1,66	

Pn—pentlandite; **Po**—pyrrhotite; **Mi**—millerite; **CS**—Coarse-grained spinel peridotite, **CGn**—Carbonate-free coarse-grained garnet peridotite, **CG**—Coarse-grained garnet/spinel with coronitic garnet peridotite, **P-FGA**—Porphyroclastic fine-grained garnet amphibole peridotite, **FGA**—Porphyroclastic fine-grained garnet amphibole peridotite, **FSA**—Fine-grained spinel (chlorite-amphibole) peridotite; na—not analyzed; bdl—below detection limit

Table C5. Rb-Sr isotope compositions (laser ablation multi-collector ICPMS) for clinopyroxene and amphibole in peridotites from the Ulten Zone

Sample (n)	Sr (ppm)	⁸⁷ Rb/ ⁸⁶ Sr	2SE	⁸⁷ Sr/ ⁸⁶ Sr	2SE	1s	⁸⁷ Sr/ ⁸⁶ Sr at 330 Ma	⁸⁷ Sr/ ⁸⁶ Sr _N
MIR-A	3036	0,002997	0,000015	0,703146	0,000020			
MIR-A	3059	0,003026	0,000014	0,703167	0,000026			0,703082
MIR-A	3036	0,002997	0,000015	0,703132	0,000020			0,703062
MIR-A	3063	0,003241	0,000020	0,703168	0,000024			0,703084
MIR-A	2975	0,003014	0,000026	0,703165	0,000022			0,703094
MIR-A	2975	0,003014	0,000026	0,703179	0,000022			

PhD Activities

			Plag Mir1 (6)	3024	0,003048	0,000020	0,703159	0,000022	0,000017			
			Rankenburg 2002 PhD				0,703096		0,000050			
			BCR-2G	344	0,496769	0,003671	0,705051	0,000064				0,704987
			BCR-2G	344	0,496769	0,003671	0,705036	0,000064				0,704966
			BCR-2G	330	0,545119	0,005709	0,704953	0,000055				0,704885
			BCR-2G	341	0,496373	0,001701	0,705032	0,000065				0,704962
			BCR-2G	336	0,564238	0,006129	0,704990	0,000072				0,704920
			BCR-2G	334	0,515375	0,003190	0,705000	0,000084				0,704915
			BCR-2G	341	0,496373	0,001701	0,705046	0,000065				0,704983
			BCR-2G (7)	339	0,515859	0,003682	0,705016	0,000067	0,000036			0,704945
			GeoREM preferred				0,705003		0,000004			
			BHVO-2G	398	0,082471	0,000464	0,703609	0,000037				0,703546
			BHVO-2G	398	0,082471	0,000464	0,703595	0,000037				0,703525
			BHVO-2G	408	0,086049	0,000871	0,703584	0,000049				0,703499
			BHVO-2G	401	0,091276	0,000799	0,703576	0,000039				0,703492
			BHVO-2G	407	0,092649	0,001061	0,703603	0,000040				0,703509
			BHVO-2G	363	0,082172	0,000275	0,703631	0,000056				0,703560
			BHVO-2G	363	0,082172	0,000275	0,703645	0,000056				0,703581
			BHVO-2G (7)	391	0,085609	0,000601	0,703606	0,000045	0,000025			0,703530
			GeoREM preferred				0,703469		0,000007			
Locality	Rock Type	Mineral	Samples	Sr (ppm)	87Rb/86Sr	2SE	87Sr/86Sr	2SE	1s	87Sr/86Sr at 330 Ma	87Sr/86Sr _N	
			P10Bcpx1	122	0,005545	0,004407	0,705217	0,000099			0,705154	
			P10B2cpx2	146	0,005299	0,001473	0,705332	0,000112			0,705269	
			P10B2cpx3	135	0,010735	0,004440	0,705400	0,000081			0,705336	
Hochwart	P-FGA	clinopyroxene	P10B (3)	135	0,007193	0,003440	0,705316	0,000097	0,000092	0,705283	0,705253	
			Kl24-2bcpx4	103	0,027171	0,007071	0,705164	0,000083			0,705100	
			Kl24-2bcpx5	95	0,010962	0,000758	0,705701	0,000153			0,705638	
			Kl24-2bcpx6	80	0,002780	0,001553	0,705222	0,000167			0,705159	
			Kl24-2bcpx7	121	0,000487	0,000154	0,705304	0,000075			0,705240	
KlapfbergAlm	P-FGA	clinopyroxene	Kl24-2b (4)	100	0,010350	0,002384	0,705348	0,000120	0,000242	0,705299	0,705284	
			VM10Acp8	163	0,000597	0,000041	0,705490	0,000047			0,705426	
			VM10Acp8	169	0,000362	0,000084	0,705336	0,000035			0,705273	
			VM10Acp8	169	0,001521	0,000565	0,705425	0,000043			0,705361	
			VM10Acp8	142	0,000083	0,000009	0,705385	0,000047			0,705322	
			VM10Acp8	136	0,000186	0,000032	0,705426	0,000093			0,705362	
			VM10Acp9	180	0,000119	0,000021	0,705358	0,000073			0,705295	
			VM10Acp9	142	0,000378	0,000055	0,705373	0,000113			0,705309	
			VM10Acp9	149	0,000055	0,000018	0,705392	0,000087			0,705329	
Hochwart	FGA	clinopyroxene	VM10A (8)	156	0,000413	0,000103	0,705398	0,000067	0,000048	0,705396	0,705335	
			UN1-1-1	95	0,054340	0,000321	0,704963	0,000112			0,704878	
			UN1-1-1	89	0,065990	0,002584	0,705731	0,000216			0,705646	
			UN1-1-2	123	0,104620	0,000468	0,705244	0,000108			0,705159	
			UN1-1-3	93	0,069856	0,001004	0,705814	0,000155			0,705729	
Samerberg	CG	clinopyroxene	UN1 cpx (4)	100	0,073702	0,001095	0,705438	0,000148	0,000404	0,705092	0,705353	
			UN2-1-1	4	0,022760	0,001215	0,706194	0,001939			0,706109	
			UN2-1-1	4	0,029662	0,000899	0,705527	0,002080			0,705442	
			UN2-1-1	4	0,026224	0,001948	0,705045	0,002689			0,704960	
			UN2-1-2	4	0,005406	0,002745	0,705736	0,002101			0,705651	
			UN2-1-2	5	0,024502	0,008382	0,704280	0,001743			0,704195	
			UN2-1-3	10	0,028381	0,000585	0,706149	0,001175			0,706065	
Samerberg	CG	clinopyroxene	UN2 cpx (6)	5	0,022822	0,002629	0,705488	0,001954	0,000729	0,705381	0,705425	
			UN3-1-1	316	0,101821	0,000617	0,705645	0,000050			0,705561	
			UN3-1-1	335	0,124094	0,000604	0,705719	0,000063			0,705634	
			UN3-1-2	319	0,131133	0,002693	0,705601	0,000057			0,705517	
			UN3-1-3	275	0,124878	0,000722	0,705755	0,000051			0,705670	
			UN3-1-3	333	0,091070	0,000399	0,705741	0,000044			0,705657	
Samerberg	P-FGA	amphibole	UN3 amp (5)	316	0,114599	0,001007	0,705692	0,000053	0,000066	0,705154	0,705629	
			UN6-1-1	234	0,127281	0,004137	0,705065	0,000115			0,704981	
			UN6-1-2	289	0,096108	0,002047	0,705386	0,000066			0,705302	
			UN6-1-2	344	0,117800	0,001373	0,705410	0,000041			0,705325	
			UN6-1-3	286	0,067879	0,000491	0,705380	0,000055			0,705296	
			UN6-1-3	303	0,108333	0,000682	0,705358	0,000058			0,705274	
Samerberg	P-FGA	amphibole	UN6 amp (5)	291	0,103480	0,001746	0,705320	0,000067	0,000144	0,704834	0,705256	
			UN7-1-1	256	0,125652	0,000895	0,705397	0,000071			0,705312	
			UN7-1-1	289	0,111503	0,000336	0,705479	0,000050			0,705394	
			UN7-1-2	276	0,106544	0,000332	0,705409	0,000073			0,705324	
			UN7-1-2	310	0,132060	0,000763	0,705444	0,000061			0,705360	
			UN7-1-3	334	0,132788	0,000540	0,705455	0,000060			0,705371	
Samerberg	P-FGA	amphibole	UN7 amp (5)	293	0,121709	0,000573	0,705437	0,000063	0,000034	0,704865	0,705373	
			UN8-2-1	230	0,090880	0,000956	0,706521	0,000073			0,706436	
			UN8-2-1	243	0,105839	0,000789	0,706638	0,000084			0,706554	
			UN8-2-2	211	0,169391	0,000973	0,706969	0,000078			0,706854	
			UN8-2-2	233	0,155804	0,000381	0,706795	0,000066			0,706703	
			UN8-2-3	247	0,158967	0,000998	0,707008	0,000078			0,706923	
Seefeld	FSA	amphibole	UN8 amp (5)	233	0,136176	0,000819	0,706786	0,000076	0,000209	0,706147	0,706723	
			UN9-1	212	0,129257	0,001178	0,707078	0,000065			0,706965	
			UN9-1	220	0,164715	0,004196	0,707137	0,000071			0,707052	

Seefeld	FGA	amphibole	UN9-2	174	0,142802	0,000865	0,707490	0,000100		0,707383
			UN9-2	174	0,132189	0,001147	0,707465	0,000092		0,707360
			UN9-3	198	0,179744	0,000801	0,707476	0,000049		0,707372
			UN9-3	182	0,181238	0,001888	0,707576	0,000080		0,707457
			UN9 amp (6)	193	0,154991	0,001679	0,707370	0,000076	0,000208	0,706642
Seefeld	FGA	amphibole	UN10-1	253	0,112834	0,000488	0,705921	0,000098		0,705852
			UN10-2	246	0,119407	0,000659	0,705894	0,000085		0,705797
			UN10-2	245	0,122177	0,000348	0,705989	0,000103		0,705923
			UN10-3	254	0,118955	0,000472	0,706084	0,000058		0,706002
			UN10 amp (4)	249	0,118343	0,000492	0,705972	0,000086	0,000084	0,705416
Masa Murada	FGA	amphibole	UN14-1	316	0,146374	0,002332	0,706383	0,000050		0,706311
			UN14-1	321	0,146214	0,000784	0,706272	0,000055		0,706188
			UN14-1	245	0,192303	0,001674	0,707450	0,000066		0,707371
			UN14-2	247	0,139278	0,000969	0,707542	0,000053		0,707435
			UN14-2	247	0,113328	0,001308	0,707443	0,000066		0,707362
			UN14-3	247	0,112386	0,000465	0,707190	0,000069		0,707106
			UN14 amp (6)	271	0,141647	0,001255	0,707047	0,000060	0,000570	0,706381
Masa Murada	FSA	amphibole	UN16-1	180	0,123337	0,001065	0,708019	0,000122		0,707952
			UN16-1	200	0,196641	0,005171	0,708113	0,000180		0,708093
			UN16-3	186	0,111538	0,000774	0,707277	0,000087		0,707160
			UN16-3	205	0,303845	0,002137	0,707787	0,000086		0,707718
			UN16-3	236	0,303213	0,003207	0,707715	0,000064		0,707604
			UN16 amp (6)	201	0,207715	0,002471	0,707782	0,000108	0,000326	0,706806

Sr abundances are estimated from signal size weighted by spot size and energy, by comparison to the known concentration in the MIR1 in-house standard. Standard deviation (1s) is given for multiple analyses. Final ratios are normalized to MIR1, using the measured vs. independently determined $^{87}\text{Sr}/^{86}\text{Sr}$ ratio (Rankenburg, 2002).

Supplementary Table C6 S and Sr concentrations and isotope compositions of various reservoirs relevant to the evolution of the Ulten Zone peridotites: full dataset of Figure 6.11.

Reservoir	[S] (ppm)	$\delta^{34}\text{S}$ (‰)	[Sr] (ppm)	$^{87}\text{Sr}/^{86}\text{Sr}$	Comment
Depleted Mantle	60-119	-1.28	9.8	0.7027	1
Continental crustal melt	600	+3.6 to +10.1	130.9	0.7162	2
Metasediment fluid	3356	-8	255	0.720	3
Metabasalt fluid	3187	-1	48-62	0.7027-0.7030	4
Metaserpentinite fluid	5800	+8	11	0.70567	5
Bulk oceanic crust	30800	-2.5	163	0.70475	6

(1) Range of S concentrations from Alt et al. (2007) and Salters and Stracke (2004); $\delta^{34}\text{S}$ of Labidi et al. (2013); Sr concentration and $^{87}\text{Sr}/^{86}\text{Sr}$ from Salters and Stracke (2004).

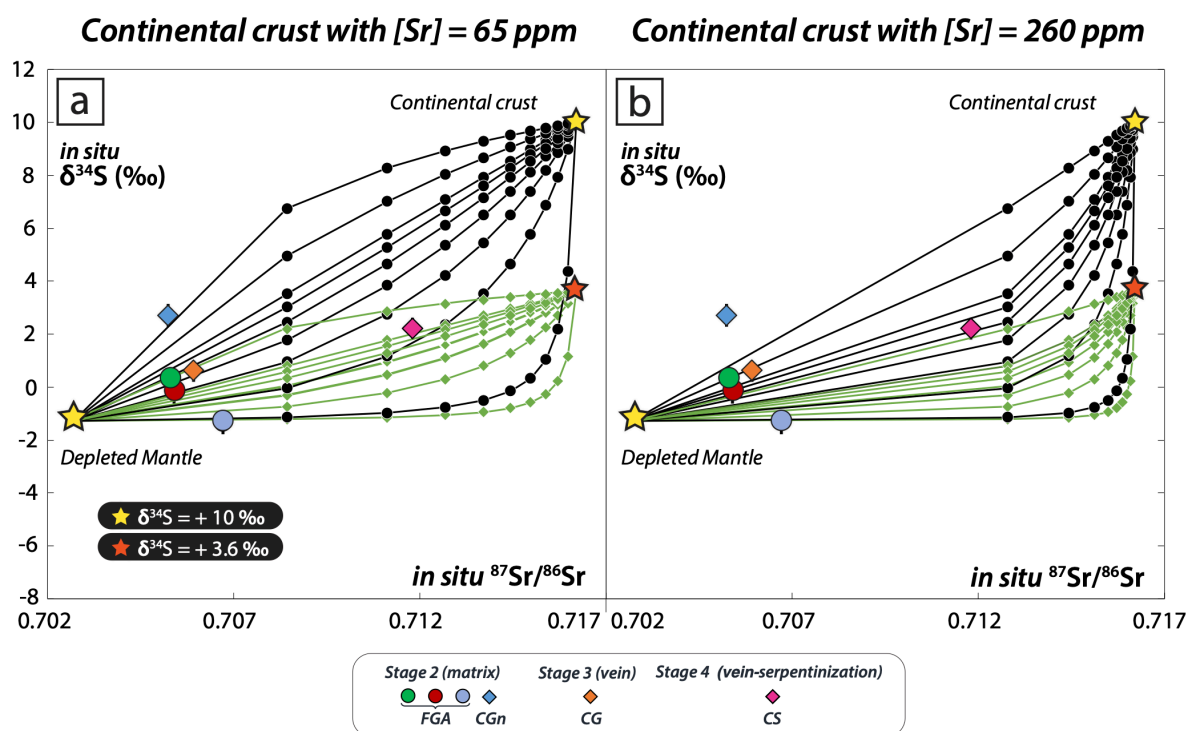
(2) S concentration is the average of the Ulten Zone garnet-kyanite paragneisses reported in Bargossi et al. (2003); $\delta^{34}\text{S}$ based on metapelites from the Italian Alps (Fiorentini et al., 2018); $^{87}\text{Sr}/^{86}\text{Sr}$ and Sr concentrations of UZ gneisses from Tumiaty et al. (2003).

(3) Average S concentrations and $\delta^{34}\text{S}$ values of Li et al. (2020); Sr concentration of fluid calculated from available amphibole/fluid partition coefficient of Sr at mantle conditions ($P=2\text{GPa}$, $T=900^\circ\text{C}$; $D_{\text{amph/fluid}}=0.26$; Fabbri et al. 2013) and average Sr concentration from amphibole (66.3 ppm; this study); $^{87}\text{Sr}/^{86}\text{Sr}$ is that modern continental crust (Peucker-Ehrenbrink and Fiske, 2019)

(4) Average S concentrations of Li et al. (2020); $\delta^{34}\text{S}$ of Li et al. 2020; Sr concentration and $^{87}\text{Sr}/^{86}\text{Sr}$ taken from altered lower dikes of Alt et al. (1996)

(5) S concentrations of serpentinite of Li et al. (2020); $\delta^{34}\text{S}$ of Li et al. (2020); (average) Sr concentration from high-pressure serpentinite mylonite of Scambelluri et al. (2001); (average) $^{87}\text{Sr}/^{86}\text{Sr}$ from HP undeformed serpentinites from Scambelluri and Tonarini (2012)

(6) S concentrations and $\delta^{34}\text{S}$ of Li et al. (2020); average Sr concentration and $^{87}\text{Sr}/^{86}\text{Sr}$ of Staudigel et al. (1995).



In this figure, we explore the effect of the Sr concentration of the continental crustal end-member on the mixing model. Both (a) half (65 ppm) and (b) double (260 ppm) the Sr concentration employed for the mixing model of Figure 6.12 are tested. We observe that, as expected, lower Sr abundance in the continental crust requires a higher percentage of crustal contamination to satisfy the data. Moreover, continental crust with a $\delta^{34}\text{S}$ of +3.6‰ and 65 ppm Sr provides a better fit with the data than crust containing 260 ppm Sr. As a whole, the mixing model suggests that continental crust with $\delta^{34}\text{S}$ of +3.6-10‰ and Sr concentrations of ~60-130 ppm is consistent with the Sr-S isotope relationships of clinopyroxene/amphibole and sulfide, respectively, of the UZ peridotite.

Supplementary annotation C1: The Mann-Whitney U Test

We applied the Mann-Whitney U Test in order to test whether any statistically significant difference occurs between the S isotope signature of pentlandite occurring in fine-grained peridotite and coarse-grained peridotite. $\delta^{34}\text{S}$ values of matrix pentlandite are ranked into two populations, defined as ‘fine-grained peridotite’ and ‘coarse-grained peridotite’. The null hypothesis H_0 is defined as ‘there is no difference between the two populations’. Because the number of analysed grains exceed $n=20$, we introduced the Z values, which is defined as follows:

$$Z = U - ((n1*n2)/2\text{Std dev})$$

The probability value (p) is then obtained with the formula

$$P = (1 - \text{normdist}(\text{abs}(z)))*2$$

We obtained Z values of 5.17916 and p values of < 0.00001 , which is taken as significant. As a result, the null hypothesis H_0 is rejected and we can state that the two populations of pentlandite grains in the fine-grained and coarse-grained peridotite are significantly different.

